WASM: Minerals, Energy and Chemical Engineering

Hydro-geophysics in High-Quality Coastal Aquifers

Alexander Ross Costall

This thesis is presented for the Degree of
Doctor of Philosophy
of
Curtin University

September 2020

Declaration

"To the best of my knowledge and belief this thesis contains no material previously published by any other person except where due acknowledgment has been made. This thesis contains no material which has been accepted for the award of any other degree or diploma in any university."

Signature:

Date:

2nd September 2020

Abstract

High-quality groundwater is stored in coastal aquifers worldwide. Groundwater held in these aquifers supports life on many scales. This includes human populations and natural ecosystems. High levels of shallow groundwater pumping, declining rainfall recharge, or rising sea levels, can all lead to seawater intrusion and contamination of fresh groundwater resources. There is a need to understand and manage groundwater at our coastal margins.

Many of the world's most productive shallow aquifers are composed of karstic limestone. In these karstic aquifers, extreme changes in hydrogeology can occur over small distances. Specific and high-quality measurements are required to characterize coastal aquifer hydraulics. My research spans the measurements and methods used to quantify hydrogeology of high-quality coastal aquifers, with emphasis on application and integration of geophysical technologies.

Electrical resistivity imaging (ERI) is a geophysical technology used to reconstruct the seawater interface and monitor seawater intrusion. An ideal outcome from electrical resistivity imaging ERI at the coastal margins is to resolve the geometry of: (i) the aquifer, (ii) the seawater wedge, and (iii) any confining layers. I examine how closely ERI can come to achieving this ideal outcome. Accurate reconstruction and monitoring of seawater intrusion is necessary for predictive numerical groundwater modelling, which is ultimately used to aid management of coastal aquifers.

A fundamental question addressed in my research is: *"Can ERI define the seawater interface in different coastal hydrogeological settings?"* To answer this question, I provide an analysis of the ERI method using datasets I have acquired at more than 20 sites selected from a 100 km stretch of Perth's coastline. Water level measurements and water chemistry data from nearby wells are compared with geophysical data. Multiple transects include both ERI and ground penetrating radar (GPR) surveys. Findings from numerical and field ERI experiments include:

1. A demonstration of how utilising multiple ERI survey configurations can improve imaging of coastal aquifer architecture, using from both numerical simulation and data from field acquisition.
2. Description of ERI outcomes and inversion artefacts that are characteristic of a range of aquifer architectures common along coastal margins, including analysis of confined and unconfined aquifers systems.
3. A clear example of how ERI has revealed greater levels of seawater intrusion with proximity to densely populated suburbs and high levels of shallow groundwater abstraction.
4. Systematic representations of how regularization parameters and inversion constraints affect the outcomes of ERI modelling.
5. High-quality examples of how ERI, GPR, and downhole logs can be combined to reveal different aspects of coastal architectures at varying scales and resolutions.

From my systematic consideration of ERI, I then move towards methods for quantifying hydraulics and water chemistry at coastal margins. This work is supported by over 30 years of data from an established seawater intrusion monitoring site located in the suburb of Quinns Rocks, Perth, Western Australia. I demonstrate that seawater intrusion has occurred, and that decoupling the influences of declining rainfall, abstraction from a regional water supply, and rising sea levels is not possible with conventional monitoring wells. I also demonstrate how estimating the rate of groundwater flow and the shape of the seawater interface is complicated by anisotropy

and heterogeneity that are common in karstic aquifers. More specifically, I find that increasing of rotation angle of anisotropy of hydraulic conductivity will move the seawater interface toward the ocean for identical rates of groundwater flow. I also compare numerical simulation at the same rate of flow for different geologically plausible random hydraulic conductivity fields. I find that the distribution of hydraulic conductivity proximal to the zone of submarine discharge can strongly impact on the shape and landward extent of the seawater wedge. In short, both anisotropy and heterogeneity strongly influence the landward extent of seawater, independent of the amount of water flowing toward the ocean.

I have developed new software that can translate outcomes from solute transport modelling into an electrical resistivity model that, in turn, is used to generate synthetic ERI survey data. Outcomes from synthetic modelling and field-based ERI data are iteratively compared to refine predictive solute transport models.

Having identified the limitations of conventional ERI and the need to accurately monitor seawater intrusion, I address the question: *"is there a way to significantly improve the accuracy of ERI outcomes along coastal margins?*"

I assess the outcomes from inversion of surface-based and borehole-based ERI data using constraints and a-priori information. From this, I conclude that borehole-based ERI has potential to significantly improve the quality of resistivity imaging along coastal margins. I find that the combination of multiple instrumented boreholes located around the seawater toe, and inversion constraints supplied by these boreholes, can be used to precisely recover the resistivity distribution and geometry of the seawater wedge, and mixing zone. I then provide numerical modelling showing how instrumented boreholes could replace time-lapse wireline logging. Automated monitoring of these instrumented boreholes could potentially replace existing monitoring techniques and generate significant volumes highly valuable data.

The perpetual balance that occurs between the vast quantities of groundwater discharging into the ocean and the landward movement of seawater must impact on the long-term health of any coastal aquifer system. Every day, people and ecosystems on all continents interact with, influence, and rely on these systems. The loss of high-quality coastal groundwater to seawater intrusion is a global concern. I hope the insights and practical conclusions from this research will lead to informed high-quality predictive groundwater modelling that ultimately results in better management of coastal aquifers systems worldwide.

Acknowledgements

To my parents, Paul and Kathy, thank you.

To my supervisor, Brett; my sincere thanks for your patience, encouragement, and support throughout these years. This was only possible through the opportunities and guidance that you gave so willingly.

To my colleagues and friends; my appreciation and gratitude.

This research was supported by an Australian Government Research Training Program (RTP) Scholarship.

List of Publications

"I warrant that I have obtained, where necessary, permission from the copyright owners to use any third-party copyright material reproduced in the thesis (e.g. questionnaires, artwork, unpublished letters), or to use any of my own published work (e.g. journal articles) in which the copyright is held by another party (e.g. publisher, co-author)."

- (See Appendix A.)

Published Refereed Journal Articles

Costall, A., Harris, B., & Pigois, J. P. (2018). Electrical Resistivity Imaging and the Saline Water Interface in High-Quality Coastal Aquifers. *Surveys in Geophysics, 39*(4), 753-816. doi:10.1007/s10712-018-9468-0

Costall, A.R., Harris, B.D., Teo, B. et al. Groundwater Throughflow and Seawater Intrusion in High Quality Coastal Aquifers. Sci Rep 10, 9866 (2020). https://doi.org/10.1038/s41598-020-66516-6

Refereed Expanded abstracts published in conference proceedings

Costall, A.* & B. Harris (2018) *Rapid estimation of shallow groundwater recharge via ground penetrating radar*, AEGC Sydney 2018, doi.org/10.1071/ASEG2018abP091

Costall, A.*, Harris, B., Pethick, A. and R. Schaa (2016) *Electric bipole antenna model study of a basin-scale fault system*, ASEG Adelaide 2016, doi.org/10.1071/ASEG2016ab324

Costall, A.*, Teo, B., & Pethick, A. (2019). *Can you use a coconut to find groundwater?* ASEG Extended Abstracts, 2019(1), 1-3. doi:10.1080/22020586.2019.12073220

Dean, T., **Costall, A**.*, Sik, N., Pethick, A., Howman, D., & Blylevens, J. (2019). *Location of buried artillery positions using near-surface geophysical techniques*. Paper presented at the SEG International Exposition and Annual Meeting, San Antonio, Texas, USA. https://doi.org/

Dean, T., **Costall, A**.*, Nguyen, N., & Howman, D. (2019). *An experimental comparison of different sledgehammers for use in seismic surveys*. In SEG Technical Program Expanded Abstracts 2019 (pp. 2953-2957), doi.org/10.1190/segam2019-3200793.1

Dean, T., **Costall, A**., Sik, N., Blylevens, J., Pethick, A., & Howman, D. (2019). *Dude, Where's My Gun? A near-surface geophysics case-study*. ASEG Extended Abstracts, 2019(1), 1-4. doi:10.1080/22020586.2019.12072912

Dean, T., Nguyen, N., & **Costall, A**. (2018). *A low-cost system and method for acquiring small refraction seismic surveys*. In SEG Technical Program Expanded Abstracts 2018 (pp. 2853-2857): Society of Exploration Geophysicists, doi.org/10.1190/segam2018-2991952.1

Harris, B., **Costall, A**., Nguyen, H., Michael, K., Ricard, L., Freifeld, B., Pethick, A. (2019). *Time lapse in-hole electrical resistivity surveying during a shallow release of CO2 gas: Harvey, Western Australia*. ASEG Extended Abstracts, 2019(1), 1-5. doi:10.1080/22020586.2019.12073174

* Presenting author

Schaa, R., Harris, B., Pethick, **A., Costall**, A., Pigois, J.-P., & Takougang, E. T. (2018). *Magnetotelluric Inversion for Characterisation of Complex Aquifer Systems*. ASEG Extended Abstracts, 2018(1), 1-6. doi: https://doi.org/10.1071/ASEG2018ABW10_2G

Schaa, R., Howman, D., **Costall, A**., Pethick, A., & Harris, B. (2017). *SRD 3.3 Prediction and Verification of Shallow CO2 Migration Electrical Resistivity Survey Run# 2 operations close-out report*. CO2CRC Publication Number RPT17-5643. CO2CRC Ltd: Australia.

Sedaghat, B., Schaa, R., Harris, B., Pethick, **A., Costall**, A., Duan, J., & Jiang, W. (2018). *Magnetotelluric, Basin Structure and Hydrodynamics; South West of Western Australia*. ASEG Extended Abstracts, 2018(1), 1-5. doi: https://doi.org/10.1071/ASEG2018ABP095

Pethick, A**., Costall, A.**, Dean, T., & Blylevens, J. (2018). *Perth's lost guns*. Preview, 2018(196), 38-41. doi:10.1071/PVv2018n196p38

Ziramov, S., Tertyshnikov, K., Pevzner, R., Urosevic, M., Harris, B., **Costall, A**., & Goodwin, J. (2016). *High resolution geophysical baseline surveys of the Otway site*. CO2CRC Publication Number RPT16-5550, CO2CRC Ltd: Melbourne.

Table of Contents

1 Introduction

1.1 Research Motivation

Access to potable groundwater is a perpetual and global issue. Many of the greatest civilizations throughout history were formed around access to high-quality water for irrigation and drinking (Frioux, 2014). In Aboriginal Australian mythos, the tale of Tiddalik serves as an allegory for resource greed and sustainable groundwater management. The demand for accessible high-quality groundwater continues to grow and existing groundwater resources are increasingly strained. As of 2015, an estimated 663 million people across the Earth are without access to potable drinking water (Unicef, 2015).

Examples of groundwater contamination and aquifer degradation are numerous and worldwide. This has dire consequence for the health of people dependent on the local groundwater supplies for drinking and quality-of-life. The Arabian Aquifer System (Saudi Arabia/Yemen) has been identified as the most-threatened aquifer system in the world, followed by the Indus (India/Pakistan) and Murzuk-Djado Basin (Northern Africa) (Odhiambo, 2017; L. Parker, 2016). There are millions, if not billions of people who rely on that water for survival.

Examples of degradation of coastal aquifers can be found for every continent around the world. Much of the coastal regions in Africa are under severe threat from over-development, yet political instability and regional conflicts stymie groundwater management programs and initiatives (Steyl *et al.*, 2010). In China, urban and industrial development has led to significant seawater intrusion across the coastal plains and throughout Laizhou bay (Shi *et al.*, 2014). In North and South America, there are multiple examples of aquifers where seawater has intruded in coastal aquifer, or where ground subsidence has permanently changed the landscape (Barlow *et al.*, 2010; Holzer *et al.*, 1985; Karegar *et al.*, 2016).

The loss of groundwater has consequences for food production and agriculture worldwide. Almost half of the worlds food supply is sourced from countries where the aquifer systems are critically threatened (Dalin *et al.*, 2017; Katz, 2016). Closer to the coast, seawater flooding contaminates groundwater used for the food production (Hoggart *et al.*, 2014; Talbot *et al.*, 2018), with examples in Vietnam (Wassmann *et al.*, 2004), Bangladesh (Alam *et al.*, 2017; World Bank, 2015), and Africa (Eswaran *et al.*, 1997). There is little doubt that groundwater and potable water supplies require immediate and sustainable action to prevent widespread loss of this resource.

1.2 Groundwater in Australia

Australia is the driest populated continent in the world (Government of Australia, 2016). Yet Australian groundwater withdrawals, per-person, are among the highest in all Organisation for Economic Cooperation and Development (OECD) countries at 696.9 m^3/capita (OECD, 2018). Rainfall patterns across Australia have changed significantly over the last 50 years, with dire consequence for the groundwater systems that depend on shallow groundwater resources (Delworth *et al.*, 2014; Harrington *et al.*, 2014; I. Smith, 2004). Sustainable management of groundwater resources is imperative to the agricultural, industrial, urban, rural, and environmental viability of Australia (Geoscience Australia, 2020).

A key management strategy for any groundwater-dependent nations is reducing the direct reliance on groundwater resources. Renewable water sources accounted for only 6% of all groundwater resource in Australia in 2006. Recent government and corporate initiatives, including greater focus on aquifer definition exploration (e.g. (Department of Regional Development WA, 2008; Department of Water WA, 2012b)), ecologically responsible groundwater usage (e.g. (Department of Water, Western Australia,. 2016; Department of Water WA, 2012a)), and renewable groundwater resources (e.g. (Water Corporation, 2016a, 2016b, 2018, 2019)) has increased the percentage of renewably sourced water in Australia to 16.74% (OECD, 2018).

Perth, the capital city of Western Australia, yields approximately 46% of its consumable water from groundwater reserves (Water Corporation, 2017). Alternative groundwater supply options, such as managed aquifer recharge (MAR) programs using treated wastewater, are already utilised in the Perth region and offset the reliance on groundwater (Water Corporation, 2019). The MAR program currently recharges the Leederville and Yarragadee aquifers with 14 GL/year of clean recycled water per-year, reducing the risk of aquifer subsidence and replenishing the groundwater resource. The MAR program is expected to increase to 28 GL/year over the next few years (EPA, 2018; Water Corporation, 2019).

Desalination plants can further supplement potable water resources. Several are operational in Perth. The desalination plant in Kwinana (Water Corporation, 2016a) began production in 2006, and supplies approximately 45 GL/year, or 18% of Perth's drinking water. An additional plant in Binningup, south of Perth (Water Corporation, 2016b), completed in 2014, provides another 100 GL/year. The total supply of Perth's water from desalination plants is estimated to be 47 % (Water Corporation, 2016a).

Changes to the groundwater system has the potential to affect more than just the people that depend on it. Groundwater dependent ecosystems (GDE) require access to groundwater on a permanent or intermittent basis to maintain local ecological processes and ecosystems (Richardson *et al.*, 2011). Groundwater is especially important to ecosystems in arid and semi-arid climates where recharge is scarce (Eamus *et al.*, 2006). Significant groundwater abstraction from shallow coastal aquifers can remove groundwater from these GDE's and also affect the quality of the groundwater, causing damage or even collapse of the local ecosystem (C. Nevill *et al.*, 2010; Groom *et al.*, 2000).

There are also economic impacts to consider. Australia's coastal ecosystems are estimated to be worth over $220 M USD (M. L. Martinez *et al.*, 2007). Worldwide, coastal ecosystems contribute 77% of global ecosystem services, such as food production, water supply, waste treatment, and more (Costanza *et al.*, 1997;

G. C. Daily, 1997). Damage to these ecosystems may have long-lasting impacts on a country's economic growth, with more severe consequence for countries that depend on these markets for survival.

Shallow groundwater systems at the coast are faced with an additional challenge compared to aquifers further inland in that they must also content with the ocean. The higher salt content of seawater can rapidly degrade drinking water reserves and damage groundwater dependent ecosystems (Reed *et al.*, 2013; W.H.O., 2011). As groundwater is removed from the shallow aquifer, the seawater is able to intrude further inland and contaminate greater volumes of groundwater (Bear, 2005).

Near-shore marine ecosystems are also affected by shallow groundwater abstraction. Submarine groundwater discharge from terrestrial-based groundwater maintains a ratio of nutrients, such as nitrogen and phosphorous, to this ecosystem (Moore, 2006). Changes to this ratio can promote algal blooms, with significant consequences for local sea life (Slomp *et al.*, 2004).

The groundwater chemistry at coastal margins typically varies according to changes in groundwater recharge. This can be relatively slow. For example, the electrical conductivity (EC) of groundwater in a monitoring well near Quinns Rocks (SIM 3-90) took almost 5 years to become saline (Kretschmer *et al.*, 2012). However, the EC measurements only present one piece of the puzzle. In karstic environments, there are extreme changes in hydrogeology that can occur over short distances. A consequence of these changes is that the seasonal variation in the water table may be very small and requires precise and frequent measurement to characterise the aquifer.

Conventional groundwater monitoring is limited by the cost of establishment and ongoing monitoring costs. A report by Sinclair Knight Merz (2012) suggest that approximately 26% of groundwater budgets are spent on water monitoring and evaluation. Automation of monitoring technologies has already been identified, and to a limited degree enacted, as a potential cost-saving and data-quality-improving method (Kern *et al.*, 2009; Sinclair Knight Merz, 2012). As of January 2020, the Water Information Reporting database reports that 59 of 407 wells (~14.5%), sampled within the last 12 months, of wells in the Perth groundwater area have time-series data, suggesting some degree of automation (Water Information Reporting database, 2019).

There is a need to understand the relationship between saline water and groundwater at coastal margins. This can only be achieved through a multidisciplinary focus using new monitoring solutions. Establishing an affordable monitoring solution for populations around the world is critical for future groundwater management problems. Australia has the means, opportunity, and reason to revitalise the status quo, and becoming a world-leader in groundwater monitoring technology.

1.3 Hydrogeology of Perth

The city of Perth, Western Australia, is the focal point of this thesis. All the datasets shown are collected from the coastal margins, within 100 km of the Swan River. The extremely high permeability Tamala Limestone results in interesting and unusual flow characteristics, while the various properties of the confining units (e.g., clay conductivity and provenance) offer unique geophysical challenges.

Perth's groundwater supply is primarily from three basin-scale aquifers (Davidson, 1995; Lasky, 1993). Figure 1.1 shows the distribution of shallow aquifer systems local to Perth. The Swan River divides the shallow superficial aquifer into the Gnangara Mound, north of the Swan River, and the Jandakot Mound, to the south. The major aquifer systems in the Perth Basin include the Superficial, Leederville, and Yarragadee. Several smaller and localized reservoirs also exist (e.g. the Mirrabooka, Kings Park, and Rockingham aquifers) but are not significant. The three major aquifers are introduced below.

The superficial aquifer extends throughout the Swan coastal plain (see sect 1.3.1). The composition of the aquifer changes from predominately clayey sediments near the Darling Scarp, to sands and sandy limestone nearer the coastline. The Gnangara Mound, to the north of the Swan River, and the Jandakot Mound, to the south, dominate the water table configuration (Davidson, 1995; Salam, 2007). Declining rainfall recharge and over-use have led to a decline in water table levels of the superficial aquifer, leading to water acidification and contamination of groundwater in some areas (S. Appleyard, 1995; S. J. Appleyard *et al.*, 2006). Groundwater abstraction, including public water entitlements and private licensed and unlicensed usage, is approximately 180 GL/year (Department of Water, Western Australia,, 2011).

The Leederville confined aquifer comprises of alternating clay/shale and sandy sediments from the Cretaceous era (Davidson, 1995; Leyland, 2012). It is present throughout the entire Swan coastal plain, with the exception of the Swan Estuary where the Kings Park formation exists instead (CSIRO, 2009). Natural groundwater recharge into the Leederville aquifer occurs where the erosion of the upper confining unit results in direct contact with the superficial formations. This occurs towards the northern areas of the Gnangara Mound. Groundwater abstraction is approximately 45 GL/year (Department of Water, Western Australia,, 2011).

The Yarragadee aquifer is a deep and extensive multi-layer confined aquifer, comprising of tilted late Jurassic era alternating sand and silty sediments that extend to the north and south of the Perth basin. Downwards leakage from the Leederville and Superficial aquifers recharge the aquifer where the upper-confining unit is absent (Davidson, 1995; Leyland, 2012). A 'recharge window' exists towards the north of the basin where direct connectivity to the superficial aquifer exists (Meredith *et al.*, 2012). Groundwater abstraction is approximately 46 GL/year (Department of Water, Western Australia,, 2011).

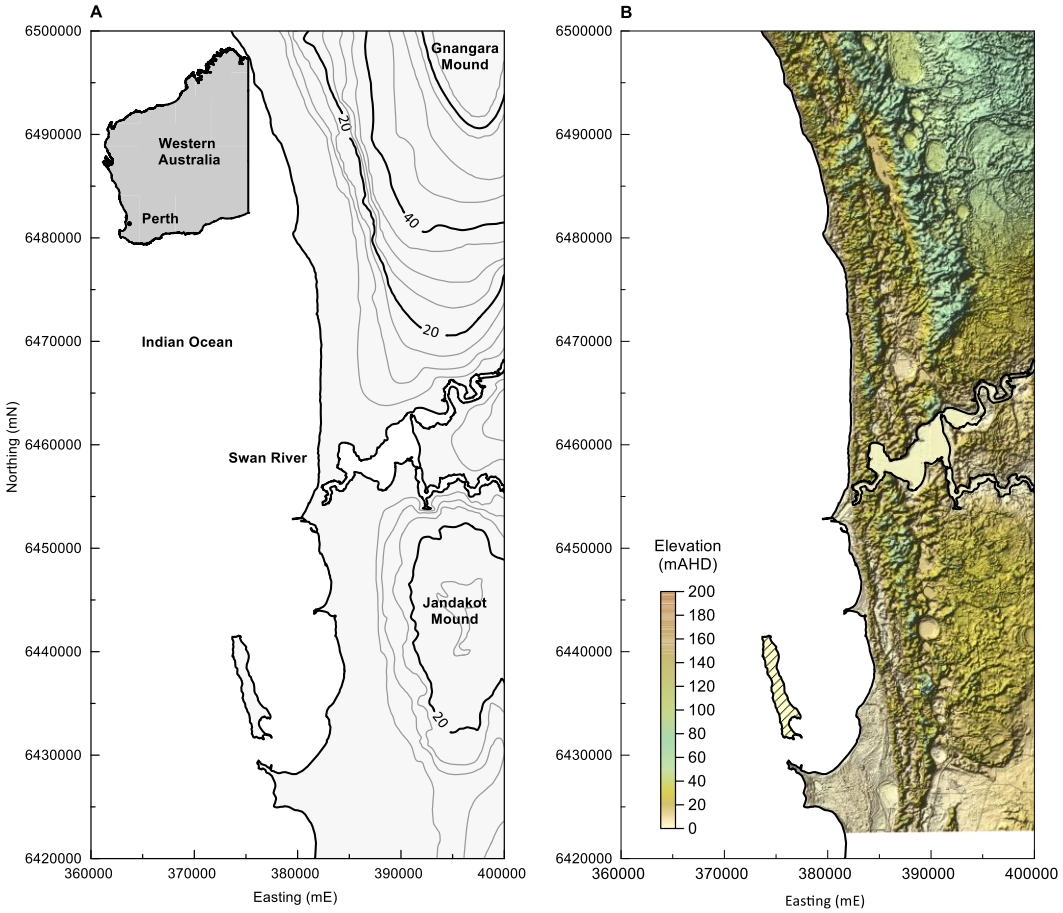

Figure 1.1: Map of groundwater contours for the Perth metropolitan area (left) (© DWER) and digital elevation model of the Perth area (right) (data sourced from https://elevation.fsdf.org.au/, reproduced under Creative Commons CC BY 3.0 AU). The Gnangara and Jandakot mounds are the primary drivers of groundwater flow in the Perth region.

1.3.1 The Swan Coastal Plain

The shallow geology of the Perth region is described as the Swan Coastal Plain (SCP). The Swan Coastal Plain is predominately formed from fluviatile (river-borne) or aeolian (air-borne) sediments (Gozzard, 2007; McArthur *et al.*, 1960). The plain generally consists of a series of geomorphic entities that are subparallel to the modern coastline.

Aeolian (i.e., wind-borne) dunes have a set of descriptive and interpretative nomenclature to describe the various features of the dune system. Figure 1.2 is a schematic showing a coastal calcarenite (i.e., lime sand) dune system including cliff and shore platform (Bird, 2011). Grains are transported by wind on the stoss slope, forming a shallow gradient hill. Grains accumulate near the crest of the dune and later collapse to form the slipface after reaching a specific angle of yield. The angle between the slip face and land surface is termed the angle of repose. Dry aeolian sand typically has an angle of repose of approximately 34 degrees (Beakawi Al-Hashemi *et al.*, 2018). This angle is dictated by grain size, shape, and moisture content of the sand.

Paleosols are ancient soil horizons buried beneath sedimentary layers (Selley, 2000). They tend to form hard crusts and are indicative of paleoclimate conditions (Retallack, 2003). Paleosols can influence groundwater flow and cave development in karstic terranes (Grimes, 2006; Mylroie, 2013). GPR imaging commonly shows the remaining slipface, any paleosols, and underlying limestone interface (Buynevich *et al.*, 2009).

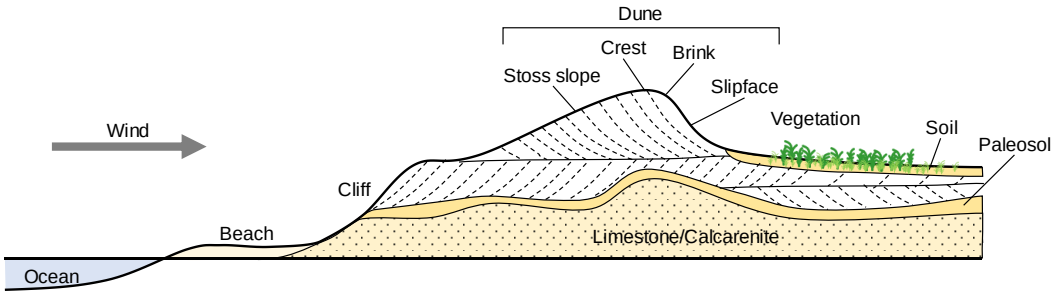

Figure 1.2: Schematic showing the anatomy of a coastal dune calcarenite system. Sand grains are blown along the stoss slope to accumulate at the crest before collapsing down the slipface. The direction of wind dictates the orientation of the slipface. Paleosols are ancient soil horizons, indicative of vegetation, that can form hard crusts and influence groundwater flow. High-frequency GPR imaging has the potential to image the different slop angles and changes in lithology, which may be useful for geotechnical or hydrogeological investigations.

Figure 1.3 shows the surface geology and distribution of dune systems in the Perth basin. The shallow geological systems approaching the coast are progressively younger in age and comprise of the Tamala Limestone, and three dominant dune systems: (i) the Bassendean, (ii) the Quindalup, and (iii) the Spearwood dunes (Bolland, 1999).

The Bassendean dune system exists throughout most of the central basin, west of the Darling Scarp. It is composed of lime sands, quartz sands, and minor concentrations of black heavy minerals. The origin of this system is from coastal calcareous sands, although much of the carbonate has been lost through leaching (McArthur *et al.*, 1960). Development of the dune system began during the interglacial period ~240,000 years ago, and took place over 100,000 years atop older marine and lacustrine deposits (Gozzard, 2007).

The Spearwood dune system is approximately 40 kyr and is a yellow to brown coloured convex and asymmetric dune system consisting of calcareous Aeolian sand, remnant from leaching of the Tamala Limestone. It features a core of eolianite and hard capping of secondary calcite underlying the sands. It is generally found west of the Bassendean dunes, and is separated by swamps and lakes (Bolland, 1999; McArthur *et al.*, 1960).

The Quindalup dunes are the youngest of the three major systems (< 10 kyr). It is a primarily nested parabolic dune complex consisting of wind-blown (aeolian) lime and quartz sands and forms parallel ridges proximal to the coast. This system tends to occupy blowouts created in the Spearwood dune system, and is otherwise separated from the Spearwood dunes via lakes or inlets (Bolland, 1999; Gozzard, 2007; McArthur *et al.*, 1960).

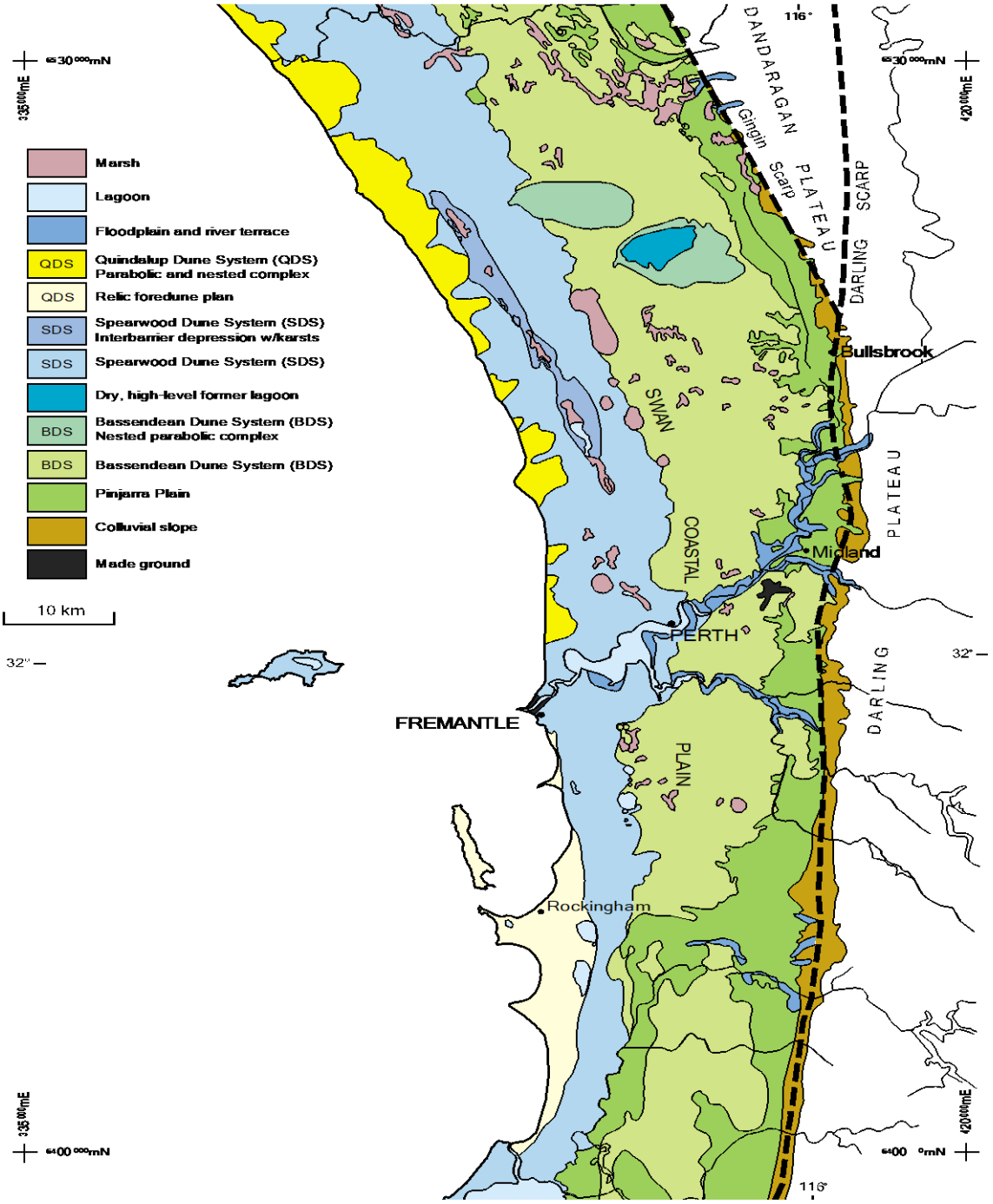

Figure 1.3: Distribution of dune systems of the Swan Coastal Plain (Modified from Gozzard 2007). The dune systems are increasingly older with proximity to the Darling Scarp. The Quindalup Dune System (QDS) is the youngest dune system and is located nearest to the coast.

1.3.2 The Tamala Limestone

The Tamala Limestone is the world's most extensive eolianite deposit (A. Smith, Massuel, & Pollock, 2012). It is a quaternary-age eolianite found extensively along the western coast of Western Australia, analogous to the Bermuda late mature Pleistocene karst. Two competing theories exist for the depositional origin: (i) glacial-age dune which have migrated across exposed shelf-margins (Sayles, 1931), and (ii) deposited during high stand system tracts (Bretz, 1960). Figure 1.4 shows an example of the Tamala Limestone from the Nambung national park, near Lancelin, which hosts a field of pinnacle karsts formed in Tamala Limestone (Hearty, 2002; Lipar *et al.*, 2015).

Figure 1.4: Example of the Tamala Limestone from 'The Pinnacles' at Nambung National Park.

Eolianites in WA are generally moderately-to-weakly-cemented fine-to-coarse carbonate sand with large-scale festoon bedding (i.e., scoop-like structures) and planar crossbedding. Exposed late-to-middle-age Pleistocene rocks can be observed in cliff-faces along the Swan River estuary throughout Perth. Early Pleistocene examples are rare, but where present tend to exhibit massive accumulations (e.g., calcrete paleosols) and extensive cave developments such as near Yanchep, north of Perth (Grimes, 1999, 2002, 2006; Hearty, 2002; Hearty *et al.*, 2008).

Coastal Tamala Limestone consists of three main lithologies: (i) wind-deposited quartz grainstone, medium- to fine grained, well-rounded sands and lithoclasts, (ii) shelly grainstone, medium- to coarse sand and gravels, and (iii) Shell and lithoclast conglomerate, deposited from high-stand systems tract (strandline), predominately gravel sized lithoclasts and shells (Semeniuk, 1985; Semeniuk *et al.*, 1982; Semeniuk & Johnson, 1985; Semeniuk & Searle, 1985; Semeniuk *et al.*, 1986). Large-scale wedges and lenses of marine sediments and sheets of massive and indurated (i.e., hardened) calcrete are also common. These lithologies relate to various stages of deposition during recent marine transgression (e.g. the last interglacial period), where the coastline Western Australia was submerged (M. E. Johnson *et al.*, 1995).

1.4 Geophysical Methods

Geophysical methods are one of the few non-invasive ways to investigate the properties the subsurface. Such properties can include (i) the differentiation of layers in an aquifer system, which may represent a sealing or confining unit, and (ii) the distribution of subsurface conductivity, which may represent changes to groundwater solute concentrations (Rubin *et al.*, 2006). Often, geophysical data provides targets for drilling campaigns or for time-lapse changes in earth properties, such as fluid or solute transport (Binley *et al.*, 2010; Binley *et al.*, 2015).

There are several empirical relationships which are commonly used to relate hydrogeological properties of the subsurface to geophysical properties. Two such relationships are (i) Archies law (Archie, 1941), which relates the resistivity of the formation to the resistivity of the water using various factors described below (see Chapter 3) and (ii) the Topp relationship (Topp *et al.*, 1980), which estimates the soil water content based on changes in dielectric properties (see 5Appendix C.1). Archies law postulates that the rock matrix is non-conductive, which is not true for clay minerals. Other equations, such as the Waxman-Smits equation (Waxman *et al.*, 1968), attempt to correct for a conductive rock matrix. Archies law is written below

$$R_t = \alpha\phi^{-m}S_w^{-n}R_w \tag{1.1}$$

Table 1.1: Definitions of hydrogeological terminology and Archies Law.

Parameter	Symbol	Description
Formation resistivity	R_t	Electrical resistivity of rock formation containing fluid.
Fluid resistivity	R_w	Electrical resistivity of fluid.
Cementation exponent	m	Effect of pore-space network on rock resistivity (ranges between 1.3-4.1, with typical consolidated sandstones values between 1.8–2.0).
Saturation exponent	n	Impact of non-conductive fluids present in pore-space (usually '1' in non-oil environments).
Fluid saturation	S_w	Saturation of the fluid in the rock.
Tortuosity	α	Correction for variation in compaction, pore structure, and grain size (usually 0.5–1.5).
Porosity	ϕ	Amount of rock that is non-matrix (i.e. can be saturated).

1.4.1 ERI

Electrical resistivity imaging (ERI) is used predominately throughout this research. It is a flexible and robust method, with surface, borehole, 2D, 3D, and marine applications, and is useful where other methods may suffer from ambient cultural noise (e.g., (Dahlin, 2001; M. H. Loke *et al.*, 2013)). Section 2.1.2 features a background of ERI. Ground penetrating radar (GPR) is another method used for shallow imaging and can yield high-resolution imagery for shallow lithology mapping (A. Costall *et al.*, 2018; Alexander Ross Costall *et al.*, 2019; Pethick *et al.*, 2018).

The propagation of electromagnetic waves, such as from ERI (in the electrostatic case) or GPR (in the high-frequency regime), is described by four fundamental equations known as Maxwell's equations. These are a compilation of works by Gauss, Ampere, and Lorentz (Maxwell, 1873). ERI uses the electrostatic case of Maxwell's equations, where the divergence of the current density (∇J) will be zero (M. H. Loke *et al.*, 2013). For GPR, the high-frequency component simply means that waves act in a non-dispersive manner and will reflect from contrasts in dielectric property (Jol, 2008). The derivation and each of Maxwell's equations are described below. Symbols are defined in Table 1-1.

Table 1-1: Commonly used symbols and their definition.

Symbol	Description	Units
D	Electric flux density	C/m^2
B	Magnetic flux density	$Wb/m^2, T$
E	Electric field intensity	$N/C, V/m$
H	Magnetic field intensity	A/m
Φ	Electric field potential	V
ρ_v	Volume charge density	C/m^3
J	Current density	A/m^2
t	Time	s
σ	Conductivity	S/m
μ	Magnetic permeability	H/m
ε	Electric permittivity	F/m

Eq. 2.1, Gauss's law, describing the electric flux proportionality of charge leaving a volume to the charge inside a volume.

$$\nabla \cdot D = \frac{\rho_v}{\varepsilon_0} \tag{1.3}$$

Eq. 2.2, Gauss's law of magnetism, which describes the total magnetic flux through a closed surface.

$$\nabla \cdot B = 0 \tag{1.4}$$

Eq. 2.3, the Maxwell-Faraday equation, describing the voltage induced by a closed loop must be proportional to the rate-of-change of magnetic flux enclosed by the loop, and finally

$$\nabla \times \mathrm{E} = -\frac{\delta \mathrm{B}}{\delta t} \tag{1.4}$$

Eq. 2.4, Ampere's circuital law with Maxwell's addition, which describes the magnetic field induced around a closed loop being proportional to the electric current and displacement currents enclosed by the loop.

$$\nabla \times \mathrm{H} = \frac{\delta \mathrm{D}}{\delta \mathrm{t}} + J \tag{1.5}$$

The constitutive equations define the relationship between physical properties (Griffiths, 1999). For electromagnetism, these equations include:

$$D = \varepsilon E \tag{1.6}$$

$$H = \frac{B}{\mu} \tag{1.7}$$

$$J = \sigma E \tag{1.8}$$

For ERI (i.e., the electrostatic case), the derivation is given by(Dey *et al.*, 1979) rewrites equation 2.7 using the conservation of stationary electric fields to yield equation 2.9.

$$E = -\nabla \Phi \tag{1.9}$$

$$J = -\sigma \nabla \Phi \tag{1.10}$$

Applying the conservation of charge over a volume yields equation 1.10, 1.11, where the divergence of the current density equals the rate of change of free charge density (Q).

$$\nabla \cdot J = -\frac{\partial Q}{\partial t} \tag{1.11}$$

$$\nabla \cdot (\sigma \nabla \Phi) = -\frac{\partial Q}{\partial t} \tag{1.12}$$

This is valid for steady-state conditions everywhere besides the source location, r_s, where it is equal to the input current, I.

$$\nabla \cdot (\sigma \nabla \Phi) = -\mathrm{I}\delta(\mathrm{r} - \mathrm{r_s}) \tag{1.13}$$

The potential field of an electrode combination can be obtained by superposition of individual potentials from each electrode (Thomas Günther, 2004; T. Günther *et al.*, 2006). For a homogeneous half space, the potential field (Φ) resulting from a point source at $\vec{r_s} = (x; y; z_s)$ is:

$$\Phi(\vec{r}) = \frac{I}{2\pi\sigma_0 |\vec{r} - \vec{r_s}|} \tag{1.14}$$

For a subsurface source (e.g. borehole or buried arrays), the solution must account for the air-ground interface by including a mirror source term, $\vec{r_s}' = (x; y; -z_s)$ such that:

$$\Phi = \frac{I}{4\pi\sigma_0}\left(\frac{1}{|\vec{r} - \vec{r_s}|} + \frac{1}{|\vec{r} - \vec{r}_s'|}\right) \tag{1.15}$$

In a typical four-pole arrangement (i.e., quadrupole), the electrical field potential (V, or Φ) is measured across two electrodes, denoted M and N (or P_1 and P_2), while an electrical current (I) is injected across two other electrodes, denoted A and B (or C_1 and C_2).

The apparent resistivity is the resistivity value that a particular voltage, current, and geometric factor would return for an idealised homogeneous half-space (Ginzburg *et al.*, 1976; Ward *et al.*, 1990). The geometric factor (K) yields the apparent resistivity (ρ_a):

$$\rho_a = K\frac{V}{I} \tag{1.16}$$

For surface-based electrodes without topography, the geometric factor is determined by the homogeneous half-space of resistivity (ρ) where K is calculated as:

$$K = \frac{2\pi}{\frac{1}{AM} - \frac{1}{AN} - \frac{1}{BM} + \frac{1}{BN}} \tag{1.17}$$

Where topographic modelling is required, the geometric factor is calculated numerically, i.e., the apparent resistivity for a constant resistivity is calculated to determine a value of K such that $\rho_{app} = \rho$.

Classical survey design uses a single geometrical arrangement (or style) of electrodes based on the characteristics of the resulting electrical field. For example, the Wenner-alpha array is considered to have a high signal-to-noise ratio, at the expensive of lateral resolution. Dahlin *et al.* (2004) compare ten of the most

common electrode arrays and detail the strengths and weaknesses of each. Combinations of classical electrode configurations, and 'optimized' arrays based on inversion resolution outcomes are gaining popularity as data acquisition technology has improved (Ishola *et al.*, 2015; M. Loke *et al.*, 2007; M. H. Loke, Wilkinson, Chambers, *et al.*, 2014; M. H. Loke, Wilkinson, *et al.*, 2015; Wilkinson *et al.*, 2012). Optimized arrays have potential to reduce the number data without compromise to imaging ability, thus increasing the efficiency of field acquisition. However, pre-made code is not readily accessible yet.

Apparent resistivity (as shown above) is based on a homogeneous half-space and cannot represent the true geo-electrical structure. Inversion modelling reconstructs a model of physical parameters that replicate a set of measurements, and is routinely used in almost all geophysical techniques (M. H. Loke *et al.*, 1995; Meju, 1994; Menke, 2012a; C. Rücker *et al.*, 2017; Snieder *et al.*, 1999).

1.4.2 GPR

Ground penetrating radar is a useful tool for shallow subsurface investigation. It is particularly useful for hydro-geological applications (A. Peter Annan, 2005; Bano *et al.*, 2001; Huisman *et al.*, 2003; Elmar Strobach, 2013). The high-frequency EM wave propagation reflects from contrasts in dielectric permittivity, such as between dry and saturated sediments (Jol, 2008; A. Martinez *et al.*, 2001; Rehman *et al.*, 2016). The term 'dielectric' describes a non-conducting material that can accommodate a propagating EM field (Cassidy, 2009). In these materials, free (i.e. unbound) charges result in EM attenuation and rapid loss of signal. Dielectric permittivity in the context of GPR is often cited as relative permittivity, relative to vacuum and defined by:

$$\varepsilon_r = \frac{\varepsilon}{\varepsilon_0} \tag{1.18}$$

Where ε_0 is the permittivity of vacuum, $8.89 * 10^{-12}$ F/m.

Table 1.2: Typical values of conductivity and relative dielectric permittivity for common subsurface materials (abbreviated from (Cassidy, 2009))

Material	***Conductivity (mS/m)***	***Relative Permittivity (ε_r)***	***Attenuation (dB/m)***
Air	0	1	0
Freshwater	0.1-10	78-88	0.1
Seawater	3000	81-88	600
Limestone (dry)	<0.001	4-8	0.4-1
Limestone (wet)	10-100	6-15	10-100
Sand (dry)	0.0001-1	3-6	0.01
Sand (wet)	0.1-10	10-30	0.06-0.3

Depth-of-investigation in GPR surveying is typically shallow (less than 20 m) and depends on both central antenna frequency and ground conditions (D. G. Smith *et al.*, 1995). Central antenna frequency also controls the resolution of the data (A. P. Annan, 2009; Jol, 2008). Table 1.3 provides examples of vertical resolution and depth of penetration for different frequency GPR antenna (Bristow, 2009; Robinson *et al.*).

Table 1.3: Approximate wavelength and vertical resolution on for various frequency GPR antennas commonly used in exploration environments.((Bristow, 2009; Robinson et al.)

Frequency (MHz)	***Wavelength (m, at v = 0.15 m/ns)***	***Resolution (cm)***
50	3	75
100	1.5	37.5
250	0.6	15
500	0.3	7.5
1000	0.15	3.75

Throughout this research, I have collected many examples of ground penetrating radar along Perth's coastal margins. These are shown throughout this research. Multiple datasets exist for a site in City Beach, located west of Perth. Here the Quindalup dunes overlay a series of partially outcropping Tamala limestone ridges. The datasets include a shielded 675 MHz, shielded 250 MHz antennae, shielded 160 MHz and an unshielded 50 MHz rough terrain antenna.

Figure 1.5 shows a section of the processed radargram from the 675 MHz dataset near to the beachfront. The zone of high conductivity associated with the seawater interface and salt-spray affected sediments can be seen where no reflectors are present. Also shown are (i) potential paleosurfaces, (ii) the change in the reflection profile associated with the water table, and (iii) a clear indication of depositional reversal. Further examples of GPR can be found throughout the chapters of this thesis.

Figure 1.6 shows a section of the processed 675 MHz radar data located further inland from the shoreline. The section highlights a set of cross-strata dipping away from the coast and terminating at a potential paleosol or limestone unconformity. Additional reflectors are present below the paleosol. The envelope attribute shown in panel B highlights the different zones of reflectivity within the section. Zones of low reflectivity can be associated with signal scattering from the Tamala Limestone.

This example of GPR data shows the potential for anisotropy of hydraulic properties, as well as the significant heterogeneity that exists throughout the Tamala limestone. This is discussed further in Chapter 3: Groundwater Throughflow and Seawater Intrusion in High-Quality Coastal Aquifers.

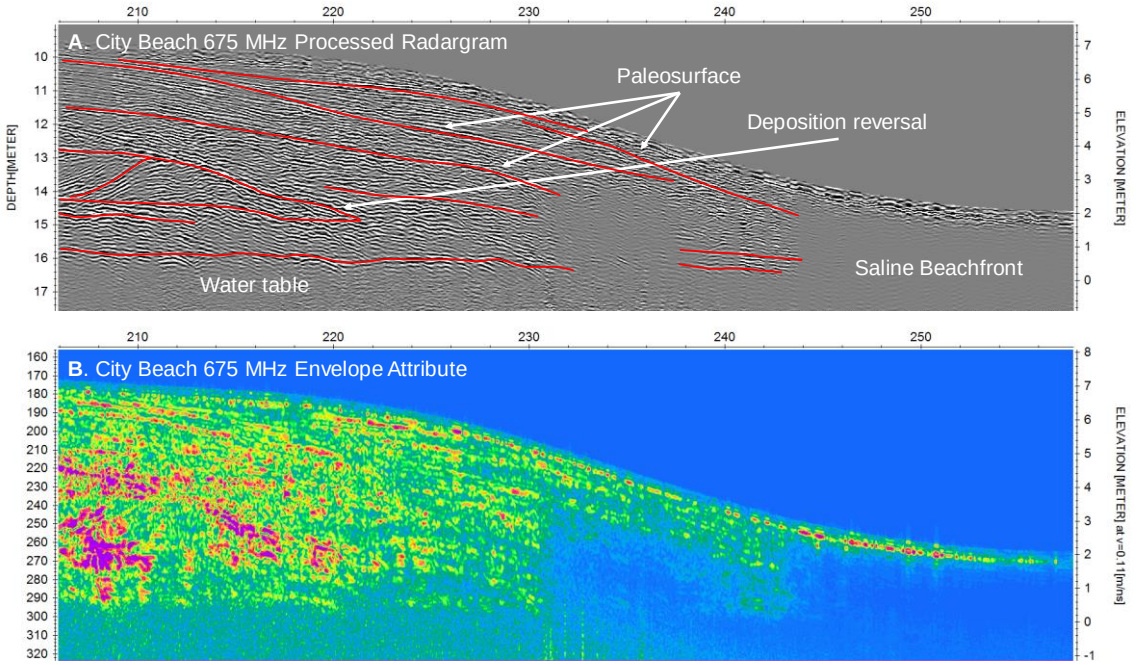

Figure 1.5: Images showing processed 675 MHz GPR data from City Beach, Perth WA. The top image shows a section of the radargram where sedimentary layers are visible on top of a semi-continuous paleosol or limestone unconformity. The lower image shows the distribution of energy from the envelope attribute, highlighting the zones of high reflectivity associated with the dunes. The high-frequency antenna can resolve fine bedding among the dunes and provide indications of limestone areas.

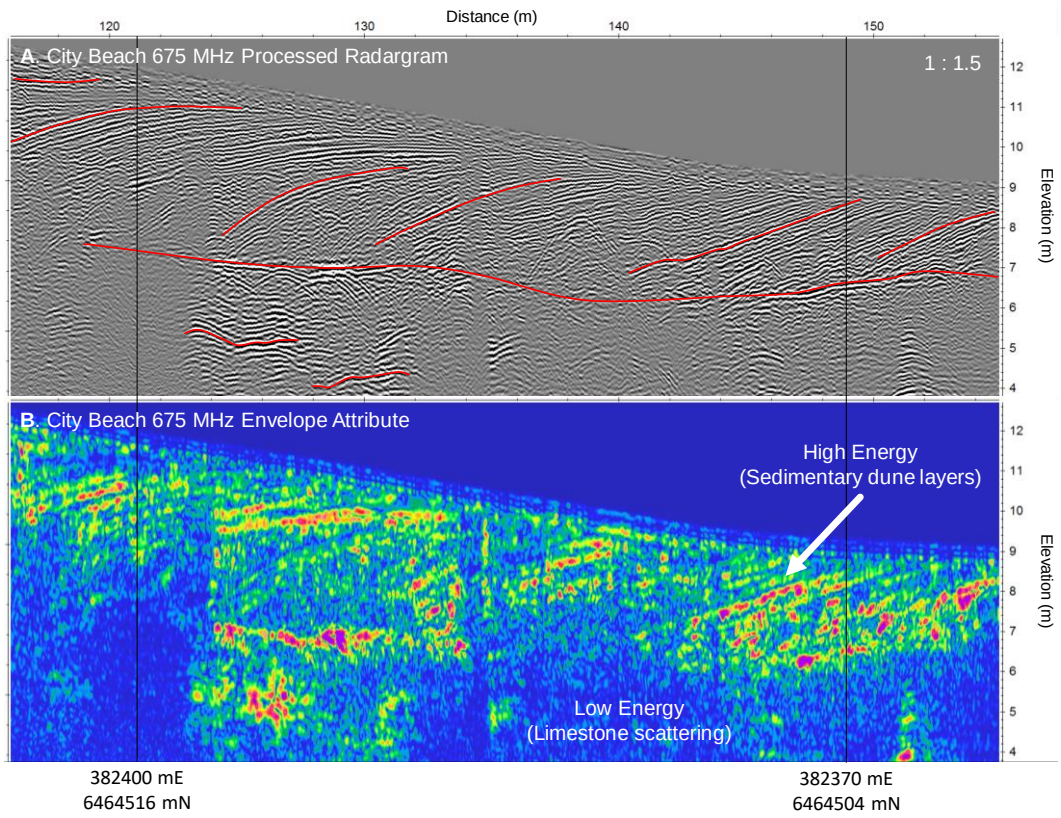

Figure 1.6: Images showing processed 675 MHz GPR data from City Beach, Perth WA. The top image shows a section of the radargram where sets of sedimentary layering within the dunes are visible on top of a prominent and semi-continuous paleosol or limestone unconformity. The lower image shows the energy attribute of the radar signal. Layers dipping away from the coast can indicate changes in prevailing wind direction and tidal levels.

1.5 Research Structure

The problem of seawater intrusion and the loss of accessible high-quality water is urgent and global. Karstic aquifers are common at coastal margins and yet the most difficult to simulate and characterise. I develop a set of research activities that focus on specific shallow coastal hydrogeology. The research is a multidisciplinary study including; (i) experimentation of ERI technologies applied along the coastal margins of Perth, (ii) the relationship between groundwater throughflow and saline water intrusion, and (iii) new imaging technologies designed to precisely resolve the saline water interface.

There are a range of questions that appear to be poorly understood or not well addressed in literature. For example; (i) which ERI array is the most practical for seawater imaging applications, (ii) what are the impacts of different inversion options on interpretation of shallow coastal hydrogeology, and (iii) to what degree are aquifer geometries can be resolved using ERI.

These questions are addressed throughout my research. The research is represented in the form of three papers. Two of these chapters are published in high-quality international journals. This research showcases numerous high-quality geophysical datasets that I have planned, acquired, processed, and interpreted throughout the course of this research.

Chapter 2 is published in Surveys in Geophysics, 2018, titled "*Electrical Resistivity Imaging and the Saline Water Interface in High-Quality Coastal Aquifer*s". In this paper, I identify areas where the technology can be improved after completing numerical experiments and an extensive field campaign throughout the coastal margins of Perth. My experiments provide evidence that certain arrays are more suitable to interpreting the lower substrate. I also find that well-control is essential for interpretation of hydrogeology of the coastal margin.

Chapter 3 is a research article published in Scientific Reports (Nature). Here I address a series of questions that stem from numerical modelling of a seawater monitoring site located in a karstic aquifer. Examples of questions include:

1. What range of hydraulic conductivity can be expected for high quality karstic aquifer systems?
2. What are the key influences on terrestrial groundwater flow and seawater intrusion?
3. What are the limitations of the methods used to quantify aquifer flow and the seawater interface?
4. How will anisotropy and heterogeneity impact the position of the seawater interface?
5. Can geophysics reveal the saline groundwater wedge, and can it assist in groundwater modelling?
6. What future monitoring technologies can to quantify the relationship in a dynamic coastal setting?

Through research in Chapters 2 and 3, I found that it was impossible for surface based ERI to recover the correction formation resistivity and geometry of the seawater interface. In Chapter 4, I include a geophysical acquisition and workflow that can precisely capture the geometry and resistivity of the seawater interface using borehole based ERI.

I intend for this thesis to be accessible and applicable to a broad audience without compromising on the underlying scientific message. The outcomes I have demonstrated are practical and achievable with current technology, and I hope that this thesis spurs further research and improvements to groundwater management at the coast.

1.6 References

Alam, M. Z., Carpenter-Boggs, L., Mitra, S., Haque, M., Halsey, J., Rokonuzzaman, M., . . . Moniruzzaman, M. (2017). Effect of salinity intrusion on food crops, livestock, and fish species at Kalapara Coastal Belt in Bangladesh. *Journal of Food Quality, 2017*.

Annan, A. P. (2005). GPR Methods for Hydrogeological Studies. In Y. Rubin & S. S. Hubbard (Eds.), *Hydrogeophysics* (pp. 185-213). Dordrecht: Springer Netherlands.

Annan, A. P. (2009). Chapter 1 - Electromagnetic Principles of Ground Penetrating Radar A2 - Jol, Harry M. In *Ground Penetrating Radar Theory and Applications* (pp. 1-40). Amsterdam: Elsevier.

Appleyard, S. (1995). The impact of urban development on recharge and groundwater quality in a coastal aquifer near Perth, Western Australia. *Hydrogeology Journal, 3*(2), 65-75.

Appleyard, S. J., Angeloni, J., & Watkins, R. (2006). Arsenic-rich groundwater in an urban area experiencing drought and increasing population density, Perth, Australia. *Applied Geochemistry, 21*(1), 83-97. doi:10.1016/j.apgeochem.2005.09.008

Archie, G. E. (1941). The Electrical Resistivity Log as an Aid in Determining Some Reservoir Characteristics. *Transactions of the AIME, 146*(01), 54-62. doi:10.2118/942054-g

Bano, M., & Girard, J. F. (2001). Radar reflections and water content estimation of aeolian sand dune. *Geophysical Research Letters, 28*(16), 3207-3210. doi:Doi 10.1029/2000gl011986

Barlow, P. M., & Reichard, E. G. (2010). Saltwater intrusion in coastal regions of North America. *Hydrogeology Journal, 18*(1), 247-260. doi:10.1007/s10040-009-0514-3

Beakawi Al-Hashemi, H. M., & Baghabra Al-Amoudi, O. S. (2018). A review on the angle of repose of granular materials. *Powder Technology, 330*, 397-417. doi:10.1016/j.powtec.2018.02.003

Bear, J. (2005). *Sea water intrusion into coastal aquifers*.

Binley, A., Cassiani, G., & Deiana, R. (2010). Hydrogeophysics: opportunities and challenges. *Bollettino di Geofisica Teorica ed Applicata, 51*(4), 267-284. Retrieved from <Go to ISI>://WOS:000285407700002

Binley, A., Hubbard, S. S., Huisman, J. A., Revil, A., Robinson, D. A., Singha, K., & Slater, L. D. (2015). The emergence of hydrogeophysics for improved understanding of subsurface processes over multiple scales. *Water Resour Res, 51*(6), 3837-3866. doi:10.1002/2015WR017016

Bird, E. C. (2011). *Coastal geomorphology: an introduction*: John Wiley & Sons.

Bolland, M. D. A. (1999). *Soils of the Swan coastal plain / by Mike Bolland*. [Perth, W.A.]: Agriculture Western Australia.

Bretz, J. H. J. G. S. o. A. B. (1960). Bermuda: A partially drowned, late mature, Pleistocene karst. *71*(12), 1729-1754.

Bristow, C. (2009). Chapter 9 - Ground Penetrating Radar in Aeolian Dune Sands A2 - Jol, Harry M. In *Ground Penetrating Radar Theory and Applications* (pp. 271-297). Amsterdam: Elsevier.

Buynevich, I. V., Jol, H. M., & FitzGerald, D. M. (2009). Coastal Environments. In *Ground Penetrating Radar Theory and Applications* (pp. 299-322). Amsterdam: Elsevier.

C. Nevill, J., J. Hancock, P., R. Murray, B., F. Ponder, W., F. Humphreys, W., L. Phillips, M., & K. Groom, P. (2010). Groundwater-dependent ecosystems and the dangers of groundwater overdraft: a review and an Australian perspective. *Pacific Conservation Biology, 16*(3), 187-208. doi:https://doi.org/10.1071/PC100187

Cassidy, N. J. (2009). Chapter 2 - Electrical and Magnetic Properties of Rocks, Soils and Fluids A2 - Jol, Harry M. In *Ground Penetrating Radar Theory and Applications* (pp. 41-72). Amsterdam: Elsevier.

Costall, A., Harris, B., & Pigois, J. P. (2018). Electrical Resistivity Imaging and the Saline Water Interface in High-Quality Coastal Aquifers. *Surveys in Geophysics, 39*(4), 753-816. doi:10.1007/s10712-018-9468-0

Costall, A. R., & Harris, B. (2019). Rapid Estimation of Volumetric Groundwater Recharge in the Vadose Zone via Ground Penetrating Radar. *ASEG Extended Abstracts, 2018*(1), 1-7. doi:10.1071/ASEG2018abP091

Costanza, R., d'Arge, R., de Groot, R., Farber, S., Grasso, M., Hannon, B., . . . van den Belt, M. (1997). The value of the world's ecosystem services and natural capital. *Nature, 387*(6630), 253-260. doi:10.1038/387253a0

CSIRO. (2009). *Groundwater Yields In South-West Western Australia: Summary Of A Report To The Australian Government From The Csiro South-West Western Australia Sustainable Yields Project*. Retrieved from

Dahlin, T. (2001). The development of DC resistivity imaging techniques. *Computers & Geosciences, 27*(9), 1019-1029. doi:Doi 10.1016/S0098-3004(00)00160-6

Dahlin, T., & Zhou, B. (2004). A numerical comparison of 2D resistivity imaging with 10 electrode arrays. *Geophysical Prospecting, 52*(5), 379-398. doi:DOI 10.1111/j.1365-2478.2004.00423.x

Daily, G. C. (1997). *Nature's services* (Vol. 3).
Dalin, C., Wada, Y., Kastner, T., & Puma, M. J. (2017). Groundwater depletion embedded in international food trade. *Nature, 543*(7647), 700-704. doi:10.1038/nature21403
Davidson, W. A. (1995). *Hydrogeology And Groundwater Resources Of The Perth Region, Western Australia* (Vol. 142): Geological Survey of WA.
Delworth, T. L., & Zeng, F. R. (2014). Regional rainfall decline in Australia attributed to anthropogenic greenhouse gases and ozone levels Latitude. *Nature Geoscience, 7*(8), 583-587. doi:10.1038/Ngeo2201
Department of Regional Development WA. (2008). Royalties for Regions. Retrieved from http://www.drd.wa.gov.au/rfr/Pages/default.aspx
Department of Water, Western Australia,. (2011). Gnangara groundwater system.
Department of Water, Western Australia,. (2016). *Environmental management of groundwater from the Gnangara Mound*. Retrieved from https://www.google.com.au/url?sa=t&rct=j&q=&esrc=s&source=web&cd=1&cad=rja&uact=8&ved=0ahUKEwigvImy4NbXAhVDspQKHdPwDWkQFggrMAA&url=http%3A%2F%2Fwww.water.wa.gov.au%2F__data%2Fassets%2Fpdf_file%2F0019%2F8209%2F109982.pdf&usg=AOvVaw2BbdrQKIguPNf0UwtZnZxO
Department of Water WA. (2012a). Perth Region Confined Aquifer Capacity (PRCAC) study. Retrieved from http://www.water.wa.gov.au/planning-for-the-future/finding-water/groundwater-investigations/perth-regional-confined-aquifer-capacity-project-prcac
Department of Water WA. (2012b). Regional Water Availability and Water for Pilbara Cities Groundwater Investigation Programs. Retrieved from http://www.water.wa.gov.au/planning-for-the-future/finding-water/groundwater-investigations/royalties-for-regions-groundwater-investigation-program
Dey, A., & Morrison, H. F. (1979). RESISTIVITY MODELLING FOR ARBITRARILY SHAPED TWO-DIMENSIONAL STRUCTURES*. *27*(1), 106-136. doi:doi:10.1111/j.1365-2478.1979.tb00961.x
Eamus, D., Froend, R., Loomes, R., Hose, G., & Murray, B. (2006). A functional methodology for determining the groundwater regime needed to maintain the health of groundwater-dependent vegetation. *Australian Journal of Botany, 54*(2), 97-114.
EPA. (2018). *Perth Groundwater Replenishment Scheme Stage 2*. Retrieved from https://www.epa.wa.gov.au/proposals/perth-groundwater-replenishment-scheme-stage-2
Eswaran, H., Almaraz, R., Reich, P., & Zdruli, P. (1997). Soil Quality and Soil Productivity in Africa. *Journal of Sustainable Agriculture, 10*(4), 75-90. doi:10.1300/J064v10n04_07
Frioux, S. (2014). Environmental History of Water Resources. In M. Agnoletti & S. Neri Serneri (Eds.), *The Basic Environmental History* (pp. 121-141). Cham: Springer International Publishing.
Geoscience Australia. (2020). Sustainable Groundwater Management. Retrieved from https://www.ga.gov.au/about/projects/water/sustainable-groundwater-management
Ginzburg, A., & Levanon, A. (1976). Determination Of A Salt-Water Interface By Electric Resistivity Depth Soundings/Détermination D'un Interface D'eau Salée À L'aide Des Mesures Verticales De Résistivité Électrique. *Hydrological Sciences Journal, 21*(4), 561-568.
Government of Australia. (2016). The Australian continent. Retrieved from http://www.australia.gov.au/about-australia/our-country/the-australian-continent
Gozzard, J. R. (2007). *Geology And Landforms Of The Perth Region*: Geological Survey of Western Australia.
Griffiths, D. J. (1999). *Introduction To Electrodynamics* (Vol. 3). Reed College: prentice Hall Upper Saddle River, NJ.
Grimes, K. G. (1999). *The Water Below: An introduction to karst hydrology and the hydrological setting of the Australian karsts.* Paper presented at the Proceedings of the 13th Australasian Conference on Cave and Karst Management. pp.
Grimes, K. G. (2002). Syngenetic and eogenetic karst: an Australian viewpoint. *Evolution of Karst: from Prekarst to Cessation. Inštitut za raziskovanje krasa, ZRC SAZU, Postojna*, 407-414.
Grimes, K. G. (2006). Syngenetic karst in Australia: a review.
Groom, B. P. K., Froend, R. H., & Mattiske, E. M. (2000). Impact of groundwater abstraction on a Banksia woodland, Swan Coastal Plain, Western Australia. *Ecological Management and Restoration, 1*(2), 117-124. doi:10.1046/j.1442-8903.2000.00033.x
Günther, T. (2004). *Inversion methods and resolution analysis for the 2D/3D reconstruction of resistivity structures from DC measurements.* (Dissertation). Retrieved from http://hdl.handle.net/11858/00-1735-0000-0001-3314-2 FID GEO-LEO e-docs database.

Günther, T., Rucker, C., & Spitzer, K. (2006). Three-dimensional modelling and inversion of dc resistivity data incorporating topography - II. Inversion. *Geophysical Journal International, 166*(2), 506-517. doi:10.1111/j.1365-246X.2006.03011.x

Harrington, N., & Cook. P. (2014). *Groundwater in Australia*. Retrieved from

Hearty, P. J. (2002). Revision of the late Pleistocene stratigraphy of Bermuda. *Sedimentary Geology, 153*(1-2), 1-21. doi:Pii S0037-0738(02)00261-0

Doi 10.1016/S0037-0738(02)00261-0

Hearty, P. J., & O'Leary, M. J. (2008). Carbonate eolianites, quartz sands, and Quaternary sea-level cycles, Western Australia: A chronostratigraphic approach. *Quaternary Geochronology, 3*(1-2), 26-55. doi:10.1016/j.quageo.2007.10.001

Hoggart, S. P. G., Hanley, M. E., Parker, D. J., Simmonds, D. J., Bilton, D. T., Filipova-Marinova, M., . . . Thompson, R. C. (2014). The consequences of doing nothing: The effects of seawater flooding on coastal zones. *Coastal Engineering, 87*, 169-182. doi:https://doi.org/10.1016/j.coastaleng.2013.12.001

Holzer, T. L., & Johnson, A. I. (1985). Land subsidence caused by ground water withdrawal in urban areas. *GeoJournal, 11*(3), 245-255. doi:10.1007/BF00186338

Huisman, J. A., Hubbard, S. S., Redman, J. D., & Annan, A. P. (2003). Measuring Soil Water Content with Ground Penetrating Radar: A Review. *Vadose Zone Journal, 2*(4), 476-491. doi:10.2136/vzj2003.4760

Ishola, K. S., Nawawi, M. N. M., & Abdullah, K. (2015). Combining Multiple Electrode Arrays for Two-Dimensional Electrical Resistivity Imaging Using the Unsupervised Classification Technique. *Pure and Applied Geophysics, 172*(6), 1615-1642. doi:10.1007/s00024-014-1007-4

Johnson, M. E., Baarli, B. G., & Scott, J. H. (1995). Colonization and Reef Growth on a Late Pleistocene Rocky Shore and Abrasion Platform in Western-Australia. *Lethaia, 28*(1), 85-98. doi:DOI 10.1111/j.1502-3931.1995.tb01596.x

Jol, H. M. (2008). *Ground Penetrating Radar Theory And Applications*: elsevier.

Karegar, M. A., Dixon, T. H., & Engelhart, S. E. (2016). Subsidence along the Atlantic Coast of North America: Insights from GPS and late Holocene relative sea level data. *Geophysical Research Letters, 43*(7), 3126-3133. doi:10.1002/2016gl068015

Katz, C. (2016). As Groundwater Dwindles, a Global Food Shock Looms. Retrieved from https://www.nationalgeographic.com/news/2016/12/groundwater-depletion-global-food-supply/

Kern, A., & Johnson, S. (2009). Improved groundwater resource management through better groundwater monitoring.

Kretschmer, P., & Degens, B. (2012). *Review Of Available Groundwater In The Superficial Aquifer For The Yanchep, Eglinton And Quinns Groundwater Subareas*. Retrieved from

Lasky, R. (1993). *A Structural Study Of The Southern Perth Basin, Western Australia*: Geological Survey of Western Australia.

Leyland, L. A. (2012). *Reinterpretation Of The Hydrogeology Of The Leederville Aquifer : Gnangara Groundwater System / By La Leyland*. Perth, W.A: Dept. of Water.

Lipar, M., & Webb, J. A. (2015). The formation of the pinnacle karst in Pleistocene aeolian calcarenites (Tamala Limestone) in southwestern Australia. *Earth-Science Reviews, 140*, 182-202. doi:10.1016/j.earscirev.2014.11.007

Loke, M., Alfouzan, F. A., & Nawawi, M. (2007). Optimisation of electrode arrays used in 2D resistivity imaging surveys. In *ASEG Extended Abstracts 2007* (pp. 1-4): Australian Society of Exploration Geophysicists (ASEG).

Loke, M. H., & Barker, R. D. (1995). Least-Squares Deconvolution of Apparent Resistivity Pseudosections. *Geophysics, 60*(6), 1682-1690. doi:Doi 10.1190/1.1443900

Loke, M. H., Chambers, J. E., Rucker, D. F., Kuras, O., & Wilkinson, P. B. (2013). Recent developments in the direct-current geoelectrical imaging method. *Journal of Applied Geophysics, 95*, 135-156. doi:10.1016/j.jappgeo.2013.02.017

Loke, M. H., Wilkinson, P. B., Chambers, J. E., & Strutt, M. (2014). Optimized arrays for 2D cross-borehole electrical tomography surveys. *Geophysical Prospecting, 62*(1), 172-189. doi:https://doi.org/10.1111/1365-2478.12072

Loke, M. H., Wilkinson, P. S., Chambers, J. E., Uhlemann, S. S., & Sorensen, J. P. R. (2015). Optimized arrays for 2-D resistivity survey lines with a large number of electrodes. *Journal of Applied Geophysics, 112*(Supplement C), 136-146. doi:10.1016/j.jappgeo.2014.11.011

Martinez, A., & Byrnes, A. P. (2001). *Modeling dielectric-constant values of geologic materials: An aid to ground-penetrating radar data collection and interpretation*: Kansas Geological Survey, University of Kansas.

Martinez, M. L., Intralawan, A., Vazquez, G., Perez-Maqueo, O., Sutton, P., & Landgrave, R. (2007). The coasts of our world: Ecological, economic and social importance. *Ecological Economics, 63*(2-3), 254-272. doi:10.1016/j.ecolecon.2006.10.022

Maxwell, J. C. (1873). *A Treatise on Electricity and Magnetism* (Vol. 1). Cambridge: Cambridge University Press.

McArthur, W. M., & Bettenay, E. J. S. P. C., Australia. (1960). The development and distribution of the soils of the Swan Coastal Plain, Western Australia. *16*.

Meju, M. A. (1994). *Geophysical Data Analysis: Understanding Inverse Problem Theory And Practice* (Vol. 6): Society of Exploration Geophysicists Tulsa,, OK.

Menke, W. (2012a). Chapter 1 - Describing Inverse Problems. In *Geophysical Data Analysis: Discrete Inverse Theory (Third Edition)* (pp. 1-14). Boston: Academic Press.

Meredith, K., Cendon, D. I., Pigois, J. P., Hollins, S., & Jacobsen, G. (2012). Using 14C and 3H to delineate a recharge 'window' into the Perth Basin aquifers, North Gnangara groundwater system, Western Australia. *Sci Total Environ, 414*, 456-469. doi:10.1016/j.scitotenv.2011.10.016

Moore, W. S. (2006). The role of submarine groundwater discharge in coastal biogeochemistry. *Journal of Geochemical Exploration, 88*(1), 389-393. doi:https://doi.org/10.1016/j.gexplo.2005.08.082

Mylroie, J. E. (2013). Coastal Karst Development in Carbonate Rocks. In M. J. Lace & J. E. Mylroie (Eds.), *Coastal Karst Landforms* (pp. 77-109). Dordrecht: Springer Netherlands.

Odhiambo, G. O. (2017). Water scarcity in the Arabian Peninsula and socio-economic implications. *Applied Water Science, 7*(5), 2479-2492. doi:10.1007/s13201-016-0440-1

OECD. (2018). Water Withdrawals (indicator) (Publication no. OECD (2018), Water withdrawals (indicator). doi: 10.1787/17729979-en).

Parker, L. (2016). What You Need to Know About the World's Water Wars. Retrieved from https://www.nationalgeographic.com/news/2016/07/world-aquifers-water-wars/

Pethick, A., Costall, A., Dean, T., & Blylevens, J. (2018). Perth's lost guns. *Preview, 2018*(196), 38-41. doi:10.1071/PVv2018n196p38

Reed, B., Shaw, R., & Chatterton, K. (2013). Technical notes on drinking-water, sanitation and hygiene in emergencies. *Loughborough (UK): World Health Organization, Water, Engineering and Development Centre*.

Rehman, F., Abouelnaga, H. S. O., & Rehman, F. (2016). Estimation of dielectric permittivity, water content, and porosity for environmental engineering and hydrogeological studies using ground penetrating radar, a short review. *Arabian Journal of Geosciences, 9*(4), 1-7. doi:ARTN 312

10.1007/s12517-016-2328-7

Retallack, G. J. (2003). 5.18 - Soils and Global Change in the Carbon Cycle over Geological Time. In H. D. Holland & K. K. Turekian (Eds.), *Treatise on Geochemistry* (pp. 1-28). Oxford: Pergamon.

Richardson, E., Irvine, E., Froend, R., Book, P., Barber, S., & Bonneville, B. (2011). Australian groundwater dependent ecosystems toolbox part 1: assessment framework. *National Water Commission, Canberra*.

Robinson, M., Bristow, C., McKinley, J., & Ruffell, A. 1.5. 5. Ground Penetrating Radar.

Rubin, Y., & Hubbard, S. S. (2006). *Hydrogeophysics* (Vol. 50): Springer Science & Business Media.

Rücker, C., Günther, T., & Wagner, F. M. (2017). pyGIMLi: An open-source library for modelling and inversion in geophysics. *Computers & Geosciences, 109*, 106-123. doi:10.1016/j.cageo.2017.07.011

Salam, R. B., Bekele, E., Hatton, T.J., Pollock, D.W and Lee-Steere, N. (2007). Sustainable Yield of Groundwater of the Gnangara Mound, Perth, Western Australia.

Sayles, R. (1931). Bermuda during the Ice Age: American Academy of Arts and Sciences, v. 66.

Selley, R. C. (2000). *Applied sedimentology*: Elsevier.

Semeniuk, V. (1985). The age structure of a Holocene barrier dune system and its implication for sealevel history reconstructions in southwestern Australia. *Marine Geology, 67*(3), 197-212. doi:https://doi.org/10.1016/0025-3227(85)90092-1

Semeniuk, V., & Johnson, D. P. (1982). Recent and Pleistocene beach/dune sequences, western Australia. *Sedimentary Geology, 32*(4), 301-328. doi:https://doi.org/10.1016/0037-0738(82)90042-2

Semeniuk, V., & Johnson, D. P. (1985). Modern and Pleistocene Rocky Shore Sequences Along Carbonate Coastlines, Southwestern Australia. *Sedimentary Geology, 44*(3-4), 225-261. doi:Doi 10.1016/0037-0738(85)90015-6

Semeniuk, V., & Searle, D. J. (1985). Distribution of Calcrete in Holocene Coastal Sands in Relationship to Climate, Southwestern Australia. *Journal of Sedimentary Petrology, 55*(1), 86-95. Retrieved from <Go to ISI>://WOS:A1985ACM0900011

Semeniuk, V., & Searle, D. J. (1986). Variability of Holocene sealevel history along the southwestern coast of Australia — Evidence for the effect of significant local tectonism. *Marine Geology, 72*(1), 47-58. doi:https://doi.org/10.1016/0025-3227(86)90098-8

Shi, L., & Jiao, J. J. (2014). Seawater intrusion and coastal aquifer management in China: a review. *Environmental Earth Sciences, 72*(8), 2811-2819. doi:10.1007/s12665-014-3186-9

Sinclair Knight Merz. (2012). An assessment of groundwater management and monitoring costs in Australia. *Waterlines Report Series*(90).

Slomp, C. P., & Van Cappellen, P. (2004). Nutrient inputs to the coastal ocean through submarine groundwater discharge: controls and potential impact. *Journal of Hydrology, 295*(1-4), 64-86. doi:10.1016/j.jhydrol.2004.02.018

Smith, D. G., & Jol, H. M. (1995). Ground Penetrating Radar: Antenna frequencies and maxiumum probable depths of penetration in quaternary sediments.

Smith, I. (2004). An assessment of recent trends in Australian rainfall. *Australian Meteorological Magazine, 53*(3), 163-173. Retrieved from <Go to ISI>://WOS:000225717400002

Snieder, R., & Trampert, J. (1999). Inverse problems in geophysics. In *Wavefield inversion* (pp. 119-190): Springer.

Steyl, G., & Dennis, I. (2010). Review of coastal-area aquifers in Africa. *Hydrogeology Journal, 18*(1), 217-225. doi:10.1007/s10040-009-0545-9

Strobach, E. (2013). Hydrogeophysical investigation of water recharge into the Gnangara Mound.

Talbot, C. J., Bennett, E. M., Cassell, K., Hanes, D. M., Minor, E. C., Paerl, H., . . . Xenopoulos, M. A. (2018). The impact of flooding on aquatic ecosystem services. *Biogeochemistry, 141*(3), 439-461. doi:10.1007/s10533-018-0449-7

Topp, G. C., Davis, J. L., & Annan, A. P. (1980). Electromagnetic Determination of Soil-Water Content - Measurements in Coaxial Transmission-Lines. *Water Resources Research, 16*(3), 574-582. doi:DOI 10.1029/WR016i003p00574

Unicef. (2015). Progress on Sanitation and Drinking-Water: 2015 Update and MDG Assessment. *World Health Organization: Geneva, Switzerland*.

W.H.O. (2011). Technical notes on drinking water, sanitation and hygiene in emergencies. *submitted from this web site: http://www. who. int/water_sanitation_health/publications/2011/tn9_how_much _water_en. pdf*.

Ward, S. H., & Society of Exploration Geophysicists. (1990). *Geotechnical And Environmental Geophysics* (Vol. 1): Society of Exploration Geophysicists Tulsa, Oklahoma.

Wassmann, R., Hien, N. X., Hoanh, C. T., & Tuong, T. P. (2004). Sea level rise affecting the Vietnamese Mekong Delta: Water elevation in the flood season and implications for rice production. *Climatic Change, 66*(1-2), 89-107. doi:DOI 10.1023/B:CLIM.0000043144.69736.b7

Water Corporation. (2016a). Perth Seawater Desalination Plant. Retrieved from https://www.watercorporation.com.au/water-supply/our-water-sources/desalination/perth-seawater-desalination-plant

Water Corporation. (2016b). Southern Seawater Desalination Plant. Retrieved from https://www.watercorporation.com.au/water-supply/our-water-sources/desalination/southern-seawater-desalination-plant

Water Corporation. (2017). Our water sources. Retrieved from https://www.watercorporation.com.au/water-supply/our-water-sources?pid=res-wss-np-spw

Water Corporation. (2018). What is the Integrated Water Supply Scheme. Retrieved from https://www.watercorporation.com.au/home/faqs/water-supply-and-services/what-is-the-integrated-water-supply-scheme

Water Corporation. (2019). Groundwater Replenishment Scheme Stage 2 Expansion. Retrieved from https://www.watercorporation.com.au/water-supply/ongoing-works/groundwater-replenishment-scheme

Water Information Reporting database. (2019). Water Information Reporting Database. Retrieved from http://wir.water.wa.gov.au. from W.A Dept. of Water, W.A Dept. Regional Development http://wir.water.wa.gov.au

Waxman, M. H., & Smits, L. J. M. (1968). Electrical Conductivities in Oil-Bearing Shaly Sands. *Society of Petroleum Engineers Journal, 8*(02), 107-122. doi:10.2118/1863-A

Wilkinson, P. B., Loke, M. H., Meldrum, P. I., Chambers, J. E., Kuras, O., Gunn, D. A., & Ogilvy, R. D. (2012). Practical aspects of applied optimized survey design for electrical resistivity tomography. *Geophysical Journal International, 189*(1), 428-440. doi:10.1111/j.1365-246X.2012.05372.x

World Bank (Producer). (2015). Salinity Intrusion in a Changing Climate Scenario will Hit Coastal Bangladesh Hard. Retrieved from https://www.worldbank.org/en/news/feature/2015/02/17/salinity-intrusion-in-changing-climate-scenario-will-hit-coastal-bangladesh-hard

2 Electrical Resistivity Imaging & the Saline Water Interface in High-Quality Coastal Aquifers

This chapter is a research article published in Surveys in Geophysics, May 2018. It includes a comparison of various conventional and combined electrical resistivity imaging arrays with the aim of identifying the hydrogeology of a shallow coastal aquifer. The principle question posed is:

"Can ERI define the saline water interface in different coastal hydrogeological settings"

To answer this question, I provide a full analysis of ERI datasets acquired along Perth's coastal margin, from acquisition to interpretation. I collected over 20 ERI data sets in total. Two of these sites have direct drill-hole support, and five have coincident ground penetrating radar data.

Some of the areas of research include:

1. The recovery of coastal hydrogeology from different arrays using an electrical forward model.
2. The impact of topography on resolving the seawater interface.
3. The outcomes and interpretation of hydrogeological architectures in field data.
4. A systematic analysis of the impact of inversion parameters on imaging outcomes
5. The value of using multiple geophysical methods to identify hydrogeological features.

This paper shows the benefits and limitations of ERI in a coastal setting with clear examples of saline water intrusion close to Perth. I conclude this paper with a table of future research options and the remaining challenges for ERI.

As of 25th November 2020, this paper has been accessed almost 5000 times and cited 11 times since publication on the 14th May 2018.

Author contributions statement can be found in Appendix B (page 204).

Citation

Costall, A., Harris, B., & Pigois, J. P. (2018). Electrical Resistivity Imaging and the Saline Water Interface in High-Quality Coastal Aquifers. Surveys in Geophysics, 39(4), 753-816. doi:10.1007/s10712-018-9468-0

This version contains minor updates to spelling and grammar compared to the published version.

Electrical Resistivity Imaging and the Saline Water Interface in High Quality Coastal Aquifer

Abstract

Population growth and changing climate continue to impact on the availability of natural resources. Urbanization of vulnerable coastal margins can place serious demands on shallow groundwater. Here, groundwater management requires definition of coastal hydrogeology, particularly the seawater interface. Electrical resistivity imaging (ERI) appears to be ideally suited for this purpose. We investigate the challenges and drivers for successful electrical resistivity imaging using field and synthetic experiments. Two decades of seawater intrusion monitoring provide a basis for creating a geo-electrical model suitable for demonstrating the significance of acquisition and inversion parameters on resistivity imaging outcomes. A key observation is that resistivity imaging with combinations of electrode arrays that include dipole–dipole quadrupoles can be configured to illuminate consequential elements of coastal hydrogeology. We extend our analysis of ERI to include a diverse set of hydrogeological settings along more than 100 km of the coastal margin passing the city of Perth, Western Australia. Of particular importance are settings with: (1) a classic seawater wedge in an unconfined aquifer, (2) a shallow unconfined aquifer over an impermeable substrate, and (3) a shallow multi-tiered aquifer system over a conductive impermeable substrate. We also demonstrate a systematic increase in the landward extent of the seawater wedge at sites located progressively closer to the highly urbanized centre of Perth. Based on field and synthetic ERI experiments from a broad range of hydrogeological settings, we tabulate current challenges and future directions for this technology. Our research contributes to resolving the globally significant challenge of managing seawater intrusion at vulnerable coastal margins.

2.1 Introduction

Of the world population in 2003, an estimated 1.2 billion people lived within 100 km of the coast (Small *et al.*, 2003). Population density along coastal margins, shown in Figure 2.1 is higher than average population densities worldwide (Small *et al.*, 2003). As global population increases, the demand on accessible fresh groundwater supplies from shallow coastal aquifers will increase, potentially resulting in the loss of potable water to seawater intrusion. This will have significant human impact (Vorosmarty *et al.*, 2000). In 2001, an estimated 85% of the Australian population were living within 50 km of the coast (Australian Bureau of Statistics, 2006). Densely populated coastlines of Thailand, Vietnam, and Bangladesh are all at high risk of seawater intrusion (Imperial College London, 2015). Populations with the greatest need to access readily available fresh water are often the ones at risk of losing this resource.

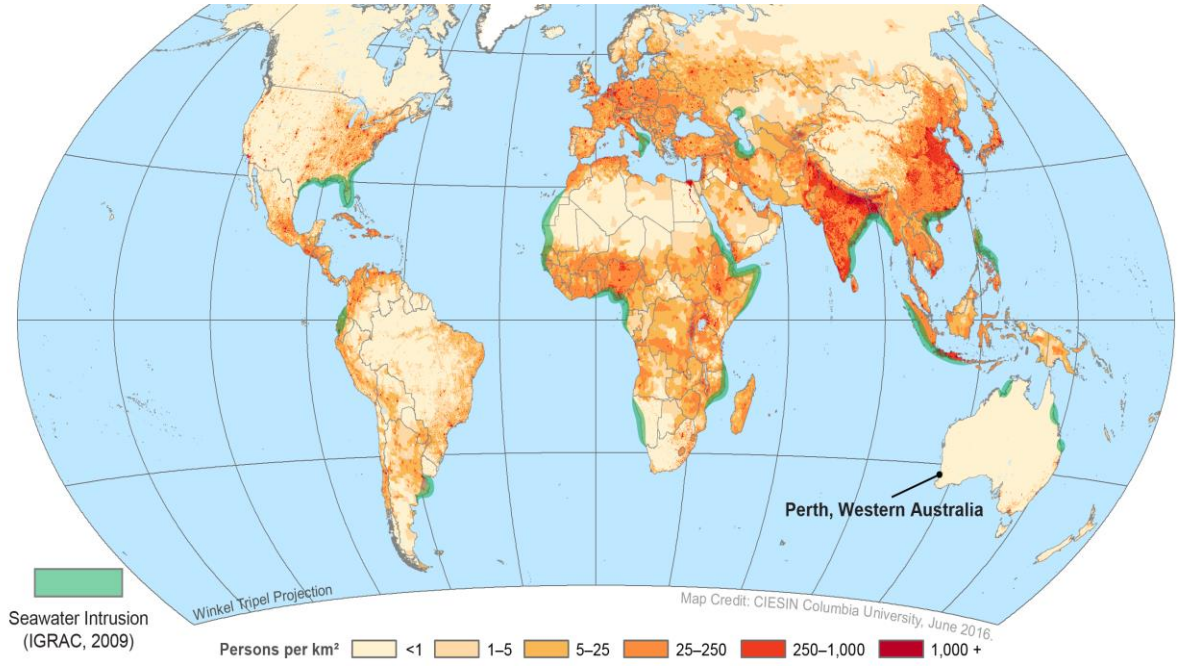

Figure 2.1: World population density map derived from gridded population of the world, version 4 (CIESIN, 2016). Countries with high population density are also at risk of losing readily accessible freshwater reserves to seawater intrusion if management strategies are not developed. Areas shaded in green around coastal margins are already identified as experiencing seawater intrusion and up-coning (Van Weert et al., 2009).

Management systems involving aquifer replenishment, such as the Groundwater Replenishment Schemes (GWRS) in Perth, Western Australia (Water Corporation, 2019) and California, USA (Water-Technology, 2016), can be designed to mitigate seawater intrusion. However, the infrastructure tends to be costly and out of reach for many developing countries. Seawater intrusion monitoring with wells is a necessary and reliable method of recovering water chemistry above and below the seawater interface. However, wells cannot map the full interface geometry and may be difficult to install in highly urbanized areas. Electrical resistivity imaging (ERI) is a potentially valuable, low-cost tool for mapping the seawater interface - but only if the resulting formation conductivity distribution can be interpreted with confidence.

Examples of ERI applied to mapping seawater intrusion use transects that are parallel, or perpendicular to the coastline (Abdul Nassir *et al.*, 2000; de Franco *et al.*, 2009; Koukadaki *et al.*, 2007; Pidlisecky *et al.*, 2016; Wilson *et al.*, 2006). Transects that run parallel to the coastline will not provide any specific geometry of the seawater

interface (e.g. perpendicular transects); however, may still provide useful information regarding changes in aquifer properties (e.g. Pidlisecky *et al.* (2016)).

Current literature on ERI and the seawater interface suggest that many challenges and knowledge gaps remain. The consequence is that ERI is applied with uncertainty regarding: (1) the connection between the inverted and true subsurface conductivity distribution, and (2) how the geo-electrical setting connects to coastal hydrogeology, particularly the geometry of the seawater interface.

For example, we found no systematic studies of ERI for a high quality, shallow coastal aquifer underlain by an impermeable substrate. This broad class of coastal aquifer system is common worldwide (e.g. Biscayne aquifer, Florida (Sonenshein, 1995), Yarkon-Taninim aquifer, Israel (Paster *et al.*, 2006; Schwarz *et al.*, 2016)). We also found no systematic comparisons of numerical modelling and field ERI experiments for a diverse aquifer system, that include detailed topography and accurate models of salinity based on seawater intrusion monitoring (SIM) wells.

Of particular interest to our study is the scenario where a high-quality, high-permeability coastal aquifer overlies a shallow clayey substrate. This is common along coastal margins, and we will show that this presents unique challenges for the application of electrical resistivity imaging. A typical setting consists of four high-contrast geo-electrical boundaries:

(i) ***The air interface***: The boundary between the ground and air represents a near-infinite change in electrical resistivity. Topographic relief along limestone-dominated coastal margins can vary significantly, from undulating sand dunes, to steep cliffs, to elongate beachfronts. Accurate elevations must be included during inversion to compute geometric factors and include the effects of the topography on the electric field distribution.

(ii) ***The water table interface***: The high electrical resistivity of the unsaturated (i.e., vadose) zone rapidly decreases across a capillary fringe as pore spaces become saturated with groundwater. This interface is near horizontal in extremely high permeability unconfined aquifers but may extend over several meters in less-permeable aquifers.

(iii) ***The seawater interface****:* The transition zone between the high conductivity aquifer saturated with seawater, and electrically resistive aquifer saturated with fresh groundwater can be sharp, existing over tens of centimetres, to extremely diffuse, existing over many kilometres, depending on the aquifer conditions.

(iv) ***The confining substrate interface:*** The clay-rich confining substrate typically prevents groundwater from flowing between the superficial aquifer and any aquifers below it. The clay is often more electrically conductive than the saturated aquifer above and may be influenced by the groundwater chemistry in the aquifers above and below.

Superimposed onto these four boundaries are contrasts resulting from variation in lithology. We suspect that lithological changes within the aquifer present a second-order impact on resistivity imaging compared to the contrasts at each of these four interfaces. One caveat is where shallow conductive clays exist close to surface. Such layers will have a strong influence on the outcome of ERI. We later provide many field and numerical experiments to explore the above.

Constraints on ERI inversion can be deployed if data from drilling, wireline logging, and/or other geophysical methods are available. Where multiple geophysical datasets exist, joint, collaborative and cooperative inversion strategies can be deployed (e.g., (Gallardo *et al.*, 2007, 2011; Le *et al.*, 2016; Marker *et al.*, 2015; Soueid Ahmed *et al.*, 2015; Takam Takougang *et al.*, 2015; J. Zhou *et al.*, 2014). We will provide field-based examples of how characterization of coastal aquifer systems can be advanced by integration of ERI with complimentary data, such as ground penetrating radar (GPR).

Ultimately, resistivity imaging and any near-surface hydro geophysical method should assist predictive transport modelling processes and contribute to decision making for long-term management of high-quality coastal groundwater resources. Our research highlights many practical applications of geophysical methods applied to seawater intrusion monitoring, with distinct benefits for groundwater management decisions.

2.1.1 Background: The Seawater Interface

The characteristic wedge shape of the seawater interface is the combined result of many factors. These include (1) the density contrasts between fresh groundwater and seawater, (2) the distribution of hydraulic properties, (3) the rate of groundwater flow towards the ocean, (4) rainfall recharge, and (5) the distribution of groundwater abstraction and recharge.

Seawater is approximately 2.5% denser than fresh water due to dissolved solids (i.e., mostly NaCl). Denser seawater tends to drive beneath the fresh water in a steady-state mixing environment (Pool *et al.*, 2011; Verruijt, 1968; Wentworth, 1947). The geometry of the theoretical seawater wedge can be obtained from the Ghyben-Herzberg approximation (Verruijt, 1968), and is a naturally occurring result of the density difference between saline and fresh water.

The ‘mixing zone’ describes the zone of variable salinity where the saline water and fresh water interact. Models for the mixing zone have historically used a simplified sharp interface which differentiates the seawater from fresh groundwater (Verruijt, 1968). Modern approximations are based on density-dependent solute-transport modelling, which accounts for variable density mixing zones (Abarca *et al.*, 2009; H.-J. G. Diersch, 2014; C. Lu, 2011; C. H. Lu *et al.*, 2013; National Water Commission, 2012; Werner *et al.*, 2013).

The width of this mixing zone can be highly variable, from millimetres in lab-based experiments (Abarca *et al.*, 2009), to kilometres in field-scale examples. Some examples include the Everglades National Park, USA, where a wide mixing zone of approximately 6 to 28 km is identified by hydrogeological tracers (Price *et al.*, 2003), and in Laizhou Bay, China where a zone approximately 1.5 to 6 km is identified (Wu *et al.*, 1993).

Figure 2.2 provides a schematic for three shallow coastal hydrogeological settings. These include (1) an unconfined aquifer, (2) an unconfined aquifer above an impermeable substrate, and (3) an aquifer containing a shallow semipervious layer above a low permeability substrate. We will analyse field ERI experiments for all these settings.

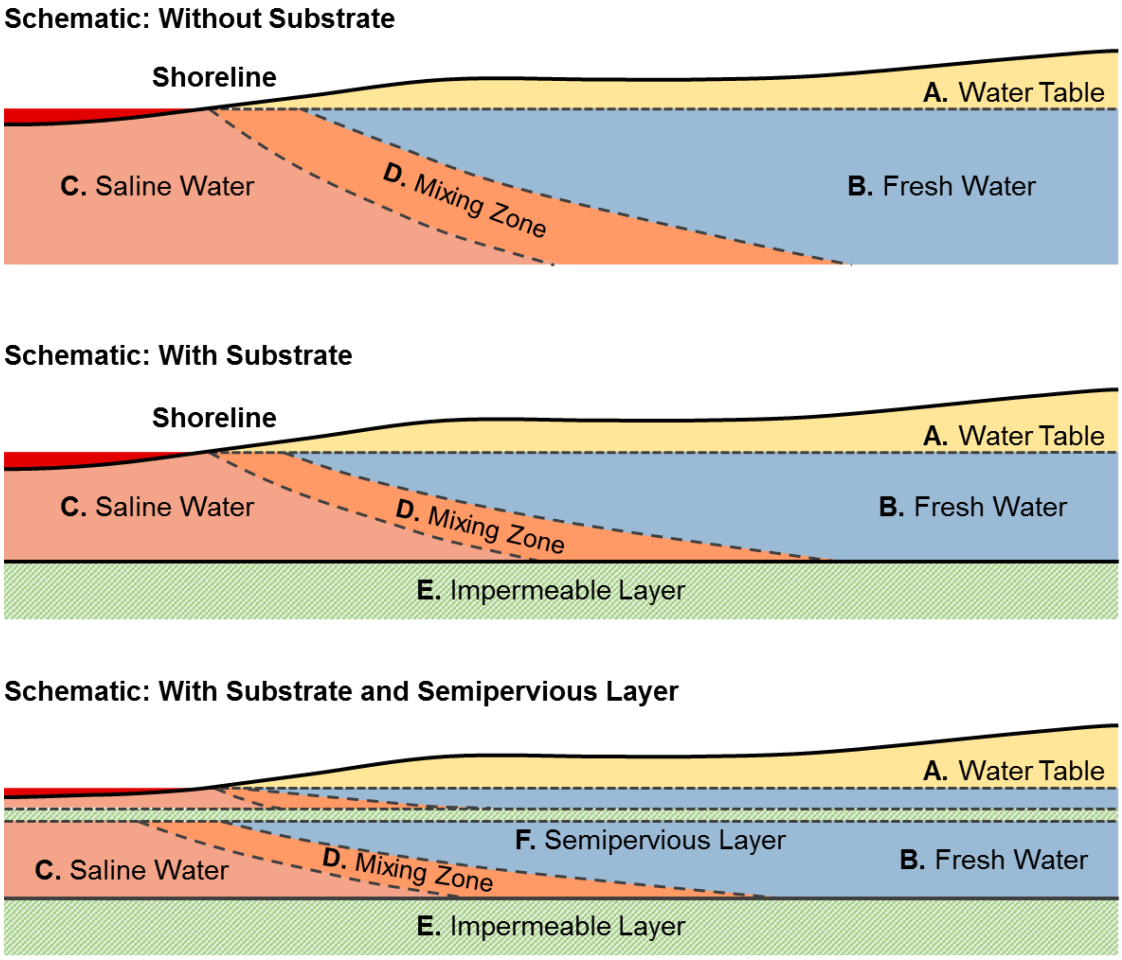

Figure 2.2: Schematic representation of three shallow coastal hydrogeological systems and respective seawater interface geometries for recovery by ERI methods. Key hydrogeological zones to be resolved by ERI are A: the phreatic water table, B: the saturated potable groundwater, C: the saturated saline groundwater, D: the mixing zone, E: an impermeable substrate, and F: a thin semi-pervious intra-aquifer clayey layer.

2.1.2 Background: Electrical Resistivity Imaging

Electrical resistivity imaging (ERI) is a geophysical method used to estimate subsurface electrical properties (Dahlin, 2001; Herman, 2001; Samouelian *et al.*, 2005). An electrical current is injected into the earth between a pair of electrodes and voltage is measured between another pair of electrodes. Multi-channel instruments allow for the rapid acquisition of various electrode configurations. A typical multi-channel array resistivity survey consists of electrodes connected to a transmitter/receiver system via a multi-core cable. The apparent resistivity (ρ) is calculated for every electrode quadrupole by equation 4.1.

$$\rho = k\frac{V}{I} \tag{2.1}$$

Where V is voltage, I is current, and k is geometric factor.

There are many different electrode configurations (Dahlin *et al.*, 2004). Some standard configurations are shown in Figure 2.3. The multiple-gradient array is relatively modern and suited to multi-channel acquisition. It has high signal-to-noise characteristics, and is similar to the pole-dipole array for some quadrupole arrangements, with other characteristics similar to a Schlumberger array (Dahlin *et al.*, 2006; M. H. Loke *et al.*, 2013).

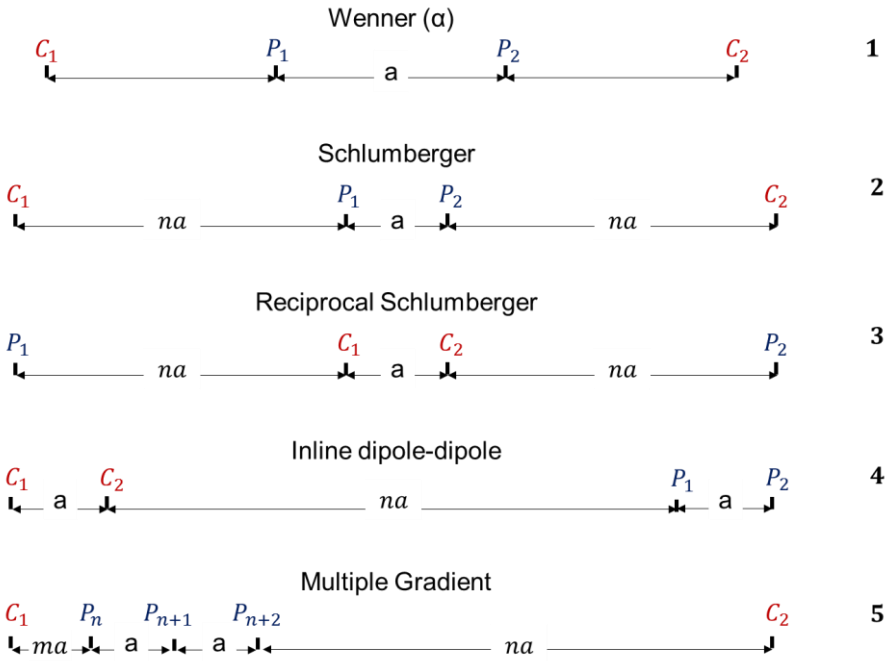

Figure 2.3: Schematic showing common electrical resistivity imaging arrays.Arrays 3, 4, and 5 are suitable for multi-channel acquisition, and thus efficient field acquisition. Current electrodes are color-coded red, while potential electrodes are in blue. The letter 'a' denotes unit spacing, whilst 'na' and 'ma' denote multiples of 'a' associated with various array parameters.

Multi-channel ERI acquisition systems are common in many exploration settings. Several authors consider methods for efficiently combining ERI arrays to improve subsurface illumination (Athanasiou *et al.*, 2007; Ishola *et al.*, 2015; M. Loke *et al.*, 2007). For any given set of electrodes, the total possible number of non-reciprocal electrode combinations is given below (Noel *et al.*, 1991; Stummer *et al.*, 2002) where *n* represents the number of electrodes present in the array.

$$N_{combinations} = \frac{[n*(n-1)*(n-2)*(n-3)]}{8} \tag{2.2}$$

For example, a 24-electrode cable has 31,878 possible 4-electrode arrangements. However, acquiring all of these electrode arrangements is prohibitively time-consuming and does not guarantee a superior outcome.

Optimized arrays, which seek the optimum ERI resolution with a given number of electrodes, is an active field of research (M. H. Loke, Wilkinson, Chambers, *et al.*, 2014; M. H. Loke, Wilkinson, Uhlemann, *et al.*, 2014; M. H. Loke, Wilkinson, *et al.*, 2015; Stummer *et al.*, 2002; Szalai *et al.*, 2013; Wilkinson *et al.*, 2012; Wilkinson *et al.*, 2006). Several methods of optimization exist, however the analysis of resolution matrices (i.e., 'Compare-R') is effective and popular. This method finds the minimum number of quadrupoles required to maximize the sum of the resolution matrix elements for a given number of electrodes (M. H. Loke *et al.*, 2013.). Some practical aspects of the optimized arrays, such as electrode polarization effects and noise mitigation are addressed by Wilkinson *et al.* (2012).

Depth of investigation for ERI is generally related to electrode separation and is < 30% of the total array length (Roy *et al.*, 1971; Szalai *et al.*, 2009). Edwards (1977) suggests that the effective median depth of investigation of a dipole-dipole array is between 14 and 22% of total line length. The actual depth-of-investigation is the result of many variables, such as electrode configuration, geo-electrical setting, signal-to-noise ratio during acquisition, and the inversion strategy deployed. Modern approximations for depth-of-investigation are made with an explicit depth-of-investigation algorithm (Christiansen *et al.*, 2012; Oldenburg *et al.*, 1999).

A comparison of electrode configurations for a range of geo-electrical settings, including analysis over a very shallow seawater interface (< 5 m depth) model, is provided by Martorana *et al.* (2009). They suggest that the dipole-dipole array is advantageous for resolving the seawater interface; however, the model study does not include topographic relief, the field examples do not span a full seawater interface, and no well data exists to verify the inferred results. We note that the modelled substrate is extremely conductive (0.2 Ω m).

The general effects of topography on outcomes from commonly used ERI arrays is examined by (Fox *et al.*, 1980; P. I. Tsourlos *et al.*, 1999). They find that incorporation of topography effects is essential. P. I. Tsourlos *et al.* (1999) concludes that slope angles of > 10° can produce significant and misleading artefacts in ERI derived conductivity images where topography is not considered. Historic 2D inversion approaches using rectangular blocks with a finite-difference inversion scheme are unable to model steep topographic changes. Modern 2D inversion software use finite-element schemes with a variety of shapes, such as triangles, hexagons, and warped rectangles, to reproduce steep or complicated surface geometries (C. Rücker *et al.*, 2006). Sloping beachfronts, limestone cliffs, and vegetated sand dunes are all common topographic features along coastal margins, and we include topography in all our analyses of ERI and coastal hydrogeology.

2.1.3 Background: Location, hydrogeology and an ERI Control Site

The coastal margin of Perth, Western Australia, has and will continue to undergo rapid urbanization. It is endowed with a range of shallow unconfined high-quality freshwater aquifer systems. This stretch of coastline is well suited for testing ERI, as a broad range of aquifer geometries exist, and seawater intrusion monitoring wells have measured the landward movement of seawater interface. Figure 2.4 show seven of the ERI test sites shown throughout this research. Many more transects were collected throughout the course of this research; however, this set provides a notable range of aquifer geometries and imaging outcomes.

Our work is presented in three parts. The first provides an analysis of ERI with numerical and field-based experiments at a long-term seawater intrusion monitoring site. In the second, well-logs and GPR highlight challenges for ERI in a complex geo-electrical and hydrogeological environment. In the third part, we compare ERI outcomes at a diverse range of coastal hydrogeological settings along approximately 100 km length of coastline. Here ERI is deployed at locations with (1) rapid urbanization in recent history, (2) historically high rates of shallow groundwater abstraction, and (3) undisturbed native coastal vegetation.

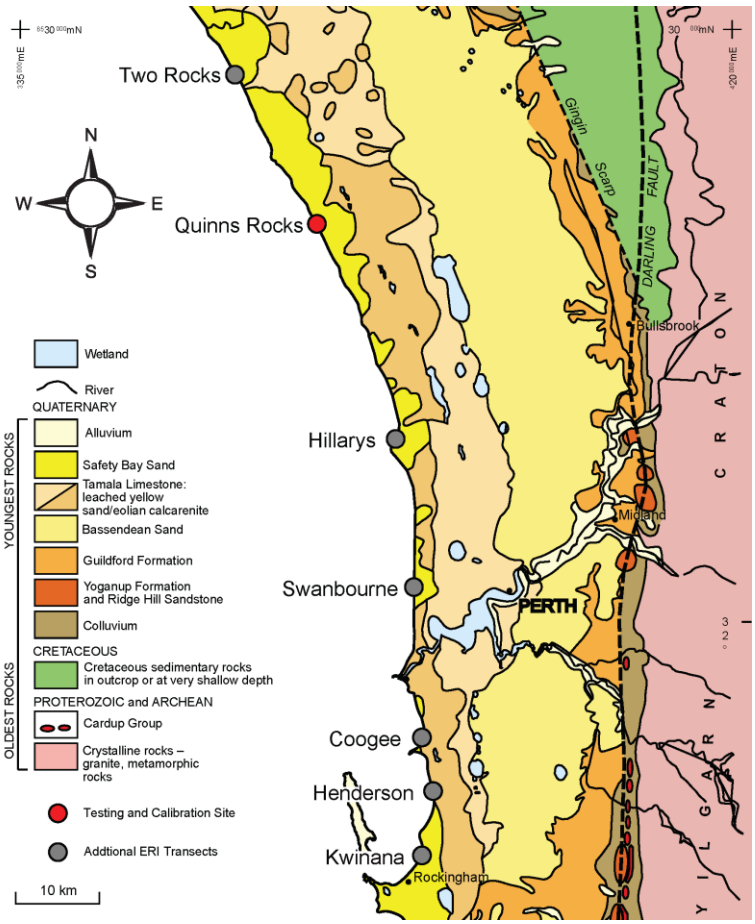

Figure 2.4: Map showing the location of ERI transects with respect to shallow geology of the Perth Basin, including the Quinns Rocks research and calibration site (shown in red). Each transect is separated by approximately 15 to 20 km, covering a total distance of approximately 100 km along the coastline of Perth, Western Australia. These transects cover a wide range of settings, with Two Rocks being a relatively undeveloped area, while the others are in highly urbanized areas. The hydrogeological settings also range from a thin (less than 30 m) high permeability aquifer over clayey substrate (e.g. Quinns Rocks, Hillarys, Swanbourne) to an aquifer over 150 m thick (e.g. Two Rocks), and finally a high-permeability unconfined aquifer with shallow clayey layers and shale substrate (e.g. Coogee, Henderson, Kwinana). Base image courtesy of the Geoscience and Resource Strategy Division, Department of Mines, Industry Regulation and Safety, modified from Gozzard (2007) by the authors with permission. © State of Western Australia 2018

2.2 Part 1: ERI – A control site for field and numerical experiments

The Quinns Rocks transect is ideally suited as an ERI research and calibration site. It is located approximately 30 km north of the Perth, Western Australia. This site has a set of established seawater intrusion monitoring (SIM) wells, with groundwater chemistry collected from 1990 to the present day. The local area has undergone extensive and rapid development over this period accompanied by significant population growth (~1,932 to 20,070 people) from 1990 to 2015 (Australian Bureau of Statistics, 2018).

Records from the SIM wells suggest that the seawater interface has moved inland over the last 20 years and is currently located between SIM 3-90 and SIM 6-90, over 180 m from the shoreline. The combination of borehole logs and water chemistry information provides the necessary inputs for creation of numerical models of subsurface groundwater and formation conductivity estimates. Synthetic ERI datasets were computed for the formation conductivity models using a variety of electrode arrays, where after identical parameters were used in the field transect.

Figure 2.5 shows the relative position of the SIM wells and the field ERI transect. Multiple ERI surveys were acquired alongside a pathway located approximately perpendicular to the shoreline. No other continuous pathways were available for use and no access was permitted in the local declared rare flora reserve surrounding the SIM wells (Ecoscape Australia Pty Ltd, 2004). The pathway is a regularly maintained pedestrian walkway, which provides reliable long-term access to the area for repeat geophysical surveys without risk of disturbance to the highly sensitive local bushland.

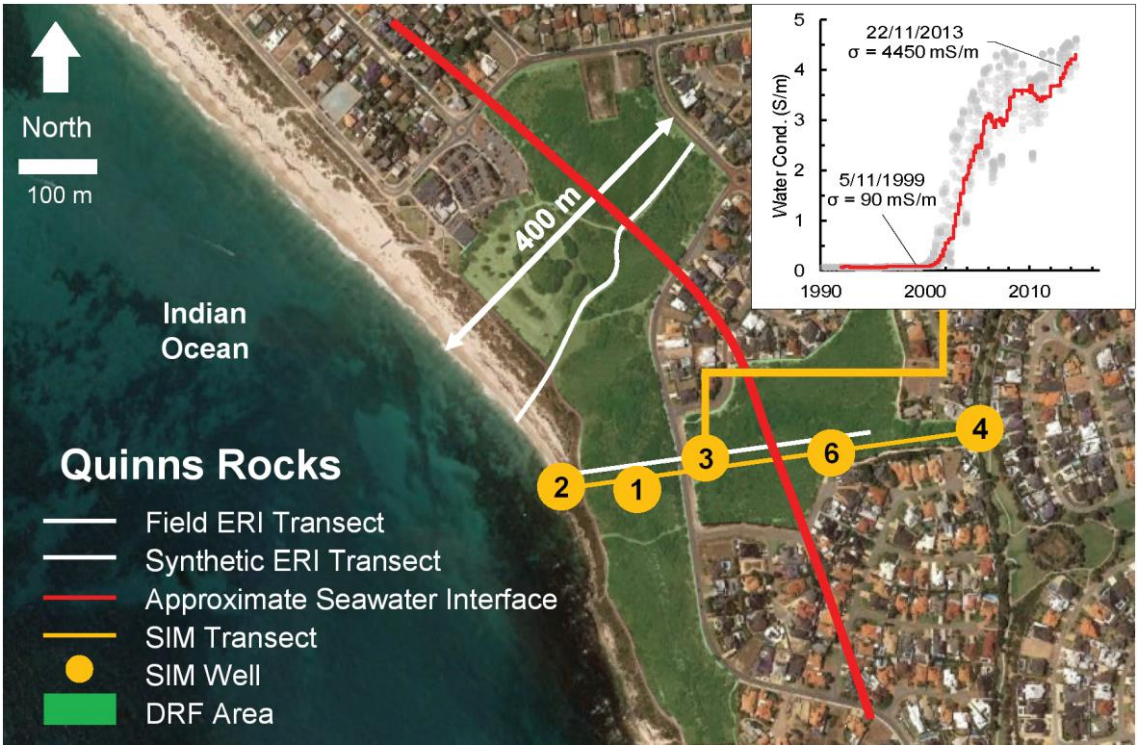

Figure 2.5: Photographic image showing the field ERI research transect and SIM wells at Quinns Rocks, Perth, Western Australia. Information from the SIM wells is used to build numerical models of both water and formation electrical conductivity. The field ERI transect runs along a pedestrian walkway, indicated by the solid white line. The graph inserted in the upper right-hand corner of the image provide a measure of seawater intrusion through time in SIM-3. The groundwater in the well was potable until approximately 2001 after which the seawater interface passed SIM-3, and salinity rapidly approached that of seawater. Prior to 1990, there were few dwellings in the Quinns Rocks area. (Base satellite imagery ©2017 Google Earth.)

2.2.1 An ERI Calibration Site: Hydrogeology and the Seawater Interface

The sedimentary facies of the near-shore environment in the Quinns Rocks area is primarily Tamala Limestone and Safety Bay Sand (Davidson, 1995). The Tamala Limestone is an expansive reach of Quaternary eolianite limestone found along the majority of coastal Western Australia. Hydraulic conductivity values associated with the Tamala Limestone from regional groundwater models are 75 to 3000 m/day, with values at Quinns Rocks ranging from 70 to 235 m/day (Kretschmer *et al.*, 2012; AJ Smith *et al.*, 2012). The wide range of values throughout the Tamala Limestone is attributed to well-developed dual-pore systems, e.g. cave systems, and secondary porosity development, e.g. (AJ Smith *et al.*, 2012) in particular areas along the coastal margin of Perth.

A hydrogeological seal of glauconitic clay and silty-shale was reported approximately 30 meters below sea level (m BSL) in lithological logs from the SIM-6 and SIM-4 wells (Water Information Reporting database, 2019). This is likely to be the Pinjar Member (Davidson, 1995; Ivkovic *et al.*, 2012; Leyland, 2012), and we refer to this layer as the clayey substrate.

The Tamala Limestone can be observed as outcrop throughout much of Perth. A sample of the limestone from the reference site was recovered. Laboratory measurements suggest a formation factor of approximately 14, and porosity of close to 35%, consistent with suggested values for the Tamala Limestone near Quinns Rocks (AJ Smith *et al.*, 2012; Anthony Smith *et al.*, 2012). These values are used to convert distribution of groundwater electrical conductivity to formation conductivity.

Figure 2.6 shows the subsurface hydrogeology for a synthetic seawater interface transect across the SIM wells at Quinns Rocks. It includes an interpretation of the seawater interface geometry from 1990 and 2017, and the associated formation resistivity distribution based on the formation factor recovered from the sample. The formation conductivity model in Figure 2.6 is used for numerical simulation of ERI data, which are compared with outcomes from a series of field ERI experiments completed at the Quinns Rocks site.

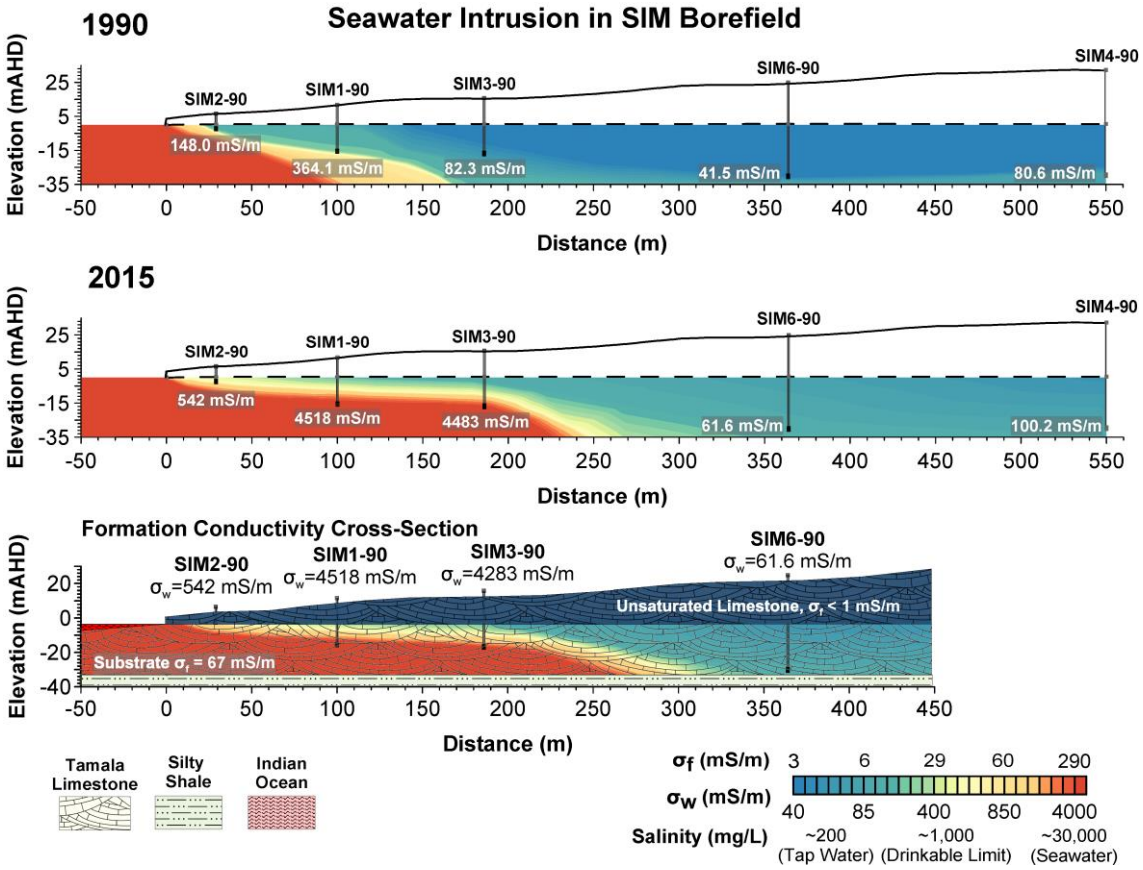

Figure 2.6: Images of Quinns Rocks groundwater solute concertation for 1990 and 2015 accompanied by a geo-electrical cross-section through the series of seawater intrusion monitoring (SIM) wells located approximately perpendicular to the coastline at the ERI control site. The model is based on geological logging, wireline logging, and water chemistry information from the SIM wells. A fifth well, SIM 4-90, is located approximately 100 m further inland and shows measurements similar to that of SIM 6.

2.2.2 ERI Inversion Strategies

The degree to which resistivity imaging can match the true subsurface resistivity distribution is driven by a combination of acquisition parameters and inversion strategy. Many strategies are possible; however, to progress our analysis across a range of geo-electrical settings we select a limited number of strategies. Several appendices are included to explicitly define inversion parameters and provide the imaging outcomes from alternative inversion strategies.

We use RES2DMOD (M. H. Loke, 2016b) for forward modelling and RES2DINV (M. H. Loke, 2016a) for inversion in this research. RES2DINV is based on a modified Occam-style 2D ERI Inversion code (M. Loke, 2003). Table 2.1 contains a summary of the parameters used to invert field and synthetic data. 2.7Appendix A.3 provides a full list of the standard inversion parameters.

Table 2.1: Summary of parameters used for inversion field and synthetic ERI data.

Parameter	Value
Initial damping factor	0.15
Minimum damping factor	0.02
Number of nodes between electrodes	8 (4 nodes, Refined mesh)
Layer thickness increase with depth	1.05
First layer thickness (% of unit step)	0.25
Damping factor increase with depth	1.05
Robust data constraint cut-off	0.05
Model block width	½ electrode step
RMS convergence threshold	5%
Line search RMS change limit	0.5
Reference resistivity for half-space	Average value of 1st iteration

We test a range of ERI inversion parameters, particularly the cut-off factor, used within RES2DINV (M. H. Loke, 2016a), and produce extensive sets of numerical resistivity imaging outcomes. These allow comparison of outcomes from different cut-off factors for the geo-electrical model shown earlier in Figure 2.6. These set of images are provided in 2.7 and reveal the impact of systematically changing roughness constraints. They also assist in selecting our "standard" parameters as shown in 2.7Appendix A.3.

We also identify an alternative inversion pathway with sufficient merit to reproduce all inversion outcomes. These are provided in 2.7Appendix A.4. For the alternate strategy, we used an 'expanded model' and a 'diagonal roughness filter'. Our standard inversion parameters represent an approach commonly deployed in literature (e.g. (Binley *et al.*, 2015; Carriere *et al.*, 2013; Krishnaraj *et al.*, 2014; M. H. Loke *et al.*, 2013)), which use a trapezoidal model (i.e., not expanded). This limits the model cells to pseudo-depth points so creating the familiar tapered edges on resistivity images. However, limiting the model in such a manner may introduce edge artefacts (M. Loke, 2016). The "standard" approach with trapezoidal model does reduce the total number of model cells; however, modern computers can handle the demands of an expanded 2D section.

As explained by Farquharson (2007), the normal roughness filter only has components in the *x* and *y* directions. This results in vertically or horizontally aligned structures (M. Loke, 2016). The diagonal roughness filter introduces two additional smoothing constraints in the diagonally up, and diagonally down directions (Farquharson, 2007). This approach can effectively generate dipping and angled interfaces while using the L1 model norm. 2.7Appendix A.4 provides resistivity imaging from the alternative inversion strategy, along with images expressing ERI resolution distribution and graphical representations of inversion misfit.

We note that all data files, including field data, model data, and inversion results, are available for the reader and we encourage comparison with our results

2.2.3 ERI Control Site: Numerical Experiments

The geoelectrical model shown in Figure 2.6 provides the basis for our analysis of ERI along coastal margins. For this setting, we have computed synthetic ERI data for Wenner, Schlumberger, and dipole-dipole electrode arrays with the parameters set out in Table 2.2. ERI inversion outcomes are assessed for individual arrays and combinations of arrays. We later compare these numerical outcomes with those from field measurements at the calibration site.

Of particular interest is a comparison of artefacts that may arise from unconstrained inversion for the three common electrode configurations, as well as any improvement or deterioration in ERI imaging that may occur by inverting combinations of electrode configurations. Note that the Schlumberger array we refer to below is the hybrid Wenner-Schlumberger configuration as described in Pazdirek *et al.* (1996).

Table 2.2: Numerical modelling array parameters from RES2DMOD

Test	Array	#No. Sensors	n	a	#No. Points	Max. K.
Model (without topography)	Wenner	44	-	14	301	10000
	Schlumberger	44	17	14	1037	10000*
	Inline dipole-dipole	44	5	14	773	10000*
Model (with topography)	Wenner	55	-	18	477	10000
	Schlumberger	55	17	18	1716	10000*
	Inline dipole-dipole	55	5	18	1168	10000*

*Limiting factor for total number of points

Figure 2.7 shows the ERI inversion outcomes for the geo-electrical model presented earlier in Figure 2.6. Our first example excludes topography. We note several examples in literature where ERI has been presented but neglects the influence of topography along coastal margins (Heen *et al.*, 2017; Igroufa *et al.*, 2010; Krishnaraj *et al.*, 2014). We take the opportunity to highlight the significance of both topographic relief and electrode configuration on ERI inversion with the numerical example.

From Figure 2.7, the inadequacies of the classic Wenner array are immediately clear as it fails to recover the substrate below the seawater wedge. Both dipole-dipole and Schlumberger arrays overshoot the substrate boundary below the wedge. Notice that the position of the substrate below the high-resistivity fresher groundwater appears well resolved in all cases. However, the existence and depth of the lower substrate could be misinterpreted from resistivity images derived from the Wenner synthetic data. The shape and resistivity of the seawater wedge are most accurately recovered from the dipole-dipole data.

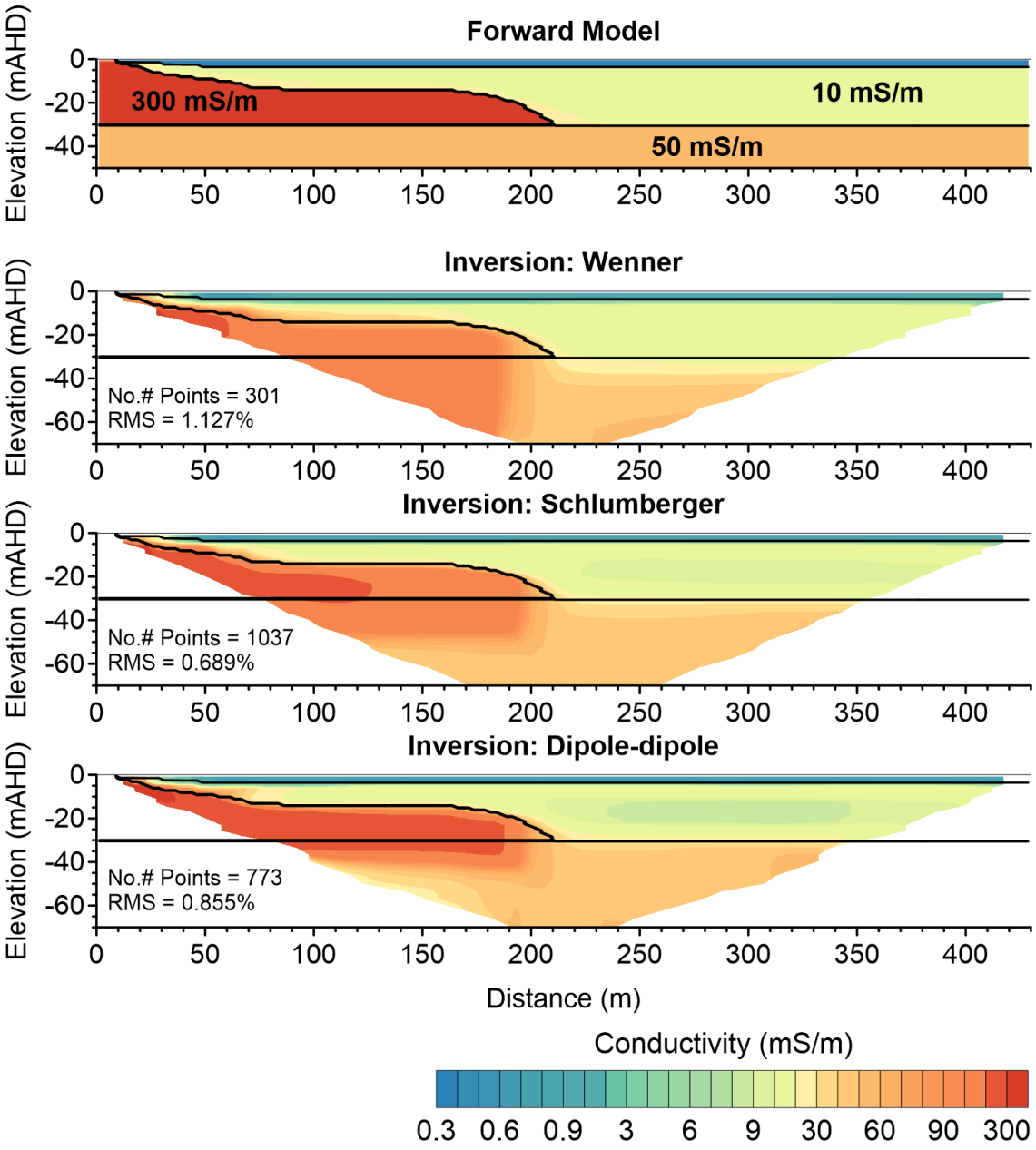

Figure 2.7: Images showing the forward geo-electrical model of formation conductivity distribution plus three inverted conductivity sections. The inverted sections are computed from synthetic ERI data of the forward model for different electrode configurations. The forward geo-electrical model is based on water chemistry and lithology from the Quinns Rocks seawater monitoring wells (i.e., Figure 2.6). The three survey configurations compared are (i) Wenner (top), (ii) Schlumberger (middle) and (iii) dipole-dipole (lower). Inversions for these models are unconstrained. The general location of the seawater interface is recovered by inversion for each example given; however, the dipole-dipole survey produced the truest representation of the full geometry of the seawater interface and lower substrate.

There are many ways to represent how well an inversion process has fit the numerical data to measurements. Global RMS error is necessary but is rarely sufficient. We will highlight some additional representations. Firstly, an appreciation of the spatial distribution of misfit can be obtained if model and field apparent resistivity pseudo-plots are compared and accompanied by an image of mismatch percent against pseudo-depth. The distribution of relative mismatch between observed and calculated values (i.e., measured data and inversion output) is a valuable tool for quality control and assessment of model fit. They may reveal an unexpected distribution of misfit or the existence of outlier data points.

We provide examples of the mismatch distribution for the forward-modelled Wenner, Schlumberger and dipole-dipole experiments in Figure 2.7 and later provide an example of the same mismatch representations for the Quinns Rocks field ERI data.

Figure 2.8 to Figure 2.13 show pseudo-plots for the observed and calculated data, as well as the percentage misfit for each data point. As expected for the forward model examples, the residual errors are small, with a Gaussian distribution, and possess an excellent match between model apparent resistivity and measured (i.e., simulated field measurements) in the cross plot. Higher levels of misfit occur in the shallow subsurface, consistent with the shallow high contrast boundary present in the forward model. The limited data density in the near-surface with the Wenner and Wenner-Schlumberger arrays are the likely source of the misfit.

We note that the Delaunay triangulation used to present the misfit plots provides a generally accurate representation of the distribution, particular where points are regularly distributed (e.g. Figure 2.9). Some electrode configurations, such as overlapping ‘n’ levels of the dipole-dipole configuration, present irregular pseudo-depth plotting points. Triangulation across these points tend to produced minor visual artefacts, such as unexpected patterns or smeared error distributions (e.g. Figure 2.10 and Figure 2.11).

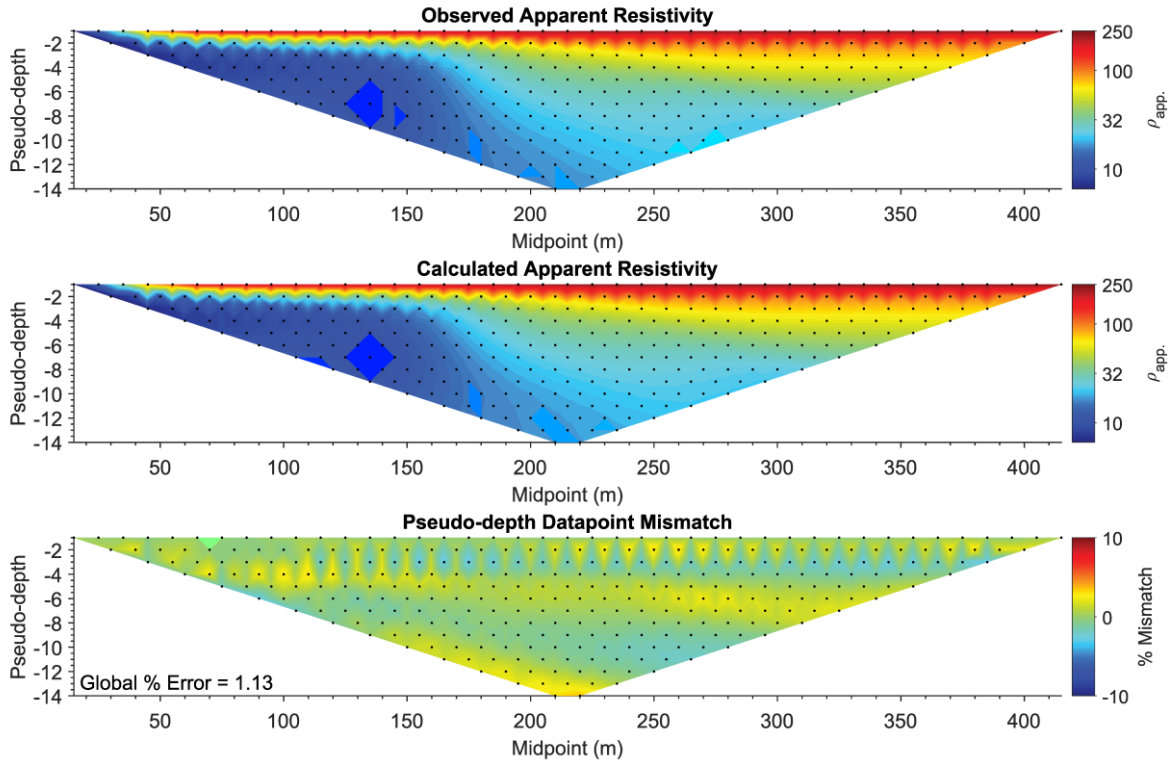

Figure 2.8: Pseudo-sections for the observed (top), and calculated (middle) apparent resistivity, and percentage mismatch (bottom) for modelled Wenner configuration. This data is calculated for a model with a shallow resistive layer, a conductive seawater wedge, and conductive lower substrate, as shown in Figure 2.7. Areas of largest misfit exist near the seawater wedge and shallow resistive interfaces.

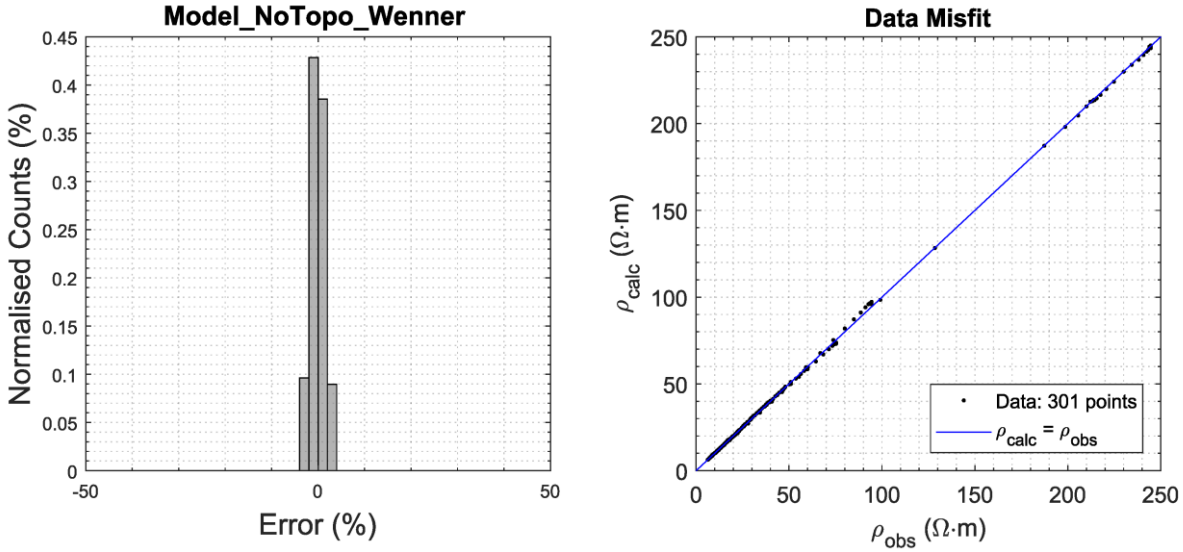

Figure 2.9: Plots showing the distribution of error and misfit between observed and calculated data.These plots describe the inversion of ERI data computed over the synthetic forward model without topography, using a Wenner configuration. The distribution of errors is Gaussian, and observations are consistent with calculated measurements.

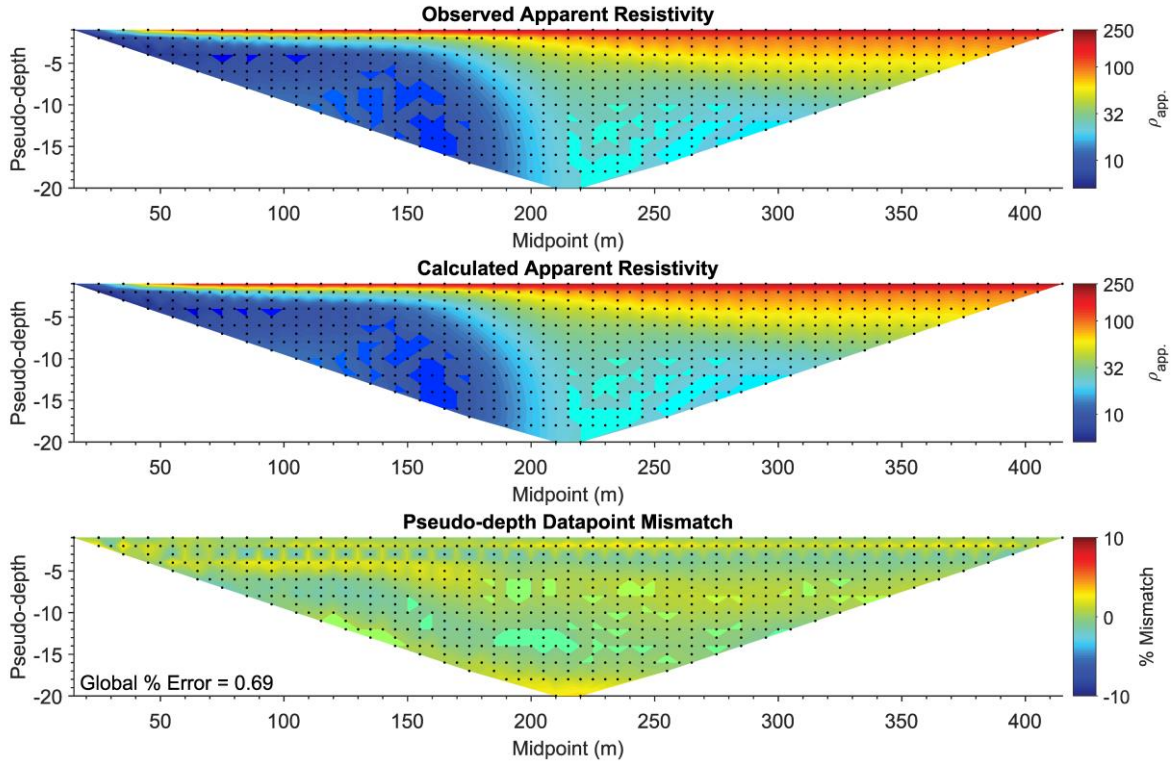

Figure 2.10: Pseudo-sections for the observed (top), and calculated apparent resistivity (middle), and percentage mismatch (bottom) between observed and calculated values for the Schlumberger configuration.

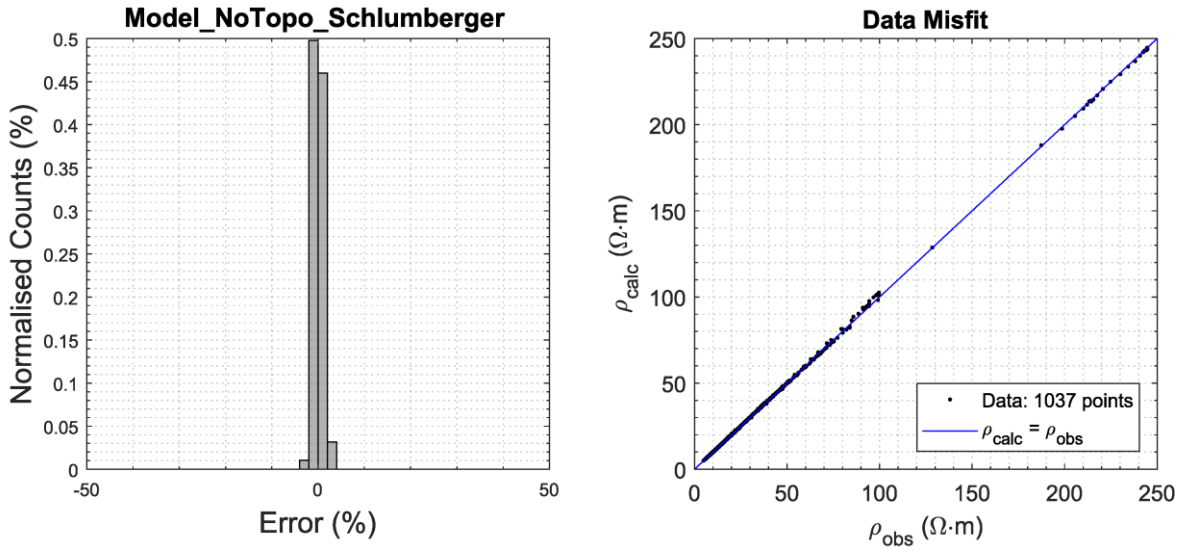

Figure 2.11: Plots showing the distribution of error and misfit between observed and calculated data for a Schlumberger configuration without topography. Elevated levels of misfit are observed in the high resistivity shallow subsurface, where the high contrast boundary exists (e.g., water table)

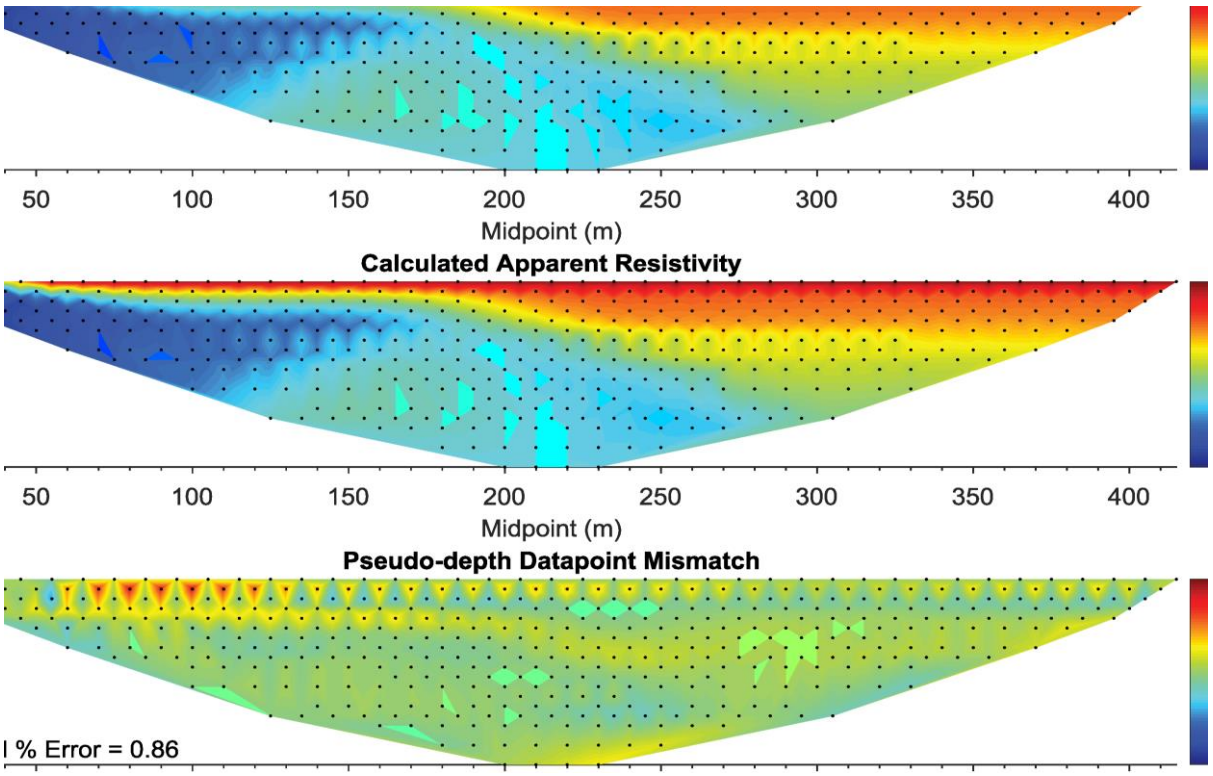

Figure 2.12: Pseudosections for the observed (top), and calculated apparent resistivity (middle), and percentage mismatch (bottom) between observed and calculated values for the dipole-dipole configuration.This model includes a shallow resistive layer, a conductive seawater wedge, and conductive lower substrate, and is without topography. Areas of largest misfit exist near the seawater wedge and shallow resistive interfaces.

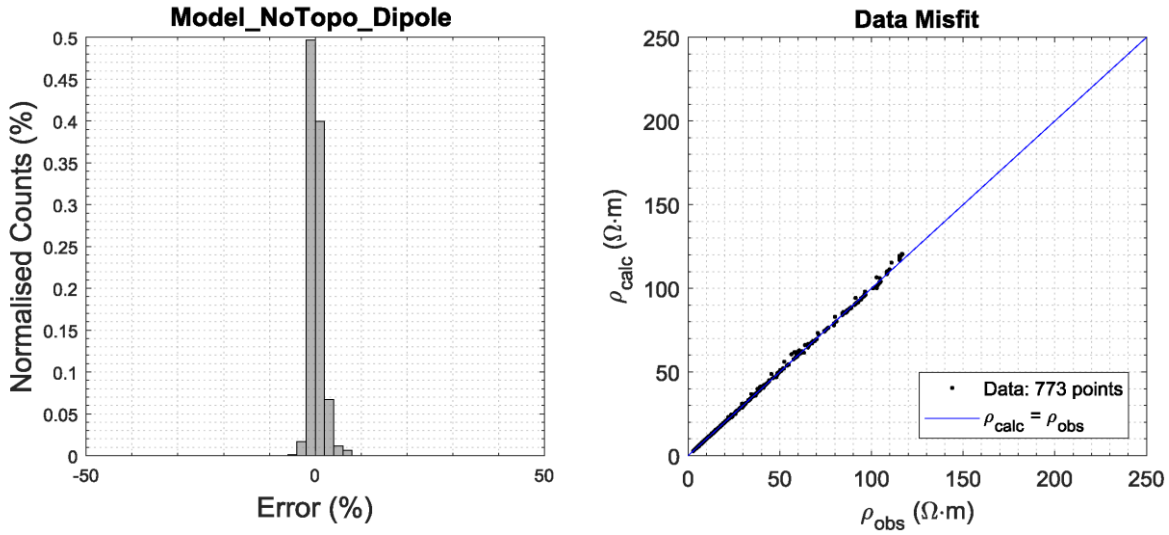

Figure 2.13: Plots showing the distribution of error and misfit between observed and calculated data for a dipole-dipole configuration without topography

Figure 2.14 shows the second example for the geo-electrical model defined by Quinns Rocks SIM wells (e.g. Figure 2.6). This model includes accurate topographic relief along the transect, recovered from 5 meter LIDAR data (. Geoscience Australia, 2017). Here, we are able to highlight the consequence of the variably thick and highly resistive unsaturated zone between the surface (i.e., ground level) and the water table on the outcome of resistivity imaging.

A comparison of dipole-dipole ERI derived conductivity distribution in Figure 2.7 and Figure 2.14 shows that topography has a significant impact on resistivity imaging. Notice the reduction in accuracy with which resistivity imaging recovers details of the seawater wedge and substrate in Figure 2.14. The recovered geo-electrical model should have uniform conductivity of 330 mS/m in the wedge, and 50 mS/m in the substrate. Similar observations are present in outcomes of field ERI data, presented later in this text.

Inversion outcomes shown in Figure 2.14 generally underestimate the conductivity of the wedge and fail to resolve the substrate below. While the location of the substrate beneath the higher-resistivity fresh groundwater is generally resolved in each case, the substrate below the conductive seawater wedge is always poorly resolved. In the worst case, the outcome of inversion of data from the Wenner array gives no indication of the existence of the uniform horizontal substrate.

Figure 2.15 extends the above analysis to include combinations of arrays. The number of data points (i.e., quadrupoles) in the combined arrays is shown on each resistivity image. Inversion parameters are identical to those used to generate resistivity images in Figure 2.7 and Figure 2.14.

Inversion of the synthetic ERI data from the combined dipole-dipole/Wenner array and dipole-dipole/ Schlumberger arrays provides significant improvement in definition of the saline groundwater wedge and lower substrate (see Figure 2.15) when compared to outcomes from individual arrays. Only the combined dipole-dipole/Schlumberger array provides clarity on the location of the substrate interface below the saline groundwater wedge. In practice, hybrid dipole-dipole surveys are relatively efficient to acquire and are readily incorporated into multichannel acquisition.

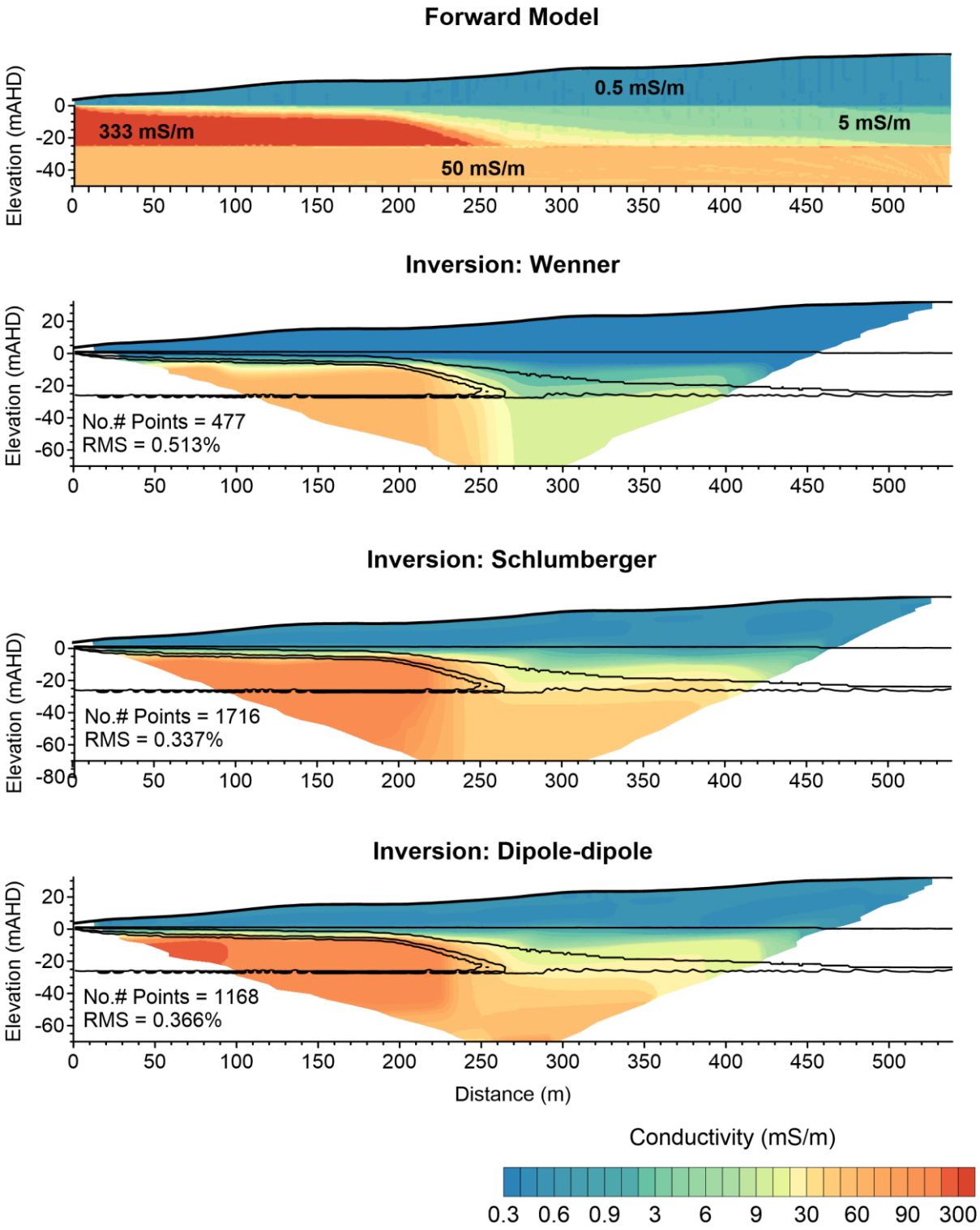

Figure 2.14: Images showing the geo-electrical model incorporating topography plus ERI derived formation conductivity distribution for standard electrode arrays. The forward geo-electrical model is converted from the Quinns Rocks hydrogeological model shown in Figure 2.6. These images can be compared with those from Figure 2.7 where the geo-electrical model excludes topography. The inclusion of topographic relief significantly affects resolution and accuracy of key interfaces in the inverted ERI conductivity distribution for conventional electrode arrays

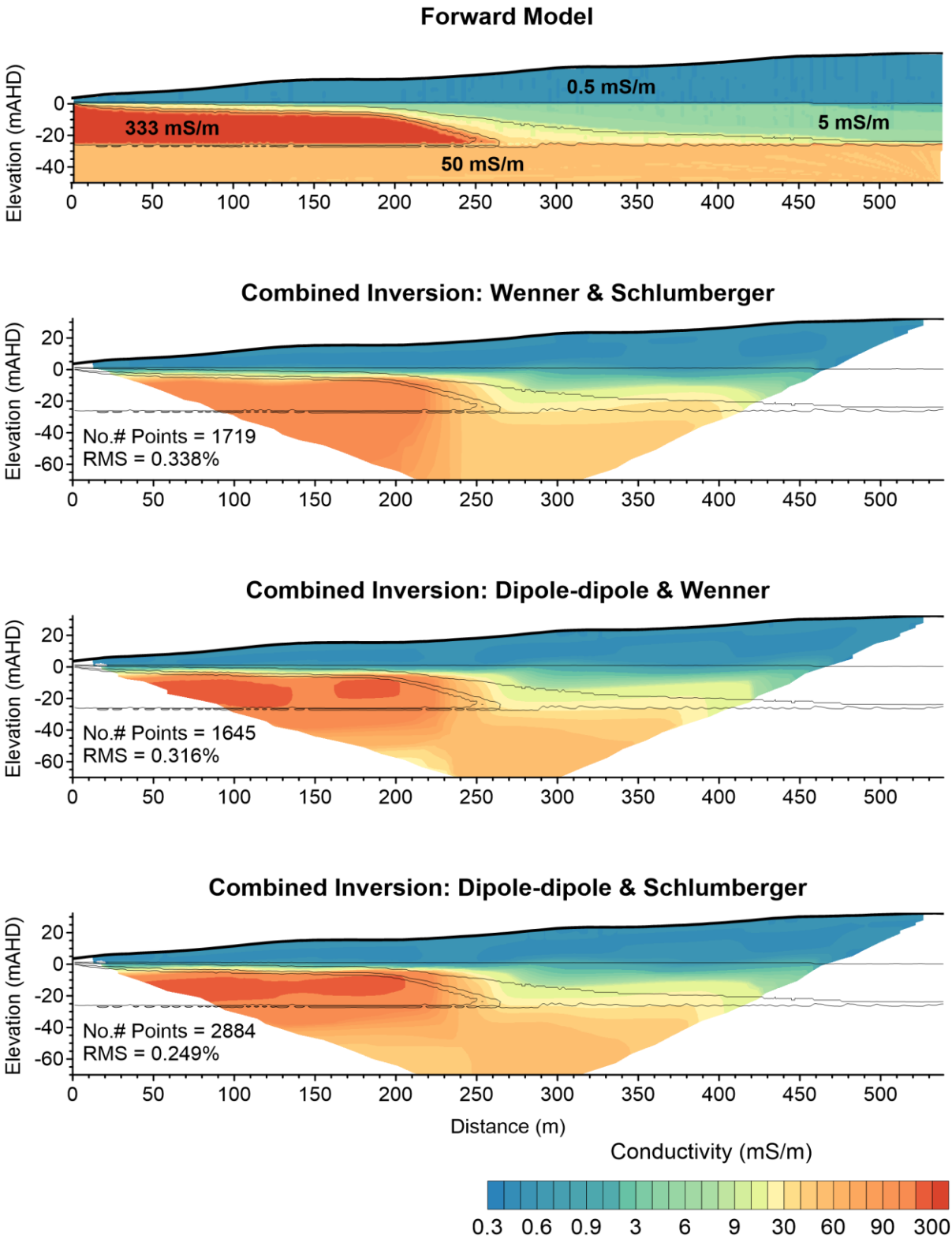

Figure 2.15: Geo-electrical model incorporating topography plus ERI derived formation conductivity distribution for combined electrode arrays.The forward geo-electrical model is converted directly from the Quinns Rocks hydrogeological model shown in Figure 2.6. These images can be compared with those from Figure 2.7 and Figure 2.14. Only the inversion of synthetic ERI data for two dipole-dipole hybrid data are able to credibly locate the high conductivity of the wedge and the depth of substrate interface below the seawater wedge.

2.2.4 ERI Control site: Field Experiments

Field experiments were completed with the SYSCAL Pro 72 ERI system (Iris Instruments). Coordinates were measured with an RTK GPS system (Navcom SF3040. The total length of the Quinns Rocks ERI transect is approximately 440 meters, with electrodes spaced every 10 meters. The electrodes were ~200 mm long, ~10 mm diameter, stainless steel pegs. Each electrode position is saturated with brackish water and resistance checks across each electrode pair are used as a quality control measure. Each electrode configuration uses an injection voltage of 400 V, 4 to 8 stacks per quadrupole with requested quality factor set to zero (i.e., no changes in successive measurements) and a 250 millisecond current injection time with a 100% duty cycle waveform.

Inversion of field data used identical parameters to those used for synthetic data. Figure 2.16 shows resistivity imaging outcomes for ERI field data from the control site. With the exception of the Schlumberger array, the field data is highly consistent with the conductivity distribution obtained from inversion of synthetic data computed for the seawater interface model at this site (e.g., Figure 2.14).

In Figure 2.16, the resistivity imaging clearly shows the substrate on the landward side of the wedge where there is higher resistivity fresher groundwater. However, below the saline wedge, the substrate is only interpretable in the dipole-dipole resistivity image. The black dotted line on the resistivity images in Figure 2.16 is the interpreted shape of the seawater interface. Without prior knowledge of shape of this interface or the existence of the substrate from drilling, there would be little prospect of accurately interpreting these key elements of coastal hydrogeology from the Wenner or Schlumberger resistivity images. These observations are consistent with those from resistivity imaging of synthetic data over the seawater interface model in section 2.2.3.

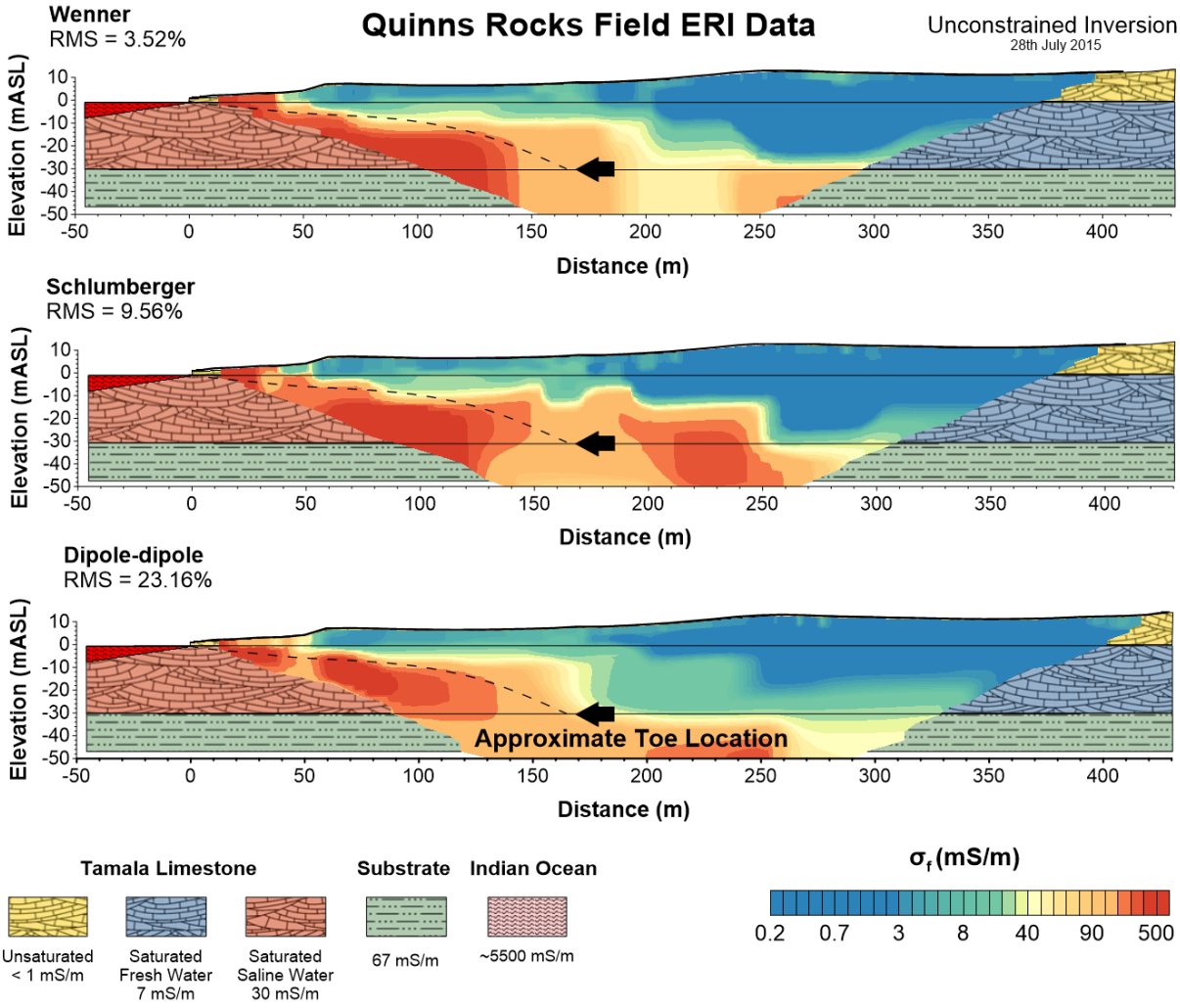

Figure 2.16: Resistivity imaging from unconstrained inversion of field ERI data for different electrode configurations. The configurations shown are Wenner (top), Schlumberger (middle) and dipole-dipole (bottom). Data was collected on 28 July 2015. The water table and the clayey substrate are located at 0 mASL and -30 mASL respectively as shown in geo-electrical model in Figure 2.6. The existence, and to some extent, the geometry of the seawater interface is revealed by all array configurations. However, the substrate is poorly resolved in both Wenner and Schlumberger examples, which is consistent with the outcome from our numerical experiments (see Figure 2.14).

Inversion of field dipole-dipole ERI data shows higher error than inversion of the data from Wenner or Schlumberger style arrays. In RES2DINV, the measure of error for the robust inversion is the mean absolute error, shown in equation 4.3.

$$E_{abs} = \frac{1}{N}\sum_{i=1}^{N}|\log(\rho_{cal}) - \log(\rho_{obs})| \quad (2.3)$$

Where $E_{abs}$the measure of error, N is the number of data points, ρ_{cal} are calculated resistivity values and ρ_{obs} are observed resistivity values.

This measure of error follows the standard definition of mean absolute error (Weisstein, 2017) and is generally preferred over root mean square error (RMSE) (Chai *et al.*, 2014; Willmott *et al.*, 2005; Willmott *et al.*, 2009). However, and more generally, all forms of global error can be exceedingly misleading. For example, the Wenner electrode configuration fails to recover any change in conductivity associated with the lower clayey substrate in both synthetic and field examples, yet the final inversion has significantly lower error than inversion of the dipole-dipole or Schlumberger data.

Measures of global error are strongly affected by quality and number of data points inverted. Wenner data has a relatively small number of low geometric factor (i.e., high quality) quadrupoles compared to dipole-dipole data, which, for the same number of electrodes, has more data points with generally higher geometric factor (i.e., lower quality).

Reducing the number of data points available for inversion tends to reduce global misfit. However, this is clearly an inappropriate strategy as it diminishes illumination of the target. General inadequacies in global error estimates leading to unrealistic models are well-documented, such as global misfit in electrical methods (Le *et al.*, 2016), and hydrologic and hydro-climatic models (Legates *et al.*, 1999).

Spatial assessment of apparent resistivity misfit distribution after inversion can be an important method for quality control of both the field data and the inversion outcome. This is illustrated in Figure 2.17 and Figure 2.18. Here we compare apparent resistivity pseudo-sections from field (i.e., observed or measured) data, and inverted (i.e., calculated) data for the Quinns Rocks Wenner electrode configuration survey. These images are accompanied by (i) a map of apparent resistivity misfit distribution, (ii) a histogram of misfit and (iii) a cross plot of measured apparent resistivity versus apparent resistivity from final inversion outcome (i.e., see comparable analysis for the synthetic example in Figure 2.8).

The misfit image shows a relatively uniform error distribution. The histogram points towards the expected normal distribution of error, and the cross plot shows relatively few outliers (i.e., points offset from the $\rho_{obs} = \rho_{calc}$ trend line). The analysis shows the quality of the match between measured and calculated ERI apparent resistivity is generally excellent. That is, the vast majority of points have exceedingly small, relatively random mismatch.

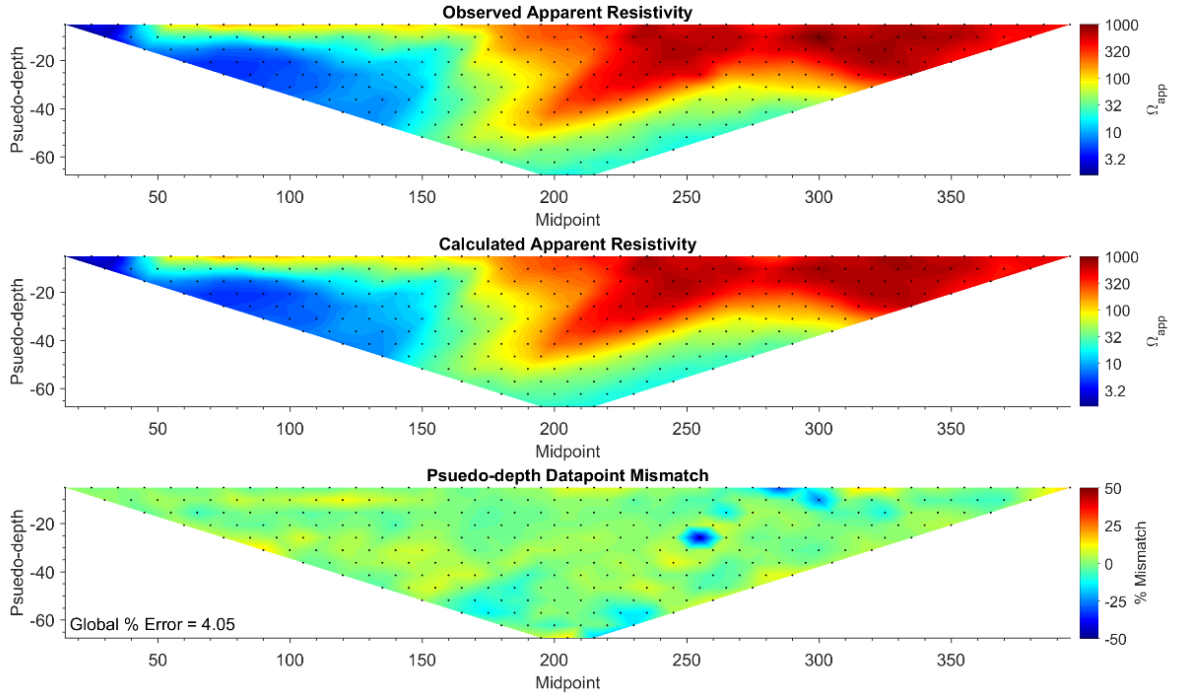

Figure 2.17: Observed (top) and resulting inverted model (middle) apparent resistivity distribution, and spatial misfit (bottom) for the Wenner configuration field data collected at Quinns Rocks.

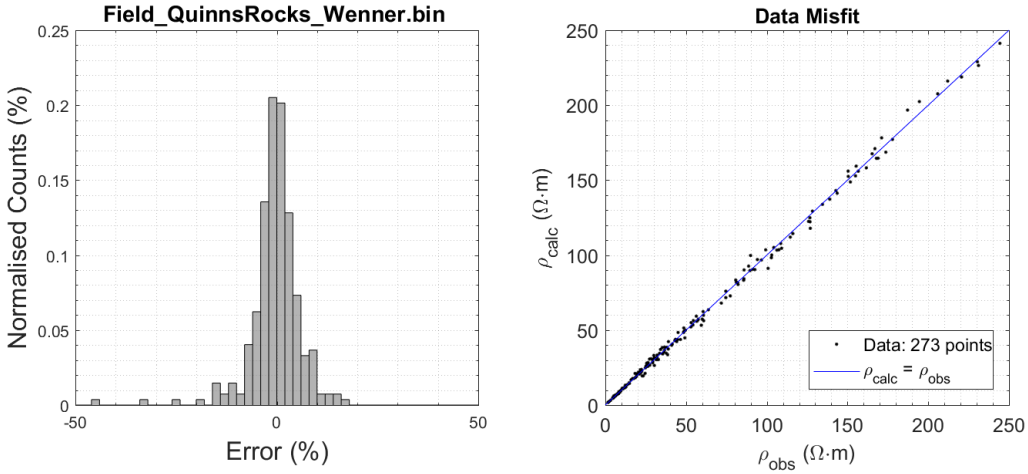

Figure 2.18: Histogram and cross-plot of misfit and error distribution in the inverted apparent resistivity image compared to the observed apparent resistivity. The error and misfit appear normally distributed throughout.

Our analysis indicates that, in the near-shore setting, the outcome of unconstrained inversion has a first order dependence on electrode configuration. While each of the arrays suggest that the seawater interface is located at approximately 170 meters inland, only the dipole-dipole based resistivity imaging provides confidence as to the existence of the substrate, which is a highly significant element of coastal hydrogeology.

2.3 Part 2: ERI in Complex Geo-Electrical / Hydrogeological Architectures

The concept of a conventional saline groundwater wedge often cannot describe the reality at dynamic coastal margins. The Cockburn area, south of Perth, Western Australia (Figure 2.4) combines high transmissivity sands, seaward-dipping stratigraphy, and an expansive high-conductivity sheet-like clay/shale substrate (Pollock *et al.*, 2006; Anthony John Smith *et al.*, 2001). For this site, drill-hole, wireline logging, and GPR data are needed to resolve key elements of the coastal hydrogeology. As with many urban ERI sites, access was restricted to pre-existing pathways.

Figure 2.19 shows the location of the ERI transects, GPR and monitoring wells C1a, and C1b. The ERI cross lines were collected to assess geo-electrical symmetry parallel to the coast. The 250 MHz shielded antenna GPR data was collected to provide detailed shallow stratigraphy (e.g. dips) and recover the shallow expression of the seawater interface near to the shoreline where ERI illumination is limited.

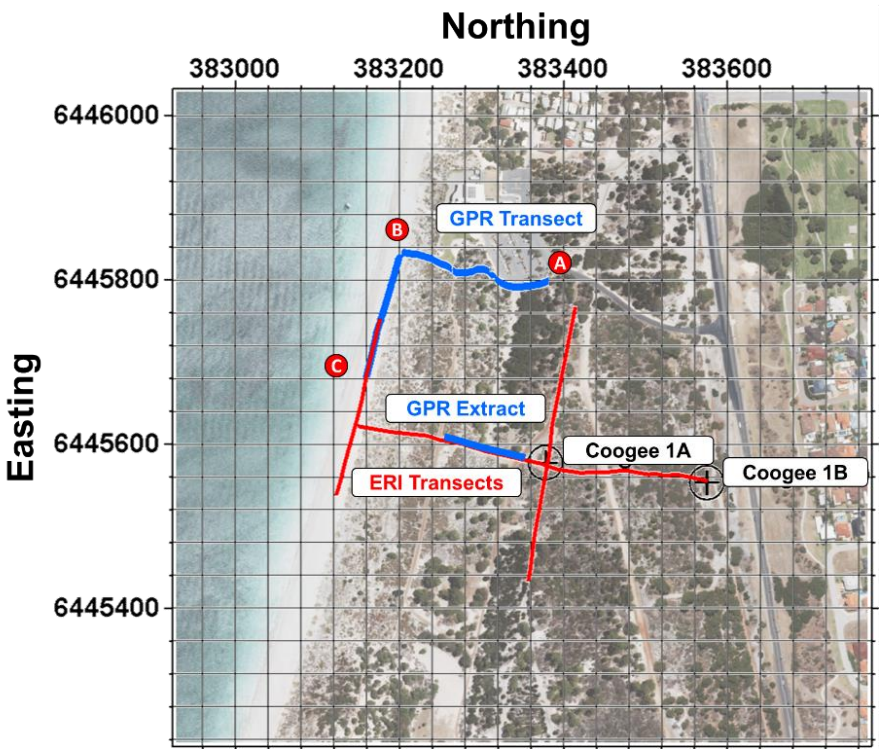

Figure 2.19: Map of the Coogee Site, showing well locations (C1a, C1b), ERI transects, and GPR. Figure 2.22 below provides a 3D perspective of the resistivity imaging. Figure 2.24 shows the annotated GPR section, where points A, B, and C, are at the start, end, and corner of the beach GPR transect respectively. [Aerial Photograph reproduced by permission of the Western Australian Land Information Authority (Landgate) 2018]

Figure 2.20 shows resistivity imaging outcomes from dipole-dipole, multiple-gradient and combined electrode configurations. The combined array includes of all quadrupoles from the multiple-gradient and dipole-dipole configurations. Inversion parameters are the same as those given in Table 2.1. Wireline electrical logs from well C1a suggest a shallow, more-conductive layer close to the water table. The dipole-dipole and combined array appear to resolve this semi-continuous layer, whereas outcomes from the multiple-gradient array are unable to resolve this layer beyond C1a. The conductivity distribution from wireline logs in Figure 2.21 compares exceedingly well with resistivity imaging from the dipole-dipole array.

Another key observation from Figure 2.20 is that the saline groundwater interface near the swash zone is not apparent in any imaging outcomes. We present evidence from GPR data below, in Figure 2.24, showing the seawater interface to be dipping steeply in the region where ERI coverage with the standard inversion strategy is low. The alternate inversion strategy presented in 2.7Appendix A.4 show the resolution of model cells is still relatively high in these areas. This strategy produces an outcome perhaps better aligned with the anticipated subsurface conductivity distribution than in the original inversion strategy.

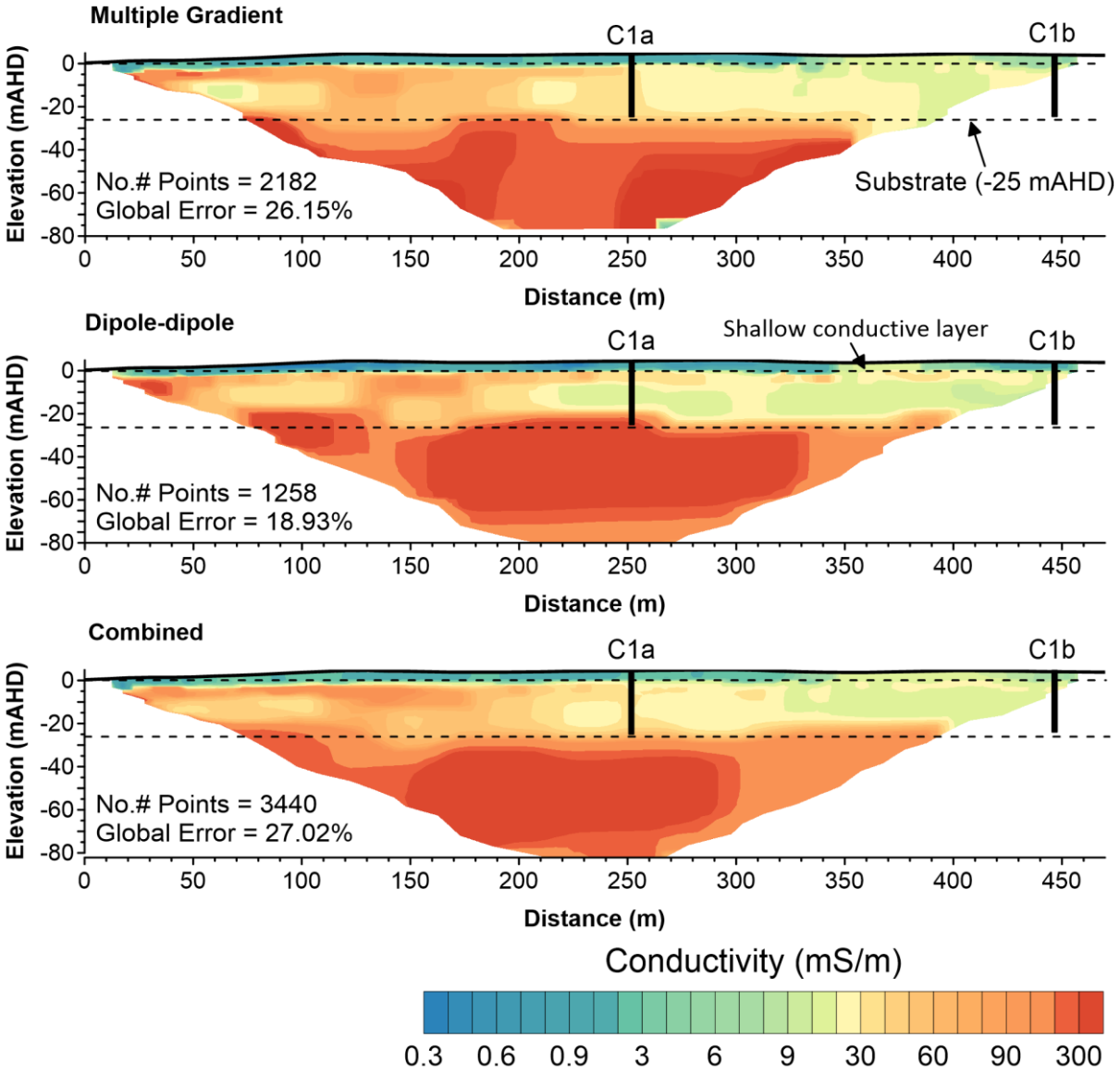

Figure 2.20: Inverted conductivity distribution from the multiple-gradient array (top), the dipole-dipole array (middle), and a combined array (bottom) at the Coogee site. A black, dashed line indicates the substrate recovered from sonic core logging at C1a and C1b. Each array is unable to locate the substrate interface from the borehole logging. It is difficult to differentiate the saline water at the base of the aquifer from the clayey substrate because both have similar high conductivity.

Figure 2.22 shows the wireline logging and lithology recovered at monitoring wells C1a and C1b. It includes resistivity images from ERI transects that pass parallel and perpendicular to the coastline. Gamma wireline logs and samples from sonic logging provide accurate depths to the shale substrate (i.e., the Kardinya Shale). The induction logs provide the depth to the saline groundwater interface within coarse sands immediately above the shale. The electrical conductivity of groundwater extracted from 2 m long well screens, set immediately above the shales, was close to 5500 mS/m.

Here, ERI is unable to differentiate the similarly conductive Kardinya Shale, from coarse sands saturated with 5500 mS/m groundwater. The saline water exists as relatively flat layer with a sharp transition (between -16 and -18 m AHD) to fresh groundwater above and shale below as indicated in Figure 2.21.

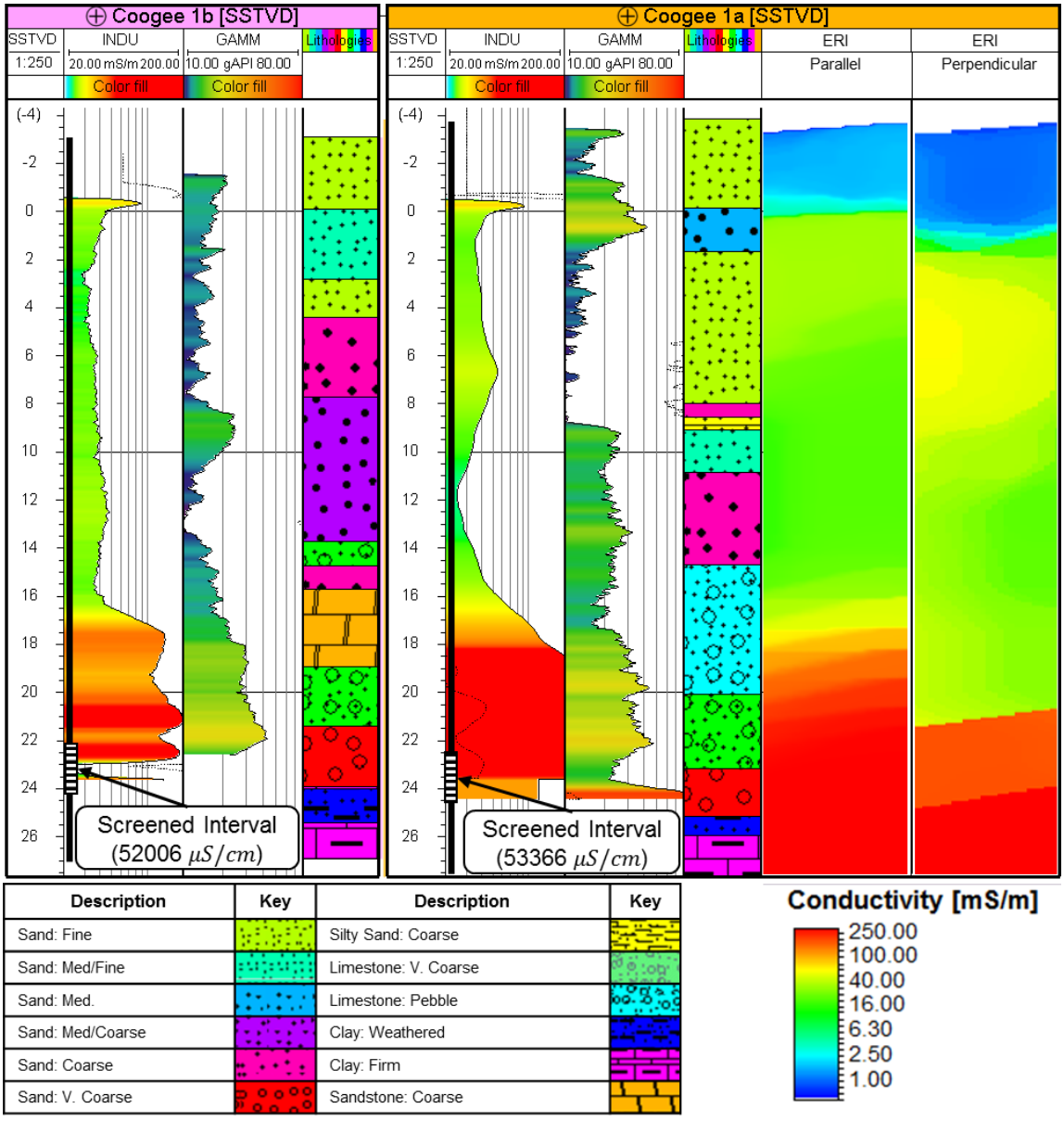

Figure 2.21: Core and geophysical logging data from C1a, and C1b, including both nearby ERI transects. Note the gamma log and core profile showing a strong response (i.e., Kardinya Shale) at 25 meters below height datum (mBHD), while the induction log shows a high response (i.e., conductive seawater) from 18 mBHD. A shallow, silty-sand layer is present at ~9 mBHD in C1a corresponding to the base of the shallow moderately-conductive unit in the ERI.

Figure 2.22 shows a 3D visualisation of the data collected at the Coogee site. The correlation of ERI resistivity and induction logging resistivity at the transition from fresh to saline groundwater for the transect parallel to the coast and passing C1a is exceptional. Transects parallel to the coast can validate the 2D assumption made for imaging of the transect perpendicular to the coast, however, are of little value if collected in isolation.

A second parallel transect was acquired along the beach within 20 m of the ocean. It shows uniform apparently layered conductivity distribution, with a resistive, 100 mS/m layer between two highly conductive layers (900 mS/m and 400 mS/m) above and below. There are two possible causes for this layer (1) submarine groundwater discharge of fresh groundwater beneath the shoreline, and (2) an artefact resulting from the presence of the ocean. That is, we suspect that parallel imaging must be affected by the large and extremely conductive ocean water (approximately 5500 mS/m), which presents strong 3D asymmetry in subsurface electrical conductivity distribution.

Figure 2.22 shows an extract from GPR collected at the site. The GPR image reveals persistent shallow dipping stratigraphy with dips approximately 15° in a north-west direction. Imaging capability below the water table is often limited by topography and signal attenuation. More so in highly conductive media such as the seawater wedge, where it totally attenuates in a very short space.

At this site, the relatively flat and low-lying topography facilitated high-quality data across much of the survey area. The fine details of the shallow stratigraphy, and the steep seawater interface angle cannot be recovered from resistivity imaging, however, may be a key element of coastal hydrogeology with a potential significance as input to flow and solute transport modelling.

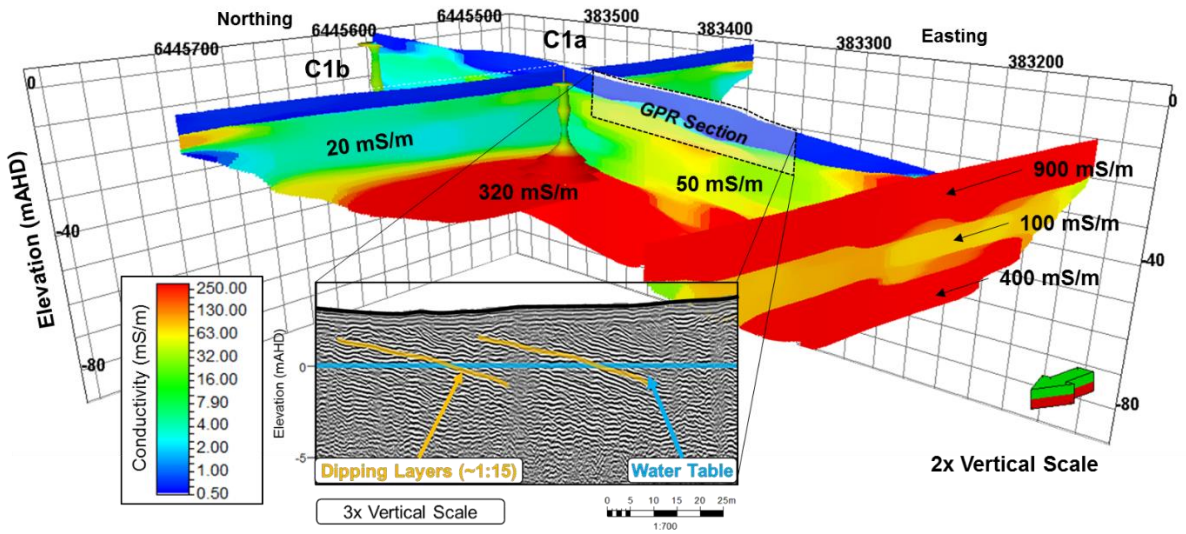

Figure 2.22: 3D visualization of the electrical conductivity distribution at Coogee, including the induction logging at C1a and C1b. A strong correlation exists between the shallow conductive layer in the induction logging and perpendicular resistivity image, as well as the depth to the conductive substrate from parallel resistivity image.

Figure 2.24 shows the GPR data proximal to the beachfront. The line travels perpendicular to the beach along a pathway before moving parallel along the top of the swash zone. The GPR signal is completely attenuated along the beachfront by the conductive subsurface, possibly from evaporated salts or wave-based salt-spray. Moving less-than 40 m away from the beach, strong GPR reflectors below the water table indicate the presence of shallow fresh groundwater.

The lower image in Figure 2.24 provides a 3D representation of the root-mean-square (RMS) amplitude attribute applied to the GPR data. The RMS amplitude is a measure of the reflectivity, and highlights where strong reflectors exist. This image particularly highlights the high-angle seawater interface close to the shore, where no reflections are observable. It closely resembles location of the shallow saline groundwater interface partially observed in the resistivity image.

We find that while the ERI provided valuable information, three specific challenges are recognized. That is ERI is unable to (1) separate the saline water from the clay substrate, (2) identify the shallow dipping layers across the site, and (3) effectively image the saline water interface close to the ocean.

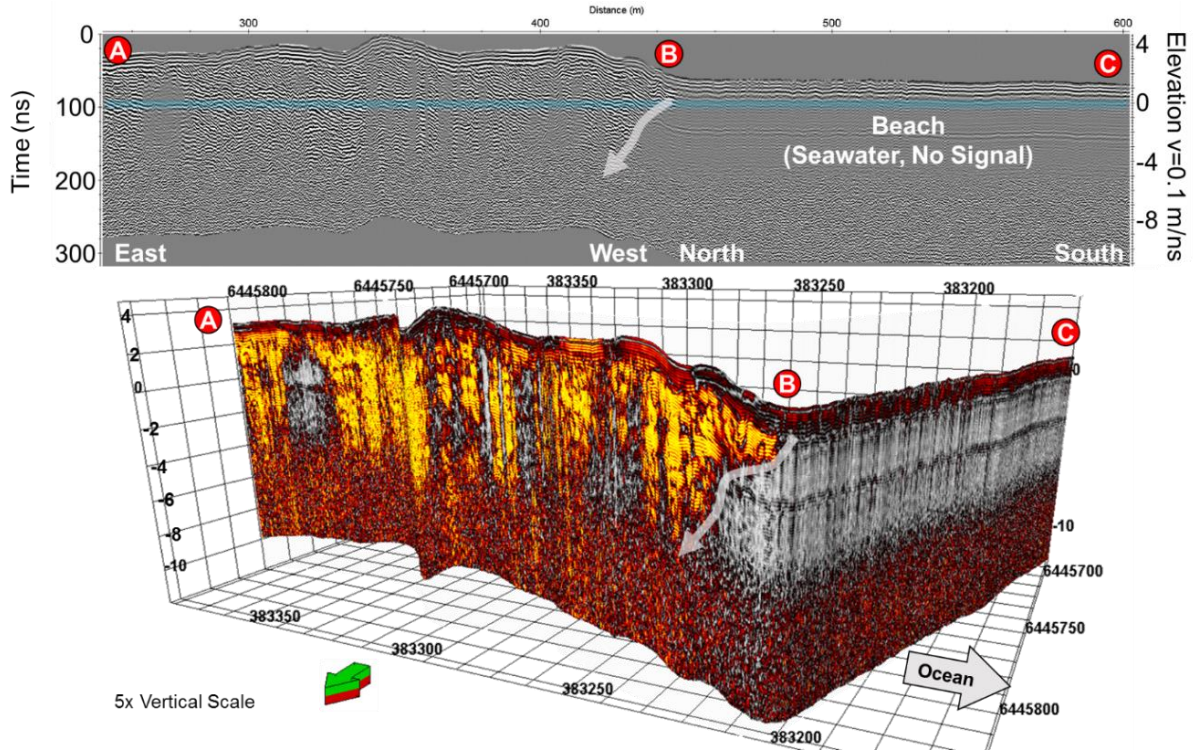

Figure 2.23

Figure 2.24: GPR transects from the Coogee site, showing the degradation of signal nearby to the ocean . The 2D profile (top) shows the reflectors visible at the east/west part of the profile, while the north/south section along the beach is attenuated. RMS amplitudes are overlain on the 3D image (bottom) highlighting the signal quality change from the resistive fresher water to the conductive seawater and beachfront sediments. Areas of landward low-RMS are related to concrete path and road crossings, rather than subsurface structures.

2.4 ERI and Aquifer Geometry: Transects along 100km of coastal margin

The elongated Perth Basin includes several distinct geo-electrical architectures and multi-tiered aquifers systems, extending for over 500 km of Western Australia's southwest coastline. Shallow unconfined aquifers exist within several hundred kilometres of Perth, and mostly overlie the Leederville and Yarragadee confined aquifer systems. Within these confined systems, high-quality potable groundwater persists for a considerable distance beyond the coastline, to ultimately exit the groundwater system as submarine discharge at the continental shelf (V. E. Post *et al.*, 2013).

The seawater interface in the unconfined aquifer (e.g. the Tamala Limestone) is typically separated from a deeper, freshwater, confined aquifer by a clayey layer, or aquiclude. In some places along the coastal margin of Perth, the aquiclude is relatively thin. It is important to recognise that, if seawater intrusion has recently occurred in the unconfined aquifer, then the seawater wedge has progressed inland over a clayey substrate historically enclosed by fresh groundwater above and below.

If the clayey substrate is dominantly a low cation exchange capacity (CEC) clay, then we might expect the substrate to be electrically resistive compared to that part of the seawater wedge which has moved inland, within the unconfined aquifer above. Such is the case where the Pinjar formation forms the shallow substrate. This scenario is common to the north of Perth city. For a substrate dominated by a high CEC clay, such as the Kardinya Shale, the electrical conductivity is likely to be high, and potentially comparable to that of the saline groundwater wedge. Where the resistivity of the seawater wedge and a high CEC clayey substrate are similar, interpretation of the interface is problematic. Further, if the seawater wedge is moving, or geoelectrical architecture is complex, then the shape of the seawater wedge in resistivity imaging outcomes may not be consistent with the classic, steady-state groundwater wedges shown in Figure 2.2.

Field sites along Perth's coastal margin are selected to demonstrate the extent to which coastal hydrogeology, including the seawater interface, can be resolved by ERI methods. We compare transects from sites where; (1) high permeability shallow sediments overlie moderate to low permeability sand and silt, (2) a thin, high-quality aquifer overlies a shallow moderately conductive impermeable substrate, and (3) a thin, exceedingly high-permeability aquifer overlies an expansive high-conductivity shale substrate (see Figure 2.2). Further, we examine distance of the seawater interface relative to the shoreline in a set of ERI transects located progressively closer to the densely populated, historically high groundwater usage coastal margin next to Perth.

Figure 2.25 and Figure 2.27 show resistivity imaging from sites along a 100 km stretch of the increasingly urbanized coastal margin of Perth. Figure 2.25 provides ERI images for distinctly different aquifer systems and Figure 2.27 provides a set of images with the seawater wedge located progressively further inland. All these key locations (see Figure 2.4) present the opportunity for long-term time lapse ERI.

The first order challenges at each ERI site were to (1) resolve the saline groundwater wedge relative to fresh groundwater within the aquifer layer, and (2) to identify the presence, nature, and depth of any low permeability substrate. We focus on these geometries because they are critical inputs to understanding, numerically modelling, and managing coastal hydrogeology.

All ERI lines commence as close to the ocean as possible and extend as far as possible inland. The transect length are limited by roads or other infrastructure. The Two Rocks and Swanbourne transects provide greatest depth of

investigation, extending 720 m inland from the shoreline. All transects had sufficient penetration to resolve the substrate materials below the shallow high-quality, high-permeability aquifer, which is generally less than 50 meters below sea level at the shoreline.

Resistivity imaging at the Two Rocks site reveals a saline groundwater wedge that is observed for the full length of the transect. The geometry of the seawater interface here is reasonable with reference to geological and wireline logs from a deep artesian monitoring bore, AM12a located about 100m from the shoreline along the transect (see Figure 2.25).

The well (AM12a) provides evidence for three stratigraphic units. These are (1) the high-permeability superficial aquifer (5 to 1000 m/day), (2) the Kings Park Formation starting at above 50 m from surface and mostly consisting of moderate to low-permeability fine sand and silt (0.1 to 15 m/day) and (3) the deep Osborne Formation, containing the impermeable Kardinya shale (10^{-4} to 10^{-6} m/day). Estimates for the hydraulic conductivity of each layer is provided in Davidson *et al.* (2008).

Wireline induction logging in AM12a (Figure 2.26) provides evidence for high electrical conductivity in the Superficial and Kings Park Formations within the saline groundwater wedge. The ERI indicates that the wedge extends a considerable distance inland, extending through shallow high-permeability sediments to the low-to-moderate permeability sediments of the Kings Park Formation. The wedge terminates at, or above, the Kardinya shale. These depths are beyond the penetration of ERI, however it is interesting to note that groundwater below the Kardinya Shale, (i.e., within the confined Leederville aquifer) are likely to be fresh or brackish (Leyland, 2011). More generally, the Leederville aquifer provides a major potable groundwater supply for Perth (. Department of Water WA, 2015).

In contrast to the Two Rocks resistivity image, the Swanbourne ERI image reveals a distinct high-conductivity saline wedge set above a horizontal substrate with much lower resistivity. Here we observe characteristic resistivity imaging artefacts within the substrate layer. Geological models in the area (Davidson, 1995; Leyland, 2012) suggest the substrate layer has a relatively uniform conductivity; however, the imaging outcomes suggest that a sharp lateral change in conductivity from 15 to 60 mS/m exists directly under the seawater toe. For our standard inversion strategy, this type of artefact commonly occurs below the transition from fresh to saline groundwater within the substrate. It is consistent with observations from resistivity imaging of numerically simulated ERI data for similar geo-electrical settings (e.g. Figure 2.25).

The Swanbourne ERI transect is a salient example of where our alternate ERI inversion strategy, as presented in 2.7Appendix A.4, offers an advantage for representing the saline water interface and substrate. For the Swanbourne Image in 2.7Appendix A.4, the possible resistivity “overshoot” and “undershoot” in the substrate on each side of the conductive saline groundwater wedge “toe” is gone.

From a hydrogeological point of view, it is reasonable that the saline groundwater wedge is located above a lower conductivity substrate, especially if the saline water wedge has moved inland. This scenario is already demonstrated in the set of Quinn Rocks SIM wells further to the north. Accurate imaging of the electrical conductivity distribution, representing the full coastal hydrogeology at sites like Swanbourne, remains as a research challenge for resistivity imaging.

In our third example (i.e., at Coogee), a thin relatively flat layer of saline groundwater is indistinguishable from the Kardinya shale substrate (see Figure 2.20. and Figure 2.25). The conductivity in two wireline logs match the ERI imaging exceedingly well; however, the two layers are not observable in the conductivity imaging. Chip samples and gamma logging are the only way to differentiate the clay substrate from the aquifer at this site.

We have discussed the sites shown in Figure 2.25 at length. These sites contrast ERI experiments with three significantly different saline water interface geometries. In Figure 2.27 we examine ERI imaging outcomes where a seawater wedge over a shallow substrate is located at successively greater distances inland.

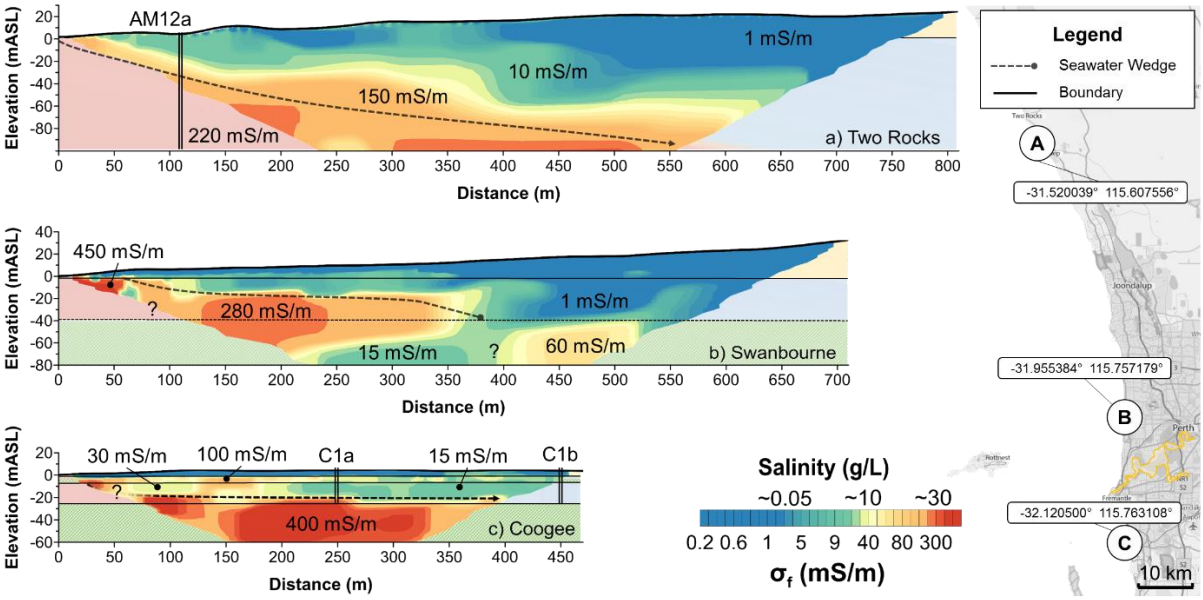

Figure 2.25: Interpretation of three classes of significant hydrogeological boundaries from the inverted conductivity distribution of ERI data, featuring: a) deep aquifer, b) shallow aquifer with moderately conductive substrate, and c) shallow aquifer with high conductivity substrate. Question marks indicate areas of some uncertainty. (Map data annotated from © OpenStreetMap contributors)

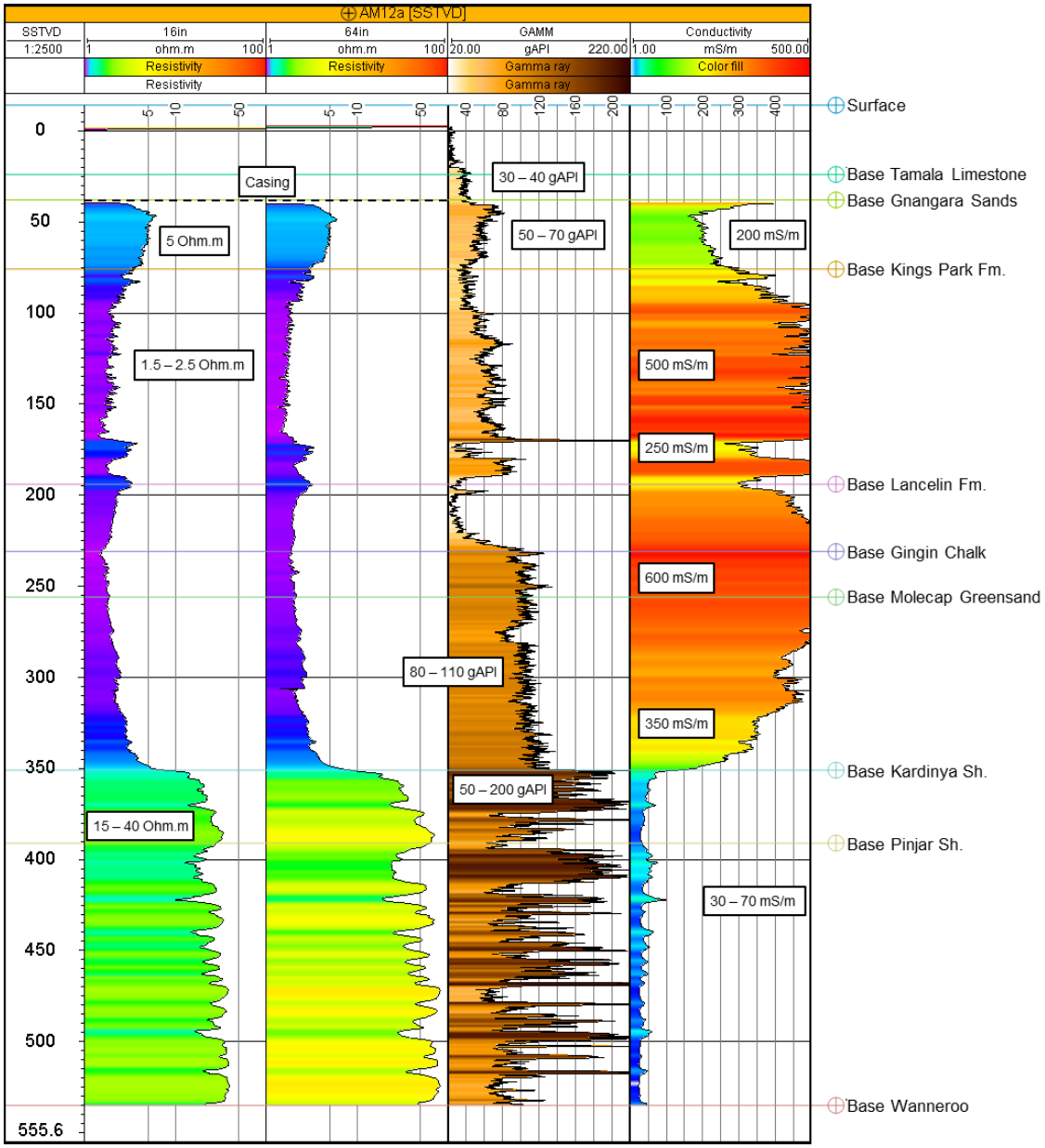

Figure 2.26: Wireline logging from the artesian monitoring well AM12a, located approximately 100 meters from the shoreline at the Two Rocks transect (see Figure 2.25). The resistivity logs suggest that conductive saline groundwater could exist to considerable depths. These logs are comparable to the resistivity-imaging outcome and indicate that the Kings Parks Formation at this site has little effect on the saline groundwater wedge distribution.

The resistivity images in Figure 2.27 present a seawater interface at ERI sites located progressively closer to the increasingly urbanized older suburbs of Perth, where historically groundwater abstraction has been highest. These suburbs are located nearby Perth, next to the saline Swan River estuary (O'Callaghan *et al.*, 2007). The position of the wedge at the northern site, Quinns Rock is constrained by five SIM wells perpendicular to the coast. These wells provide some constraints for the interpretation of the wedge geometry.

Two new sites are introduced in Figure 2.27. These are the Hillarys site, located 25 kilometres south of the Quinns Rocks, and Swanbourne ERI site, 55 kilometres south of the Quinns Rocks. These sites span suburbs which are newly developed (e.g. Quinns Rocks) to older, well-established suburbs (e.g. Swanbourne). Based on resistivity imaging outcomes, the saline groundwater wedge at the Swanbourne site has possibly moved over 300 meters inland, however this interpretation requires validation through new monitoring wells.

Local drivers for the shape and position of the saline water interface include the shape of the coastline, localized freshwater recharge (e.g. rainfall, storm water, and irrigation), aquifer transmissivity, permeability of the substrate, and local household/municipal bore field abstraction from the shallow aquifer. Despite possible local variability in wedge geometry, the resistivity imaging in Figure 2.27 provides a basis to interpret a wedge that is located at progressively greater distance inland.

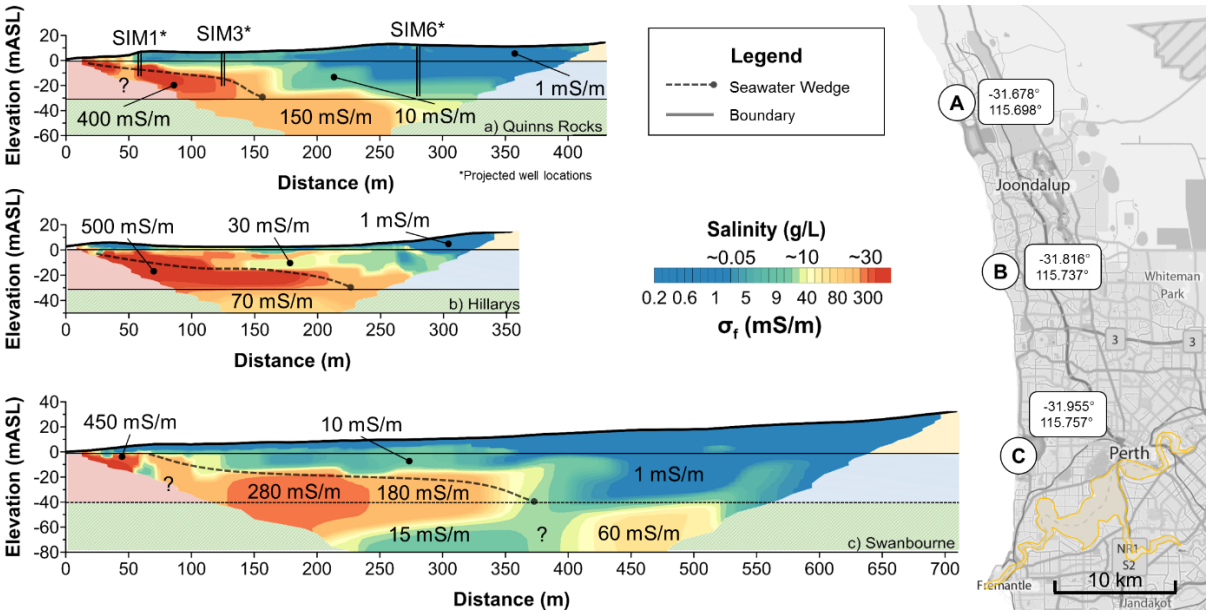

Figure 2.27: Interpreted location of the seawater interface toe progressing further inland with proximity to increasingly urbanized Perth metropolitan suburbs and the saline Swan River estuary. Questions marks indicate areas of some uncertainty. (Map data annotated from © OpenStreetMap contributors)

Confidence in the ERI interpretation could have only come from a combination of (1) analysis of outcomes from numerical modelling over comparable geo-electrical settings and (2) calibration of outcomes from a range of resistivity imaging strategies, confirmed with data gathered from drill holes.

2.5 Summary of Major outcomes

We have completed a comprehensive study of ERI applications for resolving coastal hydrogeology. During this process, we have identified benefits, limitations, and opportunities for new research that may lead to significant improvement in the method. We attempt to provide the reality of ERI application so that the technology can move forward. These major points are listed below.

Table 2.3: Summarized outcomes of experiments undertaken during this research.

	Key points	Comment	Evidence in Document
1	Imaging artefacts are identified in electrode arrays.	Imaging artefacts cannot be avoided in a complex high contrast geo-electrical setting, as exists at coastal margins. We find that some commonly deployed arrays, such as the Wenner array, cannot resolve key features of coastal hydrogeology. We were able to identify areas of potential misinterpretation through numerical modelling and systematic comparison of field ERI data with drill-hole data.	Figure 2.7
2	Topography affects imaging outcomes.	Steep topographic relief is common at many coastal margins. It should always be included at the acquisition and imaging (i.e., inversion) stages. We show the imaging outcomes may misrepresent true subsurface resistivity distribution if topography is neglected.	Figure 2.14
3	Commonly deployed arrays can be combined.	Quadrupoles from different arrays are readily combined post-acquisition to improve data density and subsurface illumination. We found that, in practice, it was useful to consider inversion outcomes from both independent and combined arrays. One reason is that some configurations were sensitive to noise (e.g. shallow pipes or fences) and tended to degrade overall imaging outcome. This only became apparent from field data imaging outcomes. It is a practical outcome with considerable consequences.	Figure 2.15 Figure 2.20
4	Perpendicular transects are better suited to resolving the seawater interface.	Coastal hydrogeology is often 2D along the coastline. Certainly, the saline groundwater interface is dominantly 2D. For this reason, the first priority should be to collect ERI perpendicular to the coastal margin. Imaging parallel to the coastal margin can add value by demonstrating the uniform geo-electrical properties parallel to the coast. However, 2D inversion may not be appropriate, especially along the beachfront, where the assumption of two dimensionality is breached.	Figure 2.22
5	ERI Inversion strategy will significantly affect the resistivity imaging outcomes.	In a setting containing large and abrupt geo-electrical contrasts (e.g. across the saline water interface, water table, or substrate), the application of an L1-style norm within the inversion strategy is likely to generate a realistic representation of conductivity distribution at the coastal margins. The L2 smoothness-constrained norm generally does not permit sufficient rate of change of conductivity to accommodate the step-like changes in conductivity contrasts that are common at coastal margins.	2.7
6	Constrained inversion can potentially improve imaging outcomes	Although constrained inversion can potentially improve imaging of key elements of coastal hydrogeology, such constraints do require detailed prior knowledge of the exact geo-electrical contrast location. It is rare that sufficiently accurate and reliable information is available, and incorrect presumption about the location of high contrast boundaries will degrade imaging outcomes.	2.7 0
7	The seawater wedge and conductive substrate may have similar electrical resistivity	Differentiating between sub horizontal saline groundwater interface and a high cation-exchange-capacity shale may difficult using electrical methods.	Figure 2.22
8	Geometry of the seawater interface	Electrical resistivity with suitable acquisition and inversion parameters can image significant coastal hydrogeological architectures, including. Classic seawater wedge in deep unconfined aquifer. Seawater wedge in shallow unconfined aquifer with impermeable substrate. Steep interface with basal layer of seawater above highly conductive impermeable substrate.	Figure 2.26
9	Value of multiple method validation	Electrical resistivity imaging is well suited to saline groundwater investigations. However, we have identified several weaknesses such as lack of resolution near the swash zone, and inability to differentiate a saline wedge from a high CEC substrate. In many situations, other geophysical technologies can also provide valuable and complementary information. For example, GPR was able to image the very shallow wedge descending below the beach zone. Seismic methods (e.g. reflection, refraction tomography, surface wave analysis) may have value, but are expensive. Wells and wireline logs offer valuable and reliable, but highly localized information - critical for understanding and managing coastal hydrogeology. We have provided several examples of integrating ERI and log data.	Figure 2.24

2.6 Conclusions and Future Work

Coastal margins around the world are often densely populated and vulnerable to seawater intrusion. Predicting the consequences of groundwater management strategies in these systems requires high quality information on solute concentration and distribution. ERI has the potential to supply this information. We have provided a comprehensive study of electrical resistivity imaging along coastal margins, including substantial evidence from seawater monitoring wells.

Electrical resistivity imaging (ERI) has the potential to resolve coastal hydrogeology in highly urbanized, intrusion-vulnerable, or environmentally sensitive settings. The geo-electrical architecture in these settings typically consists of several high-contrast geo-electrical boundaries, including the water table, seawater wedge, and substrate. These boundaries are often below beaches, undulating dunes, or steep cliffs.

Our numerical and field experiments showed that all ERI field configurations provide baseline information from which key elements of the saline water interface can be interpreted. However, each configuration exhibited limitations and characteristic artefacts. For example, inversion of data collected with the Wenner electrode configuration failed to identify a shallow clayey substrate in both numerical modelling and field data.

To assess ERI for a range of saline water interface geometries, we completed surveys at select locations along 100 kilometres of shoreline. Of particular note, is our comparison between inverted ERI conductivity distributions for a classic wedge-shaped seawater interface in a deep unconfined aquifer, and multiple sites where the high-quality aquifer with a seawater wedge terminates against a shallow clayey substrate. Our field experiments show the seawater interface mapped at successively greater distances inland while approaching the highly urbanized centre of Perth, Western Australia.

We summarize some of the challenges remaining for ERI in a coastal margin in Table 2.4. The issues identified represent areas that are developing, or not well covered in literature and regular industry practice, yet important in the full implementation of geophysical methods for assessment of seawater intrusion. We believe that future research into these areas will be valuable for accurate resolution of the seawater interface, and further improve confidence of ERI-derived conductivity distributions from coastal environments.

Table 2.4: Current and future research areas

Research Area	Comment	Examples
Cooperative Inversion	Where additional information, such as GPR, wireline logging, and lithological logs exist, these can be used to constrain inversion outcome and improve the accuracy of both significant geo-electrical boundary locations and resistivity estimates. These are generally under-utilized in coastal seawater imaging projects as ERI is typically deployed as a first-order investigative tool for monitoring well placement.	(Hamdan *et al.*, 2013; Hermans *et al.*, 2012; Steklova *et al.*, 2017)
Optimized Electrode Arrays	Optimizing electrode arrangements for the best resolution in dipping, and high-contrast geometries associated with coastal margins will prove important for reliable, routine deployment of the ERI method. Optimized arrays may also reduce the time-of-acquisition, making data cheaper to acquire.	(Ishola *et al.*, 2015; M. H. Loke, Kiflu, *et al.*, 2015; M. H. Loke, Wilkinson, Chambers, *et al.*, 2014; M. H. Loke, Wilkinson, Uhlemann, *et al.*, 2014; M. H. Loke, Wilkinson, *et al.*, 2015)
Hydraulics of the seawater wedge	Joint groundwater flow and transport modelling, coupled with geo-electrical inversion of ERI data can further improve confidence in accurately resolving features of the seawater wedge, such as the mixing zone, fresh groundwater, seawater. Inversion outcomes based on monitoring stations can then be used to better predict future movements of the seawater interface under various abstraction scenarios.	(Beaujean *et al.*, 2014; T. C. Johnson *et al.*, 2010; Nguyen *et al.*, 2009)
Joint land/marine surveying	Current instrumentation limits usage of ERI to land-bound cables. Future technology opportunities for sub-marine electrodes and weighted, waterproof cabling can potentially improve coastal resistivity imaging results by expanding surveys offshore, increasing resolution in key areas of interest.	(Crook *et al.*, 2008; Henderson *et al.*, 2010; M.H. Loke *et al.*, 2004)
Long-period time-lapse monitoring	Time-lapse ERI monitoring has proven effective in a range of scenarios; however, is little evidence in published literature of application to urban seawater intrusion monitoring. The movement of the saline wedge can occur rapidly depending on new shallow abstraction or may occur slowly over decades because of climate change (e.g. declining rainfall recharge). ERI monitoring may need to be specifically designed to capture short-term periods of interest, as well as long-term information.	(de Franco *et al.*, 2009; Ogilvy *et al.*, 2009; Ronczka *et al.*, 2015; S. S. Uhlemann *et al.*, 2016)

Acknowledgements

This research was funded by the Curtin University Postgraduate Scholarship, from Curtin University, Perth, Western Australia, and Department of Water, Western Australia. We extend our thanks to Dr. M.H. Loke for valuable discussion and commentary. We additionally extend thanks to Schlumberger for providing the Petrel E&P software platform used in this research. Supporting resistivity data, including raw data, processed files, and inversion parameter files are available from ftp and on-request from the corresponding author. Water table, water conductivity and lithological information is freely available from Water Information Reporting, (http://wir.water.wa.gov.au/). Well data is included in supporting information. Synthetic data created with RES2DMOD. Field data is processed with Iris Instrument ProSys2. All data was inverted with RES2DINV v4.05 – v4.07. Imagery created using Adobe Illustrator CC 2015, MATLAB 2017a, Microsoft PowerPoint, and Surfer 14.

2.7 Appendices

Appendix A.1 Testing of Inversion parameters on Synthetic data

For geophysical inversion, common points of discussion are: (i) the appropriateness of L_1 and L_2 norms (Claerbout *et al.*, 1973; S. C. Constable *et al.*, 1987) and (ii) the benefits and drawbacks of introducing constraints, which may themselves introduce new uncertainties. While every inversion strategy has subtle differences, the L_1, or L_2-like norms are well known in applied research and are reasonable reference points for comparison.

RES2DINV provides the ability to test inversion strategies that range between end-member L_1 and L_2-like norm approaches. This implementation is functionally similar to the Ekblom norm, (Ekblom, 1974), and uses an iteratively reweighted least-squares (IRLS) algorithm to allow sharp interfaces in subsurface structure (Farquharson, 2007).

In this implementation, if the percentage difference between observed and calculated data is > a "cut-off" value, then inversion tends to accommodate high electrical contrast in a manner consistent with application of the robust or L_1 norm (Farquharson *et al.*, 1998; M. H. Loke, 2016a). Below this threshold (i.e., the cut-off value), the inversion outcome tends towards the typical smoothness-constrained Occam style, L_2 norm (Farquharson *et al.*, 1998; M. H. Loke, 2016a). For example, selecting a high cut-off value of 1 pushes the inversion to a smoothness-constrained L_2 norm outcome while selecting a low cut-off factor of 0.001 drives the inversion closer to an outcome expected from a robust or, L_1 norm.

To highlight the effects of varying the inversion parameters in RES2DINV, we have computed images spanning the full range of available data and model cut-off values. For unconstrained inversion, these are presented in a grid of 30 conductivity-depth sections and are presented in Figure A-1. Three comparable sets of images are provided for constrained inversion, where the constraints are (i) the water table interface, (ii) the substrate interface and (iii) water table plus substrate interface. In each case, the inversion is permitted to have a sharp change at each the designated interface.

We have taken this analysis considerably further, where inversion strategies including sharp boundary constraints at (i) the water table (Figure A-1), (ii) lower substrate (Figure A-2) and (iii) a combination of the water table plus lower substrate (Figure A-3). If a relatively low cut-off factor (approaching a L_1 norm) is used, we see modest improvement compared to unconstrained inversion. However, the combination of sharp boundaries and high cut-off value (i.e., approaching the L_2-style norm) produces significant anomalies within the imaging outcomes which are easily susceptible to misinterpretation.

For geo-electrical geometries at the seawater interface, some ERI inversion outcomes can appear blocky and there may be the temptation to attribute this to mesh discretization. The discretization of finite element grids used is exceedingly fine, as indicated in Table 2.1. Attempts to create a finer mesh would simply increase calculation time with negligible benefit (e.g. Thomas Günther (2004)). The slightly blocky appearance is more likely a result of the robust regularization used in the ERI inversion. If a robust regularization is not used, the location of the lower substrate tends to be poorly represented in imaging outcomes. The alternative inversion approach dictated in 2.7Appendix A.4 appears to reduce the blocky appearance by implementing the diagonal roughness filter and extended models.

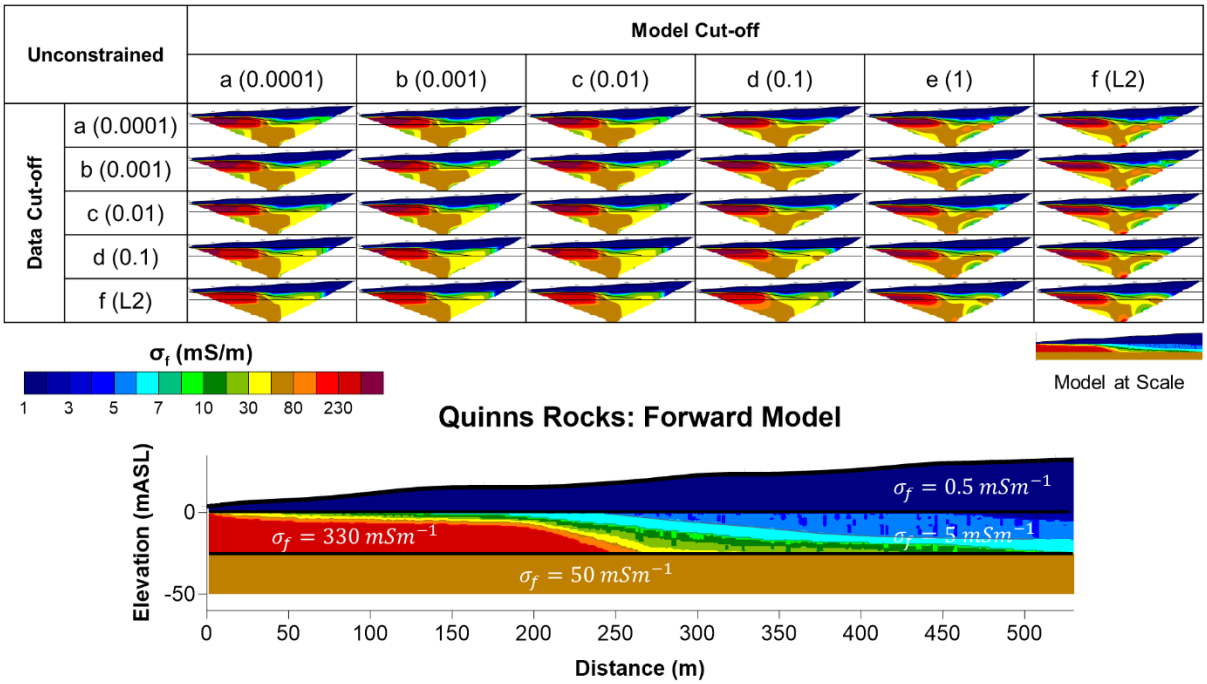

Figure A-1: Comparison of changing the model and data roughness matrix for a range of cut-off values suggested by RES2DINV (M. H. Loke, 2016a)All inversions are completed over the synthetic model with topography, and clearly show the effect of a very low cut-off value (essentially L_1 norm) compared to a high cut-off values, (essentially the L_2 norm), including a direct comparison with the robust inversion option disabled (i.e., L_2 norm only). Other inversion parameters are identical to parameters used for field data and other synthetic models presented earlier. Artefacts associated with model structure, overshoot, and undershoot are readily observed.

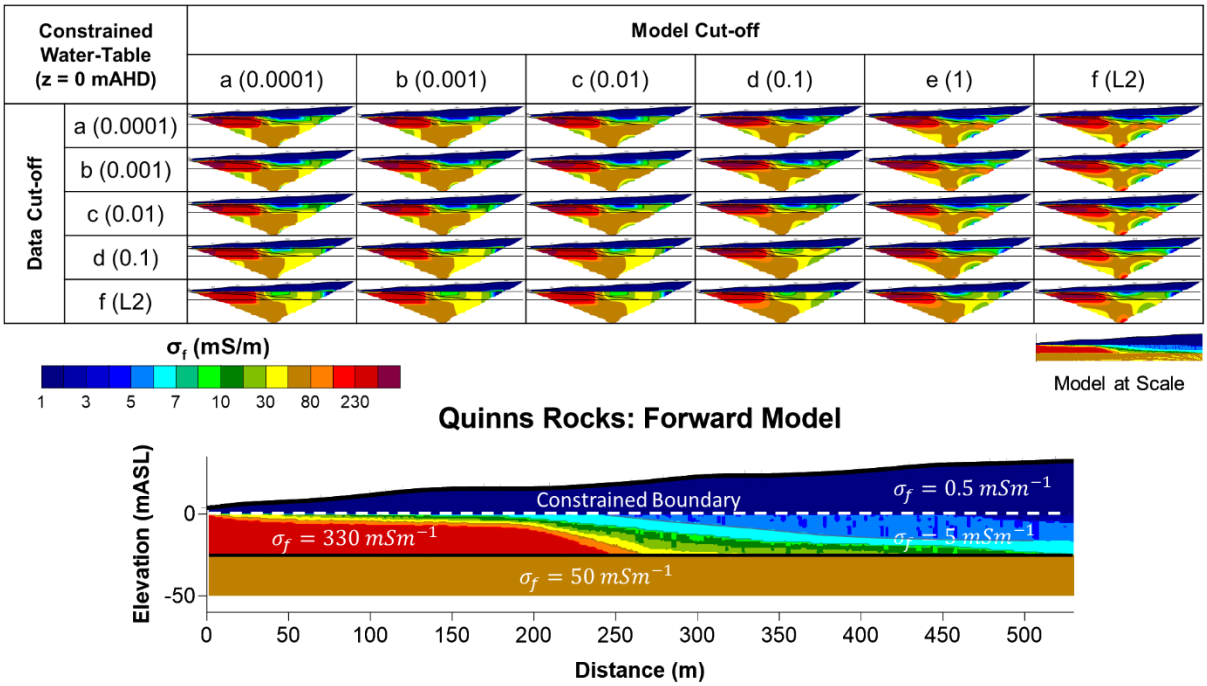

Figure A-2: Inversion of synthetic ERI data from the synthetic topography model with a sharp-boundary implemented at the water table.Lower values represent a robust, or L1 style norm, while higher values represent the smoothness-constrained L2 norm. The introduction of the sharp boundary does not significantly improve the interpretation of the sections, however the effect is most pronounced in the L2 and approaching-L2 style cut-offs, where other known boundaries are smeared.

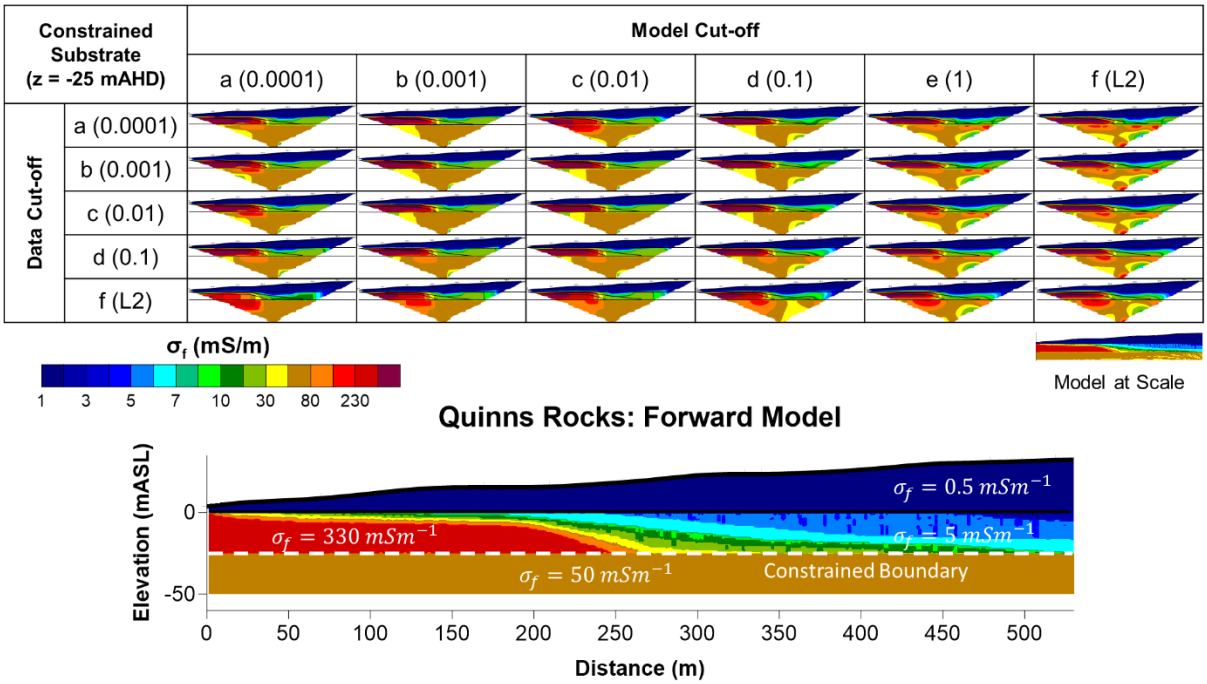

Figure A-3: Inversion of synthetic ERI data from the synthetic topography model with a sharp-boundary implemented at the lower clayey substrate.Lower values represent a robust, or L1 style norm, while higher values represent the smoothness-constrained L2 norm. This constraint introduces significantly more artefacts into the resolved lower-substrate formation conductivity at either extreme of the cut-off value. At moderate cut-offs, the conductivity in the substrate is generally continuous across the section and is consistent with the unconstrained inversion.

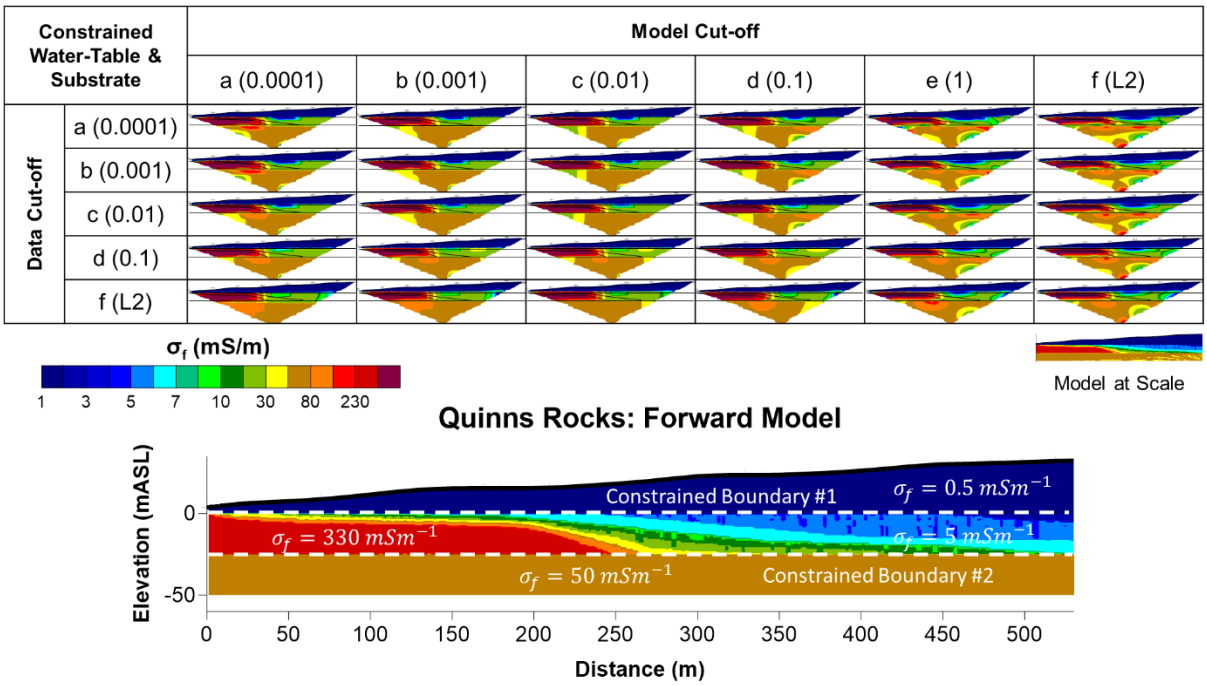

Figure A-4: Inversion of synthetic ERI data from the synthetic topography model implementing both water table and lower substrate boundaries. Lower values represent a robust, or L1 style norm, while higher values represent the smoothness-constrained L2 norm. Artefacts are introduced at either extreme of the cut-off value. Moderate cut-off values result in a relatively continuous conductivity distribution above the water table and below the substrate boundary; however, the smeared zone is no better resolved by the introduction of further constraints.

Appendix A.2 Constrained Inversion of field data

Constrained inversion incorporates additional information such as, seismic data, groundwater chemistry, wireline logs, geological descriptions and/or hydrogeological models into the inversion process. It is intended to direct the inversion process towards the best possible representation of subsurface conductivity distribution (Binley *et al.*, 2015; Jieyi Zhou, 2015; J. Zhou *et al.*, 2014).

If significant geo-electrical boundaries are known, both seed model and distribution of smoothness constraints could be manipulated to improve the outcome of inversion (e.g. (Karaoulis *et al.*, 2014; Le *et al.*, 2016; Soueid Ahmed *et al.*, 2015; J. Zhou *et al.*, 2014)). However, ERI is usually the first technique deployed, often for targeting drill holes, and constraints are often non-existent. Further, even small errors in placement high contrast boundary constraints, like the lower clay substrate, can translate to significant artefacts and considerable caution must be applied.

Figure B-1 shows the outcome of constrained ERI inversion using the water table as the constraint. Setting a 'sharp boundary constraint' allows the inversion to generate a large contrast in electrical conductivity from one side of the boundary (i.e., the water table) to the other. A flat geoelectrical interface at the water table is a highly reasonable assumption given the aquifer has a high hydraulic conductivity (> 50 m/day).

The preconditioned layer boundary probably provides a more realistic contrast between the unsaturated limestone and saturated aquifer especially near the shoreline. However, there is little difference in imaging below this interface at (i) the saline water interface, (ii) the saline water interface toe or (iii) the lower clayey substrate. Therefore, the only boundary that can be reasonably and reliably forced onto the inversion does not appear to significantly improve the outcome of the key geometries for the seawater interface. The imposition of constraint in the absence of additional information (e.g., seismic or drilling) can be undertaken but with extreme caution and with the full knowledge that any incorrect assumptions will almost certainly direct the inversion away from the best representation of subsurface conductivity distribution.

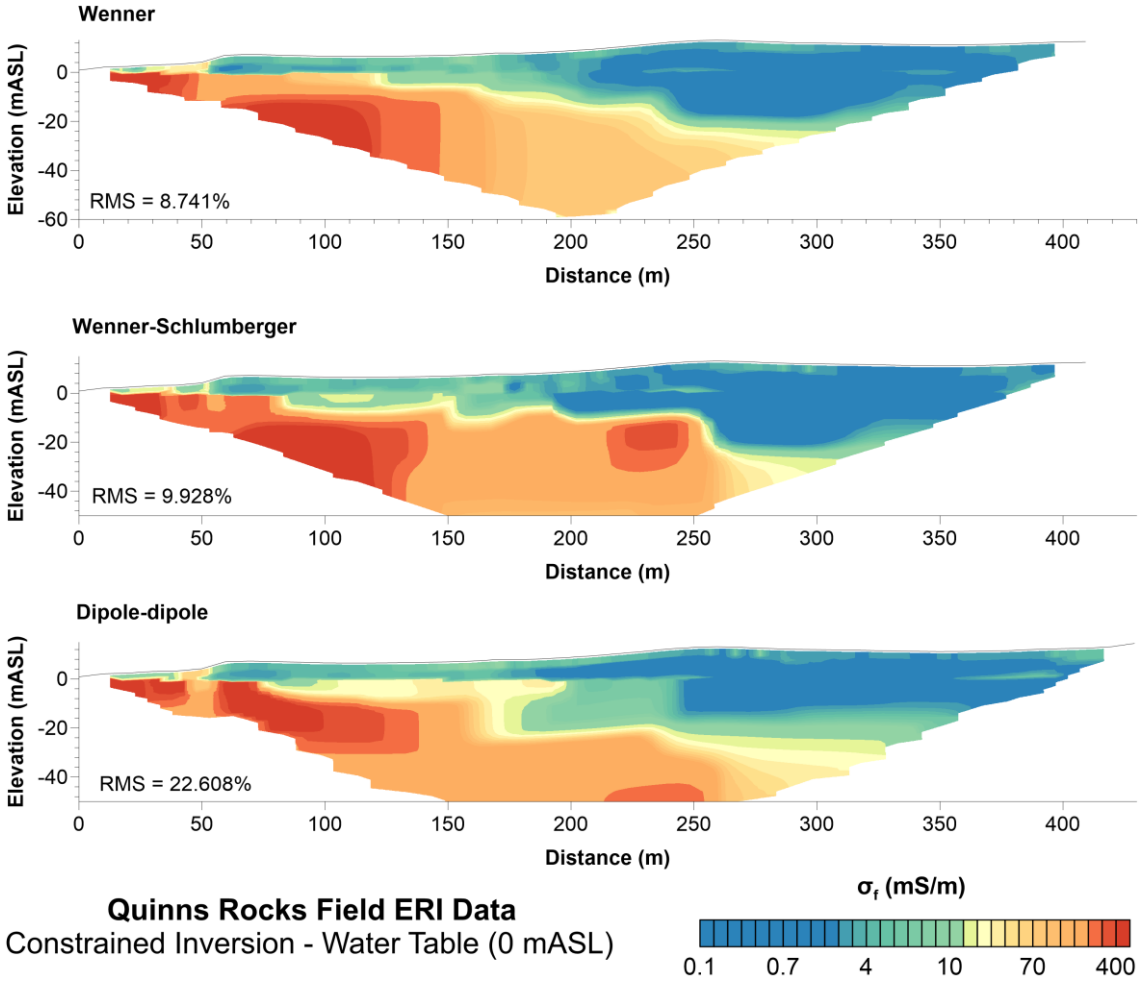

Figure 2.28

Figure A-5: Formation conductivities resulting from the guided or constrained inversion of ERI field data from each of the three electrode configurations. The sharp boundary constraint is placed on water table, which at this high-permeability coastal aquifer can be reasonably assumed flat. No additional constraints are added, as there is some uncertainty regarding the substrate's precise location, and incorrectly forcing boundaries is unlikely to accurately represent the true subsurface geo-electrical structure.

Appendix A.3 Inversion Parameters

The table below contains the inversion parameters used for inversion with RES2DINV within this chapter.

Table A-1: Full inversion parameter listing for inversion using RES2DINV. Parameters related to IP, borehole, time-lapse, and water layers have been removed for brevity.

Inversion Parameters			
Initial damping factor	0.15	Type of reference resistivity	1
Minimum damping factor	0.02	Model refinement	0.5
Local optimization option	1	Combined Marquardt and Occam inversion	0
Convergence limit for relative change	5	Type of optimisation method	2
Minimum change in RMS for line search	0.5	Convergence limit for Incomplete Gauss-Newton method	0.005
Number of iterations	10	Use data compression with Incomplete Gauss-Newton	0
Vertical to horizontal flatness filter ratio	1	Use reference model in inversion	1
Model for increase in thickness of layers	2	Damping factor for reference model	0.01
Number of nodes between adjacent electrodes	4	Use fast method to calculate Jacobian matrix.	0
Flatness filter type,	0	Use higher damping for first layer?	1
Reduce number of topographical data points?	0	Extra damping factor for first layer	5
Carry out topography modelling?	1	Type of finite-element method	1
Type of topography trend removal	1	Factor to increase model depth range	1
Type of Jacobian matrix calculation	2	Use sparse inversion method for very long survey lines	0
Increase of damping factor with depth	1.05	Optimize Jacobian matrix calculation	0
Type of topographical modelling	4	Switch electrodes for negative geometric factor	1
Robust data constrain?	1	Force consistent with the geometric factor	1
Cut-off factor for data constrain	0.05	Shift the electrodes to round up positions of electrodes	0
Robust model constraint?	1	Use active constraint balancing	0
Cut-off factor for model constraint	0.005	Type of active constraints	0
Model parameters can exceed data points?	1	Lower damping factor limit for active constraints	0.4
Use extended model?	0	Upper damping factor limit for active constraints	2.5
Reduce effect of side blocks?	1	Automatic calculation for damping factor with depth	0
Type of mesh	2	Use diagonal filter	0
Optimise damping factor?	1	Diagonal filter weight	1
Time-lapse inversion constraint	3	Limit range of data weights from error estimates?	0
Thickness of first layer (0.25 to 1.0)	0.25	Lower limit of data weights	0.3
Factor to increase thickness layer with depth	1.05	Upper limit of data weights	3
Use finite element method	1	Same data weights for different time series?	0
Width of block	1	Calculate model resolution?	1
Make sure blocks have the same width	1	Use L curve method?	0
RMS convergence limit (in percent)	0.1	Use same norms in L curve method?	0
Use logarithm of apparent resistivity	0	Allow damping factor in increase in L curve method?	1
Proceed automatically for sequential method	0	Use fast Jacobian calculation for dense data sets?	0
Limit resistivity values(0=no,1=yes)	1	Use higher damping factors at sides of model?	1
Upper limit factor (10-50)	50	Adjust damping factors for distances between the blocks?	1
Lower limit factor (0.02 to 0.1)	0.02		

Appendix A.4 Alternative Processing and Model Resolutions

In the set of images below, we recompute the datasets provided throughout this paper but include the 'diagonal roughness filter' and 'extended model' settings (Table D-1). Farquharson (2007) demonstrates how the diagonal roughness filter allow resolution of dipping interfaces in the L1-style iteratively reweighted least-square inversion approach. The interfaces tend to become vertical or horizontal during inversion otherwise.

M. Loke (2016) suggests using the 'extended model', that expands the model domain cells to the border of the model. This is compared to using a single elongate cell at the model border. This approach has two benefits; (1) it limits edge-based artefacts resulting from the relatively higher side-cell sensitivity, and (2) provides a more-realistic interpretation than the traditional pseudo-depth / midpoint plotting convention, which does not imply depth of investigation or subsurface current flow (M. Loke, 2016).

Table A-2: Modified inversion parameter settings for Appendix D

Inversion Parameter	Value
Use extended model?	1
Use diagonal filter?	1
Diagonal filter weight (0.2 to 5.0)	1.44

Outcomes using the alternate inversion approach are presented with model resolution sections. The concept of model resolution characterizes whether the data can be independently predicted or resolved (Menke, 2012b). It relates the relationship between the calculated and observed models by the resolution matrix R (M. Loke, 2016). If R = I, (i.e., the resolution matrix is an identity matrix) then every model parameter is uniquely determined. Otherwise, estimated model parameters represent weighted averages of the true model parameters (Menke, 2012b). Resolution sections can be used to estimate depth-of-investigation (i.e., (Oldenburg *et al.*, 1999)) and to aid interpretation of inversion outcomes.

Table A-3: List of figures in Appendix D. A brief description of each figure is contained in the captions. Abbreviations include W – Wenner, SC – Schlumberger, DP – Dipole-dipole, MG – Multiple Gradient.

Figure Subset		Array	Appendix Figure	Comparable In-text Figure
Fwd. Modelling (w/o topography)		W	Figure A.1	Figure 2.7
		SC	Figure A.2	Figure 2.7
		DP	Figure A.3	Figure 2.7
Fwd. Modelling (w/ topography)		W	Figure A.4	Figure 2.14
		SC	Figure A.5	Figure 2.14
		DP	Figure A.6	Figure 2.14
Fwd. Modelling (Combined Arrays)		W & SC	Figure A.7	Figure 2.15
		W & DP	Figure A.8	Figure 2.15
		SC & DP	Figure A.9	Figure 2.15
Field Data (Quinns Rocks calibration site)		W	Figure A.10	Figure 2.16
		SC	Figure A.11	Figure 2.16
		DP	Figure A.12	Figure 2.16
Field Data (Coogee site)		MG	Figure A.13	Figure 2.20
		DP	Figure A.14	Figure 2.20
		MG & DP	Figure A.15	Figure 2.20
Field Data	Hillary	DP	Figure A.16	Figure 2.25
	Swanbourne	DP	Figure A.17	Figure 2.27
	Two Rocks	DP	Figure A.18	Figure 2.25

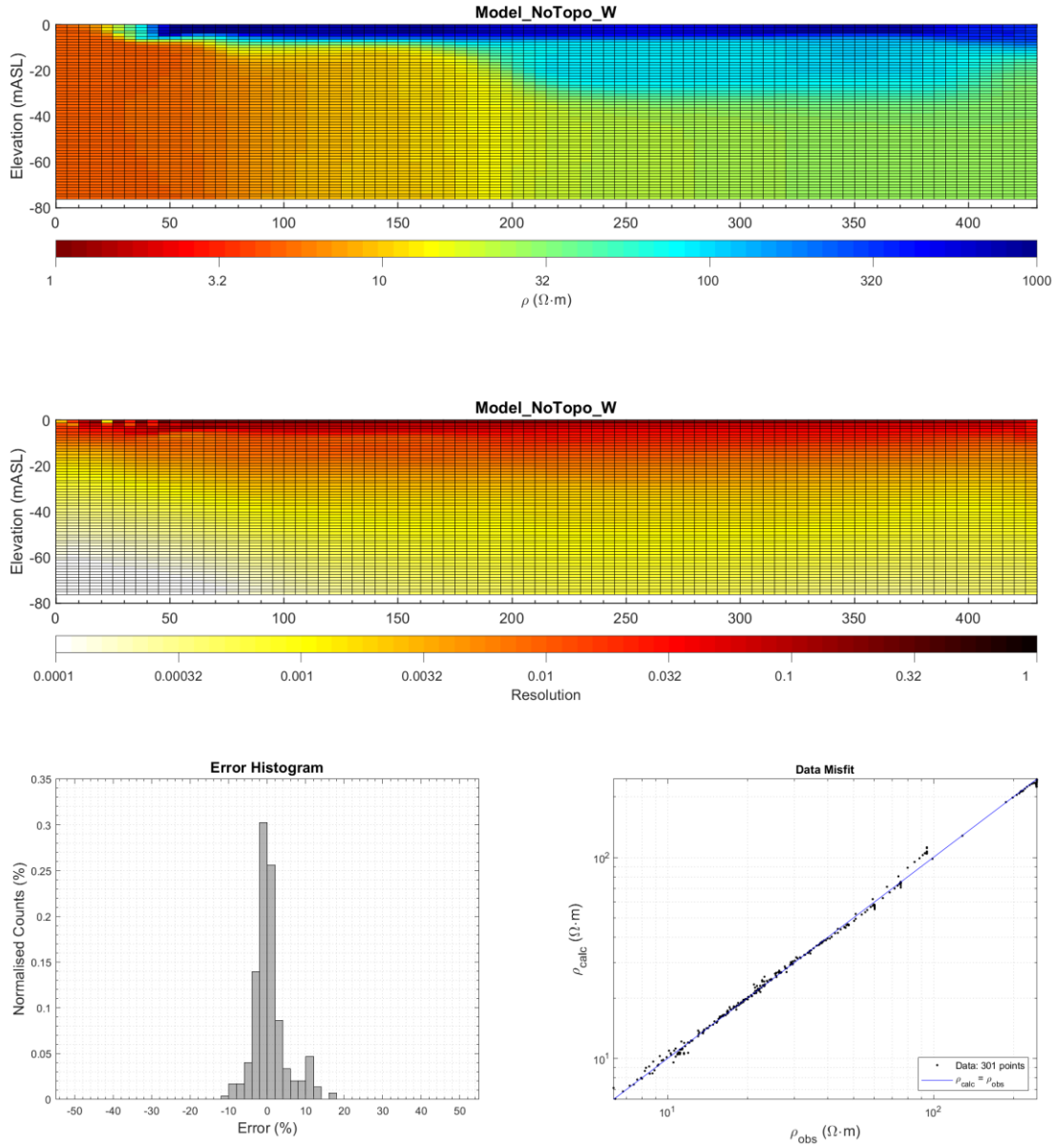

Figure A.1: Inverted conductivity distribution (top), distribution of resolution (middle), and error distribution and statistics (bottom) for the synthetic model of a seawater interface without topographic relief. This example uses the Wenner configuration.

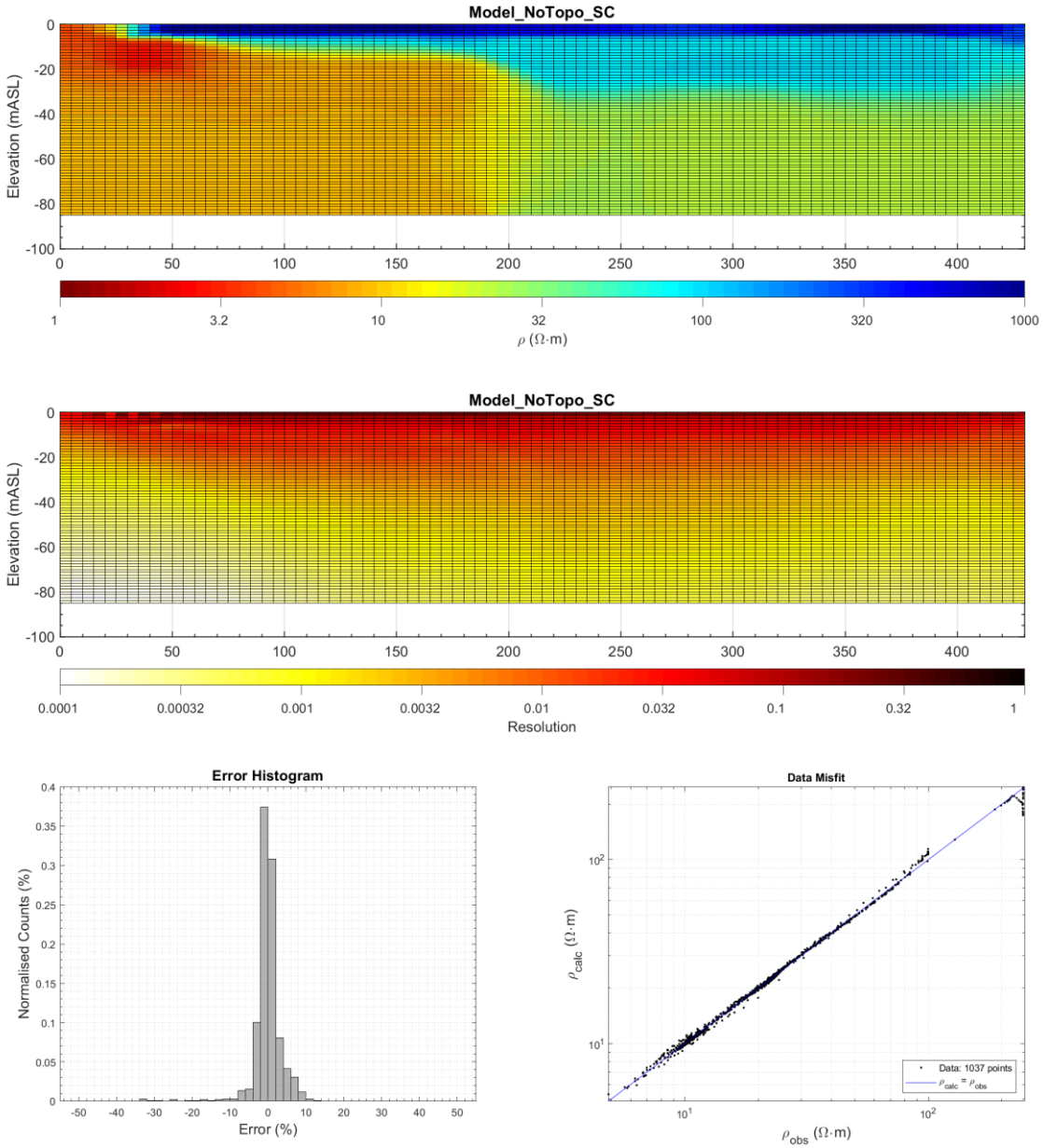

Figure A.2: Inverted conductivity distribution (top), distribution of resolution (middle), and error distribution and statistics (bottom) for the synthetic model of a seawater interface without topographic relief. This example uses the Schlumberger configuration.

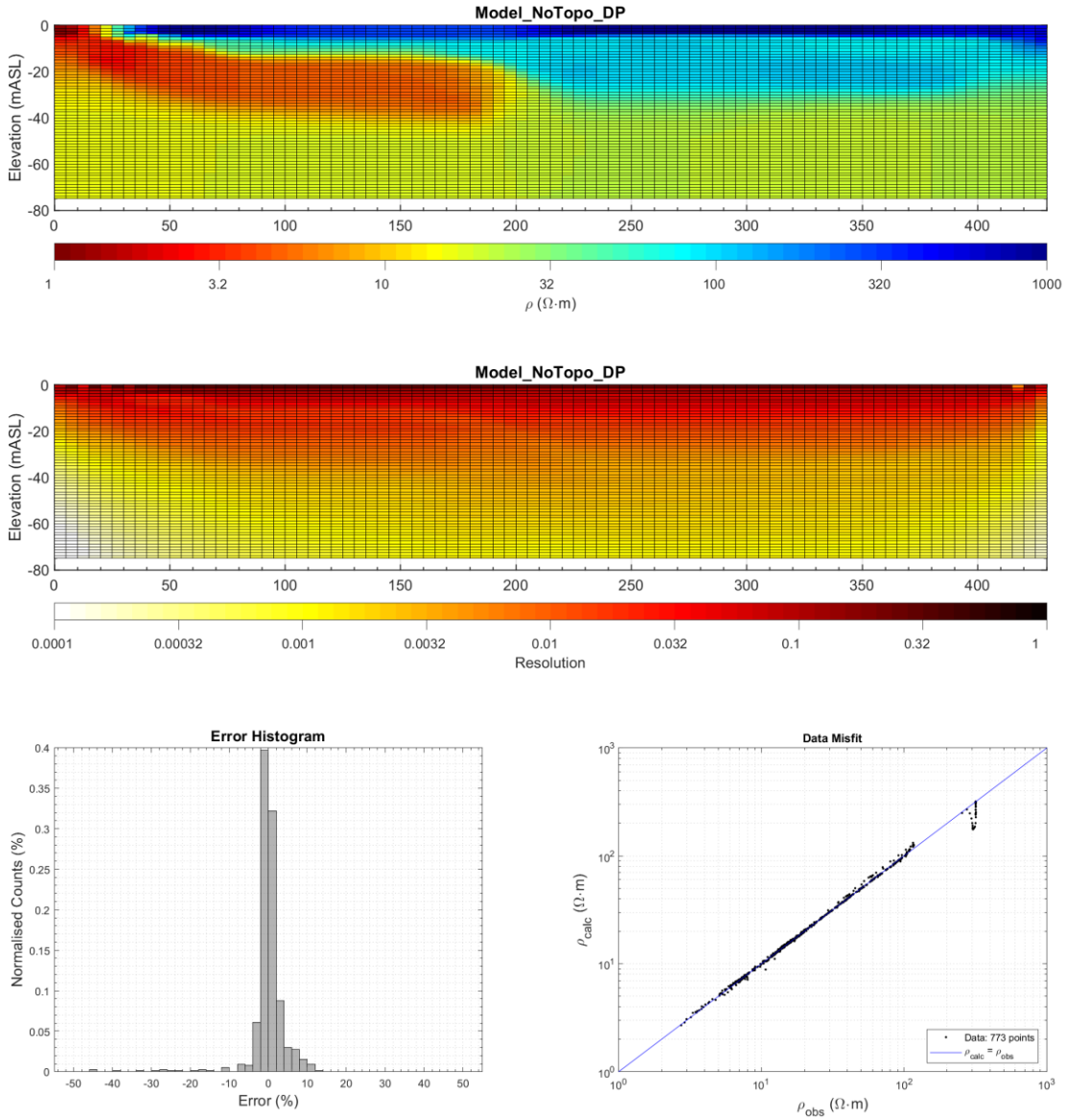

Figure A.3: inverted conductivity distribution (top), distribution of resolution (middle), and error distribution and statistics (bottom) for the synthetic model of a seawater interface without topographic relief. This example uses the dipole–dipole configuration

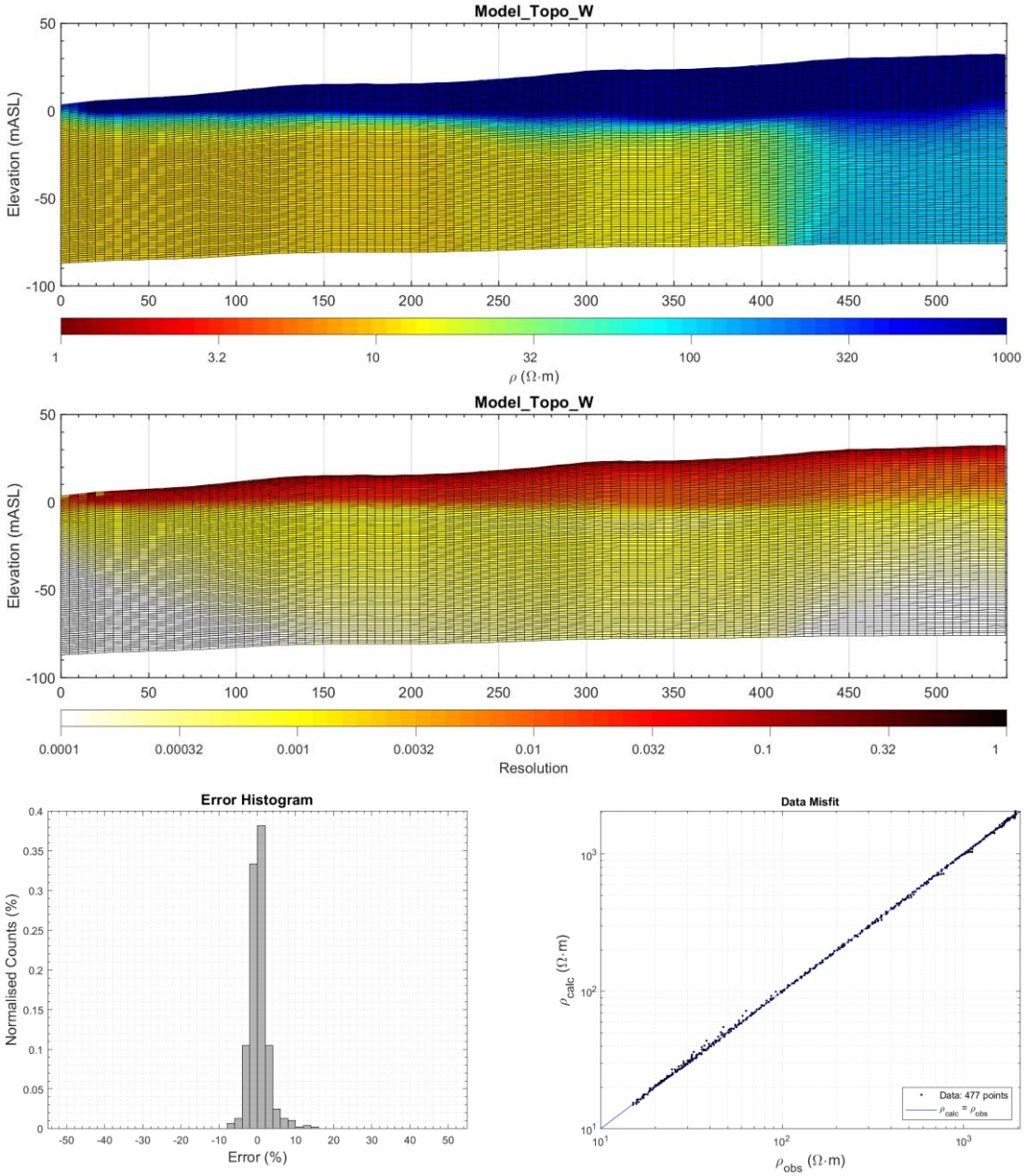

Figure A.4: Inverted conductivity distribution (top), distribution of resolution (middle), and error distribution and statistics (bottom) for the synthetic model of a seawater interface including topographic relief. This example uses the Wenner configuration.

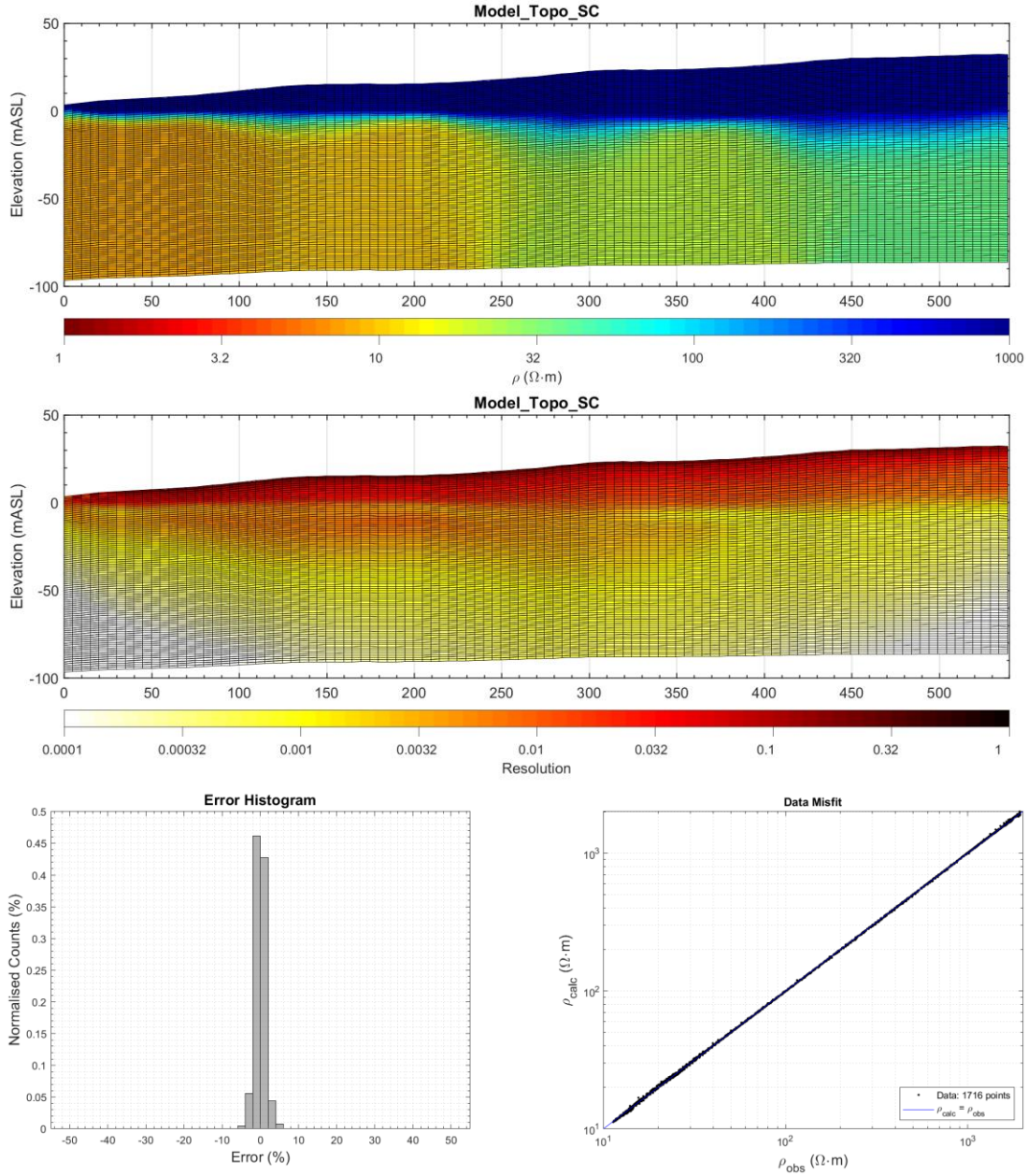

Figure A.5: Inverted conductivity distribution (top), distribution of resolution (middle), and error distribution and statistics (bottom) for the synthetic model of a seawater interface including topographic relief. This example uses the Schlumberger configuration.

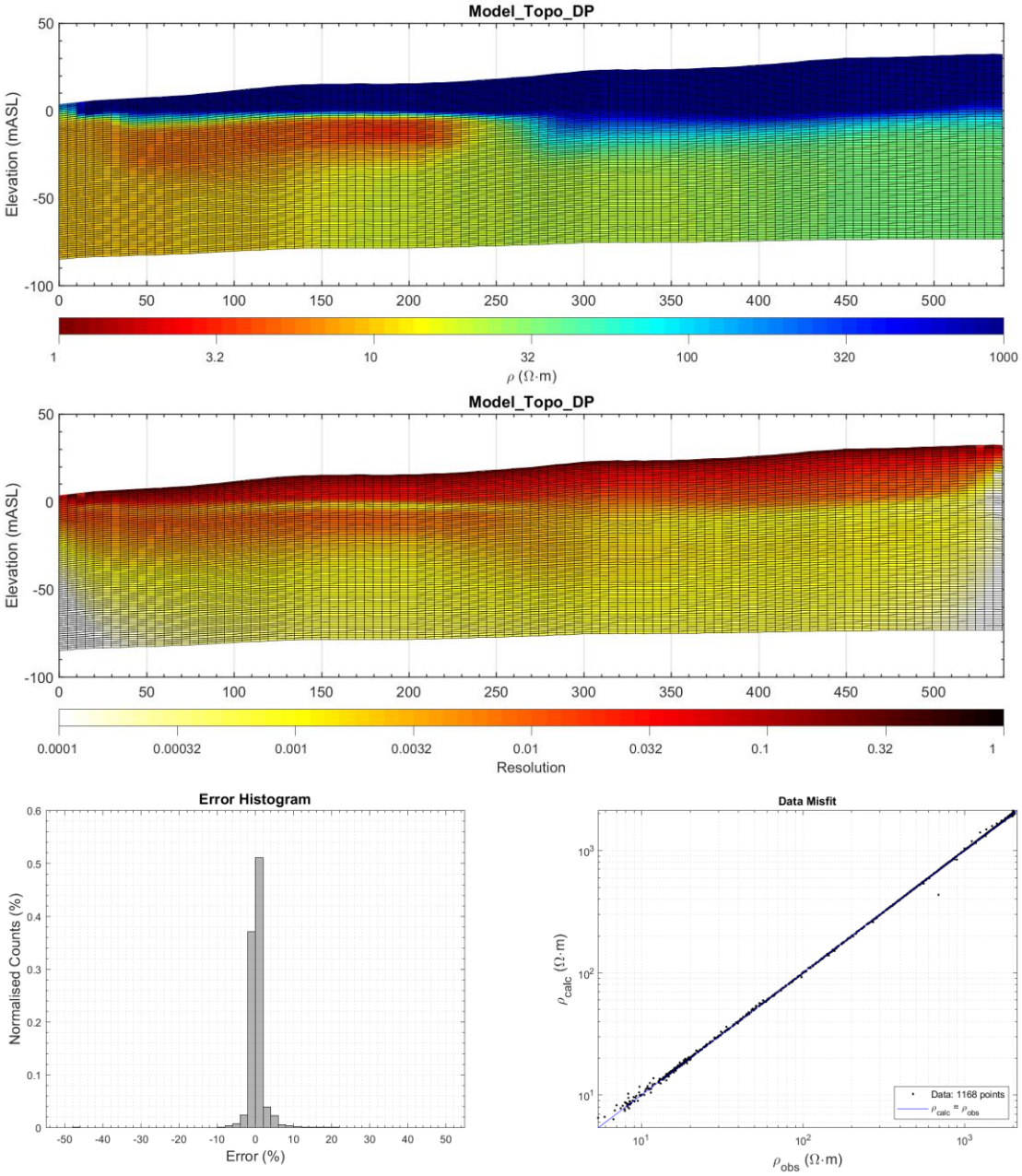

Figure A.6: Inverted conductivity distribution (top), distribution of resolution (middle), and error distribution and statistics (bottom) for the synthetic model of a seawater interface including topographic relief. This example uses the dipole–dipole configuration.

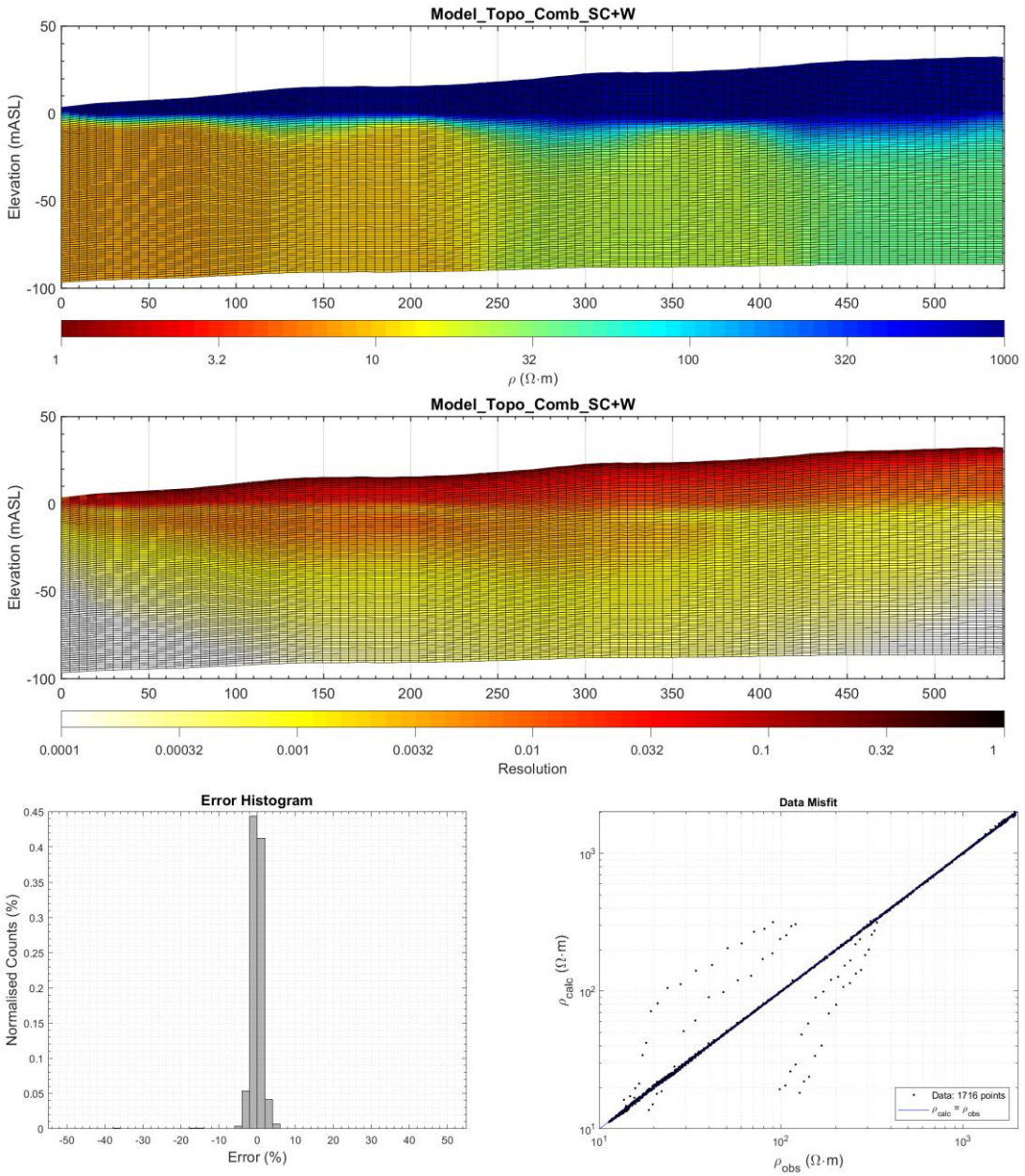

Figure A.7 Inverted conductivity distribution (top), distribution of resolution (middle), and error distribution and statistics (bottom) for the synthetic model of a seawater interface including topographic relief. This example uses the combined Wenner and Schlumberger configuration

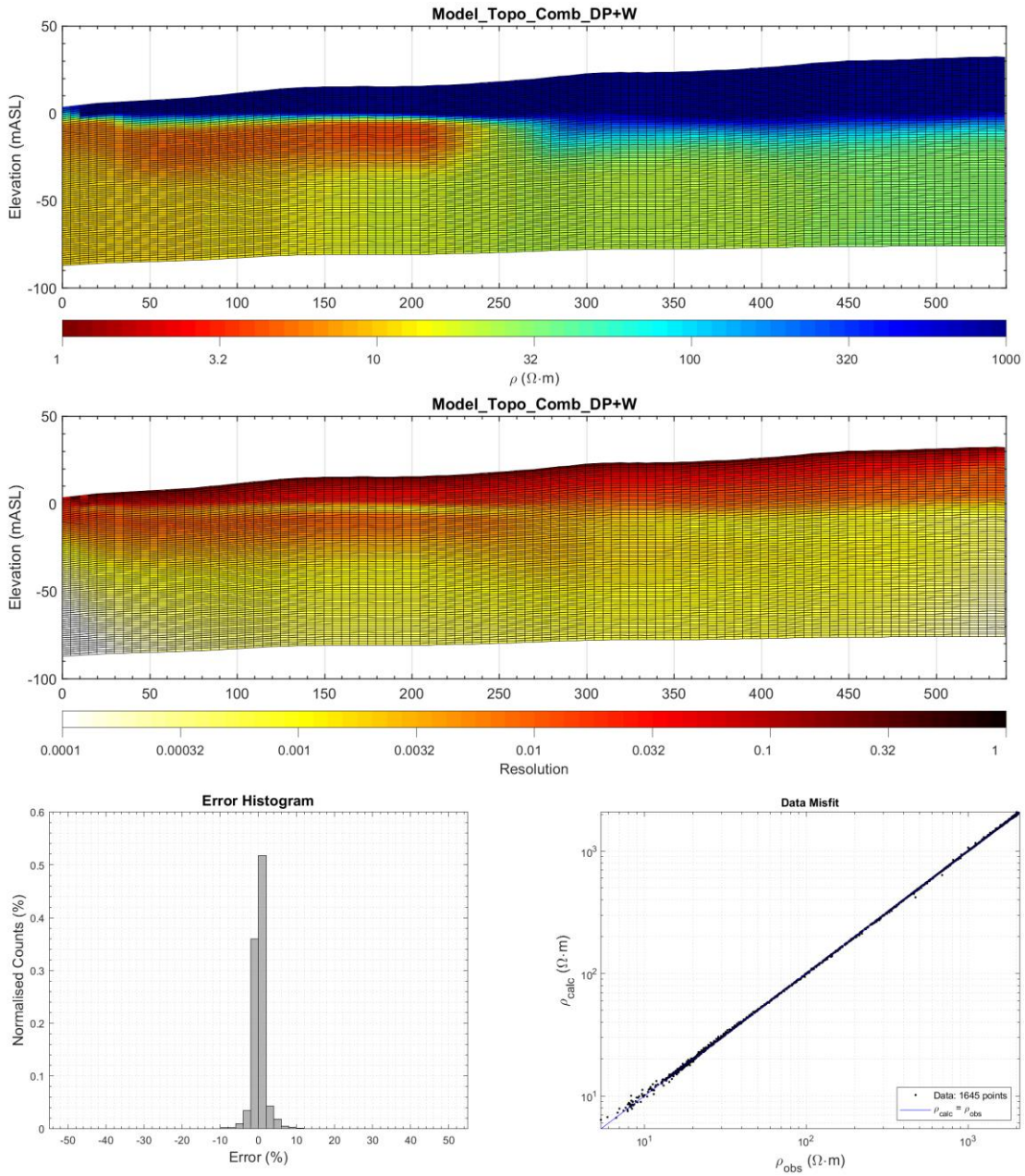

Figure A.8: Inverted conductivity distribution (top), distribution of resolution (middle), and error distribution and statistics (bottom) for the synthetic model of a seawater interface including topographic relief. This example uses the combined Wenner and dipole–dipole configuration

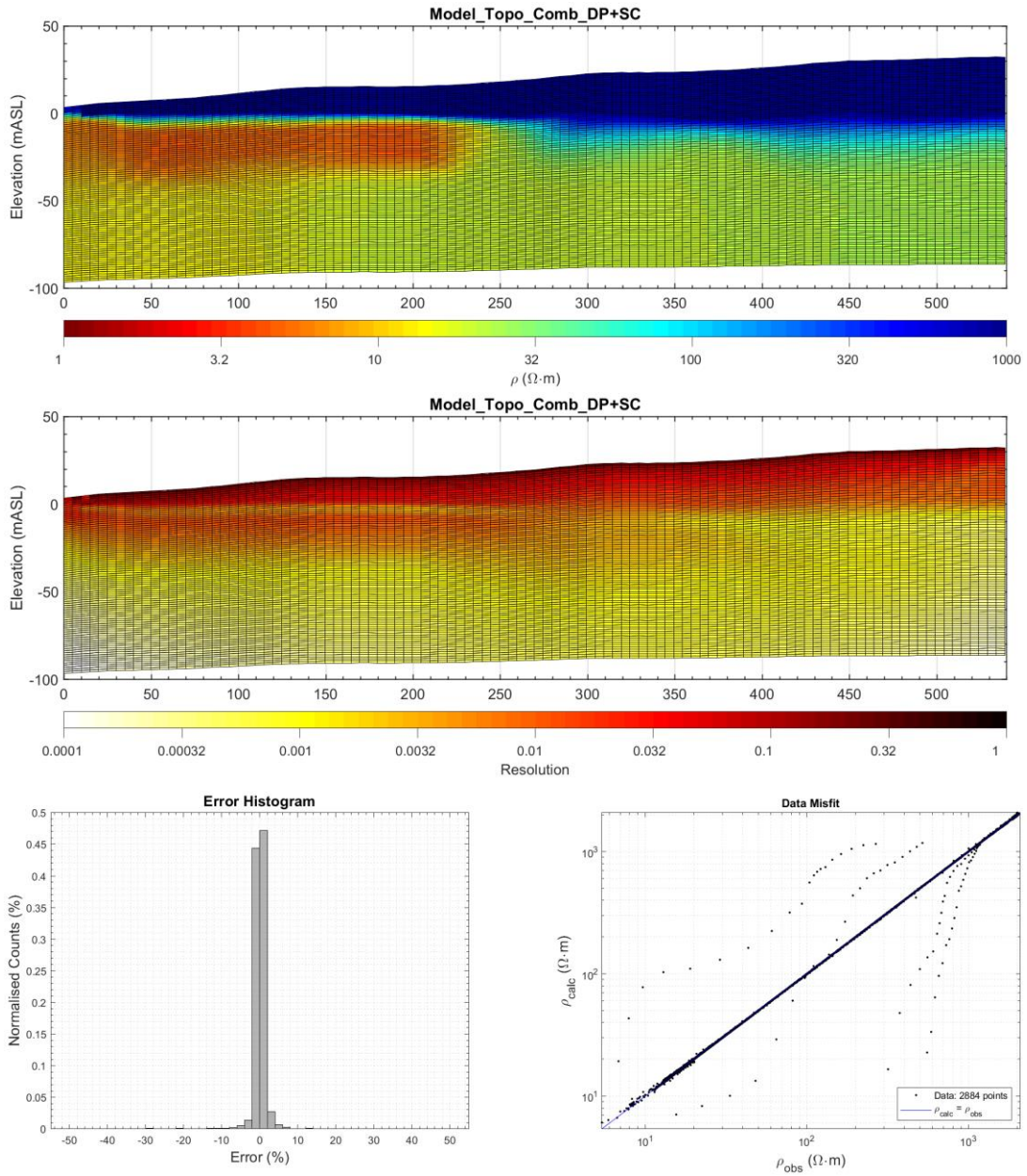

Figure A.9: Inverted conductivity distribution (top), distribution of resolution (middle), and error distribution and statistics (bottom) for the synthetic model of a seawater interface including topographic relief. This example uses the combined dipole–dipole and Schlumberger configuration

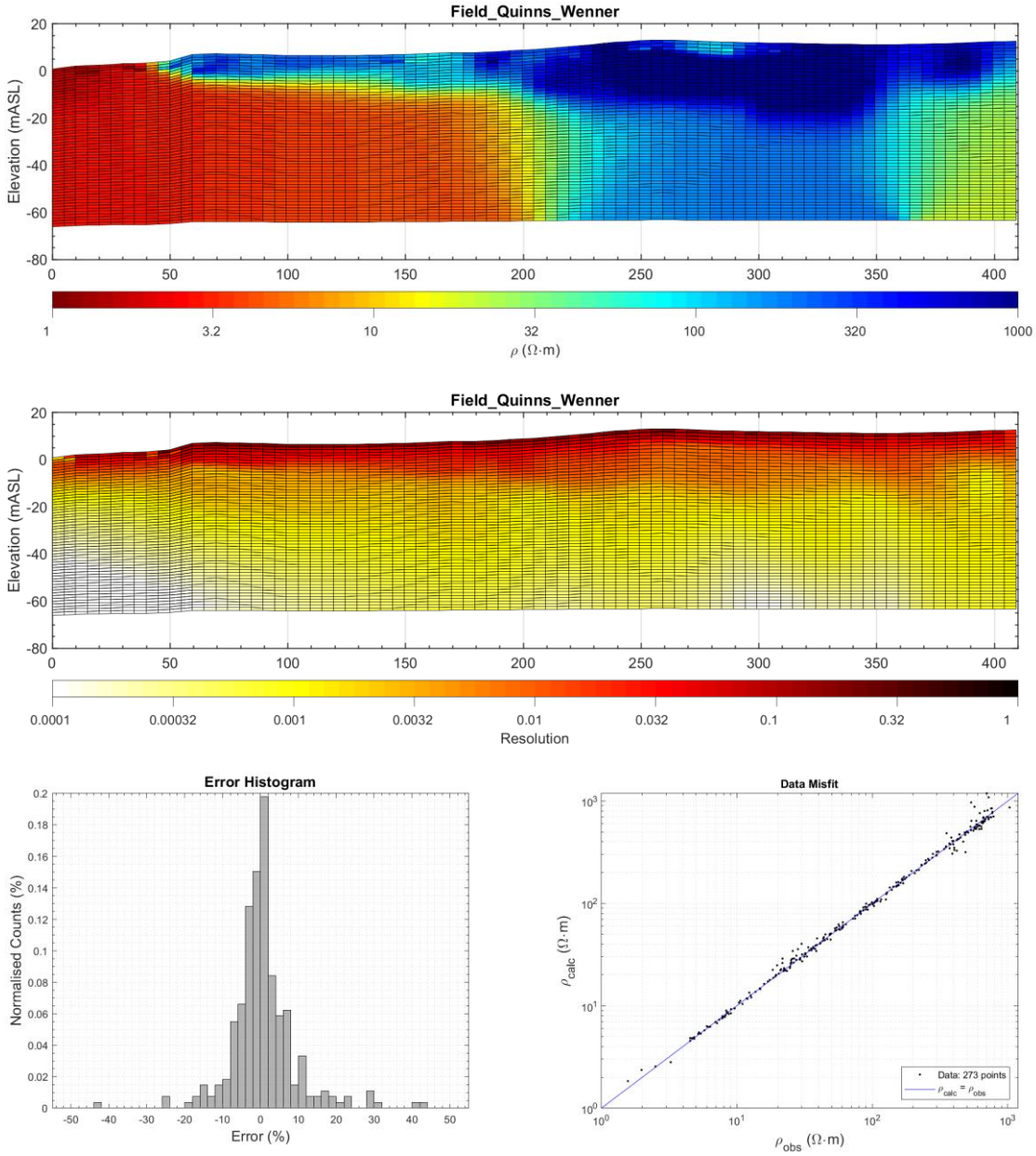

Figure A.10: Inverted conductivity distribution (top), distribution of resolution (middle), and error distribution and statistics (bottom) for the field data at the Quinns Rocks calibration site. This example uses the Wenner configuration

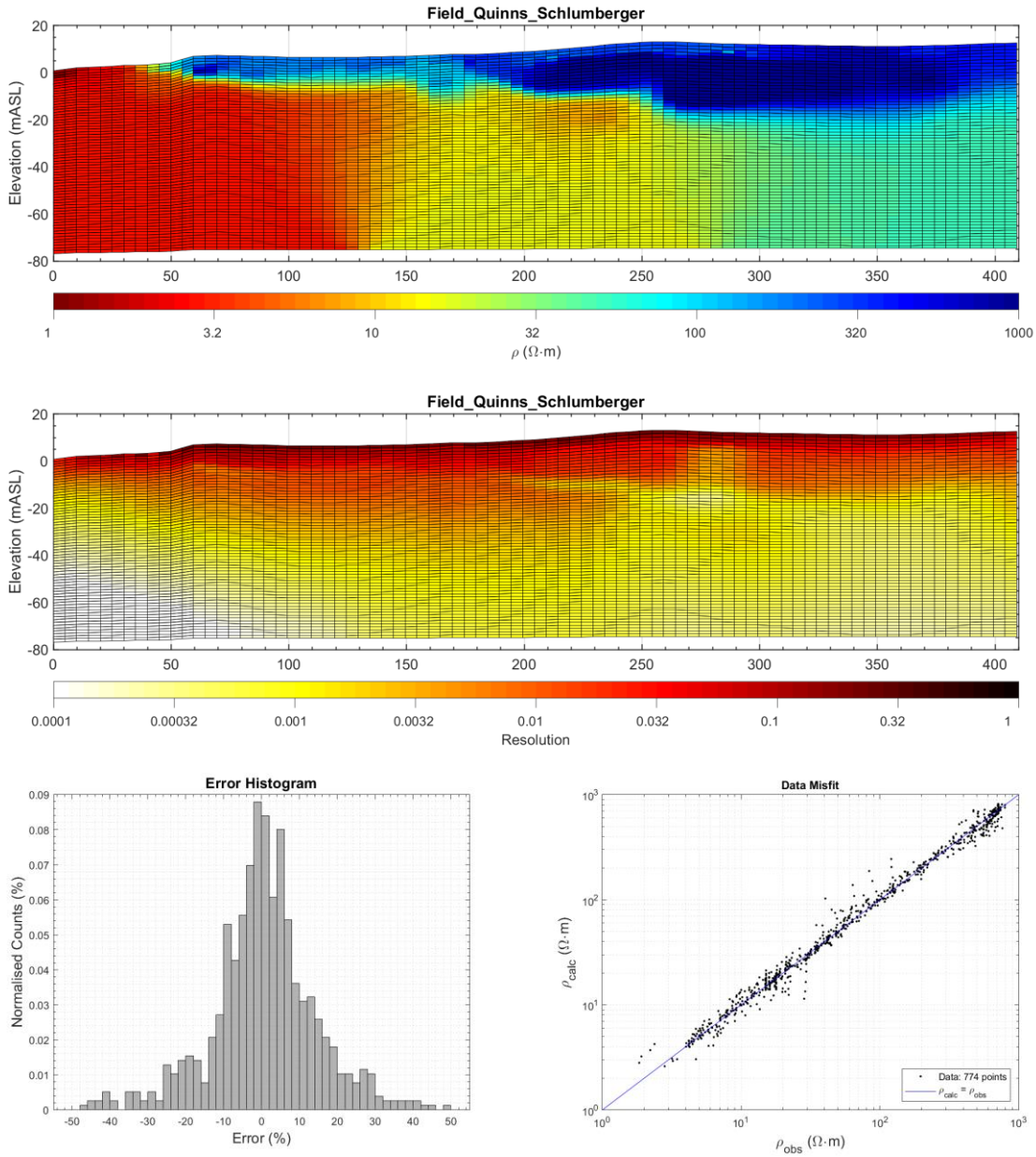

Figure A.11: Inverted conductivity distribution (top), distribution of resolution (middle), and error distribution and statistics (bottom) for the field data at the Quinns Rocks calibration site. This example uses the Schlumberger configuration.

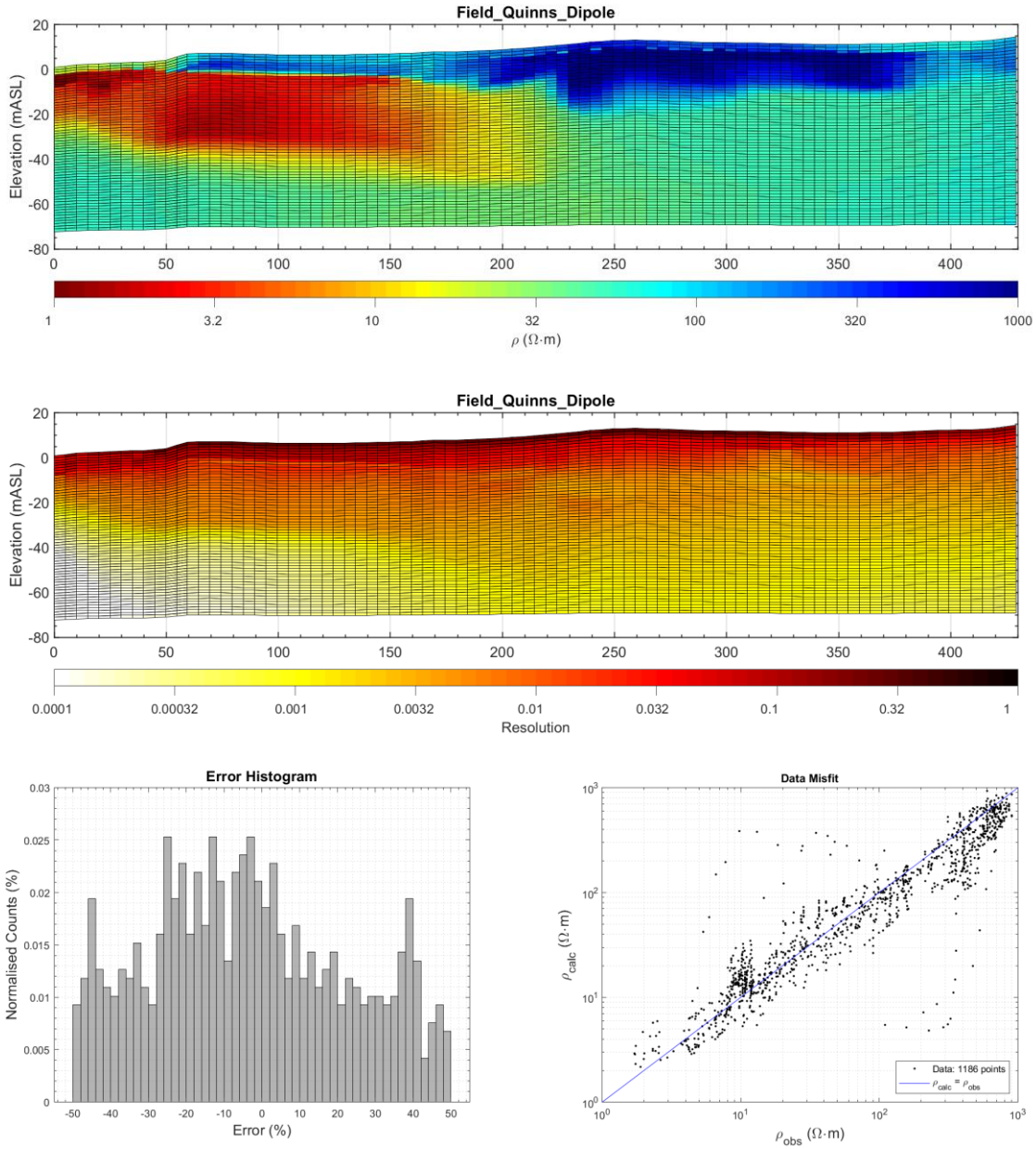

Figure A.12: Inverted conductivity distribution (top), distribution of resolution (middle), and error distribution and statistics (bottom) for the field data at the Quinns Rocks calibration site. This example uses the dipole–dipole configuration

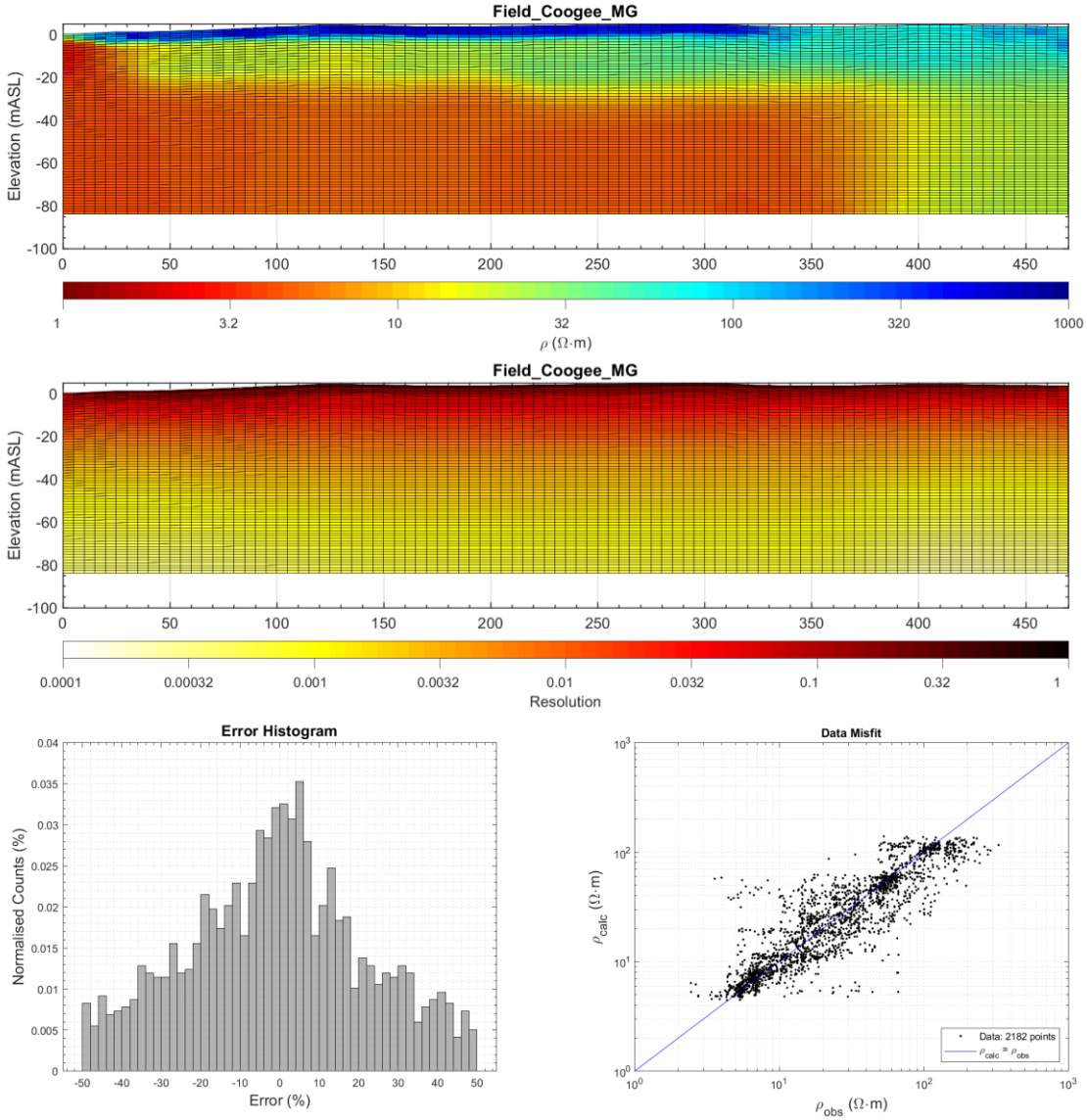

Figure A.13: Inverted conductivity distribution (top), distribution of resolution (middle), and error distribution and statistics (bottom) for the field data at the Coogee site. This example uses the multiple-gradient configuration

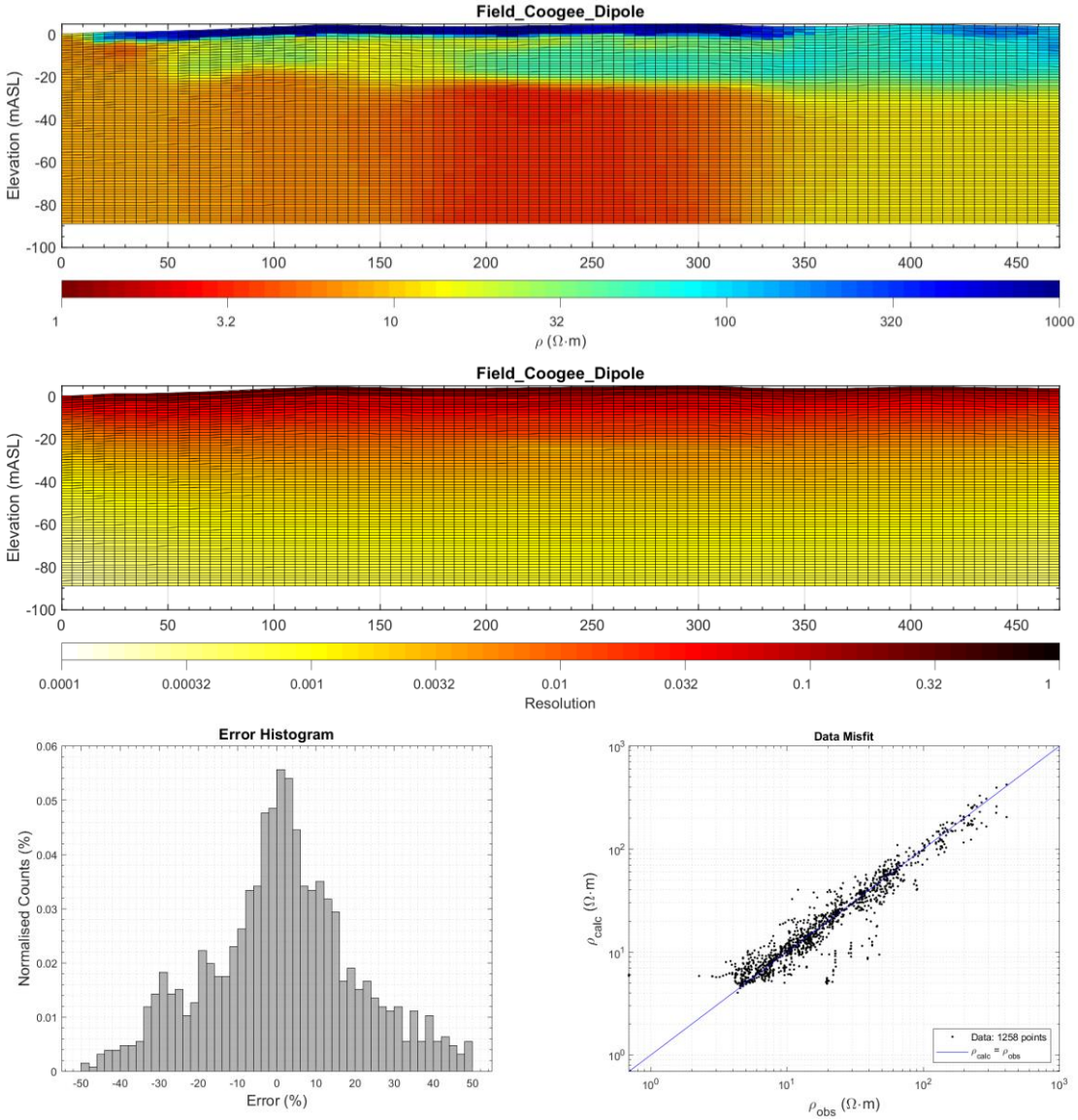

Figure A.14: Inverted conductivity distribution (top), distribution of resolution (middle), and error distribution and statistics (bottom) for the field data at the Coogee site. This example uses the dipole–dipole configuration

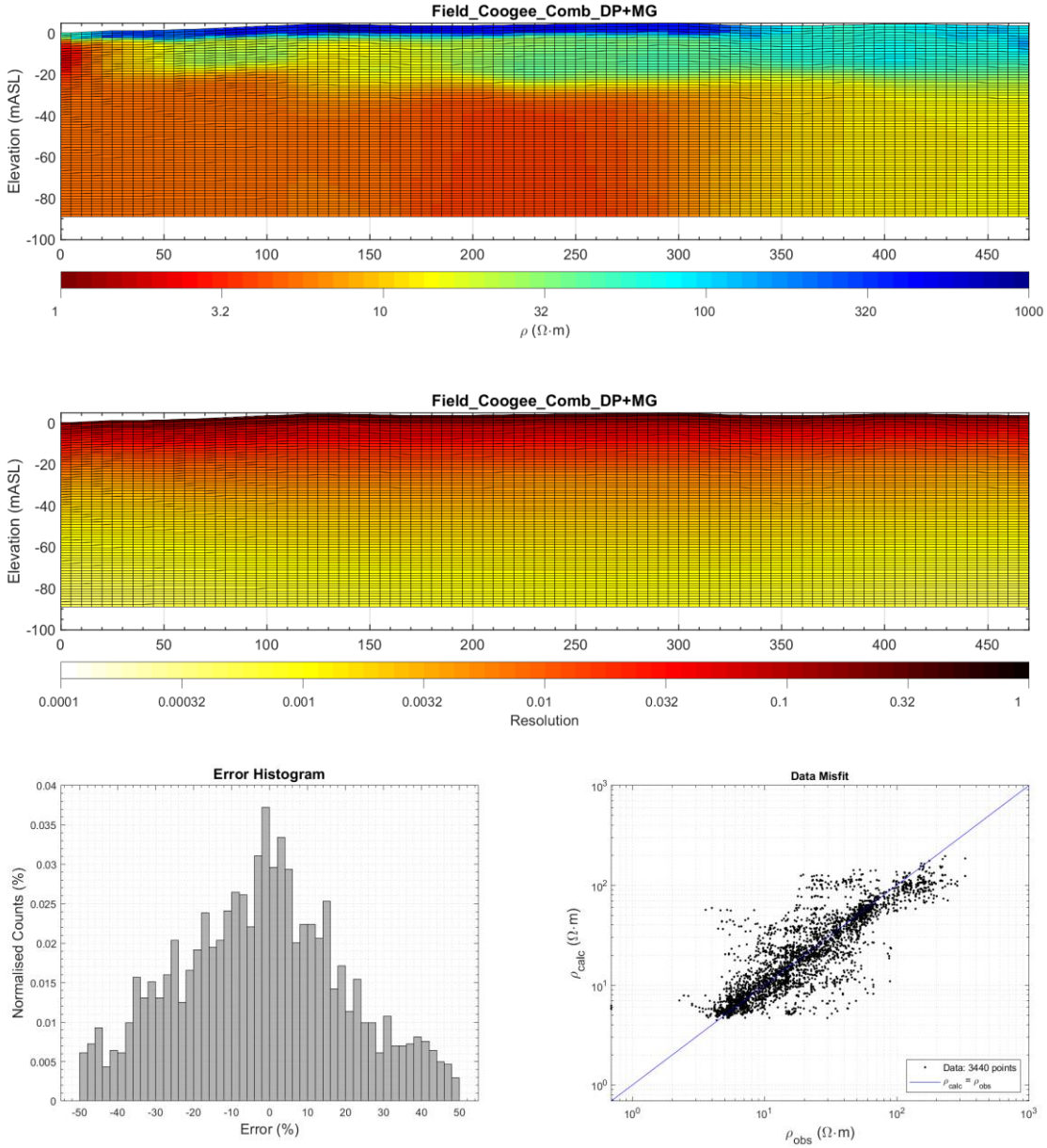

Figure A.15: Inverted conductivity distribution (top), distribution of resolution (middle), and error distribution and statistics (bottom) for the field data at the Coogee site. This example uses the combined dipole–dipole and multiple-gradient configuration

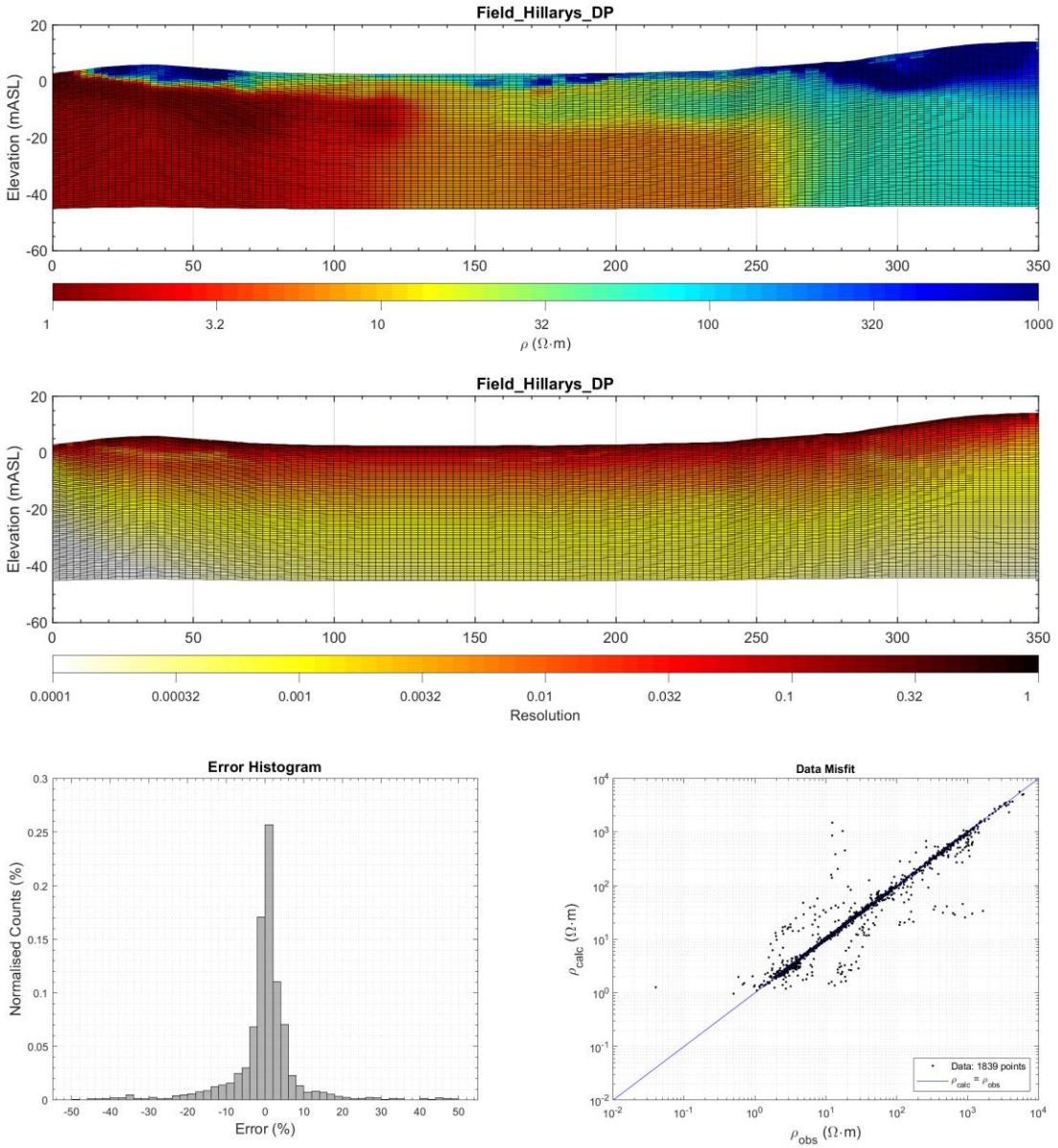

Figure A.16: Inverted conductivity distribution (top), distribution of resolution (middle), and error distribution and statistics (bottom) for the field data at the Hillarys site. This example uses the dipole–dipole configuration

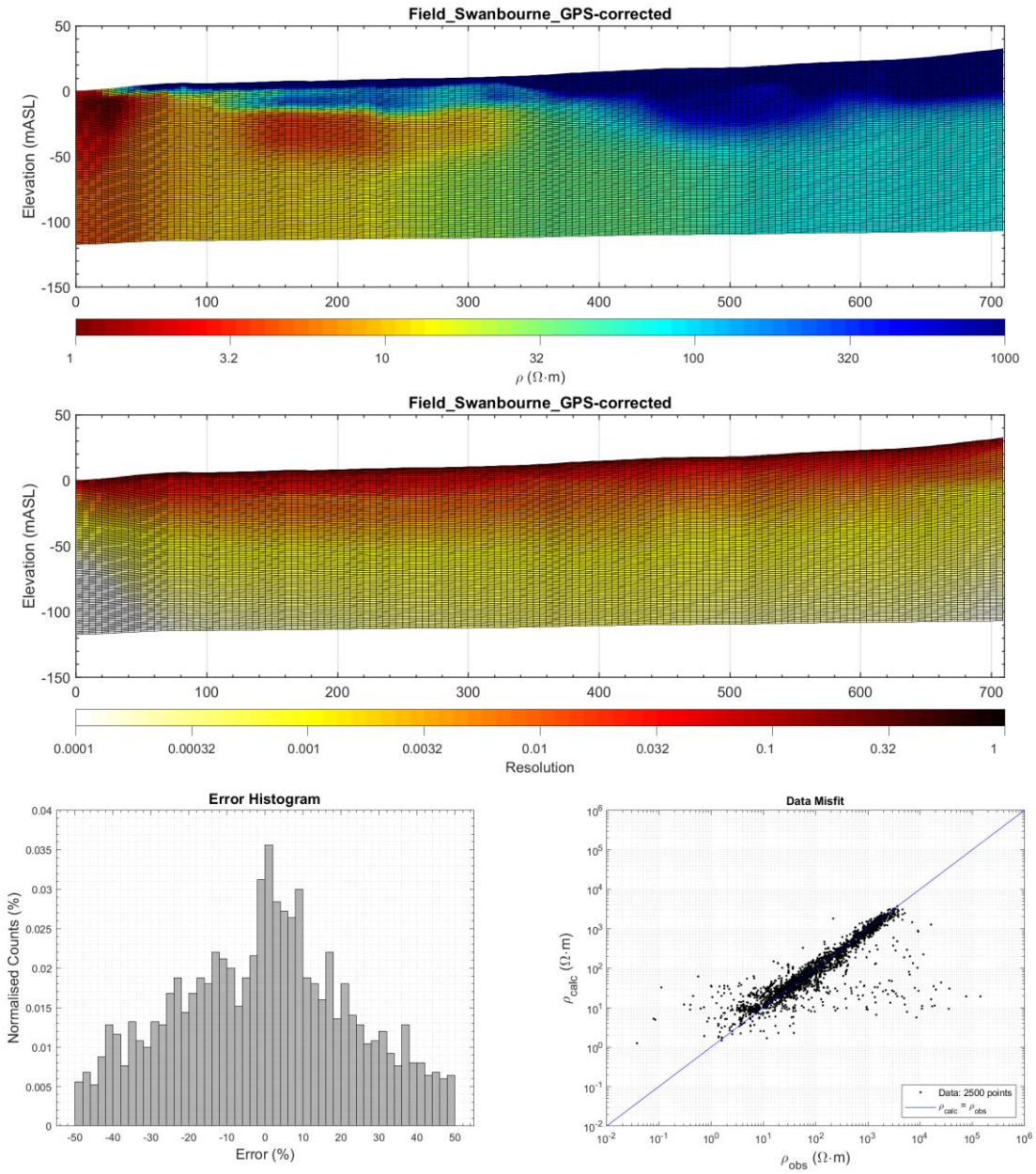

Figure A.17: Inverted conductivity distribution (top), distribution of resolution (middle), and error distribution and statistics (bottom) for the field data at the Swanbourne site. This example uses the dipole–dipole configuration

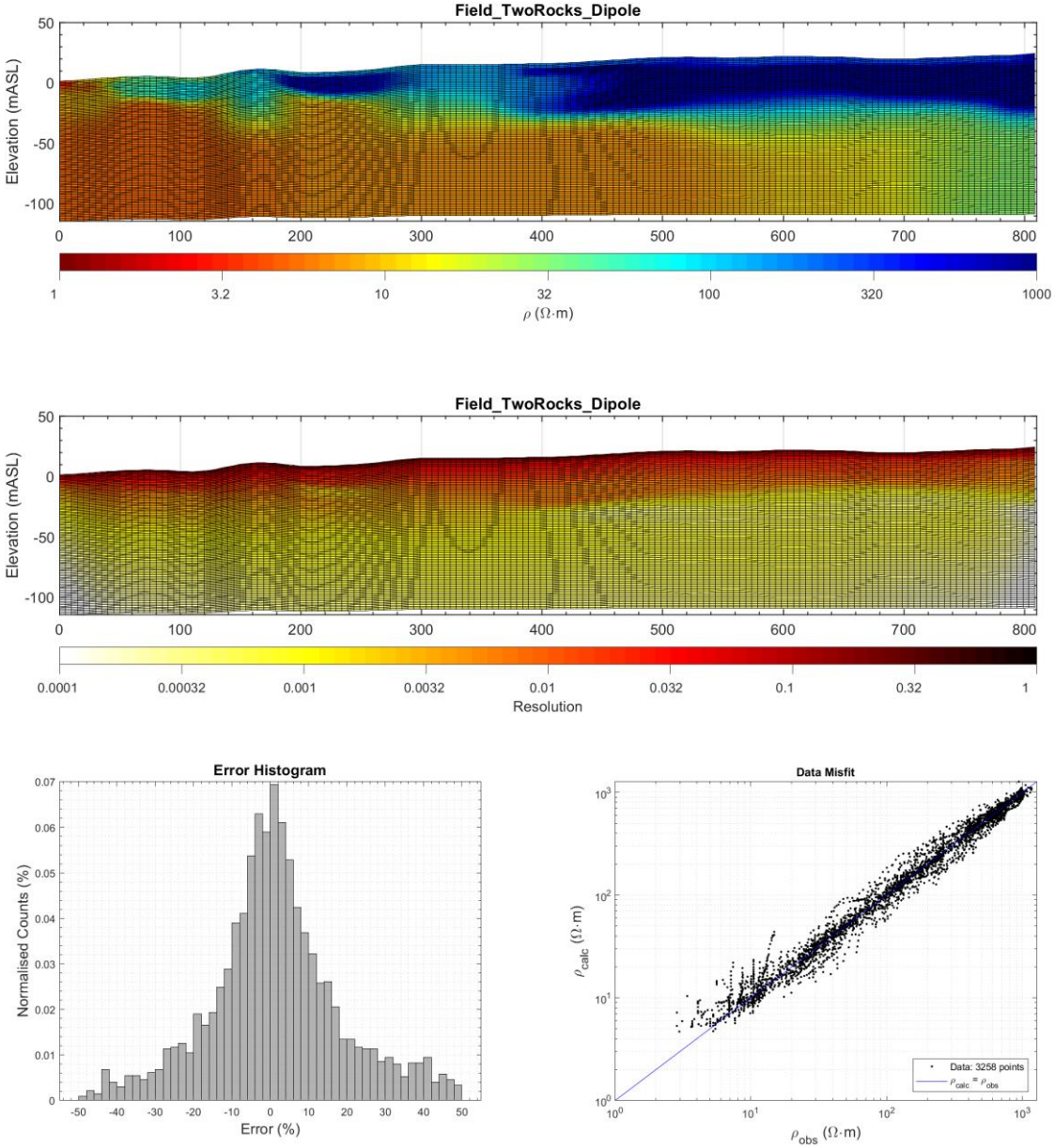

Figure A.18: Inverted conductivity distribution (top), distribution of resolution (middle), and error distribution and statistics (bottom) for the field data at the Two Rocks site. This example uses the dipole-dipole configuration

2.8 References

Abarca, E., & Clement, T. P. (2009). A novel approach for characterizing the mixing zone of a saltwater wedge. *Geophysical Research Letters, 36*(6). doi:10.1029/2008gl036995

Abdul Nassir, S. S., Loke, M. H., Lee, C. Y., & Nawawi, M. N. M. (2000). Salt-water intrusion mapping by geoelectrical imaging surveys. *Geophysical Prospecting, 48*(4), 647-661. doi:https://doi.org/10.1046/j.1365-2478.2000.00209.x

Athanasiou, E. N., Tsourlos, P. I., Papazachos, C. B., & Tsokas, G. N. (2007). Combined weighted inversion of electrical resistivity data arising from different array types. *Journal of Applied Geophysics, 62*(2), 124-140. doi:10.1016/j.jappgeo.2006.09.003

Australian Bureau of Statistics. (2006). Regional Population Growth, Australia And New Zealand. In *Year Book Australia 2004* (Vol. 3218.0): Australian Bureau of Statistics.

Australian Bureau of Statistics. (2018). Estimated Residence Population (ERP) By Statistical Area 2 (Sa2), 1991 to 2014. In: Australian Bureau of Statistics.

Beaujean, J., Nguyen, F., Kemna, A., Antonsson, A., & Engesgaard, P. (2014). Calibration of seawater intrusion models: Inverse parameter estimation using surface electrical resistivity tomography and borehole data. *Water Resources Research, 50*(8), 6828-6849. doi:10.1002/2013wr014020

Binley, A., Hubbard, S. S., Huisman, J. A., Revil, A., Robinson, D. A., Singha, K., & Slater, L. D. (2015). The emergence of hydrogeophysics for improved understanding of subsurface processes over multiple scales. *Water Resour Res, 51*(6), 3837-3866. doi:10.1002/2015WR017016

Carriere, S. D., Chalikakis, K., Senechal, G., Danquigny, C., & Emblanch, C. (2013). Combining Electrical Resistivity Tomography and Ground Penetrating Radar to study geological structuring of karst Unsaturated Zone. *Journal of Applied Geophysics, 94*, 31-41. doi:10.1016/j.jappgeo.2013.03.014

Chai, T., & Draxler, R. R. (2014). Root mean square error (RMSE) or mean absolute error (MAE)?–Arguments against avoiding RMSE in the literature. *Geoscientific Model Development, 7*(3), 1247-1250. doi:10.5194/gmd-7-1247-2014

Christiansen, A. V., & Auken, E. (2012). A global measure for depth of investigation. *Geophysics, 77*(4), Wb171-Wb177. doi:10.1190/Geo2011-0393.1

CIESIN. (2016). Gridded Population of the World, Version 4 (GPWv4): UN-Adjusted Population Count.

Claerbout, J. F., & Muir, F. (1973). Robust Modeling with Erratic Data. *Geophysics, 38*(5), 826-844. doi:Doi 10.1190/1.1440378

Constable, S. C., Parker, R. L., & Constable, C. G. (1987). Occam's inversion: A practical algorithm for generating smooth models from electromagnetic sounding data. *Geophysics, 52*(3), 289-300. doi:https://doi.org/10.1190/1.1442303

Crook, N., Binley, A., Knight, R., Robinson, D. A., Zarnetske, J., & Haggerty, R. (2008). Electrical resistivity imaging of the architecture of substream sediments. *Water Resources Research, 44*(4), n/a-n/a. doi:10.1029/2008wr006968

Dahlin, T. (2001). The development of DC resistivity imaging techniques. *Computers & Geosciences, 27*(9), 1019-1029. doi:Doi 10.1016/S0098-3004(00)00160-6

Dahlin, T., & Zhou, B. (2004). A numerical comparison of 2D resistivity imaging with 10 electrode arrays. *Geophysical Prospecting, 52*(5), 379-398. doi:DOI 10.1111/j.1365-2478.2004.00423.x

Dahlin, T., & Zhou, B. (2006). Multiple-gradient array measurements for multichannel 2D resistivity imaging. *Near Surface Geophysics, 4*(2), 113-123. doi:10.3997/1873-0604.2005037

Davidson, W. A. (1995). *Hydrogeology And Groundwater Resources Of The Perth Region, Western Australia* (Vol. 142): Geological Survey of WA.

Davidson, W. A., & Yu, X. (2008). *Perth regional aquifer modelling system (PRAMS) model development: Hydrogeology and groundwater modelling*: Department of Water.

de Franco, R., Biella, G., Tosi, L., Teatini, P., Lozej, A., Chiozzotto, B., . . . Gasparetto-Stori, G. (2009). Monitoring the saltwater intrusion by time lapse electrical resistivity tomography: The Chioggia test site (Venice Lagoon, Italy). *Journal of Applied Geophysics, 69*(3-4), 117-130. doi:https://doi.org/10.1016/j.jappgeo.2009.08.004

Department of Water WA. (2015). *Gnangara Evaluation Statement 2011-2014*. Retrieved from http://www.water.wa.gov.au/planning-for-the-future/allocation-plans/swanavon-region/gnangara-groundwater-areas-allocation-plan

Diersch, H.-J. G. (2014). *Feflow: Finite Element Modeling of Flow, Mass and Heat Transport in Porous and Fractured Media*: Springer Science & Business Media.

Ecoscape Australia Pty Ltd. (2004). *Foreshore Management Plan Mindarie – Quinns Rocks*. City of Wanneroo: Ecoscape (Australia) Pty Ltd Retrieved from http://www.wanneroo.wa.gov.au/downloads/file/1211/mindarie-quinns_rocks_foreshore_management_plan

Edwards, L. (1977). A Modified Pseudosection For Resistivity And Ip. *Geophysics, 42*(5), 1020-1036. doi:https://doi.org/10.1190/1.1440762

Ekblom, H. (1974). L p -methods for robust regression. *BIT Numerical Mathematics, 14*(1), 22-32. doi:https://doi.org/10.1007/bf01933114

Farquharson, C. G. (2007). Constructing Piecewise-Constant Models In Multidimensional Minimum-Structure Inversions. *Geophysics, 73*(1), K1-K9. doi:https://doi.org/10.1190/1.2816650

Farquharson, C. G., & Oldenburg, D. W. (1998). Non-linear inversion using general measures of data misfit and model structure. *Geophysical Journal International, 134*(1), 213-227. doi:DOI 10.1046/j.1365-246x.1998.00555.x

Fox, R. C., Hohmann, G. W., Killpack, T. J., & Rijo, L. (1980). Topographic effects in resistivity and induced-polarization surveys. *Geophysics, 45*(1), 75-93. doi:https://doi.org/10.1190/1.1441041

Gallardo, L. A., & Meju, M. A. (2007). Joint two-dimensional cross-gradient imaging of magnetotelluric and seismic traveltime data for structural and lithological classification. *Geophysical Journal International, 169*(3), 1261-1272. doi:10.1111/j.1365-246X.2007.03366.x

Gallardo, L. A., & Meju, M. A. (2011). Structure-Coupled Multiphysics Imaging in Geophysical Sciences. *Reviews of Geophysics, 49*(1). doi:Artn Rg1003

10.1029/2010rg000330

Geoscience Australia. (2017). ELVIS - Elevation Information Systsm. Retrieved from http://www.ga.gov.au/elvis/#/

Gozzard, J. R. (2007). *Geology And Landforms Of The Perth Region*: Geological Survey of Western Australia.

Günther, T. (2004). *Inversion methods and resolution analysis for the 2D/3D reconstruction of resistivity structures from DC measurements.* (Dissertation). Retrieved from http://hdl.handle.net/11858/00-1735-0000-0001-3314-2 FID GEO-LEO e-docs database.

Hamdan, H., & Vafidis, A. (2013). Joint inversion of 2D resistivity and seismic travel time data to image saltwater intrusion over karstic areas. *Environmental Earth Sciences, 68*(7), 1877-1885. doi:10.1007/s12665-012-1875-9

Heen, Z. H. A., & Muhsen, S. A. (2017). Electrical Resistivity Tomography for Coastal Sea Water Intrusion Characterization along Rafah Area, South of Gaza Strip, Palestine. *IUG Journal of Natural Studies*.

Henderson, R. D., Day-Lewis, F. D., Abarca, E., Harvey, C. F., Karam, H. N., Liu, L. B., & Lane, J. W. (2010). Marine electrical resistivity imaging of submarine groundwater discharge: sensitivity analysis and application in Waquoit Bay, Massachusetts, USA. *Hydrogeology Journal, 18*(1), 173-185. doi:10.1007/s10040-009-0498-z

Herman, R. (2001). An introduction to electrical resistivity in geophysics. *American Journal of Physics, 69*(9), 943-952. doi:Doi 10.1119/1.1378013

Hermans, T., Vandenbohede, A., Lebbe, L., Martin, R., Kemna, A., Beaujean, J., & Nguyen, F. (2012). Imaging artificial salt water infiltration using electrical resistivity tomography constrained by geostatistical data. *Journal of Hydrology, 438*, 168-180. doi:10.1016/j.jhydrol.2012.03.021

Igroufa, S., Hashim, R., & Taib, S. (2010). Mapping Of Salt-Water Intrusion By Geoelectrical Imaging In Carey Islands.

Imperial College London. (2015). Salt Water Intrusion In Bangladesh. Retrieved from https://www.imperial.ac.uk/grantham/our-work/impacts-and-adaptation/ipcc-working-group-ii/sea-level-rise/

Ishola, K. S., Nawawi, M. N. M., & Abdullah, K. (2015). Combining Multiple Electrode Arrays for Two-Dimensional Electrical Resistivity Imaging Using the Unsupervised Classification Technique. *Pure and Applied Geophysics, 172*(6), 1615-1642. doi:10.1007/s00024-014-1007-4

Ivkovic, K., Marshall, S., Morgan, L., Werner, A., Carey, H., Cook, S., . . . Caruana, L. (2012). National–Scale Vulnerability Assessment Of Seawater Intrusion: Summary Report. *Australian Government National Water Commision. Waterlines Report Series No, 85*.

Johnson, T. C., Versteeg, R. J., Ward, A., Day-Lewis, F. D., & Revil, A. (2010). Improved hydrogeophysical characterization and monitoring through parallel modeling and inversion of time-domain resistivity andinduced-polarization data. *Geophysics, 75*(4), WA27-WA41. doi:https://doi.org/10.1190/1.3475513

Karaoulis, M., Tsourlos, P., Kim, J. H., & Revil, A. (2014). 4D time-lapse ERT inversion: introducing combined time and space constraints. *Near Surface Geophysics, 12*(1), 25-34. doi:10.3997/1873-0604.2013004

Koukadaki, M. A., Karatzas, G. P., Papadopoulou, M. P., & Vafidis, A. (2007). Identification of the Saline Zone in a Coastal Aquifer Using Electrical Tomography Data and Simulation. *Water Resources Management, 21*(11), 1881. doi:10.1007/s11269-006-9135-y

Kretschmer, P., & Degens, B. (2012). *Review Of Available Groundwater In The Superficial Aquifer For The Yanchep, Eglinton And Quinns Groundwater Subareas*. Retrieved from

Krishnaraj, S., Balasubramanian, M., Gopinath, S., Saravanan, K., Prakash, R., Ravindran, A., & Sarma, V. (2014). Evaluation Of Estuarine Impact On Groundwater Salinization In Pondicherry Coastal Aquifers Using Electrical Resistivity Imagine Techniques. doi:http://doi.org/10.6084/m9.figshare.1206337

Le, C. V. A., Harris, B. D., Pethick, A. M., Takougang, E. M. T., & Howe, B. (2016). Semiautomatic and Automatic Cooperative Inversion of Seismic and Magnetotelluric Data. *Surveys in Geophysics, 37*(5), 845-896. doi:10.1007/s10712-016-9377-z

Legates, D. R., & McCabe, G. J. (1999). Evaluating the use of "goodness-of-fit" Measures in hydrologic and hydroclimatic model validation. *Water Resources Research, 35*(1), 233-241. doi:https://doi.org/10.1029/1998WR900018

Leyland, L. A. (2011). *Hydrogeology Of The Leederville Aquifer, Central Perth Basin, Western Australia*: University of Western Australia.

Leyland, L. A. (2012). *Reinterpretation Of The Hydrogeology Of The Leederville Aquifer : Gnangara Groundwater System / By La Leyland*. Perth, W.A: Dept. of Water.

Loke, M. (2003). Rapid 2d Resistivity & Ip Inversion Using The Least-Squares Method. *Geotomo Software, Manual, 122*.

Loke, M. (2016). Tutorial: 2d And 3d Electrical Imaging Surveys. Penang, Malaysia, Universiti Sains Malaysia. Retrieved from http://www.geotomosoft.com/downloads.php

Loke, M., Alfouzan, F. A., & Nawawi, M. (2007). Optimisation of electrode arrays used in 2D resistivity imaging surveys. In *ASEG Extended Abstracts 2007* (pp. 1-4): Australian Society of Exploration Geophysicists (ASEG).

Loke, M. H. (2016a). RES2DINVx64 ver. 4.05 with multi-core and 64-bit support. Retrieved from http://www.geotomosoft.com/

Loke, M. H. (2016b). Res2DMod. Retrieved from http://www.geotomosoft.com/

Loke, M. H., Chambers, J. E., Rucker, D. F., Kuras, O., & Wilkinson, P. B. (2013). Recent developments in the direct-current geoelectrical imaging method. *Journal of Applied Geophysics, 95*, 135-156. doi:10.1016/j.jappgeo.2013.02.017

Loke, M. H., Kiflu, H., Wilkinson, P. B., Harro, D., & Kruse, S. (2015). Optimized arrays for 2D resistivity surveys with combined surface and buried arrays. *Near Surface Geophysics, 13*(5), 505-517. doi:10.3997/1873-0604.2015038

Loke, M. H., & Lane., J. W. (2004). Inversion of data from electrical imaging surveys in water-covered areas. In *ASEG Extended Abstracts 2004: 17th Geophysical Conference* (pp. 1-4).

Loke, M. H., Wilkinson, P. B., Chambers, J. E., & Strutt, M. (2014). Optimized arrays for 2D cross-borehole electrical tomography surveys. *Geophysical Prospecting, 62*(1), 172-189. doi:https://doi.org/10.1111/1365-2478.12072

Loke, M. H., Wilkinson, P. B., Uhlemann, S. S., Chambers, J. E., & Oxby, L. S. (2014). Computation of optimized arrays for 3-D electrical imaging surveys. *Geophysical Journal International, 199*(3), 1751-1764. doi:10.1093/gji/ggu357

Loke, M. H., Wilkinson, P. S., Chambers, J. E., Uhlemann, S. S., & Sorensen, J. P. R. (2015). Optimized arrays for 2-D resistivity survey lines with a large number of electrodes. *Journal of Applied Geophysics, 112*(Supplement C), 136-146. doi:10.1016/j.jappgeo.2014.11.011

Lu, C. (2011). *Mixing in complex coastal hydrogeologic systems.* (Thesis). Georgia Institute of Technology, Retrieved from http://hdl.handle.net/1853/39600

Lu, C. H., Chen, Y. M., Zhang, C., & Luo, J. (2013). Steady-state freshwater-seawater mixing zone in stratified coastal aquifers. *Journal of Hydrology, 505*, 24-34. doi:10.1016/j.jhydrol.2013.09.017

Marker, P. A., Foged, N., He, X., Christiansen, A. V., Refsgaard, J. C., Auken, E., & Bauer-Gottwein, P. (2015). Performance evaluation of groundwater model hydrostratigraphy from airborne electromagnetic data and lithological borehole logs. *Hydrology and Earth System Sciences, 19*(9), 3875-3890. doi:10.5194/hess-19-3875-2015

Martorana, R., Fiandaca, G., Ponsati, A. C., & Cosentino, P. L. (2009). Comparative tests on different multi-electrode arrays using models in near-surface geophysics. *Journal of Geophysics and Engineering, 6*(1), 1-20. doi:10.1088/1742-2132/6/1/001

Menke, W. (2012b). Chapter 4 - Solution Of The Linear, Gaussian Inverse Problem, Viewpoint 2: Generalized Inverses. In *Geophysical Data Analysis: Discrete Inverse Theory (Third Edition)* (pp. 69-88). Boston: Academic Press.

National Water Commission. (2012). *National-scale vulnerability assessment of seawater intrusion: Coastal aquifer typology*. (ISSN 1448-2177). Geoscience Australia, Canberra, and National Centre for Groundwater Research and Training, Adelaide

Nguyen, F., Kemna, A., Antonsson, A., Engesgaard, P., Kuras, O., Ogilvy, R., . . . Pulido-Bosch, A. (2009). Characterization of seawater intrusion using 2D electrical imaging. *Near Surface Geophysics, 7*(5-6), 377-390. doi:https://doi.org/10.3997/1873-0604.2009025

Noel, M., & Xu, B. W. (1991). Archaeological Investigation by Electrical-Resistivity Tomography - a Preliminary-Study. *Geophysical Journal International, 107*(1), 95-102. doi:DOI 10.1111/j.1365-246X.1991.tb01159.x

O'Callaghan, J., Pattiaratchi, C., & Hamilton, D. (2007). The response of circulation and salinity in a micro-tidal estuary to sub-tidal oscillations in coastal sea surface elevation. *Continental Shelf Research, 27*(14), 1947-1965. doi:10.1016/j.csr.2007.04.004

Ogilvy, R. D., Meldrum, P. I., Kuras, O., Wilkinson, P. B., Chambers, J. E., Sen, M., . . . Tsourlos, P. (2009). Automated monitoring of coastal aquifers with electrical resistivity tomography. *Near Surface Geophysics, 7*(5-6), 367-375. doi:Doi 10.3997/1873-0604.2009027

Oldenburg, D. W., & Li, Y. G. (1999). Estimating depth of investigation in dc resistivity and IP surveys. *Geophysics, 64*(2), 403-416. doi:Doi 10.1190/1.1444545

Paster, A., Dagan, G., & Guttman, J. (2006). The salt-water body in the Northern part of Yarkon-Taninim aquifer: Field data analysis, conceptual model and prediction. *Journal of Hydrology, 323*(1-4), 154-167. doi:10.1016/j.jhydrol.2005.08.018

Pazdirek, O., & Blaha, V. (1996). *Examples of resistivity imaging using ME-100 resistivity field acquisition system.* Paper presented at the 58th EAGE Conference and Exhibition.

Pidlisecky, A., Moran, T., Hansen, B., & Knight, R. (2016). Electrical Resistivity Imaging of Seawater Intrusion into the Monterey Bay Aquifer System. *Ground Water, 54*(2), 255-261. doi:10.1111/gwat.12351

Pollock, D., Smith, A., Trefry, M., Davis, G., Johnston, C., & Gardiner, A. (2006). *Status of Groundwater Quality in the Cockburn Sound Catchment*. Retrieved from https://www.der.wa.gov.au/image/.../2006_Status_GroundwaterSUMMARY.PDF

Pool, M., & Carrera, J. (2011). A correction factor to account for mixing in Ghyben-Herzberg and critical pumping rate approximations of seawater intrusion in coastal aquifers. *Water Resources Research, 47*(5). doi:10.1029/2010wr010256

Post, V. E., Groen, J., Kooi, H., Person, M., Ge, S., & Edmunds, W. M. (2013). Offshore fresh groundwater reserves as a global phenomenon. *Nature, 504*(7478), 71-78. doi:10.1038/nature12858

Price, R. M., Top, Z., Happell, J. D., & Swart, P. K. (2003). Use of tritium and helium to define groundwater flow conditions in Everglades National Park. *Water Resources Research, 39*(9). doi:10.1029/2002wr001929

Ronczka, M., Voss, T., & Gunther, T. (2015). Cost-efficient imaging and monitoring of saltwater in a shallow aquifer by using long electrode ERT. *Journal of Applied Geophysics, 122*, 202-209. doi:10.1016/j.jappgeo.2015.08.014

Roy, A., & Apparao, A. (1971). Depth Of Investigation In Direct Current Methods. *Geophysics, 36*(5), 943-959. doi:https://doi.org/10.1190/1.1440226

Rücker, C., Günther, T., & Spitzer, K. (2006). Three-dimensional modelling and inversion of dc resistivity data incorporating topography - I. Modelling. *Geophysical Journal International, 166*(2), 495-505. doi:10.1111/j.1365-246X.2006.03010.x

Samouelian, A., Cousin, I., Tabbagh, A., Bruand, A., & Richard, G. (2005). Electrical resistivity survey in soil science: a review. *Soil & Tillage Research, 83*(2), 173-193. doi:10.1016/j.still.2004.10.004

Schwarz, J., Bear, J., & Dagan, G. (2016). Groundwater Development in Israel. *Ground Water, 54*(1), 143-148. doi:10.1111/gwat.12384

Small, C., & Nicholls, R. J. (2003). A global analysis of human settlement in coastal zones. *Journal of Coastal Research, 19*(3), 584-599. doi:http://www.jstor.org/stable/4299200

Smith, A., Massuel, S., & Pollock, D. (2012). *Geohydrology Of The Tamala Limestone Formation In The Perth Region: Origin And Role Of Secondary Porosity* (EP12568). Retrieved from Australia:

Smith, A., Massuel, S., Pollock, D., Fitzpatrick, A., Byrne, J., Johnstone, C., . . . Cahill, K. (2012). *Final Summary Report-Hydrological Controls On Mar In Perth's Coastal Aquifer* (EP125485). Retrieved from https://publications.csiro.au/rpr/pub?list=BRO&pid=csiro:EP125485

Smith, A. J., & Hick, W. P. (2001). *Hydrogeology and aquifer tidal propagation in Cockburn Sound, Western Australia* (procite:cd26e417-61cd-4a56-89b7-1ee9e32aab7a). Retrieved from

Sonenshein, R. S. (1995). Delineation of Saltwater Intrusion in the Biscayne Aquifer, Eastern Dade County, Florida. *WATER-RESOURCES INVESTIGATIONS REPORT 96-4285.* Retrieved from http://fl.water.usgs.gov/Miami/online_reports/wri964285/

Soueid Ahmed, A., Zhou, J., Jardani, A., Revil, A., & Dupont, J. P. (2015). Image-guided inversion in steady-state hydraulic tomography. *Advances in Water Resources, 82*, 83-97. doi:https://doi.org/10.1016/j.advwatres.2015.04.001

Steklova, K., & Haber, E. (2017). Joint hydrogeophysical inversion: state estimation for seawater intrusion models in 3D. *Computational Geosciences, 21*(1), 75-94. doi:10.1007/s10596-016-9595-y

Stummer, P., Maurer, H., Horstmeyer, H., & Green, A. G. (2002). Optimization of DC resistivity data acquisition: Real-time experimental design and a new multielectrode system. *IEEE Transactions on Geoscience and Remote Sensing, 40*(12), 2727-2735. doi:10.1109/Tgrs.2002.807015

Szalai, S., Koppan, A., Szokoli, K., & Szarka, L. (2013). Geoelectric imaging properties of traditional arrays and of the optimized Stummer configuration. *Near Surface Geophysics, 11*(1), 51-62. doi:10.3997/1873-0604.2012058

Szalai, S., Novak, A., & Szarka, L. (2009). Depth of Investigation and Vertical Resolution of Surface Geoelectric Arrays. *Journal of Environmental and Engineering Geophysics, 14*(1), 15-23. doi:Doi 10.2113/Jeeg14.1.15

Takam Takougang, E. M., Harris, B., Kepic, A., & Le, C. V. (2015). Cooperative Joint Inversion Of 3d Seismic And Magnetotelluric Data: With Application In A Mineral Province. *Geophysics, 80*(4), R175-R187. doi:https://doi.org/10.1190/GEO2014-0252.1

Tsourlos, P. I., Szymanski, J. E., & Tsokas, G. N. (1999). The effect of terrain topography on commonly used resistivity arrays. *Geophysics, 64*(5), 1357-1363. doi:Doi 10.1190/1.1444640

Uhlemann, S. S., Sorensen, J. P. R., House, A. R., Wilkinson, P. B., Roberts, C., Gooddy, D. C., . . . Chambers, J. E. (2016). Integrated time-lapse geoelectrical imaging of wetland hydrological processes. *Water Resources Research, 52*(3), 1607-1625. doi:10.1002/2015wr017932

Van Weert, F., van der Gun, J., & Reckman, J. (2009). *Global overview of saline groundwater occurrence and genesis* (GP 2009-1). Retrieved from International Groundwater Resources Assessment Centre: https://www.un-igrac.org/resource/global-overview-saline-groundwater-occurrence-and-genesis-0

Verruijt, A. (1968). A Note On The Ghyben-Herzberg Formula. *Hydrological Sciences Journal, 13*(4), 43-46. doi:https://doi.org/10.1080/02626666809493624

Vorosmarty, C. J., Green, P., Salisbury, J., & Lammers, R. B. (2000). Global water resources: vulnerability from climate change and population growth. *Science, 289*(5477), 284-288. doi:10.1126/science.289.5477.284

Water-Technology. (2016). Groundwater Replenishment System (GWRS), Orange County, California, United States of America. Retrieved from http://www.water-technology.net/projects/groundwaterreplenish/

Water Corporation. (2019). Groundwater Replenishment Scheme Stage 2 Expansion. Retrieved from https://www.watercorporation.com.au/water-supply/ongoing-works/groundwater-replenishment-scheme

Water Information Reporting database. (2019). Water Information Reporting Database. Retrieved from http://wir.water.wa.gov.au. from W.A Dept. of Water, W.A Dept. Regional Development http://wir.water.wa.gov.au

Weisstein, E. W. (2017). Absolute Error. Retrieved from http://mathworld.wolfram.com/AbsoluteError.html

Wentworth, C. K. (1947). Factors In The Behavior Of Ground Water In A Ghyben-Herzberg System. doi:http://hdl.handle.net/10125/12855

Werner, A. D., Bakker, M., Post, V. E. A., Vandenbohede, A., Lu, C. H., Ataie-Ashtiani, B., . . . Barry, D. A. (2013). Seawater intrusion processes, investigation and management: Recent advances and future challenges. *Advances in Water Resources, 51*, 3-26. doi:10.1016/j.advwatres.2012.03.004

Wilkinson, P. B., Loke, M. H., Meldrum, P. I., Chambers, J. E., Kuras, O., Gunn, D. A., & Ogilvy, R. D. (2012). Practical aspects of applied optimized survey design for electrical resistivity tomography. *Geophysical Journal International, 189*(1), 428-440. doi:10.1111/j.1365-246X.2012.05372.x

Wilkinson, P. B., Meldrum, P. I., Chambers, J. E., Kuras, O., & Ogilvy, R. D. (2006). Improved strategies for the automatic selection of optimized sets of electrical resistivity tomography measurement configurations. *Geophysical Journal International, 167*(3), 1119-1126. doi:10.1111/j.1365-246X.2006.03196.x

Willmott, C. J., & Matsuura, K. (2005). Advantages of the mean absolute error (MAE) over the root mean square error (RMSE) in assessing average model performance. *Climate Research, 30*(1), 79-82. doi:DOI 10.3354/cr030079

Willmott, C. J., Matsuura, K., & Robeson, S. M. (2009). Ambiguities inherent in sums-of-squares-based error statistics. *Atmospheric Environment, 43*(3), 749-752. doi:10.1016/j.atmosenv.2008.10.005

Wilson, S. R., Ingham, M., & McConchie, J. A. (2006). The applicability of earth resistivity methods for saline interface definition. *Journal of Hydrology, 316*(1-4), 301-312. doi:10.1016/j.jhydrol.2005.05.004

Wu, J. C., Xue, Y. Q., Liu, P. M., Wang, J. J., Jiang, Q. B., & Shi, H. W. (1993). Sea-Water Intrusion in the Coastal Area of Laizhou Bay, China .2. Sea-Water Intrusion Monitoring. *Ground Water, 31*(5), 740-745. doi:DOI 10.1111/j.1745-6584.1993.tb00845.x

Zhou, J. (2015). *Structure-Constrained Image-Guided Inversion Of Geophysical Data.* (Thesis). Colorado School of Mines, Retrieved from http://hdl.handle.net/11124/17066

Zhou, J., Revil, A., Karaoulis, M., Hale, D., Doetsch, J., & Cuttler, S. (2014). Image-guided inversion of electrical resistivity data. *Geophysical Journal International, 197*(1), 292-309. doi:10.1093/gji/ggu001

3 Groundwater Throughflow and Seawater Intrusion in High-Quality Coastal Aquifers

This chapter is a research article accepted for publication in Scientific Reports (Nature) on 19th May 2020. It is comprised six principle parts. In each part, I demonstrate the challenges faced by groundwater monitoring in coastal margins. These are referenced to a long-term seawater monitoring site in Perth, Western Australia where I show evidence of seawater intrusion. These parts include:

1. The extreme range of hydraulic conductivity that exists for high quality karstic aquifer systems.
2. Key influences on terrestrial groundwater flow and seawater intrusion.
3. Limitations of the methods used to quantify aquifer flow and the seawater interface.
4. Impacts of anisotropy and heterogeneity on the position of the seawater interface.
5. Application of geophysical imaging to reveal the saline groundwater wedge.
6. Monitoring technologies able to capture the rapid change in solution concentration and hydraulic head across the seawater interface.

I find that anisotropy and heterogeneity of hydraulic conductivity are a significant influence on the landward extent of saline water interface. For an aquifer that has strongly dipping anisotropy of hydraulic conductivity, I show that the position of the seawater toe can change by over 100% compared to a homogeneous aquifer with the same groundwater flow. I expand this analysis by generating spatially correlated random distributions of hydraulic conductivity that simulate the extreme heterogeneity found in the karstic aquifers of a seawater intrusion reference site in Perth, Western Australia. I show that, for the same average hydraulic conductivity and groundwater throughflow, the position of the seawater toe can vary up to 50% compared to the homogeneous distribution. In this experiment, I demonstrate the importance of the near-shore shallow hydraulic conductivity and its impact on the geometry and location of the toe of the seawater wedge.

Replicating the complex hydrogeology and groundwater flow patterns of a karstic aquifer system required development of new software that could translate a solute transport model into a forward electrical resistivity model and synthetic data. The software and workflow that I develop here are facilitate testing and simulation of various arrays and aquifer models that are expanded on in the next chapter.

As of November 2020, this research has been downloaded over 3600 times since publication on 17th June 2020. A correction to several figures in the online article was published on 30th October 2020. Author contributions statement can be found in Appendix B (page 209) and online in the published document.

Citation:

Costall, A.R., Harris, B.D., Teo, B. et al. Groundwater Throughflow and Seawater Intrusion in High Quality Coastal Aquifers. Sci Rep 10, 9866 (2020). https://doi.org/10.1038/s41598-020-66516-6

Costall, A.R., Harris, B.D., Teo, B. et al. Publisher Correction: Groundwater Throughflow and Seawater Intrusion in High Quality Coastal Aquifers. Sci Rep 10, 19088 (2020). https://doi.org/10.1038/s41598-020-75736-9

Groundwater Throughflow and Seawater Intrusion in High Quality Coastal Aquifers

Abstract

High quality coastal aquifer systems provide vast quantities of potable groundwater for millions of people worldwide. Managing this setting has economic and environmental consequences. Specific knowledge of the dynamic relationship between fresh terrestrial groundwater discharging to the ocean and seawater intrusion is necessary. We present multi- disciplinary research that assesses the relationships between groundwater throughflow and seawater intrusion. This combines numerical simulation, geophysics, and analysis of more than 30 years of data from a seawater intrusion monitoring site. The monitoring wells are set in a shallow karstic aquifer system located along the southwest coast of Western Australia, where hundreds of gigalitres of fresh groundwater flow into the ocean annually. There is clear evidence for seawater intrusion along this coastal margin.

We demonstrate how hydraulic anisotropy will impact on the landward extent of seawater for a given groundwater throughflow. Our examples show how the distance between the ocean and the seawater interface toe can shrink by over 100% after increasing the rotation angle of hydraulic conductivity anisotropy when compared to a homogeneous aquifer.

We observe extreme variability in the properties of the shallow aquifer from ground penetrating radar, hand samples, and hydraulic parameters estimated from field measurements. This motived us to complete numerical experiments with sets of spatially correlated random hydraulic conductivity fields, representative of karstic aquifers. The hydraulic conductivity proximal to the zone of submarine groundwater discharge is shown to be significant in determining the overall geometry and landward extent of the seawater interface.

Electrical resistivity imaging (ERI) data was acquired and assessed for its ability to recover the seawater interface. Imaging outcomes from field ERI data are compared with simulated ERI outcomes derived from transport modelling with a range of hydraulic conductivity distributions. This process allows for interpretation of the approximate geometry of the seawater interface, however recovery of an accurate resistivity distribution across the wedge and mixing zone remains challenging.

We reveal extremes in groundwater velocity, particularly where fresh terrestrial groundwater discharges to the ocean, and across the seawater recirculation cell. An overarching conclusion is that conventional seawater intrusion monitoring wells may not be suitable to constrain numerical simulation of the seawater intrusion. Based on these lessons, we present future options for groundwater monitoring that are specifically designed to quantify the distribution of; (i) high vertical and horizontal pressure gradients, (ii) sharp variations in subsurface flow velocity, (iii) extremes in hydraulic properties, and (iv) rapid changes in groundwater chemistry. These extremes in parameter distribution are common in karstic aquifer systems at the transition from land to ocean. Our research provides new insights into the behaviour of groundwater in dynamic, densely populated, and ecologically sensitive coastal environments found worldwide.

3.1 Introduction

Mankind has always interacted with the natural environments at coastal margins. Beaches, sand dunes, limestone cliffs, and the ocean are part of daily life for vast numbers of people. Hidden beneath the surface exists the interplay between a dense wedge of saline groundwater fuelled from the sea, and fresh terrestrial groundwater driving towards the ocean. We explore this relationship with a focus on methods for quantifying the relationship between terrestrial groundwater flowing toward the ocean and the landward extent of the seawater wedge for high-quality aquifers.

Any reduction in fresh groundwater flowing towards the ocean can potentially cause seawater intrusion. This impacts private bores, irrigation systems, and access to potable water (Bear *et al.*, 1999; Tularam *et al.*, 2009; World Health Organisation, 2011). It can also affect sensitive near-shore ecosystems that rely on the nutrients supplied from terrestrial submarine groundwater discharge (Burnett *et al.*, 2006; Johannes, 1980; Slomp *et al.*, 2004; Spiteri *et al.*, 2008). This can alter groundwater chemistry with significant environmental and economic consequences (Alonso-Rodríguez *et al.*, 2003; Goldman *et al.*, 1973; Kotera *et al.*, 2008; Tuong *et al.*, 2003; Yoshikawa *et al.*, 2007). Research into monitoring coastal groundwater systems and the seawater wedge provides inputs to managing and maintaining healthy coastal aquifers and ecosystems.

Current monitoring practices rely on wells for information on groundwater levels, chemistry, provenance, and age. These data are needed to build numerical groundwater models suitable to predict the consequences of water resource decisions. Drilling and wireline logging are typically used to infer lithology and hydraulic properties. However, this information tends to be localised and can have a dependence on the design of the well or wellfield (Elci *et al.*, 2001).

This research systematically traverses the challenges and opportunities faced in monitoring the seawater interface in a complex coastal setting. It combines elements from hydrogeology, well-based monitoring technologies, analytical seawater interface solutions, solute transport modelling of increasing complexity, and geophysical methods.

The overview shown in Figure 3.1 assists the reader in navigating our research, and includes a schematic showing the geometric relationship between groundwater wells and the seawater interface in an urban setting. An example of the type of questions addressed within each part is also provided in Figure 1. Each part of our research is summarized below.

Part 1: Here we introduce the elements of a coastal karstic aquifer system and our seawater intrusion reference site before comparing it to the hydrogeology of karstic aquifers found worldwide. We include examples of limestone sourced from the reference site and illustrate heterogeneity and dip of the shallow geology using ground penetrating radar.

Part 2: In this part we identify the influences that may impact the seawater interface at the reference site. The site has experienced significant changes in the position of the seawater interface and groundwater hydraulics throughout the monitoring period. This important site motivates our research concerning methods for characterising groundwater throughflow and the seawater interface along shallow coastal aquifer systems.

Part 3: Part 3 presents the data from the reference site and systematically explores the potential for error in predicting seawater intrusion from groundwater flow using conventional monitoring techniques. Examples from our reference site lead us more sophisticated numerical modelling.

Part 4: Here we simulate the impacts of anisotropy and heterogeneity on a coastal aquifer. We investigate the impact of dipping hydraulic conductivity anisotropy on the relationship between the landward position of the seawater interface toe and the rate of groundwater flow towards the ocean. Our numerical experiments extend to complex, extremely heterogeneous hydrogeology as found at our seawater intrusion reference site.

Part 5: This part explores the ability of geophysical techniques to accurately image the seawater interface and coastal hydrogeology. Electrical resistivity imaging (ERI) has the potential to estimate the distribution of salinity in time and space. However, imaging outcomes from ERI can be over-interpreted and we consider the implementation and practicality of ERI for recovering the seawater interface for karstic systems and the reference site.

Part 6: In Part 6 we focus on the dramatic changes in groundwater velocity that occur proximal to the seawater interface. These details have implications for both short-term and long-term monitoring strategies and solutions. This leads us toward options for new integrated monitoring systems that are tailored to shallow high-quality coastal aquifers.

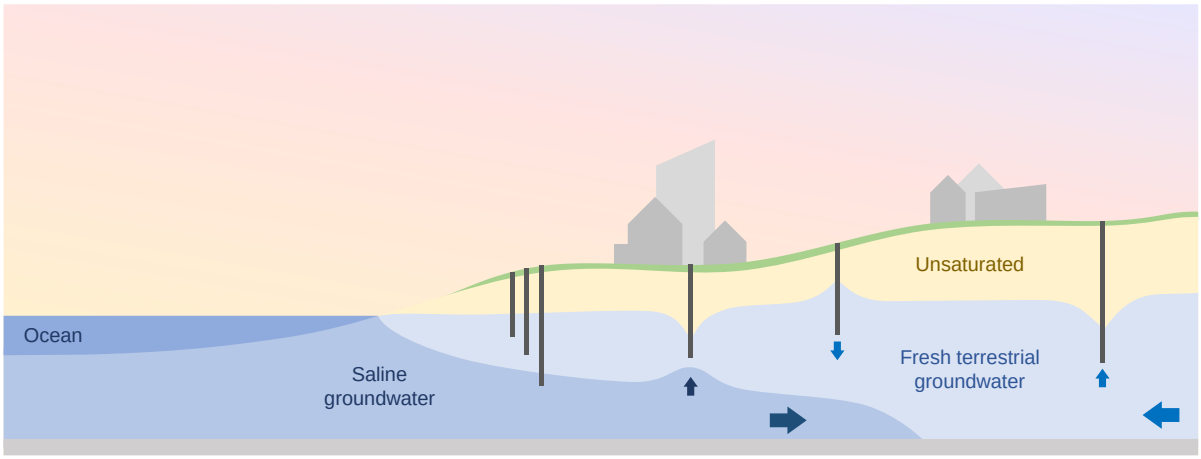

01
Coastal hydrogeology and a reference study site
What range of hydraulic conductivities are expected for high quality karstic and mixed aquifer systems?

02
Influences on groundwater flow and the seawater interface
What are the key influences on terrestrial groundwater flow and seawater intrusion?

03
Measurements and methods
What are the limitations of the measurements and methods used to quantify the relationship between aquifer flow and the seawater interface?

04
Anisotropy and complex hydraulics at coastal margins
How will anisotropy and heterogeneity impact the position of the seawater interface?

05
Electrical resistivity imaging
Can geophysics reveal the saline groundwater wedge, and can it assist in validation of groundwater modelling?

06
Groundwater velocity in karstic aquifers
Can groundwater velocity distribution quantify complex hydrogeology in dynamic coastal aquifers?

Figure 3.1: Schematic of a shallow coastal groundwater water system in an urban setting and our research outline. The multidisciplinary research is partitioned into six connected parts spanning geology, method of acquisition and processing of well data, numerical groundwater modelling and geophysical methods. An example of the type of questions addressed in each part is provided.

3.2 Coastal hydrogeology and a reference site

3.2.1 Introduction to the near-shore coastal margin

The near-shore coastal margin has nomenclature to describe the specific depositional environments and groundwater processes (Mangor *et al.*, 2017). A schematic of this terminology is shown in Figure 3.2, and includes features that are commonly associated with recent (Pleistocene) karstic aquifers such as solution pipes and cave systems (Grimes, 1999; Semeniuk & Johnson, 1985). The geometric arrangement and distribution of these post-depositional features may play a significant role in determining the geometry of the seawater interface.

At the coastal margin, higher density seawater (~1025 kg/m³) sinks beneath the less dense terrestrial groundwater (~1000 kg/m³) forming a wedge shape (Bear, 2005; R. E. Glover, 1959). The mixing zone describes the area where these two waters interact and form a solute gradient (C. H. Lu *et al.*, 2013). The extent of this zone can be highly variable, ranging from sub-meter scales to multiple kilometres (Barlow *et al.*, 2010; Price *et al.*, 2003; Zexuan Xu *et al.*, 2016), and is chemically-active, with implications for limestone dissolution and re-cementation (Back *et al.*, 1986; Randazzo *et al.*, 1985).

Groundwater throughflow and hydraulic conductivity are often used to predict the inland position of the seawater wedge, referred to as the 'toe'. Groundwater throughflow describes the volume of water flowing in the terrestrial aquifer system towards the coast (Department of Water, 2017). For our cross-sectional model, volume calculations are based on a boundary with unit length (1 m), such that groundwater throughflow is expressed in units of ML/year/m (e.g. see Section 3.4).

In addition to the zones shown in Figure 3.2, there are many temporal changes that influence the position of the seawater interface. These include effects of wave surges, beach geometry, tides, rainfall recharge, and groundwater abstraction. These variables ensure that solute distribution and hydraulic heads along coastal margins are in constant motion. In high-quality karstic aquifers, these temporal challenges are compounded by the variability in hydraulic properties associated with high-permeability caves, low-permeability cemented limestone, and anisotropy of hydraulic conductivity.

Supplementary Table S1 contains a summary table of spatial and temporal parameters that can affect the position and geometry of the seawater wedge. We will provide specific examples illustrating the potential impact of heterogeneity and anisotropy of hydraulic conductivity on the seawater wedge in Part 4.

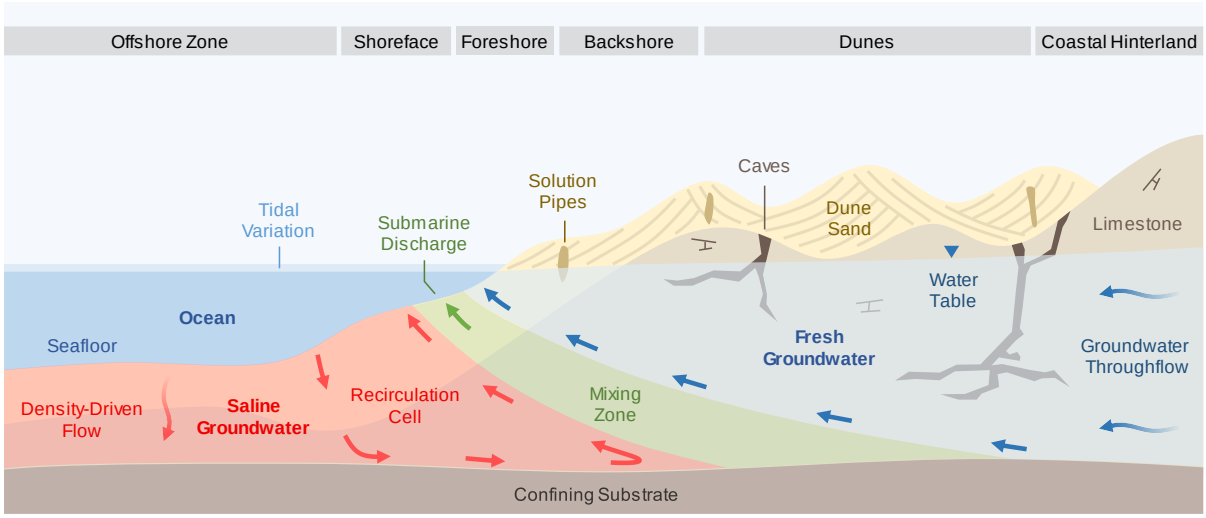

Figure 3.2: Schematic of coastal hydrogeology indicating processes and nomenclature for the seawater interface in a mixed siliciclastic and carbonate near-shore aquifer system. The permeability distribution, groundwater throughflow, and density-driven flow combine to determine the geometry of the seawater/freshwater mixing zone, patterns of groundwater flow within the seawater recirculation cell, and the distribution of submarine discharge. Temporal cycles, such as the seasonal rainfall, pumping from shallow wells, and tidal forcing drive constant groundwater movement in the coastal aquifers. 'Groundwater throughflow' describes the volume of groundwater entering the system and flowing towards the coast.

3.2.2 An urban reference site where seawater intrusion has occurred

Increase in global population density at coastal margins and associated demand for high-quality, low-cost water can significantly impact coastal aquifer systems. Our research site in Quinns Rocks, approximately 35 km north of Perth, Western Australia, has experienced a rapid increase in population and urban development during the period of monitoring. Perth, the capital of Western Australia, is one of the lowest population density cities worldwide (~323 persons per square kilometre (Australian Bureau of Statistics, 2018; Cox, 2017)). However the majority of urban sprawl is occurring along the coastal margins (Clark *et al.*, 2016).

The location of the seawater intrusion monitoring (SIM) wells at Quinns Rocks is shown in Figure 3. It includes the minimum regional groundwater level contours in the upper superficial aquifer for May 2003 (W. Department of Water, 2004). It also includes a cross-section through the SIM wells and the approximate position of the seawater interface in 2018. Regional groundwater flow is perpendicular towards the shoreline (Shoemaker, 2004). The shallow hydraulic gradients of the regional water level contours approaching the shoreline suggest high permeability in the mixed limestone aquifers typical of Perth's coastal margin (AJ Smith *et al.*, 2012; Anthony John Smith *et al.*, 2001). the details of the SIM well completions are found in Table 3.1, including location depth and screened intervals.

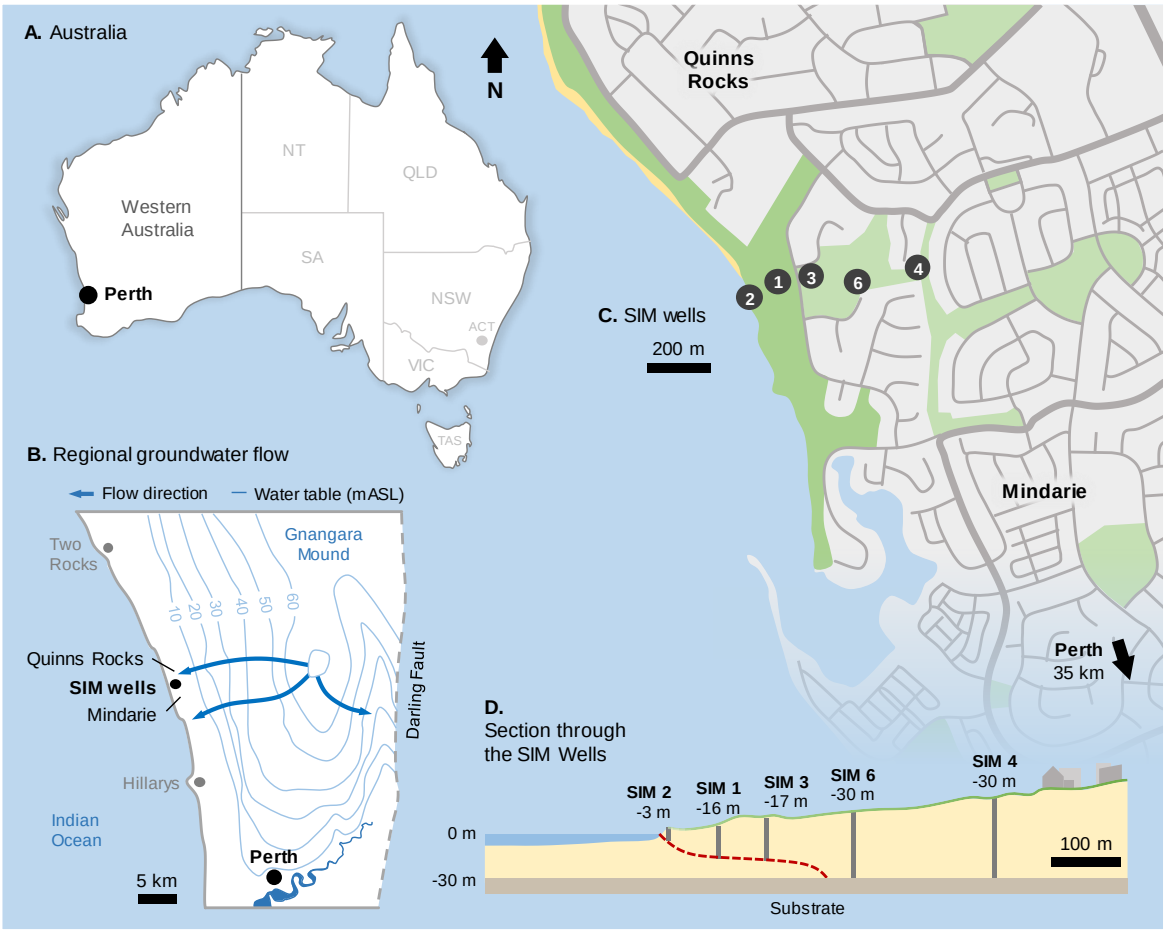

Figure 3.3: Maps providing location and characterisation of the Quinns Rocks seawater intrusion monitoring (SIM) reference site in Perth, Western Australia. ***A,*** *the location of Perth relative to Western Australia.* ***B,*** *the regional groundwater contours, which are approximately parallel to the coastline at Quinns Rocks, indicating groundwater flows towards the coast.* ***C,*** *the location of the SIM wells relative to Quinns Rocks, which have been monitored since 1990.* ***D,*** *a cross-section of the SIM wells, including the impermeable clayey substrate, and an estimate of the current position of the seawater wedge.*

Table 3.1: Details of the SIM wells including approximate distance from shoreline and depth of the screens below ground level (m BGL).

Well	**Easting**	**Northing**	**Distance from Shoreline**	**Ground Level**	**Screen Depth** (m BGL)		**Mean Screen Depth**
ID	mE	mN	(m)	(m AHD)	From	To	(m AHD)
SIM 2	376567.43	6494093.94	30	6.13	7.85	8.85	-2.22
SIM 1	376635.39	6494122.71	105	11.04	26.1	27.1	-15.56
SIM 3	376719.26	6494142.05	190	15.18	31.87	32.87	-17.19
SIM 6	376900.26	6494133.29	360	24.03	53.58	54.58	-30.05
SIM 4	377084.02	6494174.60	550	31.34	60.43	61.43	-29.59

3.2.3 The shallow geology and hydraulics at coastal margins

A fundamental step in creating a valid and practical groundwater model is to analyse local hydrogeology. Groundwater management often relies on predictive groundwater modelling to determine the future impact of groundwater allocations and water supply options. In karstic groundwater systems, aquifer hydraulics can be highly variable over short distances (Cook, 2003; Ford *et al.*, 2013; Mylroie, 2013). Localised high-permeability conduits coupled with extremely low-permeability layers of cemented limestone can form strongly anisotropic aquifer systems (Bonacci *et al.*, 2000; Ford *et al.*, 2013). These environments can influence the shape of the seawater interface and be associated with unconventional seawater wedge geometries (Calvache *et al.*, 1997; Dokou *et al.*, 2012; Zexuan Xu *et al.*, 2016; Zhongyuan Xu *et al.*, 2019).

The range of estimated values for hydraulic conductivity found in literature examples from around the world are compared with examples from the coastal margin of Perth in Figure 3.4 (Barnes, 1999; Benson *et al.*, 2015; Davidson *et al.*, 2008; Ghasemizadeh *et al.*, 2012; Gonzalez-Herrera *et al.*, 2002; Hartmann *et al.*, 2014; Kretschmer *et al.*, 2012; Mylroie, 2013; Price *et al.*, 2003; Scanlon *et al.*, 2003; Anthony Smith *et al.*, 2012; Anthony John Smith *et al.*, 2001; A. J. Smith *et al.*, 2003; Todd, 2006). The hydraulic conductivity of karstic aquifers can be orders of magnitude higher than clastic aquifers (Domenico *et al.*, 1998; Heath, 1998). The hydraulic conductivity along Perth's coastal margin is estimated to be between 10 to 10000 m/day, and the estimated average at the Quinns Rocks reference site is between 130–200 m/day (Nidagal *et al.*, 1991). Further detail on the estimates local to Quinns Rocks can be found in Supplementary Table S2, S3 and S4.

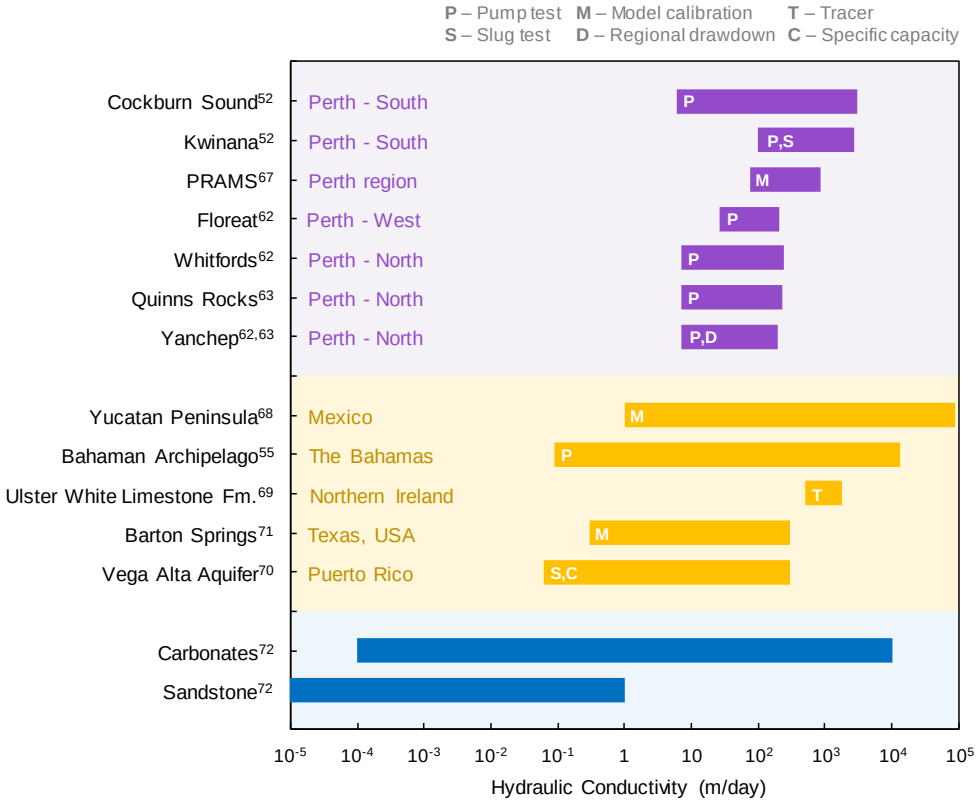

Figure 3.4: Ranges of hydraulic conductivity estimated at sites along the coastal margin of Perth (shown in purple) and other karstic environments around the world (shown in yellow). Most of the hydraulic conductivity in the Perth region fall within the mid-to-upper estimate of typical carbonate values (shown in blue). The karstic aquifers in Perth is known to contain caves and other high-permeability flow pathways that contribute to the high hydraulic conductivity.

In Perth, the shallow aquifer is dominantly comprised of the Pleistocene-Holocene-aged Tamala Limestone. The Tamala Limestone is characterized by shallow horizontal cave systems, a lack of directed conduits, cave clustering near the coast, and extensive collapse-dominated cave systems (Grimes, 1999, 2002, 2006). Evidence for these systems is found in outcrops, accessible cave systems, limestone quarries, and high-resolution ground penetrating radar. These features introduce a range of challenges in hydraulic modelling, particularly for numerical groundwater model calibration (Kretschmer *et al.*, 2012; AJ Smith *et al.*, 2012; Stringfield *et al.*, 1971).

Photographic examples of geological fabrics common in the Tamala Limestone are shown in Figure 3.5. The sample labelled Figure 3.5B is typical of a well-cemented limestone, and the sample labelled Figure 3.5A is a typical of a highly porous, high-permeability example of Tamala Limestone. This permeable sample (Figure 3.5A) shows preferential dissolution along bedding, which can form extremely high hydraulic conductivity networks throughout some layers of the aquifer. In contrast, the sample shown in Figure 3.5B is fine grained, well cemented, and likely to have significantly lower hydraulic conductivity.

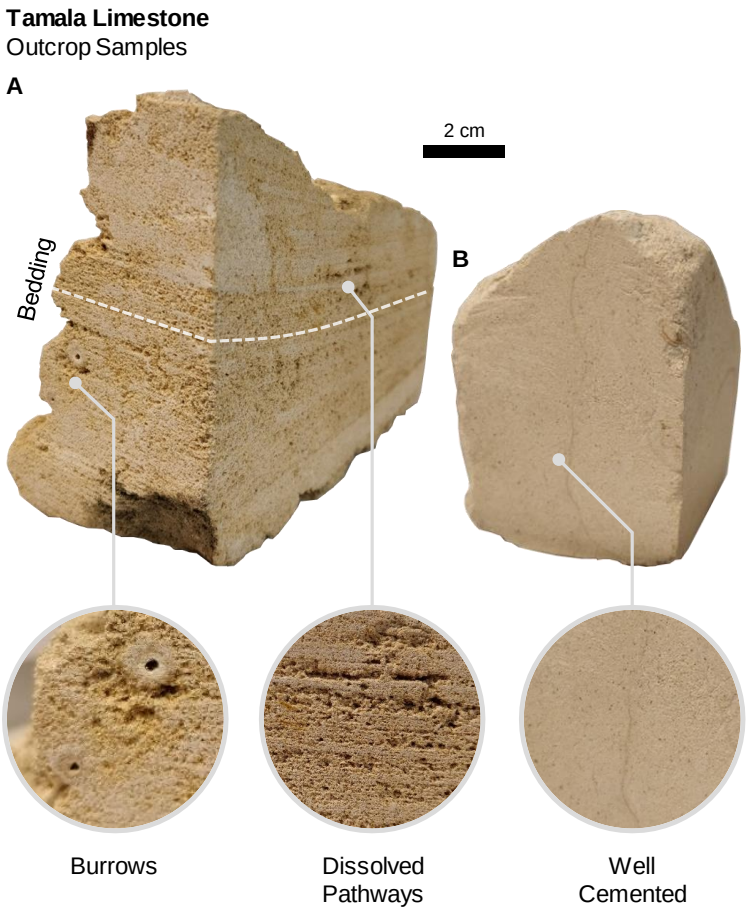

Figure 3.5: Photographs showing samples of the Tamala Limestone with different sedimentary fabrics. ***A,*** *a vuggy sample with burrows and dissolved pathways, expected to be highly permeable.* ***B,*** *a cemented massive fine-grained limestone sample, expected to have considerably lower permeability. This figure highlights the contrast in geological fabrics that directly impact hydraulic conductivity. Large-scale karsts (i.e. caves and other conduits) exist throughout the coastal margin of Western Australia.*

Geological facies at the coastal margin can vary within tens of meters of the coastline. For example, Figure 3.6presents a high-resolution 675 MHz ground penetrating radar (GPR) profile from City Beach, 10 km west of Perth CBD. Similar images have been obtained at many locations along Perth's coastal margin (A. Costall *et al.*, 2018; Alexander Ross Costall *et al.*, 2019; E. Strobach *et al.*, 2010; E. Strobach *et al.*, 2014). The GPR data reveals shallow dipping layers of modern beach and dune facies nested between limestone ridges. The dip of layers in the beach facies are estimated to be up to 16 degrees. Figure 3.6A shows an example of layers dipping towards the ocean (i.e. ~8° west), while Figure 3.6B shows layers oriented away from the ocean (dips between 13 - 16° east). Processing steps and parameters for the GPR data can be found in Supplementary Table S5.

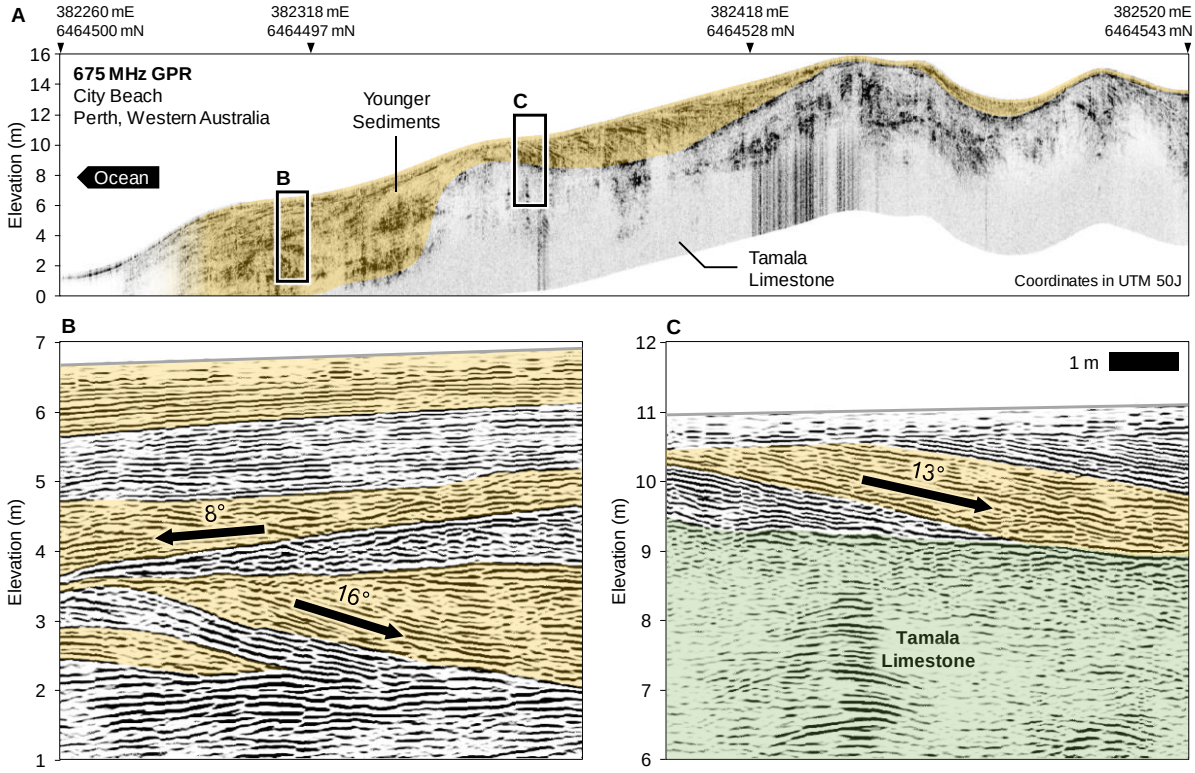

Figure 3.6: A ground penetrating radar (GPR) section at Perth's coastal margins that expresses the typical beach and dune facies and limestone ridges. ***Panel A*** *shows the GPR energy envelope attribute that highlights the unconformity between the Tamala Limestone and beach/dune facies above.* ***Panel B*** *is a GPR section showing the reflections from sedimentary layering present in the younger facies, with a prevailing dip towards the ocean.* ***Panel C*** *is a GPR section showing the reflections from sedimentary layers dipping approximately 13° landwards (away from the coast) and terminating at an unconformity. This data was collected at the suburb of City Beach, south of Quinns Rocks, using a 675 MHz antenna. Similar examples of dipping beds and limestone ridges occur throughout the coastal margin of Perth (A. Costall et al., 2018; Alexander Ross Costall et al., 2019; Semeniuk et al., 1982; Semeniuk & Johnson, 1985).*

Two important conclusions stem from the analysis of the karstic near shore setting of the Perth region. These are: (i) extreme changes in lithological character and associated hydraulic parameters are common, especially perpendicular to the shoreline, and (ii) geological layering is common and likely associated with anisotropy of hydraulic conductivity throughout Perth's coastal margin. The influences of anisotropy and complex hydraulic conductivity distributions are analysed using numerical solute transport modelling later in this research (i.e. Part 4).

3.3 What drives the relationship between groundwater throughflow and seawater intrusion?

Three influences commonly linked with seawater intrusion include greater net groundwater use (e.g. from abstraction wells), changes in net vertical flux entering the groundwater system (e.g. rainfall recharge, storm water infiltrations etc.), and sea-level rise (Badaruddin *et al.*, 2017; Barlow *et al.*, 2010; Bryan *et al.*, 2016; Ketabchi *et al.*, 2016; Werner, 2017; Werner *et al.*, 2013). Data was acquired at the Quinns Rocks reference site during a 30-year period, where all three of these factors may have contributed to fundamental changes in the geometry of the seawater interface.

We consider each of these factors with reference to available data for the Quinns Rocks reference site. Our suspicion is that, although the dataset is extensive and spans several decades and wells, isolating any one of these factors is not possible with the data that was collected. Decoupling the relative contributions of each will likely require new monitoring practices.

3.3.1 Rapid urbanisation and increased groundwater abstraction at the coastal margins

Groundwater abstraction leading to reduction in terrestrial groundwater flows is often identified as the primary driver for seawater intrusion (Cheng *et al.*, 2004; Custodio, 2012; Dausman *et al.*, 2005; Digha Opaminola *et al.*, 2015; Ferguson *et al.*, 2012; Guo *et al.*, 2019; Ivkovic *et al.*, 2012; Werner *et al.*, 2011). Sustainable groundwater management initiatives, such as augmenting rainfall recharge from urban surfaces, and managed aquifer recharge are being developed to reduce the direct dependence on shallow groundwater (Casanova *et al.*, 2016; Dillon, 2009; Teijón Ávila *et al.*, 2009; Vandenbohede *et al.*, 2009; Water-Technology, 2016; Water Corporation, 2016a, 2019). Systems of aquifer replenishment such as these, introduce another dimension to groundwater flow and reinforce the need for better groundwater monitoring solutions that are better able to decouple multiple influences.

The suburbs surrounding the Quinns Rocks reference site have undergone rapid urbanisation and population growth since 1984. The SIM wells were established to assess the impact of development and expansion of Perth's regional Integrated Water Supply Scheme (IWSS). In total, the IWSS supplies ~289 GL/year to Perth and remote mining towns (McFarlane *et al.*, 2005). This water is sourced from approximately 43% groundwater, 39% desalinated water, and 18% from surface water (Water Corporation, 2018).

The recent growth of the Quinns Rocks urban footprint is shown in Figure 3.7, and includes population and IWSS groundwater abstraction between 1984 and 2016. The local IWSS wellfield is approximately 2 km to 4 km from the coastline. Shallow groundwater abstraction from the Quinns Rocks region has supplied an average of 12 GL/year since 2003. This forms the majority of coastal groundwater abstraction and accounts for approximately 75% of local groundwater usage (Kretschmer *et al.*, 2012).

The development of a groundwater abstraction wellfield parallel to the coast and increase in urban land usage around the reference site is a strong motivation to simulate the local groundwater hydraulics and hydrogeology. Although it may seem easy to attribute the data to groundwater abstraction alone, there are other factors that may have influenced the position of the seawater wedge at this site.

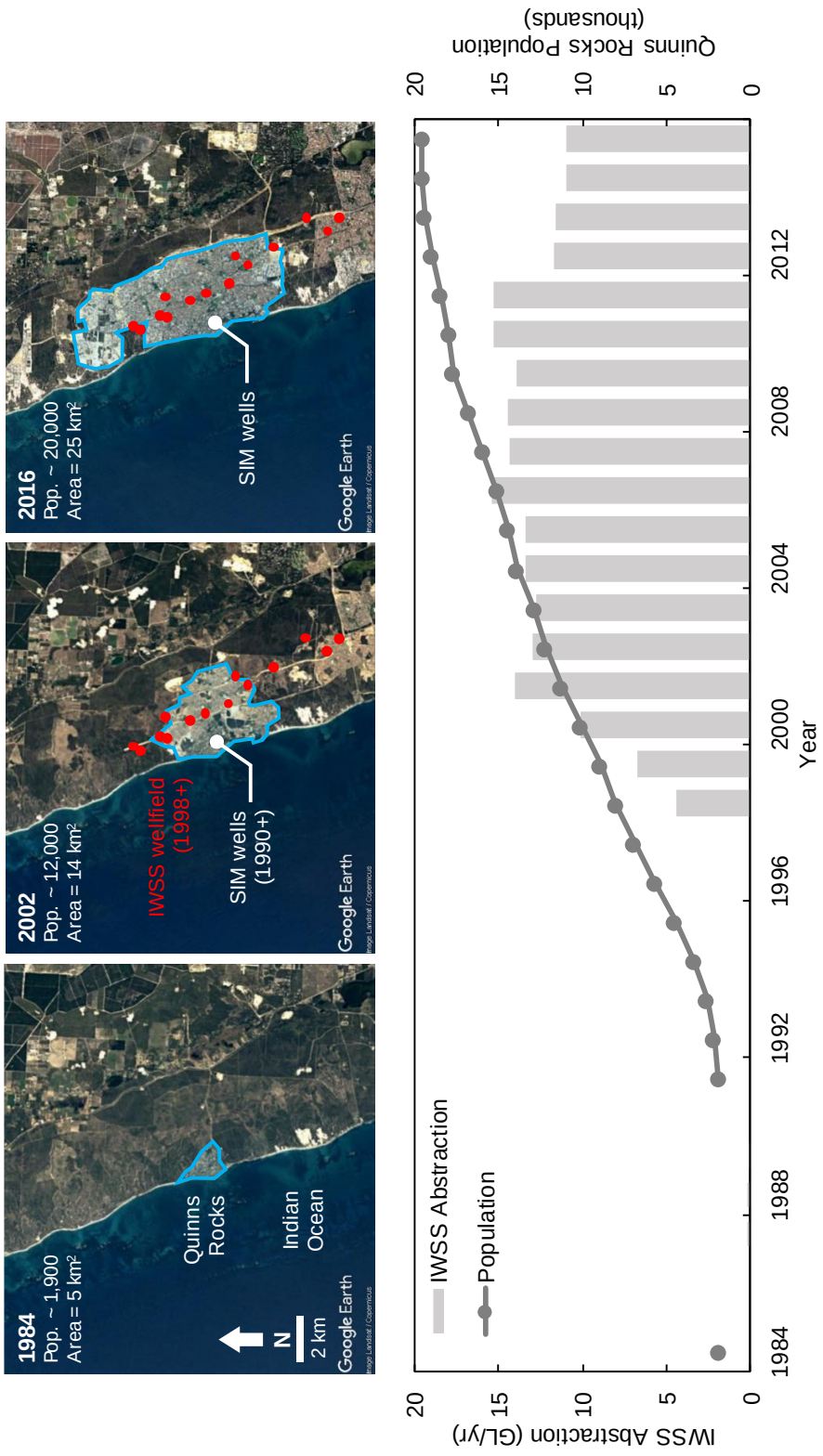

Figure 3.7: Set of satellite images showing the rapid expansion of the Quinns Rocks suburb, taken in 1984 (top left), 2002 (top middle) and 2016 (top right), and groundwater abstraction from the IWSS bore field from 1984 to 2016 (bottom) The middle satellite image contains the location of the shallow regional wellfield, developed in 1998 for the Integrated Water Supply Scheme (IWSS), and the location of the seawater intrusion monitoring (SIM) wells. The approximate annual groundwater abstraction from the local wellfield during peak production in 2002 was approximately 14 GL/year. The increase in groundwater abstraction during the monitoring period is one potential cause for seawater intrusion at the reference site. Map imagery ©2019 Google Earth, Maxar Technologies.

3.3.2 Influence of a changing climate and reduced rainfall recharge

The impacts of a rapidly changing modern climate are well-documented (Collins *et al.*, 2013; Delworth *et al.*, 2014; Parmesan *et al.*, 2003; Stern *et al.*, 2007; G.-R. Walther *et al.*, 2002). Changes in rainfall patterns and seasonal temperatures will impact groundwater systems (Bates *et al.*, 2008; Petra, 2009). For example, the reduction in winter rainfall can reduce groundwater recharge to a shallow aquifer system, reducing aquifer flows, and ultimately resulting in seawater intrusion (Mahesha *et al.*, 1996). Bryan *et al.* (2016) suggest that declining rainfall in the Perth region is the primary cause of seawater intrusion for Rottnest island, located just 20 km offshore from Perth.

Figure 3.8 shows the cumulative and seasonal (six-monthly) rainfall in Perth between 1944 and 2018. The long-term average rainfall is approximately 700 mm/year. A comparison of the first and last 20-years of the data suggests that the average rainfall has decreased from approximately 834 mm/year (1944 – 1964), to 673 mm/year (1998 to 2018).

Analysis of summer (October to March) and winter (April to September) rainfall trends suggest a minor increase of 0.03 mm/year per year in summer rainfall. However, groundwater recharge from summer rainfall is negligible due to high evapotranspiration rates in Perth (Elmar Strobach, 2013; E. Strobach *et al.*, 2014). Winter rainfall contributes to the vast majority of rainfall recharge. Analysis of rainfall trends from Figure 3.8 suggests an approximately 25% reduction over the 20-year period between 1998 and 2018 compared with the 20-year period between 1944 and 1964.

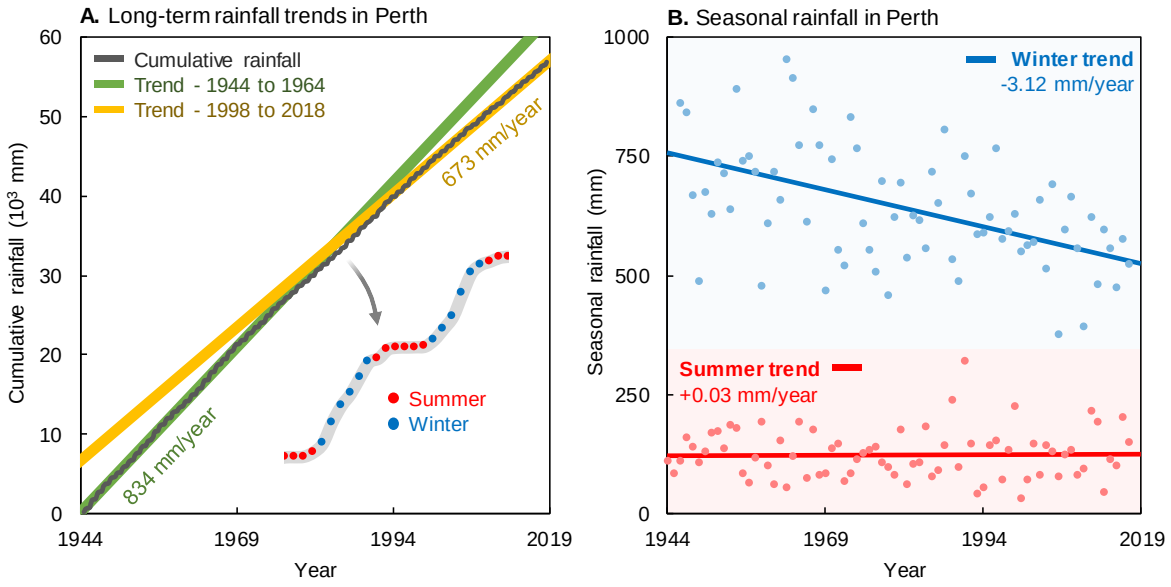

Figure 3.8: Graphs showing long-term trends in winter and summer rainfall in Perth, Western Australia. ***Panel A*** *shows the cumulative rainfall from 1944 to 2018. The average rainfall over the entire period is approximately 700 mm/year. Analysis of 20-year trends indicate that an approximately 25% reduction in rainfall has occurred since the start of measurement in 1944. The average rainfall from 1944 to 1964 was 834 mm/year, compared to data from1998 to 2018 with an average rainfall of 673 mm/year.* ***Panel B*** *shows the total seasonal rainfall for summer and winter showing that a clear decrease in winter rainfall. The decreasing winter rainfall is strong motivation for understanding the follow-on effects to the seawater interface.*

3.3.3 Influence of sea level rise

Changes in the global sea level, and sea level rise in particular, can affect the position of the seawater interface and the near-shore environment (Falkland *et al.*, 1991; Stocker *et al.*, 2013; Wassmann *et al.*, 2004; Werner *et al.*, 2013). Simulations of the impact of sea level rise suggests that relatively small increases in sea level can potentially move the seawater interface landwards by hundreds of meters (Green *et al.*, 2014; Meyer *et al.*, 2019). This can extend up to kilometres where karstic high-flow conduits are present (Zexuan Xu *et al.*, 2016; Z. Xu *et al.*, 2018).

Measurements from a tidal monitoring station located approximately 2 km south of the Quinns Rocks reference site suggest the sea level, on average, has risen by 7.63 mm/year. This is shown in Figure 3.9. The government estimate for sea-level rise, accounting for ENSO meteorological events, is 9.0 mm/year (BOM, 2011). Sea level rise accounts for between 22.8 cm and 27 cm of increased seawater head at the coast over the 30 years of monitoring. The increase in mean sea level is a possible reason behind the observations at the reference site.

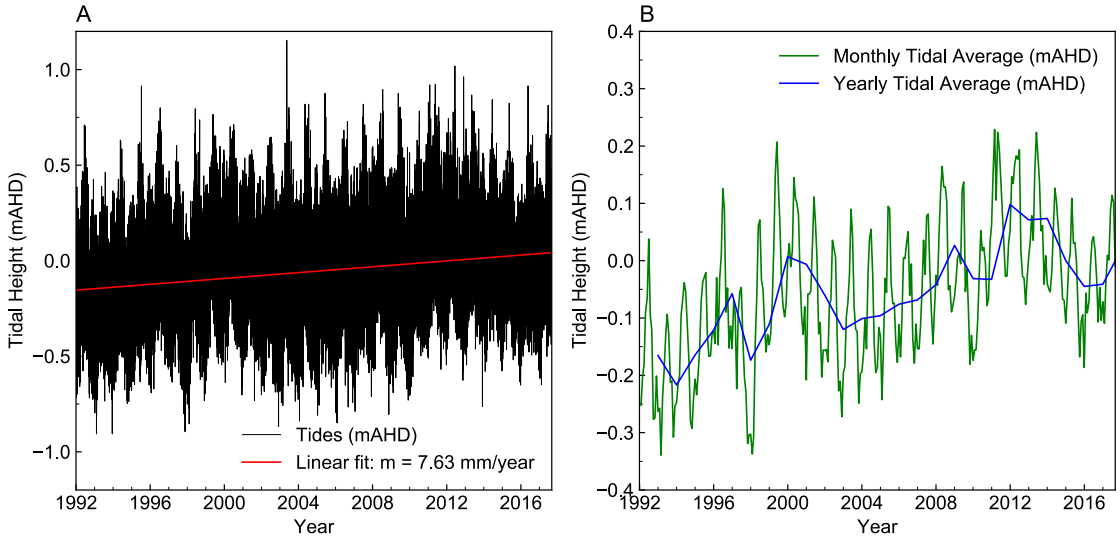

Figure 3.9: Charts showing tidal measurements from a monitoring location near the reference site in meters Australian height datum, mAHD. ***Panel A*** *shows the raw hourly data since 1992 with a linear fit overlaid.* ***Panel B*** *shows the monthly and yearly averages of the raw data. Tidal levels have risen by approximately 7.63 mm/year since monitoring began. The estimate for sea-level rise that also considers global meteorological events is 9.0 mm/year (BOM, 2011). The rise in sea level over the monitoring period is a potential factor for landward movement of the seawater interface at the reference site.*

3.4 Predicting the shape of the seawater interface: The value and limitations of historical monitoring data

Monitoring wells provide data required to inform aquifer management. The quality and value of the information gathered is highly dependent on the design and placement of the monitoring well. The demand for the precise management of aquifer systems that works in conjunction with modern numerical groundwater modelling is outpacing both the data type and quality collected from existing monitoring networks.

Water level measurements in the seawater intrusion monitoring (SIM) wells at Quinns Rocks between 1990 and 2017 are shown in Figure 3.10. Panel A shows distribution of measured water levels. The wells SIM 1 and SIM 3, nearest to the shoreline, have similar water measurements despite being approximately 80 m apart. The wells SIM 4 and SIM 6 are further inland and have similar measurements despite being over 200 m apart. The shallow hydraulic heads gradient between these wells are consistent with a highly permeable aquifer. However, significant differences in hydraulic gradients measured between each pair of SIM wells also suggests a highly heterogeneous distribution of hydraulic parameters.

Panel B of Figure 3.10 shows the variation in rainfall associated with the typical dry summer and wet winter cycles. The measured water levels are driven by seasonal rainfall cycles. In 1994, the water levels measured in SIM 2, approximately 30 m from the shoreline, vary between 0.00 mAHD (Australian height datum) during the summer months, up to 0.42 mAHD in the winter months. Daily tidal effects account for another 0.5-meter variation superimposed on the measured water levels.

Although there appears to be a substantial monitoring dataset at the Quinns Rocks reference site, we notice several inadequacies. Two key outcomes from analysis of the data in Figure 3.10 are:

I. The temporal sampling rates from manual logging are unable to capture the response of the aquifer system from tidal variations, storm surges, and other rapid events (e.g. the spike in SIM 4 in 2009)
II. Measuring a single point in depth with conventional PVC wells could mask changes in hydraulic head or solute concentration due to the extreme variability associated with karstic aquifers (e.g. SIM 1, SIM 3 measurements and depths)

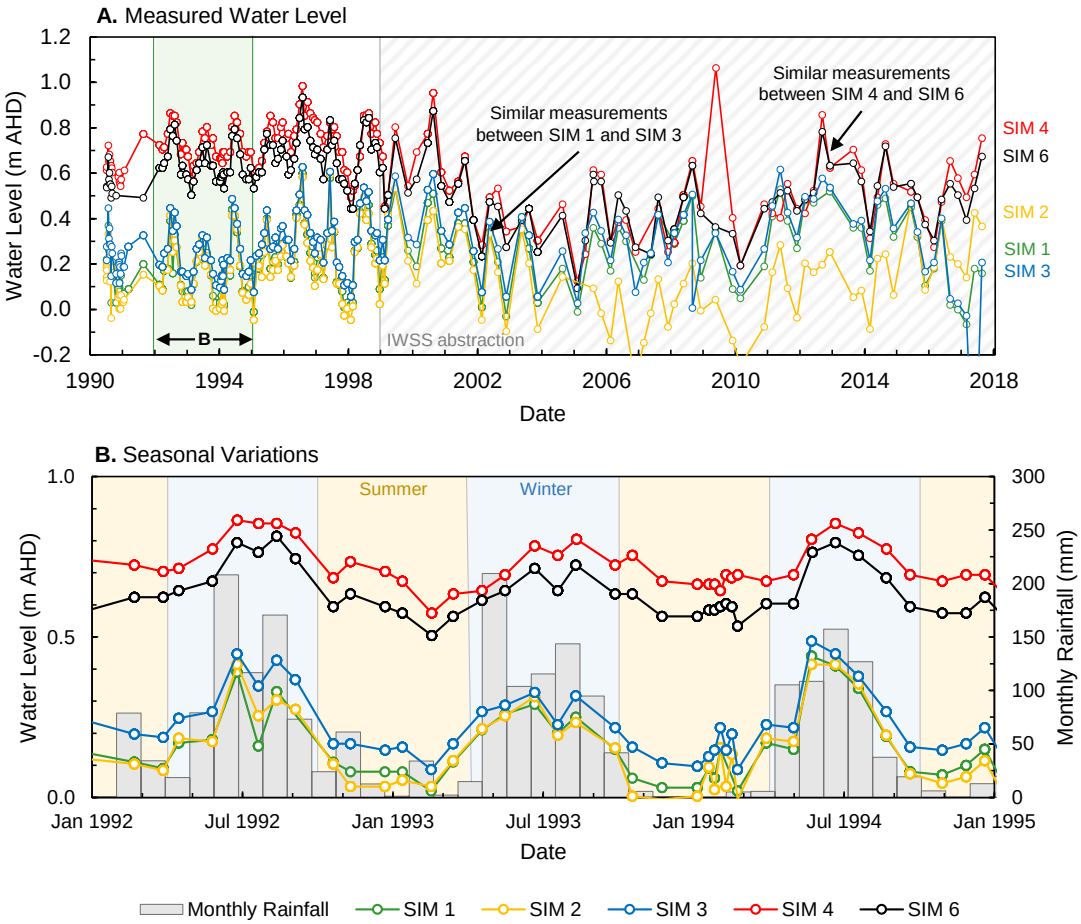

*Figure 3.10: Set of graphs comparing measured water levels in the seawater intrusion monitoring (SIM) wells to monthly rainfall. **Panel A** shows measured water levels from 1990 to 2018. The frequency of measurements decreases after the IWSS pumping begins. The measured water levels in SIM 1, SIM 2, and SIM 3, are similar despite separation of 150 m (see Figure 3, Figure 7). SIM 4 and SIM 6 also show similar measured water levels despite being separated by close to 200 m. Shallow gradients between these monitoring points suggests zones of localised extreme permeability. **Panel B** shows water levels and monthly rainfall between 1992 and 1995. Summer periods (October to March) are shaded orange, and the winter periods (April to September) are shaded blue. A clear relationship between annual rainfall cycles and water levels is present.*

3.4.1 Measurements of water chemistry - What range of seawater interface geometries fit monitoring data?

Sampling the properties of the groundwater, such as the electrical conductivity (EC), provides baseline data for identifying seawater intrusion. EC measurements can be approximated to a solute concentration (or total dissolved solids, TDS) using linear approximations (Walton, 1989), or by more advanced approximations such as the equation of state of seawater EOS-80 (UNESCO, 1981). Details on these calculations as applied at Quinns Rocks are provided in Supplementary Table S6.

Over the ~30 years of monitoring, EC data from the SIM wells clearly shows that movement of the seawater interface has occurred (see Figure 3.11). The position of the interface in 2018 is somewhere between SIM 3 and SIM 6 (i.e. between 180 and 360 m from the shoreline). The solute concentration in SIM 3 is near to that of seawater at ~30 g/L, while in SIM 6 the groundwater has always remained fresh (i.e. potable), with a TDS of 0.3 g/L.

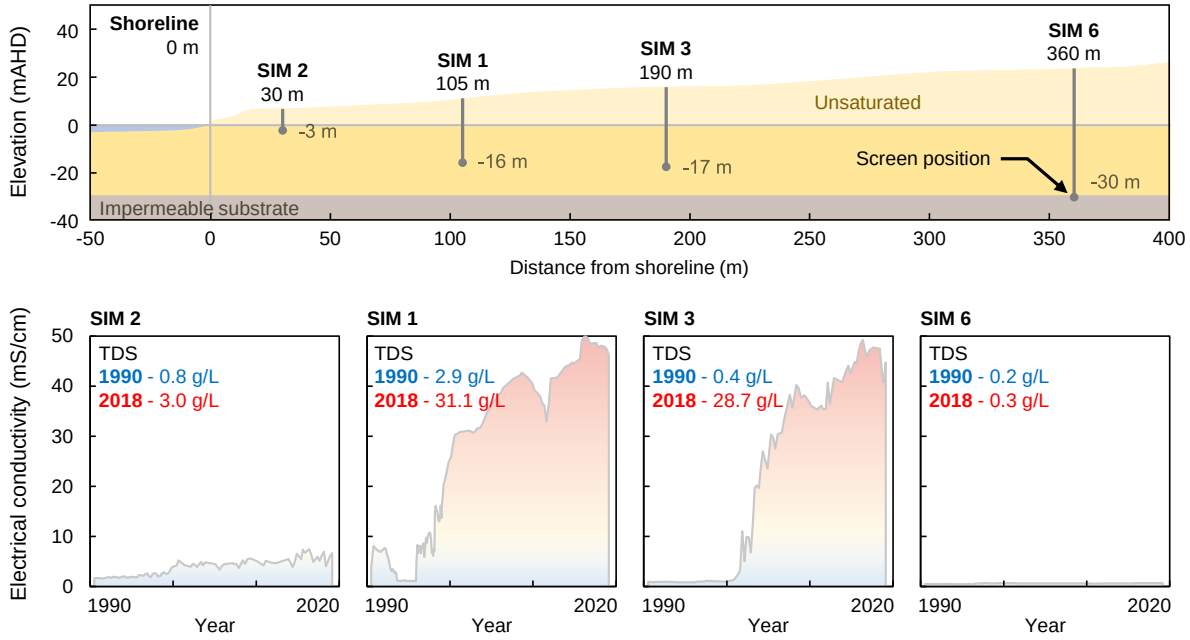

Figure 3.11: Cross-section through the SIM wells and accompanying time-lapse electrical conductivity (EC) data (1990 – 2018) showing evidence of seawater intrusion. The current position of the seawater interface is between SIM 3, where EC is equivalent to that of seawater in 2018, and SIM 6, where EC remains that of potable water in 2018.

A disadvantage of electrical conductivity measurements made in the SIM wells is that the measurements are limited to a single short-screened interval (see Table 2.1 for the screened intervals in the SIM wells). This allows for many interpretations of the shape of the seawater interface, such as the three hypothetical scenarios that may all correspond to same EC measurements within the SIM wells (see Figure 3.11). These scenarios are intended to highlight end members from a range of potential geometries of the seawater wedge over the monitoring period.

They include:

Scenario 1 (Figure 3.12A): Here the toe remains relatively stationary while the seawater interface expands vertically. This extreme may occur where there exists an inclined substrate (Ketabchi *et al.*, 2016; Koussis *et al.*, 2012), or an extremely low-permeability lithology exists near the toe (Comte *et al.*, 2017; Meyer *et al.*, 2019).

Scenario 2 (Figure 3.12B): The seawater wedge expands horizontally. This may occur if horizontal layers have extremely high horizontal hydraulic conductivity, such as directional preference conduit systems (Dafny *et al.*, 2010; Dokou *et al.*, 2012; Zexuan Xu *et al.*, 2016).

Scenario 3 (Figure 3.12C): The seawater wedge expands both horizontally and vertically. This is perhaps the most commonly reported movement in seawater intrusion literature (Badaruddin *et al.*, 2017; Bear, 2005; Bear *et al.*, 1999; H.-J. G. Diersch, 2014).

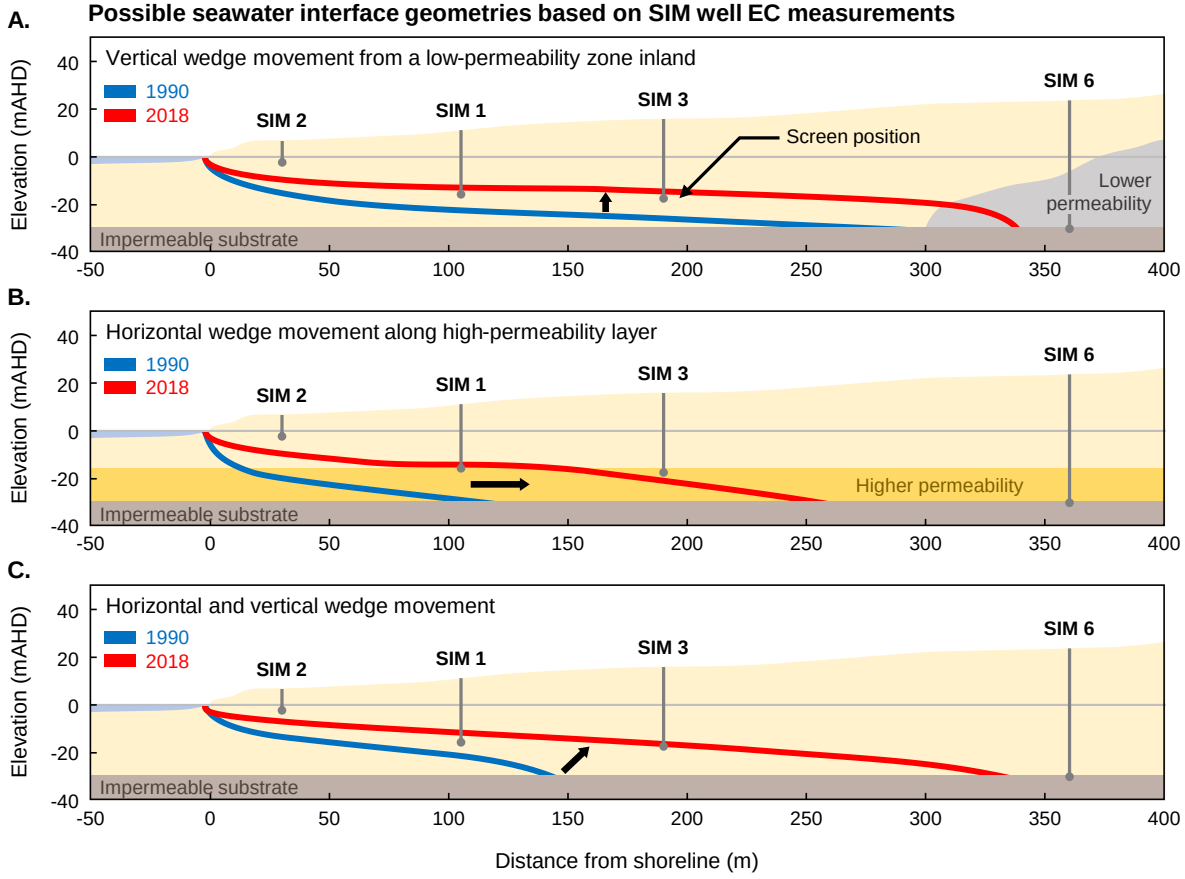

Figure 3.12: Schematic indicating the possible locations of the seawater interface based on measured solute concentrations from the SIM wells in 1990 (red line) and 2018 (blue line). ***Panel A*** *shows an example of primarily vertical movement due to a zone of reduced permeability near to the toe.* ***Panel B*** *shows an example of horizontal movement of seawater, such as along a high-permeability conduit located near to the base of the aquifer.* ***Panel C*** *shows an example of both horizontal and vertical movement inland, as would be found in a homogeneous aquifer.*

Long-term groundwater monitoring at the Quinns Rocks reference site shows that movement of the seawater interface has occurred during the monitoring period and that the seawater interface currently exists between 200 and 360 m from the shoreline. However, it is not possible to reconstruct the seawater interface or make conclusions concerning the rate of intrusion from this data alone.

3.4.2 Measurements of hydraulics across the wedge transition

Measurement of the hydraulic head at the coastal margin can present greater uncertainty than in other groundwater systems (Carrera *et al.*, 2010). These uncertainties can be driven by large variations in groundwater density and a dynamic groundwater environment. A key uncertainty from aquifers containing variable-density groundwater arises when the density of water in the well column is not constant or accurately known when the water level measurement is made.

It is often necessary to convert the measured water level in coastal wells to pressure expressed as an equivalent freshwater head for numerical modelling. In a static system, hydraulic head (h_i) is the sum of elevation head (z_i) (i.e. the depth of the well screen), and pressure head ($h_{p,i}$) (i.e. the length of water column relative to z_i) (V. Post *et al.*, 2007). This is described by

$$h_i = z_i + h_{p,i} = z_i + \frac{P_i}{\rho_i g} \quad (1)$$

Where $h_{p,i}$ is the hydraulic head from pressure at point i, P_i is the pressure at the well screen, ρ_i is the fluid density of the groundwater at the well screen, and g is the acceleration due to gravity.

If unknown variable groundwater density exists, the same hydraulic head (e.g., measured water level) could be interpreted from different hydraulic pressures. For a system with groundwater of varying density, the 'equivalent freshwater head' (Lusczynski, 1961; V. Post *et al.*, 2007) represents the column of fresh groundwater required to balance the hydraulic pressure at a particular depth and groundwater density. The equivalent freshwater head for groundwater at point i with density ρ_i is:

$$h_{f,i} = \frac{\rho_i}{\rho_f} h_i - \frac{\rho_i - \rho_f}{\rho_f} z_i \quad (2)$$

Where ρ_f is the density of fresh groundwater.

The range of densities for groundwater proximal to the seawater wedge can lead to multiple interpretations of hydraulic head. These are illustrated in Figure 3.13

1. If the well is fully screened across the aquifer, the measured water level is equal to the 'in situ' hydraulic head, as shown in Figure 13A. However, fully-screened wells (Figure 13, Well A) are susceptible to passive redistribution of groundwater along the screened interval between layers with different hydraulic properties (Levanon *et al.*, 2013). Any vertical movement or redistribution of seawater via the well-column can affect the groundwater salinity measurements with consequence for interpretation and monitoring.
2. For the equivalent freshwater head (Figure 13, Well B), the pressure at the screens is represented by the equivalent column of fresh water. The equivalent freshwater head is always higher than the measured water level when high-density groundwater is present.
3. The point-water head (Figure 13, Well C) assumes that the groundwater density at the screened interval exists throughout the well column. If there is seawater at the screened interval, the measured water level inside of the well is lower than the true water level outside of the well. This could occur if the screened interval of a monitoring well is located within the seawater wedge and has been sampled through pumping.
4. The environmental head is calculated assuming that the water within the well is stagnant, and the density of water inside the well column is equal to the average of water outside of the well (S. Davis *et al.*, 1967; V. Post *et al.*, 2007) (see Figure 13, Well D).

A consequence of the above is that the measured water level may not be a reliable input for computation of groundwater flow conditions in variable density environments. Here specific measurements are required to characterize these groundwater flow systems. We discuss suitable monitoring techniques in the conclusion.

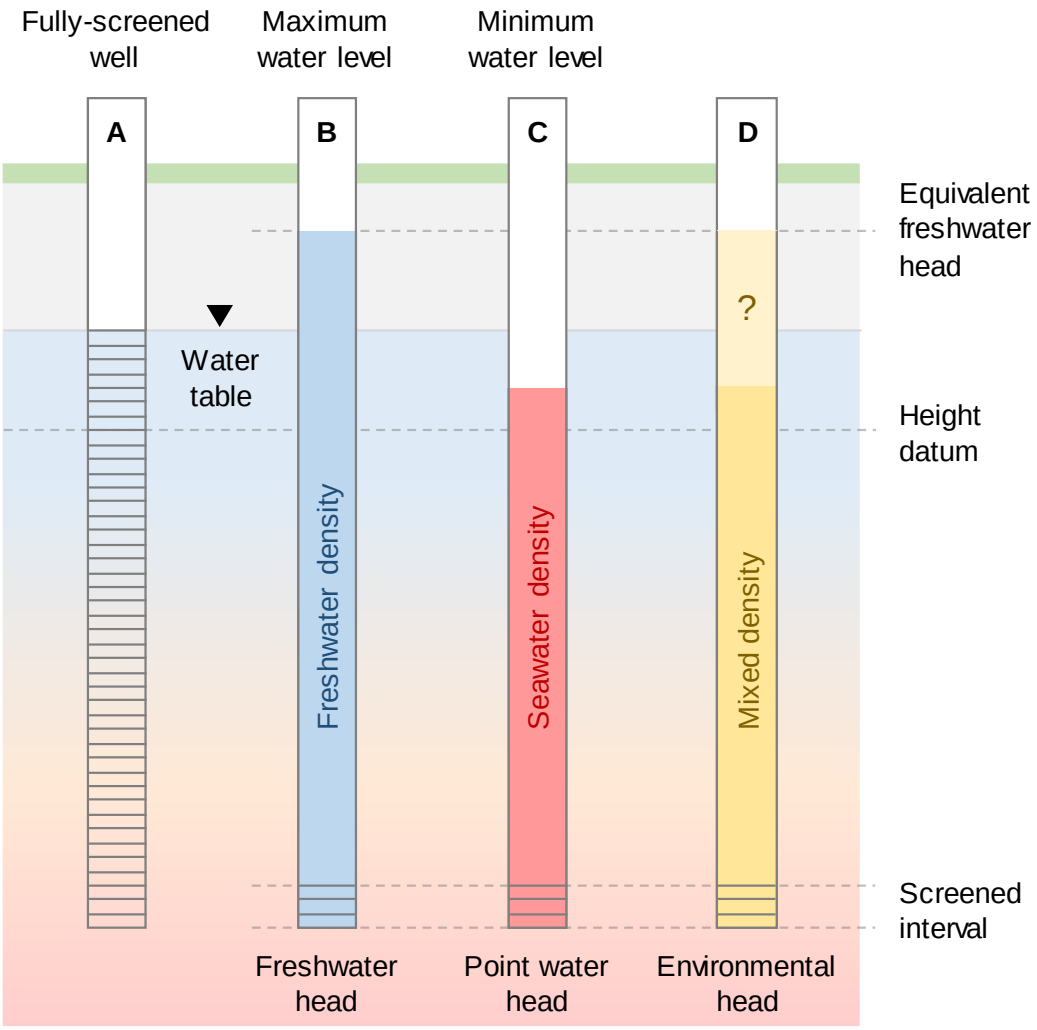

Figure 3.13: Schematic representation of uncertainty in the measurement of the hydraulic head from a well where large changes in solute concentration exist, such as at the seawater interface. The water level measured in a monitoring well is dependent on the density of water in the well column (Lusczynski, 1961; V. Post et al., 2007). ***Well A*** *is a fully screened well where the groundwater inside the well column matches that outside of the well. Here the measured water level is equivalent to the water table.* ***Well B*** *is screened below the water table. If fresh water occupies the entire water column, the measured water level will be above the water table.* ***Well C*** *shows that if the well column is filled with seawater, the measured water level will be below the water table.* ***Well D*** *assumes that the density of the water column is a mixture of fresh and saline waters. This observation is critical to compare measured water levels with numerical modelling outcomes, which are typically provided as pressure in equivalent freshwater head. If the water density in the well column is not measured at the time of the water level measurement, there is significant uncertainty in the equivalent hydraulic head calculation.*

The density of water residing in the well column is often not measured directly, and so must be assumed from the EC of water samples. This is the situation for the SIM wells at the Quinns Rocks reference site in Perth, Western Australia. Figure 3.14 provides an example from the reference site showing the difference in hydraulic head after computing the equivalent freshwater head (EFH) using the EC-derived mass density (UNESCO, 1981), compared to the measured water level (MWL). The three dates shown cover the time before seawater intrusion (Figure 3.14A), during active seawater intrusion (Figure 3.14B) and a recent date where the EFH gradient is approximately seaward (Figure 3.14C).

The well-to-well hydraulic gradients computed from the measured water levels (i.e. the blue line) in every date shown in Figure 3.14 suggests that groundwater is flowing towards the ocean. In 1992 (Figure 3.14A), all of the SIM wells contain relatively fresh groundwater and the equivalent freshwater head is similar to the MWL. However, by 2011 (Figure 3.14B) seawater had progressed beyond the screened interval in SIM 1 and SIM 3 (see Figure 3.14). The equivalent freshwater head suggests a landward hydraulic gradient between SIM 3 and SIM 6.

At first this may seem impossible or at least counterintuitive, however the water level measurements at SIM 1 and SIM 3 must be considered in the context of a seawater recirculation cell (see Figure 3.14 and Part 6) that has potentially moved inland beyond the wells. This presents the possibility of landward flow, albeit at exceedingly low velocity, in SIM1 and SIM 3 compared with expected groundwater flow towards the ocean past the screen in SIM 6, which remains fresh.

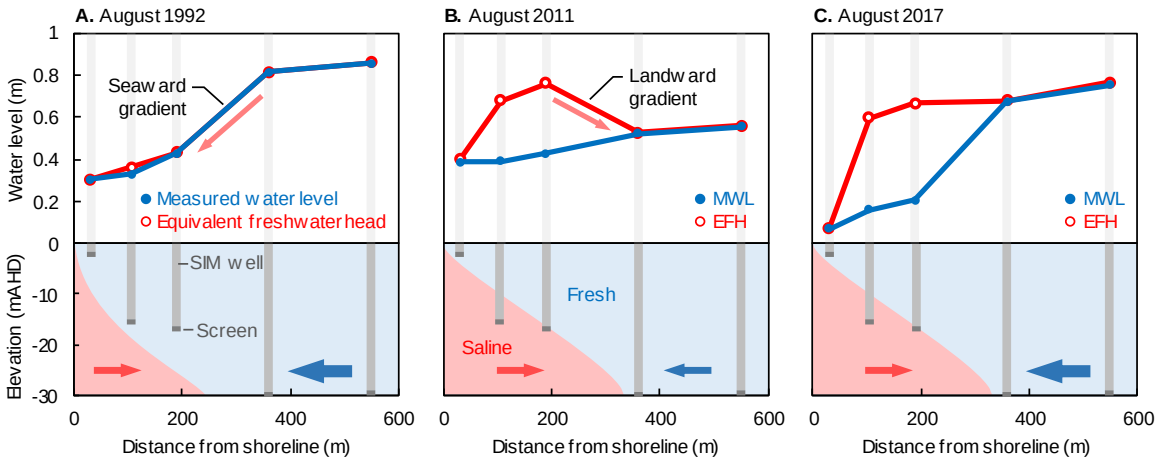

Figure 3.14: Charts and schematic showing the equivalent freshwater head compared to the measured water levels. Here the equivalent freshwater head (EFH) is calculated assuming that the water density around the well-screen exists throughout the column. ***Panel A*** *shows a measurement from 1992, which indicates that fresh water is present. Here the hydraulic gradient is towards the ocean.* ***Panel B*** *shows a measurement from 2011, where EC measurements at the well-screens suggest that high density seawater is present.* ***Panel C*** *shows a measurement from 2017, where the EFH in SIM 6 is higher than in SIM 3, suggesting no landward movement of the seawater interface is occurring. The measured water levels in Panel B suggest a seaward hydraulic gradient, however the density of water in the well columns has not been considered. Estimation of the EFH with the assumption that seawater has filled the well column for SIM 1 and SIM 3 in 2011 and 2017 presents significant changes in groundwater hydraulics in this shallow coastal aquifer system.*

3.4.3 Estimation of groundwater throughflow from hydraulic gradients

Hydraulic gradients at coastal margins can be influenced by seasonal changes in groundwater recharge, sea-level variations, and groundwater abstraction (see sections above). Estimates of throughflow based on hydraulic gradients must also be affected by how gradients are computed. For example, the gradients are dependent on how aquifer pressure is calculated (i.e. freshwater head), and localised impacts on aquifer pressure, (e.g. tidal forces and groundwater abstraction).

We estimate groundwater throughflow to the ocean based on hydraulic gradients. The question being addressed is "Can these methods provide reasonable estimates of groundwater throughflow for calculation of the landward extent of the seawater interface in a high-quality coastal aquifer system, such as at the Quinns Rocks reference site?".

There are several assumptions made when estimating groundwater throughflow using the flow-nets and hydraulic gradients. A typical flow-net analysis assumes that a homogeneous, saturated, and isotropic aquifer with known boundaries exists (Healy *et al.*, 2002). Extensions to these assumptions exist for anisotropic aquifers (Maasland, 1957) and partially saturated flow systems (Luthin *et al.*, 1955). The groundwater throughflow, *Q*, is typically estimated from (Kretschmer *et al.*, 2012)

$$Q = TiL \tag{3}$$

Where *T* is the transmissivity (m²/day), *i* is the hydraulic gradient across the aquifer (m/m), and *L* is the width of the flow-cell (m). Here we assume the flow-cell is of unit length. Transmissivity (T) is the product of the hydraulic conductivity (K) (m/day) and the thickness of the freshwater saturated aquifer (i.e., where the fresh groundwater enters the system and occupies the aquifer thickness) (m). For the Quinns Rocks reference site, Kretschmer *et al.* (2012) estimate the mean hydraulic conductivity to be 130–200 m/day, and the saturated thickness of the aquifer (i.e. depth to confining substrate) to be 30 m (Kretschmer *et al.*, 2012).

Two sets of estimates for the groundwater throughflow (Q) calculated from the hydraulic gradients of the measured water levels across the SIM wells are shown in Figure 3.15. This includes estimates for 1994, prior to regional groundwater abstraction, and in 2014 after seawater intrusion has occurred. The average groundwater throughflow is estimated to be 3 ML/year and 1 ML/year respectively. However, it is important to acknowledge the significant uncertainties that exist in the inputs to these equations, such as the impact of variable density groundwater on the hydraulic gradient, and the role of heterogeneous hydrogeology on transmissivity.

If EC measurements (and thus some estimate of density) are not made simultaneously with the measurement of water level, there may be no indication whether the measurement of hydraulic head (and thus the flow from hydraulic gradient) is affected by the impassable seawater wedge. It may seem appropriate to estimate the gradient from measurements in wells that are known to be fresh throughout the entire thickness of the aquifer, such as SIM 4 and SIM 6. As shown in Figure 3.15, the hydraulic gradients between these two wells are significantly different to the hydraulic gradient taken across all five SIM wells and yield a far lower estimate of groundwater throughflow (see Supplementary Figure S1 and S2).

The hydraulic gradients between each of the SIM wells also questions the assumption of homogeneity for the transmissivity estimate. The steep gradient between SIM 3 and SIM 6 suggests a zone of lower hydraulic conductivity between the screened intervals of these wells. Shallower inter-well gradients, such as between SIM

1, SIM 2 and SIM 3, can be indicative of high hydraulic conductivity zones. Variable hydraulic gradients across the SIM wells provides evidence that the aquifer is heterogeneous.

At best, these methods provide a first-order approximation of groundwater flow. Groundwater flow has reduced from 1994 to 2014, however, the precise value of the groundwater throughflow is uncertain. We will see that combination of water level measurements and the simple methods described above cannot provide certainty for the landward extent of the seawater interface or groundwater throughflow.

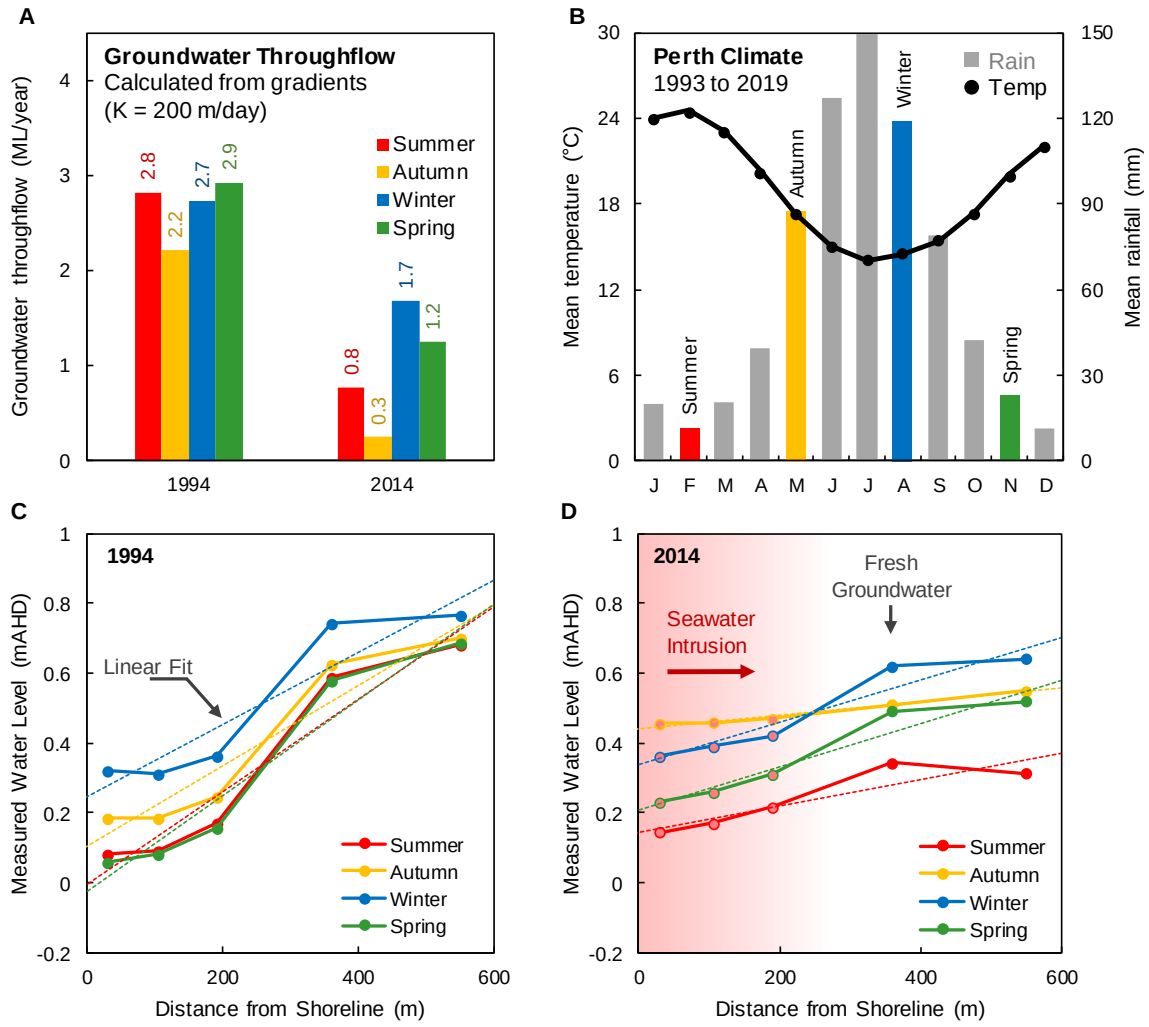

Figure 3.15: Set of charts showing seasonal variations in groundwater levels, climate and estimated throughflow at Quinns Rocks. ***Panel A*** *shows the groundwater throughflow, Q, calculated from hydraulic gradients using hydraulic conductivity K = 200 m/day. Gradients are computed from the raw measured water levels (Water Information Reporting database, 2019).* ***Panel B*** *shows the mean seasonal temperature and rainfall between 1993 and 2019.* ***Panels C, D*** *show the average seasonal groundwater levels measured in the SIM wells along with estimated linear fits for 1994 and 2014 respectively. The average groundwater throughflow during 1994 is significantly higher than in 2014, however we must acknowledge that there are significant uncertainties in the inputs to estimates of hydraulic gradient and calculation of groundwater throughflow. At best these methods provide a first-order approximation of groundwater flow.*

3.4.4 The seawater interface according to an analytical solution

Analytical solutions, such as those of Bear *et al.* (1964), R. E. Glover (1959), O. Strack (1976), and others (Bakker, 2006), estimate the position of the seawater interface based on averaged measures of hydraulics (e.g. the groundwater throughflow and average hydraulic conductivity). These solutions tend to simplify the transition between saline and fresh water to a sharp boundary, neglecting the effect of solute transport phenomena such as dispersion. They can have value in regional scale seawater intrusion studies where numerical modelling may not be practical (Ivkovic *et al.*, 2012).

The Glover solution is used to illustrate the range of possible seawater toe positions that may be derived using data at the field site with constraints from groundwater throughflow estimates. The Glover solution is a readily applied analytical solution that is routinely used to estimate the steady-state toe position of a seawater wedge. It is expressed as (R. E. Glover, 1959):

$$z^2 = \frac{2Q}{K\Delta s}x + \left(\frac{Q}{K\Delta s}\right)^2 \quad (4)$$

Here z is the depth below sea level (e.g. 0 m) to the seawater interface (m), Q is the flow per unit length of the shoreline (m²/day), K is the hydraulic conductivity of the aquifer (m/day), Δs is the density ratio of seawater to fresh water, and x is the horizontal distance inland from the shoreline (m).

The range of estimated groundwater throughflow from hydraulic gradient analysis using the average measured water level across all of the SIM wells is between 3.00 ML/year and 0.48 ML/year. At the lowest estimate of flow and using a hydraulic conductivity of 200 m/day, the Glover solution places the seawater interface at 1813 m inland from the shoreline. This estimate is not reasonable for the study site as fresh groundwater is still present at the SIM 6 monitoring well located only 360 m inland. We suspect that the gross overestimate (1813 m) for the position of the seawater interface is likely due to the inability of the solution to accommodate hydraulic complexity of the karstic system along Perth's coastal margins, although there are many uncertainties in the inputs to this solution.

In the next section, we use numerical solute transport models for a homogeneous aquifer to simulate the position of the seawater toe for comparison with the toe position calculated from the analytical solution and estimated from the field data.

3.4.5 The seawater interface according to a homogeneous numerical transport modelling

Numerical groundwater flow and solute transport modelling can replicate phenomena observed at the seawater interface, such as groundwater mixing and variable density heads. We use FEFLOW 7.2 (H.-J. G. Diersch, 2014) to simulate seawater intrusion into a high quality, high permeability coastal aquifer similar to that found at the Quinns Rocks reference site. We use a 2D cross-sectional model to describe groundwater throughflow to the ocean using units of ML/year for a unit thickness (1 m). That is, for an aquifer that is 30 m thick, the groundwater throughflow is the rate that water passes through a surface with dimensions 1 m × 30 m.

The quadrilateral mesh discretisation and boundary conditions used for the finite element model are shown in Figure 3.16. Seawater enters the model through the left boundary and along the top boundary until the coastline ($x \leq 0$ m). The density dependent hydraulic head condition ensures that seawater drives inland (H. Diersch, 2002). The flow of fresh groundwater (TDS ~358 mg/L) into the model is controlled by a fixed flux condition along the boundary at the right for $z \leq 0$ m. The substrate at the base of the model (z = -30 m) represents a no-flow boundary.

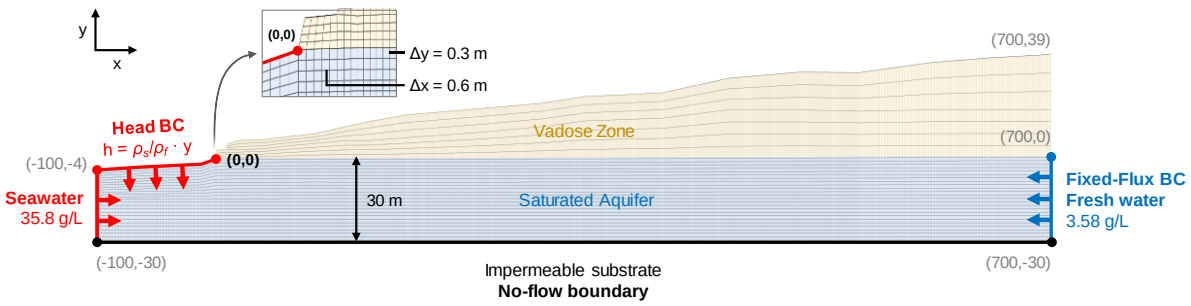

Figure 3.16: Diagram representing the finite element mesh and boundary conditions used for numerical groundwater flow and solute transport modelling . The mesh is coarse above the saturated zone as no recharge from the surface is included. Cells surrounding to the water table are included in the aquifer mesh refinement. The impact of increasing levels of refinement (e.g. number of elements) are provided in Supplementary Figure S3.

Table 3.2 summarises the material parameters used in the groundwater flow and solute transport model. Simulations were run until no further changes to the position of the seawater toe were observed. The minimum mass concentration values are described in Section 1.6, while the maximum mass concentration is estimated from the sea-surface salinity local to Perth (Bureau of Meteorology, 2012). The density ratio is set to 0.0256 after Fofonoff *et al.* (1983). The dispersivity is estimated based on Narayan *et al.* (2007); AJ Smith *et al.* (2012).

Table 3.2: Groundwater flow and solute transport modelling parameters used to generate models in FEFLOW

Parameter	Value	Unit
Hydraulic Conductivity	200	m/day
Seawater Concentration (TDS)	35800	mg/L
Freshwater Concentration (TDS)	358	mg/L
Density Ratio	0.0256	$-$
Specific Storage	10^{-4}	$1/m$
Effective Porosity	0.3	$-$
Molecular Diffusion	10^{-9}	m^2/s
Longitudinal Dispersivity	2	m
Transverse Dispersivity	0.2	m
Saturated thickness	30	m

We simulate the systematic reduction of groundwater throughflow and the show the change in solute distribution in Figure 3.17. The groundwater throughflow is reduced from 4 ML/year to 1 ML/year and covers the range of groundwater throughflow estimated for the Quinns Rocks reference site. The groundwater throughflow is not reduced again once the SIM wells furthest inland become salinized. Figure 3.17C – F shows that halving the groundwater throughflow will double the inland position of the toe for the homogeneous aquifer.

A comparison of the simulated data with measured field data from 1994 and 2014 (Figure 3.17A, B) shows that no throughflow rate can be combined with a homogeneous aquifer to achieve a suitable match. The EC in SIM 6 is the strongest constraint for the inland position of the seawater wedge, which, as of 2019 remains that of fresh water. To satisfy the solute concentration condition at SIM 6 with this homogeneous aquifer model, groundwater throughflow must remain above 2 ML/year, which results in the simulated hydraulic head being significantly higher than any of the measured values. This numerical experiment also highlights the counterintuitive shape of the simulated hydraulic gradients. As denser seawater passes the monitoring well screen, the equivalent freshwater head can rise above the hydraulic head for wells further inland (in fresher water). This is shown by the hydraulic gradient between SIM 6 and SIM 4 (Figure 3.17A, B).

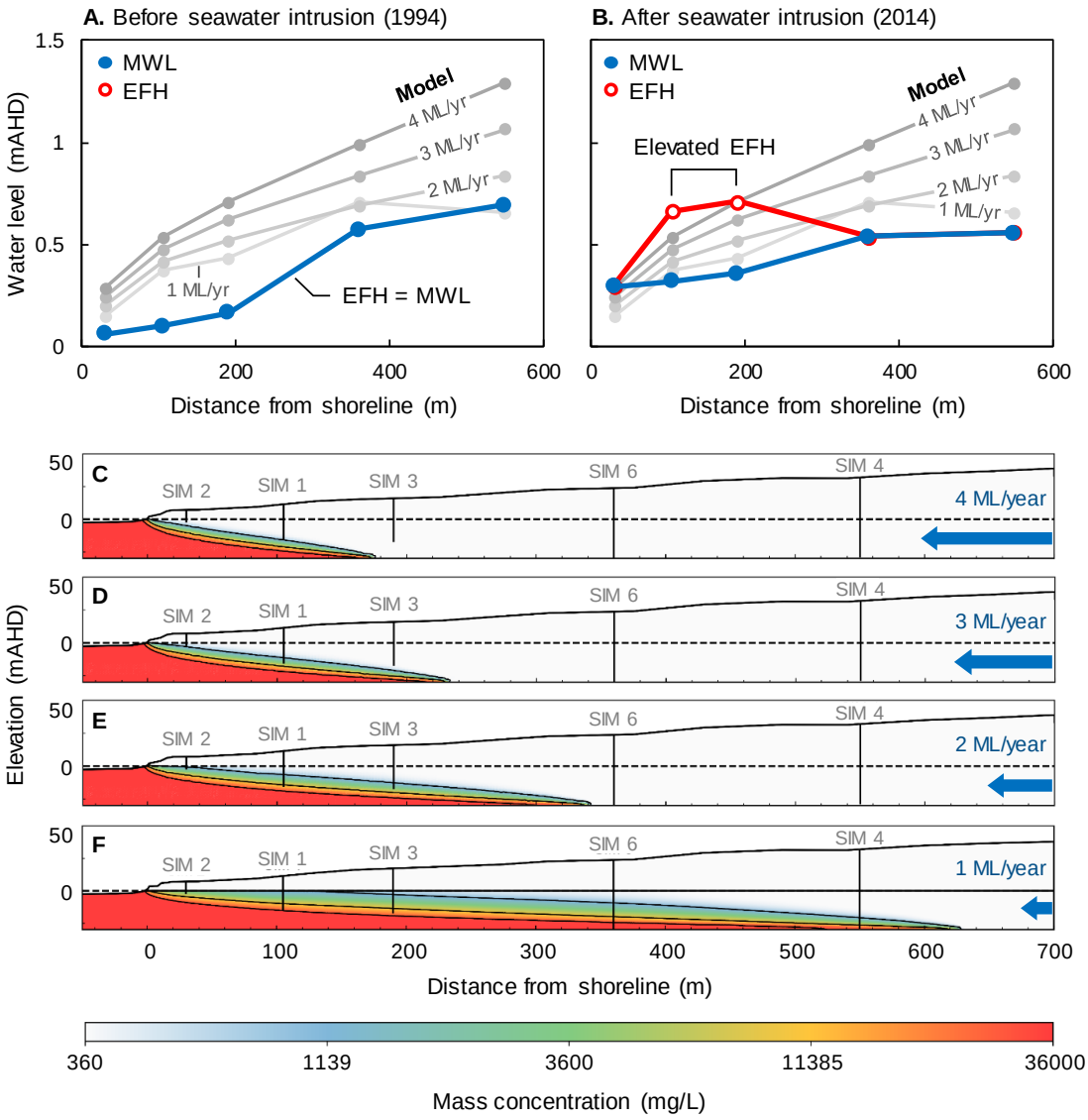

*Figure 3.17: Set of images showing the simulated seawater interfaces for a range of groundwater throughflow in a 30 m thick aquifer with hydraulic conductivity 200 m/day over an impermeable substrate (i.e., average values for the Quinns Rocks reference site). Charts **A** and **B** show the measured water levels (MWL) and equivalent freshwater head (EFH) in 1994 and 2014. The EFH is calculated assuming that the groundwater at the well screen occupies the entire well column. Images **C**, **D**, **E** and **F** show the solute concentration distribution corresponding to groundwater throughflow of 4, 3, 2, and 1 ML/year respectively. According to this homogeneous aquifer model, groundwater throughflow must remain above 2 ML/year at Quinns Rocks to maintain fresh groundwater at SIM 6; however, this results in significantly greater simulated hydraulic head than the field observations. We find that there is no combination of hydraulic conductivity and throughflow for a homogeneous aquifer that can reasonably explain both measured values of hydraulic head and solute concentration at the reference site. This points towards high contrast in hydraulic parameters within the aquifer as a strong influence on the landward extent of saline groundwater.*

3.4.6 Comparison of numerical and analytic solutions for the landward extent of seawater

The landward extent of the seawater interface is fundamental information required coastal groundwater resource management. Although the analytical solution can provide a quick answer, we suspect that in practice it may also lead to significant error.

In Figure 3.18, we compare the landward extent of the seawater toe using the analytical Glover solution with numerical simulations (see Figure 3.17). Numerical modelling with throughflow of 1 ML/year places the toe at 434 m inland (i.e. this is the landward extent of the 34 g/L contour). For the same groundwater throughflow, the Glover solution places the toe at 875 m inland. This is almost twice as far inland as compared to the numerical model (see Figure 3.17F). For a homogeneous aquifer, there is a significant difference between analytical and numerical solutions.

If we accept the simplifying assumption of a homogeneous aquifer for the Quinns Rock site, the numerical solution suggests that the reduction in groundwater throughflow between 1990 and 2018 should result in the seawater wedge moving over 500 m inland, to 750 m from the shoreline. This cannot be correct, as the groundwater in SIM 6, ~360 m from the ocean, has always remained fresh. This supports the case that neither the analytical solution nor numerical modelling with a homogeneous aquifer can reasonably estimate the landward extent of the seawater interface at Quinns Rocks. That is, no simplified model can reasonably match the measured water levels and solute concentration measured at the Quinns Rocks reference site.

The above outcome has practical consequences. As an example, approximately 23% of Western Australian households have a private shallow well used for household consumption or irrigation (Australian Bureau of Statistics, 2009). For the approximately 7,000 households local to the Quinns Rocks area (Australian Bureau of Statistics, 2016), approximately half of the dwellings are within 1 km of the coast. Over 800 shallow wells are potentially affected by groundwater management decisions at this relatively short interval of Perth’s coastal margin.

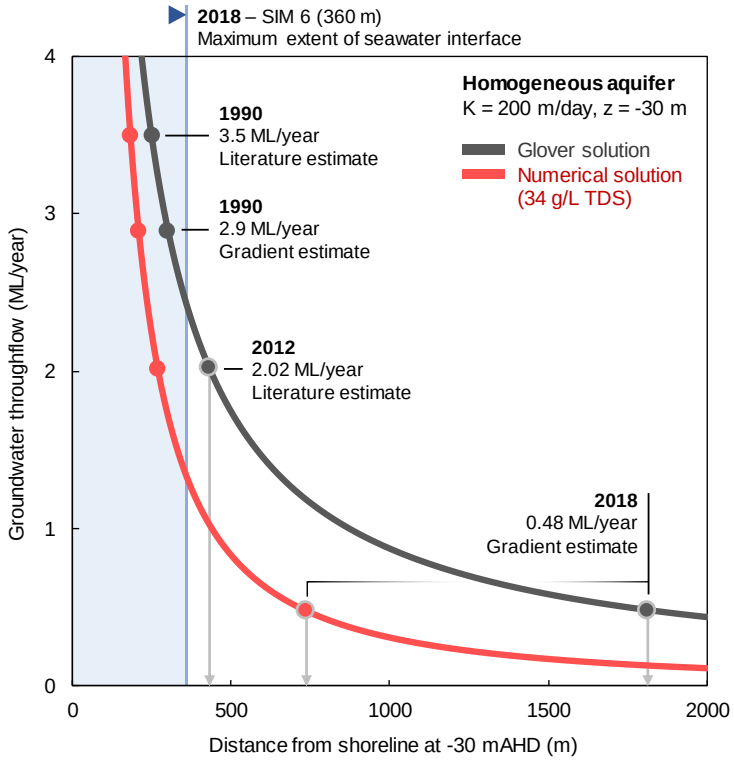

Figure 3.18: Chart comparing the landward position of the toe of the seawater wedge estimated from the Glover analytical solution (dark grey curve) and numerical simulations based on a homogeneous aquifer (red curve). We also provide a set of discrete throughflow estimates for several dates at the Quinns Rocks site to compare where these methods place the landward extent of the seawater wedge toe. These discrete groundwater throughflow estimations are derived from Kretschmer et al. (2012) and hydraulic gradient analysis (Sect. 3.1). Note that the seawater interface can be no more than 360 m inland (i.e. within the blue area) as electrical conductivity measurements in SIM 6 is screened at the base of the aquifer and remains fresh. Both methodologies significantly overestimate the landward extent of the seawater interface at Quinns Rocks. We also note the significant difference between the toe positions estimated for the lower flow rate using the numerical solution compared and that estimated from the Glover solutions (see grey arrows marked on the image).

We suspect that numerical modelling with greater levels of complexity is required; however, this leads to a new question: "What data are required to build and constrain such numerical models?". Below we consider the impact of anisotropy and strong hydraulic heterogeneity on the shape and landward extent of the seawater interface.

3.5 Complex Models: What is the role of anisotropy and heterogeneity?

3.5.1 How does anisotropy of hydraulic conductivity impact the landward extent of the seawater interface?

The hydraulic conductivity in most sedimentary environments is likely to be anisotropic (Koltermann *et al.*, 1996; Sudicky, 1986) and must influence groundwater flow patterns in some way. Anisotropy can be introduced by grain-size variations from depositional cycles, crossbedding from dune cementation and limestone diagenesis (Goggin *et al.*, 1988). For example, dune structures have dips that are typically 20° to 25°, with some aeolian systems having dips of 30° to 35° (Selley, 2000). Anisotropy is expressed as the ratio of hydraulic conductivity, K_x/K_y, where components of the conductivity tensor ($\boldsymbol{K}$) are rotated by an angle (ϕ) (H.-J. G. Diersch, 2014) as shown in Figure 3.19.

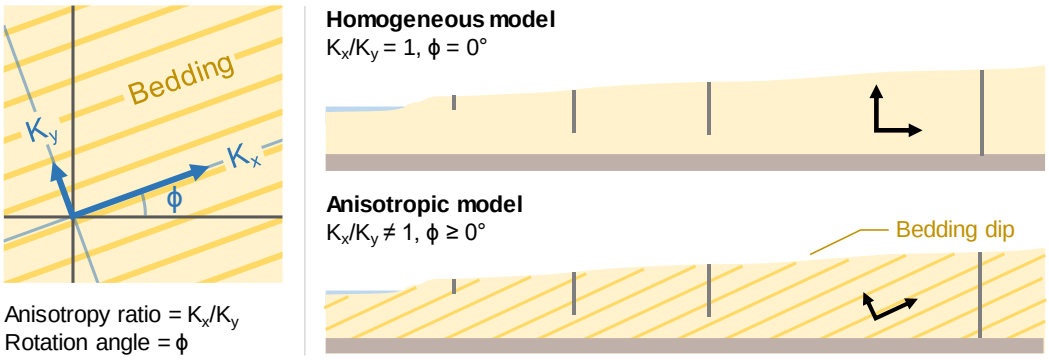

Figure 3.19: Schematic showing the ratio of anisotropy, K_x/K_y, in relation to the dip angle (ϕ) for inclined bedding planes. Dune structures have dips that are typically 20° to 25°, with some aeolian systems having dips of 30° to 35° (Selley, 2000).

Anisotropy of hydraulic parameters can significantly impact on seawater intrusion (Dagan *et al.*, 1998; Held *et al.*, 2005). Abarca, Carrera, Sánchez-Vila, and Dentz (2007) and Kerrou *et al.* (2010) use a dispersive anisotropic Henry problem (Henry, 1964) to show that the penetration of the toe is predominantly controlled by the horizontal permeability (i.e., in the direction of flow) and geometric mean of dispersivity. Qu *et al.* (2014) and Michael *et al.* (2013) show that the anisotropic ratio (K_x/K_y) and position of the seawater interface are directly proportional.

We have found no examples that approach the influence of dip angle and anisotropy on the position of the seawater interface. We systematically demonstrate the impact of increasing the angle of anisotropy on the seawater interface geometry for a groundwater throughflow of 2 ML/year. The first model (Figure 3.20A) is included for comparison with our baseline 30 m thick isotropic layer. Models for Figure 3.20B, C, and D, have the anisotropic ratio set to K_x/K_y = 10, and a rotation angle of $\phi = 0°$, 15° and 25° respectively.

An interesting observation is that the zone of submarine groundwater discharge for the anisotropic model (Figure 3.20B) extends further beneath the ocean than in the isotropic model (Figure 3.20A), despite having the toe of the seawater interface located in the same position (~270 m). Qu *et al.* (2014) suggest that the discharging zone must widen to maintain the discharge capability of the aquifer, with net seaward movement of the seawater toe. We observe this to a small extent in Figure 3.20B, where the toe moves inland from 274 m to 265 m. Quantifying the impact of anisotropy on the extent of the submarine groundwater discharge may have practical implications for near-shore coastal ecosystems that are reliant on nutrient flow from terrestrial groundwater (Moore, 2006; Slomp *et al.*, 2004) (Burnett *et al.*, 2006; Lambert *et al.*, 2003).

A key finding expressed in Figure 3.20, is that dip angle—regardless of the geological origin—has the potential to create hydraulic conductivity anisotropy and thus will also impact the landward extent of seawater at coastal margins. In Figure 3.20, all examples use identical throughflow of 2 ML/year; however, the toe of the seawater interface in this otherwise homogeneous aquifer resides at 274 m, compared to 92 m for an anisotropy of K_x/K_y = 10 at a rotation angle of 25°. This significant difference demonstrates the potential impact that anisotropy can have on the landward extent of the seawater wedge.

A more general observation is that the shape of the interface may not be a reliable mechanism for constraining groundwater throughflow and vice versa. We test this idea further below by manipulating throughflow and hydraulic conductivity anisotropy to achieve a constant hydraulic gradient.

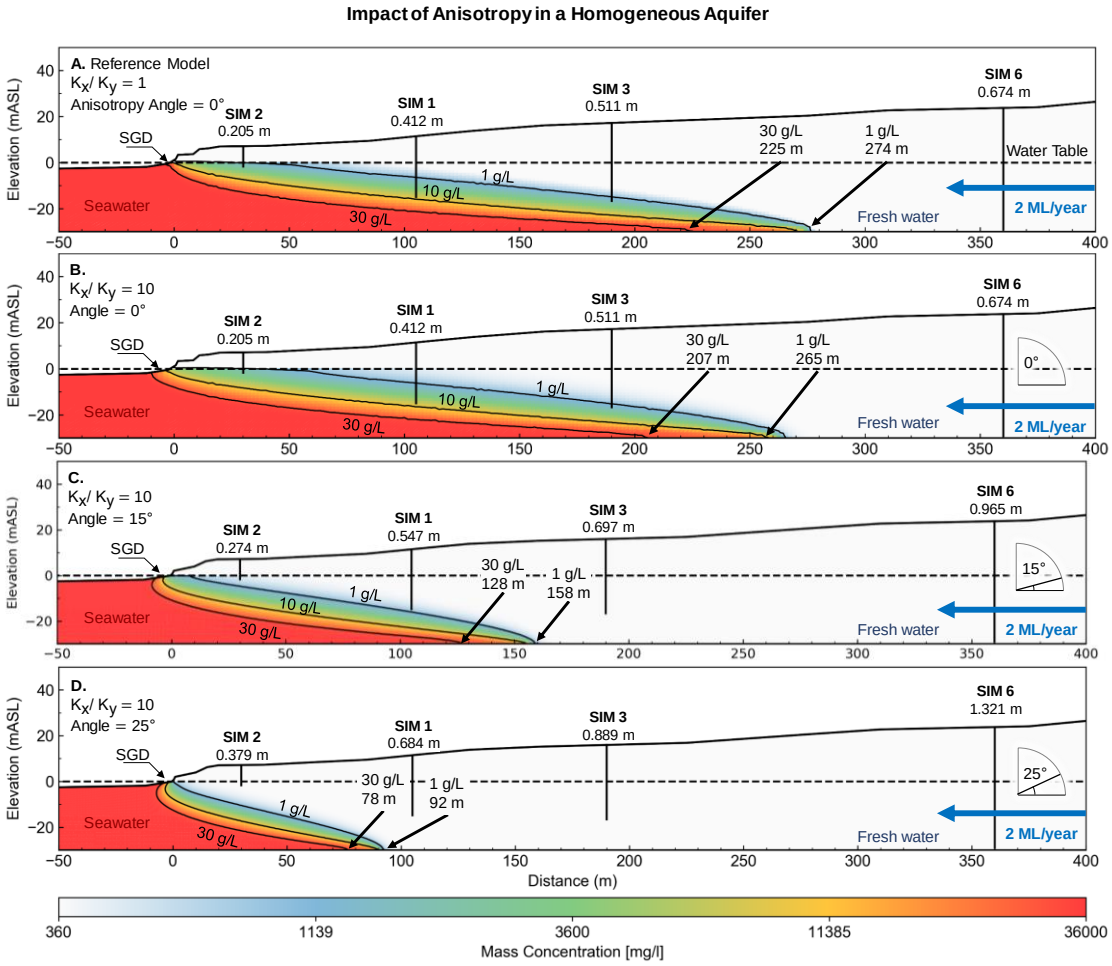

*Figure 3.20: Images showing the influence of increasing anisotropic angle on the seawater wedge geometry in a high hydraulic conductivity (200 m/day) homogeneous aquifer. In this example, the angles of anisotropy are 0° (**B**), 15° (**C**), and 25° (**D**) degrees for a constant anisotropic ratio $K_x/K_y = 10$. **Panels A** and **B** compare the isotropic and anisotropic models. The increasing angle of anisotropy is associated with higher hydraulic heads (annotated below each well), which is likely to be the primary driver behind the seaward movement of the seawater interface. The seawater wedge geometry in Panel D resembles the seawater interface geometry for a homogeneous isotropic model with a groundwater throughflow rate of 4 ML/year (see Figure 15). This demonstrates that knowing the position of the wedge toe is not a reliable indicator of throughflow and vice versa.*

3.5.2 Is the position of the wedge a reliable indicator of groundwater throughflow?

Hydraulic head is often used to constrain groundwater models. For the seawater interface, the hydraulic head gradients can be a key input to estimating throughflow to the ocean. However, the strength of this constraint in the absence of specific information regarding the hydraulic conductivity distribution needs to be carefully examined. We illustrate this point by taking a baseline scenario with hydraulic heads for a homogeneous aquifer (Figure 3.21A) and then search for combinations of hydraulic conductivity anisotropy and groundwater throughflow that generates near-identical hydraulic head distribution. We present the results as the set of images in Figure 3.21A through to Figure 3.21D. By systematically increasing rotation angle for hydraulic conductivity anisotropy and decreasing throughflow, we maintain a constant hydraulic head distribution.

An additional observation from Figure 3.21 is that the geometry of the seawater wedge at low throughflow rates (e.g. 0.699 ML/year, Figure 3.21D) can be similar to the geometry of the wedge at much higher throughflow (e.g.

2 ML/year, Figure 3.21A) by changing the hydraulic anisotropy rotation angle and or ratio. As a result, neither the groundwater throughflow estimation, nor the position of the seawater toe are reliable indicators of seawater intrusion in the absence of reliable and accurate information concerning hydraulic conductivity distribution or groundwater flow distribution.

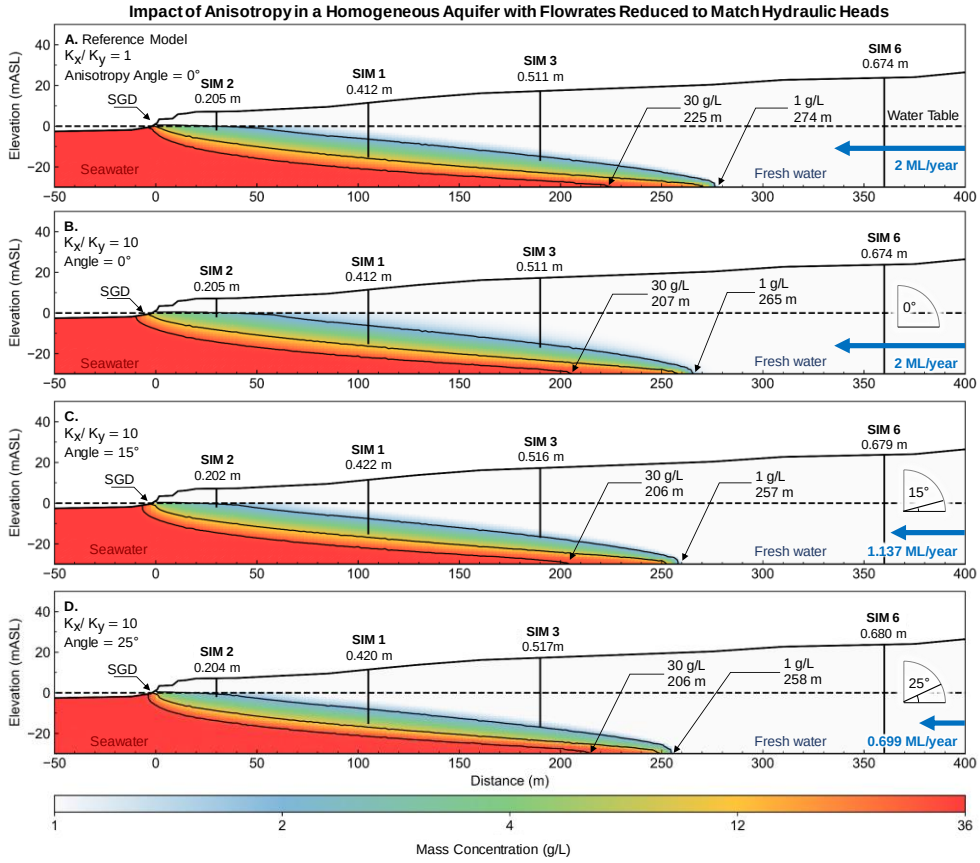

*Figure 3.21: Images showing the influence of anisotropy on the seawater wedge geometry after reducing groundwater throughflow to match hydraulic heads . The differences between the resulting seawater wedge geometry is minor. For example, the wedge geometry from the lowest flowrate (0.69 ML/year) with anisotropic angle of 25° (**Panel D**) is similar to the wedge geometry at high 2 ML/year with an angle of 0° (**Panel A**). Lower anisotropic angles result in a wider zone of submarine groundwater discharge. This figure highlights the fact that knowing the seawater wedge position alone is not an indicator for groundwater throughflow. There is a clear need for better constraints on hydraulic parameters to understand the seawater interface in these coastal aquifers.*

In the next section, we consider spatially correlated random fields as a final higher level of model complexity and compare results to field data from the Quinns Rocks reference site. One reason for providing simulations with pseudo-random distributions of hydraulic properties is to examine the implications and limitations of monitoring well design (e.g. the SIM wells). For example, this provides a platform to assess the impacts of hydraulically connected high-permeability pathways (i.e. conduits or bedding planes) on measurement from a small number of wells.

3.5.3 Taking model complexity to extremes: Spatially correlated random fields

A heterogeneous hydraulic conductivity distribution can be constructed with spatially correlated random fields (Heße *et al.*, 2014). Spatially correlated random fields can be used to generate geologically plausible distributions of subsurface parameters, such as hydraulic conductivity, porosity and dispersivity (Bellin *et al.*, 1996; Koltermann *et al.*, 1996; Li *et al.*, 2016). Each of these factors can impact the geometry (i.e., shape and landward extent) of the seawater interface (Abarca, Carrera, Sánchez-Vila, & Dentz, 2007; Al-Bitar *et al.*, 2005; Beaujean *et al.*, 2014; Comte *et al.*, 2017; Kerrou *et al.*, 2010; Werner *et al.*, 2013).

We generate a series of randomly distributed hydraulic conductivity models with values intended to span the anticipated ranges for karstic systems at the reference site as provided in Supplementary Information Table S7. The code to generate these distributions is provided in Supplementary Information Section 7, along with input parameters for generating these distributions.

The hydraulic conductivity distribution and associated solute concentration distribution for a subset of the models computed are shown in Figure 3.22. These distributions may all plausibly exist within the Tamala limestone at the Quinns Rocks reference site. Although the groundwater throughflow is set to a constant 1 ML/year, we observe significant differences in the position of the seawater toe and the geometry of the interface. The inland position of the seawater toe ranges from 201 m (Figure 3.22B) to 410 m (Figure 3.22F) in the examples shown. Despite having the same groundwater throughflow and statistically similar hydraulic conductivity distribution, the distance inland from the ocean has doubled.

A key observation from Figure 3.22 is that a low hydraulic conductivity zone located relatively close to the shoreline (e.g., Figure 3.22B, Figure 3.22C) will result in a steeper solute concentration gradient and decrease the landward extent of the seawater interface toe (e.g. Figure 3.22H, Figure 3.22I). In the example (Figure 21K, Figure 21L) higher hydraulic conductivity zones in the same area result in a flatter solute concentration gradient with the toe located further inland. Based on this, we suspect that the hydraulic conductivity of the near shore may be of greater consequence to the shape of the wedge than the distributions further inland. Establishing the hydraulic conductivity of this zone can be challenging due to tidal oscillations, high contrast in water density and the relatively extreme velocities of the groundwater moving into the zone of submarine groundwater discharge.

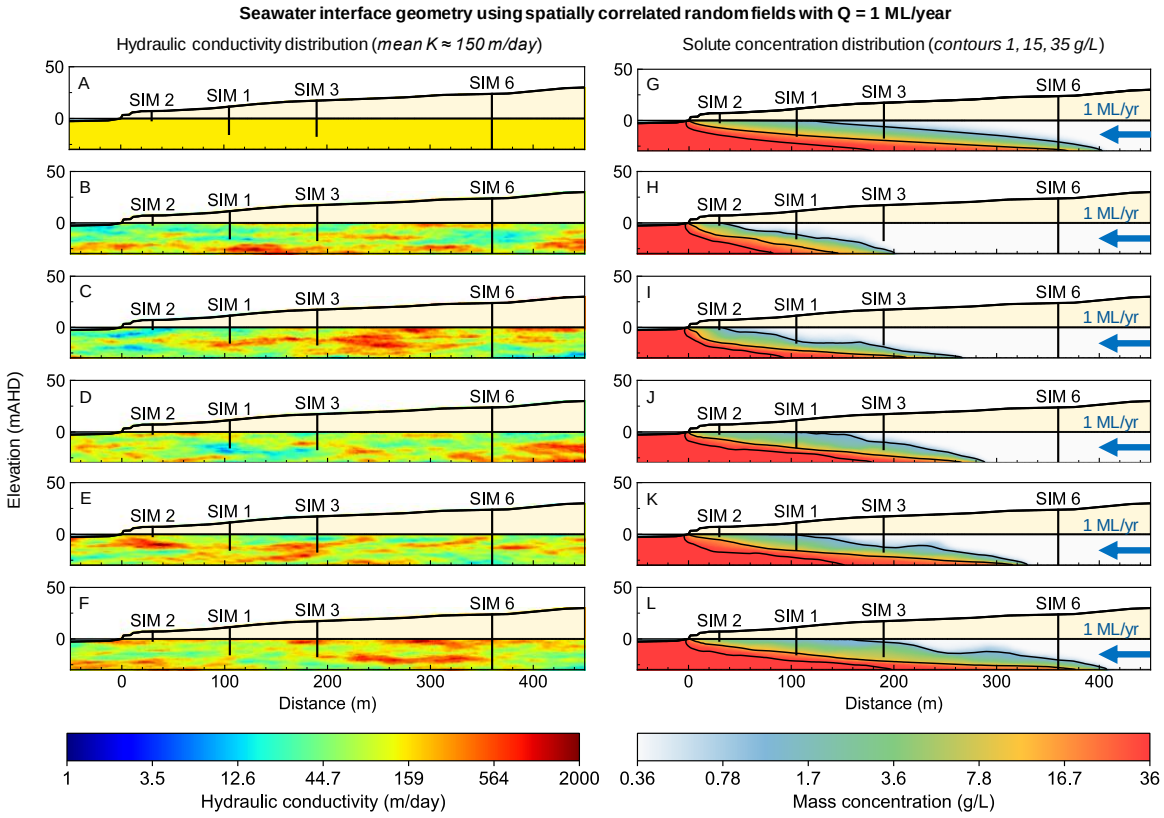

Figure 3.22: Images showing the hydraulic conductivity distribution (left column) and associated seawater interface geometry (right column) using spatially correlated random fields with a range of seeds. Despite having identical groundwater throughflow and statistically similar hydraulic conductivity distributions, the position of the seawater toe and the geometry of the wedge are significantly different.

Throughout this research we have shown that measuring the water level and EC at the screened interval of several wells may be insufficient to describe the dynamic and spatially complex hydrogeology found in karstic regions. The randomly generated models shown here further highlight the requirement to acquire specific measurements at coastal margins. This raises the question: "What set of measurement *are* necessary to explain the hydraulics and solute concentration distribution for karstic aquifers?"

Geophysical methods are often used to infer the hydrogeology of shallow aquifers, particularly the seawater wedge. Electrical resistivity imaging (ERI) is a popular technique with proven application for imaging the seawater wedge (Abdul Nassir *et al.*, 2000; Carter *et al.*, 2008; Comte *et al.*, 2007; A. Costall *et al.*, 2018). However, there are aspects of application ERI at coastal margins that need investigation. We demonstrate and discuss these in the next section.

3.6 Geophysics: How reliable is electrical resistivity-based monitoring?

Conventional groundwater monitoring with wells can provide high-quality local information, but as we have shown, may be insufficient to progress to a robust solute transport model. Geophysical measurements provide a method to investigate the volume of earth between wells; however, the imaging outcomes are subject to a range of interpretations and uncertainties. We will demonstrate a process by which solute concentration distribution from numerical groundwater modelling can be used to create numerical simulations of ERI outcomes, which can then be compared to field data.

A desirable outcome from electrical resistivity imaging (ERI) is that it recovers an accurate representation of the shallow subsurface resistivity. ERI field measurements are acquired by passing current across a pair of electrodes, while measuring the voltage drop across a second pair of electrodes. The number, orientation, spacing, and geometry of the two electrode pairs (i.e. the quadrupoles) relative to the earth's electrical structure will impact the methods ability to construct a reasonable subsurface image of electrical conductivity by inversion (Dahlin *et al.*, 2004). The dipole-dipole configuration, or combinations of dipole-dipole with other electrode arrays are considered highly reasonable for recovery the hydrogeology at the seawater interface (A. Costall *et al.*, 2018; Martorana *et al.*, 2009).

3.6.1 Converting solute to formation resistivity

The relationship between total dissolved solids in solution (TDS) and water resistivity is typically near-linear (Arps, 1953; Walton, 1989). If water resistivity is known it can then be converted to an estimate of formation resistivity via Archie's law (Archie, 1941; Winsauer *et al.*, 1952).

$$\rho_b = a\rho_w\phi^{-m}S^{-n} \tag{5}$$

Where ρ_b is the formation electrical resistivity (Ω m), ρ_w is the fluid electrical resistivity (Ω m), and ϕ is the porosity. The tortuosity factor a, and cementation exponent m, can be empirically related to the formation rock type (Archie, 1941; Azar *et al.*, 2008). *S* is the fluid saturation (between 0 and 1) and *n* is the fluid saturation exponent.

The formation resistivity is dependent on the choice of *a*, and *m*. Porosity in the Tamala Limestone is highly variable, from 0.2 to 0.5 (AJ Smith *et al.*, 2012). Tortuosity and cementation factors are based on generalised values from literature (P. W. J. Glover, 2016; Verwer *et al.*, 2011). Table 3.3 details suggested ranges of values and provides an example of the formation resistivity for a given groundwater solute concentration. For the parameters we choose, fresh groundwater and highly saline groundwater are expected to measure ~198 Ω m and 2.8 Ω m respectively.

Archie's Law was originally intended for clean sandstones (P. W. J. Glover, 2016); however there are many variations of the law including shaly sands (Asquith, 1990; Waxman *et al.*, 1968), multiple liquid phases (Paul W. J. Glover, 2010), and other various modifications (Hamamoto *et al.*, 2010; Winsauer *et al.*, 1952; Worthington, 1993). The values in Table 3.3 below are reasonable in the context of observations from well logging and ERI experiments completed in the Tamala limestone (AJ Smith *et al.*, 2012; Anthony John Smith *et al.*, 2001; Elmar Strobach, 2013).

Table 3.3: Archie's law (Archie, 1941) parameters showing variation in formation conductivity from values of 'a' and 'm'.

Parameters	Literature Values (P. W. J. Glover, 2016; AJ Smith *et al.*, 2012; Verwer *et al.*, 2011)		Simulated Values
	Sandstone	Carbonate	
Porosity (ϕ)	-	0.2 – 0.5	0.3
Tortuosity Factor (a)	0.515 – 3.45	0.425 – 1.51	1
Cementation Factor (m)	1.225 – 2.20	1.685 – 4.14	2.2
Saturation (S)	-	-	1
Saturation Exponent (n)	-	-	2

In some circumstances, formation resistivity can be derived from hydraulic conductivity (Bernabé *et al.*, 2003; Huntley, 1986; Koukadaki *et al.*, 2007); however, such relationships must be applied with considerable caution. The potential for error exists where fluid salinity is not constant, or where clays are present. Beaujean *et al.* (2014) use a modified version of Archie's law to include a relationship between hydraulic conductivity and the bulk electrical conductivity.

In coastal settings like Quinns Rocks it is highly likely that the distribution of saline and fresh water is the primary driver for the large-scale formation resistivity distribution as would be measured by an ERI survey.

3.6.2 Model generation and inversion

ERI data consists of geometry (i.e. locations of electrodes), transmitted current, and measured voltage. Inverse modelling with this data is completed to recover the subsurface distribution of electrical resistivity (i.e. the formation resistivity). The forward ERI problem is defined by the distribution of electrical fields in the ground due to a point current source. This equation is (Dey *et al.*, 1979; McGillivray, 1992)

$$-\nabla \cdot [\sigma(x,y,z)\ \nabla\phi(\mathrm{x,y,z})] = I\delta(x-x_s)\ \delta(y-y_s)\ \delta(z-z_s) \quad (6)$$

Where σ is conductivity of the medium (S/m), ϕ is electric field intensity (V/m), I is the current source (A), δ is the Dirac delta function. Inverse modelling (i.e. inversion) of geo-electrical measurements then creates a resistivity model that generates the same voltages as a set of field observations.

Electrical resistivity datasets were simulated for a formation resistivity distribution derived from solute concentration distribution using a framework built on pyGIMLi(C. Rücker *et al.*, 2017). We add 5% voltage dependent noise plus 1 μV absolute error as recommended by Friedel (2003). All scripts are freely available from the authors for review and re-use.

The synthetic data is inverted using RES2DINV (M. Loke, 1997), a commercially available resistivity and IP inversion software. It uses a modified smoothness constrained least-squares inversion method with variable smoothness and roughness constraints (M. Loke, 1997; M. H. Loke, 2016a). Inversion of geo-electrical data requires selection of many parameters that can affect electrical resistivity imaging outcomes. Key parameters include the regularisation (i.e. damping factor), error norm (Claerbout *et al.*, 1973; S. C. Constable *et al.*, 1987; A. Costall *et al.*, 2018; Farquharson *et al.*, 2003), topographical relief, a-priori inputs, and the acquisition array (Auken *et al.*, 2004; Dahlin *et al.*, 2004; Fox *et al.*, 1980; C. Rücker *et al.*, 2006)

Our numerical modelling uses a hybrid dipole-dipole and Schlumberger electrode configuration identical to that used to acquire field data at the Quinns Rocks reference site in 2015 (A. Costall *et al.*, 2018). The survey used 44 electrodes spaced at 10-meter increments. The survey extends from the shoreline to residences located 430 meters

inland. Further analysis of the field data can be found in A. Costall *et al.* (2018). All inversions are completed with a finely discretised quadrilateral mesh with robust inversion constraints (M. H. Loke *et al.*, 2003). Our data is freely available, and outcomes can be replicated using the inversion parameters supplied in Supplementary Table S8.

Figure 3.23 shows the inverted formation resistivity distribution from models created using the solute concentration of a homogeneous aquifer model (e.g. Figure 3.23A), along with the set of randomly generated heterogeneous hydraulic conductivity models shown in Figure 3.23B to F. Figure 3.23M shows the inverted formation resistivity distribution for the field data collected at the Quinns Rocks reference site.

A comparison of the forward models of formation resistivity derived for transport modelling and the inverted ERI resistivity distributions is shown in Figure 3.23. A basic observation is that the unconstrained ERI inversion outcomes do not precisely map the distribution of resistivity within the mixing zone. The geometry of the wedge is also strongly smeared. Although the toe of the seawater wedge can be approximately located from the resistivity sections, we suspect that without the forward model present the toe could be interpreted to be well over 100 m further towards the ocean.

Note that measurements in the SIM wells show that seawater intrusion has passed SIM 3, but not SIM 6, at the time of the ERI survey. However, the resistivity imaging in Figure 3.23M presents a situation where the toe could be interpreted anywhere between 180 and 270 m from the shoreline.

We have shown that using electrical imaging generates a potentially misleading reconstruction of the seawater wedge. The combination of (i) a dipping, smoothly transitioning mixing zone, and (ii) a sharp, near-horizontal high-contrast boundaries of the water table and substrate can be difficult to recover using unconstrained inversion (A. Costall *et al.*, 2018; Martorana *et al.*, 2009). The technique may be improved by using focused and optimised arrays (M. Loke *et al.*, 2007; Wilkinson *et al.*, 2012), novel acquisition techniques such as borehole-based imaging (A. Costall *et al.*, 2018; Palacios *et al.*, 2019), and constrained inversions (P. Bergmann *et al.*, 2014; Ronczka *et al.*, 2017; Wunderlich *et al.*, 2018). We focus on unconstrained inversion as under most circumstances the constrains or infrastructure required for more complex imaging will not be available.

We are presented with several conclusions regarding unconstrained inversion ERI to recover the seawater interface. These are:

i) ERI provides a valuable but highly smeared and damped version of formation resistivity distribution.
ii) ERI cannot recover precise values of resistivity for the substrate or seawater-saturated formation.
iii) Referencing the inverted ERI field data outcomes to sets of images derived from numerical transport modelling should be completed as a minimum standard of investigation.
iv) ERI should not be expected to provide exact point or geometric constraints such as the location of the toe of the seawater interface.

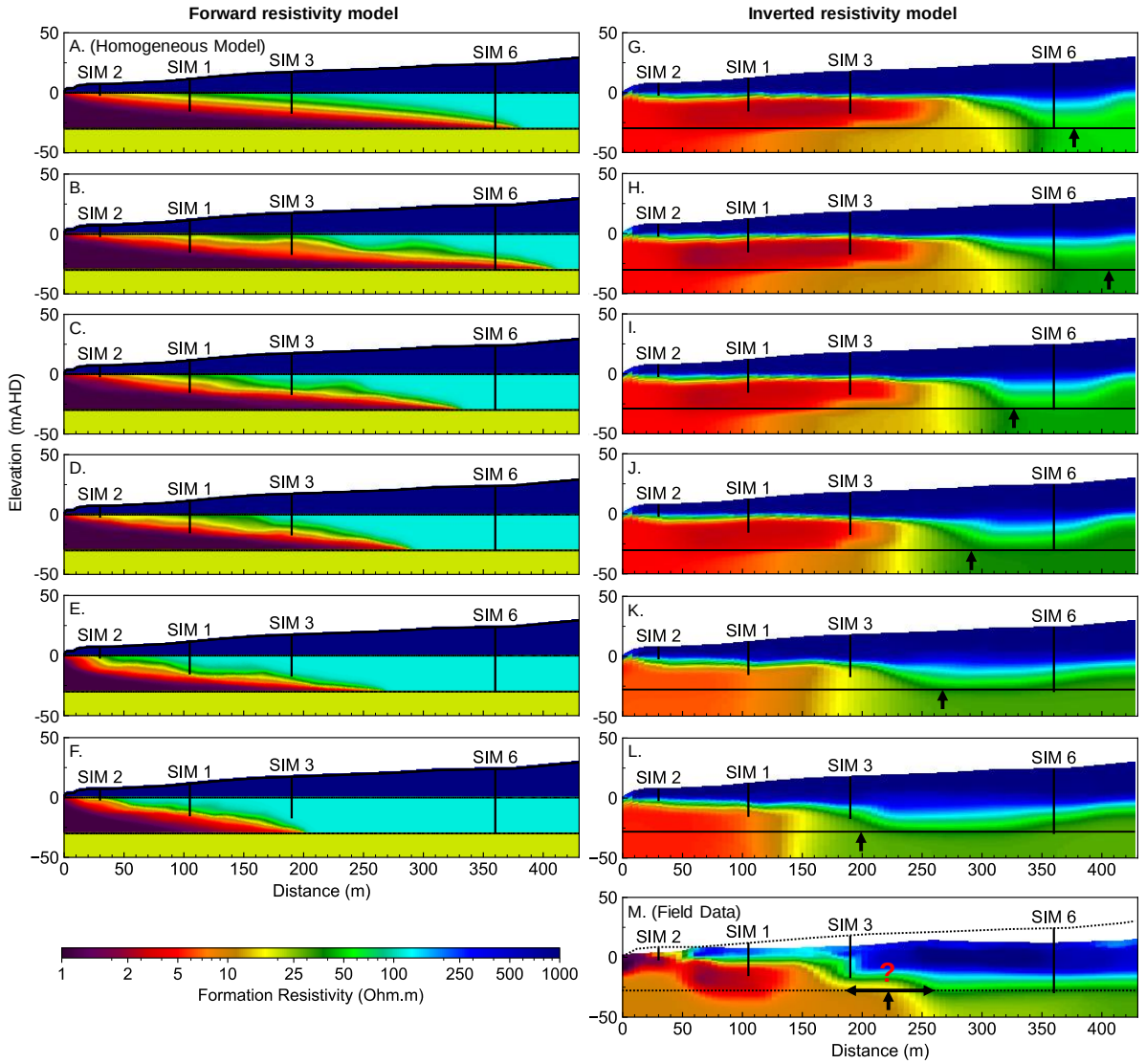

*Figure 3.23: Images showing the inverted resistivity distributions compared to the forward resistivity distributions for a range of hydraulic conductivity models. Panel **A** shows the forward resistivity distribution for a homogeneous model with 150 m/day hydraulic conductivity (e.g. Figure 3.22A). Panels **B** through **F** show the forward resistivity model based on the solute distribution for each of the randomly generated hydraulic conductivity distributions (e.g. Figure 3.22H through L). Panels **G** through **L** show the inverted resistivity outcomes of the synthetic models. Panel **M** shows the inverted resistivity distribution from field ERI data near to the Quinns Rocks reference, including the approximate projected locations of the SIM wells and topography (dashed line). The inversion outcomes from the synthetic data show the approximate location of the seawater toe and the depth of the substrate can be recovered. However, definition of the mixing zone and the wedge geometry is ambiguous and could be easily misinterpreted.*

3.7 Discussion: Capturing the dynamic hydrogeology of coastal margins

For any experiment, sufficient temporal and spatial sampling with reference to the desired outcome is fundamental. This also applies to field scale measurement systems deployed for hydrogeology. The hydraulics at coastal margins has significant differences compared to most hydrogeological setting. In Part 6, we will compute distribution of Darcy flow velocity across the seawater interface and will later consider implications for the type of monitoring systems that may be suitable for characterising this highly dynamic setting. Also, we suspect that methods for measuring groundwater flow velocity itself may present useful and currently under-utilized pathways to characterizing shallow high-quality coastal aquifers for both research and aquifer management purposes.

3.7.1 Can we use groundwater velocity to measure seawater intrusion?

There are extreme changes in flow velocity associated with the interface between seawater and fresh groundwater. Fresh terrestrial groundwater drives towards the coast but cannot pass through the denser seawater. The Darcy velocity of the fresh groundwater must increase as the flow area decreases towards the ocean (Chang *et al.*, 2012).

First, we illustrate these extremes in velocity contrast for a homogeneous aquifer. We then compare these results with flow regimes for an aquifer with a complex hydraulic conductivity distribution, as might be expected in karstic coastal aquifers. The homogeneous aquifer model is taken from Figure 3.17 (i.e. 200 m/day hydraulic conductivity with a 30 m saturated thickness), except with a greater groundwater throughflow of 5 ML/year.

Three distinct Darcy velocity regimes can be identified from Figure 3.24. These are; (i) groundwater with negligible velocity (10^{-9} m/day) at the seawater wedge face, (ii) groundwater with high velocity (~5 m/day) discharging to the ocean and (iii) groundwater with uniform velocity passing through the aquifer on the landward side of the seawater wedge (~0.4 m/day). The three flow regimes are spatially related to the seawater interface.

Monitoring wells located near to the seawater interface could observe several orders of magnitude variation in groundwater velocity, if the seawater interface moves a relatively small distance across the screens. These significant changes suggest that new seawater intrusion monitoring systems able to capture detailed vertical and horizontal changes in groundwater flow velocity and solute concentration distribution may be necessary to understand groundwater behaviour along coastal margins.

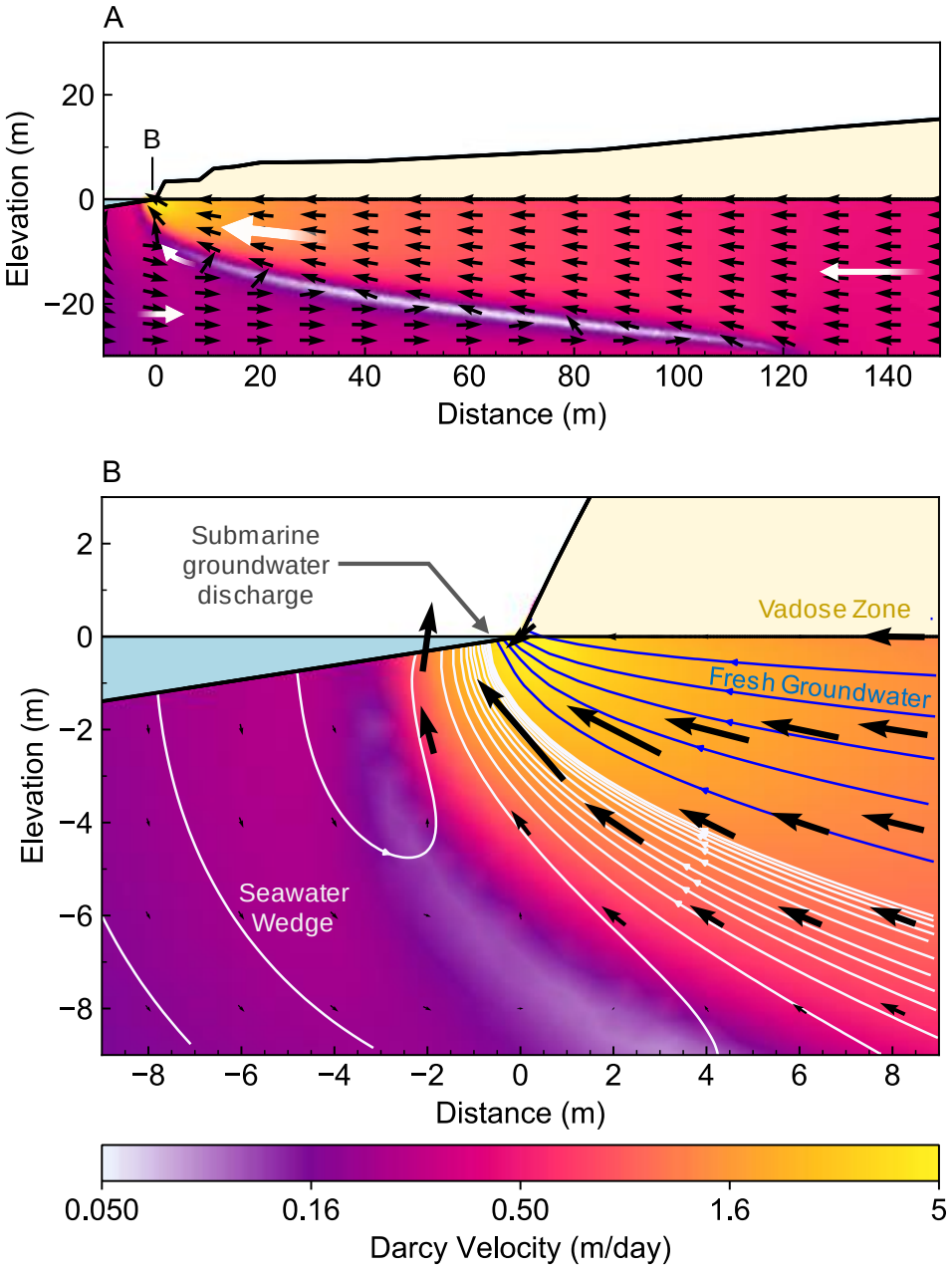

Figure 3.24: Images highlighting the extremes in Darcy velocity (m/day) that occur across a seawater wedge for a homogeneous aquifer. The velocity of fresh groundwater flowing towards the coast increases as the available area of flow decreases above the dense seawater wedge, until the fresh groundwater exits the system through the zone of submarine groundwater discharge (highlighted in Panel B). The velocity of groundwater proximal to the submarine discharge is an order of magnitude greater than the velocity of the fresh groundwater prior to being restricted by the seawater wedge. In contrast, the groundwater velocity in the seawater recirculation cell can flow in the opposite direction (i.e. towards the land) and is significantly less than that for the fresh groundwater above.

We extend analysis of Darcy velocity to the heterogeneous random-field examples first shown in Sect. 3.5.3. The distribution of arrows in Figure 3.25 is weighted by the y-component of the directional vector, highlighting areas with non-horizontal flow. A zone of extremely low velocity exists along the seawater/freshwater interface. This was also seen in the homogeneous model (Figure 3.24), however in Figure 3.25 we can contrast flow along hydraulically connected pathways with zones of low hydraulic connectivity that strongly affect flow paths and pressure gradients within the aquifer.

From this flow distribution, we conclude that the precise location of screened intervals for wells within a seawater intrusion monitoring network will likely affect the interpretation of hydraulic parameters. If we consider a pair of well screens set in a hydraulically connected conduit, the water level gradient between these wells would appear to be exceedingly low. However, these gradients will not reflect the hydraulics of full aquifer system and could lead to a strongly biased interpretation or difficulties in calibration from numerical groundwater modelling.

Our analysis suggests that additional information concerning vertical distribution of hydraulic properties, such as aquifer pressure or flow velocity distribution could significantly improve hydrogeological characterization of near shore settings. Observations from Figure 23 and 24 provide key insights required for design of new distributed seawater monitoring systems. They also link back to the difficulties encountered when attempting to interpret gradients between wells that may have screens set in rocks with significant difference hydraulic conductivity as observed throughout Part 3. The analysis of field data combined with numerical modelling and the visualization of Darcy velocity for complex hydraulic conductivity distributions (i.e. as found at reference site) points to the need for new monitoring strategies. Future options (Figure 25 and Table 4) for seawater intrusion monitoring will be presented in the conclusions.

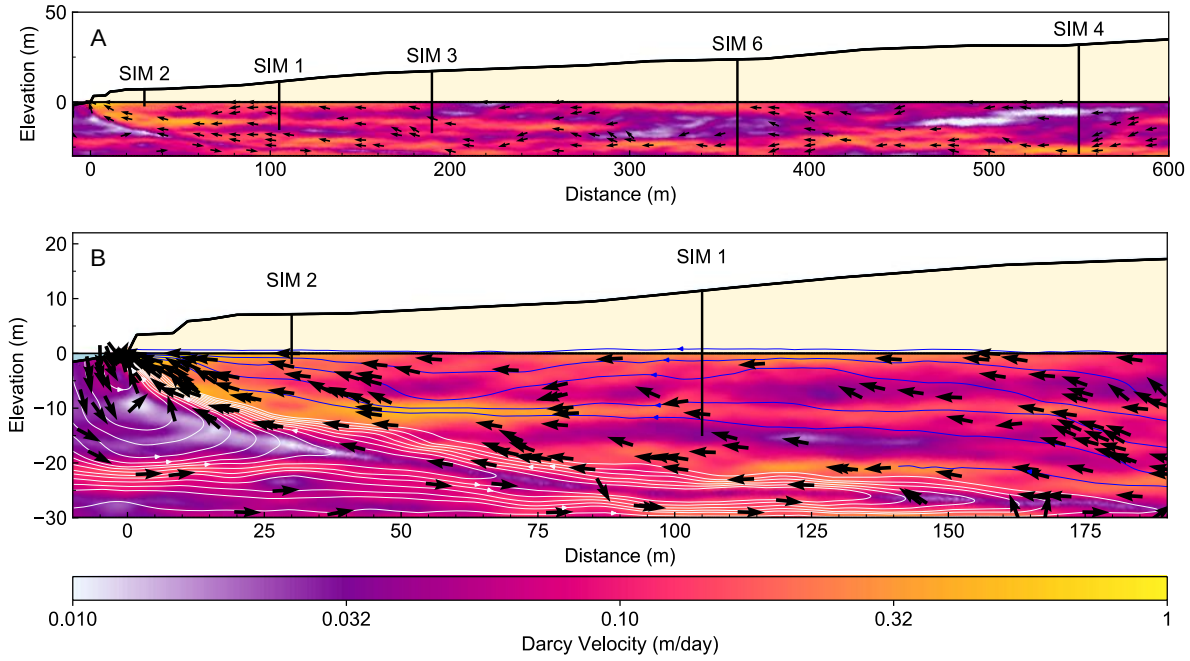

Figure 3.25: Images showing the Darcy velocity distribution for a complex hydraulic conductivity model (see Figure 3.22F). The distribution of arrows is weighted by the magnitude of the Y-component. ***Panel A*** *shows the full width of the model including zones of relatively high and low velocities related to the hydraulic conductivity distribution.* ***Panel B*** *show a zoomed in section of Darcy velocity proximal to the seawater wedge. It highlights the extremely slow groundwater velocity in the seawater recirculation cell and the complex flow directions related to hydraulic conductivity distribution in the zone of fresh terrestrial groundwater above the wedge. The screened intervals in the monitoring wells may be in high-velocity conduits or low-velocity pockets that may result in higher or lower inter-well hydraulic conductivity gradients. A distributed velocity measurement along the length of the well may identify these zones and improve calibration needed for solute transport modelling along coastal margins.*

3.8 Conclusion

The interplay between vast quantities of terrestrial groundwater discharging into the ocean and the landward ingress of seawater is central to the health of coastal aquifer systems. People and environments on all continents interact with, influence, and rely on these systems daily. The loss of high-quality coastal groundwater to seawater intrusion is a serious concern globally.

The relationship between groundwater throughflow and seawater intrusion has been dissected with numerical simulation and field data from an established seawater monitoring site in the south west of Western Australia. The site has over 30 years of conventional well-based seawater monitoring data. Here seawater intrusion has paralleled declining rainfall, rapid increase in population density, development of a regional water supply, and rising sea levels. We find that decoupling these influences is impossible without specific information concerning hydraulics and groundwater chemistry. We show that, even with the abundance of data collected at the reference site, the rate of intrusion and geometry of the interface could not be determined with confidence.

Locating the landward extent of the seawater interface is important and challenging in highly heterogeneous karstic aquifers. We found few studies that integrate long-term seawater intrusion monitoring field data into critical analysis of data acquisition strategies and various modelling approaches. We demonstrate that significant error can result from using simple analytical solutions to determine the landward extent of the seawater interface.

The landward extent of the seawater wedge is often used to guide coastal groundwater management decisions. However unresolved subsurface hydraulics may lead to considerable error in these estimates. Ground Penetrating Radar is used to reveal anisotropy and heterogeneity in karstic groundwater settings. We demonstrate the impact of dipping hydraulic anisotropy on the landward extent of seawater. Sets of images show how increasing the hydraulic anisotropy rotation angle can shift the seawater interface significantly closer to the ocean. Alternatively, the rotation angle of hydraulic anisotropy can be manipulated to maintain the landward extent of saline groundwater for vastly different aquifer throughflows.

Heterogeneity in hydraulic conductivity can also strongly impact the landward extent of the seawater interface. The outcomes from our numerical experiments with plausible spatially correlated random fields highlight the range of seawater interface geometries that can occur for systems with the same average hydraulic conductivity and groundwater throughflow. A key finding from these experiments is that the hydraulic conductivity of the aquifer proximal to the zone of submarine groundwater discharge is a key driver for the geometry and landward extent of the seawater wedge. The level of detail required to numerically simulate these heterogeneous environments cannot be obtained from conventional monitoring data which recovers water level and EC measurements from one depth interval.

Surface-based electrical resistivity imaging (ERI) is a valuable tool to establish the geometry of the seawater interface; however, determining the precise location of the toe requires the combination of ERI and solute transport modelling. That is, transport modelling is used to simulate the seawater wedge, then the solute concentration distribution is converted to formation conductivity and synthetic ERI data sets created for different wedge geometries. The simulated ERI data is inverted with the same parameters used for the field ERI data. Finally, imaging from synthetic and field data are systematically compared. Used appropriately, ERI can partially mitigate the problem of under-sampling from conventional sparsely distributed monitoring wells but – as we demonstrate

through modelling of heterogeneous aquifers – it cannot mitigate the uncertainty in measuring or predicting groundwater throughflow.

From our analysis of well-based monitoring data, numerical groundwater modelling, and representations of the extremes in groundwater velocity, we find that subsurface monitoring technologies need to be specifically designed for the nearshore coastal settings. Options for monitoring the dynamic relationship between solute concentration distribution, hydraulic property distribution, and groundwater throughflow at coastal margins are presented in Figure 26 and Table 4.

The schematic in Figure 3.26 proposes an arrangement of monitoring devices for a multi-well system capable of automated, real-time, and highly discretised sampling of hydraulic parameters. Table 3.4 details the seawater intrusion monitoring technologies that may be deployed within such a system of wells. These are provided under four categories including: (i) measurement of pressure distribution, (ii) subsurface flow characterisation, (iii) characterisation of geology (including hydraulic parameter distribution), and (iv) recovery of groundwater chemistry distribution.

These options can provide quantitative information required to understand and simulate shallow karstic hydrogeological systems along coastal margins. For example; the automated measurement of the vertical distribution of EC, flow velocity, and pressure data (Coscia *et al.*, 2012; Smerdon *et al.*, 2014; Strout *et al.*, 2005), recovery of groundwater samples at specific depths for periodic chemical analysis or tracer release, and a distributed fibreoptic system capable of measuring temperature and strain distribution (i.e. via engineered fibre) can provide highly discretised measurements throughout the aquifer (Bense *et al.*, 2016; T. Parker *et al.*, 2014; Schenato, 2017; Selker *et al.*, 2006; Shanafield *et al.*, 2018).

There is clear evidence for seawater intrusion and increased stress on coastal groundwater systems worldwide. We hope the insights and practical conclusions from this research will lead to a new era where automated real-time groundwater monitoring systems along coastal margins appropriately inform predictive groundwater modelling that ultimately leads to better management of coastal aquifers systems.

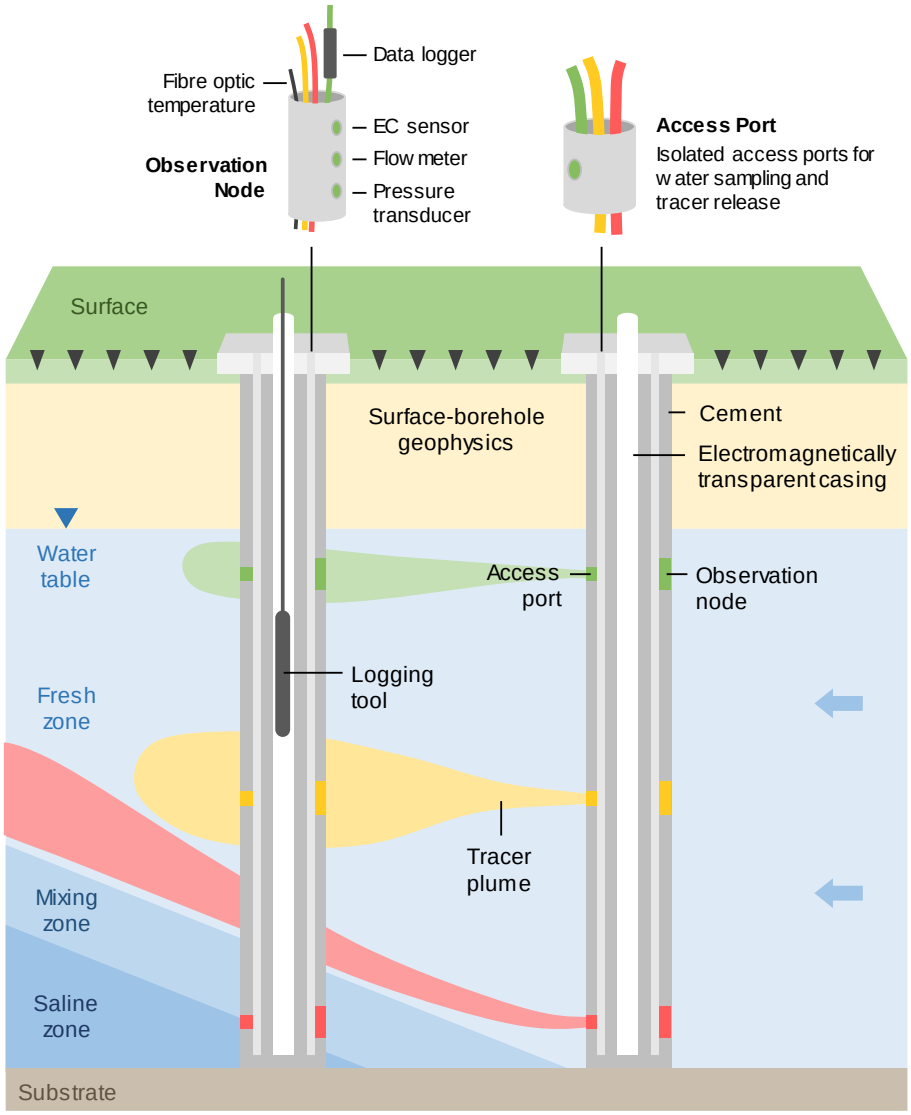

Figure 3.26: Schematic of a seawater intrusion monitoring system that would provide sufficient evidence to characterise the seawater interface in a shallow coastal aquifer. The system has multiple sampling nodes at various depths within the aquifer, with a suite of in-situ monitoring devices. These include in-situ flow meters, EC meters, and pressure piezometers. The data collected by this setup is well suited to reveal the subtle dynamics of a coastal aquifer system.

Table 3.4: Options for instrumentation and measurement of seawater intrusion monitoring wells (see). Our research identifies a range of challenges in recovering hydraulic properties and solute concentration distribution at the seawater interface. These challenges can be resolved by improved monitoring technologies. The monitoring solutions suggested below are applicable to both industry and research objectives. They should be tailored for site-specific conditions and objectives. Although the initial cost may be higher for automatic real-time monitoring of near-shore groundwater systems, the long-term costs may be lower (e.g. by replacing manual monitoring) and benefits from such systems will likely significantly outweigh initial expenditure.

	Solution (see Figure 26)	Advantages	Disadvantages	Examples
Pressure Distribution	Vertically distributed pressure sensors: Permanent monitoring outside of casing allows for measurements of true point pressures in depth.	Direct measurement of pressure without potential error associated with hydraulic head. Low per-sensor cost and automated measurement.	Difficult or impossible to recover sensors if cemented to outside of casing and can increase the well establishment costs.	Smerdon *et al.* (2014) Strout *et al.* (2005)
	Spatial distribution of monitoring wells: Measure the variation of hydraulic properties along and away from the shoreline.	3D characterisation of aquifer properties and variation parallel and perpendicular to the shoreline.	Greater number of wells required for high quality characterisation.	Coscia *et al.* (2012)
Groundwater Velocity	Flowmeters: Direct measure of flow velocity at multiple points within the aquifer.	Direct throughflow measurement that removes the uncertainty of gradient-based estimates.	Groundwater velocity can be highly variable in karstic environments, requiring multiple measurements.	This work (Sect. 5.1.1) Bayless *et al.* (2011)
	Tracers: Groundwater flow estimation and hydraulic parameterisation.	High quality estimates of various hydraulic parameters, such as dispersivity, and flow velocity.	Limited selection of tracers compatible with seawater chemistry. May require repeated physical water sampling.	Jørgensen *et al.* (2008) Stuyfzand (1992) Pulido-Leboeuf *et al.* (2003)
Geology (Dip, facies changes, etc.)	Surface/Borehole GPR	High-resolution imaging of dipping layers and geology	Requires a high electrical resistivity environment for reasonable depth-of-investigation (e.g. non-saline water).	This work (Sect. 2)
	Wireline logging data (Nuclear Magnetic Resonance, neutron logs, full waveform sonic)	High-quality wireline information along extent of borehole (e.g. can recover bound, free, and capillary water porosity along with permeability estimates)	Cost of establishment, instrumentation, and repeat logging. Measurements require repeat access to open borehole (i.e. without instrumentation) and are manual logged.	AJ Smith *et al.* (2012) Almalki *et al.* (2013) Mathieu *et al.* (1984)
	Distributed Acoustic Sensing (DAS)	High-resolution seismic imaging capable of recovering local hydrogeology. Readily automated.	Fibre-optic technology still developing and will need specifically engineered optical fibre for sufficient near-surface resolution. Interrogators are expensive.	Schenato (2017) Shanafield *et al.* (2018) T. Parker *et al.* (2014)
	Distributed Temperature Sensing (DTS)	Low-cost, low maintenance, thermal transport measurements, shared system with DAS. High accuracy temperatures.	Limited spatial resolution of thermal property.	Selker *et al.* (2006) Bense *et al.* (2016) Shanafield *et al.* (2018)
	High frequency 'sparker' seismic source	High-frequency source (plus 1000 Hz) for the high-resolution seismic imaging (combined with DAS system).	Requires access to borehole, and difficult to automate if required.	Rechtien *et al.* (1993)
	Petrophysical analysis of core samples	High-value constraints on physical and hydraulic parameters (porosity, anisotropy, dip angle, permeability).	High cost of recovering samples, which can be damaged during recovery. Further testing of samples is required. Information is highly localised.	Maliva (2016)
Solute Concentration Distribution	Water electrical conductivity sensor arrays (Galvanic, inductive, fibre-optic measurements)	Direct conductivity measurement, used with ERI for defining the formation factor.	Longevity of the electrodes (conductive probe vs inductive probe).	Possetti *et al.* (2009) Hilhorst (2000) Esteban *et al.* (1999)
	Cross-well electrical resistivity imaging	High-resolution electrical resistivity imaging and time-lapse imaging of electrical conductivity.	Limited by well location, and requires dedicated engineering at time of well development	Ogilvy *et al.* (2009) Turner *et al.* (2004)
	Surface-based electrical resistivity imaging	Flexible acquisition geometry (i.e. not limited to wells), and time-lapse imaging.	Lower resolution than cross-hole, with loss of resolution with depth. Deployment and automation may be difficult in urbanised areas.	This work (Sect. 4)
	Multi-electrode borehole monitoring	In-situ time-lapse measurement of electrical resistivity with localised imaging capability.	Non-flexible acquisition geometry and requires specific engineering at time of well development.	Michael Grinat *et al.* (2018) M Grinat *et al.* (2010)
	Time lapse induction logging	High-resolution formation conductivity proximal to well.	Difficult to automate and requires specific well construction (PVC/FRP). Other in-situ instruments may affect measurements.	Spies (1996)
	Water chemistry analysis	Repeatable and low-impact water chemistry sampling from a known depth.	Requires dedicated equipment established during well construction.	Freifeld *et al.* (2005)

3.9 Supplementary Information

Title: Groundwater Throughflow and Seawater Intrusion in High Quality Coastal Aquifers

Authors: A. R. Costall[1]*, B. D. Harris[1], B. Teo[1], R. Schaa[1], F. M. Wagner[2], J.P. Pigois[3]

This document contains information that is supplementary in nature to the main research document. Examples include processing flows, comparative tests, and tables of solutions that are not explicitly required in the manuscript but may be of interest to researchers or required to reproduce results.

All scripts, data, models, and any other information, can be found online or on request from the authors.

3.9.1 Table of Influential Parameters on Seawater Interface Model

Supplementary Table S1 lists some of the factors that can influence simulation outcomes of a seawater interface in karstic limestone aquifers. The table is split into temporal (i.e. time-varying) and spatial (varies with distance/depth) factors. Many of these factors are difficult to predict and may result in over-complication of models with regards to intended outcomes.

Supplementary Table S1: Temporal and material variables that can influence the geometry of the seawater interface.

	Factor	Comment
Temporal	Climate change (sea-level rise)	Global sea-level rise can result in the seawater wedge intruding further inland. The impact of sea-level rise on the seawater interface is a popular research topic and there are many examples of increased seawater intrusion due to global sea level rise (Abd-Elhamid *et al*., 2008; Chang *et al.*, 2011; Ketabchi *et al.*, 2016; Masterson, 2004; Werner, 2010; Werner *et al*., 2009).
	Tidal forcing and wave-surge	Daily tidal oscillations causes the very shallow (< 2 m) near-shore salinity contours to vary due to infiltration of seawater in the upper-beach face (Ataie-Ashtiani *et al.*, 1999). This can potentially double the width of the mixing zone without significant changes in the position of the seawater toe (Pool *et al.*, 2014).
	Seasonal variation in recharge	Seasonal variation in rainfall recharge results in a dynamic groundwater throughflow, which will affect the seawater interface. Other periodic cycles in ocean and groundwater levels, such as the Spring/Neap and semi-diurnal cycles also influence the seawater mixing zone and seawater circulation cell (Abarca *et al.*, 2013; Heiss *et al*., 2014).
Material	Caves and conduits	High-permeability karstic aquifer systems often contain networks of extremely high permeability caves and conduits. The orientation and density of conduits affect the geometry of the seawater interface (Sebben *et al.*, 2015; Wicks *et al.*, 1995).
	Substrate Angle	Seawater intrusion models typically assume the lower confining substrate is both flat and impermeable, however the geometry of the seawater interface is sensitive to the angle of the substrate, such that an angle of 1% (i.e. 1 m over 100 m) bed slope can move the seawater toe approximately 30–50% further inland (Ketabchi *et al.*, 2016).
	Dispersivity	Dispersivity is often highly variable and site-specific, with a range of values used throughout literature (Gelhar *et al*., 1992). For example, in a one kilometre-long unconsolidated aquifer, dispersivity estimates can range from 1.31, to 132 (Schulze-Makuch, 2005). Lowering the dispersion coefficients will reduce the zone of dispersion along the seawater/freshwater interface and tends to increase the landward extent of the toe (Shoemaker, 2004; Volker *et al.*, 1982).
	Ocean Interface Slope & Bathymetry	The shape of the intrusion face affects the geometry of the seawater interface. Examples of the marine-side face of seawater intrusion models can range from bathymetric representations (e.g. this research), to simplified wedges, and even vertical intrusion faces. High gradient slopes at the seaward wedge may reduce the simulated length of seawater intrusion, increase the residence time of seawater in the wedge, and reduce the zone of submarine groundwater discharge (Hussain *et al.*, 2016; M. Walther *et al.*, 2017)
	3D Geometries	Cave systems and conduits exist in a 3D space, and groundwater will flow preferentially through these pathways. A 2D groundwater model may not encapsulate the complexity of the seawater wedge in these environments (Abarca, Carrera, Sánchez-Vila, & Voss, 2007). Expansion to a 3D simulation space exacerbates many of the uncertainties identified throughout this paper without guarantee of more-realistic simulation outcomes.

3.9.2 Model Details and hydraulic parameters local to the Quinns Rocks reference site

Hydraulic parameters and the groundwater allocation limits for the superficial aquifer north of Perth are provided in Kretschmer *et al.* (2012). Hydraulic conductivity estimates range from 7 to 427 m/day. Nidagal *et al.* (1991) use a hydraulic conductivity of 200 m/day in estimations of groundwater throughflow. Kretschmer *et al.* (2012) suggest a lower value of 130 m/day is appropriate, based on the mean value from local tidal time lag aquifer tests.

Recharge estimates cover the flow net cell 'N' (Kretschmer *et al.*, 2012). The dimensions of the cell are 2040 wide (perpendicular from the coast), 1080 m long (parallel to the coast), with an estimated aquifer thickness of 30 meters. Volume-based calculations (e.g. fluid-flow) are calculated using an aquifer width (Δx) of one unit-length, (e.g. 1-meter) (H.-J. G. Diersch, 2014). The average Darcy flux through the throughflow surface of the model per unit area is therefore:

$$\bar{v} = \frac{\bar{Q}}{A} = \frac{\bar{Q}}{\Delta x \Delta z} \quad (1)$$

$$\bar{v} = \frac{3484\ ML/\text{year}}{1080\ \text{m}} = 3.31\frac{ML}{year.m} \quad (1)$$

Supplementary Table S2 contains the summarized statistics for the Quinns Rocks area including the SIM wells.

Supplementary Table S2: Summary of hydraulic parameter for the Quinns Rocks area, from Kretschmer et al. (2012). Full table in supplementary materials.

Quinns Rocks	K (m/day)	Q (ML/year)	Q (ML/year/m)
Mean	128.22	3484.56	3.31
Std. Error	20.46	235.38	0.17
Median	79.00	3566.00	3.30
Mode	47.00	706.15	0.52
Std. Dev.	106.34	498647.53	0.27
Kurtosis	0.94	2.10	3.02
Skewness	1.18	0.07	1.39
Range	420.00	2642.00	1.74
Minimum	7.00	2189.00	2.74
Maximum	427.00	4831.00	4.47
Count	27.00	9.00	9.00

Supplementary Table S3 contains individual well data relevant to the Quinns Rocks area.

Supplementary Table S3: Hydraulic testing of the shallow aquifer from the Quinns Rocks region. The SIM wells are bolded.

Year	Test-Type	Geology	T	b	K	BoreID
1994	8-hour constant rate	Tamala Limestone	1400	30	47	Private
1996	7-hour multi rate	Tamala Limestone	2000	30	67	Private
1993	10-hour constant rate	Tamala Limestone	1100	22	50	Private
1993	Multi rate, 8-hour constant rate	Tamala Limestone	1200	30	40	Private
1996	Multi rate, 10-hour constant rate	Tamala Limestone	1200	26	46	Private
1994	Mulit rate, 6-hour constant rate	Tamala Limestone	7000	30	233	Private
1991	**Tide time-lag & amplitude**	**Tamala Limestone**	**207**	**30**	**7**	**SIM 2/90**
1991	**Tide time-lag & amplitude**	**Tamala Limestone**	**2154**	**31**	**69**	**SIM 1/90**
1991	**Tide time-lag & amplitude**	**Tamala Limestone**	**5308**	**31**	**171**	**SIM 3/90**
1991	**Tide time-lag & amplitude**	**Tamala Limestone**	**7300**	**31**	**235**	**SIM 6/90**
1991	**Tide time-lag & amplitude**	**Tamala Limestone**	**2507**	**31**	**81**	**SIM 5/90**
1991	Tide time-lag & amplitude	Tamala Limestone	9758	31	315	SKP-GREEN
1991	Tide time-lag & amplitude	Tamala Limestone	1463	31	47	SKP-WHITE
1991	Multi-rate, 24-hour constant rate	Tamala Limestone	12824	30	427	QC
1990	Multi-rate, 12-hour constant rate	Tamala Limestone	1390	30	46	QW
1986	8-hour duration	Tamala Limestone	402.7	30	13	1/86
1994	8-hour duration	Tamala Limestone	9186	30	306	Q150 (QM10)
1994	8-hour duration	Tamala Limestone	5741	30	191	Q140 (QA10)
1994	8-hour duration	Tamala Limestone	3674	30	122	Q10 (QX10)
1990	12-hour duration	Tamala Limestone	6991	30	233	Q170 (QW10)
1996	24-hour duration	Tamala Limestone	1832	30	61	Q40 (QL10)
1997	24-hour duration	Tamala Limestone	1021	30	34	Q200 (QZ20)
1998	10-hour duration	Tamala Limestone	2296	30	77	Q190 (QZ10)
1997	24-hour duration	Tamala Limestone	2358	30	79	Q60 (QE10)
1998	10-hour duration	Tamala Limestone	5103	30	170	Q180 (QW20)
1998	10-hour duration	Tamala Limestone	4275	30	142	Q160 (QN10)
1998	12-hour duration	Tamala Limestone	4593	30	153	Q20 (QS10)

Supplementary Table S4 contains estimations of groundwater recharge relevant to the Quinns Rocks area.

Supplementary Table S4: Collation of the recharge parameters in Kretschmer et al. (2012)

Appendix	Comment	K	T	Ocean Discharge	Area	Rainfall Recharge	Recharge to flow-cell
		(m/day)	(m²/day)	(ML/year)	(km²)	(mm/year)	(ML/year.m)
B1	1976 estimate plus 1906 - 2011 recharge (757 mm/year)	10	330	1536	7.7	653.25	2.74
B2	1906 - 2011 recharge (757 mm/year)	10	330	1251	6.7	2536	3.51
B3	1975 - 2011 recharge (695 mm/year)	10	330	1251	6.7	2328	3.31
B4	2002 - 2011 recharge (630 mm/year)	10	330	1251	6.7	2111	3.11
B5	Future wet rainfall predictions, 747 mm/year	10	330	1251	6.7	2502	3.48
B6	Future median rainfall predictions, 691 mm/year	10	330	1251	6.7	2315	3.30
B7	Future dry rainfall predictions, 623 mm/year	10	330	1251	6.7	2087	3.09
B8a	Varied Spearwood Sand K, 1975 - 2011 recharge (695 mm/year)	5	165	626	6.7	2328	2.74
B8b	Varied Spearwood Sand K, 1975 - 2011 recharge (695 mm/year)	20	660	2503	6.7	2328	4.47

3.9.3 GPR Processing Flow

Ground penetrating radar (GPR) is used at a site located west of Perth, to reveal the variation in near-shore geological facies progressing inland from the ocean (see Section 3.1, Figure 6). Processing is completed using the software package ReflexW (Sandmeir, 2014). The steps are listed in Supplementary Table S5.

Supplementary Table S5: Processing steps and parameters used for the GPR image in Figure 9

Processing Step	Parameters
Subtract-mean (dewow)	4 (ns)
Static correction	-
Subtracting average	200 (ns)
Energy decay	0.01
Bandpass frequency filter	200/400/900/1500
Topography migration	0.11 m/ns
Bandpass frequency filter	200/400/900/1500
Correct 3D topography	0.11 m/ns
Time-depth conversion	0.11 m/ns

3.9.4 Comparison of EOS 80 with TDS via Evaporation

The International Equation of State of Seawater 1980 (EOS-80) (UNESCO, 1981) approximates the concentration of seawater to practical salinity units (PSU) using measurements of electrical conductivity (EC). A near-linear relationship exists between EC and the major constituent of seawater, dissolved Sodium Chloride (Arps, 1953; Walton, 1989). For reference, the conductivity of standard seawater at 15 degrees centigrade is 4.2914 S/m (Culkin *et al.*, 1980; Millero *et al.*, 2008). For a further example, Tyler *et al.* (2017) demonstrate the electrical conductivity of the global ocean (including seasonal conductivity variations).

Evaporative (180°C) testing from SIM 6 in 2005 produces 360 mg/L total dissolved solids (TDS). EC measurements of the water sample are 660 uS/cm (25°C). For comparison with Walton (1989), this yields the linear conversion factor K = 0.545 for the fresh groundwater. The equivalent estimate of mg/L using the EOS-80 scale is 0.32118 PSU (~321.18 mg/L). No evaporative tests exist for higher salinity measurements at the Quinns Rocks reference site.

Supplementary Table S6: Comparison of electrical conductivity (EC) to total dissolved salts (TDS) in SIM 6 after evaporative testing and relationship to EOS-80 conversion.

SIM 6 EC (µS/cm)	SIM 6 TDS (mg/)	Linear conversion	EOS-80 (mg/L)
660	360	0.545	321.18

3.9.5 Estimation of groundwater throughflow

Supplementary Figure S1 shows the potential estimates of groundwater throughflow using various points of measurement, such as the measured water level, the equivalent freshwater head, and the inter-well gradients between certain wells.

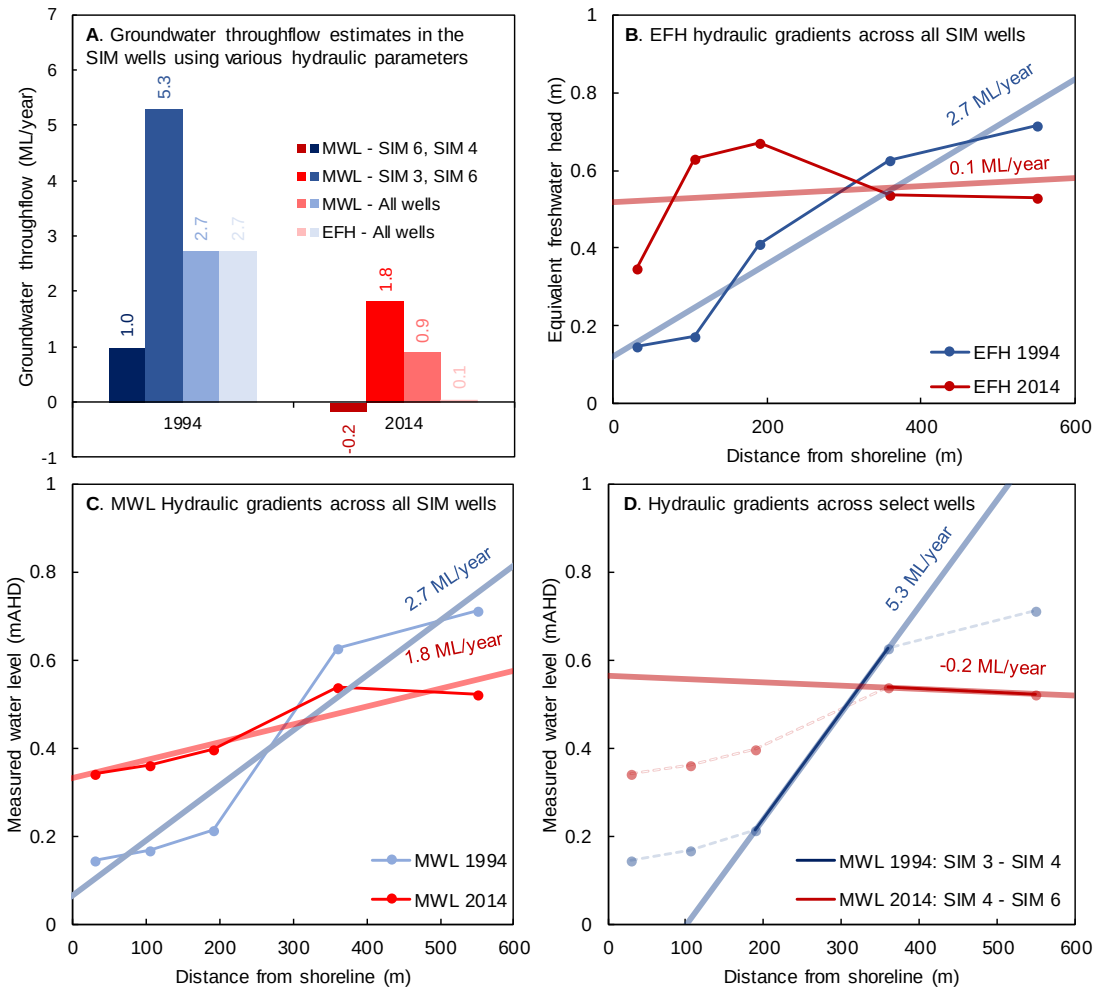

Supplementary Figure S1: Set of charts showing the potential variation in estimated groundwater throughflow derived from hydraulic gradients in a highly heterogeneous shallow coastal aquifer. ***A,*** *the groundwater throughflow derived from hydraulic gradient analysis assuming a 200 m/day homogeneous aquifer for the SIM wells in 1994, before seawater intrusion has occurred, and in 2014, after seawater intrusion has occurred and suggesting relatively low groundwater throughflow.* ***B****, the equivalent freshwater head levels, and associated line-of-best-fit.* ***C****, the measured water levels, and associated line-of-best-fit showing relatively high groundwater throughflow, and* ***D****, the lines-of-best-fit taken across selected wells, showing significant variations in the estimated groundwater throughflow. This figure highlights the implications of both a heterogeneous distribution of hydraulic conductivity, as well as the potential uncertainty associated with hydraulic gradient analysis in a coastal environment.*

Supplementary Figure S2 shows the estimated groundwater throughflow across the SIM wells throughout the monitoring period. Estimates before 2000 are similar given that seawater intrusion is not overt. After 2000, seawater is present in the SIM 1 and SIM 3 wells and strongly affects the equivalent freshwater head gradients.

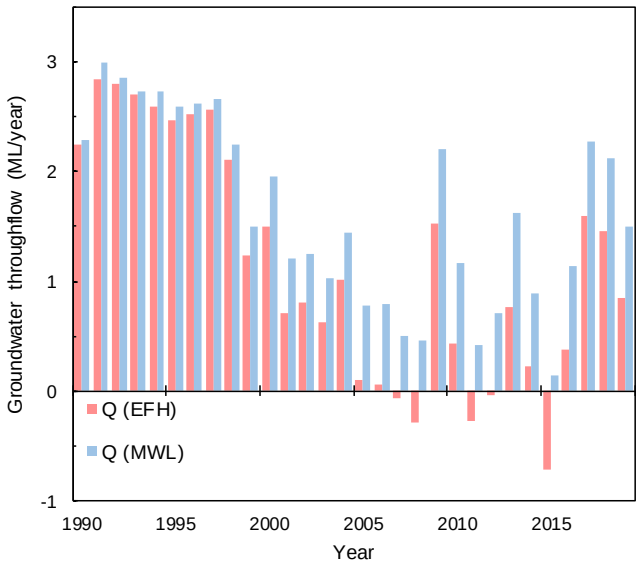

Supplementary Figure S2:Chart showing the estimated groundwater throughflow using the hydraulic gradients computed from equivalent freshwater head (EFH) and measured water level (MWL) in the SIM well series at Quinns Rocks between 1990 and 2019.

3.9.6 Effects of Model Refinement on Toe Position

This appendix contains the change in head and mass associated with increasing mess refinement. The modelled used is for a homogeneous aquifer 30 m thick and hydraulic conductivity of 130 m/d over an impermeable substrate (the mean measurement from the Quinns Rocks reference site). Groundwater through flow is set to 3.4 ML/year. Supplementary Figure S3 shows the different meshes and positions of the toe. There is negligible different in the geometry of the saline water interface or position of the toe as provided below. There is approximately one order of magnitude difference between run times for ‘A’, compared to ‘C’, below.

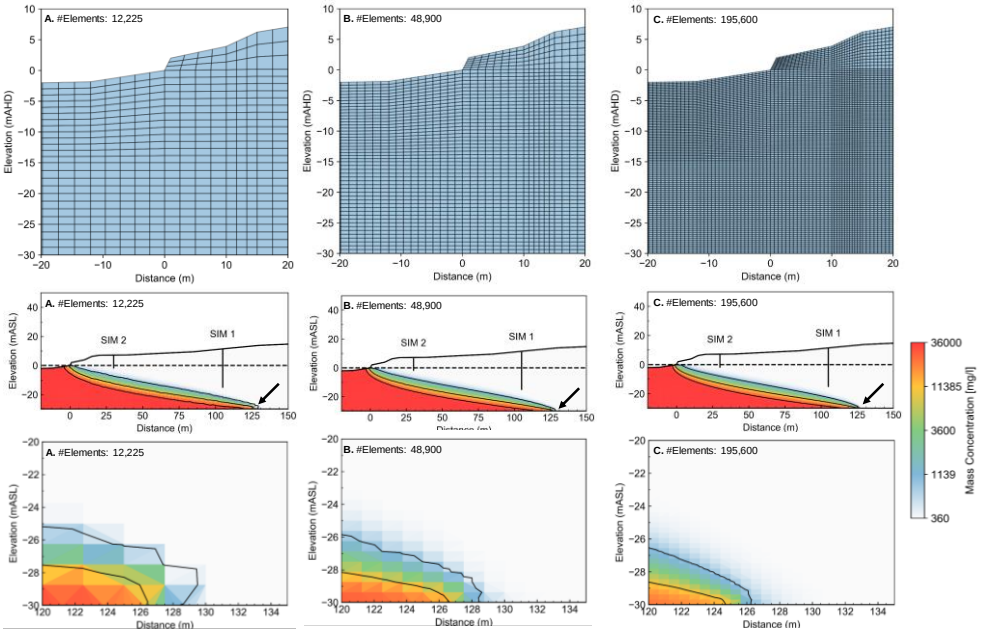

Supplementary Figure S3: Set of images showing the effect of mesh discretizaiton on the position on a simulated seawater wedge in a high hydraulic conductivity aquifer under approximately 3 ML/year-m of groundwater throughflow.

3.9.7 Random fields python script

```
import numpy as np
from matplotlib import ticker, pyplot as plt
from gstools import SRF, Exponential, transform as tf
from gstools.random import MasterRNG
import datetime as dt

def get_feflow_nodes(fid):
  from pandas import read_csv
  data = read_csv(fid, delim_whitespace = True)
  data = data[data['Y'] < 1]
  x, y = data.X.values, data.Y.values
  return x, y

def make_fields(vartype, var, scale = 1, **kwargs):
  fields = {      }
  model = Exponential(dim=2,
          var=1,
          len_scale=50,
          anis = 1./10.,
          angles=np.deg2rad(1),
          )
  for n,a in enumerate(var):
    srf = SRF(model, seed = a)
    field = srf([x, y])
    tf.normal_to_arcsin(srf)
    tf.normal_to_lognormal(srf)
    tf.zinnharvey(srf, conn="high")
    field = 100*np.exp(field)
    fields[a] = field
    print('Field:  {}\n\t  Mean:  {}\n\t  Max:  {}\n\t  Min:  {}'.format(a,  np.mean(field),
np.max(field), np.min(field)))
  return fields

def plot_fields(fields):
  fig,ax = plt.subplots(len(fields.keys()), sharex = True, sharey = True)
  fig.set_size_inches(18,12)
  for n,f in enumerate(fields.items()):
    im = ax[n].tricontourf(x, y, f[1], cmap = 'jet', norm = None, levels = 1000)
    ax[n].set_aspect('equal', adjustable='box')
    ax[n].tick_params(which = 'both', direction = 'in')
    ax[n].xaxis.set_minor_locator(ticker.AutoMinorLocator(2))
    ax[n].minorticks_on()
    ax[n].yaxis.set_minor_locator(ticker.AutoMinorLocator(2))
```

```
    ax[n].set_title(str(f[0]))
    ax[n].set_xlabel('Distance (m)')
    ax[n].set_ylabel('Elevation (mASL)')
    plt.colorbar(im, ax = ax[n], orientation = 'vertical')
  fig.set_tight_layout('tight')
  return fig, ax

def export_fields(fields):
  for f in fields:
    print(f)
    z = np.zeros((len(x),))
    xyz = np.stack((x,y,z,fields[f].T)).T
    fOut = 'GSTools_RandomField_Seed' + str(f) + '_CON_' + dt.datetime.now().strftime('%Y-%m-
%d')+'.dat'
    np.savetxt(fOut, xyz, header = "X \t Y \t Z \t COND", comments = "")
  return

#%%
rng = np.random.RandomState(MasterRNG(20190312)())
fid                                    =                                          r"\\Egpsrv08-
02\egp\Home\Staff\264401K\FEFLOW_KDrive_Backup\generic_aquifer_nodes_for_randomfields.dat"

x, y = get_feflow_nodes(fid)

seeds_ = [20191112, 20191113, 20191114, 20191115, 20191116]

fields = make_fields(vartype = 'seeds', var = seeds_, scale = 40)
fig, ax = plot_fields(fields)
export_fields(fields)
#plt.hist(fields[seeds_[-1]], bins = 100)
```

3.9.8 Random fields statistics

The statistical description of the randomly generated hydraulic conductivity fields are found below in Supplementary Table S7. The mean parameters are approximately equal to that described by field analysis of the Quinns Rocks reference site.

Supplementary Table S7: Statistical distribution of hydraulic conductivity parameters used for the random fields

	20191112	**20191113**	**20191114**	**20191115**	**20191116**	**Homogeneous**
mean	148.67	168.07	137.45	148.33	158.54	150
std	158.17	200.37	142.65	139.18	134.85	0
min	4.37	3.99	4.98	8.24	6.26	150
25%	54.13	52.27	48.65	61.23	70.35	150
50%	103.35	102.97	91.10	108.63	120.75	150
75%	182.60	204.36	171.68	186.81	202.87	150
max	2078.62	2093.58	1689.60	2699.03	2204.99	150

3.9.9 Inversion Parameters for RES2DINV

Supplementary Table S8 contains the inversion parameters used for inversion of synthetic and field data throughout the manuscript.

Supplementary Table S8: Inversion parameters used for RES2DINV (version 4.09).

Parameter	Value
Initial damping factor (0.01 to 1.00)	0.15
Minimum damping factor (0.001 to 0.75)	0.02
Local optimization option (0=No, 1=Yes)	1
Convergence limit for relative change in RMS error in percent (0.1 to 20)	5
Minimum change in RMS error for line search in percent (0.5 to 100)	0.5
Number of iterations (1 to 30)	7
Vertical to horizontal flatness filter ratio (0.25 to 4.0)	1
Model for increase in thickness of layers (0=default 10%, 1=default 25%, 2=user defined)	2
Number of nodes between adjacent electrodes (1, 2 or 4)	4
Flatness filter type, Include smoothing of model resistivity	1
Reduce number of topographical data points? (0=No,1=Yes. Recommend leave at 0)	0
Carry out topography modelling? (0=No,1=Yes)	1
Type of topography trend removal (0=Average,1=Least-squares,2=End to end)	0
Type of Jacobian matrix calculation (0=Quasi-Newton, 1=Gauss-Newton, 2=Mixed)	1
Increase of damping factor with depth (1.0 to 2.0)	1.05
Type of topographical model	4
Robust data constrain? (0=No, 1=Yes)	1
Cut-off factor for data constrain (0.0001 to 0.1))	0.05
Robust model constraint? (0=No, 1=Yes)	1
Cut-off factor for model constrain (0.0001 to 1.0)	0.005
Allow number of model parameters to exceed data points? (0=No, 1=Yes)	1
Use extended model? (0=No, 1=Yes)	0
Reduce effect of side blocks? (0=No, 1=Slight, 2=Severe, 3=Very Severe)	2
Type of mesh (0=Normal,1=Fine,2=Finest)	2
Optimise damping factor? (0=No, 1=Yes)	0
Time-lapse inversion constrain (0=None,1&2=Smooth,3=Robust)	3
Type of time-lapse inversion method (0=Simultaneous,1=Sequential)	0
Thickness of first layer (0.25 to 1.0)	0.25
Factor to increase thickness layer with depth (1.0 to 1.25)	1
Use finite element method (yes=1,no=0)	1
Width of blocks (1=normal width, 2=double, 3=triple, 4=quadruple, 5=quintuple)	1
Make sure blocks have the same width (yes=1,no=0)	0
Rms convergence limit (in percent)	0.1
Use logarithm of apparent resistivity	0
Type of ip inversion method (0=concurrent,1=sequential)	0
Proceed automatically for sequential method (1=yes,0=no)	0
IP DAMPING FACTOR (0.01 to 1.0)	0.25
Use automatic ip damping factor (yes=1,no=0)	0
CUTOFF FACTOR FOR BOREHOLE DATA (0.0005 to 0.02)	0.0001
TYPE OF CROSS-BOREHOLE MODEL (0=normal,1=half size)	0
Limit resistivity values(0=no,1=yes)	1
Upper limit factor (10-50)	50
Lower limit factor (0.02 to 0.1)	0.02
Type of reference resistivity (0=average,1=first iteration)	1
Model refinement (1.0=Normal,0.5=Half-width cells)	0.5
Combined Marquardt and Occam inversion (0=Not used,1=used)	1
Type of optimisation method (0=Gauss-Newton,2=Incomplete GN)	0
Convergence limit for Incomplete Gauss-Newton method (0.005 to 0.05)	0.005
Use data compression with Incomplete Gauss-Newton (0=No,1=Yes)	0

Use reference model in inversion (0=No,1=Yes)	1
Damping factor for reference model (0.0 to 1.0)	0.01
Use fast method to calculate Jacobian matrix. (0=No,1=Yes)	0
Use higher damping for first layer? (0=No,1=Yes)	1
Extra damping factor for first layer (1.0 to 100.0)	5
Type of finite-element method (0=Triangular,1=Trapezoidal elements)	1
Factor to increase model depth range (1.0 to 5.0)	1.05
Reduce model variations near borehole (0=No, 1=Yes)	0
Factor to control the degree variations near the boreholes are reduced (2 to 100)	5
Factor to control variation of borehole damping factor with distance (0.5 to 5.0)	1
Floating electrodes survey inversion method	1
Resistivity variation within water layer (0=allow resistivity to vary freely,1=minimise variation)	1
Use sparse inversion method for very long survey lines (0=No, 1=Yes)	0
Optimize Jacobian matrix calculation (0=No, 1=Yes)	0
Automatically switch electrodes for negative geometric factor (0=No, 1=Yes)	1
Force resistance value to be consistent with the geometric factor (0=No, 1=Yes)	0
Shift the electrodes to round up positions of electrodes (0=No, 1=Yes)	0
Use difference of measurements in time-lapse inversion (0=No,1=Yes)	0
Use active constraint balancing (0=No,1=Yes)	0
Type of active constraints (0=Normal,1=Reverse)	0
Lower damping factor limit for active constraints	0.4
Upper damping factor limit for active constraints	2.5
Water resistivity variation damping factor	8
Use automatic calculation for change of damping factor with depth (0=No,1=Yes)	0
Type of I.P. model transformation (0=None, 1=square root, 3=range)	1
Model Chargeability Lower Limit (mv/V) for range	0
Model Chargeability Upper Limit (mv/V) for range	900
Use I.P. model refinement (0=No, 1=Yes)	1
Weight for I.P. data (1 to 10)	1
I.P. model damping factor (0.05 to 1.0)	0.25
Use program estimate for I.P. model damping factor (0=No, 1=Yes)	0
Type of I.P. smoothness constraint (1=Same as resistivity, 0=Different)	1
Joint or separate I.P. inversion method (1=Separate, 0=Joint)	1
Apparent I.P. cut off value (300 to 899 mv/V)	899
Use diagonal filter (0=No, 1=Yes)	1
Diagonal filter weight (0.2 to 5.0)	1
Limit range of data weights from error estimates? (0=No, 1=Yes)	0
Lower limit of data weights (0.2 to 0.5)	0.3
Upper limit of data weights (2.0 to 5.0)	3
Use same data weights from error estimates for different time series? (0=No, 1=Yes)	0
Calculate model resolution? (0=No, 1=Yes)	1
Use L curve method? (0=No, 1=Yes)	0
Use same norms in L curve method? (0=No, 1=Yes)	0
Allow damping factor in increase in L curve method? (0=No, 1=Yes)	1
Type of borehole damping method	0
Use fast Jacobian calculation for dense data sets? (0=No,1=Yes)	0
Use higher damping factors at sides of model? (0=No,1=Yes)	1
Adjust damping factors for distances between the blocks in the model? (0=No,1=Yes)	1
Number of electrodes in segment for sparse inversion method for very long survey lines.	250
Time-lapse damping factor.	0.25
Reduce time-lapse damping with each iteration? (0=No,1=Yes)	1
Filter input data using geometric factor? (0=No,1=Yes)	0
Automatically remove negative apparent resistivity values? (0=No,1=Yes)	0
Automatically remove Gamma type arrays? (0=No,1=Yes)	0

3.9.10 References Cited within Supplementary

1 Abd-Elhamid, H. & Javadi, A. An investigation into control of saltwater intrusion considering the effects of climate change and sea level rise. *Proceeding of 20th SWIM* **2327** (2008).

2 Chang, S. W., Clement, T. P., Simpson, M. J. & Lee, K.-K. Does sea-level rise have an impact on saltwater intrusion? *Advances in Water Resources* **34**, 1283-1291, doi:10.1016/j.advwatres.2011.06.006 (2011).

3 Ketabchi, H., Mahmoodzadeh, D., Ataie-Ashtiani, B. & Simmons, C. T. Sea-level rise impacts on seawater intrusion in coastal aquifers: Review and integration. *Journal of Hydrology* **535**, 235-255, doi:10.1016/j.jhydrol.2016.01.083 (2016).

4 Masterson, J. P. *Simulated interaction between freshwater and saltwater and effects of ground-water pumping and sea-level change, Lower Cape Cod aquifer system, Massachusetts*. (US Department of the Interior, US Geological Survey, 2004).

5 Werner, A. D. A review of seawater intrusion and its management in Australia. *Hydrogeology Journal* **18**, 281-285, doi:10.1007/s10040-009-0465-8 (2010).

6 Werner, A. D. & Simmons, C. T. Impact of sea-level rise on sea water intrusion in coastal aquifers. *Ground Water* **47**, 197-204, doi:10.1111/j.1745-6584.2008.00535.x (2009).

7 Ataie-Ashtiani, B., Volker, R. E. & Lockington, D. A. Tidal effects on sea water intrusion in unconfined aquifers. *Journal of Hydrology* **216**, 17-31, doi:Doi 10.1016/S0022-1694(98)00275-3 (1999).

8 Pool, M., Post, V. E. A. & Simmons, C. T. Effects of tidal fluctuations on mixing and spreading in coastal aquifers: Homogeneous case. *Water Resources Research* **50**, 6910-6926, doi:10.1002/2014wr015534 (2014).

9 Heiss, J. W. & Michael, H. A. Saltwater-freshwater mixing dynamics in a sandy beach aquifer over tidal, spring-neap, and seasonal cycles. **50**, 6747-6766, doi:10.1002/2014wr015574 (2014).

10 Abarca, E., Karam, H., Hemond, H. F. & Harvey, C. F. Transient groundwater dynamics in a coastal aquifer: The effects of tides, the lunar cycle, and the beach profile. *Water Resources Research* **49**, 2473-2488, doi:10.1002/wrcr.20075 (2013).

11 Sebben, M. L., Werner, A. D. & Graf, T. Seawater intrusion in fractured coastal aquifers: A preliminary numerical investigation using a fractured Henry problem. *Advances in Water Resources* **85**, 93-108, doi:10.1016/j.advwatres.2015.09.013 (2015).

12 Wicks, C. & Herman, J. The Effect of Zones of High Porosity and Permeability on the Configuration of the Saline-Freshwater Mixing Zone. *Groundwater* **33**, 733-740, doi:doi:10.1111/j.1745-6584.1995.tb00019.x (1995).

13 Gelhar, L. W., Welty, C. & Rehfeldt, K. R. A critical review of data on field-scale dispersion in aquifers. **28**, 1955-1974, doi:doi:10.1029/92WR00607 (1992).

14 Schulze-Makuch, D. Longitudinal dispersivity data and implications for scaling behavior. *Ground Water* **43**, 443-456, doi:10.1111/j.1745-6584.2005.0051.x (2005).

15 Shoemaker, W. B. Important observations and parameters for a salt water intrusion model. *Ground Water* **42**, 829-840, doi:10.1111/j.1745-6584.2004.t01-2-.x (2004).

16 Volker, R. E. & Rushton, K. R. An assessment of the importance of some parameters for seawater intrusion in aquifers and a comparison of dispersive and sharp-interface modelling approaches. *Journal of Hydrology* **56**, 239-250, doi:http://dx.doi.org/10.1016/0022-1694(82)90015-4 (1982).

17 Walther, M., Graf, T., Kolditz, O., Liedl, R. & Post, V. How significant is the slope of the sea-side boundary for modelling seawater intrusion in coastal aquifers? *Journal of Hydrology* **551**, 648-659, doi:https://doi.org/10.1016/j.jhydrol.2017.02.031 (2017).

18 Hussain, M. S. & Javadi, A. A. Assessing impacts of sea level rise on seawater intrusion in a coastal aquifer with sloped shoreline boundary. *Journal of Hydro-Environment Research* **11**, 29-41, doi:10.1016/j.jher.2016.01.003 (2016).

19 Abarca, E., Carrera, J., Sánchez-Vila, X. & Voss, C. I. Quasi-horizontal circulation cells in 3D seawater intrusion. *Journal of Hydrology* **339**, 118-129, doi:https://doi.org/10.1016/j.jhydrol.2007.02.017 (2007).

20 Kretschmer, P. & Degens, B. Vol. Hydrogeological Report Series (ed Western Australian Department of Water) (2012).

21 Nidagal, V. & Davidson, W. J. G. S. o. W., Unpublished Hydrogeological Report. North coastal groundwater investigation (Burns Beach—Pipidinny). (1991).

22 Diersch, H.-J. G. *Feflow: Finite Element Modeling of Flow, Mass and Heat Transport in Porous and Fractured Media*. (Springer Science & Business Media, 2014).

23 Sandmeir, K. J. ReflexW (Manual). (2014).

24 UNESCO, I. J. U. T. P. M. S. Tenth report of the joint panel on oceanographic tables and standards. **36**, 15-19 (1981).

25 Arps, J. The effect of temperature on the density and electrical resistivity of sodium chloride solutions. *Journal of Petroleum Technology* **5**, 17-20 (1953).
26 Walton, N. R. G. Electrical Conductivity And Total Dissolved Solids—What Is Their Precise Relationship? *Desalination* **72**, 275-292 (1989).
27 Culkin, F. & Smith, N. J. I. J. o. O. E. Determination of the concentration of potassium chloride solution having the same electrical conductivity, at 15 C and infinite frequency, as standard seawater of salinity 35.0000‰(Chlorinity 19.37394‰). **5**, 22-23 (1980).
28 Millero, F. J., Feistel, R., Wright, D. G. & McDougall, T. J. The composition of Standard Seawater and the definition of the Reference-Composition Salinity Scale. *Deep-Sea Research Part I-Oceanographic Research Papers* **55**, 50-72, doi:10.1016/j.dsr.2007.10.001 (2008).
29 Tyler, R. H. *et al.* Electrical conductivity of the global ocean. **69**, 156 (2017).

3.10 References

Abarca, E., Carrera, J., Sánchez-Vila, X., & Dentz, M. (2007). Anisotropic dispersive Henry problem. *Advances in Water Resources, 30*(4), 913-926. doi:https://doi.org/10.1016/j.advwatres.2006.08.005

Abarca, E., Carrera, J., Sánchez-Vila, X., & Voss, C. I. (2007). Quasi-horizontal circulation cells in 3D seawater intrusion. *Journal of Hydrology, 339*(3), 118-129. doi:https://doi.org/10.1016/j.jhydrol.2007.02.017

Abarca, E., Karam, H., Hemond, H. F., & Harvey, C. F. (2013). Transient groundwater dynamics in a coastal aquifer: The effects of tides, the lunar cycle, and the beach profile. *Water Resources Research, 49*(5), 2473-2488. doi:10.1002/wrcr.20075

Abd-Elhamid, H., & Javadi, A. (2008). An investigation into control of saltwater intrusion considering the effects of climate change and sea level rise. *Proceeding of 20th SWIM, 2327*.

Abdul Nassir, S. S., Loke, M. H., Lee, C. Y., & Nawawi, M. N. M. (2000). Salt-water intrusion mapping by geoelectrical imaging surveys. *Geophysical Prospecting, 48*(4), 647-661. doi:https://doi.org/10.1046/j.1365-2478.2000.00209.x

Al-Bitar, A., & Ababou, R. (2005). *Random field approach to seawater intrusion in heterogeneous coastal aquifers: unconditional simulations and statistical analysis*, Berlin, Heidelberg.

Almalki, M., Harris, B., & Dupuis, J. C. (2013). Multifrequency full-waveform sonic logging in the screened interval of a large-diameter production well. *Geophysics, 78*(5), B243-B257. doi:10.1190/geo2012-0328.1

Alonso-Rodríguez, R., & Páez-Osuna, F. (2003). Nutrients, phytoplankton and harmful algal blooms in shrimp ponds: a review with special reference to the situation in the Gulf of California. *Aquaculture, 219*(1), 317-336. doi:https://doi.org/10.1016/S0044-8486(02)00509-4

Archie, G. E. (1941). The Electrical Resistivity Log as an Aid in Determining Some Reservoir Characteristics. *Transactions of the AIME, 146*(01), 54-62. doi:10.2118/942054-g

Arps, J. (1953). The effect of temperature on the density and electrical resistivity of sodium chloride solutions. *Journal of Petroleum Technology, 5*(10), 17-20.

Asquith, G. B. (1990). *Log Evaluation of Shaly Sandstones: A Practical Guide*: American Association of Petroleum Geologists.

Ataie-Ashtiani, B., Volker, R. E., & Lockington, D. A. (1999). Tidal effects on sea water intrusion in unconfined aquifers. *Journal of Hydrology, 216*(1-2), 17-31. doi:Doi 10.1016/S0022-1694(98)00275-3

Auken, E., & Christiansen, A. V. (2004). Layered And Laterally Constrained 2d Inversion Of Resistivity Data. *Geophysics, 69*(3), 752-761.

Australian Bureau of Statistics. (2009). *4656.5 - Household Choices Related to Water and Energy, WA, October 2009* Retrieved from http://www.abs.gov.au/AUSSTATS/abs@.nsf/Lookup/4656.5Main+Features1October%202009?OpenDocument

Australian Bureau of Statistics. (2016). *2016 Census QuickStats: Quinns Rocks (Code SSC51267 (SSC))*. Retrieved from http://quickstats.censusdata.abs.gov.au/census_services/getproduct/census/2016/quickstat/SSC51267

Australian Bureau of Statistics. (2018). Estimated Residence Population (ERP) By Statistical Area 2 (Sa2), 1991 to 2014. In: Australian Bureau of Statistics.

Azar, J. H., Javaherlan, A., Pishvaie, M. R., & Nabi-Bidhendi, M. (2008). An approach to defining tortuosity and cementation factor in carbonate reservoir rocks. *Journal of Petroleum Science and Engineering, 60*(2), 125-131. doi:10.1016/j.petrol.2007.05.010

Back, W., Hanshaw, B. B., Herman, J. S., & Van Driel, J. N. (1986). Differential dissolution of a Pleistocene reef in the ground-water mixing zone of coastal Yucatan, Mexico. *Geology, 14*(2), 137-140.

Badaruddin, S., Werner, A. D., & Morgan, L. K. (2017). Characteristics of active seawater intrusion. *Journal of Hydrology, 551*, 632-647. doi:10.1016/j.jhydrol.2017.04.031

Bakker, M. (2006). Analytic solutions for interface flow in combined confined and semi-confined, coastal aquifers. *Advances in Water Resources, 29*(3), 417-425. doi:10.1016/j.advwatres.2005.05.009

Barlow, P. M., & Reichard, E. G. (2010). Saltwater intrusion in coastal regions of North America. *Hydrogeology Journal, 18*(1), 247-260. doi:10.1007/s10040-009-0514-3

Barnes, S. (1999). Karstic groundwater flow characteristics in the Cretaceous Chalk aquifer, Northern Ireland. *Quarterly Journal of Engineering Geology, 32*(1), 55-68. doi:Doi 10.1144/Gsl.Qjeg.1999.032.P1.04

Bates, B., Kundzewicz, Z., & Wu, S. (2008). *Climate change and water*: Intergovernmental Panel on Climate Change Secretariat.

Bayless, E. R., Mandell, W. A., & Ursic, J. R. (2011). Accuracy of Flowmeters Measuring Horizontal Groundwater Flow in an Unconsolidated Aquifer Simulator. *31*(2), 48-62. doi:doi:10.1111/j.1745-6592.2010.01324.x

Bear, J. (2005). *Sea water intrusion into coastal aquifers*.

Bear, J., Cheng, A. H.-D., Sorek, S., Ouazar, D., & Herrera, I. (1999). *Seawater intrusion in coastal aquifers: concepts, methods and practices* (Vol. 14): Springer Science & Business Media.

Bear, J., & Dagan, G. (1964). Some exact solutions of interface problems by means of the hodograph method. *Journal of Geophysical Research, 69*(8), 1563-1572. doi:10.1029/JZ069i008p01563

Beaujean, J., Nguyen, F., Kemna, A., Antonsson, A., & Engesgaard, P. (2014). Calibration of seawater intrusion models: Inverse parameter estimation using surface electrical resistivity tomography and borehole data. *Water Resources Research, 50*(8), 6828-6849. doi:10.1002/2013wr014020

Bellin, A., Pannone, M., Fiori, A., & Rinaldo, A. (1996). On Transport in Porous Formations Characterized by Heterogeneity of Evolving Scales. *32*(12), 3485-3496. doi:10.1029/95wr02507

Bense, V., Read, T., Bour, O., Le Borgne, T., Coleman, T., Krause, S., . . . Selker, J. J. W. R. R. (2016). Distributed Temperature Sensing as a downhole tool in hydrogeology. *52*(12), 9259-9273.

Benson, R. C., & Yuhr, L. B. (2015). *Site Characterization in Karst and Pseudokarst Terraines: Practical Strategies and Technology for Practicing Engineers, Hydrologists and Geologists*: Springer.

Bergmann, P., Ivandic, M., Norden, B., Rücker, C., Kiessling, D., Lüth, S., . . . Juhlin, C. (2014). Combination of seismic reflection and constrained resistivity inversion with an application to 4D imaging of the CO2 storage site, Ketzin, Germany. *79*(2), B37-B50. doi:10.1190/geo2013-0131.1

Bernabé, Y., Mok, U., & Evans, B. (2003). Permeability-porosity Relationships in Rocks Subjected to Various Evolution Processes. *Pure and Applied Geophysics, 160*(5), 937-960. doi:10.1007/pl00012574

BOM, N. (2011). The Australian Baseline Sea Level Monitoring Project. *Annual Sea Level Data Summary Report*. Retrieved from http://www.bom.gov.au/oceanography/projects/abslmp/reports_yearly.shtml

Bonacci, O., & Roje-Bonacci, T. (2000). Interpretation of groundwater level monitoring results in karst aquifers: examples from the Dinaric karst. *Hydrological Processes, 14*(14), 2423-2438. doi:10.1002/1099-1085(20001015)14:14<2423::Aid-hyp104>3.0.Co;2-2

Bryan, E., Meredith, K. T., Baker, A., Post, V. E. A., & Andersen, M. S. (2016). Island groundwater resources, impacts of abstraction and a drying climate: Rottnest Island, Western Australia. *Journal of Hydrology, 542*, 704-718. doi:10.1016/j.jhydrol.2016.09.043

Bureau of Meteorology. (2012). Ocean Monitoring Portal. Retrieved from http://www.bom.gov.au/cosppac/apps/portal/app.html#climate

Burnett, W. C., Aggarwal, P. K., Aureli, A., Bokuniewicz, H., Cable, J. E., Charette, M. A., . . . Turner, J. V. (2006). Quantifying submarine groundwater discharge in the coastal zone via multiple methods. *Sci Total Environ, 367*(2-3), 498-543. doi:10.1016/j.scitotenv.2006.05.009

Calvache, M. L., & PulidoBosch, A. (1997). Effects of geology and human activity on the dynamics of salt-water intrusion in three coastal aquifers in southern Spain. *Environmental Geology, 30*(3-4), 215-223. doi:DOI 10.1007/s002540050149

Carrera, J., Hidalgo, J. J., Slooten, L. J., & Vazquez-Sune, E. (2010). Computational and conceptual issues in the calibration of seawater intrusion models. *Hydrogeology Journal, 18*(1), 131-145. doi:10.1007/s10040-009-0524-1

Carter, E. S., White, S. M., & Wilson, A. M. (2008). Variation in groundwater salinity in a tidal salt marsh basin, North Inlet Estuary, South Carolina. *Estuarine Coastal and Shelf Science, 76*(3), 543-552. doi:10.1016/j.ecss.2007.07.049

Casanova, J., Devau, N., & Pettenati, M. (2016). Managed Aquifer Recharge: An Overview of Issues and Options. In *Integrated Groundwater Management* (pp. 413-434): Springer.

Chang, S. W., & Clement, T. P. (2012). Experimental and numerical investigation of saltwater intrusion dynamics in flux-controlled groundwater systems. *Water Resources Research, 48*(9). doi:doi:10.1029/2012WR012134

Chang, S. W., Clement, T. P., Simpson, M. J., & Lee, K.-K. (2011). Does sea-level rise have an impact on saltwater intrusion? *Advances in Water Resources, 34*(10), 1283-1291. doi:10.1016/j.advwatres.2011.06.006

Cheng, A. H., & Ouazar, D. (2004). *Coastal aquifer management-monitoring, modeling, and case studies*: CRC Press.

Claerbout, J. F., & Muir, F. (1973). Robust Modeling with Erratic Data. *Geophysics, 38*(5), 826-844. doi:Doi 10.1190/1.1440378

Clark, G., & Johnston, E. (2016). *Coasts: Population growth and urban development: Coastal development and land use*. Australian Government Department of the Environment and Energy Retrieved from https://soe.environment.gov.au/theme/coasts/topic/2016/population-growth-and-urban-development-coastal-development-and-land-use

Collins, M., Knutti, R., Arblaster, J., Dufresne, J.-L., Fichefet, T., Friedlingstein, P., . . . Wehner, M. (2013). Chapter 12 - Long-term climate change: Projections, commitments and irreversibility. In Ipcc (Ed.), *Climate Change 2013: The Physical Science Basis. IPCC Working Group I Contribution to AR5*. Cambridge: Cambridge University Press.

Comte, J. C., & Banton, O. (2007). Cross-validation of geo-electrical and hydrogeological models to evaluate seawater intrusion in coastal aquifers. *Geophysical Research Letters, 34*(10), n/a-n/a. doi:10.1029/2007gl029981

Comte, J. C., Wilson, C., Ofterdinger, U., & Gonzalez-Quiros, A. (2017). Effect of volcanic dykes on coastal groundwater flow and saltwater intrusion: A field-scale multiphysics approach and parameter evaluation. *Water Resources Research, 53*(3), 2171-2198. doi:10.1002/2016wr019480

Constable, S. C., Parker, R. L., & Constable, C. G. (1987). Occam's inversion: A practical algorithm for generating smooth models from electromagnetic sounding data. *Geophysics, 52*(3), 289-300. doi:https://doi.org/10.1190/1.1442303

Cook, P. G. (2003). *A guide to regional groundwater flow in fractured rock aquifers*: Citeseer.

Coscia, I., Linde, N., Greenhalgh, S., Vogt, T., & Green, A. (2012). Estimating traveltimes and groundwater flow patterns using 3D time-lapse crosshole ERT imaging of electrical resistivity fluctuations induced by infiltrating river water. *Geophysics, 77*(4), E239-E250. doi:10.1190/Geo2011-0328.1

Costall, A., Harris, B., & Pigois, J. P. (2018). Electrical Resistivity Imaging and the Saline Water Interface in High-Quality Coastal Aquifers. *Surveys in Geophysics, 39*(4), 753-816. doi:10.1007/s10712-018-9468-0

Costall, A. R., & Harris, B. (2019). Rapid Estimation of Volumetric Groundwater Recharge in the Vadose Zone via Ground Penetrating Radar. *ASEG Extended Abstracts, 2018*(1), 1-7. doi:10.1071/ASEG2018abP091

Cox, W. (2017). Demographia: World Urban Areas. *13th Annual Edition ed. St. Louis: Demographia. Available: http://www. demographia. com/db-worldua. pdf. Date of access, 30*, 2017.

Culkin, F., & Smith, N. J. I. J. o. O. E. (1980). Determination of the concentration of potassium chloride solution having the same electrical conductivity, at 15 C and infinite frequency, as standard seawater of salinity 35.0000‰(Chlorinity 19.37394‰). *5*(1), 22-23.

Custodio, E. (2012). Coastal aquifer management in Europe.

Dafny, E., Burg, A., & Gvirtzman, H. (2010). Effects of Karst and geological structure on groundwater flow: The case of Yarqon-Taninim Aquifer, Israel. *Journal of Hydrology, 389*(3-4), 260-275. doi:10.1016/j.jhydrol.2010.05.038

Dagan, G., & Zeitoun, D. G. (1998). Seawater-freshwater interface in a stratified aquifer of random permeability distribution. *Journal of contaminant hydrology, 29*(3), 185-203. doi:https://doi.org/10.1016/S0169-7722(97)00013-2

Dahlin, T., & Zhou, B. (2004). A numerical comparison of 2D resistivity imaging with 10 electrode arrays. *Geophysical Prospecting, 52*(5), 379-398. doi:DOI 10.1111/j.1365-2478.2004.00423.x

Dausman, A., & Langevin, C. D. (2005). *Movement of the saltwater interface in the surficial aquifer system in response to hydrologic stresses and water-management practices, Broward County, Florida*: US Department of the Interior, US Geological Survey.

Davidson, W. A., & Yu, X. (2008). *Perth regional aquifer modelling system (PRAMS) model development: Hydrogeology and groundwater modelling*: Department of Water.

Davis, S., & DeWiest, R. (1967). Hydrology, 2nd eds., 463. *New York, London*.

Delworth, T. L., & Zeng, F. R. (2014). Regional rainfall decline in Australia attributed to anthropogenic greenhouse gases and ozone levels Latitude. *Nature Geoscience, 7*(8), 583-587. doi:10.1038/Ngeo2201

Department of Water. (2017). *Northern Perth Basin: Geology, hydrogeology and groundwater resources*. Department of Water W.A.

Department of Water, W. (2004). Perth Groundwater Atlas - Metadata: Groundwater Contours, May 2003. Retrieved from http://atlases.water.wa.gov.au/idelve/gwa/metadata_statements/gwcont_min.html

Dey, A., & Morrison, H. F. (1979). RESISTIVITY MODELLING FOR ARBITRARILY SHAPED TWO-DIMENSIONAL STRUCTURES*. *27*(1), 106-136. doi:doi:10.1111/j.1365-2478.1979.tb00961.x

Diersch, H.-J. G. (2014). *Feflow: Finite Element Modeling of Flow, Mass and Heat Transport in Porous and Fractured Media*: Springer Science & Business Media.

Diersch, H. (2002). FEFLOW-White papers vol. I. *WASY Ltd., Berlin*.

Digha Opaminola, N., & Ekanem Jessie, D. (2015). Effects of Population Density on Water Quality in Calabar Municipality Cross River State, Nigeria.

Dillon, P. (2009). Water recycling via managed aquifer recharge in Australia. *Boletin Geologico Y Minero, 120*(2), 121-130. Retrieved from <Go to ISI>://WOS:000422359700002

Dokou, Z., & Karatzas, G. P. (2012). Saltwater intrusion estimation in a karstified coastal system using density-dependent modelling and comparison with the sharp-interface approach. *Hydrological Sciences Journal-Journal Des Sciences Hydrologiques, 57*(5), 985-999. doi:10.1080/02626667.2012.690070

Domenico, P. A., & Schwartz, F. W. (1998). *Physical and chemical hydrogeology* (Vol. 506): Wiley New York.

Elci, A., Molz III, F. J., & Waldrop, W. R. (2001). Implications of Observed and Simulated Ambient Flow in Monitoring Wells. *Groundwater, 39*(6), 853-862. doi:10.1111/j.1745-6584.2001.tb02473.x

Esteban, Ó., Cruz-Navarrete, M., González-Cano, A., & Bernabeu, E. (1999). Measurement of the degree of salinity of water with a fiber-optic sensor. *Applied Optics, 38*(25), 5267-5271. doi:10.1364/AO.38.005267

Falkland, A., & Custodio, E. (1991). *Hydrology and water resources of small islands: A practical guide*: Unesco.

Farquharson, C. G., & Oldenburg, D. W. (2003). Constructing piece-wise-constant models using general measures in non-linear, minimum-structure inversion algorithms: 6th International Symposium. *Society of Exploration Geophysicists of Japan, Expanded Abstracts*, 240-243.

Ferguson, G., & Gleeson, T. (2012). Vulnerability of coastal aquifers to groundwater use and climate change. *Nature Climate Change, 2*(5), 342-345. doi:10.1038/Nclimate1413

Fofonoff, N. P., & Millard Jr, R. (1983). Algorithms for the computation of fundamental properties of seawater.

Ford, D., & Williams, P. D. (2013). *Karst hydrogeology and geomorphology*: John Wiley & Sons.

Fox, R. C., Hohmann, G. W., Killpack, T. J., & Rijo, L. (1980). Topographic effects in resistivity and induced-polarization surveys. *Geophysics, 45*(1), 75-93. doi:https://doi.org/10.1190/1.1441041

Freifeld, B. M., Trautz, R. C., Kharaka, Y. K., Phelps, T. J., Myer, L. R., Hovorka, S. D., & Collins, D. J. (2005). The U-tube: A novel system for acquiring borehole fluid samples from a deep geologic CO2 sequestration experiment. *110*(B10). doi:doi:10.1029/2005JB003735

Friedel, S. (2003). Resolution, stability and efficiency of resistivity tomography estimated from a generalized inverse approach. *Geophysical Journal International, 153*(2), 305-316. doi:DOI 10.1046/j.1365-246X.2003.01890.x

Gelhar, L. W., Welty, C., & Rehfeldt, K. R. (1992). A critical review of data on field-scale dispersion in aquifers. *28*(7), 1955-1974. doi:doi:10.1029/92WR00607

Ghasemizadeh, R., Hellweger, F., Butscher, C., Padilla, I., Vesper, D., Field, M., & Alshawabkeh, A. (2012). Review: Groundwater flow and transport modeling of karst aquifers, with particular reference to the North Coast Limestone aquifer system of Puerto Rico. *Hydrogeol J, 20*(8), 1441-1461. doi:10.1007/s10040-012-0897-4

Glover, P. W. J. (2010). A generalized Archie's law for n phases. *75*(6), E247-E265. doi:10.1190/1.3509781

Glover, P. W. J. (2016). Archie's law - a reappraisal. *Solid Earth, 7*(4), 1157-1169. doi:10.5194/se-7-1157-2016

Glover, R. E. (1959). The pattern of fresh-water flow in a coastal aquifer. *Journal of Geophysical Research, 64*(4), 457-459. doi:doi:10.1029/JZ064i004p00457

Goggin, D. J., Chandler, M. A., Kocurek, G., & Lake, L. W. (1988). Patterns of Permeability in Eolian Deposits: Page Sandstone (Jurassic), Northeastern Arizona. *SPE Formation Evaluation, 3*(02), 297-306. doi:10.2118/14893-PA

Goldman, J. C., Tenore, K. R., & Stanley, H. I. (1973). Inorganic Nitrogen Removal from Wastewater: Effect on Phytoplankton Growth in Coastal Marine Waters. *Science, 180*(4089), 955-956. doi:10.1126/science.180.4089.955

Gonzalez-Herrera, R., Sanchez-y-Pinto, I., & Gamboa-Vargas, J. (2002). Groundwater-flow modeling in the Yucatan karstic aquifer, Mexico. *Hydrogeology Journal, 10*(5), 539-552. doi:10.1007/s10040-002-0216-6

Green, N. R., & MacQuarrie, K. T. B. (2014). An evaluation of the relative importance of the effects of climate change and groundwater extraction on seawater intrusion in coastal aquifers in Atlantic Canada. *Hydrogeology Journal, 22*(3), 609-623. doi:10.1007/s10040-013-1092-y

Grimes, K. G. (1999). *The Water Below: An introduction to karst hydrology and the hydrological setting of the Australian karsts.* Paper presented at the Proceedings of the 13th Australasian Conference on Cave and Karst Management. pp.

Grimes, K. G. (2002). Syngenetic and eogenetic karst: an Australian viewpoint. *Evolution of Karst: from Prekarst to Cessation. Inštitut za raziskovanje krasa, ZRC SAZU, Postojna*, 407-414.

Grimes, K. G. (2006). Syngenetic karst in Australia: a review.

Grinat, M., Epping, D., & Meyer, R. (2018). *Long-time resistivity monitoring of a freshwater/saltwater transition zone using the vertical electrode system SAMOS.* Paper presented at the E3S Web of Conferences.

Grinat, M., Südekum, W., Epping, D., Grelle, T., & Meyer, R. (2010). *An automated electrical resistivity tomography system to monitor the freshwater/saltwater zone on a North Sea Island.* Paper presented at the Near Surface 2010-16th EAGE European Meeting of Environmental and Engineering Geophysics.

Guo, Q., Huang, J., Zhou, Z., & Wang, J. (2019). Experiment and Numerical Simulation of Seawater Intrusion under the Influences of Tidal Fluctuation and Groundwater Exploitation in Coastal Multilayered Aquifers. *Geofluids, 2019*, 17. doi:10.1155/2019/2316271

Hamamoto, S., Moldrup, P., Kawamoto, K., & Komatsu, T. (2010). Excluded-volume expansion of Archie's law for gas and solute diffusivities and electrical and thermal conductivities in variably saturated porous media. *Water Resources Research, 46*(6). doi:10.1029/2009wr008424

Hartmann, A., Goldscheider, N., Wagener, T., Lange, J., & Weiler, M. (2014). Karst water resources in a changing world: Review of hydrological modeling approaches. *52*(3), 218-242. doi:10.1002/2013rg000443

Healy, R. W., & Cook, P. G. (2002). Using groundwater levels to estimate recharge. *Hydrogeology Journal, 10*(1), 91-109. doi:10.1007/s10040-001-0178-0

Heath, R. C. (1998). *Basic ground-water hydrology* (Vol. 2220): US Department of the Interior, US Geological Survey.

Heiss, J. W., & Michael, H. A. (2014). Saltwater-freshwater mixing dynamics in a sandy beach aquifer over tidal, spring-neap, and seasonal cycles. *50*(8), 6747-6766. doi:10.1002/2014wr015574

Held, R., Attinger, S., & Kinzelbach, W. (2005). Homogenization and effective parameters for the Henry problem in heterogeneous formations. *Water Resources Research, 41*(11). doi:10.1029/2004wr003674

Henry, H. (1964). Effects of dispersion on salt encroachment in coastal aquifers: US Geological Survey Water-Supply Paper 1613-C, p. *C71-C84*.

Heße, F., Prykhodko, V., Schlüter, S., & Attinger, S. (2014). Generating random fields with a truncated power-law variogram: A comparison of several numerical methods. *Environmental Modelling & Software, 55*, 32-48. doi:https://doi.org/10.1016/j.envsoft.2014.01.013

Hilhorst, M. J. S. S. S. o. A. J. (2000). A pore water conductivity sensor. *64*(6), 1922-1925.

Huntley, D. (1986). Relations Between Permeability and Electrical Resistivity in Granular Aquifers. *Groundwater, 24*(4), 466-474. doi:10.1111/j.1745-6584.1986.tb01025.x

Hussain, M. S., & Javadi, A. A. (2016). Assessing impacts of sea level rise on seawater intrusion in a coastal aquifer with sloped shoreline boundary. *Journal of Hydro-environment Research, 11*, 29-41. doi:10.1016/j.jher.2016.01.003

Ivkovic, K., Marshall, S., Morgan, L., Werner, A., Carey, H., Cook, S., . . . Caruana, L. (2012). National–Scale Vulnerability Assessment Of Seawater Intrusion: Summary Report. *Australian Government National Water Commision. Waterlines Report Series No, 85*.

Johannes, R. E. (1980). The Ecological Significance of the Submarine Discharge of Groundwater. *Marine Ecology Progress Series, 3*(4), 365-373. doi:DOI 10.3354/meps003365

Jørgensen, N. O., Andersen, M. S., & Engesgaard, P. (2008). Investigation of a dynamic seawater intrusion event using strontium isotopes (87Sr/86Sr). *Journal of Hydrology, 348*(3), 257-269. doi:https://doi.org/10.1016/j.jhydrol.2007.10.001

Kerrou, J., & Renard, P. J. H. J. (2010). A numerical analysis of dimensionality and heterogeneity effects on advective dispersive seawater intrusion processes. *18*(1), 55-72. doi:10.1007/s10040-009-0533-0

Ketabchi, H., Mahmoodzadeh, D., Ataie-Ashtiani, B., & Simmons, C. T. (2016). Sea-level rise impacts on seawater intrusion in coastal aquifers: Review and integration. *Journal of Hydrology, 535*, 235-255. doi:10.1016/j.jhydrol.2016.01.083

Koltermann, C. E., & Gorelick, S. M. (1996). Heterogeneity in Sedimentary Deposits: A Review of Structure-Imitating, Process-Imitating, and Descriptive Approaches. *32*(9), 2617-2658. doi:doi:10.1029/96WR00025

Kotera, A., Sakamoto, T., Nguyen, D. K., & Yokozawa, M. (2008). Regional Consequences of Seawater Intrusion on Rice Productivity and Land Use in Coastal Area of the Mekong River Delta. *Japan Agricultural Research Quarterly: JARQ, 42*(4), 267-274. doi:10.6090/jarq.42.267

Koukadaki, M. A., Karatzas, G. P., Papadopoulou, M. P., & Vafidis, A. (2007). Identification of the Saline Zone in a Coastal Aquifer Using Electrical Tomography Data and Simulation. *Water Resources Management, 21*(11), 1881. doi:10.1007/s11269-006-9135-y

Koussis, A. D., Mazi, K., & Destouni, G. (2012). Analytical single-potential, sharp-interface solutions for regional seawater intrusion in sloping unconfined coastal aquifers, with pumping and recharge. *Journal of Hydrology, 416-417*, 1-11. doi:https://doi.org/10.1016/j.jhydrol.2011.11.012

Kretschmer, P., & Degens, B. (2012). *Review Of Available Groundwater In The Superficial Aquifer For The Yanchep, Eglinton And Quinns Groundwater Subareas*. Retrieved from

Lambert, M. J., & Burnett, W. C. J. B. (2003). Submarine groundwater discharge estimates at a Florida coastal site based on continuous radon measurements. *66*(1), 55-73. doi:10.1023/B:BIOG.0000006057.63478.fa

Levanon, E., Yechieli, Y., Shalev, E., Friedman, V., & Gvirtzman, H. (2013). Reliable Monitoring of the Transition Zone Between Fresh and Saline Waters in Coastal Aquifers. *Ground Water Monitoring and Remediation, 33*(3), 101-110. doi:10.1111/gwmr.12020

Li, X. Y., Zhang, L. M., & Li, J. H. (2016). Using Conditioned Random Field to Characterize the Variability of Geologic Profiles. *142*(4), 04015096. doi:doi:10.1061/(ASCE)GT.1943-5606.0001428

Loke, M. (1997). Res2DINV software user's manual. *University Sains Malaysia, Penang*.

Loke, M., Alfouzan, F. A., & Nawawi, M. (2007). Optimisation of electrode arrays used in 2D resistivity imaging surveys. In *ASEG Extended Abstracts 2007* (pp. 1-4): Australian Society of Exploration Geophysicists (ASEG).

Loke, M. H. (2016a). RES2DINVx64 ver. 4.05 with multi-core and 64-bit support. Retrieved from http://www.geotomosoft.com/

Loke, M. H., Acworth, I., & Dahlin, T. (2003). A comparison of smooth and blocky inversion methods in 2D electrical imaging surveys. *Exploration Geophysics, 34*(3), 182-187. doi:Doi 10.1071/Eg03182

Lu, C. H., Chen, Y. M., Zhang, C., & Luo, J. (2013). Steady-state freshwater-seawater mixing zone in stratified coastal aquifers. *Journal of Hydrology, 505*, 24-34. doi:10.1016/j.jhydrol.2013.09.017

Lusczynski, N. J. (1961). Head and flow of ground water of variable density. *Journal of Geophysical Research, 66*(12), 4247-4256. doi:doi:10.1029/JZ066i012p04247

Luthin, J. N., & Day, P. R. J. S. S. S. o. A. J. (1955). Lateral Flow Above a Sloping Water Table 1. *19*(4), 406-410.

Maasland, M. (1957). Soil anisotropy and land drainage. In *Drainage of agricultural lands* (Vol. 7, pp. 216-285): ASA Madison, Wis.

Mahesha, A., & Nagaraja, S. H. (1996). Effect of natural recharge on sea water intrusion in coastal aquifers. *Journal of Hydrology, 174*(3-4), 211-220. doi:Doi 10.1016/0022-1694(95)02777-7

Maliva, R. G. (2016). Aquifer Characterization Techniques.

Mangor, K., Drønen, N. K., Kærgaard, K. H., & Kristensen, S. E. (2017). Shoreline management guidelines. *DHI*. Retrieved from https://www.dhigroup.com/marine-water/ebook-shoreline-management-guidelines

Martorana, R., Fiandaca, G., Ponsati, A. C., & Cosentino, P. L. (2009). Comparative tests on different multi-electrode arrays using models in near-surface geophysics. *Journal of Geophysics and Engineering, 6*(1), 1-20. doi:10.1088/1742-2132/6/1/001

Masterson, J. P. (2004). *Simulated interaction between freshwater and saltwater and effects of ground-water pumping and sea-level change, Lower Cape Cod aquifer system, Massachusetts*: US Department of the Interior, US Geological Survey.

Mathieu, F., & Toksö: z, M. (1984). Application of full waveform acoustic logging data to the estimation of reservoir permeability. In *SEG Technical Program Expanded Abstracts 1984* (pp. 9-12): Society of Exploration Geophysicists.

McFarlane, D., Inman, M., White, S., Loh, M., Turner, A., & English, L. (2005). Integrated resource planning for the integrated water supply scheme. Client Report to WA Government. In: CSIRO: Water for a Healthy Country National Research Flagship Canberra.

McGillivray, P. R. (1992). *Forward modeling and inversion of DC resistivity and MMR data.* University of British Columbia,

Meyer, R., Engesgaard, P., & Sonnenborg, T. O. (2019). Origin and Dynamics of Saltwater Intrusion in a Regional Aquifer: Combining 3-D Saltwater Modeling With Geophysical and Geochemical Data. *Water Resources Research, 55*(3), 1792-1813. doi:10.1029/2018wr023624

Michael, H. A., Russoniello, C. J., & Byron, L. A. (2013). Global assessment of vulnerability to sea-level rise in topography-limited and recharge-limited coastal groundwater systems. *Water Resources Research, 49*(4), 2228-2240. doi:10.1002/wrcr.20213

Millero, F. J., Feistel, R., Wright, D. G., & McDougall, T. J. (2008). The composition of Standard Seawater and the definition of the Reference-Composition Salinity Scale. *Deep-Sea Research Part I-Oceanographic Research Papers, 55*(1), 50-72. doi:10.1016/j.dsr.2007.10.001

Moore, W. S. (2006). The role of submarine groundwater discharge in coastal biogeochemistry. *Journal of Geochemical Exploration, 88*(1), 389-393. doi:https://doi.org/10.1016/j.gexplo.2005.08.082

Mylroie, J. E. (2013). Coastal Karst Development in Carbonate Rocks. In M. J. Lace & J. E. Mylroie (Eds.), *Coastal Karst Landforms* (pp. 77-109). Dordrecht: Springer Netherlands.

Narayan, K. A., Schleeberger, C., & Bristow, K. L. (2007). Modelling seawater intrusion in the Burdekin Delta Irrigation Area, North Queensland, Australia. *Agricultural Water Management, 89*(3), 217-228. doi:10.1016/j.agwat.2007.01.008

Nidagal, V., & Davidson, W. J. G. S. o. W., Unpublished Hydrogeological Report. (1991). North coastal groundwater investigation (Burns Beach—Pipidinny). (1991/17).

Ogilvy, R. D., Meldrum, P. I., Kuras, O., Wilkinson, P. B., Chambers, J. E., Sen, M., . . . Tsourlos, P. (2009). Automated monitoring of coastal aquifers with electrical resistivity tomography. *Near Surface Geophysics, 7*(5-6), 367-375. doi:Doi 10.3997/1873-0604.2009027

Palacios, A., Ledo, J. J., Linde, N., Luquot, L., Bellmunt, F., Folch, A., . . . Carrera, J. (2019). Time-lapse cross-hole electrical resistivity tomography (CHERT) for monitoring seawater intrusion dynamics in a Mediterranean aquifer. *Hydrol. Earth Syst. Sci. Discuss., 2019*, 1-30. doi:10.5194/hess-2019-408

Parker, T., Shatalin, S., & Farhadiroushan, M. J. f. b. (2014). Distributed Acoustic Sensing–a new tool for seismic applications. *32*(2), 61-69.

Parmesan, C., & Yohe, G. (2003). A globally coherent fingerprint of climate change impacts across natural systems. *Nature, 421*, 37. doi:10.1038/nature01286

Petra, D. (2009). Vulnerability to the impact of climate change on renewable groundwater resources: a global-scale assessment. *Environmental Research Letters, 4*(3), 035006. Retrieved from http://stacks.iop.org/1748-9326/4/i=3/a=035006

Pool, M., Post, V. E. A., & Simmons, C. T. (2014). Effects of tidal fluctuations on mixing and spreading in coastal aquifers: Homogeneous case. *Water Resources Research, 50*(8), 6910-6926. doi:10.1002/2014wr015534

Possetti, G., Kamikawachi, R., Prevedello, C., Muller, M., Fabris, J. J. M. S., & Technology. (2009). Salinity measurement in water environment with a long period grating based interferometer. *20*(3), 034003.

Post, V., Kooi, H., & Simmons, C. (2007). Using hydraulic head measurements in variable-density ground water flow analyses. *Ground Water, 45*(6), 664-671. doi:10.1111/j.1745-6584.2007.00339.x

Price, R. M., Top, Z., Happell, J. D., & Swart, P. K. (2003). Use of tritium and helium to define groundwater flow conditions in Everglades National Park. *Water Resources Research, 39*(9). doi:10.1029/2002wr001929

Pulido-Leboeuf, P., Pulido-Bosch, A., Calvache, M. L., Vallejos, Á., & Andreu, J. M. (2003). Strontium, SO42−/Cl− and Mg2+/Ca2+ ratios as tracers for the evolution of seawater into coastal aquifers: the example of Castell de Ferro aquifer (SE Spain). *Comptes Rendus Geoscience, 335*(14), 1039-1048. doi:https://doi.org/10.1016/j.crte.2003.08.004

Qu, W. J., Li, H. L., Wan, L., Wang, X. S., & Jiang, X. W. (2014). Numerical simulations of steady-state salinity distribution and submarine groundwater discharges in homogeneous anisotropic coastal aquifers. *Advances in Water Resources, 74*, 318-328. doi:10.1016/j.advwatres.2014.10.009

Randazzo, A. F., & Bloom, J. I. (1985). Mineralogical changes along the freshwater/saltwater interface of a modern aquifer. *Sedimentary Geology, 43*(1-4), 219-239.

Rechtien, R. D., Hambacker, K. L., & R. F. Ballard, J. (1993). A high-frequency sparker source for the borehole environment. *58*(5), 660-669. doi:10.1190/1.1443450

Ronczka, M., Hellman, K., Günther, T., Wisén, R., & Dahlin, T. (2017). Electric resistivity and seismic refraction tomography: a challenging joint underwater survey at Äspö Hard Rock Laboratory. *Solid Earth, 8*(3), 671-682. doi:10.5194/se-8-671-2017

Rücker, C., Günther, T., & Spitzer, K. (2006). Three-dimensional modelling and inversion of dc resistivity data incorporating topography - I. Modelling. *Geophysical Journal International, 166*(2), 495-505. doi:10.1111/j.1365-246X.2006.03010.x

Rücker, C., Günther, T., & Wagner, F. M. (2017). pyGIMLi: An open-source library for modelling and inversion in geophysics. *Computers & Geosciences, 109*, 106-123. doi:10.1016/j.cageo.2017.07.011

Sandmeir, K. J. (2014). ReflexW (Manual).

Scanlon, B. R., Mace, R. E., Barrett, M. E., & Smith, B. (2003). Can we simulate regional groundwater flow in a karst system using equivalent porous media models? Case study, Barton Springs Edwards aquifer, USA. *Journal of Hydrology, 276*(1), 137-158. doi:https://doi.org/10.1016/S0022-1694(03)00064-7

Schenato, L. J. A. S. (2017). A review of distributed fibre optic sensors for geo-hydrological applications. *7*(9), 896.

Schulze-Makuch, D. (2005). Longitudinal dispersivity data and implications for scaling behavior. *Ground Water, 43*(3), 443-456. doi:10.1111/j.1745-6584.2005.0051.x

Sebben, M. L., Werner, A. D., & Graf, T. (2015). Seawater intrusion in fractured coastal aquifers: A preliminary numerical investigation using a fractured Henry problem. *Advances in Water Resources, 85*, 93-108. doi:10.1016/j.advwatres.2015.09.013

Selker, J. S., Thévenaz, L., Huwald, H., Mallet, A., Luxemburg, W., van de Giesen, N., . . . Parlange, M. B. (2006). Distributed fiber-optic temperature sensing for hydrologic systems. *42*(12). doi:10.1029/2006wr005326

Selley, R. C. (2000). *Applied sedimentology*: Elsevier.

Semeniuk, V., & Johnson, D. P. (1982). Recent and Pleistocene beach/dune sequences, western Australia. *Sedimentary Geology, 32*(4), 301-328. doi:https://doi.org/10.1016/0037-0738(82)90042-2

Semeniuk, V., & Johnson, D. P. (1985). Modern and Pleistocene Rocky Shore Sequences Along Carbonate Coastlines, Southwestern Australia. *Sedimentary Geology, 44*(3-4), 225-261. doi:Doi 10.1016/0037-0738(85)90015-6

Shanafield, M., Banks, E. W., Arkwright, J. W., & Hausner, M. B. (2018). Fiber-Optic Sensing for Environmental Applications: Where We Have Come From and What Is Possible. *54*(11), 8552-8557. doi:10.1029/2018wr022768

Shoemaker, W. B. (2004). Important observations and parameters for a salt water intrusion model. *Ground Water, 42*(6-7), 829-840. doi:10.1111/j.1745-6584.2004.t01-2-.x

Slomp, C. P., & Van Cappellen, P. (2004). Nutrient inputs to the coastal ocean through submarine groundwater discharge: controls and potential impact. *Journal of Hydrology, 295*(1-4), 64-86. doi:10.1016/j.jhydrol.2004.02.018

Smerdon, B. D., Smith, L. A., Harrington, G. A., Gardner, W. P., Delle Piane, C., & Sarout, J. (2014). Estimating the hydraulic properties of an aquitard from in situ pore pressure measurements. *Hydrogeology Journal, 22*(8), 1875-1887. doi:10.1007/s10040-014-1161-x

Smith, A., Massuel, S., & Pollock, D. (2012). *Geohydrology Of The Tamala Limestone Formation In The Perth Region: Origin And Role Of Secondary Porosity* (EP12568). Retrieved from Australia:

Smith, A., Massuel, S., Pollock, D., Fitzpatrick, A., Byrne, J., Johnstone, C., . . . Cahill, K. (2012). *Final Summary Report-Hydrological Controls On Mar In Perth's Coastal Aquifer* (EP125485). Retrieved from https://publications.csiro.au/rpr/pub?list=BRO&pid=csiro:EP125485

Smith, A. J., & Hick, W. P. (2001). *Hydrogeology and aquifer tidal propagation in Cockburn Sound, Western Australia* (procite:cd26e417-61cd-4a56-89b7-1ee9e32aab7a). Retrieved from

Smith, A. J., & Nield, S. P. (2003). Groundwater discharge from the superficial aquifer into Cockburn Sound Western Australia: estimation by inshore water balance. *Biogeochemistry, 66*(1-2), 125-144. doi:DOI 10.1023/B:BIOG.0000006152.27470.a9

Spies, B. R. (1996). Electrical and electromagnetic borehole measurements: A review. *Surveys in Geophysics, 17*(4), 517-556. doi:Doi 10.1007/Bf01901643

Spiteri, C., Slomp, C. P., Charette, M. A., Tuncay, K., & Meile, C. (2008). Flow and nutrient dynamics in a subterranean estuary (Waquoit Bay, MA, USA): Field data and reactive transport modeling. *Geochimica et Cosmochimica Acta, 72*(14), 3398-3412. doi:https://doi.org/10.1016/j.gca.2008.04.027

Stern, N., & Stern, N. H. (2007). *The economics of climate change: the Stern review*: cambridge University press.

Stocker, T. F., Qin, D., Plattner, G.-K., Tignor, M., Allen, S. K., Boschung, J., . . . Midgley, P. M. (2013). *Climate change 2013: The Physical Science Basis*. Retrieved from

Strack, O. (1976). A single-potential solution for regional interface problems in coastal aquifers. *Water Resources Research, 12*(6), 1165-1174. doi:doi:10.1029/WR012i006p01165

Stringfield, V. T., & LeGrand, H. E. (1971). Effects of karst features on circulation of water in carbonate rocks in coastal areas. *Journal of Hydrology, 14*(2), 139-157. doi:https://doi.org/10.1016/0022-1694(71)90003-5

Strobach, E. (2013). Hydrogeophysical investigation of water recharge into the Gnangara Mound.

Strobach, E., Harris, B. D., Dupuis, C. J., Kepic, A., & Martin, M. W. (2010). Ground-Penetrating Radar For Delineation Of Hydraulically Significant Layers In The Unsaturated Zone Of The Gnangara Mound, Wa. *ASEG Extended Abstracts, 2010*(1), 1-4. doi:http://dx.doi.org/10.1071/ASEG2010ab237

Strobach, E., Harris, B. D., Dupuis, J. C., & Kepic, A. W. (2014). Time-lapse borehole radar for monitoring rainfall infiltration through podosol horizons in a sandy vadose zone. *Water Resources Research, 50*(3), 2140-2163. doi:10.1002/2013wr014331

Strout, J. M., & Tjelta, T. I. (2005). In situ pore pressures: What is their significance and how can they be reliably measured? *Marine and Petroleum Geology, 22*(1), 275-285. doi:https://doi.org/10.1016/j.marpetgeo.2004.10.024

Stuyfzand, P. J. (1992). *Behaviour of major and trace constituents in fresh and salt intrusion waters, in the western Netherlands.* Paper presented at the Study and modelling of salt water intrusion into aquifers. In: Proceedings of the 12th salt water intrusion meeting, Barcelona. CIHS-CIMNE, Barcelona.

Sudicky, E. A. (1986). A natural gradient experiment on solute transport in a sand aquifer: Spatial variability of hydraulic conductivity and its role in the dispersion process. *Water Resources Research, 22*(13), 2069-2082. doi:10.1029/WR022i013p02069

Teijón Ávila, G., Tamoh, K., Soler Manuel, M. A., & Candela Lledó, L. (2009). Treated wastewater reuse for a seawater intrusion hydraulic barrier implementation in the Llobregat delta aquifer (Barcelona, Spain): first phase. *Options Méditerranéennes: série A: séminaires Méditerranéens*(88), 171-178.

Todd. (2006). *GROUNDWATER HYDROLOGY, 2ND ED*: Wiley.

Tularam, G., & Krishna, M. (2009). LONG TERM CONSEQUENCES OF GROUNDWATER PUMPING IN AUSTRALIA: A REVIEW OF IMPACTS AROUND THE GLOBE. *Journal of Applied Sciences in Environmental Sanitation, 4*(2).

Tuong, T. P., Kam, S. P., Hoanh, C. T., Dung, L. C., Khiem, N. T., Barr, J., & Ben, D. C. (2003). Impact of seawater intrusion control on the environment, land use and household incomes in a coastal area. *Paddy and Water Environment, 1*(2), 65-73. doi:10.1007/s10333-003-0015-2

Turner, I. L., & Acworth, R. I. J. J. o. C. R. (2004). Field measurements of beachface salinity structure using cross-borehole resistivity imaging. 753-760.

Tyler, R. H., Boyer, T. P., Minami, T., Zweng, M. M., Reagan, J. R. J. E., Planets, & Space. (2017). Electrical conductivity of the global ocean. *69*(1), 156.

UNESCO, I. J. U. T. P. M. S. (1981). Tenth report of the joint panel on oceanographic tables and standards. *36*, 15-19.

Vandenbohede, A., Van Houtte, E., & Lebbe, L. (2009). Sustainable groundwater extraction in coastal areas: a Belgian example. *Environmental Geology, 57*(4), 735-747. doi:10.1007/s00254-008-1351-8

Verwer, K., Eberli, G. P., & Weger, R. J. (2011). Effect of pore structure on electrical resistivity in carbonates. *AAPG bulletin, 95*(2), 175-190. doi:10.1306/06301010047

Volker, R. E., & Rushton, K. R. (1982). An assessment of the importance of some parameters for seawater intrusion in aquifers and a comparison of dispersive and sharp-interface modelling approaches. *Journal of Hydrology, 56*(3), 239-250. doi:http://dx.doi.org/10.1016/0022-1694(82)90015-4

Walther, G.-R., Post, E., Convey, P., Menzel, A., Parmesan, C., Beebee, T. J. C., . . . Bairlein, F. (2002). Ecological responses to recent climate change. *Nature, 416*, 389. doi:10.1038/416389a

Walther, M., Graf, T., Kolditz, O., Liedl, R., & Post, V. (2017). How significant is the slope of the sea-side boundary for modelling seawater intrusion in coastal aquifers? *Journal of Hydrology, 551*, 648-659. doi:https://doi.org/10.1016/j.jhydrol.2017.02.031

Walton, N. R. G. (1989). Electrical Conductivity And Total Dissolved Solids—What Is Their Precise Relationship? *Desalination, 72*(3), 275-292.

Wassmann, R., Hien, N. X., Hoanh, C. T., & Tuong, T. P. (2004). Sea level rise affecting the Vietnamese Mekong Delta: Water elevation in the flood season and implications for rice production. *Climatic Change, 66*(1-2), 89-107. doi:DOI 10.1023/B:CLIM.0000043144.69736.b7

Water-Technology. (2016). Groundwater Replenishment System (GWRS), Orange County, California, United States of America. Retrieved from http://www.water-technology.net/projects/groundwaterreplenish/

Water Corporation. (2016a). Perth Seawater Desalination Plant. Retrieved from https://www.watercorporation.com.au/water-supply/our-water-sources/desalination/perth-seawater-desalination-plant

Water Corporation. (2018). What is the Integrated Water Supply Scheme. Retrieved from https://www.watercorporation.com.au/home/faqs/water-supply-and-services/what-is-the-integrated-water-supply-scheme

Water Corporation. (2019). Groundwater Replenishment Scheme Stage 2 Expansion. Retrieved from https://www.watercorporation.com.au/water-supply/ongoing-works/groundwater-replenishment-scheme

Water Information Reporting database. (2019). Water Information Reporting Database. Retrieved from http://wir.water.wa.gov.au. from W.A Dept. of Water, W.A Dept. Regional Development http://wir.water.wa.gov.au

Waxman, M. H., & Smits, L. J. M. (1968). Electrical Conductivities in Oil-Bearing Shaly Sands. *Society of Petroleum Engineers Journal, 8*(02), 107-122. doi:10.2118/1863-A

Werner, A. D. (2010). A review of seawater intrusion and its management in Australia. *Hydrogeology Journal, 18*(1), 281-285. doi:10.1007/s10040-009-0465-8

Werner, A. D. (2017). On the classification of seawater intrusion. *Journal of Hydrology, 551*, 619-631. doi:10.1016/j.jhydrol.2016.12.012

Werner, A. D., Alcoe, D. W., Ordens, C. M., Hutson, J. L., Ward, J. D., & Simmons, C. T. (2011). Current Practice and Future Challenges in Coastal Aquifer Management: Flux-Based and Trigger-Level Approaches with Application to an Australian Case Study. *Water Resources Management, 25*(7), 1831-1853. doi:10.1007/s11269-011-9777-2

Werner, A. D., Bakker, M., Post, V. E. A., Vandenbohede, A., Lu, C. H., Ataie-Ashtiani, B., . . . Barry, D. A. (2013). Seawater intrusion processes, investigation and management: Recent advances and future challenges. *Advances in Water Resources, 51*, 3-26. doi:10.1016/j.advwatres.2012.03.004

Werner, A. D., & Simmons, C. T. (2009). Impact of sea-level rise on sea water intrusion in coastal aquifers. *Ground Water, 47*(2), 197-204. doi:10.1111/j.1745-6584.2008.00535.x

Wicks, C., & Herman, J. (1995). The Effect of Zones of High Porosity and Permeability on the Configuration of the Saline-Freshwater Mixing Zone. *Groundwater, 33*(5), 733-740. doi:doi:10.1111/j.1745-6584.1995.tb00019.x

Wilkinson, P. B., Loke, M. H., Meldrum, P. I., Chambers, J. E., Kuras, O., Gunn, D. A., & Ogilvy, R. D. (2012). Practical aspects of applied optimized survey design for electrical resistivity tomography. *Geophysical Journal International, 189*(1), 428-440. doi:10.1111/j.1365-246X.2012.05372.x

Winsauer, W. O., Shearin Jr, H., Masson, P., & Williams, M. (1952). Resistivity of brine-saturated sands in relation to pore geometry. *AAPG bulletin, 36*(2), 253-277.

World Health Organisation. (2011). Guidelines for drinking-water quality, 4th Edition. *WHO chronicle, 38*, 104-108.

Worthington, P. F. (1993). The Uses and Abuses of the Archie Equations .1. The Formation Factor Porosity Relationship. *Journal of Applied Geophysics, 30*(3), 215-228. doi:Doi 10.1016/0926-9851(93)90028-W

Wunderlich, T., Fischer, P., Wilken, D., Hadler, H., Erkul, E., Mecking, R., . . . Rabbel, W. (2018). Constraining electric resistivity tomography by direct push electric conductivity logs and vibracores: An exemplary study of the Fiume Morto silted riverbed (Ostia Antica, western Italy). *83*(3), B87-B103. doi:10.1190/geo2016-0660.1

Xu, Z., Bassett, S. W., Hu, B., & Dyer, S. B. (2016). Long distance seawater intrusion through a karst conduit network in the Woodville Karst Plain, Florida. *Scientific Reports, 6*, 32235. doi:10.1038/srep32235

Xu, Z., Hu, B. X., Xu, Z., & Wu, X. (2019). Simulating seawater intrusion in a complex coastal karst aquifer using an improved variable-density flow and solute transport–conduit flow process model. *Hydrogeology Journal, 27*(4), 1277-1289. doi:10.1007/s10040-018-1903-2

Xu, Z., Hu, B. X., & Ye, M. (2018). Numerical modeling and sensitivity analysis of seawater intrusion in a dual-permeability coastal karst aquifer with conduit networks. *Hydrol. Earth Syst. Sci., 22*(1), 221-239. doi:10.5194/hess-22-221-2018

Yoshikawa, T., Murata, O., Furuya, K., & Eguchi, M. (2007). Short-term covariation of dissolved oxygen and phytoplankton photosynthesis in a coastal fish aquaculture site. *Estuarine, Coastal and Shelf Science, 74*(3), 515-527. doi:https://doi.org/10.1016/j.ecss.2007.05.004

4 Borehole-based techniques and inversion constraints in Electrical Resistivity Imaging of the Seawater Interface using.

The underlying question from the data shown throughout this research is:

"Is there a way to improve the resolution of coastal hydrogeology from ERI?"

I address this question in two parts:

1. The application of inversion constraints to surface-based imaging
2. The use of boreholes-based ERI for imaging coastal hydrogeology

Inversion constraints in electrical resistivity imaging are a popular method of improving outcomes from resistivity imaging. I experiment with inversion constraints applied to electrical resistivity imaging of a shallow seawater interface over a clayey substrate. I demonstrate inversion outcomes using different electrode configurations, geometry, and inversion constraints including systematic application of '*a-priori*' data, smoothing constraints, and sharp boundary conditions.

Borehole-based imaging can overcome many of the shortcomings of surface-based methods. I demonstrate how borehole-based ERI can resolve the resistivity distribution of the mixing zone. This is not achievable with surface-based methods alone. I find that a combination of inversion constraints, such as location and resistivity of the substrate, together with multiple boreholes located proximal to the seawater toe can precisely recover the resistivity and geometry of the seawater wedge. The application of instrumented boreholes as a replacement tool for wireline logging is then discussed.

Outcomes from this chapter highlight the need for borehole-based electrical imaging systems in successful coastal seawater monitoring programs. This technology has the potential to replace and supplement existing monitoring techniques and generate significant volumes of cost-effective but highly valuable data.

This paper has been submitted to the Journal of Geophysical Research.

Precise Electrical Resistivity Imaging of the Seawater Interface Using Boreholes and Inversion Constraints

A. R. Costall[1]*, B. D. Harris[1], F. M. Wagner[2], C. Rücker[3]

1. Curtin University, Department of Exploration Geophysics
2. Institute for Applied Geophysics and Geothermal Energy, RWTH Aachen University, Aachen, Germany
3. Berlin University of Technology, Department of Applied Geophysics, Berlin, Germany

* Corresponding author; *alexander.costall@postgrad.curtin.edu.au*, ORC-ID: 0000-0001-7036-6110

Key Points

- We demonstrate how many strategies that are intended to improve recovery of formation conductivity distribution from inversion of ERI data at the seawater interface often fail to achieve the expected gains.
- We provide many examples demonstrating where solute concentration from conductivity distribution is not accurately recovered from surface-based ERI acquisition methods.
- We use numerical experiments to show that multiple targeted instrumented boreholes can resolve the precise electrical conductivity distribution of the seawater wedge at coastal margins.
- Our numerical experiments show that the combination of borehole-based and surface-based imaging applied with appropriate inversion constraints can recover the conductivity distribution of the entire seawater wedge.
- We show that cross-hole electrical resistivity imaging can be used to approximate the inland position of the toe even after the seawater wedge has moved beyond the instrumented boreholes.
- Our examples show that instrumented boreholes can be automated and used for precise time-lapse logging of electrical conductivity measurements along the borehole string.

Abstract

Knowledge of the geometry and solute concentration across the seawater interface at coastal margins is fundamental to answering the scientific questions concerning groundwater hydrodynamics in the transition between land and ocean. These data also function as input to predictive solute transport modelling that guide groundwater management practices and policy. Electrical resistivity imaging (ERI) appears to have the capacity to resolve both geometry and solute concentration of the seawater wedge and provide the necessary inputs for groundwater solute transport modelling.

Our research sets a counterpoint to the commonly held belief where enhancements in acquisition parameters, processing, and inversion constraints will guarantee improvement in precision and accuracy of ERI models. We explore the limits of surface-based ERI by systematically analysing various inversion strategies which are applied to synthetic ERI data over a known seawater wedge computed via numerical solute transport modelling. These modelling outcomes are linked with seawater interface geometries from a seawater intrusion monitoring well field. Our conclusion is that, regardless of the strategy deployed, significant differences persist between the correct resistivity distribution and that achievable by surface-based ERI of the seawater wedge.

The next stage of our research guides the way to a step change in the use of ERI for groundwater monitoring at coastal margins. We demonstrate that precise and accurate recovery of formation conductivity can be achieved: (i) along the vertical trace of individual instrumented wells, (ii) between instrumented wells, and (iii) across the entire seawater interface. It was only by combination of surface-based ERI, down-hole ERI, and specific inversion constraints, that accurate conductivity from within and across the seawater interface could be recovered. We find that down-hole measurements are needed to facilitate accurate interpretation of the geometry and solute concentration of the seawater wedge from ERI at coastal margins.

4.1 Introduction

The Earth's climate is changing. This has consequence for the lives of all people, but particularly so for those living on coastal margins. Here, shallow high-quality aquifers are an important source of water for people and the environment. Groundwater resource at coastal margins is vulnerable to seawater intrusion, which can cause long-term damage to local ecosystems and groundwater infrastructure.

Numerical groundwater modelling is sufficiently advanced to model the hydraulics and water chemistry of the near-shore environment. However, high-quality predictive models require high-quality data. Identifying the location of the seawater interface, and monitoring time-varying changes in the geometry or water chemistry, is a primary requirement for building and calibrating numerical models (Shoemaker, 2004; Werner *et al.*, 2013).

Electrical resistivity imaging (ERI) has the potential to recover the geometry and electrical conductivity seawater wedge. For A. Costall *et al.* (2018), while the existence of seawater intrusion was clear from ERI data; specific details such as the gradient of the wedge, the position of the toe, and the solute concentration could not be consistently or accurately defined. Beaujean *et al.* (2014) highlight the poor recovery of salt mass fraction (i.e., solute concentration) from within the wedge of saline water, even after using joint inversion of solute transport modelling and ERI data.

We suspect that outcomes from ERI in coastal margins can be improved by selection ERI inversion parameters and constraints. We then seek to answer a core question concerning electrical resistivity imaging along coastal margins:

> *"Is there a workable set of ERI acquisition and inversion parameters that can define the geometry and solute concentration distribution of the seawater interface in space and time?"*

It is reasonable anticipate to borehole-based imaging and inversion constraints may combined to yield better picture, but we found no clear answers to the above in existing literature.

A key part of the research is providing and representing experimental evidence for the limitations and proposed technological advances in imaging the seawater interface. The outcomes from many numerical experiments are represented in the main document which is accompanied by several appendices with supporting information and evidence. The research is organized as below:

1. Part 1: Background
    a. Groundwater modelling & conversion to electrical resistivity section
    b. Electrical Resistivity Imaging and Inversion
    c. Cross Borehole ERI
2. Part 2: Surface ERI Experiments with constraint and inversion variables
    a. Unconstrained inversion
    b. A-Priori data
    c. Sharp Boundary constraints
3. Part 3: Cross-well ERI Inversion
    a. Electrodes in the substrate
    b. Electrode spacing along the borehole
    c. Inversion outcomes from cross-borehole acquisition
4. Part 4: Combined surface and in-hole ERI with inversion constrains

4.2 Part 1: Background

4.2.1 Groundwater Modelling & conversion to electrical resistivity section

In this research, numerical modelling of groundwater flow and solute transport forms the basis of electrical resistivity models that are consistent with physics and chemistry of the seawater interface. Such transport models can be a powerful tool for managing groundwater resources and evaluating risk in groundwater management. We use the finite-element groundwater flow and solute transport software, FEFLOW (H.-J. G. Diersch, 2014) to simulate seawater intrusion into a shallow high-quality karstic aquifer.

Seawater intrusion fundamentally occurs due to density-dependent flow. Saline water is approximately 3% more dense than fresh water, which results in seawater driving below the outflowing fresh terrestrial groundwater. This flow results in the characteristic wedge shaped interface depicted throughout literature (e.g. Bear (2005); R. E. Glover (1959)). The specific geometry of the interface can change based on the distribution of hydraulic parameters and volume of groundwater discharging to the ocean.

Coastal margins can be a challenging environment for electrical resistivity surveying (A. Costall *et al.*, 2018). A primary objective for a hydro-geophysical survey of the coastal margin is to resolve the four distinct zones of electrical conductivity. These typically include (1) an unsaturated zone, (2) a freshwater zone, (3) a mixing zone, and (4) an impermeable substrate. Surveying in these environments can be difficult given the multiple high-contrast electrical boundaries found in this environment and rapid loss of imaging resolution with depth.

Figure 4.1 shows the solute transport model used to simulate electrical resistivity imaging data. It is modelled on a coastal karstic aquifer near Perth, Western Australia, and features a high hydraulic conductivity (200 m/d) homogeneous aquifer overlaying an impermeable resistivity substrate (e.g. A. Costall *et al.* (2018)). This hydrogeology is representative of many shallow coastal aquifer systems worldwide (Oiro *et al.*, 2019; Selley, 2000; Stuyfzand, 1992), and is based on a seawater intrusion monitoring site with multiple well controls and over 30 years of monitoring data. Here the toe of the seawater wedge is approximately 185 m inland from the shoreline; however, the seawater interface has potentially moved over 200 m inland since monitoring began in 1990. We examine this model later in this research.

In this model, the confining clayey substrate is set to a constant resistivity of 20 Ωm to simulate rapid landward movement of the saline water wedge over an impermeable layer, such as a low CEC clay (e.g. kaolinite). In this model, the substrate is saturated with groundwater of quality like that prior to seawater intrusion representing a resistive flat-lying feature. This situation is likely to have occurred along coastal margins of south-western Western Australia, where evidence suggests the saline water interface has move several hundred metres inland during the last 30 years of groundwater monitoring (A. Costall *et al.*, 2018; A. R. Costall *et al.*, 2020). The substrate may become saline over geological timescales as the highly saline groundwater permeates through the lower confining substrate beneath the seawater wedge.

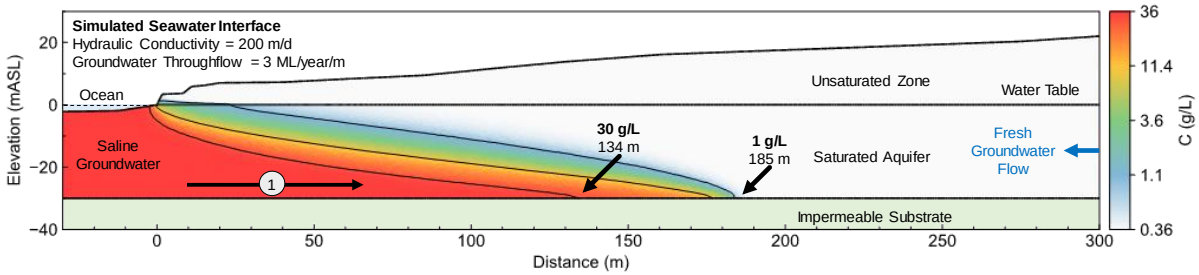

Figure 4.1: Image showing the solute concentration distribution for a baseline seawater interface scenario. This concentration distribution is from numerical simulation of a 200 m/day hydraulic conductivity aquifer with 3 ML/year of groundwater throughflow. The toe of the seawater interface in this example resides approximately 185 m from the shoreline. The full model extends to 700 m from the shoreline. This model represents a conventional seawater interface which includes an unsaturated zone, an aquifer saturated with a saline groundwater wedge intruding into fresh groundwater, and an impermeable substrate. The arrow marked with '1' shows the direction of movement of the seawater wedge above the substrate. The lateral movement of the seawater wedge is significantly greater than the downward movement of solutes through the impermeable substrate.

Numerical experiments and findings throughout this research are supported by a full library of code and reproducible modelling outcomes. The code was specifically written to convert 2D numerical solute transport data to an electrical resistivity imaging section using the near-linear relationships between salt concentration and water conductivity (Walton, 1989) and Archies law to convert from water conductivity to formation conductivity (Archie, 1941). This code is freely available online or from the author.

4.2.2 Electrical Resistivity Imaging and Inversion

Electrical resistivity imaging (ERI) is a geophysical method that measures the distribution electric field resulting from one or more charged electrodes. The electrical conductivity of the subsurface can be reconstructed using inversion modelling techniques. Common profiling techniques involve a combination of four-electrodes (i.e. quadrupoles) where two electrodes transmit a current and other pairs of electrodes measure voltage.

Synthetic acquisition array configurations and array geometry are defined using pyGIMLi (C. Rücker *et al.*, 2006; C. Rücker *et al.*, 2017). Many electrode configurations are possible, including user-defined inputs and borehole imaging. Two common arrays often used with modern simultaneous acquisition (multiple channel) systems are the multiple-gradient and dipole-dipole arrays, which are shown in Figure 4.2 (Dahlin *et al.*, 2004, 2006; M. H. Loke *et al.*, 2013).

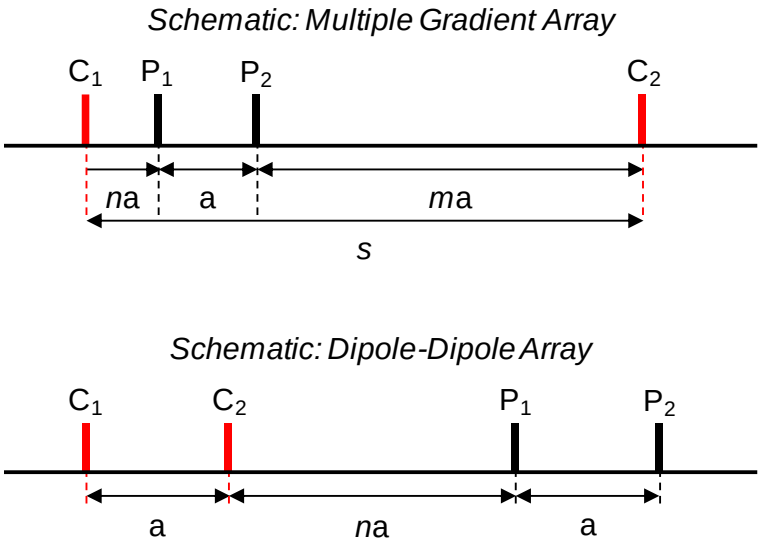

Figure 4.2: Schematic showing the arrangement of electrodes for multiple gradient array (top) and dipole-dipole array (bottom). Here, 'a' is the distance between potential electrodes (P_1, P_2); 'na' is the distance between the current electrode C_1 and nearest potential electrode P_1 expressed as a multiple of 'a'; 's' is the total distance between current electrodes.

'Optimized' arrays are becoming increasingly available as computing power increases and can be broadly categorized into two categories: (1) identify a set of electrodes and measurement combinations to maximize image resolution with the least possible measurements (M. H. Loke *et al.*, 2013; M. H. Loke, Wilkinson, Chambers, *et al.*, 2014), and (2) optimise placement of a set of electrodes with respect to a particular known target, for example borehole-based CO2 monitoring (Florian M. Wagner *et al.*, 2015). S. Uhlemann *et al.* (2018) show that a combination of the two methods can yield arrays with higher resolution than standard arrays while using fewer electrodes. Currently the algorithms used to generate such arrays are not readily available.

We use the 'Boundless Electrical Resistivity Tomography' (BERT) (Thomas Günther *et al.* (2019)) for inversion modelling. BERT is an inversion software library designed for academic use and has been used in many examples, ranging from deep borehole CO_2 monitoring applications (P. Bergmann *et al.*, 2014; Peter Bergmann *et al.*, 2012; Schmidt-Hattenberger *et al.*, 2011; Florian Michael Wagner, 2016), joint and constrained inversion of seismic and electrical resistivity methods (Ronczka *et al.*, 2017; Wunderlich *et al.*, 2018), ERI acquisition and inversion research (Bievre *et al.*, 2018; Doetsch *et al.*, 2010; Robbins *et al.*, 2018; Schmelzbach *et al.*, 2018), and frequency-dependent electrical measurements on trees for fungus detection (Martin *et al.*, 2013).

BERT uses a smoothness constrained Gauss-Newton scheme to invert ERI data (Carsten Rücker, 2010). The objective for the inversion is to fit a model vector $\boldsymbol{m} = (m_1, m_2, \dots, m_M)^T$ to a data vector $\boldsymbol{d} = (d_1, d_2, \dots, d_N)^T$ using a function f. The data functional (Φ_d) to be minimized is defined by

$$\Phi_d(m) = \sum_{i=1}^{D} \left| \frac{d_i - f_i(m)}{\varepsilon_i} \right|^2 = \left\| D\big(d - f(m)\big) \right\|_2^2 \text{ where } D = diag\left(\frac{1}{\varepsilon_i}\right) \quad (1)$$

Regularisation is imposed by an additional model functional (Φ_m), weighted by the regularization parameter λ which yields

$$\Phi(m) = \Phi_d + \lambda \Phi_m \rightarrow \min \quad (2)$$

Here, Φ_m is a squared norm of a product of a constraint matrix (**C**) and the difference between the model (**m**) and reference model ($\boldsymbol{m^0}$)

$$\Phi_m(m) = \|C(m - m^0)\|_2^2 \quad (3)$$

The full equation includes the error-derived data weights ($\boldsymbol{W_d}$), the constraint weight matrix ($\boldsymbol{W_c}$), the model control matrix ($\boldsymbol{W_m}$), and the cell interdependence matrix ($\boldsymbol{C}$)

$$\Phi(m) = \phi_d + \lambda\phi_m = \|W_d(d - f(m)\|_2^2 + \lambda\|W_m C W_C(m - m^0)\|_2^2 \quad (4)$$

Smoothness constraints (i.e. regularization) in geophysical inversion limit generation of model structure (i.e. 'unnatural' or 'non-geological' changes) (Thomas Günther, 2004). The regularization parameter λ weights the model constraints Φ_m against the data misfit Φ_d. The regularization parameter must be appropriate for the data, else over-fitting or under-fitting will occur (Meju, 1994; Menke, 2012c; Vogel, 2002).

In addition to the regularization parameter, customization of the smoothness matrix **C** can affect inversion outcomes. Below we discuss the 'first order', 'second order', and 'zeroth order' schemes. Combinations of these constraints are also possible (Carsten Rücker, 2010).

(i) A '**first-order'** smoothness constraint restricts the rate-of-change of variables in the reconstructed model (i.e. the smoothness). The Occam-style inversion (S. C. Constable *et al.*, 1987) is one example of this constraint.
(ii) A '**second-order'** imposes restrictions on the spatial derivative of the first-order constraint (i.e. the curvature) (Saunders *et al.*, 2005).
(iii) The **zeroth-order** restricts deviation from the reference model by only minimising the norm of the model difference (i.e. deviation from the start model) (Carsten Rücker, 2010).

Electrical resistivity imaging based on inversion can be completed with a broad range of strategies and parameters. These can be implemented globally, or to specific model domains where credible data exists such as from geophysical methods or borehole lithology logs (Carsten Rücker, 2010; Wunderlich *et al.*, 2018), (P. Bergmann *et al.*, 2014; Thomas Günther *et al.*, 2019; Hellman *et al.*, 2017; Ronczka *et al.*, 2017; Carsten Rücker, 2010; J. Y. Zhou *et al.*, 2016)). Strategies can permit or favour rapid changes in electrical conductivity at known geo-electrical boundaries, which may counter the effect of regularization (i.e. smoothing) to produce models that are consistent with known geology. However, the extent to which this is true or achievable in practice needs to be examined for the saline water interface.

Including specific inversion constraints could guide the models generated by inversion of ERI data towards a model which conforms with the 'true' subsurface conductivity distribution. We assess outcomes from applying various inversion constraints including:

(1) Starting resistivity (e.g. an a-priori resistivity distribution)
(2) Constraint type (e.g. first, second, or zeroth order)
(3) Relative smoothing factor (e.g. lambda λ relative to the global smoothing factor (see equation 2)),
(4) Vertical constraint weighting (e.g. preferential smoothing in vertical or horizontal plane),
(5) Upper and lower resistivity bounds (e.g. limit the range of resistivity values)
(6) Inter-region constraints (e.g. continuity across boundary).

4.2.3 Cross Borehole ERI

Cross-borehole techniques can generate high-resolution imaging at depths beyond the reach of surface-based arrays (Coscia *et al.*, 2011; W. Daily *et al.*, 1991; M. Loke, 2016; M. H. Loke, Wilkinson, Chambers, *et al.*, 2014).

Cross-borehole ERI has been used for deep imaging applications, such as CO_2 storage and sequestration (Hagrey, 2011; Schmidt-Hattenberger *et al.*, 2011; Florian Michael Wagner, 2016; F. M. Wagner *et al.*, 2015), and shallow applications, such as groundwater level and quality monitoring (Coscia *et al.*, 2011; Michael Grinat *et al.*, 2018; M Grinat *et al.*, 2010).

Time-lapse seawater intrusion imaging often uses surface-based arrays due to the ease of mobility and deployment (de Franco *et al.*, 2009; Garcia-Menendez *et al.*, 2018; Sutter *et al.*, 2017). Long-term borehole-based ERI monitoring systems can generate high-quality resistivity data but must be specifically designed to withstand high pressures and saline environments (Kuras *et al.*, 2009; Ogilvy *et al.*, 2009; Palacios *et al.*, 2019).

In-hole electrical resistivity imaging can present many additional and useful combinations of electrodes to measure the electrical field at various locations and angles when compared against surface-based measurements. Figure 4.3 shows some electrode configurations, including cross-borehole, single-borehole-to-surface and dual-borehole-to-surface examples. Although imaging that includes a single borehole and surface-based electrodes can provide some increase to resolution at depth (P. Tsourlos *et al.*, 2011; Florian M. Wagner *et al.*, 2013) multiple boreholes are required to generate high-resolution data at depth. The distance between boreholes in cross-well imaging is a significant factor in the quality of inversion outcomes and according to (LaBrecque *et al.*, 1996) this distance is ideally less than 75% of the instrumented borehole length.

Cross-borehole configurations can be arranged such that current or potential poles or dipoles are located on either or both boreholes. This results in many additional configurations that can provide data about the subsurface compared to surface-only arrays. However, not all combinations are practical or contributed significantly to imaging outcomes, for example the array shown in Figure 4.3B is highly susceptible to noise contamination (Bing *et al.*, 2000). As a result, cross-hole imaging is an active area of research for array optimisation (Leontarakis *et al.*, 2012; M. H. Loke, Wilkinson, Chambers, *et al.*, 2014; Wilkinson *et al.*, 2006).

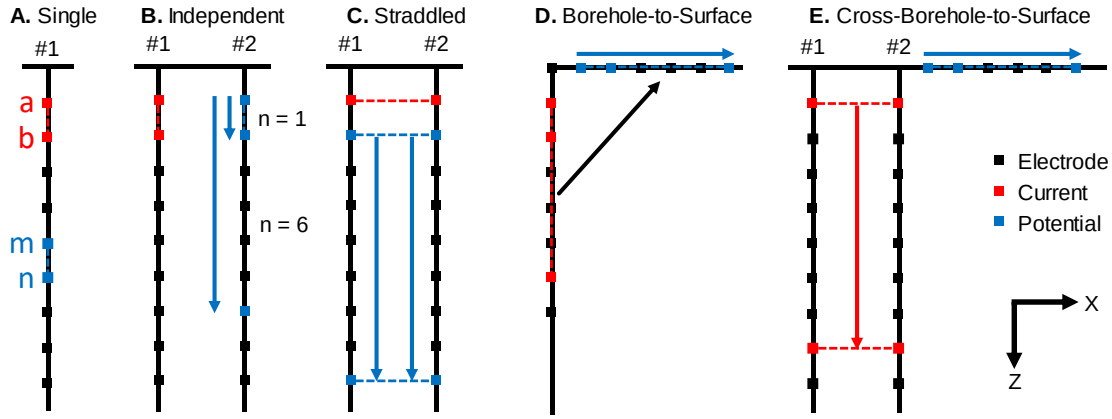

*Figure 4.3: Schematic of possible borehole-based electrode array configurations. The left-most image (A) shows a single borehole arrangement (Harris et al., 2019). Image **B** shows cross-borehole array with independent 'C' (i.e. A, B electrodes) and 'P' (i.e. M, N electrodes) dipoles (left). Many of the independent quadrupoles have high geometric factor and are filtered (e.g. Bing et al. (2000); Sasaki (1992)). Image **C** shows a cross-borehole array with 'straddled' C and P dipoles (right). Image **D** shows a single borehole-to-surface configuration (e.g. P. Tsourlos et al. (2011)). Image **E** shows a dual-borehole-to-surface configuration.*

4.3 Part 2: Surface-based ERI experiments with constraints and inversion variables

4.3.1 What are the limits of unconstrained inversion?

Unconstrained inversion is a common starting point for any electrical resistivity imaging. We first demonstrate outcomes from unconstrained inversion with the dipole-dipole and multiple-gradient configurations (see Figure 4.2). A comparison of mesh refinement can be found in Appendix A.2.

Figure 4.4 shows the outcomes from unconstrained inversion of the two arrays. The electrodes are spaced at 5-meter intervals, with 101 electrodes in total, starting at 0 m from the shoreline and extending to 500 meters inland from the shoreline. Appendix A.3 contains experiments showing the impact of electrode spacings on inversion outcomes. For our model, we find that electrode spacing larger than 10 m significantly degrade imaging outcomes, while electrodes spaced at less than 5 m did not improve the key outcomes. Each of the arrays converge to the 5% simulated noise level ($\chi^2 \approx 1$). For each of these inversions, the damping parameter (λ) is set to 20.

It may seem intuitive that more measurements would improve inversion outcomes. For ERI, this may not be the case. Here we experiment with comprehensive arrays, with limitations placed on the maximum geometric factor. These include many additional quadrupoles compared to the 'standard' array configurations. Appendix A.1 contains further details of array creation. We compare these outcomes based on the recovery the hydrogeology of the forward model. That includes the (i) the conductivity of the body of the seawater wedge, (ii) the shallow near-shore formation conductivity, (iii) the location of a confining substrate, and (iv) the position of the saline water toe.

Figure 4.4 shows the outcomes from the unconstrained inversions. Comparison of each panels indicates that there are no advantages to increasing the number of measurements in brute-force manner. The outcomes from the comprehensive arrays are, at best the same as less-dense arrays, and at worst, provide poorer outcomes. We use the standard multiple-gradient as a practical basis for further experiments; however, the position of the seawater toe and the extent of the mixing zone remain unclear. Note the resistivity of the seawater wedge is poorly recovered when compared to the forward model. Accurate recovery of the resistivity of this area is a key outcome for comparison with numerical solute transport modelling and needs to be improved.

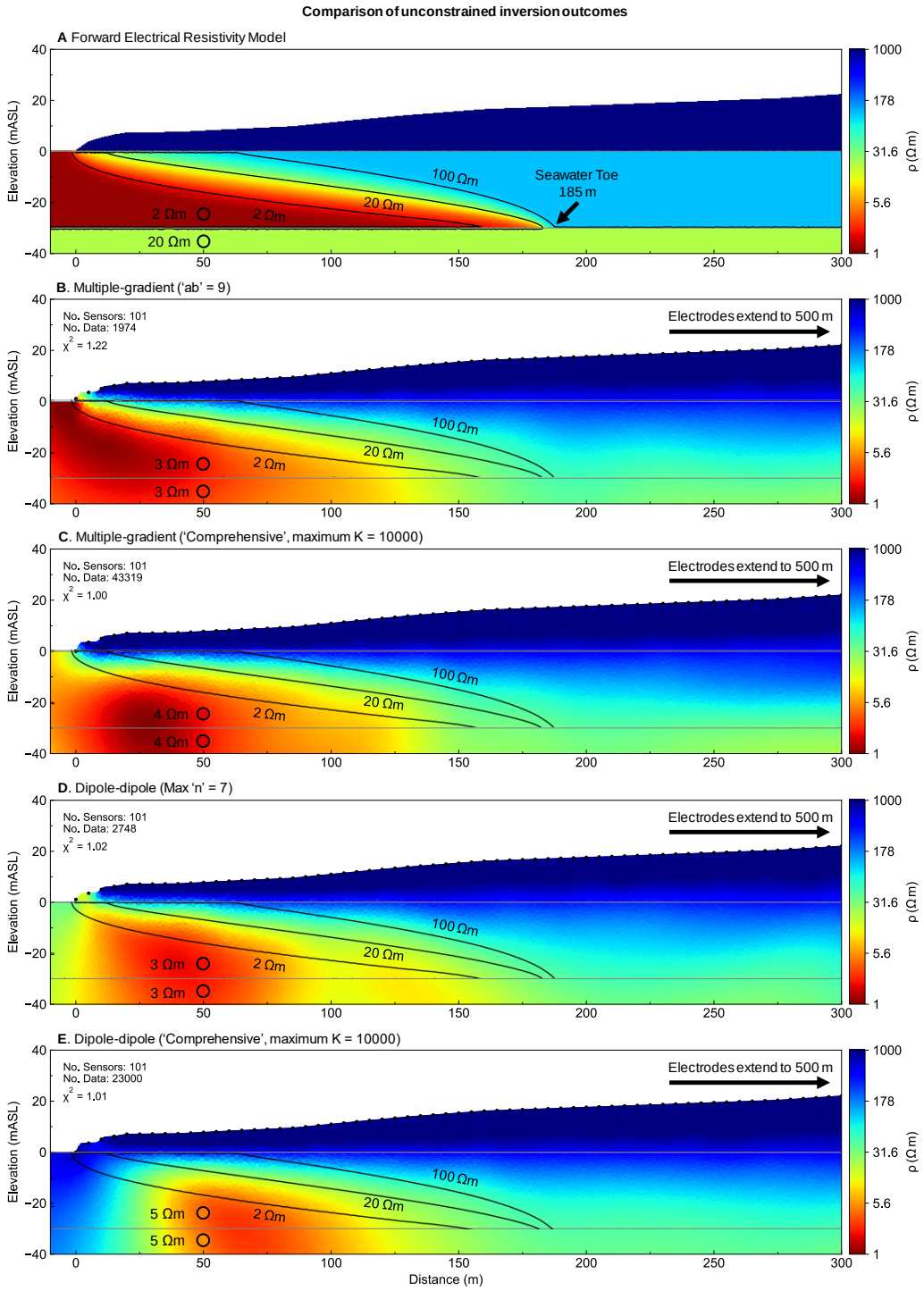

*Figure 4.4: Set of images showing the outcomes of unconstrained inversion using different electrode configurations for an electrical resistivity model of a seawater interface. Panel **A** shows the forward electrical model, Panel **B** shows the outcomes from a standard multiple gradient array, Panel **C** shows outcomes from an expanded multiple gradient array, Panel **D** shows a standard dipole-dipole, and Panel **E** shows an expanded dipole-dipole. Our set of images demonstrates that simply including extra measurements does not guarantee superior imaging outcomes. Labelled dots indicate the resistivity of the saline aquifer and substrate beneath for a point located within the body of the seawater wedge. Note that the resistivity of the wedge is poorly defined when compared to the forward model in each of these cases, particularly for the substrate beneath the seawater wedge and resistivity near the seawater toe. Accurately recovering the resistivity of the seawater wedge is fundamental to determine the salinity of the groundwater and is a key aspect we seek to resolve through this research.*

4.3.2 Does a-priori data help?

A-priori ('*from the earlier*' or, '*known before*') data has been an effective way to guide inversion outcomes towards one model. Historical applications are associated with potential field data (Boulanger *et al.*, 2001; Guillen *et al.*, 1984; Lines *et al.*, 1988; PEDERSEN, 1979), and is crucial in airborne EM inversion (Ellis, 1998). Seed models in electrical resistivity imaging have historical significance (POUS *et al.*, 1987), but are not commonplace in modern inversion workflows.

Today, ERI inversion algorithms tend to start from a homogeneous or layered half-space (Auken *et al.*, 2004; M. H. Loke *et al.*, 2013; Rubin *et al.*, 2006; C. Rücker *et al.*, 2017). This may lead to questions of end-member model complexity following damped and smoothness constrained inversions. We demonstrate the impact of a-priori data using (1) a simplified representation of the seawater wedge, (2), a full representation of the seawater wedge, and (3) a well-constrained substrate layer.

4.3.3 What are the impacts of a simple a-priori seawater wedge?

The seawater interface is a consistent feature throughout the coastal margin. It may seem sensible to include an approximation of the seawater wedge into our inversion as a starting model. Here we use a starting model that includes vadose zone, clayey substrate, freshwater saturated aquifer, and a simplified conductive seawater interface. The shape of the simplified seawater wedge is based on sharp-interface analytical approximations e.g. R. E. Glover (1959). The goal of this experiment is to demonstrate whether including a-priori information can better resolve the geometry and resistivity of the seawater wedge than unconstrained inversion.

Figure 4.5 shows the outcome from an inversion using the simplified forward model described above. There are minimal differences between this model (Figure 4.5C), and the unconstrained inversion model (Figure 4.5B). This suggests that a pre-defined starting model offers no advantage over a homogeneous half-space for this electrical setting.

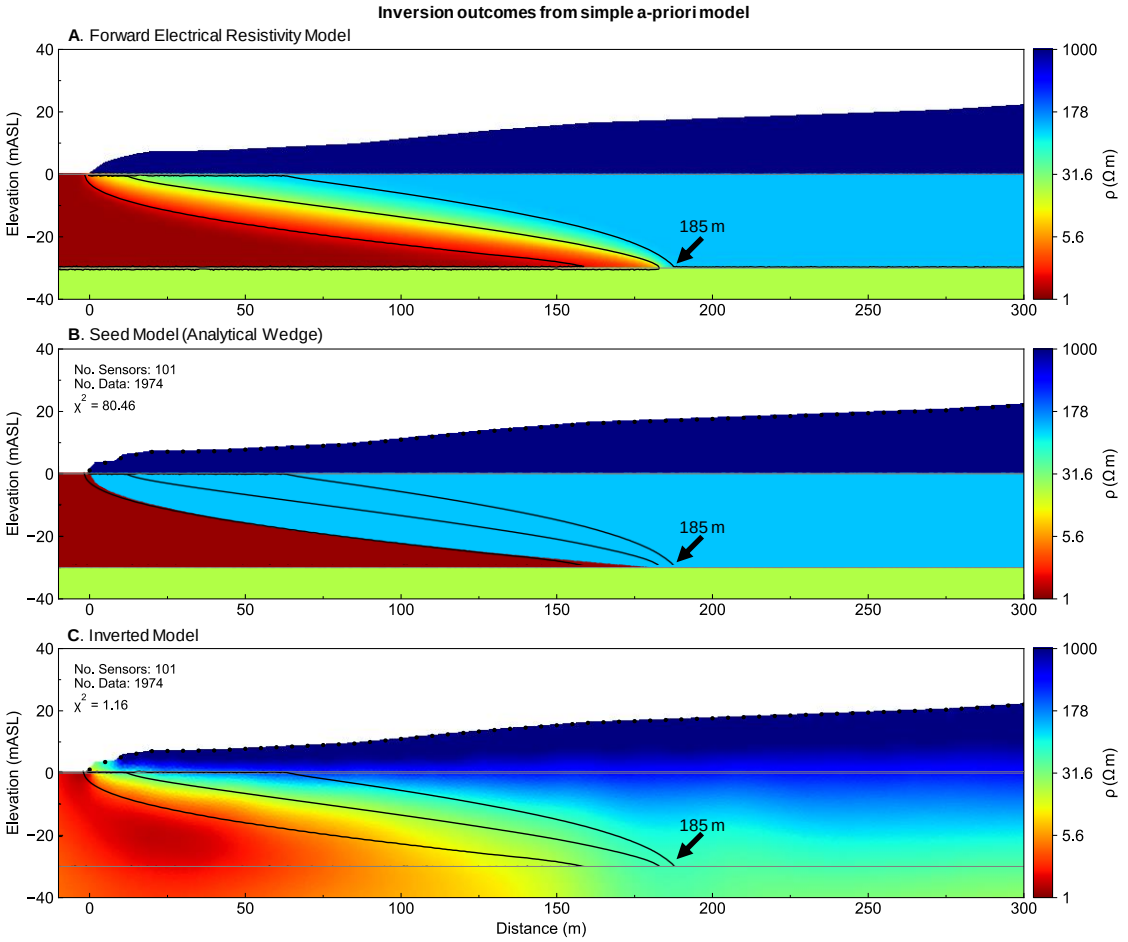

*Figure 4.5: Set of images showing the outcome from inversion given a simplfied electrical resistivity seed model which consists of a resistive unsaturated zone, a impermeable substrate, and a wedge of conductive seawater intruding into an aquifer containing fresh high-quality groundwater. Panel **A** shows a forward resistivity model resulting from solute transport modelling that includes a solute mixing zone. Panel **B** shows the simplied forward seed model, which approximates the mixing zone to a sharp boundary. Panel **C** shows the inverted resistivity model after supplying the simplified seed model as a starting model. This outcome is near-identical to the outcomes from a homogeneous halfspace, suggesting that the simplified seed model has no apprent influence on the outcomes of this inversion.*

4.3.4 Does a-priori data have any impact at all?

The result shown above question whether including forward models have any impact on the inversion outcome. Figure 4.6 shows the outcomes of inversion using a 'perfect' seed model. The outcomes from this inversion are very similar to the original input model. Some small but unsurprising differences exist in the shallow ocean-side area where sensitivity is typically very low. A key outcome from this experiment is that the inversion outcome will not unnecessarily smooth the forward model at sharp boundaries given a high-quality starting model. However, such high-quality starting models are rarely possible to supply in a field-based acquisition.

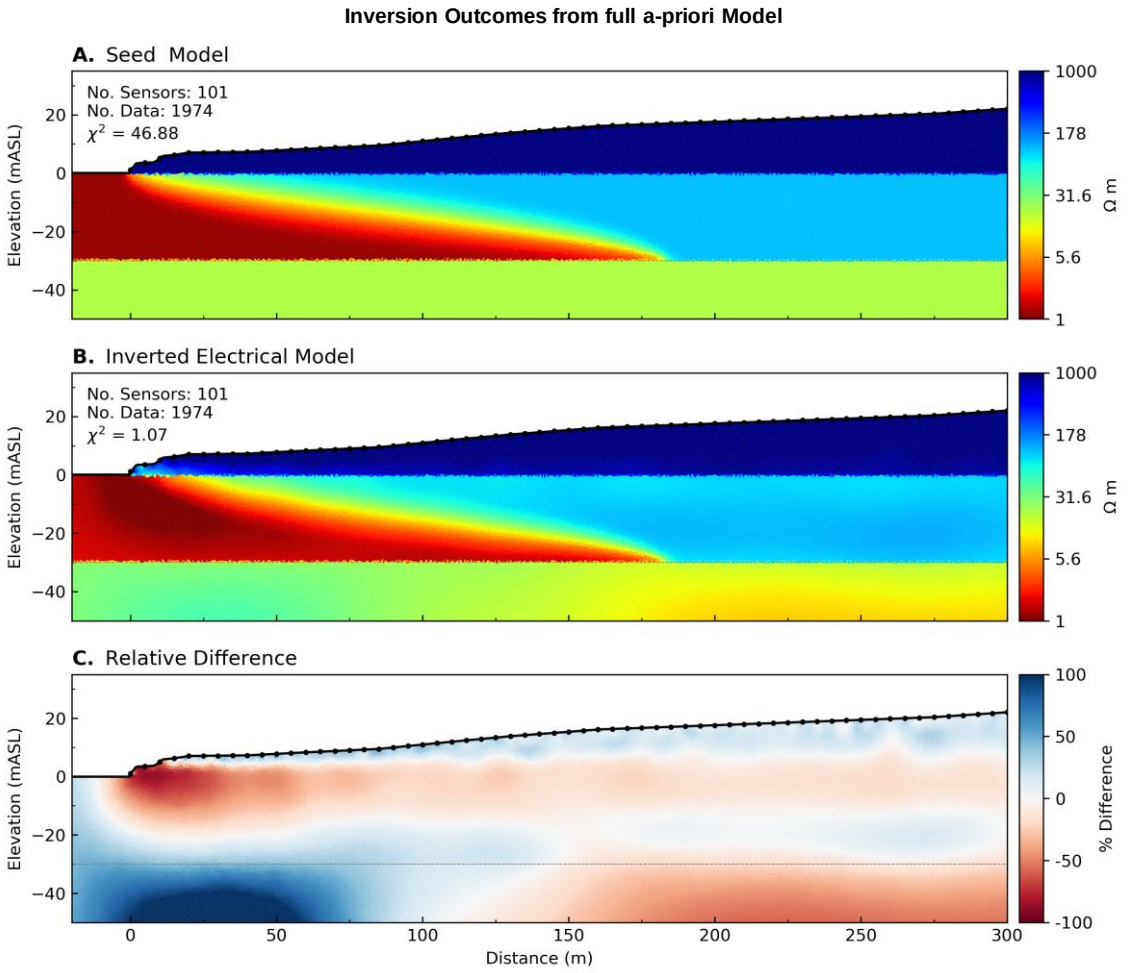

*Figure 4.6: Images showing the outcome from an inversion supplied with perfect a-priori data based on the solute transport model. Panel **A** shows the forward resistivity model calculated from solute transport modelling, Panel **B** shows the inverted resistivity model using the perfect seed model as a starting and reference model, and Panel **C** shows the percent difference between the forward and inverted models resistivity distributions. The greatest differences exist in the substrate located directly below the seawater wedge, and in the cliff edges nearest the ocean. Note the resistivity within the seawater wedge is lower in the inverted model than in the seed model (i.e. also the forward model), could result in significant over-estimation of solute concentration in the wedge. These images show that the inversion outcome does not force smooth boundaries given a high-quality starting model. Our example above shows that while the shape of the wedge is broadly correct from imaging there remains significant error in electrical resistivity distribution. This is a weakness in surface ERI imaging that we seek to resolve.*

4.4 What happens if we force a uniform substrate?

The ability to define the position and resistivity of a lower substrate is a valuable outcome for hydro-geophysical methods applied at coastal margins. However, accurately imaging the substrate is challenging for unconstrained ERI inversion (see Section 4.3.1). Although depth to substrate may be established at a regional scale from drilling data, the resistivity is often not constrained. Integrating depth and resistivity information into the inversion workflow may improve the definition of the seawater wedge from ERI. This assumption needs to be tested.

Our numerical experiments thus far, has used a first-order constraint, which limits the rate of change of resistivity during inversion (see Section 4.2.2). Here we will use a zeroth order constraint, which restricts change of the model away from selected regions of the initial or starting model.

Figure 4.7 shows the impact of changing the initial value for constrained inversion in the substrate region. Here we assign the substrate region to a zeroth order constraint and analyse the impact of assigning: (i) the correctly value substrate resistivity of 20 Ω m, and (ii) incorrect substrate resistivity values of 10 Ω m and 30 Ω m. These values are reasonable for a saturated low cation-exchange capacity clayey substrate (A. Costall *et al.*, 2018; Kibria *et al.*, 2019).

Figure 4.7B shows that, by including the correct location and resistivity of the substrate, the resistivity and geometry of the seawater wedge can reconstruct the initial forward resistivity model significantly better than any previously shown inversion. This outcome shows improvements in the definition of the shallow seawater wedge, particularly in the high conductivity saline areas and shallow mixing zone. However, there is still significant uncertainty in the location of the toe.

Figure 4.7A and Figure 4.7C show some of the potential drawbacks of forcing the inversion to adhere to a consistent, but incorrect resistivity. This has a direct consequence on the geometry of the seawater interface. Setting the value too high (30 Ω m) moves the toe landwards, while setting it too low (10 Ω m) moves the toe backwards, towards the ocean. Using identical parameters and data, setting the substrate too low (e.g., Figure 4.7A) appears to introduce further artefacts into the inversion outcome.

It is important to consider the percentage difference compared to absolute difference. Here we force the substrate to be 10 Ω m +/- the correct value, i.e., an absolute difference. However, this is also the difference between a substrate forced to be 0.5x the correct value, versus 1.5x the correct value. This may result in the greater percentage difference being a greater influence on the inversion outcomes, as shown in Figure 4.7A.

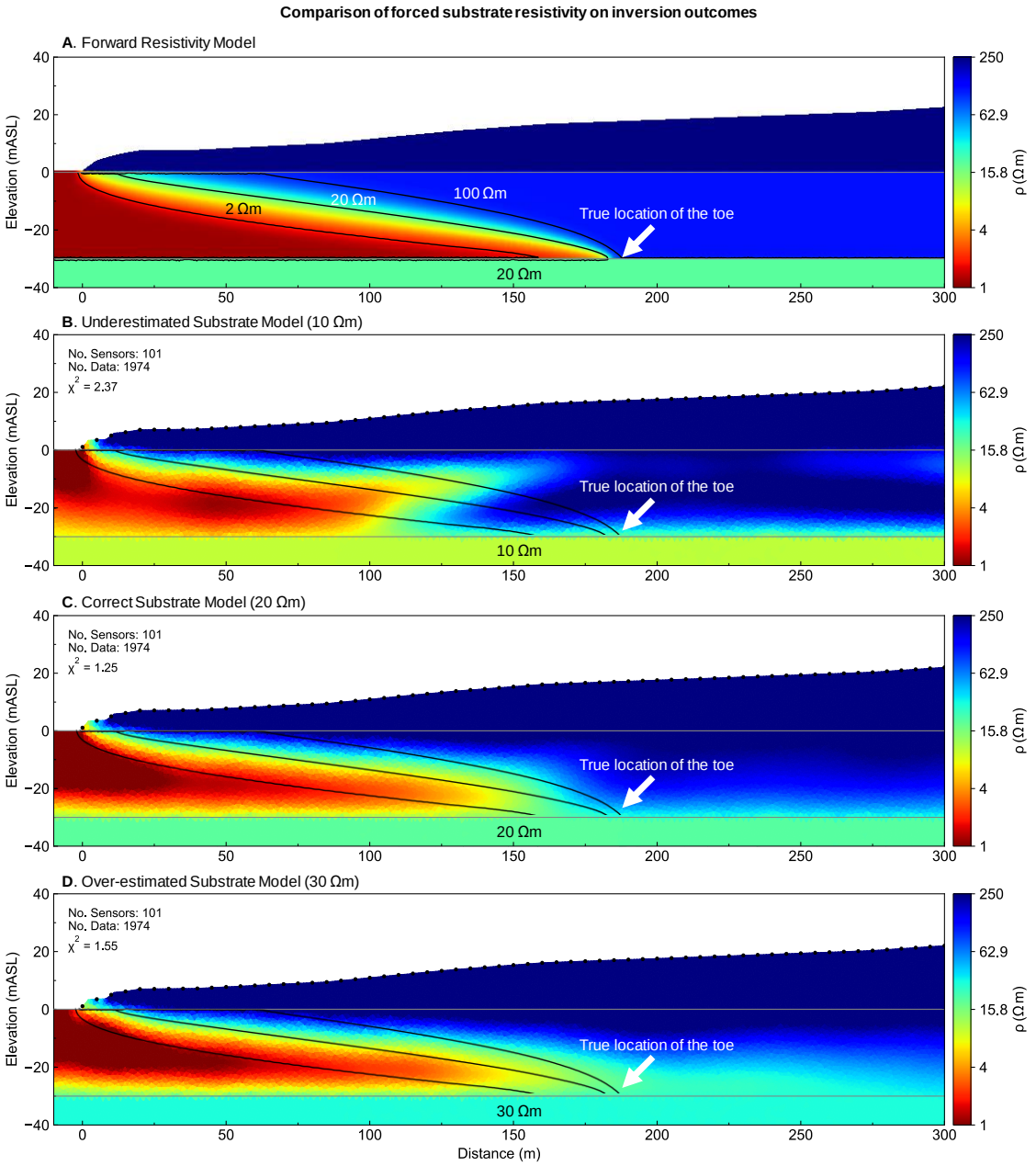

Figure 4.7: Set of images comparing outcomes for three different substrate resistivity values using a zeroth-order constraint which prevents deviation from the assigned resistivity. The substrate is set to (A) 10 Ωm (lower than the forward model), (B) 20 Ωm (the same as the forward model) and (C) 30 Ωm (higher than the forward model). Setting the substrate lower than the correct value results in the toe of the seawater wedge moving seaward, and the resistivity of the seawater wedge becoming higher, and vice versa for setting the substrate higher than the correct value. This set of images highlights the impact of incorrectly setting the substrate resistivity and reinforces the need for high quality constraints.

4.5 How effective are sharp boundary constraints at the seawater wedge?

Geophysical inversion requires a smoothing constraint which prevents generation of excessively 'structured' outcomes. As a consequence, this process may overly smooth areas with sharp geo-electrical transitions (S. C. Constable *et al.*, 1987; deGroot-Hedlin *et al.*, 1990). Explicitly defining the smoothing constraint between cells where sharp transitions allows for the has proven effective for recovering the electrical properties of between boundaries (P. Bergmann *et al.*, 2014; Coscia *et al.*, 2011; Ronczka *et al.*, 2017; Ronczka *et al.*, 2015).

Figure 4.8 shows the outcomes from inversion after systematically increasing the smoothness constraints at known high-electrical-resistivity boundaries. These boundaries exist at the water table (z = 0 m, $\Delta\rho = 1000/100$) and the lower confining substrate (z = -30 m, $\Delta\rho = 100/20$). We show outcomes from a sharp boundary with (i) no smoothness constraint (Figure 4.8B), (ii) 20% smoothness constraint (Figure 4.8C), (iii) 40% smoothness constraint (Figure 4.8D) and (iv) 100% smoothness constraint (Figure 4.8E). The last image is identical to unconstrained inversion as there are no changes to the smoothness characteristics across boundaries. All inversion outcomes converge to the simulated noise levels (e.g. $\chi^2 \approx 1$).

Appendix A.4 contains further experiments sharp boundaries located at the incorrect depths, and the impact of placing sharp boundaries on a single high-contrast boundary.

A surprising outcome is that forcing both sharp boundaries into the inversion process significantly degrades recovery of the geometry of the seawater wedge (e.g. Figure 4.8B). The resistivity distribution suggests that the 'wedge' shape has become laterally distributed within the aquifer. As the smoothness constraint is increased, the wedge returns, at the expense of boundary definition.

This experiment highlights the potential for misleading representations of the seawater wedge. We do not see a significant improvement in the definition of the wedge geometry by including these boundary constraints. Including these boundaries may be merited where the layers are well constrained and the inversion can benefit from higher resolution imaging, such as in the very-near surface or from borehole-based solutions. However, in the example shown, there is no appreciable improvement to the outcomes of surface-based ERI after including these constraints.

We have shown that, even if inversion constraints are included, there is still considerable room for interpretation in the inland position of the seawater toe. There is a need for a new approach able to precisely recover the seawater toe. Surface-based ERI is unlikely to provide the direct parameters required for groundwater modelling. This leads to investigation of the imaging potential of integrating surface and in-hole ERI data. We consider possible configuration with a view to discovering a practical solution for accurate recovery of slope, toe position and accurate resistivity distribution (i.e. for correct recovery of solute concentrations) of the seawater wedge.

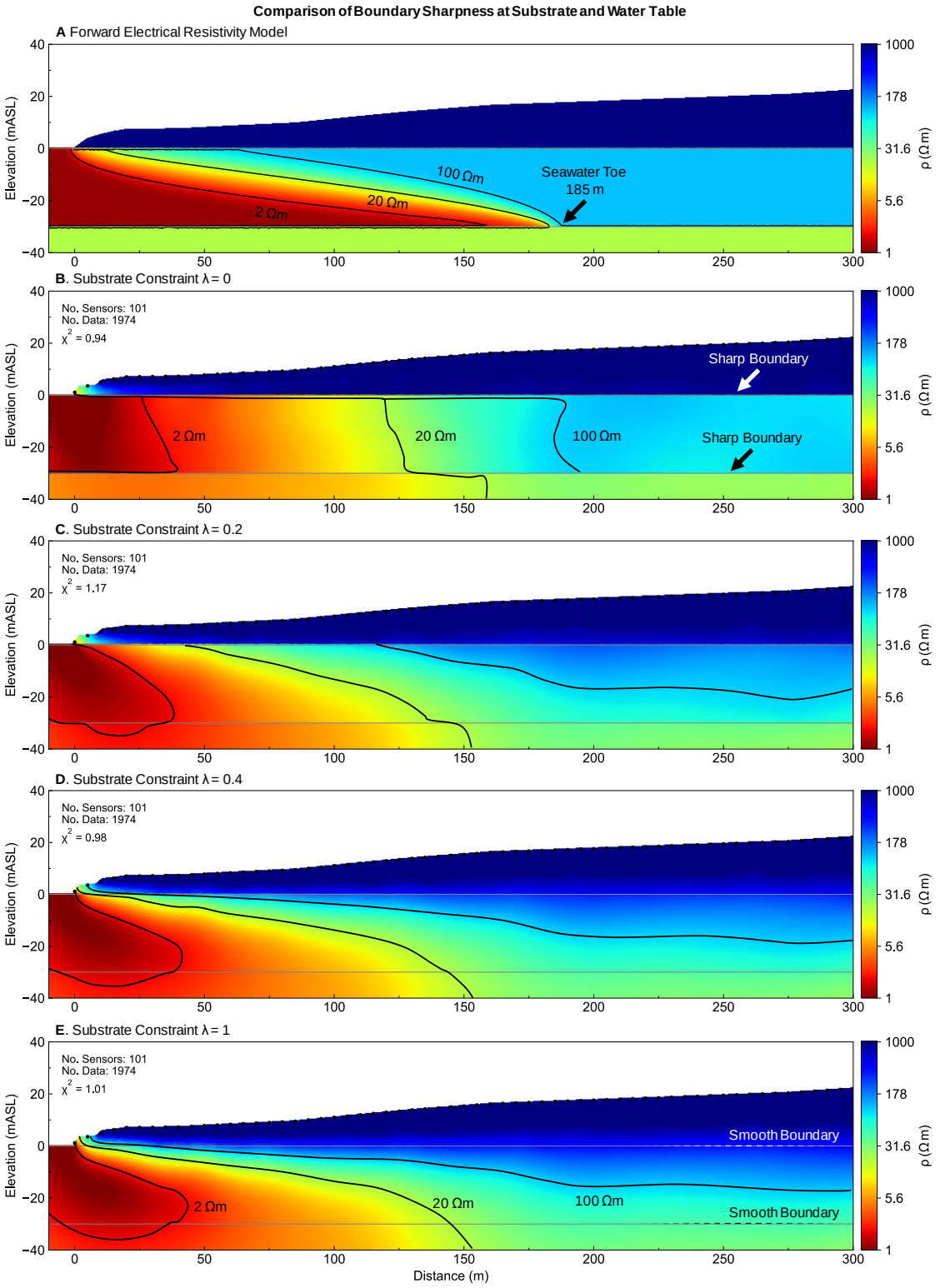

*Figure 4.8: Image showing inversion outcomes after systematically increasing the smoothness constraints across the high-contrast boundaries located at the water table and confining substrate. Panel **A** shows the forward resistivity model, indicating the correct resistivity values. Panels **B** through **E** systematically increase the smoothness constraint across the boundaries which results in smoother models. Panel **E** is identical to unconstrained inversion. Note that forcing sharp boundaries results in an apparently near-vertical mixing zone (Panel A). Even if accurately placed, sharp boundary constraints offer minimal benefit over unconstrained inversion for resolving coastal hydrogeology*

4.6 Part 3: Cross Well ERI-- Borehole-Based Imaging of the Seawater Interface

We consider two primary applications for borehole-based seawater intrusion monitoring and imaging. The first is when the position of the seawater toe is approximately known, and boreholes are placed in an optimal location to monitor the movements of the toe. The second is when the boreholes have been in-place for a period long enough for the seawater interface to move significantly further inland, and beyond the area of optimal imaging.

Figure 4.9 shows the solute distribution that represent each of these outcomes. The top image is the model shown earlier in Figure 4.1, where the seawater toe resides at 185 m from the shoreline. The bottom panel shows the solute distribution for a lower flow rate, where the seawater toe resides at 319 m. Here the position of the seawater wedge has doubled compared to the first model. We will examine ERI for this low throughflow model in the below and later in the discussion.

These two models demonstrate an extreme change in the position of the seawater toe, and are included here to examine the resolution of the seawater toe (e.g. Figure 4.9A) and the mixing zone (Figure 4.9B). In these examples, the position of the simulated cross-well electrical resistivity imaging survey is between the two wells located at 150 m and 175 m from the shoreline. We simulate boreholes that are 25 m apart, and are instrumented from 5 m above sea level (ASL) to -35 m ASL, for a total instrumented length of 40 m. The ratio of the distance between boreholes and the length of the instrumented borehole is therefore within suggested guidelines (LaBrecque *et al.*, 1996).

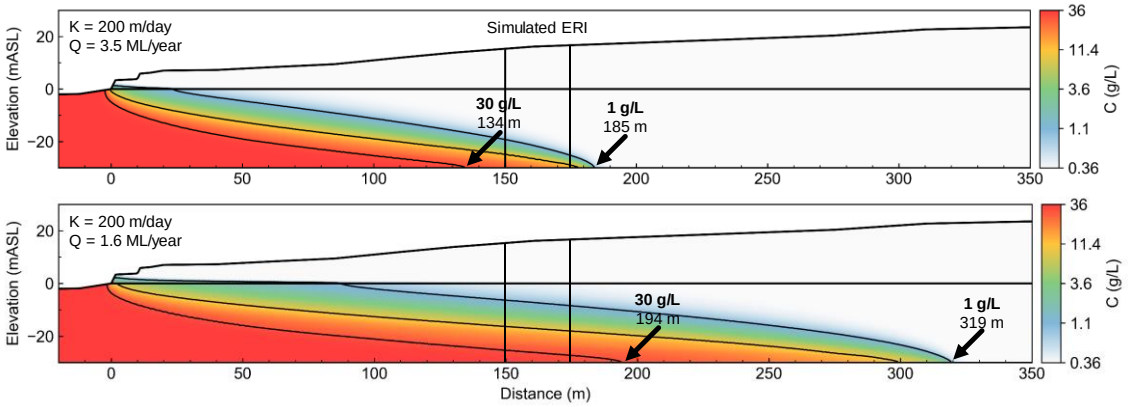

*Figure 4.9: Cross-section showing a seawater interface model where the groundwater throughflow has been reduced from 3.2 ML/year shown (**top**) to 1.6 ML/year (**bottom**),. The position of the toe has moved inland from 185 m to 320 m as a result. The location of two boreholes used for simulating cross-well ERI outcomes are shown on each panel. The boreholes are located to capture the greatest change in the geometry of the seawater wedge.*

There are practical aspects that need to be considered with any instrumented borehole. The positioning and density of electrodes are fundamental to borehole imaging. Two questions that may be common are:

1) "*How deep do the electrodes need to be*", and
2) "*How far apart do the electrodes need to be*".

4.6.1 Electrodes within the substrate

We find that placing electrodes in the substrate is critical to resolving the resistivity of the clayey substrate layer. A further advantage is that the depth to the substrate, and the material of the substrate can be explicitly determined. Figure 4.10 shows a comparison of borehole electrodes located within the substrate (left), and atop the substrate (right). Both inversions converge to the estimated error (i.e., $\chi^2 \approx 1$). As shown earlier, even small differences in the resistivity of the constrained substrate can affect imaging of the seawater wedge. Placing electrodes into the substrate provides a way to measure the resistivity of this layer with application for constrained inversion.

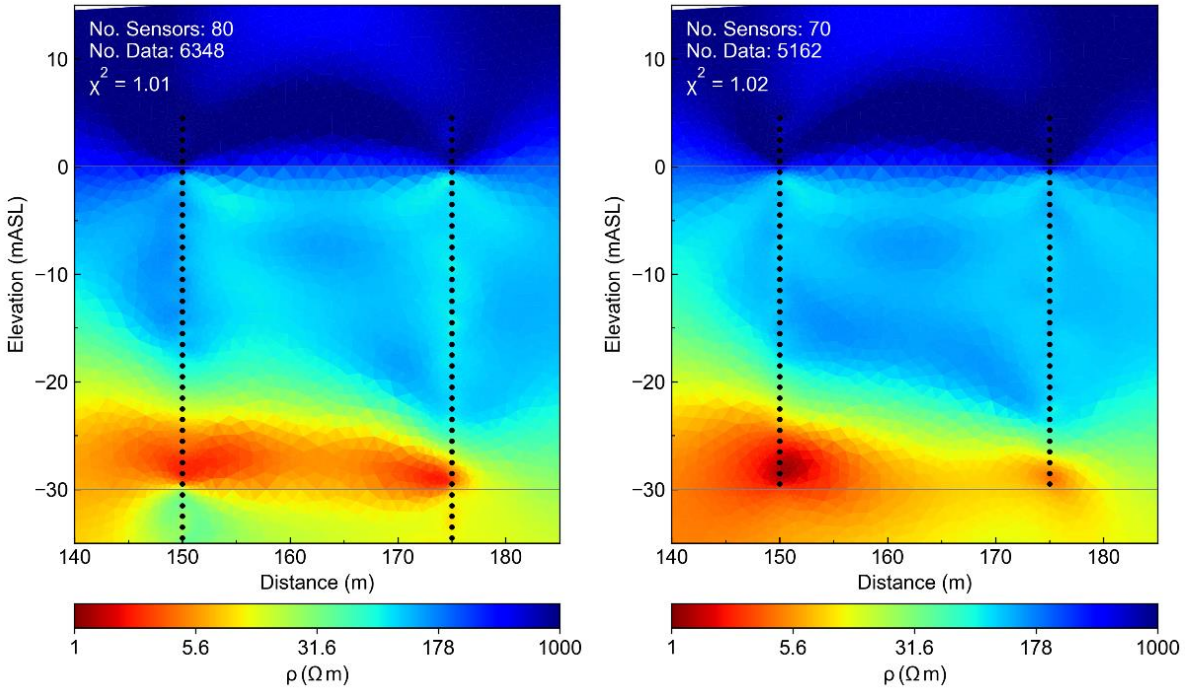

*Figure 4.10: Images showing the inversion outcome from a cross-borehole imaging arrangement where the electrodes penetrate into the substrate (**left**) and stop above the substrate (**right**). The resistivity of the substrate is only resolved when the electrodes are located within the substrate, which can also be used for as a constraint for inversion.*

4.6.2 Borehole Electrode Spacing

The field setup required for borehole imaging requires design of specific infrastructure and instrumentation for extended monitoring periods in challenging environments. Two key considerations when planning the instrumented boreholes are: (i) the distance between boreholes (i.e., inter-well resolution), and (ii) the distance between electrodes (i.e., along-well resolution).

Figure 4.11 shows the effects of reducing the electrode spacing along a borehole in a cross-well imaging scenario using 1 m, 2.5 m, and 5 m spaced electrode intervals. The difference in the volume of data for 1 m (i.e. 69570 measurements) and 5 m (i.e. 696 measurements) electrode intervals is two orders of magnitude. Note that the imaging outcomes are comparable across each of the experiments.

Outcomes from Figure 4.11 suggest that 5 m spaced electrodes provide valuable imaging of the toe of the seawater interface. However, such widely spaced electrodes will affect model resolution along the vertical well string. We explore the application of a high-density electrode string as a replacement for time-lapse induction logging in the discussion.

Optimal electrode spacing is depends on site specific objectives. For example, complex hydraulics associated with heterogeneous karstic aquifers may benefit from a concentration of sensors across extreme permeable zones. Python code that simulates the resistivity from directly from solute-transport modelling is freely available and described within see (A. R. Costall *et al.*, 2020)

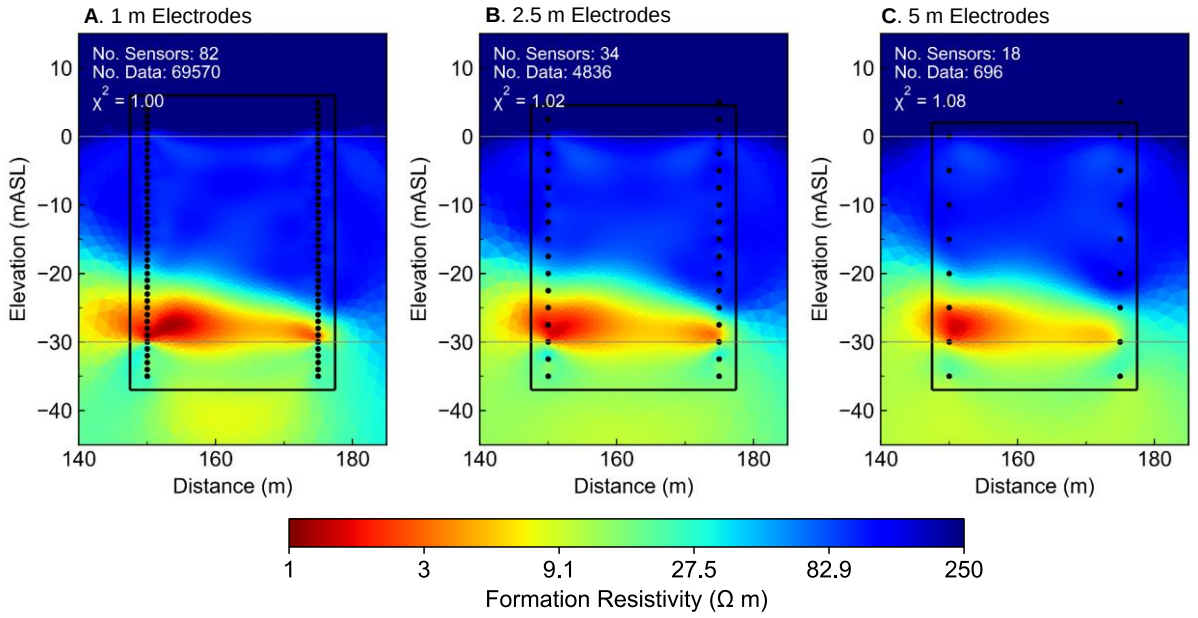

Figure 4.11: Set of images showing the outcomes of inversion using electrodes spaced at 1 m (Panel A), 2.5 m (Panel B) and 5 m (Panel C). In this example, the toe of the seawater wedge is still resolved using the 5 m spacing without significantly increasing misfit, however the landward extent of the toe is better-defined in the finely spaced electrodes. In each example, the mesh generation and inversion parameters are identical. When viewed from an interpretation perspective, all images contain valuable information about distribution of saline and fresh water, but none provide precise definition of the resistivity distribution within the wedge, so the limitation observed in surface data remains.

4.6.3 Inversion outcomes

Figure 4.12 shows a comparison of unconstrained cross-well imaging inversion outcomes for the two solute transport models (see Figure 4.9). A comprehensive electrode acquisition configuration is generated with quadrupoles filtered by maximum geometric factor (10,000) and upper limit of estimated error (10%) given a noise floor of 1 μV. Solute contours are overlain on the imaging outcomes.

The distinction between the fresh groundwater, mixing zone, and seawater wedge is clear in each of the images and boundaries between vadose zone and saturated aquifer, and aquifer and substrate are easily interpreted. The precise geometry of the wedge is less distinguishable after the wedge has moved significantly further inland, although definition of the mixing zone remains superior to any surface-based inversion outcomes.

The outcomes from these experiments are: i) boreholes located across of the seawater toe can recover a critical element of seawater wedge geometry (i.e. the terrestrial extend of seawater intrusion), and ii) boreholes located within the seawater wedge can determine the solute distribution across the mixing zone. An extension to point (ii) is that solute concentration contours can be used to infer the position of the toe or place a high confidence constraint on solute transport modelling.

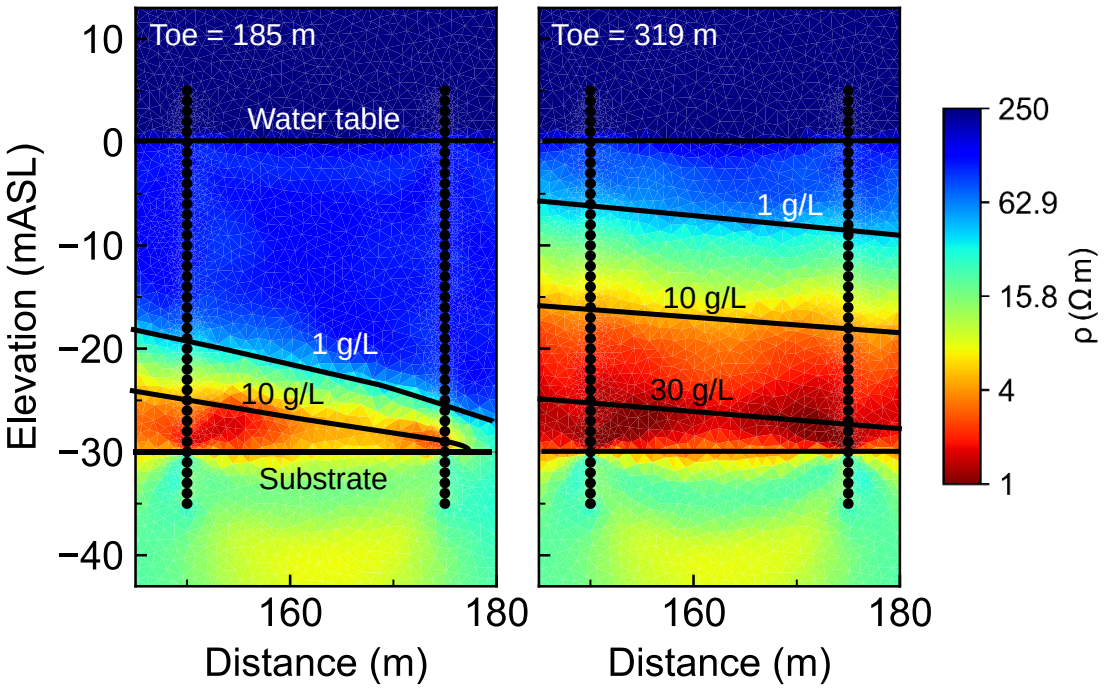

Figure 4.12: Panels comparing imaging outcomes from boreholes after large changes to groundwater flow conditions. The seawater wedge is clearly defined in the left image, where high groundwater flow conditions place the toe approximately 185 m from the shoreline. The 1 g/L contour is well resolved here. The right image shows the imaging outcomes after the wedge has moved considerably further inland, to 319 m from the shoreline. Recovering the wedge geometry is more challenging once the toe has moved beyond the boreholes.

4.7 Part 4: Combined cross-borehole and surface ERI with constraints

We have assessed unconstrained inversion of surface-based ERI and found that while it generated useful outcomes, its weakness is resolution of electrical resistivity in the seawater wedge and lower substrate. We have also assessed inversion constraints including a-priori information. Here it was possible improve recovery of seawater wedge geometry, although we demonstrate that as expected the outcome relies on accurate a-priori resistivity distributions. None of the surface based ERI methods accurately recovered electrical resistivity in the seawater wedge. We show that cross well ERI clearly present improved local definition of resistivity distribution weaknesses remain. That is only a relatively small zone between wells was resolved and every this was not perfect.

We systematically work through application of combined borehole and surface imaging including the inversion constraints shown earlier in this research. The panels in Figure 4.13 contain the forward resistivity model (A), outcomes from unconstrained inversion of surface and borehole data (B), outcomes where a sharp interface in placed at the substrate (C), and an inversion where the inversion is constrained to the correct substrate resistivity and a sharp boundary is included at the substrate (D). The surface dataset is identical to the multiple-gradient dataset presented earlier (1974 measurements) and the borehole dataset contains 4868 filtered measurements including the independent and straddled configurations (Figure 4.13B and C). Each of the inversions converge to an acceptable misfit level (e.g. $\chi^2 \approx 1$).

Figure 4.13D shows the optimal outcome where surface and borehole ERI data, in combination with resistivity constraints at the substrate, yield the full geometry of the seawater wedge. The sharp-interface boundary, Figure 4.13C, shows some improvement in the boundary definition beneath the resistivity fresh groundwater zone beyond the seawater toe; however, the resistivity within the substrate beneath the seawater wedge is poorly resolved. This

is similar to the outcomes shown in Figure 4.13B, where unconstrained inversion of surface and borehole data shows minimal improvement over inverting the datasets individually.

Cross-borehole resistivity outcomes demonstrate a significant improvement in inversion outcomes of the seawater wedge. Resistivity contours are well defined when the toe is proximal to the boreholes, which facilitates precise interpretation of the inland extent of the seawater wedge. We additionally show that the full wedge geometry can be resolved using combined surface and borehole imaging with spatial data constraints such as sharp boundary and a-priori resistivity. This is a significant improvement over any of the experiments using the arrays or techniques independently and demonstrates the potential for high-precision measurement of the seawater wedge at coastal margins.

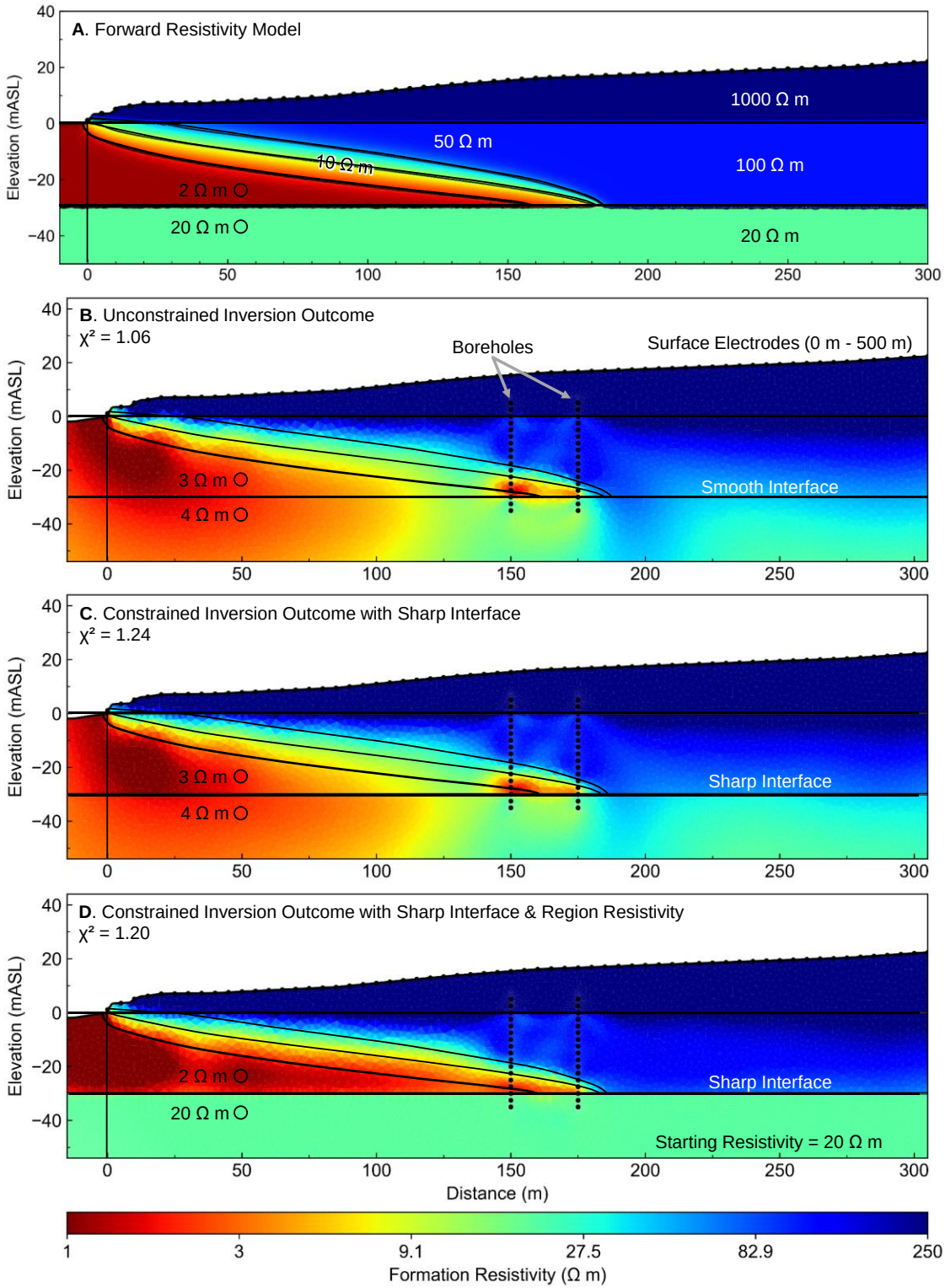

*Figure 4.13: Set of images showing resistivity imaging outcomes from constrained inversion of combined cross-borehole and surface acquisition. Panel **A** shows the forward model, Panel **B** shows outcomes from unconstrained inversion of cross-borehole and surface resistivity data, Panel **C** shows outcomes where a sharp interface in placed at the substrate, and Panel **D** shows the outcomes from inversion with correct prior substrate resistivity (20 Ohm-m) and sharp boundary located at the substrate interface. Panel **D** shows that the combination of borehole-based imaging and inversion constraints is required to recover the full geometry of the seawater wedge. This approach also demonstrates the high confidence by which the angle of the seawater wedge can be interpreted, allowing for constraints on predictive groundwater modelling.*

4.8 Discussion

Our numerical experiments show that a pair of shallow instrumented wells, in combination with surface ERI and appropriate inversion constraints, can build a clear picture of subsurface electrical conductivity across a seawater wedge. In our experiments we place the wells near the toe of the wedge, however it is unclear whether these wells are still useful after a significant landward movement of the seawater interface has occurred. We suspect the high-resolution data between the wells may remain useful to provide time lapse information.

We also suspect that instrumented boreholes present more advantages beyond improving inversion outcomes as described above. That is, instrumented boreholes present the opportunity to directly recover conductivity along the trace of each well. We discuss these concepts below.

4.8.1 What happens if the wedge moves past the instrumented wells?

The dynamic nature of the seawater front means that the seawater wedge may move a considerable distance inland and end up beyond the region of investigation provided by any two wells intended for cross-well ERI. To investigate this situation, we halve the groundwater throughflow in our solute transport model, which results in the inland position of the seawater toe moving twice as far inland, as shown in Figure 4.9. The pair of wells are now located near to the middle of the wedge. We suspect that the high resolution between the wells can resolve the solute concentration gradients, which can be used support interpretation of the landward extent of the toe.

Figure 4.14 shows the solute concentration distribution and the inverted resistivity model after lowering the groundwater flow. Once again, the solute distribution between the boreholes is well-resolved and the presence of the highly saline 30 g/L groundwater is clear. While the combination of surface and in-hole support a better ERI inversion outcome for the overall wedge there must be some loss in resolution of the exact position of the toe itself as it extends further inland (i.e. away from the instrumented wells).

Figure 4.14 also shows a zoomed section around the two wells. The high resolution between the wells means that the solute contours in the mixing zone is well constrained. Assuming a homogeneous aquifer, it is possible to extrapolate the solute contour with depth across the two wells. For example, the 50 Ωm contour (~1 g/L) is approximately 336 m inland while the position of the toe in the forward model is 319 m from the shoreline. Having an estimate of the landward position of the toe in addition to the gradient of the mixing zone can be highly useful as a constraint on solute transport modelling.

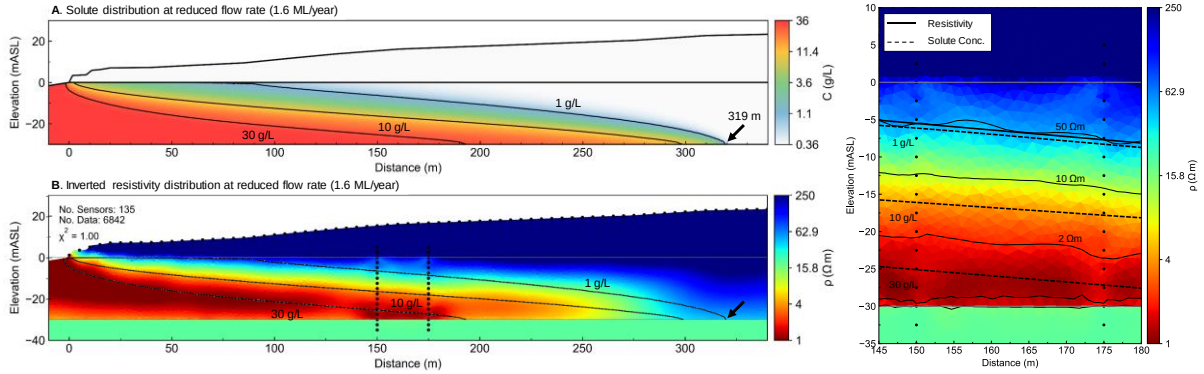

Figure 4.14: ***Left, top and bottom:*** *Pair of images showing the solute concentration distribution and the inverted resistivity distribution for a model with lower flow rates than the models demonstrated above. The seawater toe has moved inland to ~320 m from the shoreline and is now beyond the region high ERI illumination/sensitivity proximal to the bore hole. The definition of the toe from the resistivity imaging depends on the surface array and is not well resolved as a result.* ***Right:*** *zoomed image showing the solute concentration contours and formation resistivity contours. The 50 Ωm contour approximates to the 1 g/L solute boundary. A simple linear extrapolation between the two wells places the intersection of this contour at 336 m from the shoreline, compared to 319 m in the forward model.*

4.8.2 Seawater intrusion and time-lapse resistivity at instrumented wells

We find that many published examples that focus on borehole-based ERI do not include measurements along a single borehole, and instead opt for a purely cross-well application. This may impact on the quality of inversion proximal to the boreholes. We ran experiments that compare inversion outcomes from data with quadrupoles located purely along the boreholes with purely cross-well data. The electrode separation shown in these experiments is comparable to separation of downhole resistivity logging tool electrodes. Our experiments indicate that configurations that include these sets of quadrupoles can recover the high-quality resistivity information proximal to the borehole.

Figure 4.15 shows a series of vertical traces taken from an inverted conductivity distribution using two borehole imaging wells (e.g., Figure 4.14) with acquisition geometry purely acquired along the well (i.e., no cross-well quadrupoles). The wells are located 150 and 170 m away from the shoreline, and another trace is shown at 160 m, between the two wells. The data taken along the well traces is highly comparable to the forward model, indicating that the inversion from acquisition with single-well data can recover a reasonable conductivity distribution.

Figure 4.16 shows a similar experiment to that shown in Figure 4.15, except where acquisition quadrupoles are in a purely cross-well orientation. This acquisition geometry provides greater coverage of the area between the wells, which is reflected in the vertical trace taken from 160 m. Comparison of both experiments suggests that combining cross-borehole and single-borehole acquisition geometry may yield optimal imaging outcomes.

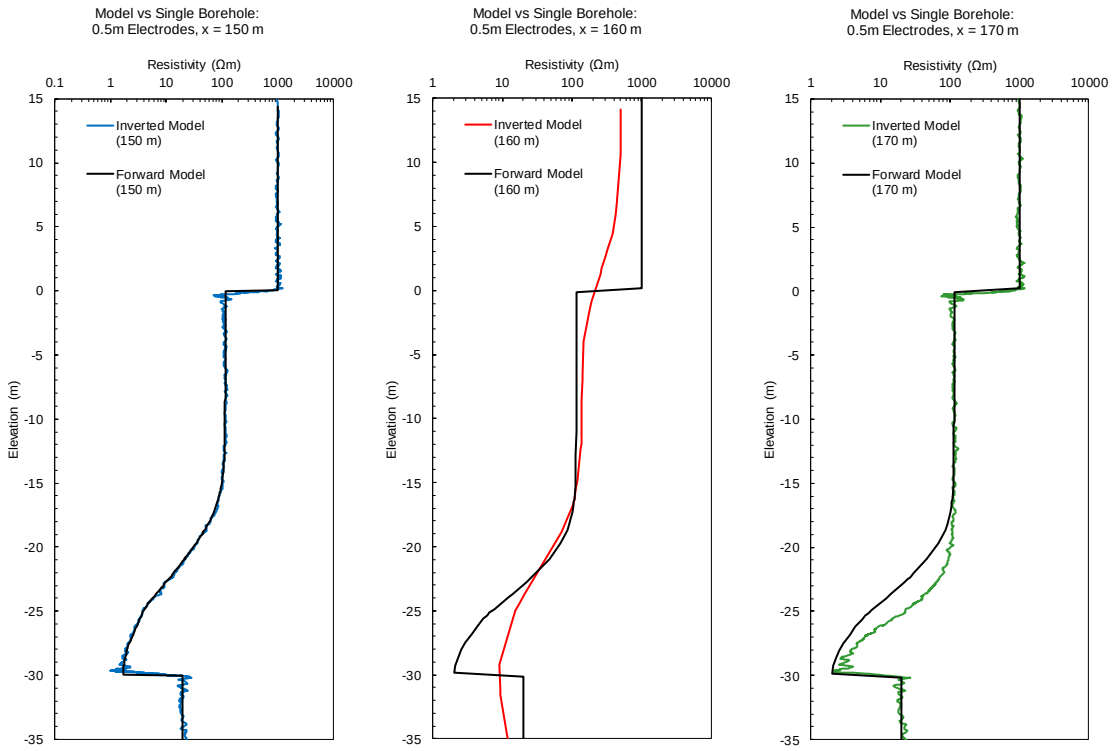

Figure 4.15: Graphs showing a vertical trace taken from the inverted resistivity model using single-borehole acquisition geometry along a well-string located 150 m (along an instrumented well), 160 m (between instrumented wells), and 170 m (along instrumented well) from the shoreline. The outcomes show that the inverted outcomes from along vertical well-traces can precisely replicate the input model in some scenarios, however struggle to maintain that precision closer to the toe. The area between the wells undershoots the conductive wedge.

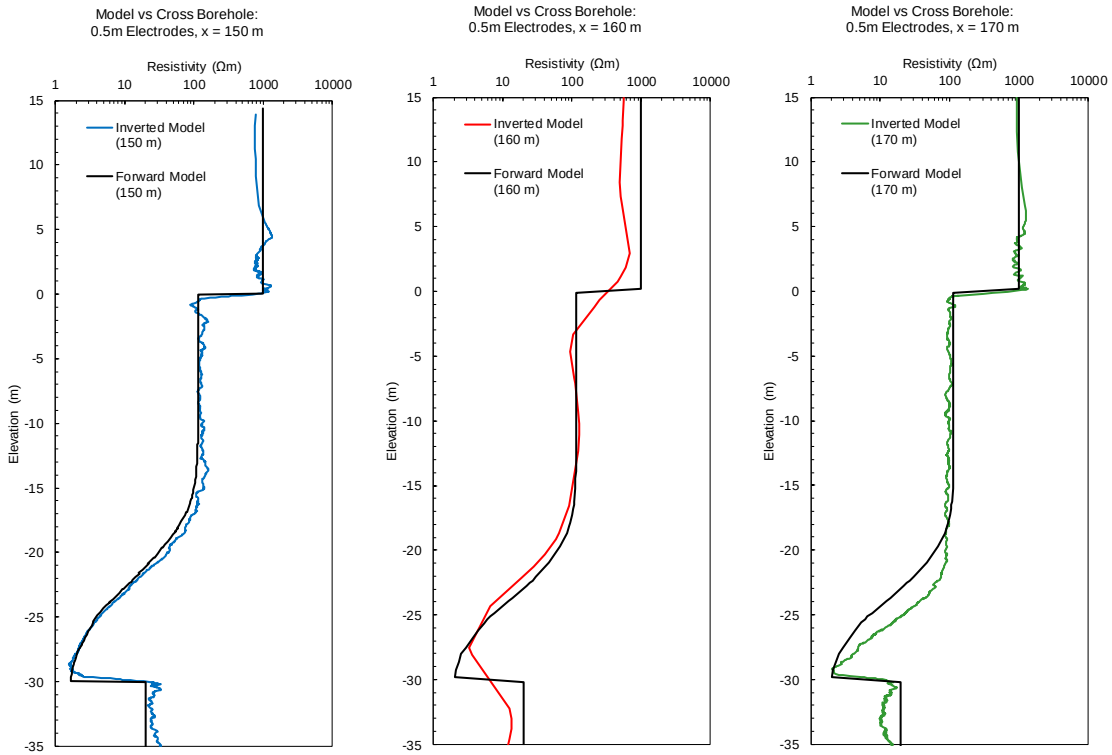

Figure 4.16: Graphs showing a vertical trace taken from the inverted resistivity model using cross-borehole acquisition geometry along a well-string located 150 m (along an instrumented well), 160 m (between instrumented wells), and 170 m (along instrumented well) from the shoreline. The outcomes show that the inverted outcomes from along vertical well-traces can precisely replicate the input model in some scenarios, however struggle to maintain that precision closer to the toe.

4.9 Conclusion

The need for high-quality data as inputs for solute transport modelling is a key driver for precise groundwater monitoring in coastal margins. Data from boreholes can provide a snapshot of this data but lack the spatial distribution of data required to build the high-quality models needed for coastal monitoring. If used appropriately, ERI can provide these inputs for these solute transport models.

ERI can be applied for many reasons. For coastal hydrogeology, it is most often used to target future monitoring bores, identify areas of saline water intrusion, and to provide inputs for solute transport modelling. Solute transport modelling requires specify geometry and groundwater solute concentration for numerical parameter estimation. If we want to recover earth properties, we need confidence in the water electrical conductivity proximal to the seawater wedge.

Surface-based ERI measurements are subject to significant interpretational error. There are several techniques that are commonly used to improve inversion outcomes. We experiment with simplified a-priori data derived from analytical groundwater solutions and find that they have minimal impacts on the inversion outcomes. We also demonstrate the impact of sharp boundary constraints and show that their impacts can, perhaps counter-intuitively, be detrimental to interpretation of the seawater wedge.

The outcomes from borehole-based resistivity imaging show substantial improvements for interpretation of the seawater wedge compared to surface-based imaging. We demonstrate that an instrumented borehole in a seawater wedge environment can be used to image the position of the seawater interface toe, and reasonably interpret variations in solute concentration in a time-varying seawater system. Our experiments highlight the importance of setting borehole sensors in the substrate.

We found it interesting that inversion of the individual borehole data appears to be absent in many borehole-based ERI research. To remedy this, we include images with inversion to near-well conductivity for each borehole string. This provides an outcome that can recover a precise representation of vertical conductivity along the trace of the borehole for small electrode spacing. This is outcome can provide a high confidence in the formation EC constraint for transport modelling (Costall, Harris 2020).

This is consequential for transport modelling proximal to the zone of submarine groundwater discharge where groundwater levels and chemistry change rapidly. This could be an optimal location for a low-cost dense array of electrodes for coastal groundwater monitoring.

We find that electrical imaging using surface and borehole-based electrodes, together with region-based inversion constraints, shows the optimal outcomes for a coastal seawater-imaging program. Borehole-based imaging can provide the data required to constrain the location and resistivity of the substrate. This compliments surface-based imaging to resolve the full geometry of the seawater wedge.

Future Experiments

Many variables exist for electrical resistivity imaging in coastal margins. We have demonstrated several of these throughout this research. Table 4.1 contains future research topics for resistivity imaging of the seawater interface. These span several levels of complexity and difficulty; however, several of the points can be simulated within the framework used to simulate the experiments within this research.

Table 4.1: Avenues of future research into cross-borehole acquisition in coastal margins.

	Future Research	Comment
Boreholes	Distance between boreholes	Our boreholes are spaced at approximately 25 meters but having boreholes closer or further apart may be required at some sites. This is easily simulated using the framework provided, which can additionally incorporate any number of boreholes. A minimum ratio of 0.5 for borehole-length to inter-borehole-separation is suggested by LaBrecque *et al.* (1996).
	Borehole imaging schemes	The dipole-dipole configuration is suggested to yield the best imaging outcomes by several authors (Bing *et al.*, 2000; P. Tsourlos *et al.*, 2011; Florian M. Wagner *et al.*, 2013). We suspect that surface-to-borehole and cross-borehole to surface applications could potentially yield efficient combinations of electrodes for subsurface imaging.
Hydraulic Models	Complex models	The seawater interface model used as our base model represents a relatively simple seawater interface, however in reality these aquifers are often highly complex and with extreme spatially variable properties.
	3D Models	The expansion to 3D is a natural conclusion for large-scale models. Having framework to generate synthetic datasets in 3D is the next step in near-shore coastal margin resistivity research. The existing frameworks could accommodate this relatively easily, however 3D solute transport models require considerably greater time and computational power than most standard desktops permit.
Resistivity Models	Influence of the ocean	The influence of the ocean on ERI arrays is seldom discussed, although must influence the electric fields near to the coast. Maurer *et al.* (2006) discuss the effects of the 'outer-space' resistivity, i.e. the area outside of the electrodes, and show that these regions can have a definite impact on the model domain. We suspect that, if not explicitly included into the inversion, the measured voltages in electrodes near to the ocean will be affected.
	Influence of cliff-faces	We base the model topography shown throughout this research on the limestone-dominated shoreline of Costall 2019. However, sloping, and elongated beachfronts are also common. We suspect that the sharp cliff-edges may affect the very shallow resistivity distribution if not correctly replicated in the inversion mesh. At sloping beachfronts, the shallow wave-dominated zone may present further challenges for the electrical field distribution (see "Influence of the ocean", above)
	Influence of substrate	The resistivity model used throughout this research assumes that the substrate is infinitely thick, which is unlikely to represent the reality of substrates worldwide. However, incorporation of deeper layers is possible with minor modification to the provided python script. We further assume the substrate is, and always was, saturated with fresh groundwater prior to seawater intrusion. If the seawater wedge spent an extended length of time above the substrate, the resistivity of the substrate is likely to be different beneath the saline wedge compared to beneath the fresh ground water.

Acknowledgements

This research is funded by the Australian Government Research Training Program Scholarship from Curtin University, Western Australia. We thank DHI WASY FEFLOW (v7.2) for the student licence granted during this research. All scripts used throughout this research are available freely online from *https://github.com/Coastal0*.

Appendix A.1 Surface Array Parameters and Combined Arrays

Surface arrays are created using pyGIMLi (C. Rücker *et al.*, 2017) and BERT (Thomas Günther *et al.*, 2019; T. Günther *et al.*, 2006; C. Rücker *et al.*, 2006). The multiple gradient configurations maintain a 9-electrode separation and expands the dipole separation (i.e. 'a') by a factor of two after each full sweep of the electrodes.

Table 4.2 contains an example for 100 electrodes, where *mn* and *ab* are spaced to 11 and 99 respectively. A total of 1932 quadrupoles are generated by this configuration. Arrays generated like this are configurable for simultaneous channel acquisition and can be tailored for requirements.

Table 4.2: Example of multiple-gradient array generated using pyGIMLi (C. Rücker et al., 2017).

a - b	m - n	a	b	m	n
9	1	1	10	2	3
		1	10	3	4
			…		
9	1	1	10	8	9
		2	11	3	4
			…		
9	1	91	100	97	98
		91	100	98	99
27	3	1	28	4	7
		1	28	7	10
			…		
27	3	73	100	91	94
		73	100	94	97
45	5	1	46	6	11
		1	46	11	16
			…		
81	9	19	100	73	82
		19	100	82	91
99	11	1	100	12	23
		1	100	23	34

In the expanded arrays (Code Sample 1), the multiple-gradient array sweeps through the range of possible 's' separations (i.e., *ab_sep* below). The code below is modified from pyGIMLi (C. Rücker *et al.*, 2017).

Code Sample 1: A modified multiple-gradient array generator to include all possible separations of current electrodes.

```
import numpy as np
confs = []
count = 0
for ab_sep in np.arange(1,(int(np.floor(nElectrodes/2)))):
  ab_sep_base = ab_sep
  ev = 2
  takeevery = 2
  max_fak = int(np.ceil(nElectrodes / ab_sep_base))
  ab_space = [ii*ab_sep_base for ii in range(max_fak) if ii % ev == 1]
  mn_space = [ii for ii in range(max_fak) if ii % takeevery == 1]
  a, b, m, n = [], [], [], []
  for ab in range(len(ab_space)): # ab spacings
    for aa in np.arange(1, nElectrodes-ab_space[ab]+1, 1): # a index
      mn = mn_space[ab]
      for mm in np.arange(aa+mn, aa+ab_space[ab]-mn, mn):
        count += 1
        a.append(int(aa))
        b.append(int(aa+ab_space[ab]))
        m.append(int(mm))
        n.append(int(mm+mn))
  abmn = np.vstack([a,b,m,n]).T
  confs.append(abmn)
confs = np.vstack(confs)
```

Combined Arrays

Combined arrays (e.g. combinations of conventional array types) can be used to improve imaging outcomes (Furman *et al.*, 2003; M. H. Loke *et al.*, 2013; W. F. Zhou *et al.*, 2002). The multiple-gradient configuration includes much of the traditional Wenner and Schlumberger arrays. However, it does not collect data outside of the current electrodes (i.e. dipole-dipole). Collecting and combining multiple datasets per-site is an effective method to increase data density and can facilitate greater interpretation through different excitation voltage patterns.

Figure 4.17 shows the unconstrained imaging outcomes for the combined multiple gradient and dipole-dipole configuration. No significant different is observable when compared to the multiple-gradient inversion outcomes shown earlier. That is, the addition of the dipole-dipole quadrupoles does not increase the interpretation of the lower confining substrate for the synthetic model. In practice, the near-surface variations in the vadose zone and other geologic noise may be better resolved by the dipole-dipole array (Costall 2018).

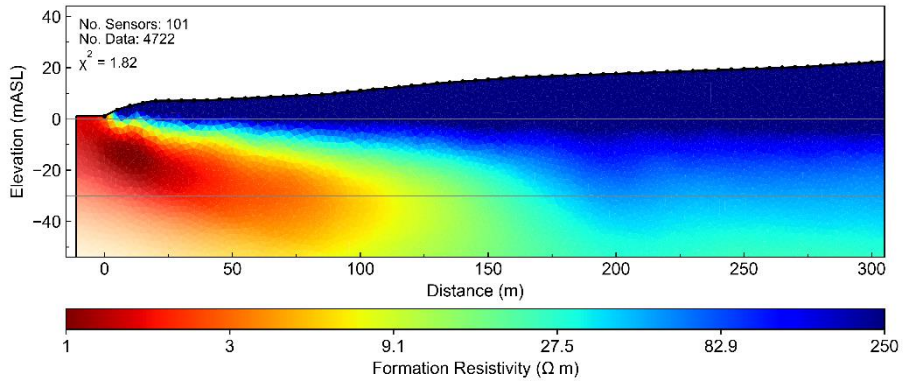

Figure 4.17: Image showing the inversion outcome for the combined dipole-dipole and multiple gradient array. We note no significant improvement over the multiple-gradient array in this synthetic model. However, in practice, it is practical to collect both dipole-dipole and multiple-gradient to analyse different aspects of noise in the model.

Appendix A.2 How does the mesh discretization affect imaging outcomes?

Mesh discretization is a common focal point for finite-element based experiments. Here we provide a set of images highlighting the effects of increasing the maximum allowable cell size in the mesh generation code. The inversion is dataset is a multiple-gradient with electrodes at 5 m intervals. The cells between electrodes (i.e. near the surface) is always refined regardless of the maximum allowable cell size.

Figure 4.18 shows the practical impacts of systematically increasing cell sizes. We observe that smaller cells are aesthetically pleasing however do not impact on the inversion outcomes. This suggests that the cells are refined in the appropriate locations. Further investigation of cell sizes is located in Carsten Rücker (2010)

Table 3 provides the summarized log for each of the inversions. Note the significant increase in inversion time for the smallest cell size. Each of these inversions converges to the simulated noise level (5%), suggesting that any improvement in reducing the cell sizes is aesthetic.

Table 4.3: Details of the inversion outcomes comparing maximum cell size. Limiting the maximum cell size to increasingly smaller numbers primarily affects the run time without significant change in the level of fit. The refinement at the surface is clearly sufficient to capture the rapid changes near electrodes.

Max. Cell Size	No. Cells	No. Iterations	RMS (%)	χ^2	Time (minutes)
50	13935	9	5.15889	1.01982	11
25	15412	9	5.15871	1.01878	14
10	22061	8	5.0868	0.996473	26
5	34325	9	5.08481	0.991731	44
1	125748	8	5.14872	1.01064	130

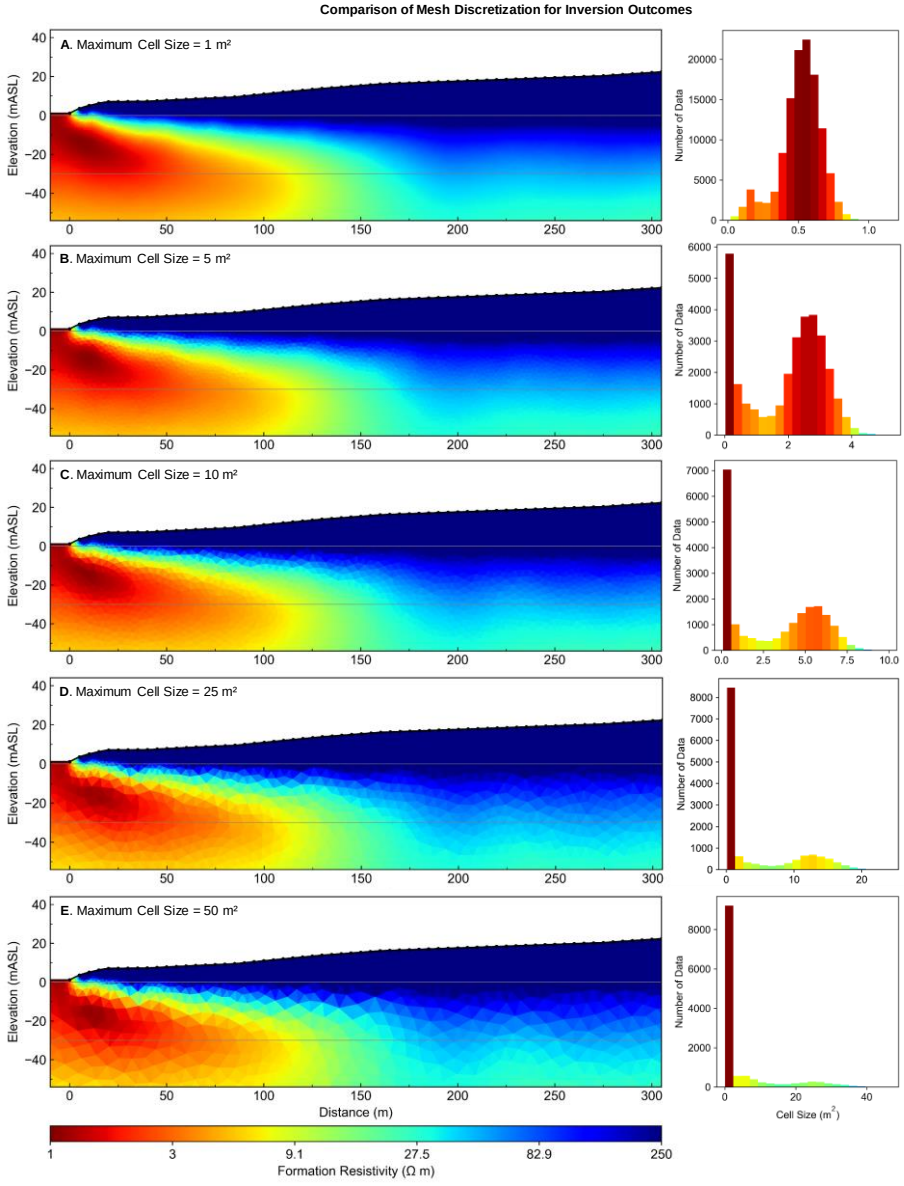

Figure 4.18: Set of images showing the systematic coarsening of the inversion mesh. The maximum allowable area is increased in each of the panels from A to E. A histogram shows the occurrences of the various cell sizes. The spike in small cell sizes is due to the fine discretization between electrodes at the surface (See Figure 4.19).

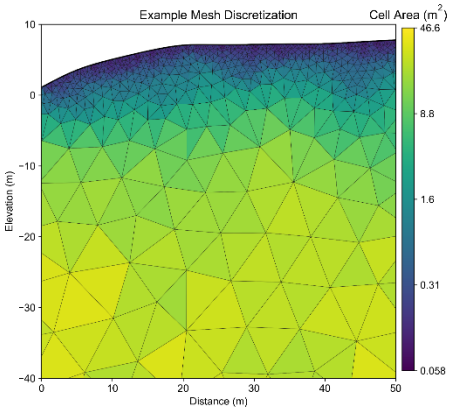

Figure 4.19: Image highlighting the fine discretization of the mesh nearby electrodes.

Figure 4.20 shows the meshes used for inversion of cross-borehole imaging. The regions include the primary mesh, which extends to several kilometres either side of the inversion mesh. This mesh is used for forward modelling only. The orange and grey regions represent the inversion mesh, which have finer cell dimensions and represent the area of interest.

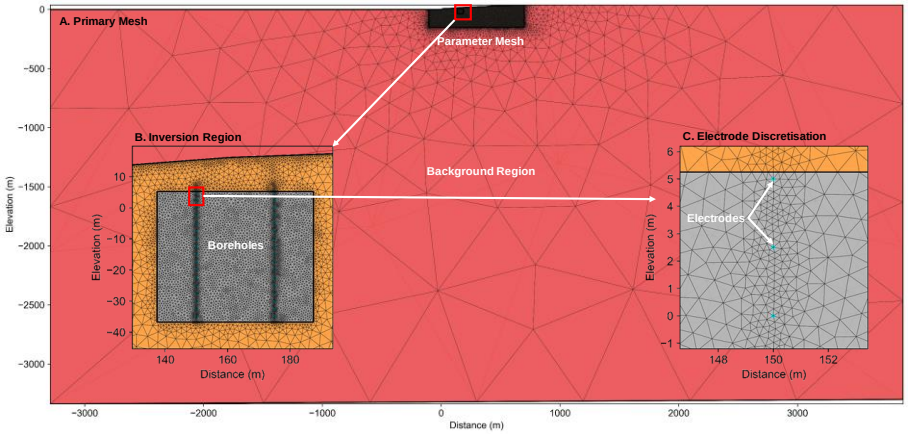

Figure 4.20: Image showing the discretization of meshes used for forward modelling (e.g. C. Rücker et al. (2006))

Appendix A.3 How do different electrode spacing affect inversion outcomes?

Electrical resistivity imaging is often a trade-off between resolution and depth-of-investigation. That is, larger electrode spacing is required to image deeper regions of the subsurface, while smaller electrode spacing is required for higher resolution imaging. Given that most instruments today have some limit to the maximum number of sensors, a compromise between resolution and depth is required.

Figure 4.21 shows the inversion outcomes from various electrode spacing of the multiple gradient style array for the model shown in Figure 4.1. Here we assume that we have a system that can measure any given number of electrodes (e.g. up to the 201 electrodes simulated in Figure 4.21 A). The electrode spacing tested includes 2.5 meters (Figure 4.21A), 5 meters (Figure 4.21B), 10 meters (Figure 4.21C), 25 meters (Figure 4.21D), and 50 meters (Figure 4.21). In these examples, the topography is derived from the positions of the electrodes, resulting in progressively smoother surfaces as the spacing increases.

We observe that closely spaced electrodes are better able to resolve the features of the seawater wedge (e.g., the water table, substrate, saline wedge, and freshwater wedge). However, there are obvious practical limitations associated with small electrode spacing. Furthermore, the landward position of the seawater wedge (i.e. the toe) can be approximated where electrodes are at 10-meter intervals or less. The overall recovery of seawater wedge geometry of the wedge and the depth of the substrate are limited throughout each of the examples. The largest simulated case with 50-meter electrode spacing is not suitable to recover any of the seawater wedge geometry.

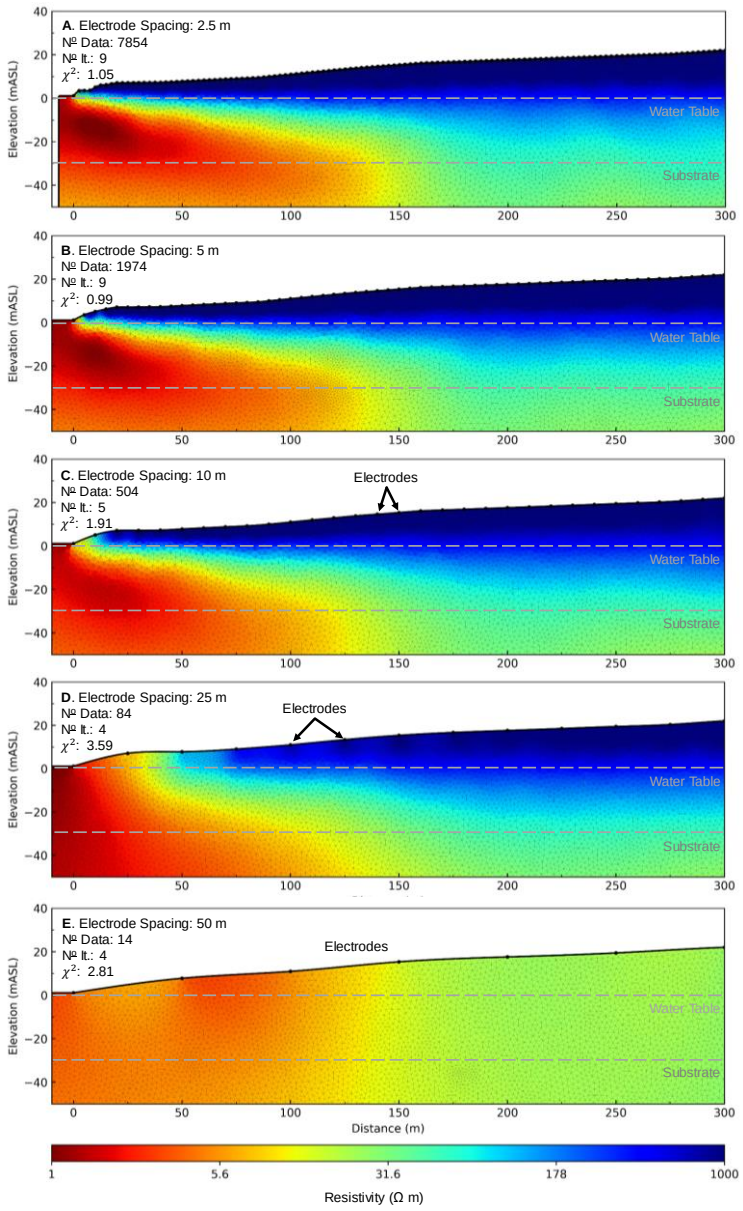

Figure 4.21: Set of images showing inversion of a seawater wedge using a multiple gradient array with increasing electrode spacing. The electrodes are spaced over the 500 m transect, from 0 to 500 m away from the shoreline, at intervals of 2.5 m (A), 5 m (B), 10 m (C), 25 m (D), and 50 m (E). The definition of the key hydrogeology (e.g. water table, substrate, saline wedge, freshwater) is generally improved using closer electrode spacing; however, this also increases the number of data and can exceed practical limitations. We use the 5-meter example later to demonstrate the use of constrained and a-priori inversion for seawater wedge characterization.

Appendix A.4 Sharp Boundaries Continued

The experiment that introduces sharp boundary constraints represents a 'best case' outcome where the location of the substrate is well constrained. We recognise two significant variables that can affect the use of sharp boundary constraints: (1) The water table includes a capillary fringe where a gradual change in the resistivity will occur. Including a sharp boundary here may enforce unrealistic resistivity changes at this boundary, and (2) shallow groundwater monitoring wells do not always reach the substrate, resulting in extrapolation of the depth to the substrate across the modelling domain.

Figure 4.22 shows an example of the imaging outcome where the substrate is located incorrectly. The substrate in the forward model is at 30 m depth; however, the substrate in these inversions is located incorrectly at 25 m (top) and 35 m (bottom) depth. The consequence is that inversions are driven to the wrong outcome when sharp boundaries are incorrectly located. This experiment highlights the dangers of forcing sharp boundaries into a model.

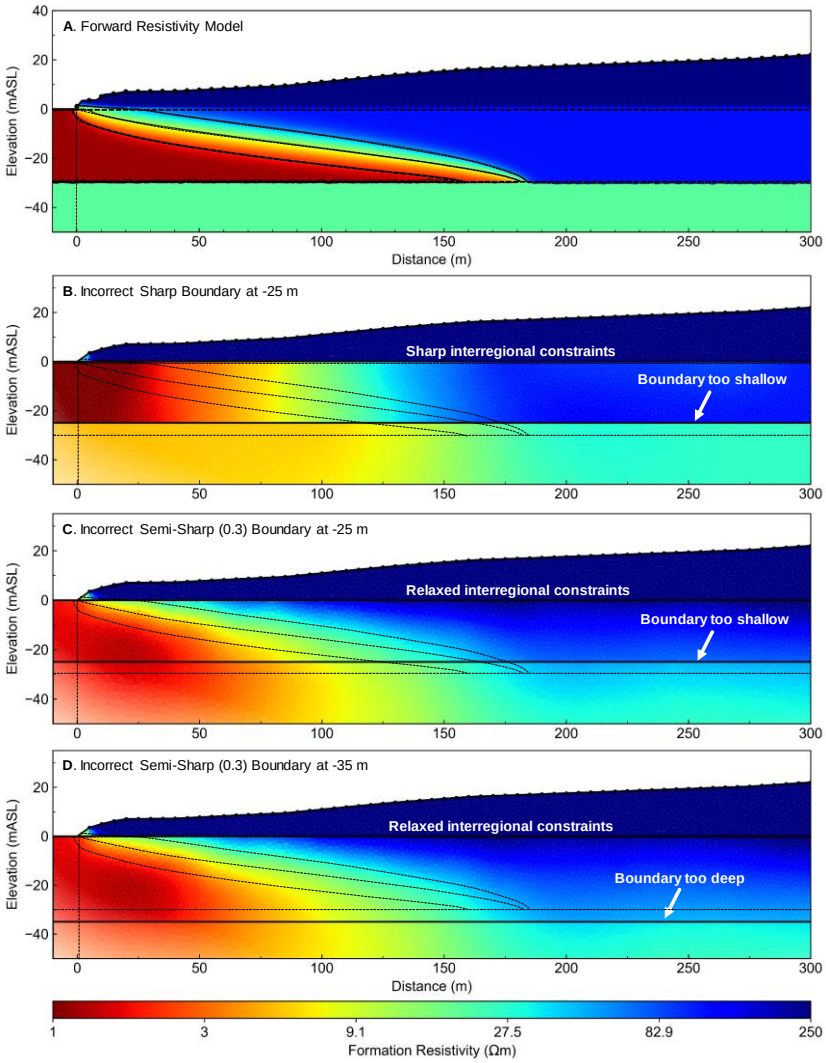

Figure 4.22: Set of images showing the inversion outcomes where the sharp boundary is placed at an incorrect depth. Panels A and B show the outcomes where the deeper sharp boundary is located at 25 meters, instead of the 30 meters in the correct model. A sharp boundary is created at the prescribed interval without impact on the level of fit or the resulting image. Panels B and C shows the outcomes from using a relaxed boundary (constraint = 0.3) where the boundary is incorrectly located too shallow (B) and too deep (C). There is little indication of this mistake in the imaging outcomes, suggesting that including a sharp boundary where the location is uncertain will degrade imaging outcomes.

Figure 4.24 shows a set of images after including a sharp boundary inversion constraint located at the water table and gradually relaxing the sharpness requirements across that boundary. Forcing this boundary to be sharp results in a reduction of the wedge-shaped geometry in favour of lateral conductivity distribution in seawater wedge. Any geometry associated with the submarine groundwater discharge is also lost. As this boundary constraint is relaxed, the wedge geometry returns. This experiment suggests that forcing a sharp boundary at the water table may not enhance inversion outcomes.

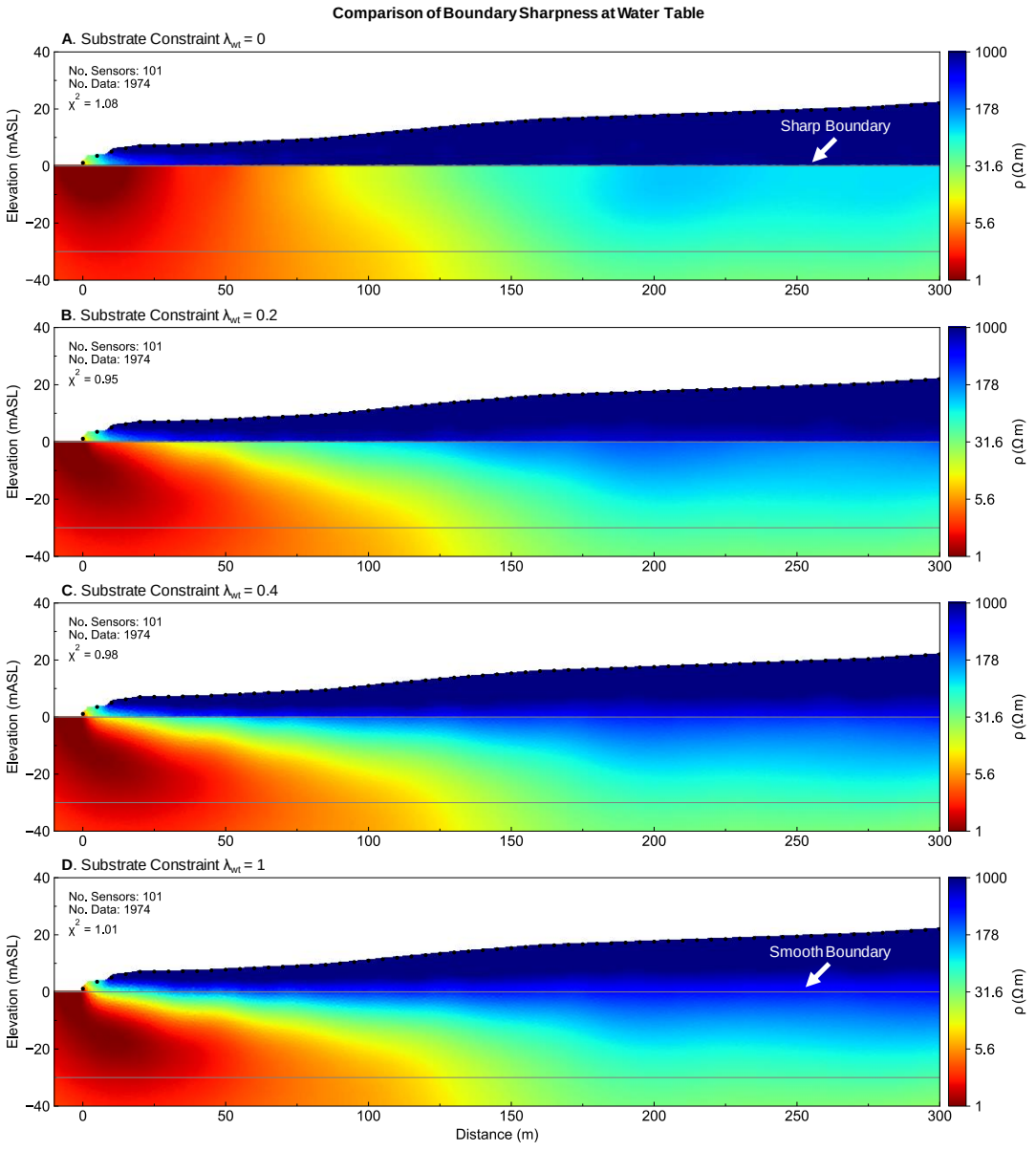

Figure 4.23: Set of images showing the outcomes of inversion after including a sharp boundary transition at the water table and gradually increasing the cross-boundary smoothing. Panel A shows the two regions (i.e., above and below the water table) as disconnected entities. Panel B through D show the systemetic re-connection of this smoothness constraint.

Figure 4.24 is a similar experiment to that shown in Figure 4.23 except the sharp boundary constraint has been placed across the lower substrate. Here the seawater wedge geometry remains unaffected however the resistivity of the substrate is impacted. Given the forward model for this region was a constant resistivity, the lateral changes we observe indicate that this boundary needs further constraints before it can be effective.

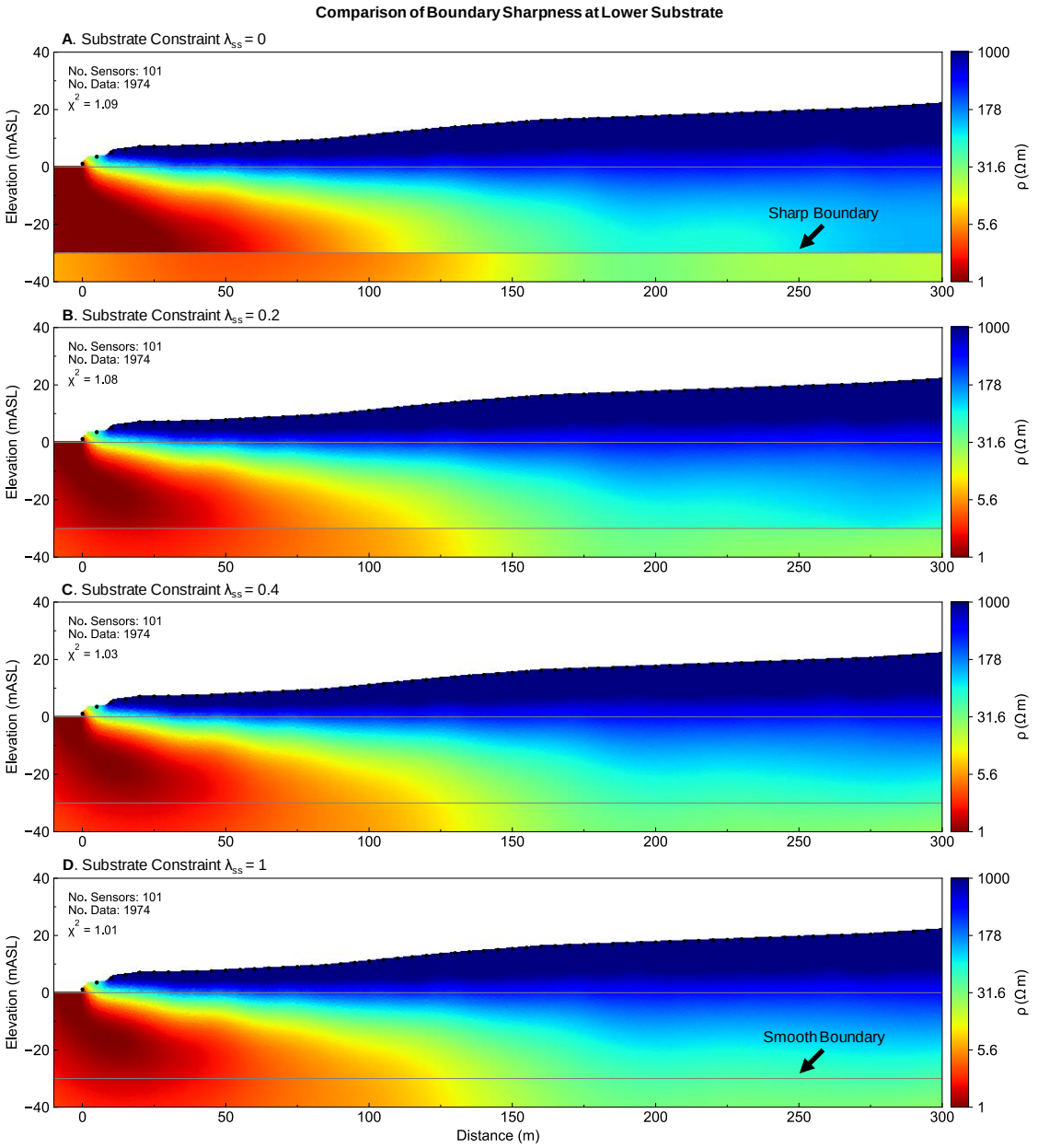

Figure 4.24: Set of images showing the outcomes of inversion after including a sharp boundary transition at the substrate and gradually increasing the cross-boundary smoothing. Panel A shows the two regions (i.e., above and below the water table) as disconnected entities. Panel B through D show the systemetic re-connection of this smoothness constraint.

Appendix A.5 How does the smoothing parameter affect the imaging outcomes?

The smoothing parameter fundamentally limits the rate-of-change of the model domain. In the seawater interface model described above, there are two distinct areas where the rate-of-change is extremely different. These are (i) the rapid changes across boundaries at the substrate and water table, and (ii) the gradual change across the mixing zone.

Here we demonstrate how the smoothing parameter in combination with defined sharp boundaries affects the inversion outcomes of the seawater interface. Earlier experiments demonstrate that including two sharp boundaries will result in the seawater interface losing the wedge-shaped geometry. In this experiment, the regions of the vadose zone and substrate remain at a constant lambda, while the smoothness constraints in the aquifer region is systematically reduced.

Figure 4.25 shows that the seawater wedge geometry is increasingly better resolved with lower smoothing constraints. While there is little indication of the wedge in the top panel of Figure 4.25, the wedge and mixing zone begin to take shape in the lower panels.

An obvious limitation to synthetic modelling is the lack of geologic noise. The reality of field data and geology means that lowering the smoothing value may result in overfitting the data. However, in this model, allowing for greater model roughness proximal to the seawater wedge can recover the geometry of the seawater wedge as the model roughness is increased.

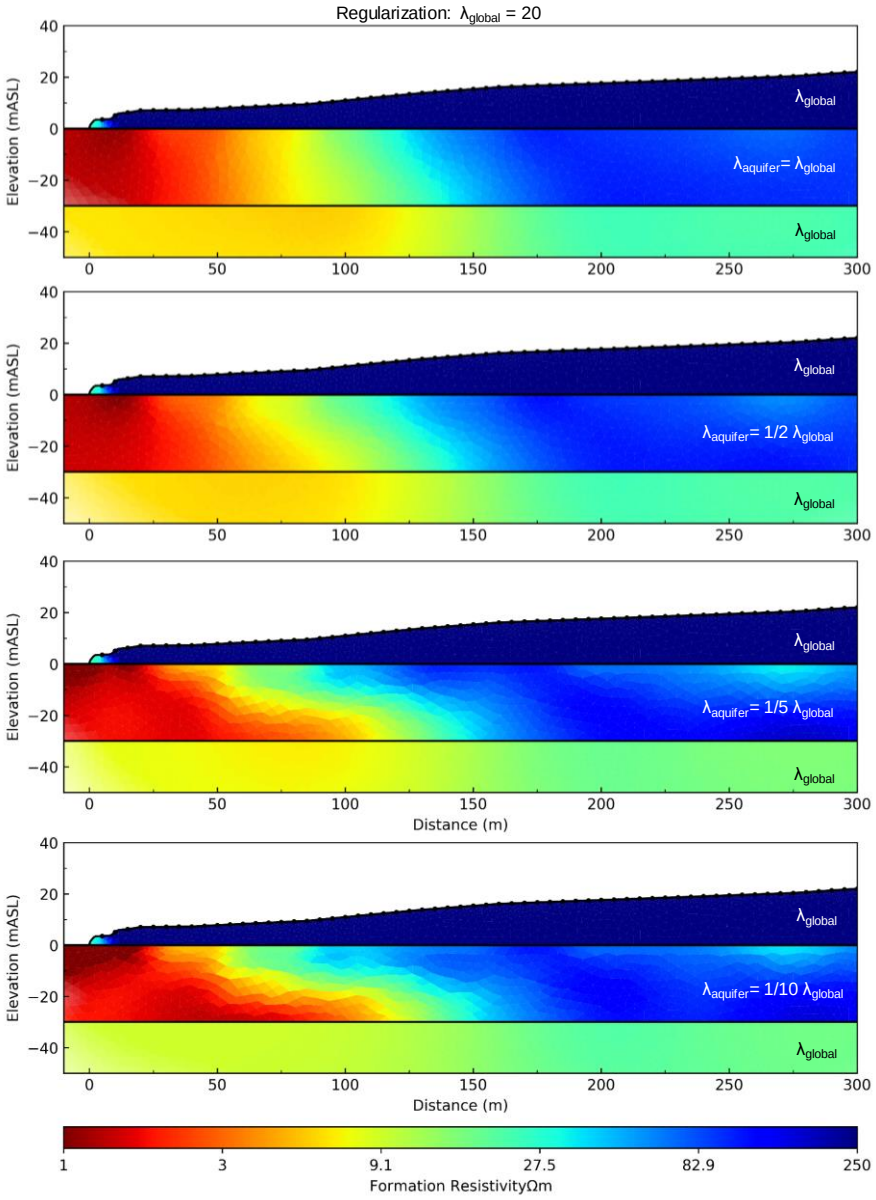

Figure 4.25: Set of images showing the effects of decreasing the smoothing parameter of the aquifer layer. As the smoothing parameter is lowered, more of the seawater wedge geometry becomes apparent. However, the smoothing parameter also needs to prevent over-fitting of noise. Reducing the smoothing parameter may result in data overfitting, particularly for noisy field data.

4.10 References

Archie, G. E. (1941). The Electrical Resistivity Log as an Aid in Determining Some Reservoir Characteristics. *Transactions of the AIME, 146*(01), 54-62. doi:10.2118/942054-g

Auken, E., & Christiansen, A. V. (2004). Layered And Laterally Constrained 2d Inversion Of Resistivity Data. *Geophysics, 69*(3), 752-761.

Bear, J. (2005). *Sea water intrusion into coastal aquifers*.

Beaujean, J., Nguyen, F., Kemna, A., Antonsson, A., & Engesgaard, P. (2014). Calibration of seawater intrusion models: Inverse parameter estimation using surface electrical resistivity tomography and borehole data. *Water Resources Research, 50*(8), 6828-6849. doi:10.1002/2013wr014020

Bergmann, P., Ivandic, M., Norden, B., Rücker, C., Kiessling, D., Lüth, S., . . . Juhlin, C. (2014). Combination of seismic reflection and constrained resistivity inversion with an application to 4D imaging of the CO2 storage site, Ketzin, Germany. *79*(2), B37-B50. doi:10.1190/geo2013-0131.1

Bergmann, P., Schmidt-Hattenberger, C., Kiessling, D., Rücker, C., Labitzke, T., Henninges, J., . . . Schütt, H. (2012). Surface-downhole electrical resistivity tomography applied to monitoring of CO2 storage at Ketzin, Germany. *77*(6), B253-B267. doi:10.1190/geo2011-0515.1

Bievre, G., Oxarango, L., Gunther, T., Goutaland, D., & Massardi, M. (2018). Improvement of 2D ERT measurements conducted along a small earth-filled dyke using 3D topographic data and 3D computation of geometric factors. *Journal of Applied Geophysics, 153*, 100-112. doi:10.1016/j.jappgeo.2018.04.012

Bing, Z., & Greenhalgh, S. A. (2000). Cross-hole resistivity tomography using different electrode configurations. *Geophysical Prospecting, 48*(5), 887-912. doi:10.1046/j.1365-2478.2000.00220.x

Boulanger, O., & Chouteau, M. (2001). Constraints in 3D gravity inversion. *Geophysical Prospecting*. Retrieved from https://onlinelibrary.wiley.com/doi/abs/10.1046/j.1365-2478.2001.00254.x

Constable, S. C., Parker, R. L., & Constable, C. G. (1987). Occam's inversion: A practical algorithm for generating smooth models from electromagnetic sounding data. *Geophysics, 52*(3), 289-300. doi:https://doi.org/10.1190/1.1442303

Coscia, I., Greenhalgh, S. A., Linde, N., Doetsch, J., Marescot, L., Gunther, T., . . . Green, A. G. (2011). 3D crosshole ERT for aquifer characterization and monitoring of infiltrating river water. *Geophysics, 76*(2), G49-G59. doi:10.1190/1.3553003

Costall, A., Harris, B., & Pigois, J. P. (2018). Electrical Resistivity Imaging and the Saline Water Interface in High-Quality Coastal Aquifers. *Surveys in Geophysics, 39*(4), 753-816. doi:10.1007/s10712-018-9468-0

Costall, A. R., Harris, B. D., Teo, B., Schaa, R., Wagner, F. M., & Pigois, J. P. (2020). Groundwater Throughflow and Seawater Intrusion in High Quality Coastal Aquifers. *Scientific Reports, 10*(1), 9866. doi:10.1038/s41598-020-66516-6

Dahlin, T., & Zhou, B. (2004). A numerical comparison of 2D resistivity imaging with 10 electrode arrays. *Geophysical Prospecting, 52*(5), 379-398. doi:DOI 10.1111/j.1365-2478.2004.00423.x

Dahlin, T., & Zhou, B. (2006). Multiple-gradient array measurements for multichannel 2D resistivity imaging. *Near Surface Geophysics, 4*(2), 113-123. doi:10.3997/1873-0604.2005037

Daily, W., & Owen, E. (1991). Cross-borehole resistivity tomography. *Geophysics, 56*(8), 1228-1235. doi:10.1190/1.1443142

de Franco, R., Biella, G., Tosi, L., Teatini, P., Lozej, A., Chiozzotto, B., . . . Gasparetto-Stori, G. (2009). Monitoring the saltwater intrusion by time lapse electrical resistivity tomography: The Chioggia test site (Venice Lagoon, Italy). *Journal of Applied Geophysics, 69*(3-4), 117-130. doi:https://doi.org/10.1016/j.jappgeo.2009.08.004

deGroot-Hedlin, C., & Constable, S. (1990). Occam's inversion to generate smooth, two-dimensional models from magnetotelluric data. *Geophysics, 55*(12), 1613-1624. doi:10.1190/1.1442813

Diersch, H.-J. G. (2014). *Feflow: Finite Element Modeling of Flow, Mass and Heat Transport in Porous and Fractured Media*: Springer Science & Business Media.

Doetsch, J. A., Coscia, I., Greenhalgh, S., Linde, N., Green, A., & Günther, T. (2010). The borehole-fluid effect in electrical resistivity imaging. *75*(4), F107-F114. doi:10.1190/1.3467824

Ellis, R. G. (1998). Inversion of airborne electromagnetic data. *Exploration Geophysics, 29*(2), 121-127. doi:https://doi.org/10.1071/EG998121

Furman, A., Ferré, T. P. A., & Warrick, A. W. (2003). A Sensitivity Analysis of Electrical Resistivity Tomography Array Types Using Analytical Element Modeling. *Vadose Zone Journal, 2*(3), 416-423. doi:10.2136/vzj2003.4160

Garcia-Menendez, O., Ballesteros, B. J., Renau-Prunonosa, A., Morell, I., Mochales, T., Ibarra, P. I., & Rubio, F. M. (2018). Using electrical resistivity tomography to assess the effectiveness of managed aquifer recharge in a salinized coastal aquifer. *Environ Monit Assess, 190*(2), 100. doi:10.1007/s10661-017-6446-9

Glover, R. E. (1959). The pattern of fresh-water flow in a coastal aquifer. *Journal of Geophysical Research, 64*(4), 457-459. doi:doi:10.1029/JZ064i004p00457

Grinat, M., Epping, D., & Meyer, R. (2018). *Long-time resistivity monitoring of a freshwater/saltwater transition zone using the vertical electrode system SAMOS.* Paper presented at the E3S Web of Conferences.

Grinat, M., Südekum, W., Epping, D., Grelle, T., & Meyer, R. (2010). *An automated electrical resistivity tomography system to monitor the freshwater/saltwater zone on a North Sea Island.* Paper presented at the Near Surface 2010-16th EAGE European Meeting of Environmental and Engineering Geophysics.

Guillen, A., & Menichetti, V. (1984). Gravity and magnetic inversion with minimization of a specific functional. *Geophysics*. Retrieved from https://library.seg.org/doi/abs/10.1190/1.1441761

Günther, T. (2004). *Inversion methods and resolution analysis for the 2D/3D reconstruction of resistivity structures from DC measurements.* (Dissertation). Retrieved from http://hdl.handle.net/11858/00-1735-0000-0001-3314-2 FID GEO-LEO e-docs database.

Boundless Electrical Resistivity Tomography—Bert 2—The User Tutorial. (2019). Günther, T., & Rücker, C. (Version 2.2.8) [Mobile application software]

Günther, T., Rucker, C., & Spitzer, K. (2006). Three-dimensional modelling and inversion of dc resistivity data incorporating topography - II. Inversion. *Geophysical Journal International, 166*(2), 506-517. doi:10.1111/j.1365-246X.2006.03011.x

Hagrey, S. A. a. (2011). CO2 plume modeling in deep saline reservoirs by 2D ERT in boreholes. *The Leading Edge, 30*(1), 24-33. doi:10.1190/1.3535429

Harris, B., Costall, A., Nguyen, H., Michael, K., Ricard, L., Freifeld, B., . . . Pethick, A. (2019). Time lapse in-hole electrical resistivity surveying during a shallow release of CO2 gas: Harvey, Western Australia. *ASEG Extended Abstracts, 2019*(1), 1-5. doi:10.1080/22020586.2019.12073174

Hellman, K., Ronczka, M., Günther, T., Wennermark, M., Rücker, C., & Dahlin, T. (2017). Structurally coupled inversion of ERT and refraction seismic data combined with cluster-based model integration. *Journal of Applied Geophysics, 143*, 169-181. doi:https://doi.org/10.1016/j.jappgeo.2017.06.008

Kibria, G., & Hossain, S. (2019). Electrical resistivity of compacted clay minerals. *Environmental Geotechnics, 6*(1), 18-25. doi:10.1680/jenge.16.00005

Kuras, O., Pritchard, J. D., Meldrum, P. I., Chambers, J. E., Wilkinson, P. B., Ogilvy, R. D., & Wealthall, G. P. (2009). Monitoring hydraulic processes with automated time-lapse electrical resistivity tomography (ALERT). *Comptes Rendus Geoscience, 341*(10-11), 868-885. doi:10.1016/j.crte.2009.07.010

LaBrecque, D. J., Ramirez, A. L., Daily, W. D., Binley, A. M., & Schima, S. A. (1996). ERT monitoring of environmental remediation processes. *Measurement Science and Technology, 7*(3), 375-383. doi:10.1088/0957-0233/7/3/019

Leontarakis, K., & Apostolopoulos, G. V. (2012). Laboratory study of the cross-hole resistivity tomography: The Model Stacking (MOST) Technique. *Journal of Applied Geophysics, 80*, 67-82. doi:https://doi.org/10.1016/j.jappgeo.2012.01.005

Lines, L., Schultz, A., & Treitel, S. (1988). Cooperative inversion of geophysical data. *Geophysics*. Retrieved from https://library.seg.org/doi/abs/10.1190/1.1442403

Loke, M. (2016). Tutorial: 2d And 3d Electrical Imaging Surveys. Penang, Malaysia, Universiti Sains Malaysia. Retrieved from http://www.geotomosoft.com/downloads.php

Loke, M. H., Chambers, J. E., Rucker, D. F., Kuras, O., & Wilkinson, P. B. (2013). Recent developments in the direct-current geoelectrical imaging method. *Journal of Applied Geophysics, 95*, 135-156. doi:10.1016/j.jappgeo.2013.02.017

Loke, M. H., Wilkinson, P. B., Chambers, J. E., & Strutt, M. (2014). Optimized arrays for 2D cross-borehole electrical tomography surveys. *Geophysical Prospecting, 62*(1), 172-189. doi:https://doi.org/10.1111/1365-2478.12072

Martin, T., & Gunther, T. (2013). Complex resistivity tomography (CRT) for fungus detection on standing oak trees. *European Journal of Forest Research, 132*(5-6), 765-776. doi:10.1007/s10342-013-0711-4

Maurer, H., & Friedel, S. (2006). Outer-space sensitivities in geoelectrical tomography. *Geophysics, 71*(3), G93-G96. doi:10.1190/1.2194891

Meju, M. A. (1994). *Geophysical Data Analysis: Understanding Inverse Problem Theory And Practice* (Vol. 6): Society of Exploration Geophysicists Tulsa,, OK.

Menke, W. (2012c). *Geophysical data analysis: Discrete inverse theory* (Vol. 45): Academic press.

Ogilvy, R. D., Meldrum, P. I., Kuras, O., Wilkinson, P. B., Chambers, J. E., Sen, M., . . . Tsourlos, P. (2009). Automated monitoring of coastal aquifers with electrical resistivity tomography. *Near Surface Geophysics, 7*(5-6), 367-375. doi:Doi 10.3997/1873-0604.2009027

Oiro, S., & Comte, J.-C. (2019). Drivers, patterns and velocity of saltwater intrusion in a stressed aquifer of the East African coast: Joint analysis of groundwater and geophysical data in southern Kenya. *Journal of African Earth Sciences, 149*, 334-347. doi:https://doi.org/10.1016/j.jafrearsci.2018.08.016

Palacios, A., Ledo, J. J., Linde, N., Luquot, L., Bellmunt, F., Folch, A., . . . Carrera, J. (2019). Time-lapse cross-hole electrical resistivity tomography (CHERT) for monitoring seawater intrusion dynamics in a Mediterranean aquifer. *Hydrol. Earth Syst. Sci. Discuss., 2019*, 1-30. doi:10.5194/hess-2019-408

PEDERSEN, L. B. (1979). CONSTRAINED INVERSION OF POTENTIAL FIELD DATA*. *27*(4), 726-748. doi:10.1111/j.1365-2478.1979.tb00993.x

POUS, J., MARCUELLO, A., & QUERALT, P. (1987). RESISTIVITY INVERSION WITH A PRIORI INFORMATION*. *Geophysical Prospecting, 35*(5), 590-603. doi:10.1111/j.1365-2478.1987.tb00837.x

Robbins, A. R., & Plattner, A. (2018). Offset-electrode profile acquisition strategy for electrical resistivity tomography. *Journal of Applied Geophysics, 151*, 66-72. doi:10.1016/j.jappgeo.2018.01.027

Ronczka, M., Hellman, K., Günther, T., Wisén, R., & Dahlin, T. (2017). Electric resistivity and seismic refraction tomography: a challenging joint underwater survey at Äspö Hard Rock Laboratory. *Solid Earth, 8*(3), 671-682. doi:10.5194/se-8-671-2017

Ronczka, M., Voss, T., & Gunther, T. (2015). Cost-efficient imaging and monitoring of saltwater in a shallow aquifer by using long electrode ERT. *Journal of Applied Geophysics, 122*, 202-209. doi:10.1016/j.jappgeo.2015.08.014

Rubin, Y., & Hubbard, S. S. (2006). *Hydrogeophysics* (Vol. 50): Springer Science & Business Media.

Rücker, C. (2010). Advanced Electrical Resistivity Modelling And Inversion Using Unstructured Discretization.

Rücker, C., Günther, T., & Spitzer, K. (2006). Three-dimensional modelling and inversion of dc resistivity data incorporating topography - I. Modelling. *Geophysical Journal International, 166*(2), 495-505. doi:10.1111/j.1365-246X.2006.03010.x

Rücker, C., Günther, T., & Wagner, F. M. (2017). pyGIMLi: An open-source library for modelling and inversion in geophysics. *Computers & Geosciences, 109*, 106-123. doi:10.1016/j.cageo.2017.07.011

Sasaki, Y. (1992). Resolution of resistivity tomography inferred from numerical simulation. *Geophysical Prospecting, 40*(4), 453-463. doi:10.1111/j.1365-2478.1992.tb00536.x

Saunders, J. H., Herwanger, J. V., Pain, C. C., Worthington, M. H., & De Oliveira, C. R. E. (2005). Constrained resistivity inversion using seismic data. *Geophysical Journal International, 160*(3), 785-796. doi:10.1111/j.1365-246X.2005.02566.x

Schmelzbach, C., Doetsch, J., Robertsson, J. O., Jordi, C., & Günther, T. (2018). Geostatistical regularization operators for geophysical inverse problems on irregular meshes. *Geophysical Journal International, 213*(2), 1374-1386. doi:10.1093/gji/ggy055 %J Geophysical Journal International

Schmidt-Hattenberger, C., Bergmann, P., Kiessling, D., Kruger, K., Rucker, C., Schutt, H., & Grp, K. (2011). Application of a Vertical Electrical Resistivity Array (VERA) for Monitoring CO2 Migration at the Ketzin Site: First Performance Evaluation. *10th International Conference on Greenhouse Gas Control Technologies, 4*, 3363-3370. doi:10.1016/j.egypro.2011.02.258

Selley, R. C. (2000). *Applied sedimentology*: Elsevier.

Shoemaker, W. B. (2004). Important observations and parameters for a salt water intrusion model. *Ground Water, 42*(6-7), 829-840. doi:10.1111/j.1745-6584.2004.t01-2-.x

Stuyfzand, P. J. (1992). *Behaviour of major and trace constituents in fresh and salt intrusion waters, in the western Netherlands.* Paper presented at the Study and modelling of salt water intrusion into aquifers. In: Proceedings of the 12th salt water intrusion meeting, Barcelona. CIHS-CIMNE, Barcelona.

Sutter, E., & Ingham, M. (2017). Seasonal saline intrusion monitoring of a shallow coastal aquifer using time-lapse DC resistivity traversing. *Near Surface Geophysics, 15*(1), 59-73. doi:10.3997/1873-0604.2016039

Tsourlos, P., Ogilvy, R., Papazachos, C., & Meldrum, P. (2011). Measurement and inversion schemes for single borehole-to-surface electrical resistivity tomography surveys. *Journal of Geophysics and Engineering, 8*(4), 487-497. doi:10.1088/1742-2132/8/4/001 %J Journal of Geophysics and Engineering

Uhlemann, S., Wilkinson, P. B., Maurer, H., Wagner, F. M., Johnson, T. C., & Chambers, J. E. (2018). Optimized survey design for electrical resistivity tomography: combined optimization of measurement configuration and electrode placement. *Geophysical Journal International, 214*(1), 108-121. doi:10.1093/gji/ggy128

Vogel, C. R. (2002). *Computational Methods for Inverse Problems*: Society for Industrial and Applied Mathematics.

Wagner, F. M. (2016). *New developments in electrical resistivity imaging with applications to geological CO_2 storage.*

Wagner, F. M., Bergmann, P., Rucker, C., Wiese, B., Labitzke, T., Schmidt-Hattenberger, C., & Maurer, H. (2015). Impact and mitigation of borehole related effects in permanent crosshole resistivity imaging: An example from the Ketzin CO2 storage site. *Journal of Applied Geophysics, 123*, 102-111. doi:10.1016/j.jappgeo.2015.10.005

Wagner, F. M., Günther, T., Schmidt-Hattenberger, C., & Maurer, H. (2015). Constructive optimization of electrode locations for target-focused resistivity monitoring. *Geophysics, 80*(2), E29-E40. doi:10.1190/geo2014-0214.1

Wagner, F. M., Möller, M., Schmidt-Hattenberger, C., Kempka, T., & Maurer, H. (2013). Monitoring freshwater salinization in analog transport models by time-lapse electrical resistivity tomography. *Journal of Applied Geophysics, 89*, 84-95. doi:https://doi.org/10.1016/j.jappgeo.2012.11.013

Walton, N. R. G. (1989). Electrical Conductivity And Total Dissolved Solids—What Is Their Precise Relationship? *Desalination, 72*(3), 275-292.

Werner, A. D., Bakker, M., Post, V. E. A., Vandenbohede, A., Lu, C. H., Ataie-Ashtiani, B., . . . Barry, D. A. (2013). Seawater intrusion processes, investigation and management: Recent advances and future challenges. *Advances in Water Resources, 51*, 3-26. doi:10.1016/j.advwatres.2012.03.004

Wilkinson, P. B., Meldrum, P. I., Chambers, J. E., Kuras, O., & Ogilvy, R. D. (2006). Improved strategies for the automatic selection of optimized sets of electrical resistivity tomography measurement configurations. *Geophysical Journal International, 167*(3), 1119-1126. doi:10.1111/j.1365-246X.2006.03196.x

Wunderlich, T., Fischer, P., Wilken, D., Hadler, H., Erkul, E., Mecking, R., . . . Rabbel, W. (2018). Constraining electric resistivity tomography by direct push electric conductivity logs and vibracores: An exemplary study of the Fiume Morto silted riverbed (Ostia Antica, western Italy). *83*(3), B87-B103. doi:10.1190/geo2016-0660.1

Zhou, J. Y., Revil, A., & Jardani, A. (2016). Stochastic structure-constrained image-guided inversion of geophysical data. *Geophysics, 81*(2), E89-E101. doi:10.1190/Geo2014-0569.1

Zhou, W. F., Beck, B. F., & Adams, A. L. (2002). Effective electrode array in mapping karst hazards in electrical resistivity tomography. *Environmental Geology, 42*(8), 922-928. doi:10.1007/s00254-002-0594-z

5 Conclusion

Coastal margins are dynamic and sensitive ecological systems. They are vulnerable to the burdens and whims of human development, and are highly desirable for housing, industry, agriculture, and aquacultures. All can affect the groundwater chemistry and hydraulics in the near-shore environment. Unsustainable groundwater abstraction, sea level rise, and changes to rainfall patterns further upset this balance. The need for high-quality information in these areas is higher now than ever before.

An established seawater intrusion monitoring site located in Perth, Western Australia, appears to be a prime reference site for numerical experiments. There is clear evidence of movement of the seawater interface from water electrical conductivity data, with multiple wells, geological logs, and time-lapse data from over thirty years of monitoring. I demonstrate how, although there is substantial data at this site, the geometry and rate of movement of the seawater wedge cannot be conclusively defined.

The shallow karstic aquifer at this site is extremely transmissive and heterogeneous. Direct evidence exists from quarries, hand samples, and regional flow nets. This has direct implications for groundwater modelling of the seawater interface. I examine the potential impacts of aquifer heterogeneity and dip angle, and show that, even if the aquifer throughflow is well-constrained, anisotropy can significantly affect the position of the seawater toe. In a dipping anisotropic environment, I demonstrate the seawater wedge can maintain the same position for multiple groundwater throughflows. This has consequence for groundwater models based on knowing the position of the seawater interface without regard for the anisotropic properties.

Spatially correlated random fields can generate geologically plausible distributions of hydraulic parameters. I use the data from the reference site to create a set of hydraulic conductivity distributions that conform to the existing data. I show that the geometry of the seawater wedge can be significantly different for the same groundwater flow and mean hydraulic conductivity. I find that the hydraulic conductivity proximal to the zone of submarine groundwater discharge is a strong influence on the geometry and landward position of the seawater wedge.

Using the monitoring well data from this site, I outline a monitoring system that is optimised for high-quality groundwater monitoring at the coastal margins. Three of the key outcomes include (i) automation of measurements including groundwater pressure, water quality, and groundwater velocity (ii) measurements made throughout the entire saturated thickness of the aquifer to capture the variability of karstic aquifers and (iii) the measurement and distribution of solutes using geophysical methods.

Electrical resistivity imaging (ERI) appears to be well-suited to provide the distribution of solutes in the shallow aquifer. However, I find that outcomes from surface based ERI are heavily dependent on acquisition and processing parameters and require specific interpretation. The technology needs to be analysed, adapted, and improved if it is to be effective in recovering the seawater interface.

I show that certain ERI acquisition configurations are more suitable than others for identifying coastal hydrogeology. For example, arrays containing dipole-dipole configurations provided improvements in the definition of key features such as the clayey aquiclude. I also show that including topography, such as dune structures, is an essential part of the imaging process (i.e., inversion). I provide a detailed comparison of multiple inversion approaches and parameters. The wealth of field data collected shows how ERI data can be used to

identify a range of aquifer architectures. I also use ERI to demonstrate the landward movement of the seawater interface along Perth's coastal margin approaching the highly developed town centre.

The introduction of multi-disciplinary research opens a range of possibility for groundwater monitoring, particularly for instrumented monitoring boreholes. I compile a table of potential groundwater monitoring solutions and propose an 'optimal' monitoring design to capture changes in this complex environment. This design incorporates the outcomes from the analysis of existing monitoring solution at the reference site and has the potential to supply high-quality data for groundwater modelling at the coast.

Borehole-based imaging and instrumented boreholes appear to provide an optimal solution for precision seawater monitoring. I have analysed the outputs from an extensive range of resistivity models, acquisition geometry, and inversion parameters to show that cross-borehole ERI can accurately resolve electrical resistivity for the vadose zone, mixing zone, seawater wedge and clayey substrate between boreholes. A key outcome is that the combination of surface and borehole-based electrodes, including constrained inversion of the substrate, is able to reveal the full geometry and resistivity of the seawater wedge.

There are no examples of cross-well imaging that include measurements from single well quadrupoles in literature. This may be due to acquisition constraints, such a limited acquisition time, or research-oriented goals. My analysis suggests that (i) electrodes in each single-well can provide a detailed resistivity trace along each well, and (ii) including quadrupoles from the single-well with conventional cross-well quadrupoles can improve tomographic imaging between wells.

Outcomes from imaging in a single borehole have additional benefits. I show that a single borehole with dense electrode spacing can yield a highly accurate map of resistivity along the trace of the borehole. This is process is automatable and can be remotely controlled, effectively replacing the wireline logging for high-risk areas. Where multiple-single boreholes are used in a coastal setting, the outcomes from inversion can indicate the simple geometry of the seawater wedge.

The topics addressed in this research show that precise monitoring of the seawater wedge is possible and achievable. The sustainable management of shallow groundwater resources has consequence for the future of humanity and all living things, and it is my hope that this research helps to create subsurface imaging technology required to guide the future of these critical aquifers.

Appendix A Permissions

This thesis utilises published material under the following papers:

> Costall, A., Harris, B., & Pigois, J. P. (2018). Electrical Resistivity Imaging and the Saline Water Interface in High-Quality Coastal Aquifers. Surveys in Geophysics, 39(4), 753-816. doi:10.1007/s10712-018-9468-0
>
> Costall, A., Harris, B., Teo, B., Schaa, R., Wagner, F. M., and Pigois, J. P. (2020). Groundwater Throughflow and Seawater Intrusion in High Quality Coastal Aquifers. Nature Scientific Reports
>
> Costall, A. R., & Harris, B. (2019). Rapid Estimation of Volumetric Groundwater Recharge in the Vadose Zone via Ground Penetrating Radar. ASEG Extended Abstracts, 2018(1), 1-7. doi:10.1071/ASEG2018abP091
>
> Costall, A. R., Harris, B. D., Pethick, A. M., & Schaa, R. (2016). Electric Bipole Antenna Model Study of a Basin Scale Fault System. ASEG Extended Abstracts, 2016(1), 1-5. doi: https://doi.org/10.1071/ASEG2016AB324

As per the SEG policy on publishing, authors have open-access permission to reuse their papers published with SEG in a thesis or dissertation. This applies to both The Leading Edge and Interpretation journals.

The policy states:

> *"Authors may reuse all or part of their papers published with SEG in a thesis or dissertation that authors write and are required to submit to satisfy criteria of degree granting institutions."*

For more details on SEG policies and permissions, please refer to:
https://seg.org/Publications/Policies-and-Permissions/Open-Access-Policy.

I have requested explicit permissions from the publishing bodies and have included their approval below.

Gmail

Alex Costall <costall.alex@gmail.com>

RE: FW: Query regarding publication of article in PhD thesis: Journal 10712/GEOP - Article 9468 Ticket ID 64495

2 messages

Journalpermissions <journalpermissions@springernature.com> 25 June 2019 at 21:07
To: "costall.alex@gmail.com" <costall.alex@gmail.com>
Cc: OR Support <ORsupport@springernature.com>

Dear Alex,

Thank you for your recent Springer Nature permissions request. This work is licensed under the Creative Commons Attribution 4.0 International License, which permits unrestricted use, distribution, modification, and reproduction in any medium, provided you:

1) give appropriate acknowledgment to the original author(s) including the publication source,

2) provide a link to the Creative Commons license, and indicate if changes were made.

You are not required to obtain permission to reuse this article, but you must follow the above two requirements.

Images or other third party material included in the article are encompassed under the Creative Commons license, unless indicated otherwise in the credit line. If the material is not included under the Creative Commons license, users will need to obtain permission from the license holder to reproduce the material.

To view a copy of the Creative Commons license, please visit http://creativecommons.org/licenses/by/4.0/

Please let me know if you have any questions.

Best wishes,

Oda

Oda Siqveland

Rights Executive

SpringerNature

Gmail Alex Costall <costall.alex@gmail.com>

RE: Proofs for your article in Scientific Reports (66516) - [Reminder-2]

Journalpermissions <journalpermissions@springernature.com> 28 July 2020 at 21:31
To: "costall.alex@gmail.com" <costall.alex@gmail.com>
Cc: Jemima Williamson <jemima.williamson@nature.com>

Dear Alex,

Thank you for your recent email. Per your retained rights you can reuse your article in your thesis/dissertation without obtaining permission from us. If the material is being reused prior to publication by us, please make your editor/editorial contact aware of your intended use.

Copyright statement should read – 'Accepted and soon to be published; article name, journal, and publisher name'.

If you have any further questions, please contact me directly.

Best wishes,

Oda

--

Oda Siqveland

(she/her/hers)

Rights Executive

Springer Nature

The Campus, 4 Crinan Street, London N1 9XW, United Kingdom

T +44 (0) 207 014 6851

oda.siqveland@springernature.com

springernature.com

BLACK LIVES MATTER

Gmail Alex Costall <costall.alex@gmail.com>

Re: ASEG Website - Contact Enquiry

Ian James <ian@terraspect.com> 11 June 2019 at 12:02
Reply-To: ian@terraspect.com
To: Alexander Costall <costall.alex@gmail.com>
Cc: webmaster@aseg.org.au

Hi Alex,

Thanks for the email. I asked around and I believe all you will need to do is to ask the authors permission to use the material, and to cite the publication where the material is used (which I expect you'd do anyway). As you are the previous author, this should be pretty straightforward. I expect Brett will also be happy for you to use the material - so all good.

Good luck with the rest of the PhD!

Cheers,

Ian

Ian James

T | +61 (0)488 497 117

E | ian@terraspect.com

On 07/06/2019 14:38, Alexander Costall via Australian Society of Exploration Geophysicists wrote:

> Hi ASEG Webmaster,
>
> A contact enquiry has been made on the ASEG website.
>
> The details of the enquiry are as follows:
> Name: Alexander Costall
> Contact Number: 0468300974
> Email Address: costall.alex@gmail.com
> Message:
> G'day,
>
> I would like to apply for permission to re-use the material from the 2018
> expanded abstract 'Rapid Estimation of Volumetric Groundwater Recharge in the
> Vadose Zone via Ground Penetrating Radar' (linked below) for submission to an
> ASEG published research article, and for further publication in my phd
> thesis.
>
> Could you please assist me with the correct procedure to obtain such
> permissions?
>
> http://www.publish.csiro.au/ex/ASEG2018ABP091
>
> Regards,
>
> Alex
>
> Time Submitted:
> Submitted on Friday, June 7, 2019 - 14:38

Appendix B Attribution of Authorship

Costall, A., Harris, B., & Pigois, J. P. (2018). E*lectrical Resistivity Imaging and the Saline Water Interface in High-Quality Coastal Aquifers*. Surveys in Geophysics, 39(4), 753-816. doi:10.1007/s10712-018-9468-0

9/3/2020 Gmail - Attribution of Authorship: Electrical Resistivity Imaging and the Saline Water Interface in High-Quality Coastal Aquifers

Gmail Alex Costall <costall.alex@gmail.com>

Attribution of Authorship: Electrical Resistivity Imaging and the Saline Water Interface in High-Quality Coastal Aquifers

3 messages

Alex Costall <costall.alex@gmail.com> 2 September 2020 at 20:12
To: Brett Harris <b.harris@curtin.edu.au>, Jon-Philippe Pigois <jon-philippe.pigois@dwer.wa.gov.au>

Dear Brett and JP,

Prior to submission of my thesis I require the approval of co-authors and relevant attribution statements.

Could you please review the table below and advise whether you acknowledge and agree with the attribution statement, and that you approve the use of this work in my thesis. Written confirmation will be sufficient.

Costall, A., Harris, B., & Pigois, J. P. (2018). E*lectrical Resistivity Imaging and the Saline Water Interface in High-Quality Coastal Aquifers*. Surveys in Geophysics, 39(4), 753-816. doi:10.1007/s10712-018-9468-0

Author	Conception & Design	Data Acquisition	Data Processing	Data Analysis	Paper Writing	Paper Review
A. Costall	x	x	x	x	x	x
I acknowledge that the above represents my contribution to the research output. Signed:						
B. Harris	x			x	x	x
I acknowledge that the above represents my contribution to the research output. Signed:						
J.P. Pigois						x
I acknowledge that the above represents my contribution to the research output. Signed:						

Kind Regards,

Alexander Costall
PhD Student | Exploration Geophysics | Curtin University
Tel | (+61) 8 9266 3408
Mobile | (+61) 0468 300 974
Email | alex.costall@curtin.edu.au

Gmail

Alex Costall <costall.alex@gmail.com>

Attribution of Authorship: Electrical Resistivity Imaging and the Saline Water Interface in High-Quality Coastal Aquifers

JP Pigois <jon-philippe.pigois@dwer.wa.gov.au> 3 September 2020 at 08:11
To: Alex Costall <costall.alex@gmail.com>, Brett Harris <b.harris@curtin.edu.au>

Hi Alex,

I approve and agree with the attribution statement.

Cheers

JP

Jon-Philippe (JP) Pigois

Senior Hydrogeologist

Swan Avon Region

Department of Water and Environmental Regulation

7 Ellam Street, Victoria Park WA 6100

T: (+61) 6250 8024

E: jon-philippe.pigois@dwer.wa.gov.au | www.dwer.wa.gov.au

Twitter: @DWER_WA

[Quoted text hidden]

Gmail

Alex Costall <costall.alex@gmail.com>

Attribution of Authorship: Electrical Resistivity Imaging and the Saline Water Interface in High-Quality Coastal Aquifers

Brett Harris <B.Harris@curtin.edu.au> 3 September 2020 at 08:12
To: Alex Costall <costall.alex@gmail.com>, Jon-Philippe Pigois <jon-philippe.pigois@dwer.wa.gov.au>

Thanks Alex,

The table looks fine to me.

Best Regards

Brett

Brett Harris
Professor

Discipline Lead | Exploration Geophysics

Western Australian School of Mines: Minerals, Energy and Chemical Engineering
Faculty of Science and Engineering

Curtin University
Tel | +61 8 9266 3408
Mobile | +61 410 65 7268

Email | b.harris@curtin.edu.au
Web | www.curtin.edu.au

Curtin University
CENTRE FOR EXPLORATION GEOPHYSICS

From: Alex Costall <costall.alex@gmail.com>
Sent: Wednesday, 2 September 2020 8:13 PM

[Quoted text hidden]

[Quoted text hidden]

Attributions for the article below are located under the Author Information section of the published article (see "Contributions")

Costall, A.R., Harris, B.D., Teo, B. et al. Groundwater Throughflow and Seawater Intrusion in High Quality Coastal Aquifers. Sci Rep 10, 9866 (2020). https://doi.org/10.1038/s41598-020-66516-6

Contributions

A.C., B.H., wrote the paper using input and feedback from all co-authors; A.C., B.H., B.T., R.S., F.W., and J.P. reviewed and contributed scientific discussion to the manuscript; A.C. designed and ran experiments with advice from B.H.; B.T. and A.C. designed figures with input from B.H.

Appendix C Other Publications

Appendix C.1 Rapid Estimation of Volumetric Groundwater Recharge in the Vadose Zone Via Ground Penetrating Radar

This expanded abstract was presented at AEGC 2018 in Sydney. It explores the concept of vadose zone recharge using changes in velocity and the time delay to a known reflector, e.g., the water table.

RAPID ESTIMATION OF VOLUMETRIC GROUNDWATER RECHARGE IN THE VADOSE ZONE VIA GROUND PENETRATING RADAR

Mr Alexander Ross Costall*
Curtin University
26 Dick Perry Avenue, W.A
Alex.costall@curtin.edu.au

Professor Brett Harris
Curtin University
26 Dick Perry Avenue, W.A
b.harris@curtin.edu.au

*presenting author asterisked

SUMMARY

Saturation in the vadose zone is known to reduce the ground penetrating radar (GPR) electromagnetic wave velocities. We examine the impact of increased water content in highly-permeable beach and dune systems on GPR velocities along coastal margin of Perth, Western Australia. We acquire repeat GPR transects in May and August before and after annual high rainfall periods. The assumption of exceedingly flat water table reflector permits us to estimated change in GPR velocity at successive dates. This change in velocity can be translated to an estimated change in water saturation via the Topp relationship which is an imperial mapping of water saturation to dielectric permittivity.

Key words: Ground Penetrating Radar, Water-Table, Vadose-zone recharge

INTRODUCTION

Ground Penetrating Radar (GPR) is an effective tool for shallow high-resolution geophysical investigation. The speed and simplicity of acquisition lends itself to rapid detection and evaluation of subsurface features. Variations in relative dielectric permittivity below the ground cause high-frequency electromagnetic waves to be reflected from layers with sufficient electrical impedance contrast.

The vadose zone in semi-arid quartz or limestone coastal environments is usually highly resistive and internal structure of beach and dune sediments can be exceedingly well resolved by GPR. However, it is the high-contrast boundary at the water table that often provides the strongest GPR reflection. Other reflections in the vadose zone are typically the result of grain-size or mineralogy changes, including high concentrations of heavy minerals (exceeding 2.9 $g.cm^{-3}$) such as those formed from storm-lag deposits (Buynevich *et al.*, 2009). Changes in depositional environments are identifiable in GPR.

Examples where GPR has been applied include stratigraphic mapping (J. L. Davis *et al.*, 1989), soil-water content definition (Huisman *et al.*, 2003), porosity estimation (Bradford *et al.*, 2009; Turesson, 2006), and water table/vadose zone depth evaluation (Elmar Strobach, 2013; E. Strobach *et al.*, 2010). The dominant factors controlling the depth of investigation for GPR are antennae bandwidth, and ground conductivity. Higher-frequency antennas tend to be able to resolve close spaced layers at the expense of depth penetration. Highly conductive media, such as clays and saline water, will attenuate the GPR signal and dramatically reducing the investigation depth. The velocity of an electromagnetic wave in a medium is (BurVal Working Group *et al.*, 2006);

$$v = \frac{c}{\sqrt{\varepsilon_r \mu_r \frac{1 + \sqrt{\left(1 + \left(\frac{\sigma}{\omega \varepsilon}\right)^2\right)}}{2}}} \quad (1)$$

In the case of low-loss materials such as clean, dry, quartz sands, equation (**1**) reduces to

$$v = \frac{c}{\sqrt{\varepsilon_r}} \quad (2)$$

Changes in surface elevation such as dunes are significant for imaging and analysis of GPR data. Sand dunes in Perth can extend to 40 metres above-sea-level (ASL) in the northern-most suburbs such that depth to the water table will be outside the range of most shielded GPR systems. We target accuracy of less than 10cm which can be achieved with real-time kinematic (RTK) global-position-systems (GPS). This is necessary for precise mapping of the water table GPR reflector.

METHOD AND RESULTS

The velocity of the GPR electromagnetic pulse is related to electrical permittivity. Water has a high relative electrical permittivity (e.g. 80) and thus even a small change in water saturations can significantly impact GPR velocity in the vadose zone (Topp *et al.*, 1980). The Topp relationship (Topp *et al.*, 1980) (equations 3, and 4) shown in Figure 5.1, is an empirically derived relationship between dielectric permittivity and water saturation. The empirical nature of the relationship tends to break down at very low (i.e. < 5%) and very high (i.e. > 40%) water saturation, resulting in a wider margin of error at these extremes (Elmar Strobach, 2013).

$$\varepsilon'_{e,r} = 3.03 + 0.3\theta_v + 146\,\theta_v^2 - 76.7\theta_v^3 \quad (3)$$

$$\theta_v = -5.3 * 10^{-2} + 2.92 * 10^{-2}\varepsilon_{e,r} - 5.5 * 10^{-4}\varepsilon_{e,r}^2 + 4.3 * 10^{-6}\varepsilon_{e,r}^3 \quad (4)$$

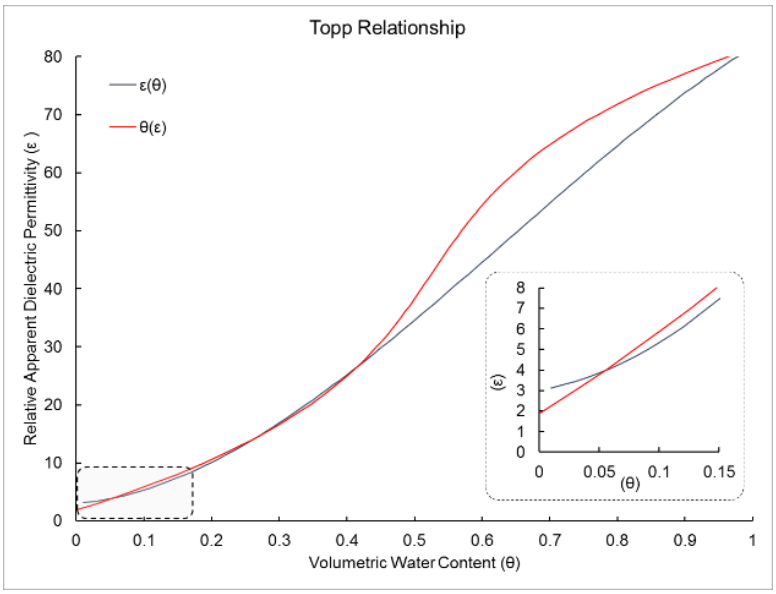

Figure 5.1: Graph of the 'Topp relationship' (Topp et al., 1980) relating the volumetric water content and dielectric permittivity of a medium. Note the difference between the forward and reverse relationships at lower volumetric water contents, prominent at high (i.e. > 40%) volumetric water content. Graph shown from equations 3 and 4 (Topp et al., 1980).

We refer to water in the vadose zone (i.e. between the ground surface and phreatic water table), as 'volumetric unsaturated zone water content' or simply volumetric water content. Rate of rainfall infiltration through the unsaturated zone will depend on rainfall, evapotranspiration, and unsaturated hydraulics of the sediments. Water

saturation will affect the relative dielectric permittivity ($\boldsymbol{\varepsilon}$) as shown by the Topp relationship (Figure 5.1), and reduce the GPR pulse velocity, e.g. Figure 5.2. Changes in water saturation can be estimated from repeat GPR surveys.

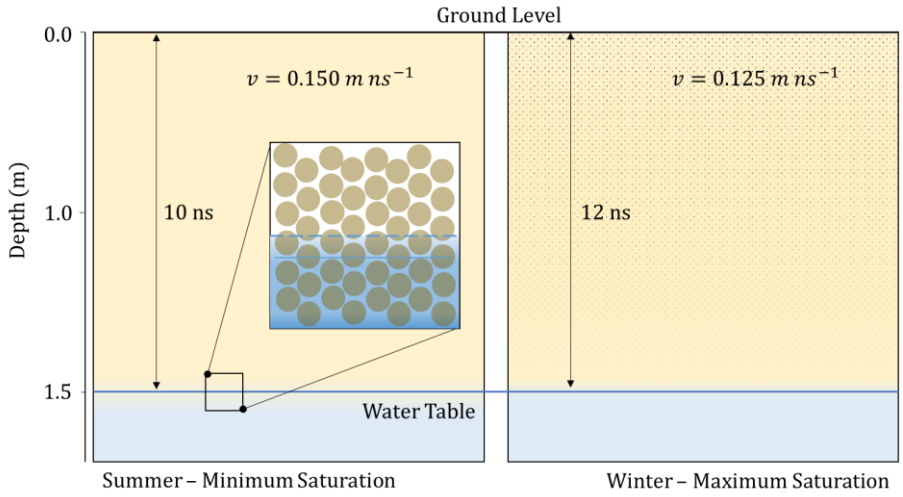

Figure 5.2: Representation of the velocity reduction effect of water saturation, as inferred from the Topp relationship. An increase in water content will increase the relative apparent dielectric permittivity and reducing the GPR wave velocity. This schematic shows a highly permeable media, such as a coarse beach sand. For high permeability sediments, the impact of rainfall recharge on the water table will be negligible near to the ocean (e.g. a known head boundary dictated by tidal forcing). The capillary fringe in a coarse sand environment is also expected to be negligible.

Data collected by a local monitoring station at Swanbourne suggests that rainfall for the year 2014 was unusually low, at 581.2 mm for the entire year. This is considerably lower than both the historical average since 1993 (when these records began), and the preceding two years. E. Strobach *et al.* (2014) suggests rainfall at several location in the Bassendean Sand of the Gnangara mound aquifer system may infiltrate at rates of close to 2 metres per 3-month period. It's possible that infiltration rates through the sands at the city beach site could be similar or faster than of the Bassendean Sands.

Worldwide study locations suggest infiltration rates of 34.5% for permeable skeletal soil of low water-holding capacity (Allison *et al.*, 1978), while Stephens *et al.* (1986) suggests up to 20% for coarse-grained sands with very small percentage of silt and clay. Local infiltration studies from Banksia woodland vegetation in the Gnangara mound suggest a value of 194 mm/year for approximately 800 mm of rainfall, i.e. 24% (Sharma *et al.*, 1983), which agree with geophysical infiltration studies by E. Strobach *et al.* (2014).

We assume a near-flat water table at mean sea level, over the length of the GPR transect. A nearby well suggests a water-table gradient of 1.07 mm/m in October and 0.61 mm/m in May. These numbers suggest that the maximum rise in the water table from the ocean to the end of the GPR transect is less 18 cm in May, and less than 30 cm in August.

Four transects, shown in Figure 5.3, were collected on the 2nd May 2014 and then again on the 8th August 2014 using the common offset radar method. These transects were measured with the Mala ProEx GPR system in combination with a 250 MHz towed sled-style shielded antenna. Radar measurements were made ten times a second (10 Hz) and synchronised with a Thales Z-Max real-time kinematic (RTK) global positioning system

(GPS) for precise elevation control. Each trace is stacked four times to improve signal-to-noise ratio. Processing steps undertaken are common between vintages (i.e. May and August transects), including de-wow, static correction, subtracting average, band-pass filtering and an energy-decay gain function.

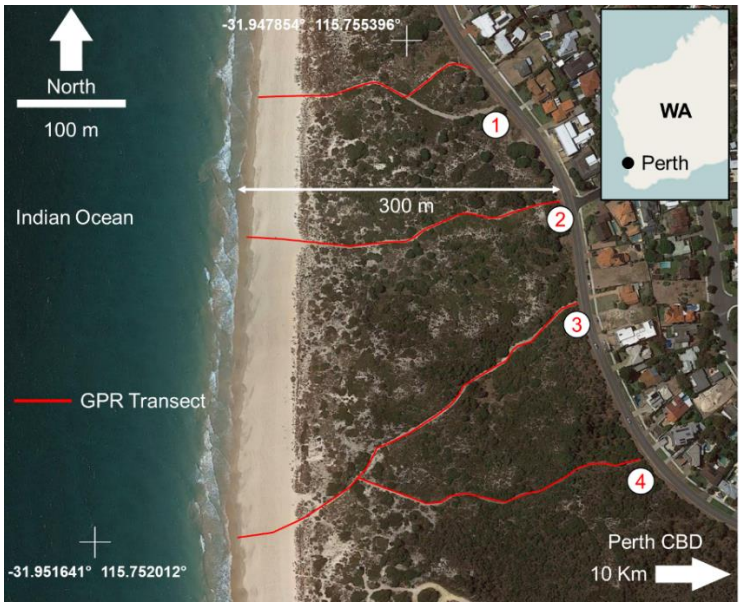

Figure 5.3: Location and orientation of the ground penetrating radar (GPR) transects featured in this paper. Shallow geology is described predominantly Tamala Limestone and Safety Bay sands. Total perpendicular length from the coastline is approximately 300 m.

After diffraction velocity analysis of the sections, a depth-conversion velocity of 0.145 m/ns is found to be appropriate. This value satisfies the flat water-table reflection assumption for May. Velocities ranging from 0.1 to 0.2 m/ns were tested however 0.145 m/ns was optimal (i.e. provided a flat water table reflector), and agreed with the majority of diffractions. Butler (2005) suggests 0.15 m/ns is reasonable for dry sands, in agreement with our finding.

Figure 5.4 shows that using a velocity of 0.145 m/ns for time to depth conversion of the August GPR data fails to flatten the water table reflector. The August water-table reflection is clearly bowed in the centre of the profile. The geometry of the reflector at 0.145m/ns may be due to lithological changes, such as lower-porosity limestone, or finer sands.

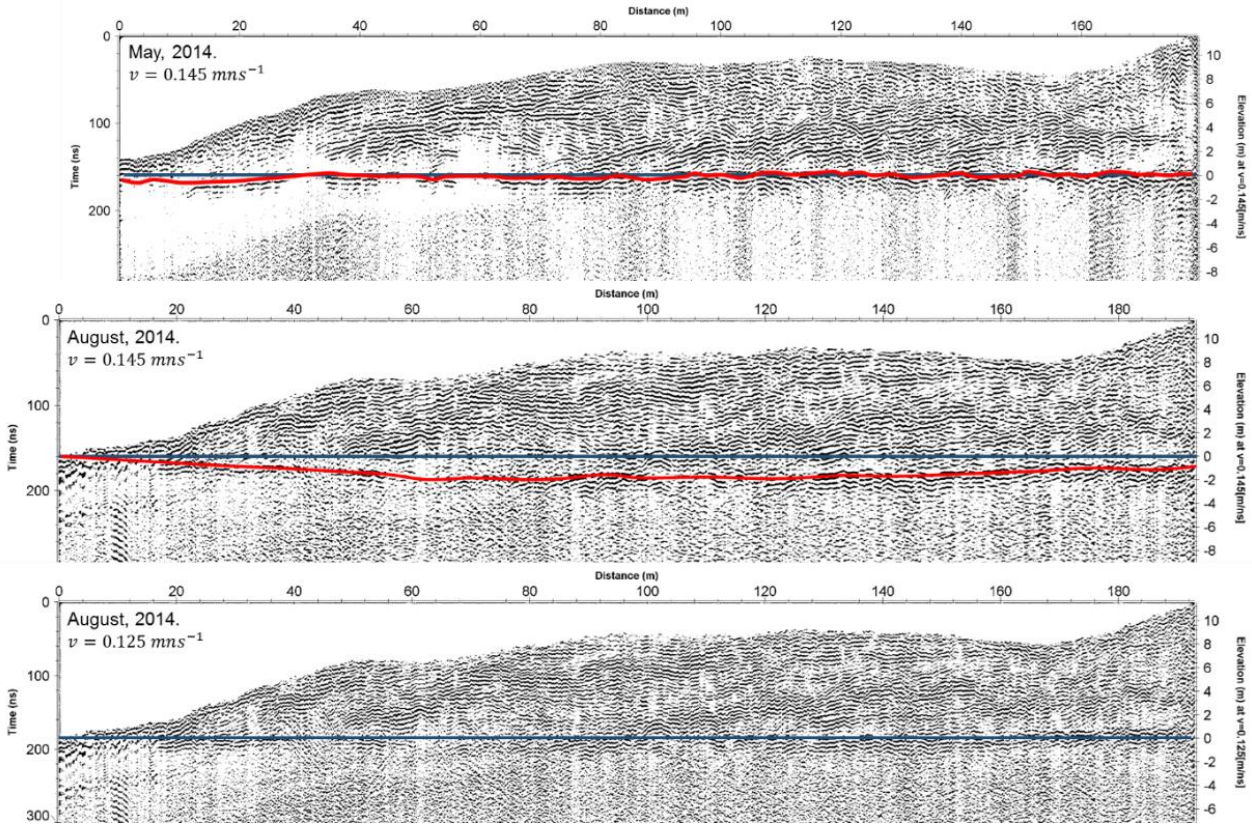

Figure 5.4: Processed GPR data from Line 1a, taken from May (top) and August (middle, bottom). A blue line represents an idealised flat water-table assumption at 0 m ASL. The upper and middle sections are migrated with a velocity of 0.145 m/ns, where the August transect violates the flat-water table assumption. The difference in the water-table reflection is an assumed result of water suspended in the zone above the water table, resulting in a slower velocity wave.

Diffraction hyperbola analysis of the August transect suggests a velocity of 0.125 m/ns is the appropriate velocity. We assume the change in velocity is dominantly due to additional water in the immediate subsurface. A 0.02 m/ns velocity change can be linked to an approximately 3.5% increase in the water content within the saturated zone, using the Topp Relationship. As expected, there is an increase in water in the vadose zone in August when compared to May.

Table 5.1: Calculation of the saturation difference via Topp relationship.

v (m/ns)	Ɛ	θ	Θ (%)	Δ Θ (%)
0.145	4.275	0.062	6.211	3.547
0.125	5.752	0.098	9.758	

Figure 5.5 shows the May transects from the investigation site in 3D. All transects show common features including the water-table, and dune-structures. However, limestone spurs are only observed in Line 2 and 4, and correlate with areas of higher topographical relief. A horizontal continuous layer above the water-table can be seen across many of the profiles here. This layer is too high to be the water-table (~2m above sea level), however we speculate this may represent a hydraulically altered layer from periods of higher water table levels, or the capillary fringe.

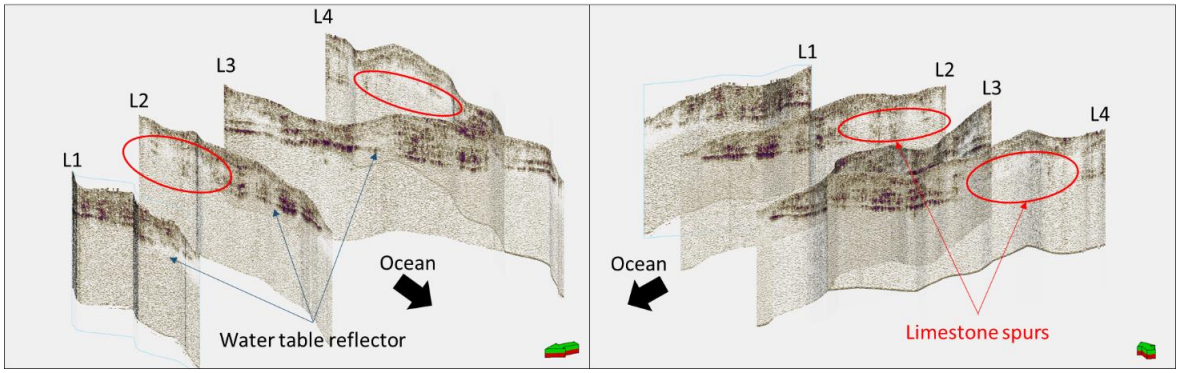

Figure 5.5: Visualisation of GPR data from the investigation site. The water-table reflector is prominently shown, and the limestone spur can be readily identified. Left and right images show the May GPR data from the north and south respectively.

Figure 5.6 highlights the reflectors identified from the Line 1 transect. A strong water table reflector continuous throughout the profile was readily identified, however no reflectors could be identified below the water table, likely due to a combination of saline water at the coast, and elevation throughout the dunes.

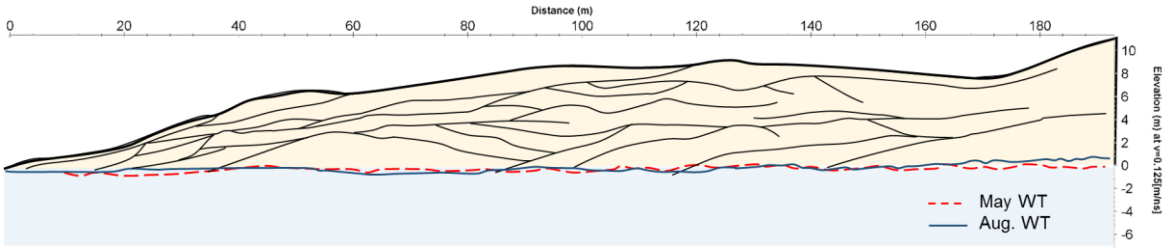

Figure 5.6: Schematic interpretation of GPR reflectors seen in Line 1. May and August water table reflectors are interpreted at the velocities 0.145 m/ns and 0.125 m/ns, showing the flat-water table approximation dependency on volumetric water content in the vadose zone. No sub-water table reflectors were identified.

DISCUSSION

Several assumptions are made throughout this experiment, which include assumptions on the homogeneity of the subsurface, as well as the rate-of-movement through the vadose zone. It is clear that the homogeneity of some sections is incorrect, given the obvious differences in subsurface reflectors across the profile, e.g. limestone spurs, however the section for which the analysis was used (Line 1) is obviously more uniform than other sections, such as Line 2, and Line 4. The water-table is difficult or impossible to resolve in most cases as the limestone appears to have scattered the GPR signal, and so we have based our analysis mostly on line 1, which offers the clearest image of the primary features required for our analysis.

Given the potential rate of infiltration associated with dune sands can be rapid, the long time period between each survey may have resulted in recharge events fully migrating through the vadose zone to the water table. Transition rates in the coarse beach sand will be rapid, however on the built-up vegetated dune faces, the fine-grained wind-borne sediments will naturally decrease this rate. A solution would be to repeat the surveys on a regular, short-period basis, to determine the exact changes present, as well as performing measurements in the laboratory to determine the rate of movement though the sands.

Tidal fluctuations of the order of 0.5 – 1 metre will affect the water table reflector near the coast. The GPR measurements made during this study were at similar tidal levels, however if more regular surveys are planned, the tidal fluctuations must be considered.

CONCLUSIONS

We demonstrate that GPR can be effective for time-lapse water infiltration monitoring, showing a decrease in velocity associated with increased volumetric water content in accordance with the Topp relationship. We estimate that, over the time period between measurements, the saturated water volume has increased by approximately 3.5% as inferred by a bulk velocity change of 0.02 m/ns. With the two surveys acquired for this pilot study, we are unable to estimate the physical amount of water in the vadose zone using changes in water-table reflection associated with an increase in vadose-zone water saturation. However, it can be used to further quantitatively assess groundwater recharge through geophysical measures, and with regular monitoring, the hydraulic parameters of the dune structure could be inferred.

ACKNOWLEDGMENTS

We wish to sincerely thank and acknowledge the work and assistance of Dr. Andrew Greenwood and Dr. Andrew Pethick in the collection of GPR data, and technical advice, and Dr. Elmar Strobach for assistance and valuable commentary on processing and interpretation of the dataset.

REFERENCES

Allison, G., & Hughes, M. (1978). The use of environmental chloride and tritium to estimate total recharge to an unconfined aquifer. *Soil Research, 16*(2), 181-195.

Bradford, J. H., Clement, W. P., & Barrash, W. (2009). Estimating porosity with ground-penetrating radar reflection tomography: A controlled 3-D experiment at the Boise Hydrogeophysical Research Site. *Water Resources Research, 45*(4).

BurVal Working Group, Kirsch, R., Rumpel, H.-M., Scheer, W., & Wiederhold, H. (2006). *Groundwater resources in buried valleys: a challenge for geosciences*: Leibniz Institute for Applied Geosciences (GGA-Institut).

Butler, D. K. (2005). *Near-surface geophysics*: Society of Exploration Geophysicists Tulsa.

Buynevich, I. V., Jol, H. M., & FitzGerald, D. M. (2009). Coastal Environments. In *Ground Penetrating Radar Theory and Applications* (pp. 299-322). Amsterdam: Elsevier.

Davis, J. L., & Annan, A. P. (1989). Ground-Penetrating Radar for High-Resolution Mapping of Soil and Rock Stratigraphy1. *Geophysical Prospecting, 37*(5), 531-551. doi:10.1111/j.1365-2478.1989.tb02221.x

Huisman, J. A., Hubbard, S. S., Redman, J. D., & Annan, A. P. (2003). Measuring Soil Water Content with Ground Penetrating Radar: A Review. *Vadose Zone Journal, 2*(4), 476-491. doi:10.2136/vzj2003.4760

Sharma, M., Farrington, P., & Fernie, M. (1983). *Localized groundwater recharge on the" Gnangara Mound", Western Australia.* Paper presented at the international conference on groundwater and man.

Stephens, D. B., & Knowlton, R. (1986). Soil-Water Movement and Recharge through Sand at a Semiarid Site in New-Mexico. *Water Resources Research, 22*(6), 881-889. doi:DOI 10.1029/WR022i006p00881

Strobach, E. (2013). Hydrogeophysical investigation of water recharge into the Gnangara Mound.

Strobach, E., Harris, B. D., Dupuis, C. J., Kepic, A., & Martin, M. W. (2010). Ground-Penetrating Radar For Delineation Of Hydraulically Significant Layers In The Unsaturated Zone Of The Gnangara Mound, Wa. *ASEG Extended Abstracts, 2010*(1), 1-4. doi:http://dx.doi.org/10.1071/ASEG2010ab237

Strobach, E., Harris, B. D., Dupuis, J. C., & Kepic, A. W. (2014). Time-lapse borehole radar for monitoring rainfall infiltration through podosol horizons in a sandy vadose zone. *Water Resources Research, 50*(3), 2140-2163. doi:10.1002/2013wr014331

Topp, G. C., Davis, J. L., & Annan, A. P. (1980). Electromagnetic Determination of Soil-Water Content - Measurements in Coaxial Transmission-Lines. *Water Resources Research, 16*(3), 574-582. doi:DOI 10.1029/WR016i003p00574

Turesson, A. (2006). Water content and porosity estimated from ground-penetrating radar and resistivity. *Journal of Applied Geophysics, 58*(2), 99-111. doi:10.1016/j.jappgeo.2005.04.004

Appendix C.2 Electric Bipole Antenna Model Study of a Basin Scale Fault System

This expanded abstract was presented at ASEG 2016, Adelaide. It is a model study of long-offset transient EM source for identifying the characteristics of the Badaminna fault.

Expanded Abstract: Electric Bipole Antenna Model Study of a Basin Scale Fault System

***Alexander Ross Costall**
Curtin University
a.costall@curtin.edu.au

Dr. Brett Harris
Curtin University
b.harris@curtin.edu.au

Dr. Andrew Pethick
Curtin University
a.pethick@curtin.edu.au

Dr. Ralf Schaa
Curtin University
r.schaa@curtin.edu.au

SUMMARY

The generation of electric fields with electric bipole transmitters are applicable at a wide range physical scales and for many subsurface exploration endeavours. Increase in transmitter power for a wide range of waveforms combined with receiver sensitivity has led to deeper exploration with electromagnetic methods. We investigate optimal design of grounded bipole EM system for generate electromagnetic fields over a basin-scale fault in Perth, W.A. The technical objective is to recover detailed electrical conductivity distribution proximal to and within a large fault system to depths of as much as 1000m below the surface. The ultimate geological imperative for the exercise is reveal possible change in solute concentration or hydraulic across these large fault systems. For example imaging of the difference composition of fault core zone would be a valuable outcome. We investigate various combinations of receiving and transmitting antenna geometries in preparation for a field campaign intended to resolve electrical parameters and structures of this large fault system.

Introduction

The Long-Offset Transient Electro-Magnetics, LOTEM, is a deep exploration, Time-Domain electromagnetic method. Modern examples of LOTEM application, range from hydrocarbon exploration (K.-M. Strack *et al.*, 1989) to analysis of the internal structure volcanoes (Haroon *et al.*, 2015; Hördt *et al.*, 2000) and even crustal studies (K. M. Strack *et al.*, 1990). The Long-Offset concept is gaining renewed interest, with successful application of similarly constructed frequency domain systems becoming also commonplace in today's exploration markets. As LOTEM is sensitive to deep, resistive targets, the methodology is well placed for hydrocarbon, CO2, and freshwater aquifer identification. It is also relatively inexpensive can be high complementary to seismic reflection data.

Recently, the controlled source electromagnetic (CSEM) method have been applied in offshore environments, where oil and gas reservoirs presented suitable higher resistivity targets. Land Based, long-offset CSEM and controlled source audio magneto-telluric (CSAMT) methods, both use a frequency domain signal to generate a far-offset plane-wave, and are believed to recover information to depths of 1 Km (Zonge, 1992). Typical land-based CSEM applications involve the definition of deep, high resistivity targets, such as geologically sequestered CO2, and hydrocarbon deposits (Grayver *et al.*, 2014; Lovatini *et al.*, 2013; Wirianto *et al.*, 2010a, 2010b).

Modern land EM acquisition is starting to take on characteristic of common in for seismic surveys. An example is the MTEM system where it is claimed multiple transmitters and receivers are used to generate data. This method

can transmit a step current change waveform (square-wave) or Pseudo-Random Binary Sequence (PRBS) to simulate a delta-pulse function in the transmitter. One of the major issues relating to use of MTEM is the precision in timing required to accurately deconvolve the transmitted waveform from the received waveform (Wright *et al.*, 2002). This also means introducing complications into the TEM measurement process (Anderson *et al.*, 2008; Chen *et al.*, 2015; S. Constable *et al.*, 2007; Guo-Qiang *et al.*, 2013; Hobbs *et al.*, 2008; PGS, 2007; SEG, 2010; Streich, 2015; Wright *et al.*, 2002; Zhdanov, 2010; Ziolkowski *et al.*, 2007; Ziolkowski *et al.*, 2010). Our research aims to investigate different waveforms and survey geometries to optimize recovery of conductivity distribution in and proximal to large fault systems.

The Badaminna fault is a basin-scale extensional fault system, running roughly North/South across the entire Vlaming sub-basin (Marshal *et al.*, 1993; Nicholas *et al.*, 2013). Figure 5.7 indicates the extent of the fault through the basin. This fault intersects both the Leederville, and Yarragadee aquifers. This presents an opportunity to investigate the feasibility of long-offset electromagnetic methods applied to deep groundwater exploration and fault system characterisation. This fault system is suitable for our investigation as both deep wells and detailed seismic transects cross the fault. Airborne EM data is also available, allowing near-surface constraint on electrical conductivity distribution to approximately 300m.

Basin hydrodynamics is often intimately connected to large-scale solution concentration distribution. So, building a large-scale picture of solution concentration across basin scale fault systems can be a key input to understanding the influence of large fault systems on basin hydraulics (e.g. groundwater flow). These are key considerations in building realistic groundwater models and such issues are currently being addressed by the Department of Water in Western Australia (Water, 2016). The long-offset or deep sounding electromagnetic methods could prove effective in recovering detailed information about solute concentration of the Yarragadee and Leederville aquifers which exist on each side and are displaced by Badaminna fault system (Davidson, 1995; Glasson, 2011)

We intend to use a large-scale grounded bipole antenna source to investigate the structure of the Badaminna fault system. Our grounded bipole system will utilise modern multi-component electric and magnetic field receivers in a dense array.

Method and Results

The relative offset of receivers and transmitted waveform contribute to the depth of investigation and resolving capability of the EM system. The software to support 1D, 2D and 3D forward and inverse modelling of frequency domain systems has existed in various forms for considerable time. (Barnett, 1984; Farquharson *et al.*, 1993; Farquharson *et al.*, 1999; Haber *et al.*, 2007; Nekut, 1987; Scholl, 2005). Full three-dimensional Inversion of time domain EM data in complex setting is still evolving and generally required the initial model to be close to the final inverted outcome. Full 3D inversion of deep penetrating time domain CSEM data is one challenge not quite fully resolved by today's computational geophysics.

Identifying which combination and orientation of transmitter and receiver antennas will be most effective require forward modelling. A poor choice of receiver orientation may result in negligible amplitudes, effectively wasting time deploying and collecting the data. To plan for the deep penetrating EM survey, we created a number of geo-electrical models based around information from existing seismic and well logs. We compare outcome from are range of field configurations and for a range of possible geo-electrical models.

Modelling is completed with Marco, part of the P223 AMIRA software suite (Raiche *et al.*, 2007). We show one example here that uses an extremely low frequency 0.25 Hz 50 % duty cycle bipolar square waveform to assess various configurations of transmitter and receiver orientation. Figure 5.8 shows the earth model used with Marco. It is a simplified, representation of the Badaminna fault system, comprising of a conductive vertical "fault zone" and alternating shale and sandstone layers. Figure 5.8. Units are mV/Amp. For the modelling, the transmitter current is always 1 Ampere.

Transmitter receiver geometries are shown in Figure 5.9. Each transmitter is modelled with receivers in Ex, and Ey orientations. Results depicted in Figure 5.10 onwards show the effect of the fault on signal amplitudes. These are seen to be quite prominently in the far-offset, north-south driving bipole in the Ex component (also known as the broadside configuration). During early decay times, the footprint presented by the fault zone is approximately 600 m wide – three times greater than the physical width of the fault body (indicated by dotted white lines).

The fault appear to have less impact on in-line transmitter-receiver geometries as shown in Figure 5.11 and Figure 5.12 (far and near offsets respectively). Analysis of the target percentage effect indicates the long-offset transmitters show largest differences across the fault zone. We have computed a range of different models and present one example here.

Conclusions

In this paper we present initial modelled results from simplified large scale geo-electrical structures as they may appear from various grounded bipole antennae configurations used in the field. We aim to identify the best orientation and transmitter/receiver combinations in order to resolve electrical parameters of this deep large-scale fault system. The investigation of these structures is important for groundwater considerations, and antennae design including transmitter waveform are critical element in the successful planning and design of deep penetrating land-based EM surveys. Initial models show the longer offset geometries which drive current along the fault potentially has a greater impact on the received signal amplitudes. We are in the process of investigating the effects of different waveforms and possible field configurations prior to collecting data in the field.

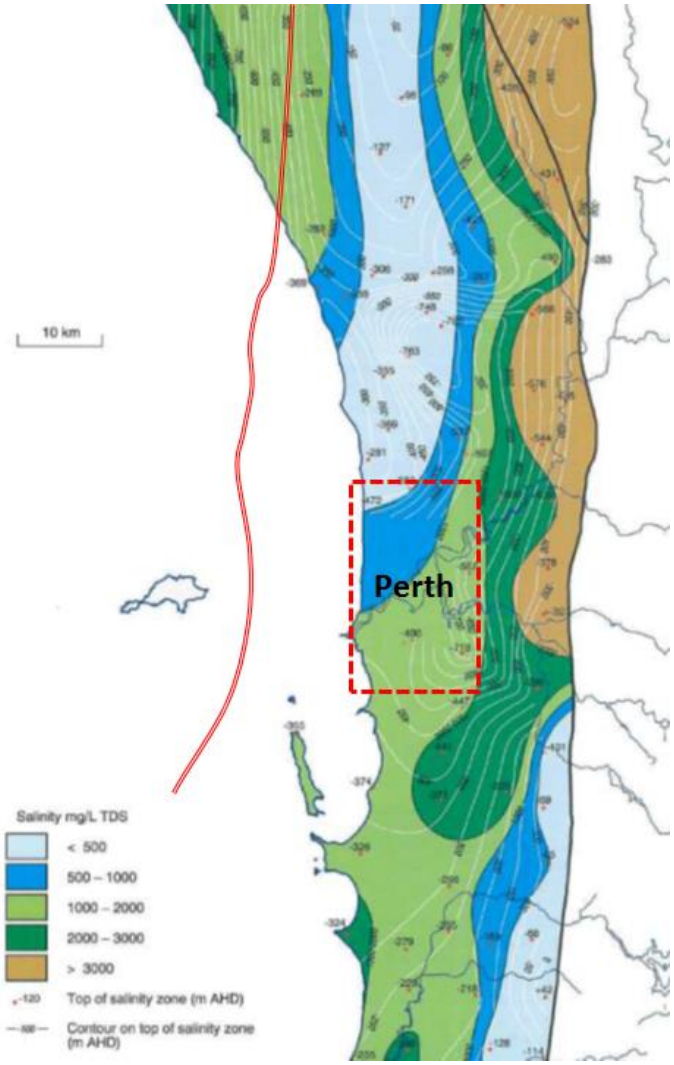

Figure 5.7: Salinity distribution of the Yarragadee aquifer, modified after (Davidson, 1995)

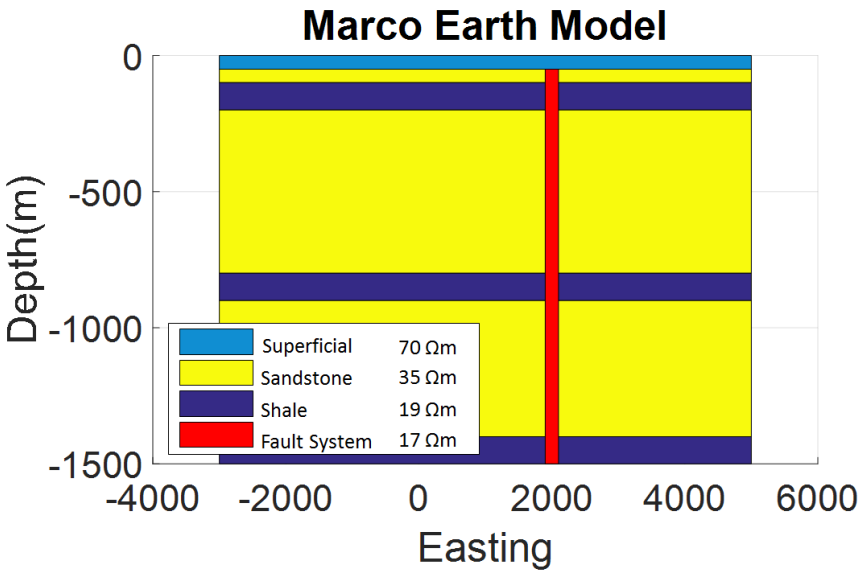

Figure 5.8: An example of a simplified geo-electrical earth model use for testing a range of survey parameters. Several geo-electrical models were developed to assess the signal strength and distribution in time and space.

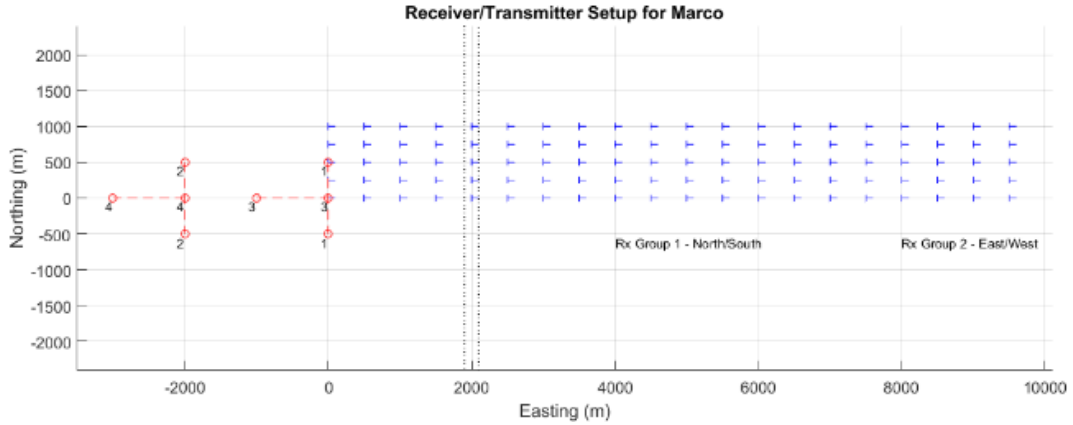

Figure 5.9: Modelled receiver and transmitter setup (plan view). Dotted line indicates location of the fault zone.

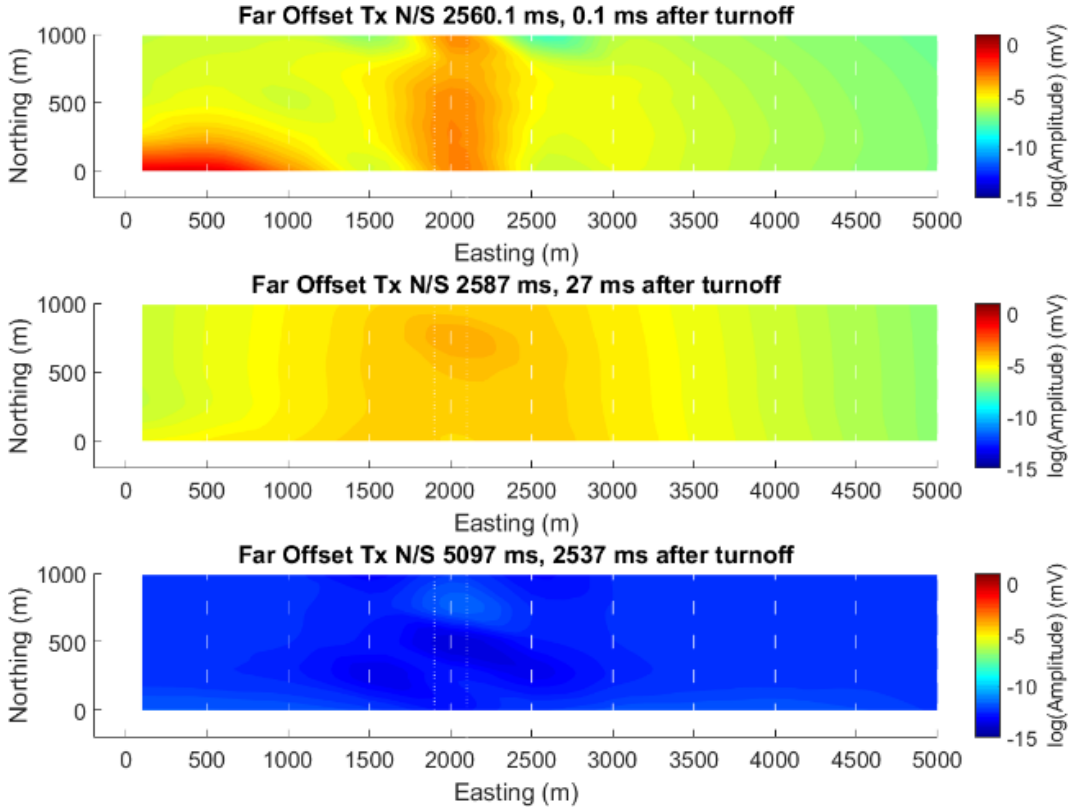

Figure 5.10: Near offset Ex Component from N/S Bipole. This shows the effect of the fault zone most prominently, showing a strong anomaly over the top of the prism representing the fault zone.

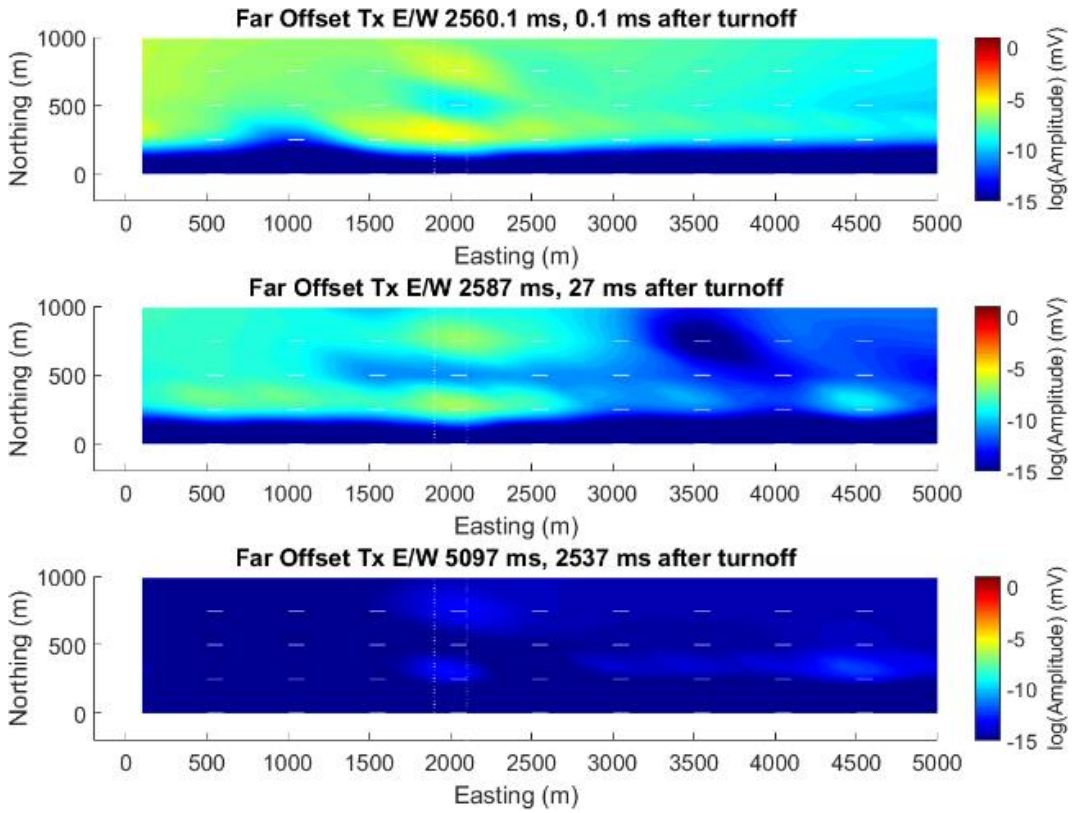

Figure 5.11: Far offset Ex component from E/W bipole. This shows a peculiar 'streak' horizontally at 500 m – possibly due to layering or fault presence.

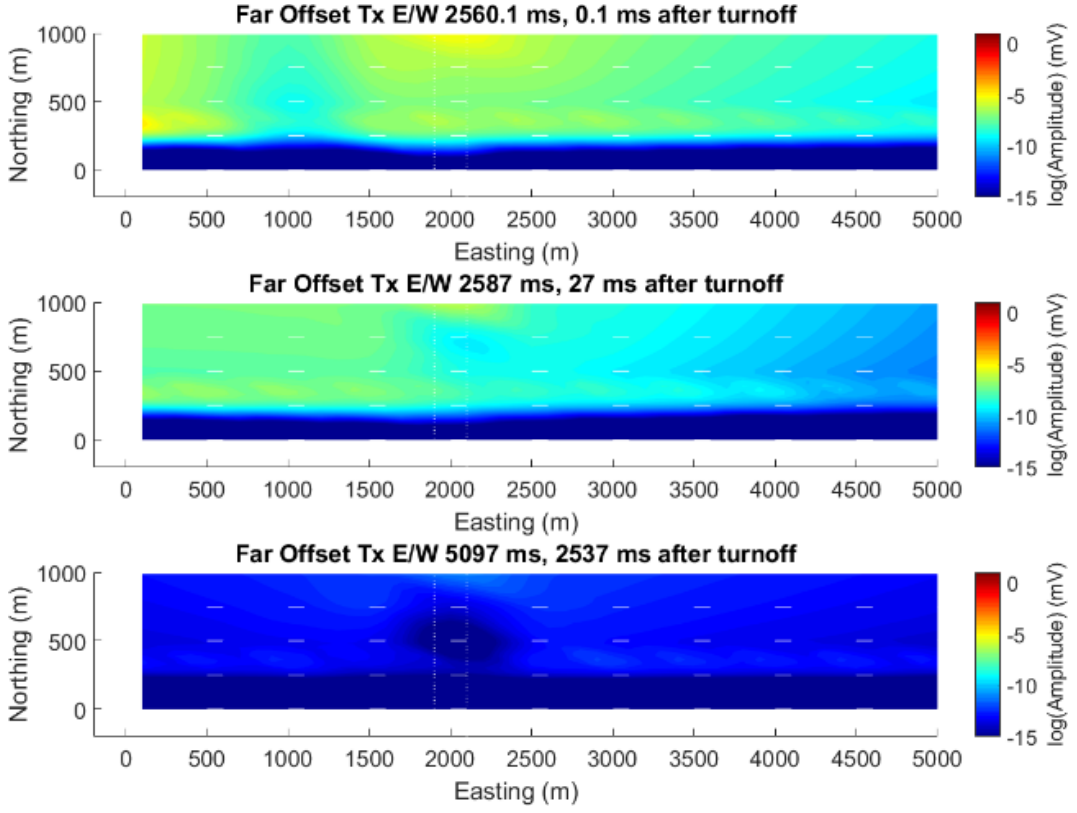

Figure 5.12: Near-offset Ex component from E/W bipole

References

Anderson, C., Long, A., Ziolkowski, A., Hobbs, B., & Wright, D. (2008). Multi-transient EM technology in practice. *First break, 26*(3).

Barnett, C. T. (1984). Simple Inversion of Time-Domain Electromagnetic Data. *Geophysics, 49*(7), 925-933. doi:Doi 10.1190/1.1441738

Chen, W.-y., Xue, G., Muhammad, Y. K., Gelius, L., Zhou, N.-n., Li, H., & Zhong, H.-s. (2015). Application of Short-Offset TEM (SOTEM) Technique in Mapping Water-Enriched Zones of Coal Stratum, an Example from East China. *Pure and Applied Geophysics, 172*(6), 1643-1651.

Constable, S., & Srnka, L. J. (2007). Special Section--Marine Controlled-Source Electromagnetic Methods-An Introduction To Marine Controlled-Source Electromagnetic Methods For Hydrocarbon Exploration. *Geophysics, 72*(2), WA3.

Davidson, W. A. (1995). *Hydrogeology And Groundwater Resources Of The Perth Region, Western Australia* (Vol. 142): Geological Survey of WA.

Farquharson, C. G., & Oldenburg, D. W. (1993). Inversion of Time-Domain Electromagnetic Data for a Horizontally Layered Earth. *Geophysical Journal International, 114*(3), 433-442. doi:DOI 10.1111/j.1365-246X.1993.tb06977.x

Farquharson, C. G., Oldenburg, D. W., & Li, Y. G. (1999). An approximate inversion algorithm for time-domain electromagnetic surveys. *Journal of Applied Geophysics, 42*(2), 71-80. doi:Doi 10.1016/S0926-9851(99)00023-3

Glasson, S. (2011). *Investigation Of Salinity Within The Yarragadee Aquifer In The Perth Area.* University of Western Australia,

Grayver, A. V., Streich, R., & Ritter, O. (2014). 3D inversion and resolution analysis of land-based CSEM data from the Ketzin CO2 storage formation. *Geophysics, 79*(2), E101-E114. doi:10.1190/geo2013-0184.1

Guo-Qiang, X., Wei-Ying, C., Nan-Nan, Z., Hai, L., & Hua-Sen, Z. (2013). Understanding of Grounded-Wire TEM Sounding with Near-Source Configuration. *Journal of Geophysics & Remote Sensing*.

Haber, E., Oldenburg, D. W., & Shekhtman, R. (2007). Inversion of time domain three-dimensional electromagnetic data. *Geophysical Journal International, 171*(2), 550-564. doi:10.1111/j.1365-246X.2007.03365.x

Haroon, A., Adrian, J., Bergers, R., Gurk, M., Tezkan, B., Mammadov, A. L., & Novruzov, A. G. (2015). Joint inversion of long-offset and central-loop transient electromagnetic data: Application to a mud volcano exploration in Perekishkul, Azerbaijan. *Geophysical Prospecting, 63*(2), 478-494. doi:10.1111/1365-2478.12157

Hobbs, B., & Sopher, D. (2008). *Constrained Sharp Boundary Inversion Of Multi-Transient Em Data.* Paper presented at the Cspg, Cseg, Cwls Convention.

Hördt, A., & Müller, M. (2000). Understanding LOTEM data from mountainous terrain. *Geophysics, 65*(4), 1113-1123. doi:10.1190/1.1444804

Lovatini, A., Kumar, R., Al-Saeed, M., Khalid, A., Pezzoli, M., Battaglini, A., . . . Roth, J. (2013). *Land Controlled-Source Electromagnetic Surveying For Viscous Oil Characterization In Kuwait.* Paper presented at the 75th Eage Conference & Exhibition Incorporating Spe Europec 2013.

Marshal, J., Ramsay, D., Moore, A., Shafik, S., Graham, T., & Needham, J. (1993). The Vlaming Sub-Basin, Offshore South Perth Basin Continental Margins Program Folio 7. *Geoscience Australia, Canberra*.

Nekut, A. G. (1987). Direct Inversion of Time-Domain Electromagnetic Data. *Geophysics, 52*(10), 1431-1435. doi:Doi 10.1190/1.1442256

Nicholas, W., Borissova, I., Radke, L., Tran, M., Bernardel, G., Jorgensen, D., . . . Whiteway, T. (2013). Seabed Environments And Shallow Geology Of The Vlaming Sub-Basin, Western Australia.

PGS. (2007). Multi-Transient Em Technology At Pgs.

Raiche, A., Sugeng, F., & Wilson, G. (2007). Practical 3D EM inversion? The P223F software suite. *ASEG Extended Abstracts, 2007*(1), 1-5.

Scholl, C. (2005). *The Influence Of Multidimensional Structures On The Interpretation Of Lotem Data With One-Dimensional Models And The Application To Data From Israel.* Universität zu Köln,

SEG. (2010). *Geophysics Today: 75th Anniversery Edition Compedium*.

Strack, K.-M., Hanstein, T., LeBrocq, K., Moss, D., Vozoff, K., & Wolfgram, P. (1989). Case histories of LOTEM surveys in hydrocarbon prospective area. *First break, 7*(12), 467-477.

Strack, K. M., Lueschen, E., & Koetz, A. W. (1990). Long-offset transient electromagnetic (LOTEM) depth soundings applied to crustal studies in the Black Forest and Swabian Alb, Federal Republic of Germany. *Geophysics, 55*(7), 834-842. doi:10.1190/1.1442897

Streich, R. (2015). Controlled-Source Electromagnetic Approaches for Hydrocarbon Exploration and Monitoring on Land. *Surveys in Geophysics, 37*(1), 47-80. doi:10.1007/s10712-015-9336-0

Water, D. o. (2016). Perth Region Confined Aquifer Capacity (Prcac) Study. Retrieved from http://www.water.wa.gov.au/planning-for-the-future/finding-water/groundwater-investigations/perth-regional-confined-aquifer-capacity-project-prcac

Wirianto, M., Mulder, W., & Slob, E. (2010a). *Exploiting the Airwave for Land CSEM Reservoir Monitoring.* Paper presented at the 72nd EAGE Conference and Exhibition incorporating SPE EUROPEC 2010.

Wirianto, M., Mulder, W., & Slob, E. (2010b). A feasibility study of land CSEM reservoir monitoring in a complex 3-D model. *Geophysical Journal International, 181*(2), 741-755.

Wright, D., Ziolkowski, A., & Hobbs, B. (2002). Hydrocarbon detection and monitoring with a multicomponent transient electromagnetic (MTEM) survey. *The Leading Edge, 21*(9), 852-864. doi:doi:10.1190/1.1508954

Zhdanov, M. S. (2010). Electromagnetic geophysics: Notes from the past and the road ahead. *Geophysics, 75*(5), A49-A66. doi:10.1190/1.3483901

Ziolkowski, A., Carson, R., & Wright, D. (2007). *New Technology To Acquire, Process, And Interpret Transient Em Data.* Paper presented at the Egm 2007 International Workshop.

Ziolkowski, A., Parr, R., Wright, D., Nockles, V., Limond, C., Morris, E., & Linfoot, J. (2010). Multi-Transient Electromagnetic Repeatability Experiment Over The North Sea Harding Field‡. *Geophysical Prospecting, 58*(6), 1159-1176.

Zonge, K. L. (1992). Introduction To Csamt. *Practical Geophysics II for the Exploration Geologist*, 439-523.

Abarca, E., Carrera, J., Sánchez-Vila, X., & Dentz, M. (2007). Anisotropic dispersive Henry problem. *Advances in Water Resources, 30*(4), 913-926. doi:https://doi.org/10.1016/j.advwatres.2006.08.005

Abarca, E., Carrera, J., Sánchez-Vila, X., & Voss, C. I. (2007). Quasi-horizontal circulation cells in 3D seawater intrusion. *Journal of Hydrology, 339*(3), 118-129. doi:https://doi.org/10.1016/j.jhydrol.2007.02.017

Abarca, E., & Clement, T. P. (2009). A novel approach for characterizing the mixing zone of a saltwater wedge. *Geophysical Research Letters, 36*(6). doi:10.1029/2008gl036995

Abarca, E., Karam, H., Hemond, H. F., & Harvey, C. F. (2013). Transient groundwater dynamics in a coastal aquifer: The effects of tides, the lunar cycle, and the beach profile. *Water Resources Research, 49*(5), 2473-2488. doi:10.1002/wrcr.20075

Abd-Elhamid, H., & Javadi, A. (2008). An investigation into control of saltwater intrusion considering the effects of climate change and sea level rise. *Proceeding of 20th SWIM, 2327*.

Abdul Nassir, S. S., Loke, M. H., Lee, C. Y., & Nawawi, M. N. M. (2000). Salt-water intrusion mapping by geoelectrical imaging surveys. *Geophysical Prospecting, 48*(4), 647-661. doi:https://doi.org/10.1046/j.1365-2478.2000.00209.x

Al-Bitar, A., & Ababou, R. (2005). *Random field approach to seawater intrusion in heterogeneous coastal aquifers: unconditional simulations and statistical analysis*, Berlin, Heidelberg.

Alam, M. Z., Carpenter-Boggs, L., Mitra, S., Haque, M., Halsey, J., Rokonuzzaman, M., . . . Moniruzzaman, M. (2017). Effect of salinity intrusion on food crops, livestock, and fish species at Kalapara Coastal Belt in Bangladesh. *Journal of Food Quality, 2017*.

Allison, G., & Hughes, M. (1978). The use of environmental chloride and tritium to estimate total recharge to an unconfined aquifer. *Soil Research, 16*(2), 181-195.

Almalki, M., Harris, B., & Dupuis, J. C. (2013). Multifrequency full-waveform sonic logging in the screened interval of a large-diameter production well. *Geophysics, 78*(5), B243-B257. doi:10.1190/geo2012-0328.1

Alonso-Rodríguez, R., & Páez-Osuna, F. (2003). Nutrients, phytoplankton and harmful algal blooms in shrimp ponds: a review with special reference to the situation in the Gulf of California. *Aquaculture, 219*(1), 317-336. doi:https://doi.org/10.1016/S0044-8486(02)00509-4

Anderson, C., Long, A., Ziolkowski, A., Hobbs, B., & Wright, D. (2008). Multi-transient EM technology in practice. *First break, 26*(3).

Annan, A. P. (2005). GPR Methods for Hydrogeological Studies. In Y. Rubin & S. S. Hubbard (Eds.), *Hydrogeophysics* (pp. 185-213). Dordrecht: Springer Netherlands.

Annan, A. P. (2009). Chapter 1 - Electromagnetic Principles of Ground Penetrating Radar A2 - Jol, Harry M. In *Ground Penetrating Radar Theory and Applications* (pp. 1-40). Amsterdam: Elsevier.

Appleyard, S. (1995). The impact of urban development on recharge and groundwater quality in a coastal aquifer near Perth, Western Australia. *Hydrogeology Journal, 3*(2), 65-75.

Appleyard, S. J., Angeloni, J., & Watkins, R. (2006). Arsenic-rich groundwater in an urban area experiencing drought and increasing population density, Perth, Australia. *Applied Geochemistry, 21*(1), 83-97. doi:10.1016/j.apgeochem.2005.09.008

Archie, G. E. (1941). The Electrical Resistivity Log as an Aid in Determining Some Reservoir Characteristics. *Transactions of the AIME, 146*(01), 54-62. doi:10.2118/942054-g

Arps, J. (1953). The effect of temperature on the density and electrical resistivity of sodium chloride solutions. *Journal of Petroleum Technology, 5*(10), 17-20.

Asquith, G. B. (1990). *Log Evaluation of Shaly Sandstones: A Practical Guide*: American Association of Petroleum Geologists.

Ataie-Ashtiani, B., Volker, R. E., & Lockington, D. A. (1999). Tidal effects on sea water intrusion in unconfined aquifers. *Journal of Hydrology, 216*(1-2), 17-31. doi:Doi 10.1016/S0022-1694(98)00275-3

Athanasiou, E. N., Tsourlos, P. I., Papazachos, C. B., & Tsokas, G. N. (2007). Combined weighted inversion of electrical resistivity data arising from different array types. *Journal of Applied Geophysics, 62*(2), 124-140. doi:10.1016/j.jappgeo.2006.09.003

Auken, E., & Christiansen, A. V. (2004). Layered And Laterally Constrained 2d Inversion Of Resistivity Data. *Geophysics, 69*(3), 752-761.

Australian Bureau of Statistics. (2006). Regional Population Growth, Australia And New Zealand. In *Year Book Australia 2004* (Vol. 3218.0): Australian Bureau of Statistics.

Australian Bureau of Statistics. (2009). *4656.5 - Household Choices Related to Water and Energy, WA, October 2009* Retrieved from http://www.abs.gov.au/AUSSTATS/abs@.nsf/Lookup/4656.5Main+Features1October%202009?OpenDocument

Australian Bureau of Statistics. (2016). *2016 Census QuickStats: Quinns Rocks (Code SSC51267 (SSC))*. Retrieved from http://quickstats.censusdata.abs.gov.au/census_services/getproduct/census/2016/quickstat/SSC51267

Australian Bureau of Statistics. (2018). Estimated Residence Population (ERP) By Statistical Area 2 (Sa2), 1991 to 2014. In: Australian Bureau of Statistics.

Azar, J. H., Javaherlan, A., Pishvaie, M. R., & Nabi-Bidhendi, M. (2008). An approach to defining tortuosity and cementation factor in carbonate reservoir rocks. *Journal of Petroleum Science and Engineering, 60*(2), 125-131. doi:10.1016/j.petrol.2007.05.010

Back, W., Hanshaw, B. B., Herman, J. S., & Van Driel, J. N. (1986). Differential dissolution of a Pleistocene reef in the ground-water mixing zone of coastal Yucatan, Mexico. *Geology, 14*(2), 137-140.

Badaruddin, S., Werner, A. D., & Morgan, L. K. (2017). Characteristics of active seawater intrusion. *Journal of Hydrology, 551*, 632-647. doi:10.1016/j.jhydrol.2017.04.031

Bakker, M. (2006). Analytic solutions for interface flow in combined confined and semi-confined, coastal aquifers. *Advances in Water Resources, 29*(3), 417-425. doi:10.1016/j.advwatres.2005.05.009

Bano, M., & Girard, J. F. (2001). Radar reflections and water content estimation of aeolian sand dune. *Geophysical Research Letters, 28*(16), 3207-3210. doi:Doi 10.1029/2000gl011986

Barlow, P. M., & Reichard, E. G. (2010). Saltwater intrusion in coastal regions of North America. *Hydrogeology Journal, 18*(1), 247-260. doi:10.1007/s10040-009-0514-3

Barnes, S. (1999). Karstic groundwater flow characteristics in the Cretaceous Chalk aquifer, Northern Ireland. *Quarterly Journal of Engineering Geology, 32*(1), 55-68. doi:Doi 10.1144/Gsl.Qjeg.1999.032.P1.04

Barnett, C. T. (1984). Simple Inversion of Time-Domain Electromagnetic Data. *Geophysics, 49*(7), 925-933. doi:Doi 10.1190/1.1441738

Bates, B., Kundzewicz, Z., & Wu, S. (2008). *Climate change and water*: Intergovernmental Panel on Climate Change Secretariat.

Bayless, E. R., Mandell, W. A., & Ursic, J. R. (2011). Accuracy of Flowmeters Measuring Horizontal Groundwater Flow in an Unconsolidated Aquifer Simulator. *31*(2), 48-62. doi:doi:10.1111/j.1745-6592.2010.01324.x

Beakawi Al-Hashemi, H. M., & Baghabra Al-Amoudi, O. S. (2018). A review on the angle of repose of granular materials. *Powder Technology, 330*, 397-417. doi:10.1016/j.powtec.2018.02.003

Bear, J. (2005). *Sea water intrusion into coastal aquifers*.

Bear, J., Cheng, A. H.-D., Sorek, S., Ouazar, D., & Herrera, I. (1999). *Seawater intrusion in coastal aquifers: concepts, methods and practices* (Vol. 14): Springer Science & Business Media.

Bear, J., & Dagan, G. (1964). Some exact solutions of interface problems by means of the hodograph method. *Journal of Geophysical Research, 69*(8), 1563-1572. doi:10.1029/JZ069i008p01563

Beaujean, J., Nguyen, F., Kemna, A., Antonsson, A., & Engesgaard, P. (2014). Calibration of seawater intrusion models: Inverse parameter estimation using surface electrical resistivity tomography and borehole data. *Water Resources Research, 50*(8), 6828-6849. doi:10.1002/2013wr014020

Bellin, A., Pannone, M., Fiori, A., & Rinaldo, A. (1996). On Transport in Porous Formations Characterized by Heterogeneity of Evolving Scales. *32*(12), 3485-3496. doi:10.1029/95wr02507

Bense, V., Read, T., Bour, O., Le Borgne, T., Coleman, T., Krause, S., . . . Selker, J. J. W. R. R. (2016). Distributed Temperature Sensing as a downhole tool in hydrogeology. *52*(12), 9259-9273.

Benson, R. C., & Yuhr, L. B. (2015). *Site Characterization in Karst and Pseudokarst Terraines: Practical Strategies and Technology for Practicing Engineers, Hydrologists and Geologists*: Springer.

Bergmann, P., Ivandic, M., Norden, B., Rücker, C., Kiessling, D., Lüth, S., . . . Juhlin, C. (2014). Combination of seismic reflection and constrained resistivity inversion with an application to 4D imaging of the CO2 storage site, Ketzin, Germany. *79*(2), B37-B50. doi:10.1190/geo2013-0131.1

Bergmann, P., Schmidt-Hattenberger, C., Kiessling, D., Rücker, C., Labitzke, T., Henninges, J., . . . Schütt, H. (2012). Surface-downhole electrical resistivity tomography applied to monitoring of CO2 storage at Ketzin, Germany. *77*(6), B253-B267. doi:10.1190/geo2011-0515.1

Bernabé, Y., Mok, U., & Evans, B. (2003). Permeability-porosity Relationships in Rocks Subjected to Various Evolution Processes. *Pure and Applied Geophysics, 160*(5), 937-960. doi:10.1007/pl00012574

Bievre, G., Oxarango, L., Gunther, T., Goutaland, D., & Massardi, M. (2018). Improvement of 2D ERT measurements conducted along a small earth-filled dyke using 3D topographic data and 3D computation of geometric factors. *Journal of Applied Geophysics, 153*, 100-112. doi:10.1016/j.jappgeo.2018.04.012

Bing, Z., & Greenhalgh, S. A. (2000). Cross-hole resistivity tomography using different electrode configurations. *Geophysical Prospecting, 48*(5), 887-912. doi:10.1046/j.1365-2478.2000.00220.x

Binley, A., Cassiani, G., & Deiana, R. (2010). Hydrogeophysics: opportunities and challenges. *Bollettino di Geofisica Teorica ed Applicata, 51*(4), 267-284. Retrieved from <Go to ISI>://WOS:000285407700002

Binley, A., Hubbard, S. S., Huisman, J. A., Revil, A., Robinson, D. A., Singha, K., & Slater, L. D. (2015). The emergence of hydrogeophysics for improved understanding of subsurface processes over multiple scales. *Water Resour Res, 51*(6), 3837-3866. doi:10.1002/2015WR017016

Bird, E. C. (2011). *Coastal geomorphology: an introduction*: John Wiley & Sons.

Bolland, M. D. A. (1999). *Soils of the Swan coastal plain / by Mike Bolland*. [Perth, W.A.]: Agriculture Western Australia.

BOM, N. (2011). The Australian Baseline Sea Level Monitoring Project. *Annual Sea Level Data Summary Report*. Retrieved from http://www.bom.gov.au/oceanography/projects/abslmp/reports_yearly.shtml

Bonacci, O., & Roje-Bonacci, T. (2000). Interpretation of groundwater level monitoring results in karst aquifers: examples from the Dinaric karst. *Hydrological Processes, 14*(14), 2423-2438. doi:10.1002/1099-1085(20001015)14:14<2423::Aid-hyp104>3.0.Co;2-2

Boulanger, O., & Chouteau, M. (2001). Constraints in 3D gravity inversion. *Geophysical Prospecting*. Retrieved from https://onlinelibrary.wiley.com/doi/abs/10.1046/j.1365-2478.2001.00254.x

Bradford, J. H., Clement, W. P., & Barrash, W. (2009). Estimating porosity with ground-penetrating radar reflection tomography: A controlled 3-D experiment at the Boise Hydrogeophysical Research Site. *Water Resources Research, 45*(4).

Bretz, J. H. J. G. S. o. A. B. (1960). Bermuda: A partially drowned, late mature, Pleistocene karst. *71*(12), 1729-1754.

Bristow, C. (2009). Chapter 9 - Ground Penetrating Radar in Aeolian Dune Sands A2 - Jol, Harry M. In *Ground Penetrating Radar Theory and Applications* (pp. 271-297). Amsterdam: Elsevier.

Bryan, E., Meredith, K. T., Baker, A., Post, V. E. A., & Andersen, M. S. (2016). Island groundwater resources, impacts of abstraction and a drying climate: Rottnest Island, Western Australia. *Journal of Hydrology, 542*, 704-718. doi:10.1016/j.jhydrol.2016.09.043

Bureau of Meteorology. (2012). Ocean Monitoring Portal. Retrieved from http://www.bom.gov.au/cosppac/apps/portal/app.html#climate

Burnett, W. C., Aggarwal, P. K., Aureli, A., Bokuniewicz, H., Cable, J. E., Charette, M. A., . . . Turner, J. V. (2006). Quantifying submarine groundwater discharge in the coastal zone via multiple methods. *Sci Total Environ, 367*(2-3), 498-543. doi:10.1016/j.scitotenv.2006.05.009

BurVal Working Group, Kirsch, R., Rumpel, H.-M., Scheer, W., & Wiederhold, H. (2006). *Groundwater resources in buried valleys: a challenge for geosciences*: Leibniz Institute for Applied Geosciences (GGA-Institut).

Butler, D. K. (2005). *Near-surface geophysics*: Society of Exploration Geophysicists Tulsa.

Buynevich, I. V., Jol, H. M., & FitzGerald, D. M. (2009). Coastal Environments. In *Ground Penetrating Radar Theory and Applications* (pp. 299-322). Amsterdam: Elsevier.

C. Nevill, J., J. Hancock, P., R. Murray, B., F. Ponder, W., F. Humphreys, W., L. Phillips, M., & K. Groom, P. (2010). Groundwater-dependent ecosystems and the dangers of groundwater overdraft: a review and an Australian perspective. *Pacific Conservation Biology, 16*(3), 187-208. doi:https://doi.org/10.1071/PC100187

Calvache, M. L., & PulidoBosch, A. (1997). Effects of geology and human activity on the dynamics of salt-water intrusion in three coastal aquifers in southern Spain. *Environmental Geology, 30*(3-4), 215-223. doi:DOI 10.1007/s002540050149

Carrera, J., Hidalgo, J. J., Slooten, L. J., & Vazquez-Sune, E. (2010). Computational and conceptual issues in the calibration of seawater intrusion models. *Hydrogeology Journal, 18*(1), 131-145. doi:10.1007/s10040-009-0524-1

Carriere, S. D., Chalikakis, K., Senechal, G., Danquigny, C., & Emblanch, C. (2013). Combining Electrical Resistivity Tomography and Ground Penetrating Radar to study geological structuring of karst Unsaturated Zone. *Journal of Applied Geophysics, 94*, 31-41. doi:10.1016/j.jappgeo.2013.03.014

Carter, E. S., White, S. M., & Wilson, A. M. (2008). Variation in groundwater salinity in a tidal salt marsh basin, North Inlet Estuary, South Carolina. *Estuarine Coastal and Shelf Science, 76*(3), 543-552. doi:10.1016/j.ecss.2007.07.049

Casanova, J., Devau, N., & Pettenati, M. (2016). Managed Aquifer Recharge: An Overview of Issues and Options. In *Integrated Groundwater Management* (pp. 413-434): Springer.

Cassidy, N. J. (2009). Chapter 2 - Electrical and Magnetic Properties of Rocks, Soils and Fluids A2 - Jol, Harry M. In *Ground Penetrating Radar Theory and Applications* (pp. 41-72). Amsterdam: Elsevier.

Chai, T., & Draxler, R. R. (2014). Root mean square error (RMSE) or mean absolute error (MAE)?–Arguments against avoiding RMSE in the literature. *Geoscientific Model Development, 7*(3), 1247-1250. doi:10.5194/gmd-7-1247-2014

Chang, S. W., & Clement, T. P. (2012). Experimental and numerical investigation of saltwater intrusion dynamics in flux-controlled groundwater systems. *Water Resources Research, 48*(9). doi:doi:10.1029/2012WR012134

Chang, S. W., Clement, T. P., Simpson, M. J., & Lee, K.-K. (2011). Does sea-level rise have an impact on saltwater intrusion? *Advances in Water Resources, 34*(10), 1283-1291. doi:10.1016/j.advwatres.2011.06.006

Chen, W.-y., Xue, G., Muhammad, Y. K., Gelius, L., Zhou, N.-n., Li, H., & Zhong, H.-s. (2015). Application of Short-Offset TEM (SOTEM) Technique in Mapping Water-Enriched Zones of Coal Stratum, an Example from East China. *Pure and Applied Geophysics, 172*(6), 1643-1651.

Cheng, A. H., & Ouazar, D. (2004). *Coastal aquifer management-monitoring, modeling, and case studies*: CRC Press.

Christiansen, A. V., & Auken, E. (2012). A global measure for depth of investigation. *Geophysics, 77*(4), Wb171-Wb177. doi:10.1190/Geo2011-0393.1

CIESIN. (2016). Gridded Population of the World, Version 4 (GPWv4): UN-Adjusted Population Count.

Claerbout, J. F., & Muir, F. (1973). Robust Modeling with Erratic Data. *Geophysics, 38*(5), 826-844. doi:Doi 10.1190/1.1440378

Clark, G., & Johnston, E. (2016). *Coasts: Population growth and urban development: Coastal development and land use*. Australian Government Department of the Environment and Energy Retrieved from https://soe.environment.gov.au/theme/coasts/topic/2016/population-growth-and-urban-development-coastal-development-and-land-use

Collins, M., Knutti, R., Arblaster, J., Dufresne, J.-L., Fichefet, T., Friedlingstein, P., . . . Wehner, M. (2013). Chapter 12 - Long-term climate change: Projections, commitments and irreversibility. In Ipcc (Ed.), *Climate Change 2013: The Physical Science Basis. IPCC Working Group I Contribution to AR5*. Cambridge: Cambridge University Press.

Comte, J. C., & Banton, O. (2007). Cross-validation of geo-electrical and hydrogeological models to evaluate seawater intrusion in coastal aquifers. *Geophysical Research Letters, 34*(10), n/a-n/a. doi:10.1029/2007gl029981

Comte, J. C., Wilson, C., Ofterdinger, U., & Gonzalez-Quiros, A. (2017). Effect of volcanic dykes on coastal groundwater flow and saltwater intrusion: A field-scale multiphysics approach and parameter evaluation. *Water Resources Research, 53*(3), 2171-2198. doi:10.1002/2016wr019480

Constable, S., & Srnka, L. J. (2007). Special Section--Marine Controlled-Source Electromagnetic Methods-An Introduction To Marine Controlled-Source Electromagnetic Methods For Hydrocarbon Exploration. *Geophysics, 72*(2), WA3.

Constable, S. C., Parker, R. L., & Constable, C. G. (1987). Occam's inversion: A practical algorithm for generating smooth models from electromagnetic sounding data. *Geophysics, 52*(3), 289-300. doi:https://doi.org/10.1190/1.1442303

Cook, P. G. (2003). *A guide to regional groundwater flow in fractured rock aquifers*: Citeseer.

Coscia, I., Greenhalgh, S. A., Linde, N., Doetsch, J., Marescot, L., Gunther, T., . . . Green, A. G. (2011). 3D crosshole ERT for aquifer characterization and monitoring of infiltrating river water. *Geophysics, 76*(2), G49-G59. doi:10.1190/1.3553003

Coscia, I., Linde, N., Greenhalgh, S., Vogt, T., & Green, A. (2012). Estimating traveltimes and groundwater flow patterns using 3D time-lapse crosshole ERT imaging of electrical resistivity fluctuations induced by infiltrating river water. *Geophysics, 77*(4), E239-E250. doi:10.1190/Geo2011-0328.1

Costall, A., Harris, B., & Pigois, J. P. (2018). Electrical Resistivity Imaging and the Saline Water Interface in High-Quality Coastal Aquifers. *Surveys in Geophysics, 39*(4), 753-816. doi:10.1007/s10712-018-9468-0

Costall, A. R., & Harris, B. (2019). Rapid Estimation of Volumetric Groundwater Recharge in the Vadose Zone via Ground Penetrating Radar. *ASEG Extended Abstracts, 2018*(1), 1-7. doi:10.1071/ASEG2018abP091

Costall, A. R., Harris, B. D., Teo, B., Schaa, R., Wagner, F. M., & Pigois, J. P. (2020). Groundwater Throughflow and Seawater Intrusion in High Quality Coastal Aquifers. *Scientific Reports, 10*(1), 9866. doi:10.1038/s41598-020-66516-6

Costanza, R., d'Arge, R., de Groot, R., Farber, S., Grasso, M., Hannon, B., . . . van den Belt, M. (1997). The value of the world's ecosystem services and natural capital. *Nature, 387*(6630), 253-260. doi:10.1038/387253a0

Cox, W. (2017). Demographia: World Urban Areas. *13th Annual Edition ed. St. Louis: Demographia. Available: http://www. demographia. com/db-worldua. pdf. Date of access, 30*, 2017.

Crook, N., Binley, A., Knight, R., Robinson, D. A., Zarnetske, J., & Haggerty, R. (2008). Electrical resistivity imaging of the architecture of substream sediments. *Water Resources Research, 44*(4), n/a-n/a. doi:10.1029/2008wr006968

CSIRO. (2009). *Groundwater Yields In South-West Western Australia: Summary Of A Report To The Australian Government From The Csiro South-West Western Australia Sustainable Yields Project*. Retrieved from

Culkin, F., & Smith, N. J. I. J. o. O. E. (1980). Determination of the concentration of potassium chloride solution having the same electrical conductivity, at 15 C and infinite frequency, as standard seawater of salinity 35.0000‰(Chlorinity 19.37394‰). *5*(1), 22-23.

Custodio, E. (2012). Coastal aquifer management in Europe.

Dafny, E., Burg, A., & Gvirtzman, H. (2010). Effects of Karst and geological structure on groundwater flow: The case of Yarqon-Taninim Aquifer, Israel. *Journal of Hydrology, 389*(3-4), 260-275. doi:10.1016/j.jhydrol.2010.05.038

Dagan, G., & Zeitoun, D. G. (1998). Seawater-freshwater interface in a stratified aquifer of random permeability distribution. *Journal of contaminant hydrology, 29*(3), 185-203. doi:https://doi.org/10.1016/S0169-7722(97)00013-2

Dahlin, T. (2001). The development of DC resistivity imaging techniques. *Computers & Geosciences, 27*(9), 1019-1029. doi:Doi 10.1016/S0098-3004(00)00160-6

Dahlin, T., & Zhou, B. (2004). A numerical comparison of 2D resistivity imaging with 10 electrode arrays. *Geophysical Prospecting, 52*(5), 379-398. doi:DOI 10.1111/j.1365-2478.2004.00423.x

Dahlin, T., & Zhou, B. (2006). Multiple-gradient array measurements for multichannel 2D resistivity imaging. *Near Surface Geophysics, 4*(2), 113-123. doi:10.3997/1873-0604.2005037

Daily, G. C. (1997). *Nature's services* (Vol. 3).

Daily, W., & Owen, E. (1991). Cross-borehole resistivity tomography. *Geophysics, 56*(8), 1228-1235. doi:10.1190/1.1443142

Dalin, C., Wada, Y., Kastner, T., & Puma, M. J. (2017). Groundwater depletion embedded in international food trade. *Nature, 543*(7647), 700-704. doi:10.1038/nature21403

Dausman, A., & Langevin, C. D. (2005). *Movement of the saltwater interface in the surficial aquifer system in response to hydrologic stresses and water-management practices, Broward County, Florida*: US Department of the Interior, US Geological Survey.

Davidson, W. A. (1995). *Hydrogeology And Groundwater Resources Of The Perth Region, Western Australia* (Vol. 142): Geological Survey of WA.

Davidson, W. A., & Yu, X. (2008). *Perth regional aquifer modelling system (PRAMS) model development: Hydrogeology and groundwater modelling*: Department of Water.

Davis, J. L., & Annan, A. P. (1989). Ground-Penetrating Radar for High-Resolution Mapping of Soil and Rock Stratigraphy1. *Geophysical Prospecting, 37*(5), 531-551. doi:10.1111/j.1365-2478.1989.tb02221.x

Davis, S., & DeWiest, R. (1967). Hydrology, 2nd eds., 463. *New York, London*.

de Franco, R., Biella, G., Tosi, L., Teatini, P., Lozej, A., Chiozzotto, B., . . . Gasparetto-Stori, G. (2009). Monitoring the saltwater intrusion by time lapse electrical resistivity tomography: The Chioggia test site (Venice Lagoon, Italy). *Journal of Applied Geophysics, 69*(3-4), 117-130. doi:https://doi.org/10.1016/j.jappgeo.2009.08.004

deGroot-Hedlin, C., & Constable, S. (1990). Occam's inversion to generate smooth, two-dimensional models from magnetotelluric data. *Geophysics, 55*(12), 1613-1624. doi:10.1190/1.1442813

Delworth, T. L., & Zeng, F. R. (2014). Regional rainfall decline in Australia attributed to anthropogenic greenhouse gases and ozone levels Latitude. *Nature Geoscience, 7*(8), 583-587. doi:10.1038/Ngeo2201

Department of Regional Development WA. (2008). Royalties for Regions. Retrieved from http://www.drd.wa.gov.au/rfr/Pages/default.aspx

Department of Water. (2017). *Northern Perth Basin: Geology, hydrogeology and groundwater resources*. Department of Water W.A.

Department of Water, Western Australia,. (2011). Gnangara groundwater system.

Department of Water, Western Australia,. (2016). *Environmental management of groundwater from the Gnangara Mound*. Retrieved from https://www.google.com.au/url?sa=t&rct=j&q=&esrc=s&source=web&cd=1&cad=rja&uact=8&ved=0ahUKEwigvImy4NbXAhVDspQKHdPwDWkQFggrMAA&url=http%3A%2F%2Fwww.water.wa.gov.au%2F__data%2Fassets%2Fpdf_file%2F0019%2F8209%2F109982.pdf&usg=AOvVaw2BbdrQKIguPNf0UwtZnZxO

Department of Water, W. (2004). Perth Groundwater Atlas - Metadata: Groundwater Contours, May 2003. Retrieved from http://atlases.water.wa.gov.au/idelve/gwa/metadata_statements/gwcont_min.html

Department of Water WA. (2012a). Perth Region Confined Aquifer Capacity (PRCAC) study. Retrieved from http://www.water.wa.gov.au/planning-for-the-future/finding-water/groundwater-investigations/perth-regional-confined-aquifer-capacity-project-prcac

Department of Water WA. (2012b). Regional Water Availability and Water for Pilbara Cities Groundwater Investigation Programs. Retrieved from http://www.water.wa.gov.au/planning-for-the-future/finding-water/groundwater-investigations/royalties-for-regions-groundwater-investigation-program

Department of Water WA. (2015). *Gnangara Evaluation Statement 2011-2014*. Retrieved from http://www.water.wa.gov.au/planning-for-the-future/allocation-plans/swanavon-region/gnangara-groundwater-areas-allocation-plan

Dey, A., & Morrison, H. F. (1979). RESISTIVITY MODELLING FOR ARBITRARILY SHAPED TWO-DIMENSIONAL STRUCTURES*. *27*(1), 106-136. doi:doi:10.1111/j.1365-2478.1979.tb00961.x

Diersch, H.-J. G. (2014). *Feflow: Finite Element Modeling of Flow, Mass and Heat Transport in Porous and Fractured Media*: Springer Science & Business Media.

Diersch, H. (2002). FEFLOW-White papers vol. I. *WASY Ltd., Berlin*.

Digha Opaminola, N., & Ekanem Jessie, D. (2015). Effects of Population Density on Water Quality in Calabar Municipality Cross River State, Nigeria.

Dillon, P. (2009). Water recycling via managed aquifer recharge in Australia. *Boletin Geologico Y Minero, 120*(2), 121-130. Retrieved from <Go to ISI>://WOS:000422359700002

Doetsch, J. A., Coscia, I., Greenhalgh, S., Linde, N., Green, A., & Günther, T. (2010). The borehole-fluid effect in electrical resistivity imaging. *75*(4), F107-F114. doi:10.1190/1.3467824

Dokou, Z., & Karatzas, G. P. (2012). Saltwater intrusion estimation in a karstified coastal system using density-dependent modelling and comparison with the sharp-interface approach. *Hydrological Sciences Journal-Journal Des Sciences Hydrologiques, 57*(5), 985-999. doi:10.1080/02626667.2012.690070

Domenico, P. A., & Schwartz, F. W. (1998). *Physical and chemical hydrogeology* (Vol. 506): Wiley New York.

Eamus, D., Froend, R., Loomes, R., Hose, G., & Murray, B. (2006). A functional methodology for determining the groundwater regime needed to maintain the health of groundwater-dependent vegetation. *Australian Journal of Botany, 54*(2), 97-114.

Ecoscape Australia Pty Ltd. (2004). *Foreshore Management Plan Mindarie – Quinns Rocks*. City of Wanneroo: Ecoscape (Australia) Pty Ltd Retrieved from http://www.wanneroo.wa.gov.au/downloads/file/1211/mindarie-quinns_rocks_foreshore_management_plan

Edwards, L. (1977). A Modified Pseudosection For Resistivity And Ip. *Geophysics, 42*(5), 1020-1036. doi:https://doi.org/10.1190/1.1440762

Ekblom, H. (1974). L p -methods for robust regression. *BIT Numerical Mathematics, 14*(1), 22-32. doi:https://doi.org/10.1007/bf01933114

Elci, A., Molz III, F. J., & Waldrop, W. R. (2001). Implications of Observed and Simulated Ambient Flow in Monitoring Wells. *Groundwater, 39*(6), 853-862. doi:10.1111/j.1745-6584.2001.tb02473.x

Ellis, R. G. (1998). Inversion of airborne electromagnetic data. *Exploration Geophysics, 29*(2), 121-127. doi:https://doi.org/10.1071/EG998121

EPA. (2018). *Perth Groundwater Replenishment Scheme Stage 2*. Retrieved from https://www.epa.wa.gov.au/proposals/perth-groundwater-replenishment-scheme-stage-2

Esteban, Ó., Cruz-Navarrete, M., González-Cano, A., & Bernabeu, E. (1999). Measurement of the degree of salinity of water with a fiber-optic sensor. *Applied Optics, 38*(25), 5267-5271. doi:10.1364/AO.38.005267

Eswaran, H., Almaraz, R., Reich, P., & Zdruli, P. (1997). Soil Quality and Soil Productivity in Africa. *Journal of Sustainable Agriculture, 10*(4), 75-90. doi:10.1300/J064v10n04_07

Falkland, A., & Custodio, E. (1991). *Hydrology and water resources of small islands: A practical guide*: Unesco.

Farquharson, C. G. (2007). Constructing Piecewise-Constant Models In Multidimensional Minimum-Structure Inversions. *Geophysics, 73*(1), K1-K9. doi:https://doi.org/10.1190/1.2816650

Farquharson, C. G., & Oldenburg, D. W. (1993). Inversion of Time-Domain Electromagnetic Data for a Horizontally Layered Earth. *Geophysical Journal International, 114*(3), 433-442. doi:DOI 10.1111/j.1365-246X.1993.tb06977.x

Farquharson, C. G., & Oldenburg, D. W. (1998). Non-linear inversion using general measures of data misfit and model structure. *Geophysical Journal International, 134*(1), 213-227. doi:DOI 10.1046/j.1365-246x.1998.00555.x

Farquharson, C. G., & Oldenburg, D. W. (2003). Constructing piece-wise-constant models using general measures in non-linear, minimum-structure inversion algorithms: 6th International Symposium. *Society of Exploration Geophysicists of Japan, Expanded Abstracts*, 240-243.

Farquharson, C. G., Oldenburg, D. W., & Li, Y. G. (1999). An approximate inversion algorithm for time-domain electromagnetic surveys. *Journal of Applied Geophysics, 42*(2), 71-80. doi:Doi 10.1016/S0926-9851(99)00023-3

Ferguson, G., & Gleeson, T. (2012). Vulnerability of coastal aquifers to groundwater use and climate change. *Nature Climate Change, 2*(5), 342-345. doi:10.1038/Nclimate1413

Fofonoff, N. P., & Millard Jr, R. (1983). Algorithms for the computation of fundamental properties of seawater.

Ford, D., & Williams, P. D. (2013). *Karst hydrogeology and geomorphology*: John Wiley & Sons.

Fox, R. C., Hohmann, G. W., Killpack, T. J., & Rijo, L. (1980). Topographic effects in resistivity and induced-polarization surveys. *Geophysics, 45*(1), 75-93. doi:https://doi.org/10.1190/1.1441041

Freifeld, B. M., Trautz, R. C., Kharaka, Y. K., Phelps, T. J., Myer, L. R., Hovorka, S. D., & Collins, D. J. (2005). The U-tube: A novel system for acquiring borehole fluid samples from a deep geologic CO2 sequestration experiment. *110*(B10). doi:doi:10.1029/2005JB003735

Friedel, S. (2003). Resolution, stability and efficiency of resistivity tomography estimated from a generalized inverse approach. *Geophysical Journal International, 153*(2), 305-316. doi:DOI 10.1046/j.1365-246X.2003.01890.x

Frioux, S. (2014). Environmental History of Water Resources. In M. Agnoletti & S. Neri Serneri (Eds.), *The Basic Environmental History* (pp. 121-141). Cham: Springer International Publishing.

Furman, A., Ferré, T. P. A., & Warrick, A. W. (2003). A Sensitivity Analysis of Electrical Resistivity Tomography Array Types Using Analytical Element Modeling. *Vadose Zone Journal, 2*(3), 416-423. doi:10.2136/vzj2003.4160

Gallardo, L. A., & Meju, M. A. (2007). Joint two-dimensional cross-gradient imaging of magnetotelluric and seismic traveltime data for structural and lithological classification. *Geophysical Journal International, 169*(3), 1261-1272. doi:10.1111/j.1365-246X.2007.03366.x

Gallardo, L. A., & Meju, M. A. (2011). Structure-Coupled Multiphysics Imaging in Geophysical Sciences. *Reviews of Geophysics, 49*(1). doi:Artn Rg1003

10.1029/2010rg000330

Garcia-Menendez, O., Ballesteros, B. J., Renau-Prunonosa, A., Morell, I., Mochales, T., Ibarra, P. I., & Rubio, F. M. (2018). Using electrical resistivity tomography to assess the effectiveness of managed aquifer recharge in a salinized coastal aquifer. *Environ Monit Assess, 190*(2), 100. doi:10.1007/s10661-017-6446-9

Gelhar, L. W., Welty, C., & Rehfeldt, K. R. (1992). A critical review of data on field-scale dispersion in aquifers. *28*(7), 1955-1974. doi:doi:10.1029/92WR00607

Geoscience Australia. (2017). ELVIS - Elevation Information Systsm. Retrieved from http://www.ga.gov.au/elvis/#/

Geoscience Australia. (2020). Sustainable Groundwater Management. Retrieved from https://www.ga.gov.au/about/projects/water/sustainable-groundwater-management

Ghasemizadeh, R., Hellweger, F., Butscher, C., Padilla, I., Vesper, D., Field, M., & Alshawabkeh, A. (2012). Review: Groundwater flow and transport modeling of karst aquifers, with particular reference to the North Coast Limestone aquifer system of Puerto Rico. *Hydrogeol J, 20*(8), 1441-1461. doi:10.1007/s10040-012-0897-4

Ginzburg, A., & Levanon, A. (1976). Determination Of A Salt-Water Interface By Electric Resistivity Depth Soundings/Détermination D'un Interface D'eau Salée À L'aide Des Mesures Verticales De Résistivité Électrique. *Hydrological Sciences Journal, 21*(4), 561-568.

Glasson, S. (2011). *Investigation Of Salinity Within The Yarragadee Aquifer In The Perth Area.* University of Western Australia,

Glover, P. W. J. (2010). A generalized Archie's law for n phases. *75*(6), E247-E265. doi:10.1190/1.3509781

Glover, P. W. J. (2016). Archie's law - a reappraisal. *Solid Earth, 7*(4), 1157-1169. doi:10.5194/se-7-1157-2016

Glover, R. E. (1959). The pattern of fresh-water flow in a coastal aquifer. *Journal of Geophysical Research, 64*(4), 457-459. doi:doi:10.1029/JZ064i004p00457

Goggin, D. J., Chandler, M. A., Kocurek, G., & Lake, L. W. (1988). Patterns of Permeability in Eolian Deposits: Page Sandstone (Jurassic), Northeastern Arizona. *SPE Formation Evaluation, 3*(02), 297-306. doi:10.2118/14893-PA

Goldman, J. C., Tenore, K. R., & Stanley, H. I. (1973). Inorganic Nitrogen Removal from Wastewater: Effect on Phytoplankton Growth in Coastal Marine Waters. *Science, 180*(4089), 955-956. doi:10.1126/science.180.4089.955

Gonzalez-Herrera, R., Sanchez-y-Pinto, I., & Gamboa-Vargas, J. (2002). Groundwater-flow modeling in the Yucatan karstic aquifer, Mexico. *Hydrogeology Journal, 10*(5), 539-552. doi:10.1007/s10040-002-0216-6

Government of Australia. (2016). The Australian continent. Retrieved from http://www.australia.gov.au/about-australia/our-country/the-australian-continent

Gozzard, J. R. (2007). *Geology And Landforms Of The Perth Region*: Geological Survey of Western Australia.

Grayver, A. V., Streich, R., & Ritter, O. (2014). 3D inversion and resolution analysis of land-based CSEM data from the Ketzin CO2 storage formation. *Geophysics, 79*(2), E101-E114. doi:10.1190/geo2013-0184.1

Green, N. R., & MacQuarrie, K. T. B. (2014). An evaluation of the relative importance of the effects of climate change and groundwater extraction on seawater intrusion in coastal aquifers in Atlantic Canada. *Hydrogeology Journal, 22*(3), 609-623. doi:10.1007/s10040-013-1092-y

Griffiths, D. J. (1999). *Introduction To Electrodynamics* (Vol. 3). Reed College: prentice Hall Upper Saddle River, NJ.

Grimes, K. G. (1999). *The Water Below: An introduction to karst hydrology and the hydrological setting of the Australian karsts.* Paper presented at the Proceedings of the 13th Australasian Conference on Cave and Karst Management. pp.

Grimes, K. G. (2002). Syngenetic and eogenetic karst: an Australian viewpoint. *Evolution of Karst: from Prekarst to Cessation. Inštitut za raziskovanje krasa, ZRC SAZU, Postojna*, 407-414.

Grimes, K. G. (2006). Syngenetic karst in Australia: a review.

Grinat, M., Epping, D., & Meyer, R. (2018). *Long-time resistivity monitoring of a freshwater/saltwater transition zone using the vertical electrode system SAMOS.* Paper presented at the E3S Web of Conferences.

Grinat, M., Südekum, W., Epping, D., Grelle, T., & Meyer, R. (2010). *An automated electrical resistivity tomography system to monitor the freshwater/saltwater zone on a North Sea Island.* Paper presented at the Near Surface 2010-16th EAGE European Meeting of Environmental and Engineering Geophysics.

Groom, B. P. K., Froend, R. H., & Mattiske, E. M. (2000). Impact of groundwater abstraction on a Banksia woodland, Swan Coastal Plain, Western Australia. *Ecological Management and Restoration, 1*(2), 117-124. doi:10.1046/j.1442-8903.2000.00033.x

Guillen, A., & Menichetti, V. (1984). Gravity and magnetic inversion with minimization of a specific functional. *Geophysics*. Retrieved from https://library.seg.org/doi/abs/10.1190/1.1441761

Günther, T. (2004). *Inversion methods and resolution analysis for the 2D/3D reconstruction of resistivity structures from DC measurements.* (Dissertation). Retrieved from http://hdl.handle.net/11858/00-1735-0000-0001-3314-2 FID GEO-LEO e-docs database.

Boundless Electrical Resistivity Tomography—Bert 2—The User Tutorial. (2019). Günther, T., & Rücker, C. (Version 2.2.8) [Mobile application software]

Günther, T., Rucker, C., & Spitzer, K. (2006). Three-dimensional modelling and inversion of dc resistivity data incorporating topography - II. Inversion. *Geophysical Journal International, 166*(2), 506-517. doi:10.1111/j.1365-246X.2006.03011.x

Guo-Qiang, X., Wei-Ying, C., Nan-Nan, Z., Hai, L., & Hua-Sen, Z. (2013). Understanding of Grounded-Wire TEM Sounding with Near-Source Configuration. *Journal of Geophysics & Remote Sensing*.

Guo, Q., Huang, J., Zhou, Z., & Wang, J. (2019). Experiment and Numerical Simulation of Seawater Intrusion under the Influences of Tidal Fluctuation and Groundwater Exploitation in Coastal Multilayered Aquifers. *Geofluids, 2019*, 17. doi:10.1155/2019/2316271

Haber, E., Oldenburg, D. W., & Shekhtman, R. (2007). Inversion of time domain three-dimensional electromagnetic data. *Geophysical Journal International, 171*(2), 550-564. doi:10.1111/j.1365-246X.2007.03365.x

Hagrey, S. A. a. (2011). CO2 plume modeling in deep saline reservoirs by 2D ERT in boreholes. *The Leading Edge, 30*(1), 24-33. doi:10.1190/1.3535429

Hamamoto, S., Moldrup, P., Kawamoto, K., & Komatsu, T. (2010). Excluded-volume expansion of Archie's law for gas and solute diffusivities and electrical and thermal conductivities in variably saturated porous media. *Water Resources Research, 46*(6). doi:10.1029/2009wr008424

Hamdan, H., & Vafidis, A. (2013). Joint inversion of 2D resistivity and seismic travel time data to image saltwater intrusion over karstic areas. *Environmental Earth Sciences, 68*(7), 1877-1885. doi:10.1007/s12665-012-1875-9

Haroon, A., Adrian, J., Bergers, R., Gurk, M., Tezkan, B., Mammadov, A. L., & Novruzov, A. G. (2015). Joint inversion of long-offset and central-loop transient electromagnetic data: Application to a mud volcano exploration in Perekishkul, Azerbaijan. *Geophysical Prospecting, 63*(2), 478-494. doi:10.1111/1365-2478.12157

Harrington, N., & Cook. P. (2014). *Groundwater in Australia*. Retrieved from

Harris, B., Costall, A., Nguyen, H., Michael, K., Ricard, L., Freifeld, B., . . . Pethick, A. (2019). Time lapse in-hole electrical resistivity surveying during a shallow release of CO2 gas: Harvey, Western Australia. *ASEG Extended Abstracts, 2019*(1), 1-5. doi:10.1080/22020586.2019.12073174

Hartmann, A., Goldscheider, N., Wagener, T., Lange, J., & Weiler, M. (2014). Karst water resources in a changing world: Review of hydrological modeling approaches. *52*(3), 218-242. doi:10.1002/2013rg000443

Healy, R. W., & Cook, P. G. (2002). Using groundwater levels to estimate recharge. *Hydrogeology Journal, 10*(1), 91-109. doi:10.1007/s10040-001-0178-0

Hearty, P. J. (2002). Revision of the late Pleistocene stratigraphy of Bermuda. *Sedimentary Geology, 153*(1-2), 1-21. doi:Pii S0037-0738(02)00261-0

Doi 10.1016/S0037-0738(02)00261-0

Hearty, P. J., & O'Leary, M. J. (2008). Carbonate eolianites, quartz sands, and Quaternary sea-level cycles, Western Australia: A chronostratigraphic approach. *Quaternary Geochronology, 3*(1-2), 26-55. doi:10.1016/j.quageo.2007.10.001

Heath, R. C. (1998). *Basic ground-water hydrology* (Vol. 2220): US Department of the Interior, US Geological Survey.

Heen, Z. H. A., & Muhsen, S. A. (2017). Electrical Resistivity Tomography for Coastal Sea Water Intrusion Characterization along Rafah Area, South of Gaza Strip, Palestine. *IUG Journal of Natural Studies*.

Heiss, J. W., & Michael, H. A. (2014). Saltwater-freshwater mixing dynamics in a sandy beach aquifer over tidal, spring-neap, and seasonal cycles. *50*(8), 6747-6766. doi:10.1002/2014wr015574

Held, R., Attinger, S., & Kinzelbach, W. (2005). Homogenization and effective parameters for the Henry problem in heterogeneous formations. *Water Resources Research, 41*(11). doi:10.1029/2004wr003674

Hellman, K., Ronczka, M., Günther, T., Wennermark, M., Rücker, C., & Dahlin, T. (2017). Structurally coupled inversion of ERT and refraction seismic data combined with cluster-based model integration. *Journal of Applied Geophysics, 143*, 169-181. doi:https://doi.org/10.1016/j.jappgeo.2017.06.008

Henderson, R. D., Day-Lewis, F. D., Abarca, E., Harvey, C. F., Karam, H. N., Liu, L. B., & Lane, J. W. (2010). Marine electrical resistivity imaging of submarine groundwater discharge: sensitivity analysis and application in Waquoit Bay, Massachusetts, USA. *Hydrogeology Journal, 18*(1), 173-185. doi:10.1007/s10040-009-0498-z

Henry, H. (1964). Effects of dispersion on salt encroachment in coastal aquifers: US Geological Survey Water-Supply Paper 1613-C, p. *C71-C84*.

Herman, R. (2001). An introduction to electrical resistivity in geophysics. *American Journal of Physics, 69*(9), 943-952. doi:Doi 10.1119/1.1378013

Hermans, T., Vandenbohede, A., Lebbe, L., Martin, R., Kemna, A., Beaujean, J., & Nguyen, F. (2012). Imaging artificial salt water infiltration using electrical resistivity tomography constrained by geostatistical data. *Journal of Hydrology, 438*, 168-180. doi:10.1016/j.jhydrol.2012.03.021

Heße, F., Prykhodko, V., Schlüter, S., & Attinger, S. (2014). Generating random fields with a truncated power-law variogram: A comparison of several numerical methods. *Environmental Modelling & Software, 55*, 32-48. doi:https://doi.org/10.1016/j.envsoft.2014.01.013

Hilhorst, M. J. S. S. S. o. A. J. (2000). A pore water conductivity sensor. *64*(6), 1922-1925.

Hobbs, B., & Sopher, D. (2008). *Constrained Sharp Boundary Inversion Of Multi-Transient Em Data.* Paper presented at the Cspg, Cseg, Cwls Convention.

Hoggart, S. P. G., Hanley, M. E., Parker, D. J., Simmonds, D. J., Bilton, D. T., Filipova-Marinova, M., . . . Thompson, R. C. (2014). The consequences of doing nothing: The effects of seawater flooding on coastal zones. *Coastal Engineering, 87*, 169-182. doi:https://doi.org/10.1016/j.coastaleng.2013.12.001

Holzer, T. L., & Johnson, A. I. (1985). Land subsidence caused by ground water withdrawal in urban areas. *GeoJournal, 11*(3), 245-255. doi:10.1007/BF00186338

Hördt, A., & Müller, M. (2000). Understanding LOTEM data from mountainous terrain. *Geophysics, 65*(4), 1113-1123. doi:10.1190/1.1444804

Huisman, J. A., Hubbard, S. S., Redman, J. D., & Annan, A. P. (2003). Measuring Soil Water Content with Ground Penetrating Radar: A Review. *Vadose Zone Journal, 2*(4), 476-491. doi:10.2136/vzj2003.4760

Huntley, D. (1986). Relations Between Permeability and Electrical Resistivity in Granular Aquifers. *Groundwater, 24*(4), 466-474. doi:10.1111/j.1745-6584.1986.tb01025.x

Hussain, M. S., & Javadi, A. A. (2016). Assessing impacts of sea level rise on seawater intrusion in a coastal aquifer with sloped shoreline boundary. *Journal of Hydro-environment Research, 11*, 29-41. doi:10.1016/j.jher.2016.01.003

Igroufa, S., Hashim, R., & Taib, S. (2010). Mapping Of Salt-Water Intrusion By Geoelectrical Imaging In Carey Islands.

Imperial College London. (2015). Salt Water Intrusion In Bangladesh. Retrieved from https://www.imperial.ac.uk/grantham/our-work/impacts-and-adaptation/ipcc-working-group-ii/sea-level-rise/

Ishola, K. S., Nawawi, M. N. M., & Abdullah, K. (2015). Combining Multiple Electrode Arrays for Two-Dimensional Electrical Resistivity Imaging Using the Unsupervised Classification Technique. *Pure and Applied Geophysics, 172*(6), 1615-1642. doi:10.1007/s00024-014-1007-4

Ivkovic, K., Marshall, S., Morgan, L., Werner, A., Carey, H., Cook, S., . . . Caruana, L. (2012). National–Scale Vulnerability Assessment Of Seawater Intrusion: Summary Report. *Australian Government National Water Commision. Waterlines Report Series No, 85*.

Johannes, R. E. (1980). The Ecological Significance of the Submarine Discharge of Groundwater. *Marine Ecology Progress Series, 3*(4), 365-373. doi:DOI 10.3354/meps003365

Johnson, M. E., Baarli, B. G., & Scott, J. H. (1995). Colonization and Reef Growth on a Late Pleistocene Rocky Shore and Abrasion Platform in Western-Australia. *Lethaia, 28*(1), 85-98. doi:DOI 10.1111/j.1502-3931.1995.tb01596.x

Johnson, T. C., Versteeg, R. J., Ward, A., Day-Lewis, F. D., & Revil, A. (2010). Improved hydrogeophysical characterization and monitoring through parallel modeling and inversion of time-domain resistivity andinduced-polarization data. *Geophysics, 75*(4), WA27-WA41. doi:https://doi.org/10.1190/1.3475513

Jol, H. M. (2008). *Ground Penetrating Radar Theory And Applications*: elsevier.

Jørgensen, N. O., Andersen, M. S., & Engesgaard, P. (2008). Investigation of a dynamic seawater intrusion event using strontium isotopes (87Sr/86Sr). *Journal of Hydrology, 348*(3), 257-269. doi:https://doi.org/10.1016/j.jhydrol.2007.10.001

Karaoulis, M., Tsourlos, P., Kim, J. H., & Revil, A. (2014). 4D time-lapse ERT inversion: introducing combined time and space constraints. *Near Surface Geophysics, 12*(1), 25-34. doi:10.3997/1873-0604.2013004

Karegar, M. A., Dixon, T. H., & Engelhart, S. E. (2016). Subsidence along the Atlantic Coast of North America: Insights from GPS and late Holocene relative sea level data. *Geophysical Research Letters, 43*(7), 3126-3133. doi:10.1002/2016gl068015

Katz, C. (2016). As Groundwater Dwindles, a Global Food Shock Looms. Retrieved from https://www.nationalgeographic.com/news/2016/12/groundwater-depletion-global-food-supply/

Kern, A., & Johnson, S. (2009). Improved groundwater resource management through better groundwater monitoring.

Kerrou, J., & Renard, P. J. H. J. (2010). A numerical analysis of dimensionality and heterogeneity effects on advective dispersive seawater intrusion processes. *18*(1), 55-72. doi:10.1007/s10040-009-0533-0

Ketabchi, H., Mahmoodzadeh, D., Ataie-Ashtiani, B., & Simmons, C. T. (2016). Sea-level rise impacts on seawater intrusion in coastal aquifers: Review and integration. *Journal of Hydrology, 535*, 235-255. doi:10.1016/j.jhydrol.2016.01.083

Kibria, G., & Hossain, S. (2019). Electrical resistivity of compacted clay minerals. *Environmental Geotechnics, 6*(1), 18-25. doi:10.1680/jenge.16.00005

Koltermann, C. E., & Gorelick, S. M. (1996). Heterogeneity in Sedimentary Deposits: A Review of Structure-Imitating, Process-Imitating, and Descriptive Approaches. *32*(9), 2617-2658. doi:doi:10.1029/96WR00025

Kotera, A., Sakamoto, T., Nguyen, D. K., & Yokozawa, M. (2008). Regional Consequences of Seawater Intrusion on Rice Productivity and Land Use in Coastal Area of the Mekong River Delta. *Japan Agricultural Research Quarterly: JARQ, 42*(4), 267-274. doi:10.6090/jarq.42.267

Koukadaki, M. A., Karatzas, G. P., Papadopoulou, M. P., & Vafidis, A. (2007). Identification of the Saline Zone in a Coastal Aquifer Using Electrical Tomography Data and Simulation. *Water Resources Management, 21*(11), 1881. doi:10.1007/s11269-006-9135-y

Koussis, A. D., Mazi, K., & Destouni, G. (2012). Analytical single-potential, sharp-interface solutions for regional seawater intrusion in sloping unconfined coastal aquifers, with pumping and recharge. *Journal of Hydrology, 416-417*, 1-11. doi:https://doi.org/10.1016/j.jhydrol.2011.11.012

Kretschmer, P., & Degens, B. (2012). *Review Of Available Groundwater In The Superficial Aquifer For The Yanchep, Eglinton And Quinns Groundwater Subareas*. Retrieved from

Krishnaraj, S., Balasubramanian, M., Gopinath, S., Saravanan, K., Prakash, R., Ravindran, A., & Sarma, V. (2014). Evaluation Of Estuarine Impact On Groundwater Salinization In Pondicherry Coastal Aquifers Using Electrical Resistivity Imagine Techniques. doi:http://doi.org/10.6084/m9.figshare.1206337

Kuras, O., Pritchard, J. D., Meldrum, P. I., Chambers, J. E., Wilkinson, P. B., Ogilvy, R. D., & Wealthall, G. P. (2009). Monitoring hydraulic processes with automated time-lapse electrical resistivity tomography (ALERT). *Comptes Rendus Geoscience, 341*(10-11), 868-885. doi:10.1016/j.crte.2009.07.010

LaBrecque, D. J., Ramirez, A. L., Daily, W. D., Binley, A. M., & Schima, S. A. (1996). ERT monitoring of environmental remediation processes. *Measurement Science and Technology, 7*(3), 375-383. doi:10.1088/0957-0233/7/3/019

Lambert, M. J., & Burnett, W. C. J. B. (2003). Submarine groundwater discharge estimates at a Florida coastal site based on continuous radon measurements. *66*(1), 55-73. doi:10.1023/B:BIOG.0000006057.63478.fa

Lasky, R. (1993). *A Structural Study Of The Southern Perth Basin, Western Australia*: Geological Survey of Western Australia.

Le, C. V. A., Harris, B. D., Pethick, A. M., Takougang, E. M. T., & Howe, B. (2016). Semiautomatic and Automatic Cooperative Inversion of Seismic and Magnetotelluric Data. *Surveys in Geophysics, 37*(5), 845-896. doi:10.1007/s10712-016-9377-z

Legates, D. R., & McCabe, G. J. (1999). Evaluating the use of "goodness-of-fit" Measures in hydrologic and hydroclimatic model validation. *Water Resources Research, 35*(1), 233-241. doi:https://doi.org/10.1029/1998WR900018

Leontarakis, K., & Apostolopoulos, G. V. (2012). Laboratory study of the cross-hole resistivity tomography: The Model Stacking (MOST) Technique. *Journal of Applied Geophysics, 80*, 67-82. doi:https://doi.org/10.1016/j.jappgeo.2012.01.005

Levanon, E., Yechieli, Y., Shalev, E., Friedman, V., & Gvirtzman, H. (2013). Reliable Monitoring of the Transition Zone Between Fresh and Saline Waters in Coastal Aquifers. *Ground Water Monitoring and Remediation, 33*(3), 101-110. doi:10.1111/gwmr.12020

Leyland, L. A. (2011). *Hydrogeology Of The Leederville Aquifer, Central Perth Basin, Western Australia*: University of Western Australia.

Leyland, L. A. (2012). *Reinterpretation Of The Hydrogeology Of The Leederville Aquifer : Gnangara Groundwater System / By La Leyland*. Perth, W.A: Dept. of Water.

Li, X. Y., Zhang, L. M., & Li, J. H. (2016). Using Conditioned Random Field to Characterize the Variability of Geologic Profiles. *142*(4), 04015096. doi:doi:10.1061/(ASCE)GT.1943-5606.0001428

Lines, L., Schultz, A., & Treitel, S. (1988). Cooperative inversion of geophysical data. *Geophysics*. Retrieved from https://library.seg.org/doi/abs/10.1190/1.1442403

Lipar, M., & Webb, J. A. (2015). The formation of the pinnacle karst in Pleistocene aeolian calcarenites (Tamala Limestone) in southwestern Australia. *Earth-Science Reviews, 140*, 182-202. doi:10.1016/j.earscirev.2014.11.007

Loke, M. (1997). Res2DINV software user's manual. *University Sains Malaysia, Penang*.

Loke, M. (2003). Rapid 2d Resistivity & Ip Inversion Using The Least-Squares Method. *Geotomo Software, Manual, 122*.

Loke, M. (2016). Tutorial: 2d And 3d Electrical Imaging Surveys. Penang, Malaysia, Universiti Sains Malaysia. Retrieved from http://www.geotomosoft.com/downloads.php

Loke, M., Alfouzan, F. A., & Nawawi, M. (2007). Optimisation of electrode arrays used in 2D resistivity imaging surveys. In *ASEG Extended Abstracts 2007* (pp. 1-4): Australian Society of Exploration Geophysicists (ASEG).

Loke, M. H. (2016a). RES2DINVx64 ver. 4.05 with multi-core and 64-bit support. Retrieved from http://www.geotomosoft.com/

Loke, M. H. (2016b). Res2DMod. Retrieved from http://www.geotomosoft.com/

Loke, M. H., Acworth, I., & Dahlin, T. (2003). A comparison of smooth and blocky inversion methods in 2D electrical imaging surveys. *Exploration Geophysics, 34*(3), 182-187. doi:Doi 10.1071/Eg03182

Loke, M. H., & Barker, R. D. (1995). Least-Squares Deconvolution of Apparent Resistivity Pseudosections. *Geophysics, 60*(6), 1682-1690. doi:Doi 10.1190/1.1443900

Loke, M. H., Chambers, J. E., Rucker, D. F., Kuras, O., & Wilkinson, P. B. (2013). Recent developments in the direct-current geoelectrical imaging method. *Journal of Applied Geophysics, 95*, 135-156. doi:10.1016/j.jappgeo.2013.02.017

Loke, M. H., Kiflu, H., Wilkinson, P. B., Harro, D., & Kruse, S. (2015). Optimized arrays for 2D resistivity surveys with combined surface and buried arrays. *Near Surface Geophysics, 13*(5), 505-517. doi:10.3997/1873-0604.2015038

Loke, M. H., & Lane., J. W. (2004). Inversion of data from electrical imaging surveys in water-covered areas. In *ASEG Extended Abstracts 2004: 17th Geophysical Conference* (pp. 1-4).

Loke, M. H., Wilkinson, P. B., Chambers, J. E., & Strutt, M. (2014). Optimized arrays for 2D cross-borehole electrical tomography surveys. *Geophysical Prospecting, 62*(1), 172-189. doi:https://doi.org/10.1111/1365-2478.12072

Loke, M. H., Wilkinson, P. B., Uhlemann, S. S., Chambers, J. E., & Oxby, L. S. (2014). Computation of optimized arrays for 3-D electrical imaging surveys. *Geophysical Journal International, 199*(3), 1751-1764. doi:10.1093/gji/ggu357

Loke, M. H., Wilkinson, P. S., Chambers, J. E., Uhlemann, S. S., & Sorensen, J. P. R. (2015). Optimized arrays for 2-D resistivity survey lines with a large number of electrodes. *Journal of Applied Geophysics, 112*(Supplement C), 136-146. doi:10.1016/j.jappgeo.2014.11.011

Lovatini, A., Kumar, R., Al-Saeed, M., Khalid, A., Pezzoli, M., Battaglini, A., . . . Roth, J. (2013). *Land Controlled-Source Electromagnetic Surveying For Viscous Oil Characterization In Kuwait.* Paper presented at the 75th Eage Conference & Exhibition Incorporating Spe Europec 2013.

Lu, C. (2011). *Mixing in complex coastal hydrogeologic systems.* (Thesis). Georgia Institute of Technology, Retrieved from http://hdl.handle.net/1853/39600

Lu, C. H., Chen, Y. M., Zhang, C., & Luo, J. (2013). Steady-state freshwater-seawater mixing zone in stratified coastal aquifers. *Journal of Hydrology, 505*, 24-34. doi:10.1016/j.jhydrol.2013.09.017

Lusczynski, N. J. (1961). Head and flow of ground water of variable density. *Journal of Geophysical Research, 66*(12), 4247-4256. doi:doi:10.1029/JZ066i012p04247

Luthin, J. N., & Day, P. R. J. S. S. S. o. A. J. (1955). Lateral Flow Above a Sloping Water Table 1. *19*(4), 406-410.

Maasland, M. (1957). Soil anisotropy and land drainage. In *Drainage of agricultural lands* (Vol. 7, pp. 216-285): ASA Madison, Wis.

Mahesha, A., & Nagaraja, S. H. (1996). Effect of natural recharge on sea water intrusion in coastal aquifers. *Journal of Hydrology, 174*(3-4), 211-220. doi:Doi 10.1016/0022-1694(95)02777-7

Maliva, R. G. (2016). Aquifer Characterization Techniques.

Mangor, K., Drønen, N. K., Kærgaard, K. H., & Kristensen, S. E. (2017). Shoreline management guidelines. *DHI*. Retrieved from https://www.dhigroup.com/marine-water/ebook-shoreline-management-guidelines

Marker, P. A., Foged, N., He, X., Christiansen, A. V., Refsgaard, J. C., Auken, E., & Bauer-Gottwein, P. (2015). Performance evaluation of groundwater model hydrostratigraphy from airborne electromagnetic data and lithological borehole logs. *Hydrology and Earth System Sciences, 19*(9), 3875-3890. doi:10.5194/hess-19-3875-2015

Marshal, J., Ramsay, D., Moore, A., Shafik, S., Graham, T., & Needham, J. (1993). The Vlaming Sub-Basin, Offshore South Perth Basin Continental Margins Program Folio 7. *Geoscience Australia, Canberra*.

Martin, T., & Gunther, T. (2013). Complex resistivity tomography (CRT) for fungus detection on standing oak trees. *European Journal of Forest Research, 132*(5-6), 765-776. doi:10.1007/s10342-013-0711-4

Martinez, A., & Byrnes, A. P. (2001). *Modeling dielectric-constant values of geologic materials: An aid to ground-penetrating radar data collection and interpretation*: Kansas Geological Survey, University of Kansas.

Martinez, M. L., Intralawan, A., Vazquez, G., Perez-Maqueo, O., Sutton, P., & Landgrave, R. (2007). The coasts of our world: Ecological, economic and social importance. *Ecological Economics, 63*(2-3), 254-272. doi:10.1016/j.ecolecon.2006.10.022

Martorana, R., Fiandaca, G., Ponsati, A. C., & Cosentino, P. L. (2009). Comparative tests on different multi-electrode arrays using models in near-surface geophysics. *Journal of Geophysics and Engineering, 6*(1), 1-20. doi:10.1088/1742-2132/6/1/001

Masterson, J. P. (2004). *Simulated interaction between freshwater and saltwater and effects of ground-water pumping and sea-level change, Lower Cape Cod aquifer system, Massachusetts*: US Department of the Interior, US Geological Survey.

Mathieu, F., & Toksö: z, M. (1984). Application of full waveform acoustic logging data to the estimation of reservoir permeability. In *SEG Technical Program Expanded Abstracts 1984* (pp. 9-12): Society of Exploration Geophysicists.

Maurer, H., & Friedel, S. (2006). Outer-space sensitivities in geoelectrical tomography. *Geophysics, 71*(3), G93-G96. doi:10.1190/1.2194891

Maxwell, J. C. (1873). *A Treatise on Electricity and Magnetism* (Vol. 1). Cambridge: Cambridge University Press.

McArthur, W. M., & Bettenay, E. J. S. P. C., Australia. (1960). The development and distribution of the soils of the Swan Coastal Plain, Western Australia. *16*.

McFarlane, D., Inman, M., White, S., Loh, M., Turner, A., & English, L. (2005). Integrated resource planning for the integrated water supply scheme. Client Report to WA Government. In: CSIRO: Water for a Healthy Country National Research Flagship Canberra.

McGillivray, P. R. (1992). *Forward modeling and inversion of DC resistivity and MMR data.* University of British Columbia,

Meju, M. A. (1994). *Geophysical Data Analysis: Understanding Inverse Problem Theory And Practice* (Vol. 6): Society of Exploration Geophysicists Tulsa,, OK.

Menke, W. (2012a). Chapter 1 - Describing Inverse Problems. In *Geophysical Data Analysis: Discrete Inverse Theory (Third Edition)* (pp. 1-14). Boston: Academic Press.

Menke, W. (2012b). Chapter 4 - Solution Of The Linear, Gaussian Inverse Problem, Viewpoint 2: Generalized Inverses. In *Geophysical Data Analysis: Discrete Inverse Theory (Third Edition)* (pp. 69-88). Boston: Academic Press.

Menke, W. (2012c). *Geophysical data analysis: Discrete inverse theory* (Vol. 45): Academic press.

Meredith, K., Cendon, D. I., Pigois, J. P., Hollins, S., & Jacobsen, G. (2012). Using 14C and 3H to delineate a recharge 'window' into the Perth Basin aquifers, North Gnangara groundwater system, Western Australia. *Sci Total Environ, 414*, 456-469. doi:10.1016/j.scitotenv.2011.10.016

Meyer, R., Engesgaard, P., & Sonnenborg, T. O. (2019). Origin and Dynamics of Saltwater Intrusion in a Regional Aquifer: Combining 3-D Saltwater Modeling With Geophysical and Geochemical Data. *Water Resources Research, 55*(3), 1792-1813. doi:10.1029/2018wr023624

Michael, H. A., Russoniello, C. J., & Byron, L. A. (2013). Global assessment of vulnerability to sea-level rise in topography-limited and recharge-limited coastal groundwater systems. *Water Resources Research, 49*(4), 2228-2240. doi:10.1002/wrcr.20213

Millero, F. J., Feistel, R., Wright, D. G., & McDougall, T. J. (2008). The composition of Standard Seawater and the definition of the Reference-Composition Salinity Scale. *Deep-Sea Research Part I-Oceanographic Research Papers, 55*(1), 50-72. doi:10.1016/j.dsr.2007.10.001

Moore, W. S. (2006). The role of submarine groundwater discharge in coastal biogeochemistry. *Journal of Geochemical Exploration, 88*(1), 389-393. doi:https://doi.org/10.1016/j.gexplo.2005.08.082

Mylroie, J. E. (2013). Coastal Karst Development in Carbonate Rocks. In M. J. Lace & J. E. Mylroie (Eds.), *Coastal Karst Landforms* (pp. 77-109). Dordrecht: Springer Netherlands.

Narayan, K. A., Schleeberger, C., & Bristow, K. L. (2007). Modelling seawater intrusion in the Burdekin Delta Irrigation Area, North Queensland, Australia. *Agricultural Water Management, 89*(3), 217-228. doi:10.1016/j.agwat.2007.01.008

National Water Commission. (2012). *National-scale vulnerability assessment of seawater intrusion: Coastal aquifer typology*. (ISSN 1448-2177). Geoscience Australia, Canberra, and National Centre for Groundwater Research and Training, Adelaide

Nekut, A. G. (1987). Direct Inversion of Time-Domain Electromagnetic Data. *Geophysics, 52*(10), 1431-1435. doi:Doi 10.1190/1.1442256

Nguyen, F., Kemna, A., Antonsson, A., Engesgaard, P., Kuras, O., Ogilvy, R., . . . Pulido-Bosch, A. (2009). Characterization of seawater intrusion using 2D electrical imaging. *Near Surface Geophysics, 7*(5-6), 377-390. doi:https://doi.org/10.3997/1873-0604.2009025

Nicholas, W., Borissova, I., Radke, L., Tran, M., Bernardel, G., Jorgensen, D., . . . Whiteway, T. (2013). Seabed Environments And Shallow Geology Of The Vlaming Sub-Basin, Western Australia.

Nidagal, V., & Davidson, W. J. G. S. o. W., Unpublished Hydrogeological Report. (1991). North coastal groundwater investigation (Burns Beach—Pipidinny). (1991/17).

Noel, M., & Xu, B. W. (1991). Archaeological Investigation by Electrical-Resistivity Tomography - a Preliminary-Study. *Geophysical Journal International, 107*(1), 95-102. doi:DOI 10.1111/j.1365-246X.1991.tb01159.x

O'Callaghan, J., Pattiaratchi, C., & Hamilton, D. (2007). The response of circulation and salinity in a micro-tidal estuary to sub-tidal oscillations in coastal sea surface elevation. *Continental Shelf Research, 27*(14), 1947-1965. doi:10.1016/j.csr.2007.04.004

Odhiambo, G. O. (2017). Water scarcity in the Arabian Peninsula and socio-economic implications. *Applied Water Science, 7*(5), 2479-2492. doi:10.1007/s13201-016-0440-1

OECD. (2018). Water Withdrawals (indicator) (Publication no. OECD (2018), Water withdrawals (indicator). doi: 10.1787/17729979-en).

Ogilvy, R. D., Meldrum, P. I., Kuras, O., Wilkinson, P. B., Chambers, J. E., Sen, M., . . . Tsourlos, P. (2009). Automated monitoring of coastal aquifers with electrical resistivity tomography. *Near Surface Geophysics, 7*(5-6), 367-375. doi:Doi 10.3997/1873-0604.2009027

Oiro, S., & Comte, J.-C. (2019). Drivers, patterns and velocity of saltwater intrusion in a stressed aquifer of the East African coast: Joint analysis of groundwater and geophysical data in southern Kenya. *Journal of African Earth Sciences, 149*, 334-347. doi:https://doi.org/10.1016/j.jafrearsci.2018.08.016

Oldenburg, D. W., & Li, Y. G. (1999). Estimating depth of investigation in dc resistivity and IP surveys. *Geophysics, 64*(2), 403-416. doi:Doi 10.1190/1.1444545

Palacios, A., Ledo, J. J., Linde, N., Luquot, L., Bellmunt, F., Folch, A., . . . Carrera, J. (2019). Time-lapse cross-hole electrical resistivity tomography (CHERT) for monitoring seawater intrusion dynamics in a Mediterranean aquifer. *Hydrol. Earth Syst. Sci. Discuss., 2019*, 1-30. doi:10.5194/hess-2019-408

Parker, L. (2016). What You Need to Know About the World's Water Wars. Retrieved from https://www.nationalgeographic.com/news/2016/07/world-aquifers-water-wars/

Parker, T., Shatalin, S., & Farhadiroushan, M. J. f. b. (2014). Distributed Acoustic Sensing–a new tool for seismic applications. *32*(2), 61-69.

Parmesan, C., & Yohe, G. (2003). A globally coherent fingerprint of climate change impacts across natural systems. *Nature, 421*, 37. doi:10.1038/nature01286

Paster, A., Dagan, G., & Guttman, J. (2006). The salt-water body in the Northern part of Yarkon-Taninim aquifer: Field data analysis, conceptual model and prediction. *Journal of Hydrology, 323*(1-4), 154-167. doi:10.1016/j.jhydrol.2005.08.018

Pazdirek, O., & Blaha, V. (1996). *Examples of resistivity imaging using ME-100 resistivity field acquisition system.* Paper presented at the 58th EAGE Conference and Exhibition.

PEDERSEN, L. B. (1979). CONSTRAINED INVERSION OF POTENTIAL FIELD DATA*. *27*(4), 726-748. doi:10.1111/j.1365-2478.1979.tb00993.x

Pethick, A., Costall, A., Dean, T., & Blylevens, J. (2018). Perth's lost guns. *Preview, 2018*(196), 38-41. doi:10.1071/PVv2018n196p38

Petra, D. (2009). Vulnerability to the impact of climate change on renewable groundwater resources: a global-scale assessment. *Environmental Research Letters, 4*(3), 035006. Retrieved from http://stacks.iop.org/1748-9326/4/i=3/a=035006

PGS. (2007). Multi-Transient Em Technology At Pgs.

Pidlisecky, A., Moran, T., Hansen, B., & Knight, R. (2016). Electrical Resistivity Imaging of Seawater Intrusion into the Monterey Bay Aquifer System. *Ground Water, 54*(2), 255-261. doi:10.1111/gwat.12351

Pollock, D., Smith, A., Trefry, M., Davis, G., Johnston, C., & Gardiner, A. (2006). *Status of Groundwater Quality in the Cockburn Sound Catchment*. Retrieved from https://www.der.wa.gov.au/image/.../2006_Status_GroundwaterSUMMARY.PDF

Pool, M., & Carrera, J. (2011). A correction factor to account for mixing in Ghyben-Herzberg and critical pumping rate approximations of seawater intrusion in coastal aquifers. *Water Resources Research, 47*(5). doi:10.1029/2010wr010256

Pool, M., Post, V. E. A., & Simmons, C. T. (2014). Effects of tidal fluctuations on mixing and spreading in coastal aquifers: Homogeneous case. *Water Resources Research, 50*(8), 6910-6926. doi:10.1002/2014wr015534

Possetti, G., Kamikawachi, R., Prevedello, C., Muller, M., Fabris, J. J. M. S., & Technology. (2009). Salinity measurement in water environment with a long period grating based interferometer. *20*(3), 034003.

Post, V., Kooi, H., & Simmons, C. (2007). Using hydraulic head measurements in variable-density ground water flow analyses. *Ground Water, 45*(6), 664-671. doi:10.1111/j.1745-6584.2007.00339.x

Post, V. E., Groen, J., Kooi, H., Person, M., Ge, S., & Edmunds, W. M. (2013). Offshore fresh groundwater reserves as a global phenomenon. *Nature, 504*(7478), 71-78. doi:10.1038/nature12858

POUS, J., MARCUELLO, A., & QUERALT, P. (1987). RESISTIVITY INVERSION WITH A PRIORI INFORMATION*. *Geophysical Prospecting, 35*(5), 590-603. doi:10.1111/j.1365-2478.1987.tb00837.x

Price, R. M., Top, Z., Happell, J. D., & Swart, P. K. (2003). Use of tritium and helium to define groundwater flow conditions in Everglades National Park. *Water Resources Research, 39*(9). doi:10.1029/2002wr001929

Pulido-Leboeuf, P., Pulido-Bosch, A., Calvache, M. L., Vallejos, Á., & Andreu, J. M. (2003). Strontium, SO42−/Cl− and Mg2+/Ca2+ ratios as tracers for the evolution of seawater into coastal aquifers: the example of Castell de Ferro aquifer (SE Spain). *Comptes Rendus Geoscience, 335*(14), 1039-1048. doi:https://doi.org/10.1016/j.crte.2003.08.004

Qu, W. J., Li, H. L., Wan, L., Wang, X. S., & Jiang, X. W. (2014). Numerical simulations of steady-state salinity distribution and submarine groundwater discharges in homogeneous anisotropic coastal aquifers. *Advances in Water Resources, 74*, 318-328. doi:10.1016/j.advwatres.2014.10.009

Raiche, A., Sugeng, F., & Wilson, G. (2007). Practical 3D EM inversion? The P223F software suite. *ASEG Extended Abstracts, 2007*(1), 1-5.

Randazzo, A. F., & Bloom, J. I. (1985). Mineralogical changes along the freshwater/saltwater interface of a modern aquifer. *Sedimentary Geology, 43*(1-4), 219-239.

Rechtien, R. D., Hambacker, K. L., & R. F. Ballard, J. (1993). A high-frequency sparker source for the borehole environment. *58*(5), 660-669. doi:10.1190/1.1443450

Reed, B., Shaw, R., & Chatterton, K. (2013). Technical notes on drinking-water, sanitation and hygiene in emergencies. *Loughborough (UK): World Health Organization, Water, Engineering and Development Centre*.

Rehman, F., Abouelnaga, H. S. O., & Rehman, F. (2016). Estimation of dielectric permittivity, water content, and porosity for environmental engineering and hydrogeological studies using ground penetrating radar, a short review. *Arabian Journal of Geosciences, 9*(4), 1-7. doi:ARTN 312

10.1007/s12517-016-2328-7

Retallack, G. J. (2003). 5.18 - Soils and Global Change in the Carbon Cycle over Geological Time. In H. D. Holland & K. K. Turekian (Eds.), *Treatise on Geochemistry* (pp. 1-28). Oxford: Pergamon.
Richardson, E., Irvine, E., Froend, R., Book, P., Barber, S., & Bonneville, B. (2011). Australian groundwater dependent ecosystems toolbox part 1: assessment framework. *National Water Commission, Canberra*.
Robbins, A. R., & Plattner, A. (2018). Offset-electrode profile acquisition strategy for electrical resistivity tomography. *Journal of Applied Geophysics, 151*, 66-72. doi:10.1016/j.jappgeo.2018.01.027
Robinson, M., Bristow, C., McKinley, J., & Ruffell, A. 1.5. 5. Ground Penetrating Radar.
Ronczka, M., Hellman, K., Günther, T., Wisén, R., & Dahlin, T. (2017). Electric resistivity and seismic refraction tomography: a challenging joint underwater survey at Äspö Hard Rock Laboratory. *Solid Earth, 8*(3), 671-682. doi:10.5194/se-8-671-2017
Ronczka, M., Voss, T., & Gunther, T. (2015). Cost-efficient imaging and monitoring of saltwater in a shallow aquifer by using long electrode ERT. *Journal of Applied Geophysics, 122*, 202-209. doi:10.1016/j.jappgeo.2015.08.014
Roy, A., & Apparao, A. (1971). Depth Of Investigation In Direct Current Methods. *Geophysics, 36*(5), 943-959. doi:https://doi.org/10.1190/1.1440226
Rubin, Y., & Hubbard, S. S. (2006). *Hydrogeophysics* (Vol. 50): Springer Science & Business Media.
Rücker, C. (2010). Advanced Electrical Resistivity Modelling And Inversion Using Unstructured Discretization.
Rücker, C., Günther, T., & Spitzer, K. (2006). Three-dimensional modelling and inversion of dc resistivity data incorporating topography - I. Modelling. *Geophysical Journal International, 166*(2), 495-505. doi:10.1111/j.1365-246X.2006.03010.x
Rücker, C., Günther, T., & Wagner, F. M. (2017). pyGIMLi: An open-source library for modelling and inversion in geophysics. *Computers & Geosciences, 109*, 106-123. doi:10.1016/j.cageo.2017.07.011
Salam, R. B., Bekele, E., Hatton, T.J., Pollock, D.W and Lee-Steere, N. (2007). Sustainable Yield of Groundwater of the Gnangara Mound, Perth, Western Australia.
Samouelian, A., Cousin, I., Tabbagh, A., Bruand, A., & Richard, G. (2005). Electrical resistivity survey in soil science: a review. *Soil & Tillage Research, 83*(2), 173-193. doi:10.1016/j.still.2004.10.004
Sandmeir, K. J. (2014). ReflexW (Manual).
Sasaki, Y. (1992). Resolution of resistivity tomography inferred from numerical simulation. *Geophysical Prospecting, 40*(4), 453-463. doi:10.1111/j.1365-2478.1992.tb00536.x
Saunders, J. H., Herwanger, J. V., Pain, C. C., Worthington, M. H., & De Oliveira, C. R. E. (2005). Constrained resistivity inversion using seismic data. *Geophysical Journal International, 160*(3), 785-796. doi:10.1111/j.1365-246X.2005.02566.x
Sayles, R. (1931). Bermuda during the Ice Age: American Academy of Arts and Sciences, v. 66.
Scanlon, B. R., Mace, R. E., Barrett, M. E., & Smith, B. (2003). Can we simulate regional groundwater flow in a karst system using equivalent porous media models? Case study, Barton Springs Edwards aquifer, USA. *Journal of Hydrology, 276*(1), 137-158. doi:https://doi.org/10.1016/S0022-1694(03)00064-7
Schenato, L. J. A. S. (2017). A review of distributed fibre optic sensors for geo-hydrological applications. *7*(9), 896.
Schmelzbach, C., Doetsch, J., Robertsson, J. O., Jordi, C., & Günther, T. (2018). Geostatistical regularization operators for geophysical inverse problems on irregular meshes. *Geophysical Journal International, 213*(2), 1374-1386. doi:10.1093/gji/ggy055 %J Geophysical Journal International
Schmidt-Hattenberger, C., Bergmann, P., Kiessling, D., Kruger, K., Rucker, C., Schutt, H., & Grp, K. (2011). Application of a Vertical Electrical Resistivity Array (VERA) for Monitoring CO2 Migration at the Ketzin Site: First Performance Evaluation. *10th International Conference on Greenhouse Gas Control Technologies, 4*, 3363-3370. doi:10.1016/j.egypro.2011.02.258
Scholl, C. (2005). *The Influence Of Multidimensional Structures On The Interpretation Of Lotem Data With One-Dimensional Models And The Application To Data From Israel.* Universität zu Köln,
Schulze-Makuch, D. (2005). Longitudinal dispersivity data and implications for scaling behavior. *Ground Water, 43*(3), 443-456. doi:10.1111/j.1745-6584.2005.0051.x
Schwarz, J., Bear, J., & Dagan, G. (2016). Groundwater Development in Israel. *Ground Water, 54*(1), 143-148. doi:10.1111/gwat.12384
Sebben, M. L., Werner, A. D., & Graf, T. (2015). Seawater intrusion in fractured coastal aquifers: A preliminary numerical investigation using a fractured Henry problem. *Advances in Water Resources, 85*, 93-108. doi:10.1016/j.advwatres.2015.09.013
SEG. (2010). *Geophysics Today: 75th Anniversery Edition Compedium*.
Selker, J. S., Thévenaz, L., Huwald, H., Mallet, A., Luxemburg, W., van de Giesen, N., . . . Parlange, M. B. (2006). Distributed fiber-optic temperature sensing for hydrologic systems. *42*(12). doi:10.1029/2006wr005326
Selley, R. C. (2000). *Applied sedimentology*: Elsevier.

Semeniuk, V. (1985). The age structure of a Holocene barrier dune system and its implication for sealevel history reconstructions in southwestern Australia. *Marine Geology, 67*(3), 197-212. doi:https://doi.org/10.1016/0025-3227(85)90092-1

Semeniuk, V., & Johnson, D. P. (1982). Recent and Pleistocene beach/dune sequences, western Australia. *Sedimentary Geology, 32*(4), 301-328. doi:https://doi.org/10.1016/0037-0738(82)90042-2

Semeniuk, V., & Johnson, D. P. (1985). Modern and Pleistocene Rocky Shore Sequences Along Carbonate Coastlines, Southwestern Australia. *Sedimentary Geology, 44*(3-4), 225-261. doi:Doi 10.1016/0037-0738(85)90015-6

Semeniuk, V., & Searle, D. J. (1985). Distribution of Calcrete in Holocene Coastal Sands in Relationship to Climate, Southwestern Australia. *Journal of Sedimentary Petrology, 55*(1), 86-95. Retrieved from <Go to ISI>://WOS:A1985ACM0900011

Semeniuk, V., & Searle, D. J. (1986). Variability of Holocene sealevel history along the southwestern coast of Australia — Evidence for the effect of significant local tectonism. *Marine Geology, 72*(1), 47-58. doi:https://doi.org/10.1016/0025-3227(86)90098-8

Shanafield, M., Banks, E. W., Arkwright, J. W., & Hausner, M. B. (2018). Fiber-Optic Sensing for Environmental Applications: Where We Have Come From and What Is Possible. *54*(11), 8552-8557. doi:10.1029/2018wr022768

Sharma, M., Farrington, P., & Fernie, M. (1983). *Localized groundwater recharge on the" Gnangara Mound", Western Australia.* Paper presented at the international conference on groundwater and man.

Shi, L., & Jiao, J. J. (2014). Seawater intrusion and coastal aquifer management in China: a review. *Environmental Earth Sciences, 72*(8), 2811-2819. doi:10.1007/s12665-014-3186-9

Shoemaker, W. B. (2004). Important observations and parameters for a salt water intrusion model. *Ground Water, 42*(6-7), 829-840. doi:10.1111/j.1745-6584.2004.t01-2-.x

Sinclair Knight Merz. (2012). An assessment of groundwater management and monitoring costs in Australia. *Waterlines Report Series*(90).

Slomp, C. P., & Van Cappellen, P. (2004). Nutrient inputs to the coastal ocean through submarine groundwater discharge: controls and potential impact. *Journal of Hydrology, 295*(1-4), 64-86. doi:10.1016/j.jhydrol.2004.02.018

Small, C., & Nicholls, R. J. (2003). A global analysis of human settlement in coastal zones. *Journal of Coastal Research, 19*(3), 584-599. doi:http://www.jstor.org/stable/4299200

Smerdon, B. D., Smith, L. A., Harrington, G. A., Gardner, W. P., Delle Piane, C., & Sarout, J. (2014). Estimating the hydraulic properties of an aquitard from in situ pore pressure measurements. *Hydrogeology Journal, 22*(8), 1875-1887. doi:10.1007/s10040-014-1161-x

Smith, A., Massuel, S., & Pollock, D. (2012). *Geohydrology Of The Tamala Limestone Formation In The Perth Region: Origin And Role Of Secondary Porosity* (EP12568). Retrieved from Australia:

Smith, A., Massuel, S., Pollock, D., Fitzpatrick, A., Byrne, J., Johnstone, C., . . . Cahill, K. (2012). *Final Summary Report-Hydrological Controls On Mar In Perth's Coastal Aquifer* (EP125485). Retrieved from https://publications.csiro.au/rpr/pub?list=BRO&pid=csiro:EP125485

Smith, A. J., & Hick, W. P. (2001). *Hydrogeology and aquifer tidal propagation in Cockburn Sound, Western Australia* (procite:cd26e417-61cd-4a56-89b7-1ee9e32aab7a). Retrieved from

Smith, A. J., & Nield, S. P. (2003). Groundwater discharge from the superficial aquifer into Cockburn Sound Western Australia: estimation by inshore water balance. *Biogeochemistry, 66*(1-2), 125-144. doi:DOI 10.1023/B:BIOG.0000006152.27470.a9

Smith, D. G., & Jol, H. M. (1995). Ground Penetrating Radar: Antenna frequencies and maxiumum probable depths of penetration in quaternary sediments.

Smith, I. (2004). An assessment of recent trends in Australian rainfall. *Australian Meteorological Magazine, 53*(3), 163-173. Retrieved from <Go to ISI>://WOS:000225717400002

Snieder, R., & Trampert, J. (1999). Inverse problems in geophysics. In *Wavefield inversion* (pp. 119-190): Springer.

Sonenshein, R. S. (1995). Delineation of Saltwater Intrusion in the Biscayne Aquifer, Eastern Dade County, Florida. *WATER-RESOURCES INVESTIGATIONS REPORT 96-4285.* Retrieved from http://fl.water.usgs.gov/Miami/online_reports/wri964285/

Soueid Ahmed, A., Zhou, J., Jardani, A., Revil, A., & Dupont, J. P. (2015). Image-guided inversion in steady-state hydraulic tomography. *Advances in Water Resources, 82*, 83-97. doi:https://doi.org/10.1016/j.advwatres.2015.04.001

Spies, B. R. (1996). Electrical and electromagnetic borehole measurements: A review. *Surveys in Geophysics, 17*(4), 517-556. doi:Doi 10.1007/Bf01901643

Spiteri, C., Slomp, C. P., Charette, M. A., Tuncay, K., & Meile, C. (2008). Flow and nutrient dynamics in a subterranean estuary (Waquoit Bay, MA, USA): Field data and reactive transport modeling. *Geochimica et Cosmochimica Acta, 72*(14), 3398-3412. doi:https://doi.org/10.1016/j.gca.2008.04.027

Steklova, K., & Haber, E. (2017). Joint hydrogeophysical inversion: state estimation for seawater intrusion models in 3D. *Computational Geosciences, 21*(1), 75-94. doi:10.1007/s10596-016-9595-y

Stephens, D. B., & Knowlton, R. (1986). Soil-Water Movement and Recharge through Sand at a Semiarid Site in New-Mexico. *Water Resources Research, 22*(6), 881-889. doi:DOI 10.1029/WR022i006p00881

Stern, N., & Stern, N. H. (2007). *The economics of climate change: the Stern review*: cambridge University press.

Steyl, G., & Dennis, I. (2010). Review of coastal-area aquifers in Africa. *Hydrogeology Journal, 18*(1), 217-225. doi:10.1007/s10040-009-0545-9

Stocker, T. F., Qin, D., Plattner, G.-K., Tignor, M., Allen, S. K., Boschung, J., . . . Midgley, P. M. (2013). *Climate change 2013: The Physical Science Basis*. Retrieved from

Strack, K.-M., Hanstein, T., LeBrocq, K., Moss, D., Vozoff, K., & Wolfgram, P. (1989). Case histories of LOTEM surveys in hydrocarbon prospective area. *First break, 7*(12), 467-477.

Strack, K. M., Lueschen, E., & Koetz, A. W. (1990). Long-offset transient electromagnetic (LOTEM) depth soundings applied to crustal studies in the Black Forest and Swabian Alb, Federal Republic of Germany. *Geophysics, 55*(7), 834-842. doi:10.1190/1.1442897

Strack, O. (1976). A single-potential solution for regional interface problems in coastal aquifers. *Water Resources Research, 12*(6), 1165-1174. doi:doi:10.1029/WR012i006p01165

Streich, R. (2015). Controlled-Source Electromagnetic Approaches for Hydrocarbon Exploration and Monitoring on Land. *Surveys in Geophysics, 37*(1), 47-80. doi:10.1007/s10712-015-9336-0

Stringfield, V. T., & LeGrand, H. E. (1971). Effects of karst features on circulation of water in carbonate rocks in coastal areas. *Journal of Hydrology, 14*(2), 139-157. doi:https://doi.org/10.1016/0022-1694(71)90003-5

Strobach, E. (2013). Hydrogeophysical investigation of water recharge into the Gnangara Mound.

Strobach, E., Harris, B. D., Dupuis, C. J., Kepic, A., & Martin, M. W. (2010). Ground-Penetrating Radar For Delineation Of Hydraulically Significant Layers In The Unsaturated Zone Of The Gnangara Mound, Wa. *ASEG Extended Abstracts, 2010*(1), 1-4. doi:http://dx.doi.org/10.1071/ASEG2010ab237

Strobach, E., Harris, B. D., Dupuis, J. C., & Kepic, A. W. (2014). Time-lapse borehole radar for monitoring rainfall infiltration through podosol horizons in a sandy vadose zone. *Water Resources Research, 50*(3), 2140-2163. doi:10.1002/2013wr014331

Strout, J. M., & Tjelta, T. I. (2005). In situ pore pressures: What is their significance and how can they be reliably measured? *Marine and Petroleum Geology, 22*(1), 275-285. doi:https://doi.org/10.1016/j.marpetgeo.2004.10.024

Stummer, P., Maurer, H., Horstmeyer, H., & Green, A. G. (2002). Optimization of DC resistivity data acquisition: Real-time experimental design and a new multielectrode system. *IEEE Transactions on Geoscience and Remote Sensing, 40*(12), 2727-2735. doi:10.1109/Tgrs.2002.807015

Stuyfzand, P. J. (1992). *Behaviour of major and trace constituents in fresh and salt intrusion waters, in the western Netherlands.* Paper presented at the Study and modelling of salt water intrusion into aquifers. In: Proceedings of the 12th salt water intrusion meeting, Barcelona. CIHS-CIMNE, Barcelona.

Sudicky, E. A. (1986). A natural gradient experiment on solute transport in a sand aquifer: Spatial variability of hydraulic conductivity and its role in the dispersion process. *Water Resources Research, 22*(13), 2069-2082. doi:10.1029/WR022i013p02069

Sutter, E., & Ingham, M. (2017). Seasonal saline intrusion monitoring of a shallow coastal aquifer using time-lapse DC resistivity traversing. *Near Surface Geophysics, 15*(1), 59-73. doi:10.3997/1873-0604.2016039

Szalai, S., Koppan, A., Szokoli, K., & Szarka, L. (2013). Geoelectric imaging properties of traditional arrays and of the optimized Stummer configuration. *Near Surface Geophysics, 11*(1), 51-62. doi:10.3997/1873-0604.2012058

Szalai, S., Novak, A., & Szarka, L. (2009). Depth of Investigation and Vertical Resolution of Surface Geoelectric Arrays. *Journal of Environmental and Engineering Geophysics, 14*(1), 15-23. doi:Doi 10.2113/Jeeg14.1.15

Takam Takougang, E. M., Harris, B., Kepic, A., & Le, C. V. (2015). Cooperative Joint Inversion Of 3d Seismic And Magnetotelluric Data: With Application In A Mineral Province. *Geophysics, 80*(4), R175-R187. doi:https://doi.org/10.1190/GEO2014-0252.1

Talbot, C. J., Bennett, E. M., Cassell, K., Hanes, D. M., Minor, E. C., Paerl, H., . . . Xenopoulos, M. A. (2018). The impact of flooding on aquatic ecosystem services. *Biogeochemistry, 141*(3), 439-461. doi:10.1007/s10533-018-0449-7

Teijón Ávila, G., Tamoh, K., Soler Manuel, M. A., & Candela Lledó, L. (2009). Treated wastewater reuse for a seawater intrusion hydraulic barrier implementation in the Llobregat delta aquifer (Barcelona, Spain): first phase. *Options Méditerranéennes: série A: séminaires Méditerranéens*(88), 171-178.

Todd. (2006). *GROUNDWATER HYDROLOGY, 2ND ED*: Wiley.

Topp, G. C., Davis, J. L., & Annan, A. P. (1980). Electromagnetic Determination of Soil-Water Content - Measurements in Coaxial Transmission-Lines. *Water Resources Research, 16*(3), 574-582. doi:DOI 10.1029/WR016i003p00574

Tsourlos, P., Ogilvy, R., Papazachos, C., & Meldrum, P. (2011). Measurement and inversion schemes for single borehole-to-surface electrical resistivity tomography surveys. *Journal of Geophysics and Engineering, 8*(4), 487-497. doi:10.1088/1742-2132/8/4/001 %J Journal of Geophysics and Engineering

Tsourlos, P. I., Szymanski, J. E., & Tsokas, G. N. (1999). The effect of terrain topography on commonly used resistivity arrays. *Geophysics, 64*(5), 1357-1363. doi:Doi 10.1190/1.1444640

Tularam, G., & Krishna, M. (2009). LONG TERM CONSEQUENCES OF GROUNDWATER PUMPING IN AUSTRALIA: A REVIEW OF IMPACTS AROUND THE GLOBE. *Journal of Applied Sciences in Environmental Sanitation, 4*(2).

Tuong, T. P., Kam, S. P., Hoanh, C. T., Dung, L. C., Khiem, N. T., Barr, J., & Ben, D. C. (2003). Impact of seawater intrusion control on the environment, land use and household incomes in a coastal area. *Paddy and Water Environment, 1*(2), 65-73. doi:10.1007/s10333-003-0015-2

Turesson, A. (2006). Water content and porosity estimated from ground-penetrating radar and resistivity. *Journal of Applied Geophysics, 58*(2), 99-111. doi:10.1016/j.jappgeo.2005.04.004

Turner, I. L., & Acworth, R. I. J. J. o. C. R. (2004). Field measurements of beachface salinity structure using cross-borehole resistivity imaging. 753-760.

Tyler, R. H., Boyer, T. P., Minami, T., Zweng, M. M., Reagan, J. R. J. E., Planets, & Space. (2017). Electrical conductivity of the global ocean. *69*(1), 156.

Uhlemann, S., Wilkinson, P. B., Maurer, H., Wagner, F. M., Johnson, T. C., & Chambers, J. E. (2018). Optimized survey design for electrical resistivity tomography: combined optimization of measurement configuration and electrode placement. *Geophysical Journal International, 214*(1), 108-121. doi:10.1093/gji/ggy128

Uhlemann, S. S., Sorensen, J. P. R., House, A. R., Wilkinson, P. B., Roberts, C., Gooddy, D. C., . . . Chambers, J. E. (2016). Integrated time-lapse geoelectrical imaging of wetland hydrological processes. *Water Resources Research, 52*(3), 1607-1625. doi:10.1002/2015wr017932

UNESCO, I. J. U. T. P. M. S. (1981). Tenth report of the joint panel on oceanographic tables and standards. *36*, 15-19.

Unicef. (2015). Progress on Sanitation and Drinking-Water: 2015 Update and MDG Assessment. *World Health Organization: Geneva, Switzerland*.

Van Weert, F., van der Gun, J., & Reckman, J. (2009). *Global overview of saline groundwater occurrence and genesis* (GP 2009-1). Retrieved from International Groundwater Resources Assessment Centre: https://www.un-igrac.org/resource/global-overview-saline-groundwater-occurrence-and-genesis-0

Vandenbohede, A., Van Houtte, E., & Lebbe, L. (2009). Sustainable groundwater extraction in coastal areas: a Belgian example. *Environmental Geology, 57*(4), 735-747. doi:10.1007/s00254-008-1351-8

Verruijt, A. (1968). A Note On The Ghyben-Herzberg Formula. *Hydrological Sciences Journal, 13*(4), 43-46. doi:https://doi.org/10.1080/02626666809493624

Verwer, K., Eberli, G. P., & Weger, R. J. (2011). Effect of pore structure on electrical resistivity in carbonates. *AAPG bulletin, 95*(2), 175-190. doi:10.1306/06301010047

Vogel, C. R. (2002). *Computational Methods for Inverse Problems*: Society for Industrial and Applied Mathematics.

Volker, R. E., & Rushton, K. R. (1982). An assessment of the importance of some parameters for seawater intrusion in aquifers and a comparison of dispersive and sharp-interface modelling approaches. *Journal of Hydrology, 56*(3), 239-250. doi:http://dx.doi.org/10.1016/0022-1694(82)90015-4

Vorosmarty, C. J., Green, P., Salisbury, J., & Lammers, R. B. (2000). Global water resources: vulnerability from climate change and population growth. *Science, 289*(5477), 284-288. doi:10.1126/science.289.5477.284

W.H.O. (2011). Technical notes on drinking water, sanitation and hygiene in emergencies. *submitted from this web site: http://www. who. int/water_sanitation_health/publications/2011/tn9_how_much _water_en. pdf*.

Wagner, F. M. (2016). *New developments in electrical resistivity imaging with applications to geological CO_2 storage.*

Wagner, F. M., Bergmann, P., Rucker, C., Wiese, B., Labitzke, T., Schmidt-Hattenberger, C., & Maurer, H. (2015). Impact and mitigation of borehole related effects in permanent crosshole resistivity imaging: An example from the Ketzin CO2 storage site. *Journal of Applied Geophysics, 123*, 102-111. doi:10.1016/j.jappgeo.2015.10.005

Wagner, F. M., Günther, T., Schmidt-Hattenberger, C., & Maurer, H. (2015). Constructive optimization of electrode locations for target-focused resistivity monitoring. *Geophysics, 80*(2), E29-E40. doi:10.1190/geo2014-0214.1

Wagner, F. M., Möller, M., Schmidt-Hattenberger, C., Kempka, T., & Maurer, H. (2013). Monitoring freshwater salinization in analog transport models by time-lapse electrical resistivity tomography. *Journal of Applied Geophysics, 89*, 84-95. doi:https://doi.org/10.1016/j.jappgeo.2012.11.013

Walther, G.-R., Post, E., Convey, P., Menzel, A., Parmesan, C., Beebee, T. J. C., . . . Bairlein, F. (2002). Ecological responses to recent climate change. *Nature, 416*, 389. doi:10.1038/416389a

Walther, M., Graf, T., Kolditz, O., Liedl, R., & Post, V. (2017). How significant is the slope of the sea-side boundary for modelling seawater intrusion in coastal aquifers? *Journal of Hydrology, 551*, 648-659. doi:https://doi.org/10.1016/j.jhydrol.2017.02.031

Walton, N. R. G. (1989). Electrical Conductivity And Total Dissolved Solids—What Is Their Precise Relationship? *Desalination, 72*(3), 275-292.

Ward, S. H., & Society of Exploration Geophysicists. (1990). *Geotechnical And Environmental Geophysics* (Vol. 1): Society of Exploration Geophysicists Tulsa, Oklahoma.

Wassmann, R., Hien, N. X., Hoanh, C. T., & Tuong, T. P. (2004). Sea level rise affecting the Vietnamese Mekong Delta: Water elevation in the flood season and implications for rice production. *Climatic Change, 66*(1-2), 89-107. doi:DOI 10.1023/B:CLIM.0000043144.69736.b7

Water-Technology. (2016). Groundwater Replenishment System (GWRS), Orange County, California, United States of America. Retrieved from http://www.water-technology.net/projects/groundwaterreplenish/

Water Corporation. (2016a). Perth Seawater Desalination Plant. Retrieved from https://www.watercorporation.com.au/water-supply/our-water-sources/desalination/perth-seawater-desalination-plant

Water Corporation. (2016b). Southern Seawater Desalination Plant. Retrieved from https://www.watercorporation.com.au/water-supply/our-water-sources/desalination/southern-seawater-desalination-plant

Water Corporation. (2017). Our water sources. Retrieved from https://www.watercorporation.com.au/water-supply/our-water-sources?pid=res-wss-np-spw

Water Corporation. (2018). What is the Integrated Water Supply Scheme. Retrieved from https://www.watercorporation.com.au/home/faqs/water-supply-and-services/what-is-the-integrated-water-supply-scheme

Water Corporation. (2019). Groundwater Replenishment Scheme Stage 2 Expansion. Retrieved from https://www.watercorporation.com.au/water-supply/ongoing-works/groundwater-replenishment-scheme

Water, D. o. (2016). Perth Region Confined Aquifer Capacity (Prcac) Study. Retrieved from http://www.water.wa.gov.au/planning-for-the-future/finding-water/groundwater-investigations/perth-regional-confined-aquifer-capacity-project-prcac

Water Information Reporting database. (2019). Water Information Reporting Database. Retrieved from http://wir.water.wa.gov.au. from W.A Dept. of Water, W.A Dept. Regional Development http://wir.water.wa.gov.au

Waxman, M. H., & Smits, L. J. M. (1968). Electrical Conductivities in Oil-Bearing Shaly Sands. *Society of Petroleum Engineers Journal, 8*(02), 107-122. doi:10.2118/1863-A

Weisstein, E. W. (2017). Absolute Error. Retrieved from http://mathworld.wolfram.com/AbsoluteError.html

Wentworth, C. K. (1947). Factors In The Behavior Of Ground Water In A Ghyben-Herzberg System. doi:http://hdl.handle.net/10125/12855

Werner, A. D. (2010). A review of seawater intrusion and its management in Australia. *Hydrogeology Journal, 18*(1), 281-285. doi:10.1007/s10040-009-0465-8

Werner, A. D. (2017). On the classification of seawater intrusion. *Journal of Hydrology, 551*, 619-631. doi:10.1016/j.jhydrol.2016.12.012

Werner, A. D., Alcoe, D. W., Ordens, C. M., Hutson, J. L., Ward, J. D., & Simmons, C. T. (2011). Current Practice and Future Challenges in Coastal Aquifer Management: Flux-Based and Trigger-Level Approaches with Application to an Australian Case Study. *Water Resources Management, 25*(7), 1831-1853. doi:10.1007/s11269-011-9777-2

Werner, A. D., Bakker, M., Post, V. E. A., Vandenbohede, A., Lu, C. H., Ataie-Ashtiani, B., . . . Barry, D. A. (2013). Seawater intrusion processes, investigation and management: Recent advances and future challenges. *Advances in Water Resources, 51*, 3-26. doi:10.1016/j.advwatres.2012.03.004

Werner, A. D., & Simmons, C. T. (2009). Impact of sea-level rise on sea water intrusion in coastal aquifers. *Ground Water, 47*(2), 197-204. doi:10.1111/j.1745-6584.2008.00535.x

Wicks, C., & Herman, J. (1995). The Effect of Zones of High Porosity and Permeability on the Configuration of the Saline-Freshwater Mixing Zone. *Groundwater, 33*(5), 733-740. doi:doi:10.1111/j.1745-6584.1995.tb00019.x

Wilkinson, P. B., Loke, M. H., Meldrum, P. I., Chambers, J. E., Kuras, O., Gunn, D. A., & Ogilvy, R. D. (2012). Practical aspects of applied optimized survey design for electrical resistivity tomography. *Geophysical Journal International, 189*(1), 428-440. doi:10.1111/j.1365-246X.2012.05372.x

Wilkinson, P. B., Meldrum, P. I., Chambers, J. E., Kuras, O., & Ogilvy, R. D. (2006). Improved strategies for the automatic selection of optimized sets of electrical resistivity tomography measurement configurations. *Geophysical Journal International, 167*(3), 1119-1126. doi:10.1111/j.1365-246X.2006.03196.x

Willmott, C. J., & Matsuura, K. (2005). Advantages of the mean absolute error (MAE) over the root mean square error (RMSE) in assessing average model performance. *Climate Research, 30*(1), 79-82. doi:DOI 10.3354/cr030079

Willmott, C. J., Matsuura, K., & Robeson, S. M. (2009). Ambiguities inherent in sums-of-squares-based error statistics. *Atmospheric Environment, 43*(3), 749-752. doi:10.1016/j.atmosenv.2008.10.005

Wilson, S. R., Ingham, M., & McConchie, J. A. (2006). The applicability of earth resistivity methods for saline interface definition. *Journal of Hydrology, 316*(1-4), 301-312. doi:10.1016/j.jhydrol.2005.05.004

Winsauer, W. O., Shearin Jr, H., Masson, P., & Williams, M. (1952). Resistivity of brine-saturated sands in relation to pore geometry. *AAPG bulletin, 36*(2), 253-277.

Wirianto, M., Mulder, W., & Slob, E. (2010a). *Exploiting the Airwave for Land CSEM Reservoir Monitoring.* Paper presented at the 72nd EAGE Conference and Exhibition incorporating SPE EUROPEC 2010.

Wirianto, M., Mulder, W., & Slob, E. (2010b). A feasibility study of land CSEM reservoir monitoring in a complex 3-D model. *Geophysical Journal International, 181*(2), 741-755.

World Bank (Producer). (2015). Salinity Intrusion in a Changing Climate Scenario will Hit Coastal Bangladesh Hard. Retrieved from https://www.worldbank.org/en/news/feature/2015/02/17/salinity-intrusion-in-changing-climate-scenario-will-hit-coastal-bangladesh-hard

World Health Organisation. (2011). Guidelines for drinking-water quality, 4th Edition. *WHO chronicle, 38*, 104-108.

Worthington, P. F. (1993). The Uses and Abuses of the Archie Equations .1. The Formation Factor Porosity Relationship. *Journal of Applied Geophysics, 30*(3), 215-228. doi:Doi 10.1016/0926-9851(93)90028-W

Wright, D., Ziolkowski, A., & Hobbs, B. (2002). Hydrocarbon detection and monitoring with a multicomponent transient electromagnetic (MTEM) survey. *The Leading Edge, 21*(9), 852-864. doi:doi:10.1190/1.1508954

Wu, J. C., Xue, Y. Q., Liu, P. M., Wang, J. J., Jiang, Q. B., & Shi, H. W. (1993). Sea-Water Intrusion in the Coastal Area of Laizhou Bay, China .2. Sea-Water Intrusion Monitoring. *Ground Water, 31*(5), 740-745. doi:DOI 10.1111/j.1745-6584.1993.tb00845.x

Wunderlich, T., Fischer, P., Wilken, D., Hadler, H., Erkul, E., Mecking, R., . . . Rabbel, W. (2018). Constraining electric resistivity tomography by direct push electric conductivity logs and vibracores: An exemplary study of the Fiume Morto silted riverbed (Ostia Antica, western Italy). *83*(3), B87-B103. doi:10.1190/geo2016-0660.1

Xu, Z., Bassett, S. W., Hu, B., & Dyer, S. B. (2016). Long distance seawater intrusion through a karst conduit network in the Woodville Karst Plain, Florida. *Scientific Reports, 6*, 32235. doi:10.1038/srep32235

Xu, Z., Hu, B. X., Xu, Z., & Wu, X. (2019). Simulating seawater intrusion in a complex coastal karst aquifer using an improved variable-density flow and solute transport–conduit flow process model. *Hydrogeology Journal, 27*(4), 1277-1289. doi:10.1007/s10040-018-1903-2

Xu, Z., Hu, B. X., & Ye, M. (2018). Numerical modeling and sensitivity analysis of seawater intrusion in a dual-permeability coastal karst aquifer with conduit networks. *Hydrol. Earth Syst. Sci., 22*(1), 221-239. doi:10.5194/hess-22-221-2018

Yoshikawa, T., Murata, O., Furuya, K., & Eguchi, M. (2007). Short-term covariation of dissolved oxygen and phytoplankton photosynthesis in a coastal fish aquaculture site. *Estuarine, Coastal and Shelf Science, 74*(3), 515-527. doi:https://doi.org/10.1016/j.ecss.2007.05.004

Zhdanov, M. S. (2010). Electromagnetic geophysics: Notes from the past and the road ahead. *Geophysics, 75*(5), A49-A66. doi:10.1190/1.3483901

Zhou, J. (2015). *Structure-Constrained Image-Guided Inversion Of Geophysical Data.* (Thesis). Colorado School of Mines, Retrieved from http://hdl.handle.net/11124/17066

Zhou, J., Revil, A., Karaoulis, M., Hale, D., Doetsch, J., & Cuttler, S. (2014). Image-guided inversion of electrical resistivity data. *Geophysical Journal International, 197*(1), 292-309. doi:10.1093/gji/ggu001

Zhou, J. Y., Revil, A., & Jardani, A. (2016). Stochastic structure-constrained image-guided inversion of geophysical data. *Geophysics, 81*(2), E89-E101. doi:10.1190/Geo2014-0569.1

Zhou, W. F., Beck, B. F., & Adams, A. L. (2002). Effective electrode array in mapping karst hazards in electrical resistivity tomography. *Environmental Geology, 42*(8), 922-928. doi:10.1007/s00254-002-0594-z

Ziolkowski, A., Carson, R., & Wright, D. (2007). *New Technology To Acquire, Process, And Interpret Transient Em Data.* Paper presented at the Egm 2007 International Workshop.

Ziolkowski, A., Parr, R., Wright, D., Nockles, V., Limond, C., Morris, E., & Linfoot, J. (2010). Multi-Transient Electromagnetic Repeatability Experiment Over The North Sea Harding Field‡. *Geophysical Prospecting, 58*(6), 1159-1176.

Zonge, K. L. (1992). Introduction To Csamt. *Practical Geophysics II for the Exploration Geologist*, 439-523.